ASME
SETTING THE STANDARD

Transactions of the ASME, Journal of Applied Mechanics (ISSN 0021-8936) is published bimonthly (Jan., Mar., May, July, Sept., Nov.) by The American Society of Mechanical Engineers, Three Park Avenue, New York, NY 10016. Periodicals postage paid at New York, NY and additional mailing offices. POSTMASTER: Send address changes to Transactions of the ASME, Journal of Applied Mechanics, c/o THE AMERICAN SOCIETY OF MECHANICAL ENGINEERS, 22 Law Drive, Box 2300, Fairfield, NJ 07007-2300. **CHANGES OF ADDRESS** must be received at Society headquarters seven weeks before they are to be effective. Please send old label and new address. **STATEMENT from By-Laws.** The Society shall not be responsible for statements or opinions advanced in papers or printed in its publications (B7.1, Para. 3).

Journal of Applied Mechanics

Published Bimonthly by ASME

VOLUME 75 • NUMBER 1 • JANUARY 2008

RESEARCH PAPERS

(Contents continued on inside back cover)

This journal is printed on acid-free paper, which exceeds the ANSI Z39.48-1992 specification for permanence of paper and library materials. ♾™
♻ 85% recycled content, including 10% post-consumer fibers.

Journal of Applied Mechanics Volume 75, Number 1 JANUARY 2008

TECHNICAL BRIEFS

DESIGN INNOVATION

The ASME Journal of Applied Mechanics is abstracted and indexed in the following:

Alloys Index, Aluminum Industry Abstracts, Applied Science & Technology Index, Ceramic Abstracts, Chemical Abstracts, Civil Engineering Abstracts, Compendex (The electronic equivalent of Engineering Index), Computer & Information Systems Abstracts, Corrosion Abstracts, Current Contents, EEA (Earthquake Engineering Abstracts Database), Electronics & Communications Abstracts Journal, Engineered Materials Abstracts, Engineering Index, Environmental Engineering Abstracts, Environmental Science and Pollution Management, Fluidex, Fuel & Energy Abstracts, GeoRef, Geotechnical Abstracts, INSPEC, International Aerospace Abstracts, Journal of Ferrocement, Materials Science Citation Index, Mechanical Engineering Abstracts, METADEX (The electronic equivalent of Metals Abstracts and Alloys Index), Metals Abstracts, Nonferrous Metals Alert, Polymers Ceramics Composites Alert, Referativnyi Zhurnal, Science Citation Index, SciSearch (Electronic equivalent of Science Citation Index), Shock and Vibration Digest, Solid State and Superconductivity Abstracts, Steels Alert, Zentralblatt MATH

Gang-Feng Wang[1]
MOE Key Laboratory for Strength and Vibration,
Department of Engineering Mechanics,
Xi'an Jiaotong University,
Xi'an 710049, China
e-mail: wanggangfeng@tsinghua.org.cn

Xi-Qiao Feng
Department of Engineering Mechanics,
Tsinghua University,
Beijing 100084, China

Tie-Jun Wang
MOE Key Laboratory for Strength and Vibration,
Department of Engineering Mechanics,
Xi'an Jiaotong University,
Xi'an 710049, China

Wei Gao
Department of Engineering Mechanics,
Tsinghua University,
Beijing 100084, China

Surface Effects on the Near-Tip Stresses for Mode-I and Mode-III Cracks

Based on the surface elasticity theory and using a local asymptotic approach, we analyzed the influences of surface energy on the stress distributions near a blunt crack tip. The dependence relationship of the crack-tip stresses on surface elastic parameters is obtained for both mode-I and mode-III cracks. It is found that when the curvature radius of a crack front decreases to nanometers, surface energy significantly affects the stress intensities near the crack tip. Using a kind of surface elements, we also performed finite element simulations to examine the surface effects on the near-tip stresses. The obtained analytical solution agrees well with the numerical results. [DOI: 10.1115/1.2712233]

Keywords: crack, surface elasticity, stress, nanomechanics

1 Introduction

Analysis of deformations and stresses at crack tips is a fundamental issue for understanding the failure behavior of engineering materials and structures. At macroscopic scale, the crack front profile is usually considered to be infinitely sharp, and the corresponding elastic and elastic-plastic crack-tip fields have been well established in the classical fracture mechanics. In physical nature, however, most crack tips are not ideally sharp but blunt with a finite curvature radius, e.g., on the order of microns or nanometers. First, only when the spacing between the two surfaces of a crack is larger enough beyond some physical limits (e.g., the cut-off radius of Lennard-Jones potential), are the surfaces free from atomic interaction. Second, the atoms near a crack tip experience a local environment different from those in the bulk, and their tendency to minimize the system free energy may also cause blunting of the crack tip.

Atomic simulation is very powerful in pursuing the details of deformations and evolution processes at nanoscale, and has been employed to investigate fracture problems [1–4]. Through massively parallel atomistic simulations, Buehler and Gao [1] and Buehler et al. [2] reported the dynamical fracture instabilities due to local hyperelasticity at crack tips. Abraham et al. [4] developed a concurrent multiscale method spanning the continuum to quantum length scales to study brittle fracture problems.

Recently, continuum mechanics models of surface elasticity have also been adopted to explore the features of mechanical deformations at nanoscale by incorporating the effects of surface/interface energy [5–9]. The generic and mathematical formulation of surface elasticity theory was presented by Gurtin and Murdoch [10] and Gurtin et al. [11], in which a surface is regarded as a two-dimensional membrane adhered to the bulk without slipping. Experiments on some elementary deformation modes, such as uniaxial stretching of plates, bending of beams, and torsion of bars, showed that the predictions from the surface elasticity theory agrees well with the results from directly atomic simulations [5,6]. Therefore, the surface elasticity theory has been employed to elucidate many size-dependent phenomena at nanoscale, for examples, the deformation around a spherical nanoinhomogeneity [7], the effective modulus of elastic solid with nanocavities [12,13] and nanoinclusions [14,15]. In addition, based on the analysis for an elliptic void, Wu [16] addressed the effect of surface stress on the deformation of a crack, in which only the constant residual surface stress is considered.

Through the embedded atom method, Hoagland et al. [17] examined the deformation field near a crack tip. They found that the stresses calculated from atomic models are in a good agreement with the predictions of linear elastic fracture mechanics except in a small vicinity of the crack tip, where the effects of surface energy should be accounted for. Therefore, local analysis near a crack tip may capture the key features of surface effects on crack tip fields. Creager and Paris [18] and Smith [19] investigated the stress distributions near the tip of a blunt crack in the light of classical elastic theory. In the present paper, we will use Gurtin's surface elasticity theory to examine the surface effects on the deformations and stresses in the immediate vicinity of a blunt crack tip.

The paper is organized as follows. The basic equations of Gurtin's surface elasticity theory are reviewed briefly in Sec. 2. In Secs. 3 and 4, the stress distributions near the tips of mode-III and mode-I cracks are determined through a local approach. In Sec. 5, the obtained theoretical results are compared to our finite element simulations with surface effects.

2 Basic Equations of Surface Elasticity

In Gurtin's surface elasticity theory [11], a surface is regarded as an elastic but negligibly thin membrane, which is adhered to the underlying bulk material without slipping and has elastic constants different from the bulk. The surface stress tensor is a function of the surface strain tensor, which depends on the deformation of the bulk material. The equilibrium and constitutive equations in the bulk of the material are the same as those in the classical theory of elasticity, but the presence of surface stress gives rise to a nonclassical boundary condition. Only several basic equations of the surface elasticity theory are reviewed here. For its detailed mathematical formulation, the reader may refer to Gurtin and Murdoch [10] and Gurtin et al. [11].

[1]Corresponding author.

Contributed by the Applied Mechanics Division of ASME for publication in the JOURNAL OF APPLIED MECHANICS. Manuscript received May 10, 2006; final manuscript received October 23, 2006; published online December 27, 2007. Review conducted by Zhigang Suo.

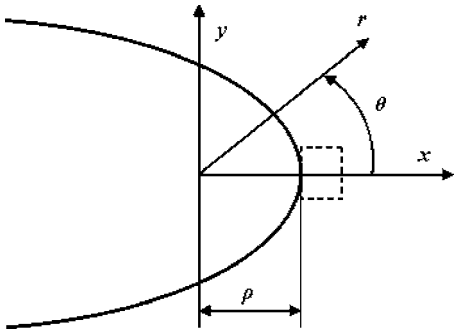

Fig. 1 A blunt crack with a finite curvature radius at its tip

In the absence of body forces, the equilibrium equations and the isotropic constitutive relations in the bulk read

$$\sigma_{ij,j} = 0 \tag{1}$$

$$\sigma_{ij} = 2G\varepsilon_{ij} + \lambda\varepsilon_{kk}\delta_{ij} \tag{2}$$

where G and λ are the Lame constants, σ_{ij} and ε_{ij} are the stress tensor and strain tensor in the bulk material, respectively. The strain tensor is related to the displacement vector u_i by

$$\varepsilon_{ij} = \tfrac{1}{2}(u_{i,j} + u_{j,i}) \tag{3}$$

Throughout the paper, Einstein's summation convention is adopted for all repeated Latin indices (1, 2, 3) and Greek indices (1, 2).

Assume that the surface adheres perfectly to the bulk material without slipping. The equilibrium conditions on the surface are obtained as

$$t_\alpha + \sigma^s_{\beta\alpha,\beta} = 0, \quad \sigma_{ij}n_i n_j = \sigma^s_{\alpha\beta}\kappa_{\alpha\beta} \tag{4}$$

where n_i denotes the outward normal vector to the surface, t_α is the negative of the tangential component of the traction $t_i = \sigma_{ij}n_j$ along the α_i direction of surface, $\kappa_{\alpha\beta}$ is the surface curvature tensor.

The surface stress tensor $\sigma^s_{\alpha\beta}$ is related to the surface energy density $\Gamma(\varepsilon_{\alpha\beta})$ by

$$\sigma^s_{\alpha\beta} = \tau^0\delta_{\alpha\beta} + \frac{\partial\Gamma}{\partial\varepsilon_{\alpha\beta}} \tag{5}$$

where $\delta_{\alpha\beta}$ is the Kronecker δ, $\varepsilon_{\alpha\beta}$ the second-rank tensor of surface strains, and τ^0 the residual surface tension under unstrained condition. For an isotropic surface, the surface stresses are given by

$$\sigma^s_{\alpha\beta} = \tau^0\delta_{\alpha\beta} + 2(\mu^s - \tau^0)\delta_{\alpha\gamma}\varepsilon_{\gamma\beta} + (\lambda^s + \tau^0)\varepsilon_{\gamma\gamma}\delta_{\alpha\beta} \tag{6}$$

where μ^s and λ^s are surface elastic constants.

3 Near-Tip Deformation for Mode-III Crack

Now we consider the deformation near a two-dimensional crack tip, which has an initially blunt shape of curvature radius ρ. Refer to a Cartesian coordinate system (x,y) and a polar coordinate system (r,θ), as shown in Fig. 1. The origin of the coordinate systems is located at the curvature center of the crack tip, and the z-axis is normal to the x-y plane.

For mode-III problems, the only nonvanishing displacement w along z-axis satisfies the Laplace's equation

$$\frac{\partial^2 w}{\partial x^2} + \frac{\partial^2 w}{\partial y^2} = 0 \tag{7}$$

The displacement w can be given by an analytical function $F(z)$ of $z = x + y\mathrm{i}$ as

$$Gw = \mathrm{Re}[F(z)] \tag{8}$$

and the stress components are expressed as

$$\sigma_{r3} - \mathrm{i}\sigma_{\theta 3} = \exp(\mathrm{i}\theta)\frac{\mathrm{d}F}{\mathrm{d}z} \tag{9}$$

As it has been found from atomic simulations [17], the influence of surface energy is localized near the crack tip. Therefore, we use a local analysis to focus on an immediate vicinity of the crack tip for $|z-\rho| \ll \rho$. Hereby, $F(z)$ can be expressed in power series of $(z-\rho)$ as

$$F(z) = a_0 + \mathrm{i}b_0 + (a_1 + \mathrm{i}b_1)(z-\rho) + (a_2 + \mathrm{i}b_2)(z-\rho)^2 + o\{(z-\rho)^2\} \tag{10}$$

where a_0, b_0, a_1, b_1, a_2, and b_2 are real constants. Then to the first order of $(z-\rho)$, the stresses are given from Eqs. (9) and (10) as

$$\begin{aligned}\sigma_{r3} &= a_1\cos\theta - b_1\sin\theta + 2r(a_2\cos 2\theta - b_2\sin 2\theta) - 2\rho(a_2\cos\theta \\ &\quad - b_2\sin\theta) \\ \sigma_{\theta 3} &= -(b_1\cos\theta + a_1\sin\theta) - 2r(b_2\cos 2\theta + a_2\sin 2\theta) \\ &\quad + 2\rho(b_2\cos\theta + a_2\sin\theta)\end{aligned} \tag{11}$$

The corresponding nonvanishing strain components are

$$\varepsilon_{r3} = \varepsilon_{3r} = \frac{\sigma_{r3}}{2G}, \quad \varepsilon_{\theta 3} = \varepsilon_{3\theta} = \frac{\sigma_{\theta 3}}{2G} \tag{12}$$

Then one obtains the surface stress components on the crack surface

$$\sigma^s_{3\theta} = \sigma^s_{\theta 3} = 2G^s\varepsilon_{3\theta}, \quad \sigma^s_{33} = \sigma^s_{\theta\theta} = \tau^0 \tag{13}$$

with $G^s = \mu^s - \tau^0$.

On the crack surface near the tip $(r=\rho)$, the surface boundary condition in Eq. (4) reduces to

$$\sigma_{r3} = -\frac{\partial\sigma^s_{\theta 3}}{r\partial\theta} \tag{14}$$

Substitution of Eqs. (11)–(13) into Eq. (14) leads to

$$\begin{aligned}&a_1\cos\theta - b_1\sin\theta + 2\rho(a_2\cos 2\theta - b_2\sin 2\theta) - 2\rho(a_2\cos\theta \\ &\quad - b_2\sin\theta) \\ &= -\frac{G^s}{G\rho}[b_1\sin\theta - a_1\cos\theta + 4\rho(b_2\sin 2\theta - a_2\cos 2\theta) \\ &\quad + 2\rho(a_2\cos\theta - b_2\sin\theta)]\end{aligned} \tag{15}$$

For a small value of θ near the crack tip, we expand Eq. (15) in terms of θ up to the square order; that is,

$$\begin{aligned}&a_1 - \theta(b_1 + 2\rho b_2) - \theta^2\left(\frac{a_1}{2} + 3\rho a_2\right) \\ &\quad = \frac{G^s}{G\rho}\left[2\rho a_2 + a_1 - \theta(b_1 + 6\rho b_2) - \theta^2\left(\frac{a_1}{2} + 7\rho a_2\right)\right]\end{aligned} \tag{16}$$

Comparing the factors of 1, θ and θ^2 at the two sides of Eq. (16) gives

$$a_1 = a_2 = 0, \quad b_2 = -\frac{b_1}{2\rho}\left(\frac{\rho G - G^s}{\rho G - 3G^s}\right) \tag{17}$$

Then the shear stress at the crack tip $(r=\rho,\ \theta=0)$ is obtained as

$$\sigma^p_{\theta 3} = \sigma_{\theta 3}(\rho, 0) = -b_1 \tag{18}$$

If no effect of surface elasticity is considered, Eq. (18) should reduce to the solution of classical linear elasticity. Therefore, the parameter b_1 can be determined from the linear elastic fracture mechanics. Since the surface constants do not appear in Eq. (18), surface energy does not affect the stresses at the tip of a mode-III crack.

However, at a distance t ahead of the crack tip ($r=\rho+t$, $\theta=0$), the shear stress is given by

$$\frac{\sigma_{\theta 3}}{\sigma_{\theta 3}^{p}} = 1 - \frac{t}{\rho}k \tag{19}$$

with $k=(\rho G-G^s)/(\rho G-3G^s)$.

Equation (19) clearly demonstrates that the stress depends not only on t, ρ, and $\sigma_{\theta 3}^{p}$ but also on the surface constant G^s. Its last term stands for the relative influence of surface elasticity on the stress. For metals, G^s/G is usually on the order of nanometers [5,7,12]. Therefore, it is only when the curvature radius ρ is of the order of nanometers that the effects of surface energy become significant. For a very blunt crack ($\rho \gg G^s/G$), $k \to 1$ and the result reduces to that of classical elasticity analysis [19]. For a very sharp crack ($\rho \ll G^s/G$ and $k \to 1/3$), however, the solution in Eq. (19) is different distinctly from that of classical elasticity.

4 Near-Tip Deformation for Mode-I Crack

Then we consider the deformation near the tip of a mode-I crack under plane-strain conditions. In this case, $\varepsilon_{\theta\theta}$ is the only nonzero surface strain on the crack surface, and the surface stress $\sigma_{\theta\theta}^{s}$ is given by

$$\sigma_{\theta\theta}^{s} = \tau^0 + E^s \varepsilon_{\theta\theta} \tag{20}$$

with $E^s=2\mu^s+\lambda^s-\tau^0$ being the surface elastic modulus.

On the crack surface near the tip, the surface boundary conditions in Eq. (4) are simplified as

$$\sigma_{rr} = \frac{\sigma_{\theta\theta}^{(s)}}{\rho}, \quad \sigma_{r\theta} = -\frac{\partial \sigma_{\theta\theta}^{(s)}}{\rho \partial \theta} \tag{21}$$

According to the complex variable formulation [20], the stresses in the bulk can be expressed by two analytic functions $\phi(z)$ and $\psi(z)$ of $z=x+iy$ as

$$\sigma_{rr}+\sigma_{\theta\theta} = 2[\phi(z)+\overline{\phi(z)}],$$

$$\sigma_{\theta\theta}-\sigma_{rr}+2i\sigma_{r\theta} = 2[\bar{z}\phi'(z)+\psi(z)]\exp(2i\theta) \tag{22}$$

Because of the special significance of the stress values at the crack tip for the initiation of fracture, we are concerned mainly with the surface elasticity effects on the stress strength in the immediate vicinity of the crack tip ($|z-\rho| \ll \rho$). The analytic functions $\phi(z)$ and $\psi(z)$ can be expressed in the form of power series as

$$\phi(z) = (a_0+ib_0)+(a_1+ib_1)(z-\rho)+(a_2+ib_2)(z-\rho)^2+o\{(z-\rho)^2\}$$

$$\psi(z) = (c_0+id_0)+(c_1+id_1)(z-\rho)+o\{(z-\rho)\} \tag{23}$$

where a_0, b_0, a_1, b_1, a_2, b_2, c_0, d_0, c_1, and d_1 are all real constants. Substituting Eq. (23) into (22) leads to the following expressions of stress components to the first order of $(z-\rho)$:

$$\sigma_{rr}+\sigma_{\theta\theta} = 2[2a_0+(a_1+ib_1)(z-\rho)+(a_1-ib_1)(\bar{z}-\rho)]$$

$$\sigma_{\theta\theta}-\sigma_{rr}+2i\sigma_{r\theta} = 2\exp(2i\theta)\{\bar{z}[a_1+ib_1+2(a_2+ib_2)(z-\rho)]+c_0+id_0+(c_1+id_1)(z-\rho)\} \tag{24}$$

On the crack surface $z=\rho\exp(i\theta)$, the stress components are expressed as

$$\sigma_{rr} = 2a_0-2\rho a_1+\rho a_1\cos\theta-\rho b_1\sin\theta-c_0\cos 2\theta+d_0\sin 2\theta-2\rho^2 a_2(\cos 2\theta-\cos\theta)+2\rho^2 b_2(\sin 2\theta-\sin\theta)-\rho c_1(\cos 3\theta-\cos 2\theta)+\rho d_1(\sin 3\theta-\sin 2\theta)$$

$$\sigma_{r\theta} = \rho a_1\sin\theta+\rho b_1\cos\theta+d_0\cos 2\theta+c_0\sin 2\theta+2\rho^2 a_2(\sin 2\theta-\sin\theta)+2\rho^2 b_2(\cos 2\theta-\cos\theta)+\rho d_1(\cos 3\theta-\cos 2\theta)+\rho c_1(\sin 3\theta-\sin 2\theta)$$

$$\sigma_{\theta\theta} = 2a_0+(3\cos\theta-2)\rho a_1-3\rho b_1\sin\theta+c_0\cos 2\theta-d_0\sin 2\theta+2\rho^2 a_2(\cos 2\theta-\cos\theta)-2\rho^2 b_2(\sin 2\theta-\sin\theta)+\rho c_1(\cos 3\theta-\cos 2\theta)-\rho d_1(\sin 3\theta-\sin 2\theta)$$

$$\sigma_{zz} = \nu(\sigma_{rr}+\sigma_{\theta\theta}) \tag{25}$$

For the considered plane-strain problem, the strain $\varepsilon_{\theta\theta}$ is given by

$$\varepsilon_{\theta\theta} = \frac{1}{2G}[(1-\nu)\sigma_{\theta\theta}-\nu\sigma_{rr}] \tag{26}$$

where ν is the Poisson's ratio.

From Eqs. (25), (26), and (20), one can obtain the surface stress $\sigma_{\theta\theta}^{s}$ on the crack surface. Analogously to the derivation in Sec. 3, we substitute the stresses and surface stress into the boundary conditions in Eq. (21), expand the relations in terms of θ up to the square order and compare the coefficients of 1, θ, and θ^2. Then the constants a_1, b_1, a_2, b_2, c_1, and d_1 are obtained in terms of a_0, b_0, c_0, and d_0 as

$$a_1 = \frac{2a_0-c_0-\tau^0/\rho-2a_0\eta+4\eta\nu a_0-\eta c_0}{(\eta+1)\rho}$$

$$b_1 = \frac{1+\eta}{3\eta-4\nu\eta-1}\left(\frac{d_0}{\rho}\right)$$

$$c_1 = \{4a_0-c_0+(32\nu^2 a_0-8\nu c_0+7c_0+12a_0-40\nu a_0)\eta^2+(6c_0-8\nu c_0-16a_0+24\nu a_0)\eta+(6\eta-8\eta\nu-2)\tau^0/\rho\}/\{(1+\eta)^2\rho\}$$

$$d_1 = \left(\frac{1-2\eta}{1-6\eta}\right)\left(\frac{3d_0}{\rho}\right)$$

$$a_2 = 3\{-2a_0+(1+4\eta\nu-3\eta)\tau^0/\rho-12\eta\nu a_0-4\eta c_0+8\eta a_0-6a_0+4\eta\nu c_0+(20\nu a_0-16\nu^2 a_0+4\nu c_0-4c_0-6a_0)\eta^2\}/\{2(1+\eta)^2\rho^2\}$$

$$b_2 = \left(\frac{4\eta-1}{1-6\eta}\right)\left(\frac{3d_0}{\rho^2}\right) \tag{27}$$

where the nondimensional parameter $\eta=E^s/(2G\rho)$ signifies the surface effects.

Then the stresses at the crack tip ($r=\rho$, $\theta=0$) are determined as

$$\sigma_{yy}^{p} = \sigma_{yy}^{0}\left(\frac{1+\eta\nu}{1+\eta}\right)-\frac{\tau^0}{(1+\eta)\rho}$$

$$\sigma_{xy}^{p} = \frac{4d_0\eta(\nu-1)}{1-3\eta+4\eta\nu}$$

$$\sigma_{xx}^{p} = \sigma_{yy}^{0}\frac{\eta(1-\nu)}{1+\eta}+\frac{\tau^0}{(1+\eta)\rho} \tag{28}$$

where $\sigma_{yy}^{0}=4a_0$ stands for the stress $\sigma_{yy}(\rho,0)$ at the crack tip without surface effects. It is seen from Eq. (28) that the surface energy significantly alters the near-tip stresses, which rely on the surface constants and the curvature radius of the crack tip.

Equation (28) should reduce to the solution of classical linear elastic fracture mechanics if the effect of surface elasticity is neglected (i.e., $\eta=0$ and $\tau^0=0$). Therefore, the parameters a_0 and d_0 can be determined from the well-known K-field solution of linear elasticity. From the solution for a blunt mode-I crack [18], it is obtained $\sigma_{yy}^{0}=4a_0=2K_I/\sqrt{\pi\rho}$ and $d_0=0$, where K_I is the stress intensity factor in the far field.

For $\eta=0$ and $\tau^0 \neq 0$, Eq. (28) reduces to $\sigma_{yy}^{p}/\sigma_{yy}^{0}=1-\tau^0/(\sigma_{yy}^{0}\rho)$. The contribution from surface energy is completely determined by the residual surface stress and the root radius. For a very blunt crack ($\rho \gg \tau^0/\sigma_{yy}^{0}$), $\sigma_{yy}^{p}/\sigma_{yy}^{0} \to 1$ and then the influ-

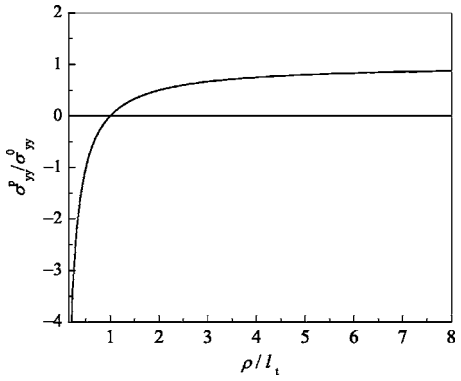

Fig. 2 Variation of $\sigma_{yy}^p/\sigma_{yy}^0$ with respect to the curvature radius for $\eta=0$

ence of surface energy is negligible. But for a very sharp crack ($\rho \sim \tau^0/\sigma_{yy}^0$), the contribution from surface energy should be taken into account. For a mode-I crack, the variation of $\sigma_{yy}^p/\sigma_{yy}^0$ with respect to the curvature radius of the crack tip is shown in Fig. 2, where $l_t=\tau^0/\sigma_{yy}^0$. The curvature radius not only affects the magnitude of stress, but changes its deformation state from stretching to compression. A positive residual surface stress in front of a mode-I crack may postpone its propagation and therefore enhances the fracture toughness of the material. But a negative residual surface stress will lower the fracture toughness of the material. These conclusions are in qualitative agreement with those in Wu [16], where the stress intensity factor is analyzed using the assumption of constant surface stress.

For $\tau^0=0$ and $\eta \neq 0$, Eq. (28) simplifies to $\sigma_{yy}^p/\sigma_{yy}^0=(1+\eta\nu)/(1+\eta)$. For metals, $l_s=E^s/(2G)$ is usually on the order of nanometers [5,7,12]. Therefore, it is seen from Eq. (28) and $\eta=l_s/\rho$ that only when the curvature radius at the crack tip reduces to nanometers do the surface effects become significant. For a very blunt crack ($\rho \gg l_s$), $\eta \to 0$ and $\sigma_{yy}^p/\sigma_{yy}^0 \to 1$, whereas for a very sharp crack ($\rho \ll l_s$), $\eta \to \infty$ and $\sigma_{yy}^p/\sigma_{yy}^0 \to \nu$. With the decrease in the crack root curvature radius, the stress ratio $\sigma_{yy}^p/\sigma_{yy}^0$ reduces continuously from 1 to ν, as shown in Fig. 3.

5 Finite Element Formulation of Surface Elasticity

To examine the accuracy of the analytical solution in Eq. (28), we also carried out finite element simulations to calculate the stress distributions near the crack tip. The surface element developed recently by Gao et al. [13] is used to account for the effects of surface elasticity.

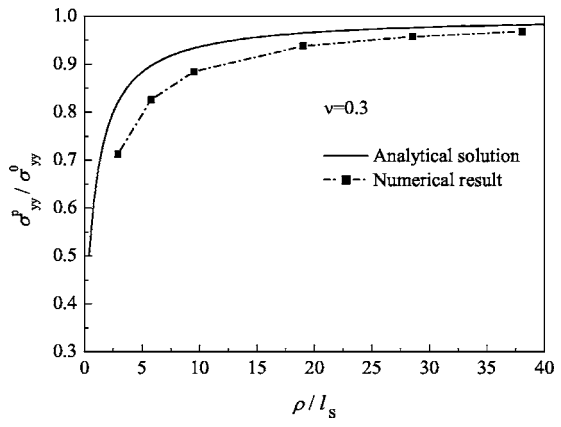

Fig. 3 Variation of $\sigma_{yy}^p/\sigma_{yy}^0$ with respect to the curvature radius for $\tau^0=0$

The total potential energy Π in the surface elasticity theory consists of three parts, the bulk elastic energy U^b, the surface elastic energy U^s, and the work of external force W, i.e.,

$$\prod = U^b + U^s - W \tag{29}$$

U^b and W can be calculated from the bulk elements as in the classical elasticity.

For elements on surfaces or interfaces, we incorporate the influence of surface energy. The surface energy for each surface element is given by [13]

$$U^s = \int_\Omega \int \{\sigma^s\}^T d\{\varepsilon^s\} d\Omega \tag{30}$$

where Ω is the area of surface element, $\{\sigma^s\}$ and $\{\varepsilon^s\}$ are the surface stress matrix and the surface strain matrix, respectively. Substituting Eq. (5) into Eq. (30), the surface energy is rewritten as

$$U^s = \frac{1}{2}\int_\Omega \{\varepsilon^s\}^T[S]\{\varepsilon^s\} d\Omega + \int_\Omega \{\varepsilon^s\}^T\{F\} d\Omega \tag{31}$$

where $[S]$ and $[F]$ stand for the surface elastic matrix and residual surface stress matrix, respectively. For a surface adhered perfectly to the bulk, the surface strains of a surface element can be determined by its adjacent bulk element via the relation

$$\{\varepsilon^s\} = [B^s]\{\delta_e\} \tag{32}$$

where $[B^s]$ is the strain-displacement matrix of the surface element, and $\{\delta_e\}$ the nodal displacement matrix of bulk element. Therefore, the surface energy can be expressed as

$$U^s = \tfrac{1}{2}\{\delta_e\}^T[K_e^s]\{\delta_e\} + \{\delta_e\}^T\{P_e^s\} \tag{33}$$

where $[K_e^s]$ and $\{P_e^s\}$ are the surface stiffness matrix and the surface residual stress matrix, respectively. They are defined as

$$[K_e^s] = \int_\Omega \{B^s\}^T[S]\{B^s\} d\Omega \tag{34}$$

$$\{P_e^s\} = \int_\Omega \{B^s\}^T\{F\} d\Omega \tag{35}$$

According to the principle of minimum potential energy, the relationships between the nodal displacements and the nodal forces read

$$\{[K_e] + [K_e^s]\}\{\delta_e\} = [P_e] - [P_e^s] \tag{36}$$

for surface elements, and

$$[K_e]\{\delta_e\} = [P_e] \tag{37}$$

for bulk elements, respectively, where $[K_e]$ is the stiffness matrix, and $[P_e]$ is the nodal force matrix of bulk elements.

The above finite element method is adopted here to investigate the deformation near a blunted crack tip with the effect of surface energy. In our calculations, the front tip of a semi-infinity crack is assumed to have the shape of a circular arc, and we take the following surface constants of aluminum [7]: $\lambda^s=6.842$ N/m, $\mu^s=-0.3755$ N/m, and $\tau^0=0$.

Our numerical simulations show that the stress distributions with surface elasticity effects have a good agreement with the predictions of linear elastic fracture mechanics except in a small vicinity of the crack tip, where the surface energy has a significant influence. Similar results were also obtained directly from atomic simulation [17]. The calculated circumferential stress σ_{yy}^p in Eq. (28) at the crack tip normalized by σ_{yy}^0 is plotted in Fig. 3 as a function of the root curvature radius ρ. It is seen that the analytical solution and the numerical result for the stresses at the crack tip

agree reasonably well. Therefore, the local analysis adopted in the present paper can capture the most prominent features of surface effects on the near-tip stresses and deformations.

6 Conclusions

In the present paper, we adopt an asymptotic method to investigate the effects of surface energy on the stresses near a crack tip with finite root radius. The analytical relations between the surface constants and the stresses at the crack tip are obtained. The results show that only when the curvature radius at the crack tip reduces to nanometers do the surface effects become significant. For mode-III cracks, surface energy does not affect the stresses at crack tips, while it does influence the stresses at a small distance ahead of the crack tip. For mode-I cracks, the surface energy evidently alters the stress magnitudes at the crack tips. The obtained analytical solution agrees reasonable well with the results of our finite element numerical simulations, in which the effects of surface energy have been incorporated. This study might be helpful for understanding some size-dependent fracture phenomena, especially for micro- or nanosized devices and systems.

Acknowledgment

The support from the National Natural Science Foundation of China (Grants No. 10602042, No. 10121202, and No. 10525210), the 973 project (Grant No. 2004CB619303), and the Program for NCET by the Ministry of Education of China are acknowledged.

References

[1] Buehler, M. J., and Gao, H. J., 2006, "Dynamical Fracture Instabilities Due to Local Hyperelasticity at Crack Tips," Nature (London), **439**, pp. 307–310.
[2] Buehler, M. J., Abraham, F. F., and Gao, H. J., 2003, "Hyperelasticity Governs Dynamic Fracture at a Critical Length Scale," Nature (London), **426**, pp. 141–146.
[3] Buehler, M. J., Gao, H. J., and Huang, Y. G., 2004, "Continuum and Atomistic Studies of the Near-Crack Field of a Rapidly Propagating Crack in a Harmonic Lattice," Theor. Appl. Fract. Mech., **41**, pp. 21–42.
[4] Abraham, F. F., Broughton, J. Q., Bernstein, N., and Kaxiras, E., 1998, "Spanning the Continuum to Quantum Length Scales in a Dynamic Simulation of Brittle Fracture," Europhys. Lett., **44**, pp. 783–787.
[5] Miller, R. E., and Shenoy, V. B., 2000, "Size-Dependent Elastic Properties of Nanosized Structural Elements," Nanotechnology, **11**, pp. 139–147.
[6] Shenoy, V. B., 2002, "Size-Dependent Rigidities of Nanosized Torsional Elements," Int. J. Solids Struct., **39**, pp. 4039–4052.
[7] Sharma, P., Ganti, S., and Bhate, N., 2003, "Effect of Surfaces on the Size-Dependent Elastic State of Nanoinhomogeneities," Appl. Phys. Lett., **82**, pp. 535–537.
[8] Cammarata, R. C., Sieradzki, K., and Spaepen, F., 2000, "Simple Model for Interface Stresses With Application to Misfit Dislocation Generation in Epitaxial Thin Films," J. Appl. Phys., **87**, pp. 1227–1234.
[9] Dingreville, R., Qu, J. M., and Cherkaoui, M., 2005, "Surface Free Energy and Its Effect on the Elastic Behavior of Nano-Sized Particles, Wires and Films," J. Mech. Phys. Solids, **53**, pp. 1827–1854.
[10] Gurtin, M. E., and Murdoch, A. I., 1975, "A Continuum Theory of Elastic Material Surfaces," Arch. Ration. Mech. Anal., **57**, pp. 291–323.
[11] Gurtin, M. E., Weissmuller, J., and Larche, F., 1998, "A General Theory of Curved Deformable Interfaces in Solids at Equilibrium," Philos. Mag. A, **78**, pp. 1093–1109.
[12] Yang, F. Q., 2004, "Size-Dependent Effective Modulus of Elastic Composite Materials: Spherical Nanocavities at Dilute Concentrations," J. Appl. Phys., **95**, pp. 3516–3520.
[13] Gao, W., Yu, S. W., and Huang, G. Y., 2006, "Finite Element Characterization of the Size-Dependent Mechanical Behaviour in Nanosystems," Nanotechnology, **17**, pp. 1118–1122.
[14] Sharma, P., and Ganti, S., 2004, "Size-Dependent Eshelby's Tensor for Embedded Nano-Inclusions Incorporating Surface/Interface Energies," ASME, ASME J. Appl. Mech., **71**, pp. 663–670.
[15] Duan, H. L., Wang, J., Huang, Z. P., and Karihaloo, B. L., 2005, "Size-Dependent Effective Elastic Constants of Solids Containing Nano-Inhomogeneities With Interface Stress," J. Mech. Phys. Solids, **53**, pp. 1574–1596.
[16] Wu, C. H., 1999, "The Effect of Surface Stress on the Configurational Equilibrium of Voids and Cracks," J. Mech. Phys. Solids, **47**, pp. 2469–2492.
[17] Horgland, R. G., Daw, M. S., and Hirth, J. P., 1991, "Some Aspects of Forces and Fields in Atomic Models of Crack Tips," J. Mater. Res., **6**, pp. 2565–2571.
[18] Creager, M., and Paris, P. C., 1967, "Elastic Field Equations for Blunt Cracks With Reference to Stress Corrosion Cracking," Int. J. Fract. Mech., **3**, pp. 247–252.
[19] Smith, E., 2004, "A Comparison of Mode I and Mode III Results for the Elastic Stress Distribution in the Immediate Vicinity of a Blunt Notch," Int. J. Eng. Sci., **42**, pp. 473–481.
[20] England, A. E., 1971, *Complex Variable Methods in Elasticity*, Wiley, New York.

Instability of a Hollow Elastic Cylinder Under Tension, Torsion, and Inflation

Leonid M. Zubov
Professor
Department of Mathematics,
Mechanics and Computer Science,
South Federal University,
Bolshaya Sadovaya, 105,
Rostov-on-Don, 344006, Russia
e-mail: zubovl@yandex.ru

Denis N. Sheidakov
Department of Mechanics and Mathematics
Problems,
South Scientific Center of the Russian Academy
of Science,
Chekhova, 41,
Rostov-on-Don, 344006, Russia
e-mail: sheidakov@donpac.ru

Background. Many papers on the elastic stability of both thin-walled and massive (three-dimensional) bodies regard the bifurcation of equilibrium in the case of compressive loads. Although, the elastic instability may also occur under tensile stresses. Method of Approach. In the present paper on the basis of three-dimensional equations of the nonlinear elasticity the instability of a stretched infinite hollow cylinder under torsion and inflation is investigated. The bifurcational method of stability analysis is used. Results. The critical surfaces and stability region in the space of loading parameters are defined for a Biderman material and special model of incompressible medium, which possess essential material nonlinearity. The influence of a wall thickness on the instability of a hollow cylinder is analyzed. Conclusions. Based on the obtained results, a simple and efficient practical criterion of stability under tension is formulated. This criterion can be represented in the form of the Drucker postulate, given in terms of external loads.
[DOI: 10.1115/1.2723824]

Keywords: nonlinear elasticity, stability of deformable bodies, criterion of stability

1 Introduction

The problem of equilibrium and motion stability for deformable bodies is of major importance both from theoretical and practical points of view. For the elastic medium the problem of equilibrium stability is extensively investigated for thin and thin-walled bodies in the form of rods, plates, and shells [1–6]. In the last decades the stability theory of three-dimensional elastic bodies has developed significantly. Different methods and approaches for the stability analysis of massive bodies as well as a solution of some instability problems, based on a three-dimensional elasticity, are presented in [7–16].

A common approach for the investigation of equilibrium stability in the elasticity theory is the bifurcational method. Within the framework of this method the stability analysis is reduced to the solution of a homogeneous boundary-value problem, linearized in the vicinity of a basic state, i.e., to the determination of eigenvalues (critical loads) and eigenfunctions (instability modes). The conservatism of external loads is the necessary condition for the correctness of the bifurcational method. In papers on the elastic stability of both thin-walled and massive (three-dimensional) bodies the bifurcation of equilibrium under compressive loads is considered most often. Though, the elastic instability may also occur under tensile stresses. Specifically, it is commonly known from the tension tests for rods that after reaching the local maximum of a load-extension curve, the process of a homogeneous deformation became unstable. The circular cylindrical form of a stretched sample changes into the axisymmetric mode of equilibrium, i.e., the neck is formed. The instability under tensile stresses has the following features in the comparison with the instability under compression:

(1) Most often the instability of stretched bodies occurs under large deformations, which demands the complete account of a geometrical and material nonlinearity in the equations of the elasticity theory.
(2) The instability under tensile loads is only possible for some models of nonlinearly elastic materials.

In Refs. [17–19] from the standpoint of three-dimensional elasticity the stability problem for an elastic rod under uniaxial tension has been investigated. The effect of torsion on the stability of a solid circular cylinder under tension has been analyzed in [20]. The instability of a stretched hollow cylinder that is inflated by an internal pressure has been studied in [21–23].

In the present paper on the basis of a three-dimensional nonlinear elasticity we consider the stability problem for a hollow circular infinite cylinder under three-parameter stress: the axial tension, torsion, and inflation. This problem is connected with the standard test types for materials in the experimental mechanics of deformable bodies.

2 The Prestressed State

The set of elastostatics equations for an isotropic incompressible solid [12,24–26] consists of the equilibrium equation

$$\operatorname{div} \mathbf{T} = 0 \tag{1}$$

and the constitutive relation

$$\mathbf{T} = \kappa_1(I_1,I_2)\mathbf{F} - \kappa_2(I_1,I_2)\mathbf{g} - p_1\mathbf{E}$$

$$\kappa_1(I_1,I_2) = 2\frac{\partial W}{\partial I_1} \quad \kappa_2(I_1,I_2) = 2\frac{\partial W}{\partial I_2}$$

$$\mathbf{F} = \sum_{m,n,s=1}^{3} \frac{\partial X_s}{\partial x_n}\frac{\partial X_m}{\partial x_n}\mathbf{i}_s\mathbf{i}_m \quad I_1 = \operatorname{tr}\mathbf{F} = \sum_{n,s=1}^{3} \frac{\partial X_s}{\partial x_n}\frac{\partial X_s}{\partial x_n}$$

$$I_2 = \frac{1}{2}(\operatorname{tr}^2\mathbf{F} - \operatorname{tr}\mathbf{F}^2) \tag{2}$$

In these formulas $\mathbf{T}$ is the Cauchy stress tensor, $\mathbf{F}$ is the Finger strain measure, $\mathbf{g}=\mathbf{F}^{-1}$ is the Almanci strain measure, I_1, I_2 are the first and second invariants of the tensor $\mathbf{F}$, $\mathbf{E}$ is the unit tensor, p_1 is the component of the stress in the incompressible solid, not defined by strains, $W(I_1, I_2)$ is the strain-energy function of an elastic body, x_n $(n=1,2,3)$ are Cartesian coordinates in the refer-

Contributed by the Applied Mechanics Division of ASME for publication in the JOURNAL OF APPLIED MECHANICS. Manuscript received February 23, 2006; final manuscript received February 4, 2007; published online December 27, 2007. Review conducted by Edmundo Corona.

ence configuration, X_s $(s=1,2,3)$ are Cartesian coordinates in the strained state, $\mathbf{i}_m$ $(m=1,2,3)$ are the basis vectors of the Cartesian coordinate system, div is the divergence operator in Eulerian coordinates, which can be rectangular (Cartesian) or curvilinear. In Cartesian coordinates the divergence operator has the following form div $\mathbf{T}=\mathbf{i}_k\cdot\partial\mathbf{T}/\partial X_k$. Symbol tr denotes the trace of a second-rank tensor.

We will use the cylindrical coordinate system. Consider the deformation of a torsion, tension, and inflation for a hollow circular cylinder [12,24] of incompressible material. It is given by the relations

$$R=\sqrt{\omega+\alpha^{-1}(r^2-r_1^2)}\quad \Phi=\varphi+\psi z\quad Z=\alpha z\quad \alpha,\psi,\omega=\text{const} \tag{3}$$

Here r,φ,z are cylindrical coordinates in the reference configuration of a body (Lagrangian coordinates), R,Φ,Z are cylindrical coordinates in the strained state (Eulerian coordinates), α is the stretching coefficient along the cylinder axis, ψ is the angle of twist per unit length, ω is the inner radius square of the deformed hollow cylinder, and r_1 is the inner radius of the hollow cylinder in the reference state.

The expressions for the Finger strain measure $\mathbf{F}$ and Almanci strain measure $\mathbf{g}$, corresponding to the deformation (3), have the following form:

$$\mathbf{F}=f_2(R)\mathbf{e}_R\mathbf{e}_R+f_1(R)f_2^{-1}(R)\mathbf{e}_\Phi\mathbf{e}_\Phi+\alpha\psi R(\mathbf{e}_\Phi\mathbf{e}_Z+\mathbf{e}_Z\mathbf{e}_\Phi)+\alpha^2\mathbf{e}_Z\mathbf{e}_Z$$

$$\mathbf{g}=f_2^{-1}(R)\mathbf{e}_R\mathbf{e}_R+\alpha^2 f_2(R)\mathbf{e}_\Phi\mathbf{e}_\Phi-\alpha\psi R f_2(R)(\mathbf{e}_\Phi\mathbf{e}_Z+\mathbf{e}_Z\mathbf{e}_\Phi)+f_1(R)\mathbf{e}_Z\mathbf{e}_Z \tag{4}$$

$$I_1=f_2(R)+f_1(R)f_2^{-1}(R)+\alpha^2\quad I_2=f_2^{-1}(R)+\alpha^2 f_2(R)+f_1(R)$$

$$f_1(R)=\alpha^{-2}(r_1^2\psi^2+\alpha\psi^2[R^2-\omega]+1)$$

$$f_2(R)=(\alpha R)^{-2}(r_1^2+\alpha[R^2-\omega])$$

$$\mathbf{e}_R=\mathbf{i}_1\cos\Phi+\mathbf{i}_2\sin\Phi\quad \mathbf{e}_\Phi=-\mathbf{i}_1\sin\Phi+\mathbf{i}_2\cos\Phi\quad \mathbf{e}_Z=\mathbf{i}_3 \tag{5}$$

where $\mathbf{e}_R,\mathbf{e}_\Phi,\mathbf{e}_Z$ is the orthonormal basis of the Eulerian cylindrical coordinates.

If outer lateral surface of the cylinder is free, then, taking Eqs. (1), (2), and (4) into account, the relation for the Cauchy stress tensor has the form

$$\mathbf{T}=\sigma_R(R)\mathbf{e}_R\mathbf{e}_R+\sigma_\Phi(R)\mathbf{e}_\Phi\mathbf{e}_\Phi+\tau_{\Phi Z}(R)(\mathbf{e}_\Phi\mathbf{e}_Z+\mathbf{e}_Z\mathbf{e}_\Phi)+\sigma_Z(R)\mathbf{e}_Z\mathbf{e}_Z$$

$$\sigma_R(R)=\int_R^{R_0}[(f_2(\rho)-f_1(\rho)f_2^{-1}(\rho))\kappa_1(\rho)+(\alpha^2 f_2(\rho)-f_2^{-1}(\rho))\kappa_2(\rho)]\frac{d\rho}{\rho}$$

$$\sigma_\Phi(R)=f_1(R)f_2^{-1}(R)\kappa_1(R)-\alpha^2 f_2(R)\kappa_2(R)-p_1(R)$$

$$\sigma_Z(R)=\alpha^2\kappa_1(R)-f_1(R)\kappa_2(R)-p_1(R)$$

$$\tau_{\Phi Z}(R)=\alpha\psi R[\kappa_1(R)+f_2(R)\kappa_2(R)]$$

$$p_1(R)=f_2(R)\kappa_1(R)-f_2^{-1}(R)\kappa_2(R)-\sigma_R(R)$$

$$R_0=\sqrt{\omega+\alpha^{-1}(r_0^2-r_1^2)} \tag{6}$$

Here r_0 and R_0 are the outer radii of the hollow cylinder before and after deformation, respectively.

The axial load K and torque M, acting at any cross section of the cylinder, and the internal pressure p, applied at the inner lateral surface, are the functions of the three loading parameters α,ψ,ω, defined by the formulas

$$K(\alpha,\psi,\omega)=2\pi\int_{R_1}^{R_0}\sigma_Z(R)RdR\quad M(\alpha,\psi,\omega)=2\pi\int_{R_1}^{R_0}\tau_{\Phi Z}(R)R^2dR$$

$$p(\alpha,\psi,\omega)=-\sigma_R(R_1)\quad R_1=\sqrt{\omega} \tag{7}$$

where R_1 is the deformed inner radius.

3 The Perturbed Equilibrium

We will consider a small perturbation of the prestressed equilibrium state, defined in the previous section. The linearized equilibrium equations for the incompressible solid, which describes the perturbed state, have the form [12,27,28]

$$\operatorname{div}\Theta=0\quad \Theta=\mathbf{T}^{\cdot}-(\operatorname{grad}\mathbf{u})^T\cdot\mathbf{T}\quad \mathbf{T}^{\cdot}=\left[\frac{d}{d\eta}\mathbf{T}(\mathbf{R}+\eta\mathbf{u})\right]_{\eta=0}$$

$$\operatorname{div}\mathbf{u}=0\quad \mathbf{u}=u_1\mathbf{e}_R+u_2\mathbf{e}_\Phi+u_3\mathbf{e}_Z$$

$$\operatorname{grad}\mathbf{u}=\mathbf{e}_R\frac{\partial\mathbf{u}}{\partial R}+\mathbf{e}_\Phi\frac{\partial\mathbf{u}}{R\partial\Phi}+\mathbf{e}_Z\frac{\partial\mathbf{u}}{\partial Z} \tag{8}$$

In these formulas Θ is the linearized Piola stress tensor, $\mathbf{R}$ is the radius-vector in the prestressed state, grad is the gradient operator, and $\mathbf{u}$ is the perturbance vector. The linearized boundary conditions at the lateral surfaces of the hollow cylinder

$$\mathbf{e}_R\cdot\Theta=p\mathbf{e}_R\cdot(\operatorname{grad}\mathbf{u})^T\ \text{for}\ R=R_1$$

$$\mathbf{e}_R\cdot\Theta=0\ \text{for}\ R=R_0 \tag{9}$$

express the fact that the internal pressure p is the tracking load and there are no loads at the outer surface in the perturbed state.

Taking Eq. (2) into account, the expression for the tensor Θ becomes [28]

$$\Theta=\kappa_1\mathbf{F}\cdot\operatorname{grad}\mathbf{u}+\kappa_2[(\operatorname{grad}\mathbf{u})\cdot\mathbf{g}+\mathbf{g}\cdot(\operatorname{grad}\mathbf{u})^T+(\operatorname{grad}\mathbf{u})^T\cdot\mathbf{g}]+p_1(\operatorname{grad}\mathbf{u})^T+\kappa_1^{\cdot}\mathbf{F}-\kappa_2^{\cdot}\mathbf{g}+q\mathbf{E}\quad q=-p_1^{\cdot}$$

$$\kappa_i^{\cdot}=2\kappa_{i1}\operatorname{tr}(\mathbf{F}\cdot\operatorname{grad}\mathbf{u})-2\kappa_{i2}\operatorname{tr}(\mathbf{g}\cdot\operatorname{grad}\mathbf{u})\quad \kappa_{ij}=\frac{d\kappa_i}{dI_j}\ i,j=1,2 \tag{10}$$

We will seek the perturbance vector components u_1,u_2,u_3 and linearized function of the hydrostatic pressure $q=-p_1^{\cdot}$ in the form

$$u_1=U_1(R)\cos(n\Phi+\lambda Z)\quad u_2=U_2(R)\sin(n\Phi+\lambda Z)$$

$$u_3=U_3(R)\sin(n\Phi+\lambda Z)\quad q=Q(R)\cos(n\Phi+\lambda Z)\ \lambda\geqslant 0$$

$$n=0,1,2,\ldots \tag{11}$$

where λ is a real number. This representation permits the separation of variables Φ,Z in the linearized equilibrium equations (8) and boundary conditions (9), and reduces the stability analysis to the solution of a linear homogeneous boundary-value problem for a set of ordinary differential equations.

Taking Eqs. (10) and (11) into account, the linearized equilibrium Eq. (8) can be written as follows (in these formulas the accent denotes a derivative with respect to R),

$$\left(p_1+f_2\kappa_1+3\frac{\kappa_2}{f_2}+2f_2^2\kappa_{11}-4\kappa_{12}+2\frac{\kappa_{22}}{f_2^2}\right)U_1''+\left(\frac{p_1}{R}+p_1'+\left[f_2'+\frac{f_2}{R}\right]\kappa_1+f_2\kappa_1'+3\left[\frac{1}{R}-\frac{f_2'}{f_2}\right]\frac{\kappa_2}{f_2}+3\frac{\kappa_2'}{f_2}+2f_2\left[2f_2'+\frac{f_2}{R}\right]\kappa_{11}+2f_2^2\kappa_{11}'-4\frac{\kappa_{12}}{R}-4\kappa_{12}'+2\left[\frac{1}{R}-2\frac{f_2'}{f_2}\right]\frac{\kappa_{22}}{f_2^2}+2\frac{\kappa_{22}'}{f_2^2}\right)U_1'+\left(-\left[\frac{nf_3}{R}+\alpha\lambda\gamma+\frac{f_1}{R^2f_2}\right]\kappa_1-\left[\lambda^2+\frac{n^2}{R^2}\right.\right.$$

$$+3\frac{\alpha^2 f_2^2}{R^2}\Big]\frac{\kappa_2}{f_2}-\frac{p_1}{R^2}+\frac{2}{R}\Big[f_1'-\frac{f_1^2}{Rf_2^2}\Big]\kappa_{11}+2\frac{f_1\kappa_{11}'}{R}+\frac{4}{R}\Big[\frac{f_1f_2'}{f_2^3}$$
$$-\frac{f_1'}{2f_2^2}+\frac{\alpha^2 f_1}{R}-\alpha^2 f_2 f_2'\Big]\kappa_{12}-\frac{2}{R}\Big[\alpha^2 f_2^2+\frac{f_1}{f_2^2}\Big]\kappa_{12}'$$
$$-2\frac{\alpha^4 f_2^2\kappa_{22}}{R^2}+2\frac{\alpha^2\kappa_{22}'}{R}\Big)U_1+\Big(\frac{np_1}{R}+\Big[f_4+\frac{n}{Rf_2^2}\Big]f_2\kappa_2$$
$$+2f_2f_3\kappa_{11}-2f_2^2\Big[f_4+\frac{f_3}{f_2^3}\Big]\kappa_{12}+2f_4\kappa_{22}\Big)U_2'+2\Big(-\frac{np_1}{2R^2}$$
$$-\frac{f_3\kappa_1}{R}-\Big[f_4+\frac{n}{Rf_2^2}+2\frac{\alpha^2 n}{R}\Big]\frac{f_2\kappa_2}{2R}+f_3\Big[\frac{f_2}{R}+f_2'+\frac{f_2f_3'}{f_3}$$
$$-\frac{f_1}{Rf_2}\Big]\kappa_{11}+f_2f_3\kappa_{11}'-\alpha f_2^2\Big[\frac{\alpha f_4}{R}+\frac{2\lambda\psi}{f_2^2}\Big]\kappa_{22}+f_4\kappa_{22}'$$
$$+\Big[\frac{f_1f_4}{R}-2f_2f_4f_2'+2\alpha\lambda\psi f_2^2-\frac{f_3}{Rf_2}-\frac{f_3'}{f_2}+\frac{\alpha^2 f_2f_3}{R}$$
$$+\frac{f_3f_2'}{f_2^2}\Big]\kappa_{12}-f_2^2\Big[f_4+\frac{f_3}{f_2^3}\Big]\kappa_{12}'\Big)U_2+\Big(\lambda p_1+\Big[\frac{\lambda}{f_2}+f_2f_5\Big]\kappa_2$$
$$+2\gamma\alpha f_2\kappa_{11}-2f_2^2\Big[f_5+\frac{\gamma\alpha}{f_2^3}\Big]\kappa_{12}+2f_5\kappa_{22}\Big)U_3'+2\Big(\frac{\alpha\psi m f_2\kappa_2}{R}$$
$$+\alpha\gamma\Big[\frac{f_2}{R}-\frac{f_1}{Rf_2}+f_2'\Big]\kappa_{11}+\alpha\gamma f_2\kappa_{11}'+\Big[\frac{\gamma\alpha^3 f_2}{R}-\frac{\gamma\alpha}{Rf_2}$$
$$+2\alpha\psi m f_2f_2'+\frac{\gamma\alpha f_2'}{f_2^2}+(f_1-f_2^2)\frac{f_5}{R}-\lambda f_2f_1'-\lambda f_1f_2'\Big]\kappa_{12}$$
$$-[f_2^2f_5+\gamma\alpha]\kappa_{12}'+\Big[(1-\alpha^2 f_2^2)\frac{f_5}{R}+f_5'\Big]\kappa_{22}+f_5\kappa_{22}'\Big)U_3$$
$$+Q'=0$$

$$\Big(-\frac{np_1}{R}-f_2\Big[f_4+\frac{n}{Rf_2^2}\Big]\kappa_2-2f_2f_3\kappa_{11}+2\Big[f_2^2f_4+\frac{f_3}{f_2}\Big]\kappa_{12}$$
$$-2f_4\kappa_{22}\Big)U_1'+\Big(-\frac{np_1}{R^2}-\frac{np_1'}{R}-\frac{2f_3\kappa_1}{R}-\Big[\frac{3f_2f_4}{R}+f_2'f_4+\frac{n}{R^2f_2}$$
$$-\frac{f_2'n}{Rf_2^2}\Big]\kappa_2-\Big[f_2f_4+\frac{n}{Rf_2}\Big]\kappa_2'-\frac{2f_1f_3\kappa_{11}}{Rf_2}+\frac{2}{R}[\alpha^2 f_2f_3$$
$$+f_1f_4]\kappa_{12}-\frac{2\alpha^2 f_2^2f_4\kappa_{22}}{R}\Big)U_1+f_2(\kappa_1+\alpha^2\kappa_2)U_2''+f_2\Big(\Big[\frac{f_2'}{f_2}$$
$$+\frac{1}{R}\Big][\kappa_1+\alpha^2\kappa_2]+\kappa_1'+\alpha^2\kappa_2'\Big)U_2'+\Big(-\frac{n^2p_1}{R^2}-\frac{p_1'}{R}-\Big[\frac{nf_3}{R}$$
$$+\alpha\lambda\gamma+\frac{f_1}{R^2f_2}\Big]\kappa_1-\Big[\frac{\alpha^2f_2'}{R}+\frac{1}{R^2f_2}-\frac{f_2'}{Rf_2^2}+\frac{3nf_2f_4}{R}$$
$$+\alpha\lambda\gamma f_2\Big]\kappa_2-[1+\alpha^2f_2^2]\frac{\kappa_2'}{Rf_2}-2f_3^2\kappa_{11}+4f_2f_3f_4\kappa_{12}$$
$$-2f_2^2f_4^2\kappa_{22}\Big)U_2-\alpha\psi Rf_2\kappa_2U_3''-\alpha\psi([Rf_2'+3f_2]\kappa_2+Rf_2\kappa_2')U_3'$$
$$+\Big(-\frac{\lambda np_1}{R}+f_2\Big[\frac{n\alpha\gamma}{R}-\frac{nf_5}{R}-2\lambda f_4\Big]\kappa_2-2\alpha\gamma f_3\kappa_{11}$$
$$-2f_2^2f_4f_5\kappa_{22}+2f_2[f_3f_5+\alpha\gamma f_4]\kappa_{12}\Big)U_3-\frac{n}{R}Q=0$$

$$\Big(-\lambda p_1-\Big[f_2f_5+\frac{\lambda}{f_2}\Big]\kappa_2-2\alpha\gamma f_2\kappa_{11}+2\Big[f_2^2f_5+\frac{\alpha\gamma}{f_2}\Big]\kappa_{12}$$
$$-2f_5\kappa_{22}\Big)U_1'+\Big(-\frac{\lambda p_1}{R}-\lambda p_1'+\Big[\frac{\lambda f_2'}{f_2^2}-\lambda f_1'-\frac{\lambda}{Rf_2}-\frac{f_2f_5}{R}$$
$$+\alpha\psi m\Big[f_2'+\frac{2f_2}{R}\Big]\Big]\kappa_2-\Big[f_2f_5+\frac{\lambda}{f_2}\Big]\kappa_2'-\frac{2\alpha\gamma f_1\kappa_{11}}{Rf_2}$$
$$+\frac{2}{R}[\alpha^3\gamma f_2+f_1f_5]\kappa_{12}-\frac{2\alpha^2f_2^2f_5\kappa_{22}}{R}\Big)U_1-\alpha\psi Rf_2\kappa_2U_2''$$
$$-\alpha\psi([f_2+Rf_2']\kappa_2+Rf_2\kappa_2')U_2'+\Big(-\frac{\lambda np_1}{R}+f_2\Big[\alpha\psi\Big[\frac{1}{R}+\frac{f_2'}{f_2}\Big]$$
$$+\lambda f_3-\lambda f_4-\frac{2nf_5}{R}\Big]\kappa_2+\alpha\psi f_2\kappa_2'-2\alpha\gamma f_3\kappa_{11}+2f_2[f_3f_5$$
$$+\alpha\gamma f_4]\kappa_{12}-2f_2^2f_4f_5\kappa_{22}\Big)U_2+(f_2\kappa_1+f_1\kappa_2)U_3''+\Big(\Big[f_2'$$
$$+\frac{f_2}{R}\Big]\kappa_1+\Big[f_1'+\frac{f_1}{R}\Big]\kappa_2+f_2\kappa_1'+f_1\kappa_2'\Big)U_3'+\Big(-\lambda^2p_1-\Big(\frac{nf_3}{R}$$
$$+\alpha\lambda\gamma\Big)\kappa_1-f_2\Big(\frac{nf_3}{R}+3\lambda f_5\Big)\kappa_2-2\alpha^2\gamma^2\kappa_{11}+4\alpha\gamma f_2f_5\kappa_{12}$$
$$-2f_2^2f_5^2\kappa_{22}\Big)U_3-\lambda Q=0$$

$$U_1'+\frac{1}{R}U_1+\frac{n}{R}U_2+\lambda U_3=0$$

$$\gamma=\psi m+\alpha\lambda\quad f_3=\frac{nf_1}{Rf_2}+\alpha\psi R\lambda\quad f_4=\frac{\alpha^2 n}{R}-\alpha\psi R\lambda$$

$$f_5=\frac{\lambda f_1}{f_2}-\alpha\psi m \tag{12}$$

The boundary conditions (9) on the lateral surfaces will take the form

$$\Big(\frac{p_1-p}{2}+\frac{f_2\kappa_1}{2}+\frac{3\kappa_2}{2f_2}+f_2^2\kappa_{11}-2\kappa_{12}+\frac{\kappa_{22}}{f_2^2}\Big)U_1'+\Big(f_1\kappa_{11}$$
$$-\frac{f_1+\alpha^2f_2^4}{f_2^2}\kappa_{12}+\alpha^2\kappa_{22}\Big)\frac{U_1}{R}+\Big(f_2f_3\kappa_{11}-\frac{f_3+f_2^3f_4}{f_2}\kappa_{12}$$
$$+f_4\kappa_{22}\Big)U_2+\Big(f_2\alpha\gamma\kappa_{11}-\frac{\alpha\gamma+f_2^3f_5}{f_2}\kappa_{12}+f_5\kappa_{22}\Big)U_3+\frac{Q}{2}=0$$

$$\Big(\lambda[p_1+p]+\frac{\lambda+f_2^2f_5}{f_2}\kappa_2\Big)U_1+\alpha\psi Rf_2\kappa_2U_2'-\alpha\psi f_2\kappa_2U_2$$
$$-(f_2\kappa_1+f_1\kappa_2)U_3'=0$$

$$\Big(\frac{p_1+p}{R}n+\Big[\frac{n}{R}+f_2^2f_4\Big]\frac{\kappa_2}{f_2}\Big)U_1-f_2(\kappa_1+\alpha^2\kappa_2)U_2'+\Big(p_1+p$$
$$+\frac{1+\alpha^2f_2^2}{f_2}\kappa_2\Big)\frac{U_2}{R}+\alpha\psi Rf_2\kappa_2U_3'=0\quad\text{at } R=R_1 \tag{13}$$

$$\left(\frac{p_1}{2}+\frac{f_2\kappa_1}{2}+\frac{3\kappa_2}{2f_2}+f_2^2\kappa_{11}-2\kappa_{12}+\frac{\kappa_{22}}{f_2^2}\right)U_1'+\left(f_1\kappa_{11}-\frac{f_1+\alpha^2 f_2^4}{f_2^2}\kappa_{12}+\alpha^2\kappa_{22}\right)\frac{U_1}{R}+\left(f_2f_3\kappa_{11}-\frac{f_3+f_2^3f_4}{f_2}\kappa_{12}+f_4\kappa_{22}\right)U_2+\left(f_2\alpha\gamma\kappa_{11}-\frac{\alpha\gamma+f_2^3f_5}{f_2}\kappa_{12}+f_5\kappa_{22}\right)U_3+\frac{Q}{2}=0$$

$$\left(\lambda p_1+\frac{\lambda+f_2^2f_5}{f_2}\kappa_2\right)U_1+\alpha\psi Rf_2\kappa_2U_2'-\alpha\psi f_2\kappa_2U_2-(f_2\kappa_1+f_1\kappa_2)U_3'=0$$

$$\left(\frac{np_1}{R}+\left[\frac{n}{R}+f_2^2f_4\right]\frac{\kappa_2}{f_2}\right)U_1-f_2(\kappa_1+\alpha^2\kappa_2)U_2'+\left(p_1+\frac{1+\alpha^2f_2^2}{f_2}\kappa_2\right)\frac{U_2}{R}+\alpha\psi Rf_2\kappa_2U_3'=0 \quad \text{at } R=R_0 \qquad (14)$$

4 The Numerical Results

We have carried out the stability analysis of an infinite hollow cylinder under torsion, tension, and inflation for two models of incompressible material. The strain energy for a Biderman material [26,29,30] is given by the relation

$$W(I_1,I_2)=d_0(I_2-3)+d_1(I_1-3)+d_2(I_1-3)^2+d_3(I_1-3)^3$$

$$d_0\geqslant 0 \quad d_1\geqslant 0 \quad d_3\geqslant 0 \quad d_1+d_3\geqslant 0 \quad 3d_2+\sqrt{15d_1d_3}\geqslant 0 \qquad (15)$$

A power-law material [31,32] has the strain energy in the form

$$W(I_1,I_2)=d(I_1-3)^\beta \; d>0 \; \beta\geqslant 1/2 \qquad (16)$$

All numerical results, presented in this paper, are obtained for the next set of material constants: for a Biderman material $d_0=0$, $d_1=27$, $d_2=-60$, $d_3=80$, and for a power-law material $d=1$, $\beta=0.51$. For the given values of coefficients Hadamard's condition [12,30] is satisfied for both materials.

To obtain conditions under which the boundary-value problem (12)–(14) has a nonzero solution, we have used the numerical method, suggested previously [28]. This method is based on a finite-difference approximation for the set of ordinary differential equations. Its efficiency has been tested on the stability problem for a stretched infinite hollow cylinder with respect to small axisymmetric perturbations (the pure necking instability). An explicit bifurcation criterion for this problem can be derived from Eqs. (12)–(14), if one considers $\psi=0$, $n=0$, $p=0$ ($R=r/\sqrt{\alpha}$). We have compared the stability analysis results, obtained using this explicit criterion and suggested numerical method. The disarrangement has been less than 0.05%.

By means of the approximate solution of the linear homogeneous boundary-value problem (12)–(14), we construct the stability region in the space of the loading parameters α,ψ,ω. This procedure is described below. According to Eq. (11), the instability mode for an infinite hollow cylinder under torsion, tension, and inflation is characterized by two non-negative parameters: the integral parameter n and the real parameter λ. For the sufficiently great number of the instability modes, which corresponds to the values of n and λ in the zero to several hundreds range, we obtain the critical relations between the loading parameters α,ψ,ω. Using these relations, the critical surfaces in the space of the parameters α,ψ,ω are constructed. By analyzing obtained results, we draw certain conclusions about these surface behaviors with further increase in n and λ. This allows us to construct the bifurcational stability region in the space of the loading parameters α,ψ,ω, i.e., the region in which the boundary-value problem (12)–(14) has only zero solution. The boundary of this region consists of the critical surfaces segments. The selection of these segments is dictated by the arrangement of the whole set of critical surfaces and fulfilled substantially by sight, as shown in the graphs below.

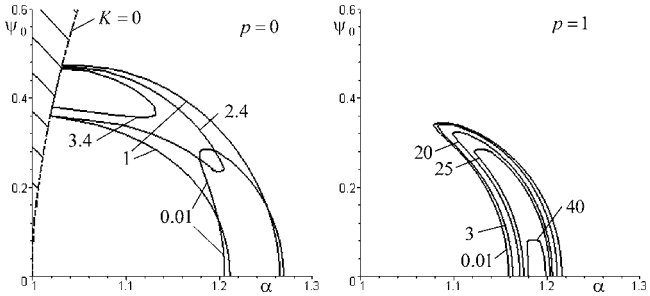

Fig. 1 Sections of the critical surfaces for the Biderman material in the case of axisymmetric instability

Using the expression for the internal pressure (7), we map the results, obtained in the space of the loading parameters α,ψ,ω, into the space of the parameters α,ψ,p. The main reason for this is that from the practical point of view the internal pressure is a more suitable parameter of inflation, because generally it is quite difficult to control the deformed inner radius of the tube (in contrast to the pressure) during experiments. But the use of the internal pressure as a parameter has one major limitation. Namely, for both considered material models the function $p(R_1)$ shows a local maximum (followed by a local minimum for a Biderman material), i.e., the pressure p is not a single-valued function of the deformed inner radius R_1 ($\omega=R_1^2$). For this reason we will only consider the radius R_1 before the local maximum of the function $p(R_1)$. We choose not to consider the radius after the local maximum, because it is difficult to realize the descending branch of the pressure curve $p(R_1)$ during actual experiments.

We have analyzed the cylinder instability for the case of a tensile axial load only. The curve which is noted $K=0$ in the graphs below corresponds to the case of a zero axial load. The area located to the left of this curve (in the graphs this area is hatched) corresponds to the case of a compressive axial load, which is of no interest in this paper.

Let $\chi=h/r_0$, where $h=r_0-r_1$ is a wall thickness of the hollow cylinder in the reference state. For all graphs presented in this paper $\chi=0.1$, $\psi_0=\psi r_0$. In Figs. 1 and 2 some results for the case of axisymmetric instability ($n=0$) are presented. In these graphs we have plotted sections of the critical surfaces by the planes $p=$const. All curves are symmetric about axis α and on each curve the corresponding value of the parameter λ is noted. For $\lambda=0$ the boundary-value problem (12)–(14) have only trivial solutions for both materials. The critical surfaces for the power-law material, which corresponds to the values of $\lambda<0.01$, are almost undistinguishable from the critical surface, corresponding to $\lambda=0.01$. Ac-

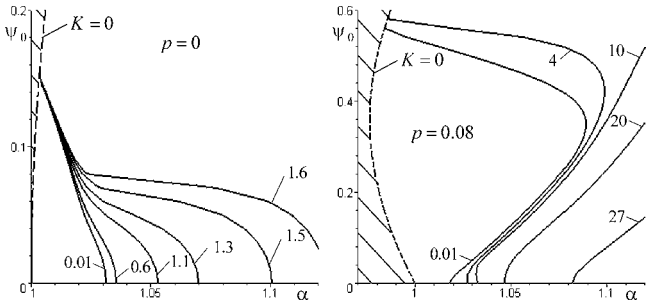

Fig. 2 Sections of the critical surfaces for the power-law material in the case of axisymmetric instability

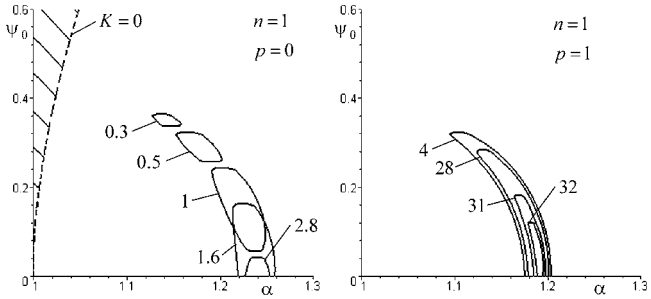

Fig. 3 Sections of the critical surfaces for the Biderman material in the case of asymmetric instability

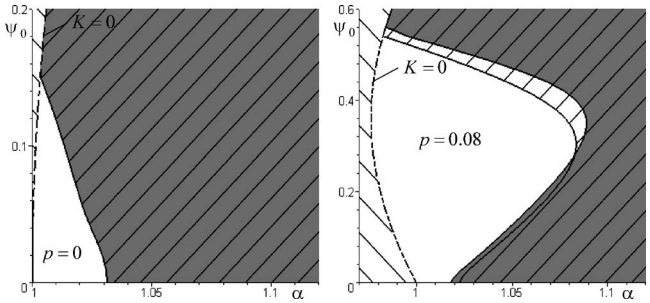

Fig. 5 Sections of the stability region for the power-law material

cording to the obtained results, the first instability mode can correspond to the different values of the parameter λ for the different load paths. For example, in the case of the uniaxial tension ($\psi_0=0$, $p=0$) the first instability mode for both materials corresponds to the arbitrarily small positive λ. But for a Biderman material in the case of the sufficiently strong twisting ($\psi_0 > 0.3, p=0$) there is no cylinder instability for $\lambda \leqslant 0.01$ (Fig. 1), and the first instability mode corresponds to $\lambda > 0.01$. Thus, the stability region boundary does not coincide with any critical surface, obtained for some value of the parameter λ.

Sections of the critical surfaces for the case of asymmetric instability ($n>0$) are plotted in Fig. 3.

According to the stability analysis, the region of asymmetric instability ($n \geqslant 1$) is embedded in the region of existence for the axisymmetric solutions of the linearized boundary-value problem (12)–(14). This fact is easily seen if one compares the graphs, presented in Figs. 1–3. Therefore, to construct the stability region in the case of a tensile axial load it is sufficient to consider the problem of stability with respect to axisymmetric perturbations ($n=0$) only. Results, obtained for both considered materials, confirm this fact.

In Figs. 4 and 5 the sections of the stability region are plotted. In these graphs the instability region is filled. This means that there is no instability of the infinite hollow cylinder for any load path (i.e., any curve in the space of the loading parameters), which does not have common points with the filled instability region. For thin-walled cylinders ($\chi<0.1$) we have determined that the stability regions in the space of the parameters α, ψ_0, ω_0 ($\omega_0=\omega/r_0^2$), corresponding to the different values of χ, are almost undistinguishable.

5 The Practical Criterion of Stability

Consider a potential energy per unit length for the stretched, twisted, and inflated hollow cylinder, as a function of the parameters α, ψ, ω, defined by the formula

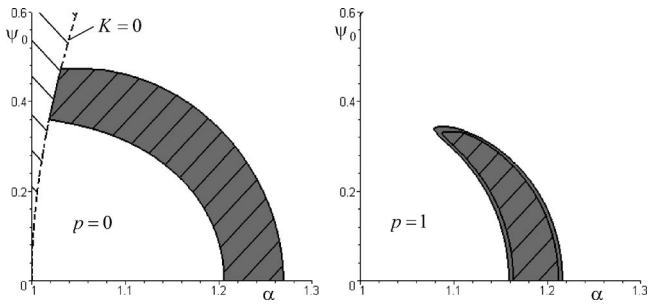

Fig. 4 Sections of the stability region for the Biderman material

$$\Pi(\alpha,\psi,\omega) = 2\pi \int_{r_1}^{r_0} rW(I_1(r), I_2(r))dr \tag{17}$$

For the axial load K, torque M, and internal pressure p, the following energy relations can be easily proved, using Eqs. (3), (5)–(7), and (17):

$$K(\alpha,\psi,\omega) = \frac{\partial \Pi(\alpha,\psi,\omega)}{\partial \alpha} \quad M(\alpha,\psi,\omega) = \frac{\partial \Pi(\alpha,\psi,\omega)}{\partial \psi}$$

$$p_0(\alpha,\psi,\omega) = \frac{\partial \Pi(\alpha,\psi,\omega)}{\partial \omega} \quad p_0(\alpha,\psi,\omega) = \alpha\pi p(\alpha,\psi,\omega) \tag{18}$$

The condition of strict convexity for the potential energy per unit length Π, as a function of the axial stretching α, angle of twist ψ, and deformed inner radius square ω, is equivalent to the three inequalities,

$$\frac{\partial^2 \Pi}{\partial \alpha^2} > 0 \quad \frac{\partial^2 \Pi}{\partial \alpha^2}\frac{\partial^2 \Pi}{\partial \psi^2} - \left(\frac{\partial^2 \Pi}{\partial \alpha \partial \psi}\right)^2 > 0$$

$$\frac{\partial^2 \Pi}{\partial \alpha^2}\frac{\partial^2 \Pi}{\partial \psi^2}\frac{\partial^2 \Pi}{\partial \omega^2} + 2\frac{\partial^2 \Pi}{\partial \alpha \partial \omega}\frac{\partial^2 \Pi}{\partial \alpha \partial \psi}\frac{\partial^2 \Pi}{\partial \psi \partial \omega} - \frac{\partial^2 \Pi}{\partial \psi^2}\left(\frac{\partial^2 \Pi}{\partial \alpha \partial \omega}\right)^2 - \frac{\partial^2 \Pi}{\partial \alpha^2}\left(\frac{\partial^2 \Pi}{\partial \psi \partial \omega}\right)^2 - \frac{\partial^2 \Pi}{\partial \omega^2}\left(\frac{\partial^2 \Pi}{\partial \alpha \partial \psi}\right)^2 > 0 \tag{19}$$

Using energy relations (18), this condition can be represented in the form of the Drucker postulate [33], i.e., the requirement that the work of the generalized forces increments on small increments of generalized displacements must be positive

$$dKd\alpha + dMd\psi + dp_0 d\omega > 0$$

In the case of the uniaxial tension ($\psi=0$, $p=0$) there is a theorem, proven for a compressible cylinder, having an arbitrary cross section [17], and for both hollow and solid circular cylinder of incompressible material [20]. According to this theorem, there is no instability for the stretched cylinder on the ascending branch of the load-extension curve $K(\alpha)$. Since for the uniaxial tension $K(\alpha)=\partial \Pi(\alpha)/\partial \alpha$, then the requirement of strict convexity for the function $\Pi(\alpha)$ is the sufficient condition for the equilibrium stability of a hollow cylinder under uniaxial tension. We must emphasize that this statement is valid for the case of a tensile axial load only and incorrect for the cylinder under compression. From the practical point of view a quite adequate accuracy for the criterion of a potential energy convexity was found earlier [20] for the stability problem of a stretched and twisted cylinder.

For the infinite hollow cylinder under tension, torsion, and inflation the result of a comparison between the stability region, determined by solving the linearized boundary-value problem (12)–(14), and the convexity region for the potential energy Π is presented in Figs. 4 and 5. In these graphs the nonconvexity region (a region, for which the convexity condition (19) does not hold) is backward-hatched. As shown in the graphs, for a zero

internal pressure ($p=0$) there is almost no difference between these regions. Moreover, there is no instability in the convexity region. For a nonzero pressure the cylinder instability in the convexity region of the potential energy Π is possible, but the differences between the stability region and the convexity region are not too large. These results are independent of the hollow cylinder geometry.

6 Concluding Remark

Within the framework of the bifurcational approach we have investigated the stability problem for a hollow circular infinite cylinder under tension, torsion, and inflation. The stability analysis has been carried out on the basis of the exact three-dimensional equations of the nonlinear elasticity for an isotropic incompressible body. For two models of material (a Biderman material and a power-law material) the critical surfaces and the stability region in the space of the loading parameters have been defined numerically. According to obtained results, to construct the stability region in the case of a tensile axial load, it is sufficient to consider the stability problem with respect to axisymmetric perturbations ($n=0$) only. It has been determined that the stability region boundary consists of the critical surfaces segments, which are obtained for different values of λ. For thin-walled hollow cylinders ($\chi<0.1$) we have defined that the stability region in the space of the parameters α, ψ_0, ω_0 is almost independent of a wall thickness. By comparing the stability region and convexity region for the potential energy per unit length Π, as a function of the axial stretching α, angle of twist ψ, and deformed inner radius square ω, we have determined that the condition of strict convexity for the potential energy $\Pi(\alpha, \psi, \omega)$ can be used as a sufficiently accurate practical criterion of stability for the stretched hollow cylinder under torsion and inflation. This condition can be represented in the form of the Drucker postulate, i.e., the requirement that the work of the generalized forces increments on small increments of generalized displacements must be positive.

Acknowledgment

This research was supported by the Russian Foundation for Basic Research (05-01-00638 and 06-01-00726).

References

[1] Timoshenko, S. P., and Gere, J. M., 1961, *Theory of Elastic Stability*, McGraw-Hill, NY.
[2] Volmir, A. S., 1967, *Stability of Deformable Systems*, Nauka, Moscow.
[3] Tvergaard, V., 1976, "Buckling Behavior of Plate and Shell Structure," in *Proceedings of the 14th IUTAM Congress*, North-Holland, Amsterdam, pp. 233–247.
[4] Budiansky, B., and Hutchinson, J. W., 1979, "Buckling: Progress and Challenge," *Trends in Solid Mechanics*, J. F. Besseling and A. M. A. Van der Heijden, eds., University Press, Delft.
[5] Steigmann, D. J., 1990, "Tension-Field Theory," Proc. R. Soc. London, Ser. A, **429**, pp. 141–173.
[6] Haughton, D. M., 2001, "Elastic Membranes," *Nonlinear Elasticity: Theory and Applications*, Y. B. Fu and R. W. Ogden, eds., Cambridge University Press, Cambridge, UK, pp. 233–267.
[7] Green, A. E., and Adkins, J. E., 1960, *Large Deformations and Non-Linear Continuum Mechanics*, Oxford University Press, Oxford.
[8] Sensenig, C. B., 1964, "Instability of Thick Elastic Solids," Commun. Pure Appl. Math., **17**(4), pp. 451–491.
[9] Biot, M. A., 1965, *Mechanics of Incremental Deformations*, Wiley, New York.
[10] Knops, R. J., and Wilkes, E. W., 1973, *Theory of Elastic Stability*, Springer, Berlin.
[11] Wesolowski, Z., 1974, *Dynamic Problems of Non-Linear Theory of Elasticity*, Panstwowe Wydawnictwo Naukowe, Warsaw.
[12] Lurye, A. I., 1980, *The Non-Linear Theory of Elasticity*, Nauka, Moscow.
[13] Zubov, L. M., 1997, *Nonlinear Theory of Dislocations and Disclinations in Elastic Bodies*, Springer-Verlag, Berlin.
[14] Fu, Y. B., and Ogden, R. W., 1999, "Nonlinear Stability Analysis of Pre-Stressed Elastic Bodies," Continuum Mech. Thermodyn., **11**, pp. 141–172.
[15] Guz, A. N., 1999, *Fundamentals of the Three-Dimensional Theory of Stability of Deformable Bodies*, Springer Verlag, Berlin.
[16] Beatty, M. F., 1987, "Topics in Finite Elasticity: Hyperelasticity of Rubber, Elastomers, and Biological Tissues-with Examples," Appl. Mech. Rev., **40**, pp. 1699–1734.
[17] Spector, S. J., 1984, "On the Absence of Bifurcation for Elastic Bars in Uniaxial Tension," Arch. Ration. Mech. Anal., **85**(2), pp. 171–199.
[18] Zubov, L. M., and Rudev, A. N., 1996, "The Instability of a Stretched Non-Linearly Elastic Beam," Prikl. Mat. Mekh., **60**(5), pp. 786–798.
[19] Lastenko, M. S., and Zubov, L. M., 2002, "A Model of Neck Formation on a Rod under Tension," Revista Colombiana de Matematicas, **36**(1), pp. 49–57.
[20] Zubov, L. M., and Sheidakov, D. N., 2005, "The Effect of Torsion on the Stability of an Elastic Cylinder under Tension," Prikl. Mat. Mekh., **69**(1), pp. 53–60.
[21] Haughton, D. M., and Ogden, R. W., 1979, "Bifurcation of Inflated Circular Cylinders of Elastic Material under Axial Loading. I. Membrane Theory for Thin-Walled Tubes," J. Mech. Phys. Solids, **27**(3), pp. 179–212.
[22] Haughton, D. M., and Ogden, R. W., 1979, "Bifurcation of Inflated Circular Cylinders of Elastic Material under Axial Loading. II. Exact Theory for Thick-Walled Tubes," J. Mech. Phys. Solids, **27**(5–6), pp. 489–512.
[23] Chen, Y. C., and Haughton, D. M., 2003, "Stability and Bifurcation of Inflation of Elastic Cylinders," Proc. R. Soc. London, Ser. A, **459**, pp. 137–156.
[24] Ogden, R. W., 1997, *Non-Linear Elastic Deformations*, Mineola, Dover.
[25] Antman, S. S., 1995, *Nonlinear Problems of Elasticity*, Springer, New York.
[26] Oden, J. T., 1972, *Finite Elements of Nonlinear Continua*, McGraw-Hill, New York.
[27] Zubov, L. M., 1971, "Variational Principles of the Non-Linear Theory of Elasticity. The Case of the Superposition of a Small Deformation on a Finite One," Prikl. Mat. Mekh., **35**(5), pp. 848–852.
[28] Zubov, L. M., and Moiseyenko, S. I., 1981, "The Buckling of an Elastic Cylinder under Torsion and Compression," Izv. Akad. Nauk SSSR, Mekh. Tverd. Tela, **5**, pp. 78–84.
[29] Biderman, V. L., 1958, "Problems of Rubber Articles Analysis," *Strength Analysis*, Mashgiz, Moscow, Vol. 3, pp. 40–87.
[30] Zubov, L. M., and Rudev, A. N., 1994, "Indications That Hadamard's Condition is Satisfied for Highly Elastic Materials," Izv. Ross. Akad. Nauk, Mekh. Tverd. Tela, **6**, pp. 21–31.
[31] Zubov, L. M., and Rudev, A. N., 1993, "Features of the Loss of Stability for a Non-Linearly Elastic Rectangular Beam," Prikl. Mat. Mekh., **57**(3), pp. 65–83.
[32] Algin, V. A., and Zubov, L. M., 2000, "The Stability of an Elastic Ring Made of Physically Non-Linear Material," Izv. Vuzov. Severo-Kavkaz. Region. Estest. nauki, **2**, pp. 14–16.
[33] Kachanov, L. M., 1974, *Principles of Fracture Mechanics*, Nauka, Moscow.

Dynamic Response Characteristics of a Nonviscously Damped Oscillator

S. Adhikari[1]
Department of Aerospace Engineering,
University of Bristol,
Queens Building,
University Walk,
Bristol BS8 1TR, UK
e-mail: s.adhikari@bristol.ac.uk

The characteristics of the frequency response function of a nonviscously damped linear oscillator are considered in this paper. It is assumed that the nonviscous damping force depends on the past history of velocity via a convolution integral over an exponentially decaying kernel function. The classical dynamic response properties, known for viscously damped oscillators, have been generalized to such nonviscously damped oscillators. The following questions of fundamental interest have been addressed: (a) Under what conditions can the amplitude of the frequency response function reach a maximum value?, (b) At what frequency will it occur?, and (c) What will be the value of the maximum amplitude of the frequency response function? Introducing two nondimensional factors, namely, the viscous damping factor and the nonviscous damping factor, we have provided exact answers to these questions. Wherever possible, attempts have been made to relate the new results with equivalent classical results for a viscously damped oscillator. It is shown that the classical concepts based on viscously damped systems can be extended to a nonviscously damped system only under certain conditions. [DOI: 10.1115/1.2755096]

1 Introduction

The characterization of dissipative forces is crucial for the design of safety critical engineering structures subjected to dynamic forces. Viscous damping is the most common approach for the modeling of dissipative or damping forces in engineering structures. This model assumes that the instantaneous generalized velocities are the only relevant variables that determine damping. Viscous damping models are used widely for their simplicity and mathematical convenience, even though the energy dissipation behavior of real structural materials may not be accurately represented by simple viscous models. Increasing use of modern composite materials, high-damping elements, and active control mechanisms in the aerospace and automotive industries in recent years demands sophisticated treatment of the dissipative forces for proper analysis and design. It is well known that, in general, a physically realistic model of damping in such cases will not be viscous. Damping models in which the dissipative forces depend on any quantity other than the instantaneous generalized velocities are nonviscous damping models.

Recognizing the need to incorporate generalized dissipative forces within the equations of motion, several authors have used nonviscous damping models. Within the scope of linear models, the damping force can, in general [1], be expressed by

$$f_d(t) = \int_0^t g(t-\tau)\dot{u}(\tau)\mathrm{d}\tau \tag{1}$$

Bagley and Torvik [2], Torvik and Bagley [3], Gaul et al. [4] and Maia et al. [5] have considered damping modeling in terms of fractional derivatives of the displacements, which can be obtained by properly choosing the damping kernel function $g(t)$ in Eq. (1). This type of problem has also been treated extensively within the viscoelasticity literature; see, for example, the books by Bland [6] and Christensen [7] and references therein. Among various other nonviscous damping models, the "Biot model" [8] or "exponential damping model" is particularly promising and has been used by many authors [9–14]. With this model, the damping force is expressed as

$$f_d(t) = \sum_{k=1}^{n} c_k \int_0^t \mu_k e^{-\mu_k(t-\tau)}\dot{u}(\tau)\mathrm{d}\tau \tag{2}$$

Here, c_k are the damping constants, μ_k are the relaxation parameters, n is the number of relaxation parameters required to describe the damping behavior, and $u(t)$ is the displacement as a function of time. In the context of viscoelastic materials, the physical basis for exponential models has been well established; see, for example, Ref. [15]. A selected literature review including the justifications for considering the exponential damping model may be found in Ref. [13]. Adhikari and Woodhouse [16] proposed a few methods by which the damping parameters in Eq. (2) can be obtained from experimental measurements.

Methods for the analysis of linear systems with damping of the form (2) have been considered by many authors; for example [1,9–13,17,18]. Although these publications provide excellent analytical and numerical tools for the analysis of nonviscously damped systems, most of the physical understandings are still from the point of view of a viscously damped oscillator. In this paper, we address the dynamic response characteristics of a nonviscously damped oscillator with energy dissipation characteristics given by Eq. (2) with $n=1$. The outline of the paper is as follows. In Sec. 2, the equation of motion is introduced and the exact analytical solutions of the eigenvalues are derived. The conditions for sustainable oscillatory motion are discussed in Sec. 3.1. The critical damping factors of a nonviscously damped oscillator are discussed in Sec. 3.2. The frequency response function of the system is derived in Sec. 4. The characteristics of the response amplitude are discussed in Sec. 5. In Sec. 6, a simplified analysis of dynamic response is proposed. Finally, our main findings are summarized in Sec. 7.

2 Background

The equation of motion of the system with damping characteristics given by Eq. (2) with $n=1$ can be expressed as

[1]Current address: School of Engineering, University of Wales Swansea, Singleton Park, Swansea SA2 8PP, UK.

Contributed by the Applied Mechanical Division of ASME for publication in the JOURNAL OF APPLIED MECHANICS. Manuscript received October 6, 2005; final manuscript received February 28, 2007; published online January 11, 2008. Review conducted by N. Sri Namachchivaya.

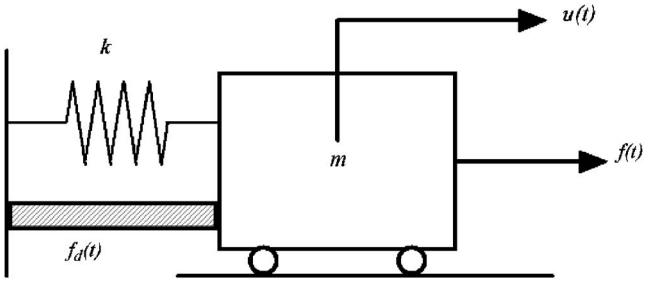

Fig. 1 A single-degree-of-freedom nonviscously damped oscillator with the damping force $f_d(t)=\int_0^t c\mu e^{-\mu(t-\tau)}\dot{u}(\tau)\mathrm{d}\tau$

$$m\ddot{u}(t)+\int_0^t c\mu e^{-\mu(t-\tau)}\dot{u}(\tau)\mathrm{d}\tau+ku(t)=f(t) \tag{3}$$

together with the initial conditions

$$u(0)=u_0 \quad \text{and } \dot{u}(0)=\dot{u}_0 \tag{4}$$

The system is shown in Fig. 1. Here, m is the mass of the oscillator, k is the spring stiffness, $f(t)$ is the applied forcing, and $(\bullet)$ represents a derivative with respect to time. Qualitative properties of the eigenvalues of this system have been discussed in detail by Adhikari [19]. Here, we review some basic results.

Transforming Eq. (3) into the Laplace domain, one obtains

$$s^2m\bar{u}(s)+sc\left(\frac{\mu}{s+\mu}\right)\bar{u}(s)+k\bar{u}(s)=\bar{f}(s)+m\dot{u}_0+\left(sm+c\frac{\mu}{s+\mu}\right)u_0 \tag{5}$$

where s is the complex Laplace domain parameter and $\overline{(\bullet)}$ is the Laplace transform of $(\bullet)$. For convenience, we introduce the constants ω_n, ζ, and β as follows:

$$\omega_n=\sqrt{\frac{k}{m}} \quad \zeta=\frac{c}{2\sqrt{km}} \quad \beta=\frac{\omega_n}{\mu} \tag{6}$$

Here, ω_n is the undamped natural frequency, ζ is the viscous damping factor, and β is the nonviscous damping factor. When $\zeta\to 0$, the oscillator is effectively undamped. When $\beta\to 0$, then $\mu\to\infty$, and the oscillator is effectively viscously damped. We will use these limiting cases frequently to develop our physical understandings of the results to be derived in this paper. In the context of multiple-degree-of-freedom dynamic systems, Adhikari and Woodhouse [20] have proposed four nonviscosity indices in order to quantify nonviscous damping. The nonviscous damping factor β proposed here also serves a similar purpose. Using the constants in (6), Eq. (5) can be rewritten as

$$\bar{d}(s)\bar{u}(s)=\bar{p}(s) \tag{7}$$

where the dynamic stiffness coefficient $\bar{d}(s)$ and the equivalent forcing function $\bar{p}(s)$ are given by

$$\bar{d}(s)=s^2+s2\zeta\omega_n\left(\frac{\omega_n}{s\beta+\omega_n}\right)+\omega_n^2 \tag{8}$$

and

$$\bar{p}(s)=\frac{\bar{f}(s)}{m}+\dot{u}_0+\left(s+2\zeta\omega_n\frac{\omega_n}{s\beta+\omega_n}\right)u_0 \tag{9}$$

The aim of a dynamic analysis is often to obtain the dynamic response, either in the time domain or in the frequency domain. For a single-degree-of-freedom (SDOF) oscillator, it is a relatively simple task; one can either directly integrate Eq. (3) with the initial conditions (4), or alternatively can invert the coefficient associated with $\bar{u}(s)$ in Eq. (7). Such an approach is not suitable for multiple degree-of-freedom systems with nonproportional damping and may not provide much physical insight. We pursue an approach that involves eigensolutions of the oscillator. The eigenvalues are the zeros of the dynamic stiffness coefficient and can be obtained by setting $\bar{d}(s)=0$. Therefore, using Eq. (8), the eigenvalues are the solutions of the characteristic equation:

$$\beta s^3+\omega_n s^2+(\beta\omega_n^2+2\zeta\omega_n^2)s+\omega_n^3=0 \tag{10}$$

In contrast to a viscously damped oscillator where one obtains a quadratic equation.

The three roots of Eq. (10) can appear in two distinct forms: (a) One root is real and the other two roots are in a complex conjugate pair, or (b) all roots are real. Case (a) represents an *underdamped oscillator*, which usually arises when the "small damping" assumption is made. The complex conjugate pair of roots corresponds to the "vibration" of the oscillator, while the third root corresponds to a purely dissipative motion. Case (b) represents an *overdamped oscillator* in which the system cannot sustain any oscillatory motion. For simplicity, we introduce a nondimensional frequency parameter

$$r=\frac{s}{\omega_n}\in\mathbb{C} \tag{11}$$

and transform the characteristics of Eq. (10) to

$$\beta r^3+r^2+(\beta+2\zeta)r+1=0 \tag{12}$$

or

$$r^3+\sum_{j=0}^{2}a_jr^j=0 \tag{13}$$

The constants associated with the powers of r are given by

$$a_0=\frac{1}{\beta} \quad a_1=1+2\frac{\zeta}{\beta} \quad a_2=\frac{1}{\beta} \tag{14}$$

The cubic Eq. (13) can be solved exactly in closed form; see, for example [[21] Sec. 3.8]. Define the following constants

$$Q=\frac{3a_1-a_2^2}{9}=\frac{(3\beta^2+6\beta\zeta-1)}{9\beta^2} \tag{15}$$

and

$$R=\frac{9a_2a_1-27a_0-2a_2^3}{54}=-\frac{(9\beta^2-9\beta\zeta+1)}{27\beta^3} \tag{16}$$

From these, calculate the negative of the discriminant

$$D=Q^3+R^2=\frac{1}{27\beta^4}(\beta^4+6\beta^3\zeta+2\beta^2+12\beta^2\zeta^2-10\beta\zeta+1+8\beta\zeta^3-\zeta^2) \tag{17}$$

and define two new constants

$$S=\sqrt[3]{R+\sqrt{D}} \quad \text{and } T=\sqrt[3]{R-\sqrt{D}} \tag{18}$$

Using these constants, the roots of Eq. (13) can be expressed by the Cardanos formula as

$$r_1=-\frac{a_2}{3}-\frac{1}{2}(S+T)+\mathrm{i}\frac{\sqrt{3}}{2}(S-T) \tag{19}$$

$$r_2=-\frac{a_2}{3}-\frac{1}{2}(S+T)-\mathrm{i}\frac{\sqrt{3}}{2}(S-T) \tag{20}$$

and

$$r_3=-\frac{a_2}{3}+(S+T) \tag{21}$$

These are the normalized eigenvalues of the system. The actual eigenvalues, that is the solutions of Eq. (10), can be obtained as

$\lambda_j = \omega_n r_j$, $j=1,2,3$. If the nonviscous damping factor β is zero, Eq. (12) reduces to the quadratic equation

$$r^2 + 2\zeta r + 1 = 0 \tag{22}$$

which, as expected, is the characteristic equation of a viscously damped oscillator. For this special case, the two solutions of Eq. (22) are given by

$$r_1 = -\zeta + i\sqrt{1-\zeta^2} \quad r_2 = -\zeta - i\sqrt{1-\zeta^2} \tag{23}$$

Since the nature of these solutions is very well understood, we will compare the new results with them.

3 Characteristic of the Eigenvalues

3.1 Conditions for Oscillatory Motion. The conditions for oscillatory motion have been discussed by Muravyov and Hutton [10] and more recently by Muller [22] and Adhikari [19]. Here, we briefly review the answers to the following questions of fundamental interest:

- Under what conditions can a nonviscously damped oscillator sustain oscillatory motions?
- Is there any critical damping factor for a nonviscously damped oscillator so that, beyond this value, the oscillator becomes overdamped?

For a viscously damped oscillator, the answer to the above questions is well known. From Eq. (23) it is clear that if the viscous damping factor ζ is more than 1, then the oscillator becomes overdamped and consequently it will not be able to sustain any oscillatory motions. This simple fact is no longer true for a nonviscously damped oscillator.

Roots r_1 and r_2 in Eqs. (19) and (20), respectively, will be in a complex conjugate pair, provided $S-T\neq 0$. The motion corresponding to the complex conjugate roots r_1 and r_2 is oscillatory (and decaying) in nature, while the motion corresponding to the real root r_3 is a pure nonoscillatory decay. Considering the expressions of S and T in Eq. (18), it is easy to observe that the system can oscillate provided $D>0$. Therefore, the critical condition is given by

$$D(\zeta,\beta) = 0 \tag{24}$$

From the expression of D in (17), this condition can be rewritten as

$$8\beta\zeta^3 + (12\beta^2 - 1)\zeta^2 + (6\beta^3 - 10\beta)\zeta + (1 + 2\beta^2 + \beta^4) = 0 \tag{25}$$

In Fig. 2, the surface $D(\zeta,\beta)=0$ is plotted for $0\leqslant\zeta\leqslant 6$ and $0\leqslant\beta\leqslant 0.5$. This plot shows the parameter domain where the system can have oscillatory motion. For a viscously damped oscillator, $\beta=0$, which is represented by the X-axis of Fig. 2. Along the X-axis when $\zeta>1$, the oscillatory motion is not possible, which is well known. But the scenario changes in an interesting way for nonzero β (i.e., for a nonviscously damped oscillator). For example, if $\beta\approx 0.1$, the system can have oscillatory motion even when $\zeta>2$, which is more than twice the critical viscous damping factor! Conversely, there are also regions where the system may not have oscillatory motion even when $\zeta<1$. Perhaps the most interesting observation from Fig. 2 is that if β is more than about 0.2, then the oscillator will *always* have oscillatory motions, no matter what the value of the viscous damping factor is. Therefore, there is a critical value of ζ, say ζ_c, *below* which the system will always have an oscillatory motion. Similarly, there is a critical value of β, say β_c, *above* which the system will always have an oscillatory motion. In the previous work [19], the exact critical values of ζ and β were obtained and the following basic result was proved:

THEOREM 3.1. *A nonviscously damped oscillator will have oscillatory motions if* $\zeta<4/(3\sqrt{3})$ or $\beta>1/(3\sqrt{3})$.

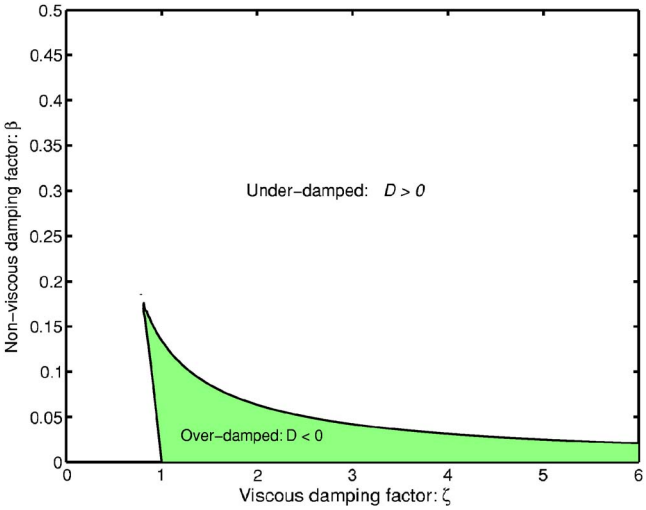

Fig. 2 The boundary between oscillatory and nonoscillatory motion

In the next section, the precise parameter region, where oscillatory motion is possible, is defined using the concept of critical damping factors.

3.2 Critical Damping Factors. In Fig. 3, we have (again) plotted the surface $D(\zeta,\beta)=0$ concentrating around the critical values of ζ and β. The shaded region corresponds to the parameter combinations for which oscillatory motion is not possible. A nonviscously damped oscillator will *always* have oscillatory motions if $\zeta<\zeta_c$ and/or $\beta>\beta_c$ (parameter regions C_1 and A in the figure). If $\beta<\beta_c$, then it is possible to have overdamped motion even if $\zeta<1$, as in the parameter region B, shown in Fig. 3. When $\beta<\beta_c$, there are two distinct parameter regions (shown as C_1 and C_2 in the figure) in which oscillatory motion is possible. Therefore, one can think of two critical damping factors for a nonviscously damped oscillator.

Using the notations ζ_L and ζ_U, the oscillator will have overdamped motion when $\zeta_L<\zeta<\zeta_U$. We call ζ_L the lower critical damping factor and ζ_U the upper critical damping factor.

To obtain the critical damping factors, it is required to solve $D=0$ for ζ, which is a cubic equation in ζ. In the previous work

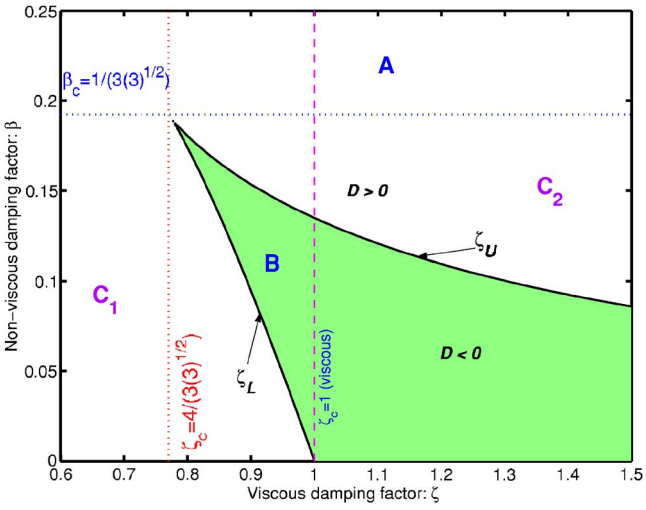

Fig. 3 Critical values of ζ and β for oscillatory motion

[19], it was proved that the lower and the upper critical damping factors of a nonviscously damped oscillator are given by

$$\zeta_L = \frac{1}{24\beta}\{1 - 12\beta^2 + 2\sqrt{1 + 216\beta^2} + \cos[(4\pi + \theta_c)/3]\} \quad (26)$$

and

$$\zeta_U = \frac{1}{24\beta}[1 - 12\beta^2 + 2\sqrt{1 + 216\beta^2} + \cos(\theta_c/3)] \quad (27)$$

where

$$\theta_c = \arccos\left[\frac{1 - 5832\beta^4 - 540\beta^2}{(216\beta^2 + 1)^{3/2}}\right] \quad (28)$$

Equations (26) and (27) are plotted in Fig. 3. When $\beta \to \beta_c$, the critical damping factors approach each other and eventually when $\beta = \beta_c$, both critical damping factors become the same and equal to ζ_c. The existence of two critical damping factors is a new concept compared to a viscously damped oscillator. In the limiting case when $\beta \to 0$, it can be verified that $\zeta_L \to 1$ and $\zeta_U \to \infty$. This indeed implies that a viscously damped oscillator has only one critical damping factor, and that is $\zeta = 1$. These results can be summarized in the following theorem:

THEOREM 3.2. *When* $\beta < 1/(3\sqrt{3})$, *a nonviscously damped oscillator will have oscillatory motions if and only if* $\zeta \notin [\zeta_L, \zeta_U]$.

4 The Frequency Response Function

The results given in the previous section define the conditions under which a nonviscously damped oscillator can sustain oscillatory motions. The rest of the paper is aimed at gaining insights into the nature of the dynamic response. The frequency response function of linear systems contains complete information regarding the dynamic response. The direct computation of the frequency response function of a SDOF system is a trivial task. To gain further insight into the dynamic response characteristics, it is often useful to express the frequency response function in terms of the eigenvalues of the system. The aim of this section is to establish a connection to the results given in the previous section, which gives the expression of the eigenvalues as a function of ζ and β.

We begin with the normalized frequency response function $\bar{h}(s)$, which is defined as the solution of Eq. (7) with the forcing function $\bar{p}(s) = 1$. Therefore, from Eq. (7) one obtains

$$\bar{h}(s) = \frac{1}{\bar{d}(s)} \quad \text{where } \bar{d}(s) = s^2 + s2\zeta\omega_n\left(\frac{\omega_n}{s\beta + \omega_n}\right) + \omega_n^2 \quad (29)$$

Noting that $\bar{d}(s)$ has zeros at $s = \lambda_j$, $j = 1, 2, 3$, where the eigenvalues $\lambda_j = \omega_n r_j$, the frequency response function can be conveniently expressed by the pole-residue form as

$$\bar{h}(s) = \sum_{j=1}^{3} \frac{R_j}{s - \lambda_j} \quad (30)$$

Here, the residues

$$R_j = \lim_{s \to \lambda_j} \frac{s - \lambda_j}{\bar{d}(s)} = \frac{1}{\partial \bar{d}(s)/\partial s|_{s=\lambda_j}} = \frac{1}{2}\frac{1}{\lambda_j + \zeta\omega_n[\omega_n/(\beta\lambda_j + \omega_n)]^2} \quad (31)$$

Because λ_1 and λ_2 appear in a complex conjugate pair, it is convenient to write $\lambda_1 = \lambda$ and $\lambda_2 = \lambda^*$, where $(\bullet)^*$ denotes the complex conjugation. We denote the real eigenvalue $\lambda_3 = \nu$. Using these notations and substituting $s = i\omega$, the frequency response function in Eq. (30) can be expressed as

$$\bar{h}(i\omega) = \frac{R_\lambda}{i\omega - \lambda} + \frac{R_\lambda^*}{i\omega - \lambda^*} + \frac{R_\nu}{i\omega - \nu} \quad (32)$$

where

$$R_\lambda = \frac{1}{2}\frac{1}{\lambda + \zeta\omega_n[1 + (\beta\lambda/\omega_n)]^{-2}} \quad R_\nu = \frac{1}{2}\frac{1}{\nu + \zeta\omega_n[1 + (\beta\nu/\omega_n)]^{-2}} \quad (33)$$

For the special cases when the system is undamped ($\zeta = 0$), or viscously damped ($\beta = 0$), Eq. (32) reduces to its corresponding familiar forms as follows:

- For undamped systems, $\zeta = 0$ and ν does not exist. The eigenvalue λ is purely imaginary so that $\lambda = i\omega_n$. From Eq. (33), one obtains $R_\lambda = 1/(2i\omega_n)$. Substitution of these values in Eq. (32) results in

$$\bar{h}(i\omega) = \frac{1}{2i\omega_n}\frac{1}{i\omega - i\omega_n} - \frac{1}{2i\omega_n}\frac{1}{i\omega + i\omega_n} = \frac{1}{2i\omega_n}\left[\frac{1}{i\omega - i\omega_n} - \frac{1}{i\omega + i\omega_n}\right] = \frac{1}{\omega_n^2 - \omega^2} \quad (34)$$

- For viscously damped systems, $\beta = 0$ and ν does not exist. The eigenvalue λ can be expressed as

$$\lambda = -\zeta\omega_n + i\omega_d \quad \text{where } \omega_d = \omega_n\sqrt{1 - \zeta^2} \quad (35)$$

From Eq. (33), one obtains $R_\lambda = 1/[2(-\zeta\omega_n + i\omega_d + \zeta\omega_n)] = 1/(2i\omega_d)$. Substituting these in Eq. (32), one obtains

$$\bar{h}(i\omega) = \frac{1}{2i\omega_d}\frac{1}{i\omega - (-\zeta\omega_n + i\omega_d)} - \frac{1}{2i\omega_d}\frac{1}{i\omega - (-\zeta\omega_n - i\omega_d)} = \frac{1}{2i\omega_d}\left[\frac{2i\omega_d}{(\zeta\omega_n + i\omega)^2 - (i\omega_d)^2}\right] = \frac{1}{\omega_n^2 + 2i\omega\zeta\omega_n - \omega^2} \quad (36)$$

In the time domain, the impulse response function can be obtained by taking the inverse Laplace transform of $\bar{h}(s)$ as

$$h(t) = \mathrm{Re}\left\{\frac{e^{\lambda t}}{\lambda + \zeta\omega_n[1 + (\beta\lambda/\omega_n)]^{-2}}\right\} + \frac{1}{2}\frac{e^{\nu t}}{\nu + \zeta\omega_n[1 + (\beta\nu/\omega_n)]^{-2}} \quad (37)$$

The first term in Eq. (37) is oscillating in nature because λ is complex, while the second term is purely decaying in nature as ν is real and negative.

It is convenient to define a nondimensional driving frequency parameter

$$\tilde{\omega} = \frac{\omega}{\omega_n} \quad (38)$$

Substituting $s = i\omega = i\tilde{\omega}\omega_n$ in Eq. (29), one has

$$\bar{h}(i\omega) = \frac{1}{\omega_n^2}\left[\frac{1}{-\tilde{\omega}^2 + 2i\zeta\tilde{\omega}(1/i\beta\tilde{\omega} + 1) + 1}\right] \quad (39)$$

Separating the real and imaginary parts, the nondimensional frequency response function can be expressed as

$$G(i\omega) = \omega_n^2\bar{h}(i\omega) = \frac{1 + i\beta\tilde{\omega}}{(1 - \tilde{\omega}^2) + i\tilde{\omega}(2\zeta + \beta - \beta\tilde{\omega}^2)} \quad (40)$$

From Eq. (40), the amplitude of vibration can be obtained as

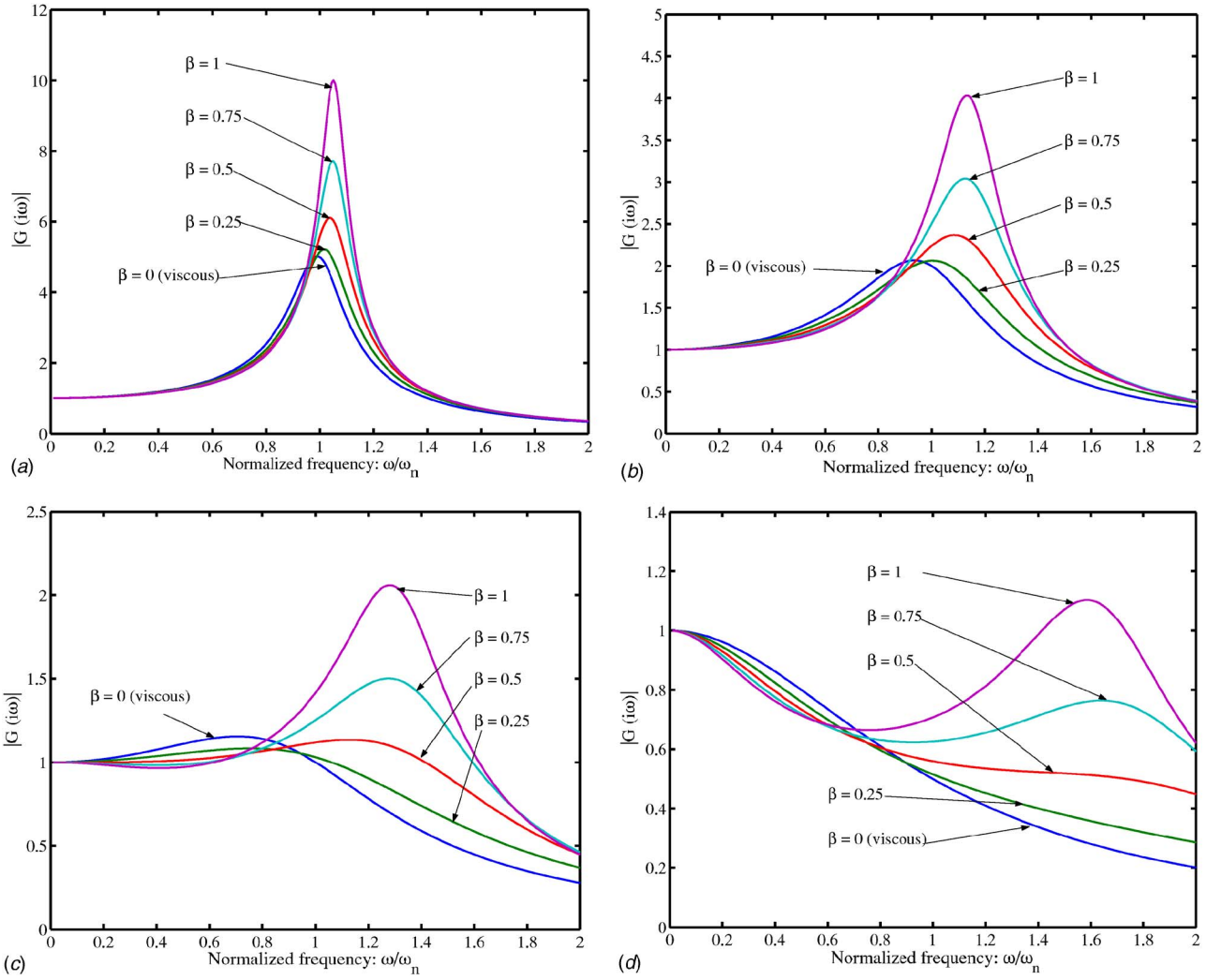

Fig. 4 Amplitude of the nondimensional frequency response $|G(i\omega)|$ as a function of the normalized frequency ω/ω_n for different values of ζ and β. (*a*) ζ=0.1. (*b*) ζ=0.25. (*c*) ζ=0.5. (*d*) ζ=1.0.

$$|G(i\omega)| = \sqrt{G(i\omega)G^*(i\omega)} = \sqrt{\frac{1+\beta^2\tilde{\omega}^2}{(1-\tilde{\omega}^2)^2+\tilde{\omega}^2(2\zeta+\beta-\beta\tilde{\omega}^2)^2}} \tag{41}$$

Figure 4 shows the amplitude of the nondimensional frequency response $|G(i\omega)|$ as a function of the normalized frequency ω/ω_n. The numerical values of β and ζ are selected such that Fig. 4 represents the general overall behavior. In the static case, that is when $\omega/\omega_n=0$, the amplitude of vibration is 1. Therefore, as the frequency changes, the values of $|G(i\omega)|$ in Eq. (41) can be regarded as the amplification factors.

When $\beta<\beta_c=1/(3\sqrt{3})$, the frequency response function is similar to that of the viscously damped system. This is expected because the value of β is relatively small. The amplitude of the peak response of the nonviscously damped system is more than that of the viscously damped system. In general, the higher the values of β, the higher the values of the amplitudes of the peak response. Another interesting fact can be seen from Fig. 4 is that the dynamic response amplitude has a peak even when $\zeta>1/\sqrt{2}$. For example, in Fig. 4(*d*), the viscously damped system does not have any response peak as $\zeta=1$ (critical viscous damping). However, for the nonviscously damped system, the response amplitude has a peak when $\beta=1$ or $\beta=0.75$, but not if $\beta<0.5$. These interesting response behaviors are explored further in the next section.

5 Characteristics of the Response Amplitude

The maximum vibration amplitude of a linear system near the resonance is of fundamental engineering interest because it can lead to damage or even failure of a structure. For a viscously damped system, it is well known that if $\zeta<1/\sqrt{2}$, then the frequency response function has a peak when $\omega/\omega_n=\sqrt{1-2\zeta^2}$. At this frequency, the amplitude of the maximum dynamic response is given by

$$|G|_{\max} = \frac{1}{2\zeta\sqrt{1-\zeta^2}} \tag{42}$$

Recently, Vinokur [23] derived a closed-form expression of the frequency point where the vibration amplitude of a hysteretically damped system reaches its maximum value. We are interested in the equivalent results for nonviscously damped systems. Specifically, we ask the following questions of fundamental engineering interest:

- Under what conditions can the amplitude of the frequency response function reach a maximum value?
- At what frequency will it occur?
- What will be the value of the maximum amplitude of the frequency response function?

5.1 The Frequency for the Maximum Response Amplitude. For notational convenience, denoting

$$x = \tilde{\omega}^2 = \frac{\omega^2}{\omega_n^2} \tag{43}$$

from Eq. (41), the amplitude of the dynamic response can be expressed as

$$|G|^2 = \frac{1 + \beta^2 x}{(1-x)^2 + x(2\zeta + \beta - \beta x)^2} \tag{44}$$

For the maximum value of $|G|$, we set

$$\frac{\partial |G|^2}{\partial x} = 0 \tag{45}$$

or

$$\frac{2x^2\beta^2 - 2\beta^2 x - 2\beta^3\zeta x^2 - \beta^4 x^2 + \beta^4 x^3 - 1 + x + 2\zeta^2 + 2\zeta\beta - 4\zeta x\beta}{[(1-x)^2 + x(2\zeta + \beta - \beta x)^2]^2} = 0 \tag{46}$$

At the solution point, it is also required that

$$\frac{\partial^2 |G|^2}{\partial x^2} < 0 \tag{47}$$

that in turn implies satisfying

$$\begin{aligned} &3\beta^6 x^5 + (9\beta^4 - 12\zeta\beta^5 - 6\beta^6)x^4 + (9\beta^2 + 12\zeta^2\beta^4 - 18\beta^4 - 40\beta^3\zeta \\ &\quad + 12\zeta\beta^5 + 3\beta^6)x^3 + (60\beta^2\zeta^2 + 9\beta^4 + 3 + 60\beta^3\zeta - 24\zeta\beta \\ &\quad - 18\beta^2)x^2 + (9\beta^2 - 24\beta^3\zeta - 48\zeta^3\beta + 12\zeta^2 + 36\zeta\beta - 6 \\ &\quad - 72\beta^2\zeta^2)x + 3 + 4\beta^3\zeta - 16\zeta^2 - 12\zeta\beta + 20\beta^2\zeta^2 + 32\zeta^3\beta \\ &\quad + 16\zeta^4 < 0 \end{aligned} \tag{48}$$

The numerator of Eq. (46) is a cubic equation in x and can be expressed as

$$x^3 + \sum_{j=0}^{2} c_j x^j = 0 \tag{49}$$

where

$$c_0 = \frac{2\zeta\beta + 2\zeta^2 - 1}{\beta^4} \quad c_1 = \frac{1 - 2\beta^2 - 4\zeta\beta}{\beta^4} \quad c_2 = \frac{2 - 2\zeta\beta - \beta^2}{\beta^2} \tag{50}$$

The three roots of Eq. (49) can either be all real or one real and one complex conjugate pair. The nature of the roots depends on the discriminant, which can be obtained from the constants

$$Q_x = \frac{3c_1 - c_2^2}{9} = -\frac{1}{9\beta^4}(1 + 2\zeta\beta + \beta^2)^2 \tag{51}$$

and

$$\begin{aligned} R_x &= \frac{9c_2c_1 - 27c_0 - 2c_2^3}{54} \\ &= \frac{1}{27\beta^6}[8\zeta^3\beta^3 + (12\beta^4 - 15\beta^2)\zeta^2 + (-15\beta^3 - 21\beta + 6\beta^5)\zeta \\ &\quad + 3\beta^4 + 3\beta^2 + 1 + \beta^6] \end{aligned} \tag{52}$$

as

$$\begin{aligned} D_x = Q_x^3 + R_x^2 = -\frac{\zeta}{27\beta^{11}}&[16\beta^4\zeta^4 + (13\beta^3 + 40\beta^5)\zeta^3 \\ &+ (18\beta^4 + 36\beta^6 - 18\beta^2)\zeta^2 + (-13\beta - 12\beta^3 + 15\beta^5 + 14\beta^7)\zeta \\ &+ 2 + 8\beta^2 + 12\beta^4 + 2\beta^8 + 8\beta^6] \end{aligned} \tag{53}$$

If $D_x > 0$, then Eq. (49) has one complex conjugate pair and only one real solution. It turns out that when $D_x > 0$, the real solution is always negative and, therefore, is not of interest in this study. However, when $D_x < 0$, all the roots of Eq. (49) become real. We define an angle θ as

$$\cos(\theta) = (R_x/\sqrt{-Q_x^3}) = \frac{8\zeta^3\beta^3 + (12\beta^4 - 15\beta^2)\zeta^2 + (6\beta^5 - 15\beta^3 - 21\beta)\zeta + 3\beta^4 + 3\beta^2 + 1 + \beta^6}{(1 + \beta^2 + 2\zeta\beta)^3} \tag{54}$$

Using θ, the three real solutions of Eq. (49) can be given using Dickson's formula [24] as

$$x_1 = 2\sqrt{-Q_x}\cos\left(\frac{\theta}{3}\right) - c_2/3 \tag{55}$$

$$x_2 = 2\sqrt{-Q_x}\cos\left(\frac{2\pi + \theta}{3}\right) - c_2/3 \tag{56}$$

and

$$x_3 = 2\sqrt{-Q_x}\cos\left(\frac{4\pi + \theta}{3}\right) - c_2/3 \tag{57}$$

Among the above three solutions, we need to choose a positive solution that also satisfies Eq. (48). From numerical calculations, it turns out that only x_1 in Eq. (55) satisfies the condition in Eq. (48). Substituting Q_x from (51) and c_2 from (50) into Eq. (55), the normalized excitation frequency for which the amplitude of the frequency response function reaches its maximum value is given by

$$x_{\max} = \frac{1}{3\beta^2}\{(1 + 2\zeta\beta + \beta^2)[2\cos(\theta/3) + 1] - 3\} \tag{58}$$

For convenience, we define the notation $\omega_{\max}$ as

$$x_{\max} = \frac{\omega_{\max}^2}{\omega_n^2} \tag{59}$$

we have

$$\omega_{\max} = \frac{\omega_n}{\beta}\sqrt{(1 + 2\zeta\beta + \beta^2)[2\cos(\theta/3) + 1]/3 - 1} \tag{60}$$

This is the extension of the well known result for viscously damped systems for which $\omega_{\max} = \omega_n\sqrt{1 - 2\zeta^2}$.

Figure 5 shows the contours of $\omega_{\max}/\omega_n$ obtained from Eq. (60), as a function of ζ and β. The value of $\omega_{\max}$ is the frequency where the amplitude of the frequency response function reaches its maximum value.

For a better understanding, Fig. 5 is divided into three regions. In region A where $\zeta \lesssim 0.5$ and β is small, $\omega_{\max}/\omega_n < 1$. This implies that in this parameter region, the frequency at which the amplitude of the frequency response function reaches its maximum appears *below* the system's natural frequency. Contour line 0

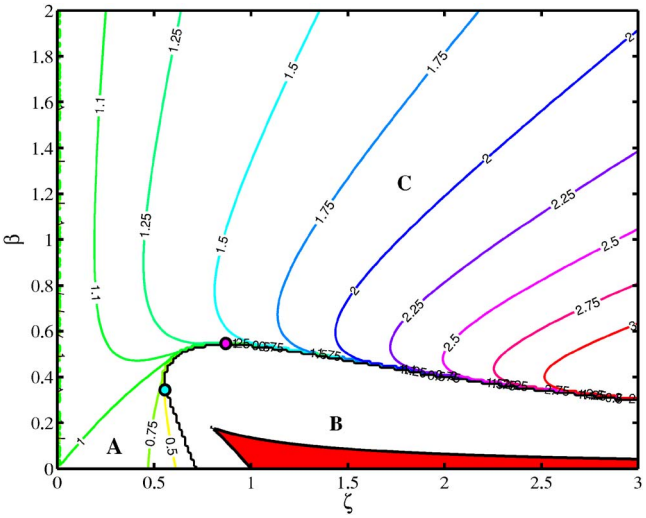

Fig. 5 Contours of the normalized excitation frequency corresponding to the maximum value of the amplitude of the frequency response function ω_{max}/ω_n as a function of ζ and β

separates the region B from A and C. In region B, $\beta \lesssim 0.5$ and $\zeta \gtrsim 1/\sqrt{2}$ and the amplitude of the frequency response function does not have any maximum value. This implies that within this parameter region, it is not possible to find a positive real solution of the cubic Eq. (49) and the system response decays gradually, as in 4(*d*) for $\beta=0$ and $\beta=0.25$. The shaded portion inside region B (shown before in Figs. 2 and 3) corresponds to the parameter region where the system cannot have any oscillatory motions. Clearly, within this overdamped region, it is not possible for the dynamic response amplitude to reach a maximum value. In region C, where $\zeta \gtrsim 1$ and $\beta \gtrsim 0.5$, observe that $\omega_{max}/\omega_n > 1$. The contour plots in Fig. 5 also show a general trend that ω_{max}/ω_n increases for increasing values of ζ and β.

An interesting contour line in Fig. 5 is line 1. For these parameter combinations of ζ and β, the frequency at which the amplitude of the frequency response function reaches the maximum value coincides exactly with the undamped natural frequency. This surprising observation implies that the system may be heavily damped ($\zeta > 0.5$), but still can have a peak at ω_n, for some appropriate values of β. Another interesting fact observed from Fig. 5 is that there exist a critical value of ζ, say ζ_{mL}, *below* which the amplitude of the frequency response will always have a maximum value for any values of β. Similarly, there is also a critical value of β, say β_{mU}, *above* which the amplitude of the frequency response will always have a maximum value for any values of ζ. The explanation of these observations, including the derivation of the exact values of ζ_{mL} and β_{mU}, are considered in the next subsections.

5.1.1 Critical Parameter Values for the Maximum Response Amplitude. Suppose a general complex solution of Eq. (49) is expressed as

$$x = \sigma + i\psi \tag{61}$$

for arbitrary $\sigma, \psi \in \mathbb{R}$. Substituting x from the above equation in (49) and separating the real and imaginary parts, we have

$$-2\beta^4\sigma^3 + (4\beta^3\zeta + 2\beta^4 - 4\beta^2)\sigma^2 + (6\beta^4\psi^2 - 2 + 4\beta^2 + 8\zeta\beta)\sigma - 4\zeta\beta - (4\beta^3\zeta + 2\beta^4 - 4\beta^2)\psi^2 - 4\zeta^2 + 2 = 0 \tag{62}$$

and

$$-6\beta^4\sigma^2\psi + (-8\psi\beta^2 + 8\psi\beta^3\zeta + 4\psi\beta^4)\sigma + 2\beta^4\psi^3 + 4\psi\beta^2 + 8\psi\zeta\beta - 2\psi = 0 \tag{63}$$

Eliminating σ from Eqs. (62) and (63) and substituting $\psi=0$ (because we are interested only in the real solution) in the resulting equation, after some algebra one has

$$\mathcal{M}(\zeta,\beta) = 0 \tag{64}$$

where

$$\mathcal{M}(\zeta,\beta) = 16\beta^3\zeta^3 + (24\beta^4 - 3\beta^2)\zeta^2 + (12\beta^5 - 15\beta - 3\beta^3)\zeta + 2 + 6\beta^2 + 6\beta^4 + 2\beta^6 \tag{65}$$

The parameters ζ and β must satisfy Eq. (64) in order to have a real solution. Therefore, in view of Fig. 5, the values of β_{mU} and ζ_{mL} can be obtained from the following optimization problems, respectively:

$$\beta_{mU}\text{: max } \beta \text{ subject to } \mathcal{M}(\zeta,\beta) = 0 \tag{66}$$

and

$$\zeta_{mL}\text{: min } \zeta \text{ subject to } \mathcal{M}(\zeta,\beta) = 0 \tag{67}$$

First, consider the constrained optimization problem in Eq. (66). Using the Lagrange multiplier γ_1, we construct the Lagrangian

$$\mathcal{L}_1(\zeta,\beta) = \beta + \gamma_1\mathcal{M}(\zeta,\beta) \tag{68}$$

The optimization problem shown in Eq. (66) can be solved by setting

$$\frac{\partial\mathcal{L}_1}{\partial\zeta} = 0 \tag{69a}$$

and

$$\frac{\partial\mathcal{L}_1}{\partial\beta} = 0 \tag{69b}$$

Differentiating the Lagrangian in Eq. (68), the above two conditions result

$$\gamma_1[48\beta^3\zeta^2 + (-6\beta^2 + 48\beta^4)\zeta - 15\beta + 12\beta^5 - 3\beta^3] = 0 \tag{70}$$

and

$$1 + \gamma_1[48\beta^2\zeta^3 + (-6\beta + 96\beta^3)\zeta^2 + (-15 + 60\beta^4 - 9\beta^2)\zeta + 12\beta + 24\beta^3 + 12\beta^5] = 0 \tag{71}$$

Because the Lagrange multiplier γ_1 cannot be zero, solving Eq. (70) one has

$$\zeta = -\frac{1+\beta^2}{2\beta} \tag{72a}$$

or

$$\zeta = \frac{5-4\beta^2}{8\beta} \tag{72b}$$

Ignoring the first solution, which is always negative, and substituting $\zeta=(5-4\beta^2)/8\beta$ in the constraint Eq. (64) and simplifying we have

$$\beta^4 + 2\beta^2 - 11/16 = 0 \tag{73}$$

There is only one feasible solution to the above equation, which can be obtained as

$$\beta_{mU} = \tfrac{1}{2}\sqrt{3\sqrt{3}-4} = 0.5468 \tag{74}$$

For this value of β, the value of ζ can be obtained from Eq. (72*b*) as

$$\zeta_{mU} = \tfrac{3}{4}\sqrt{(12\sqrt{3}-6)/11} = 0.8695 \tag{75}$$

The point (ζ_{mU}, β_{mU}) is shown by a dot in Fig. 5. From this plot, it can be observed that if $\beta > \beta_{mU}$, then there always exists a

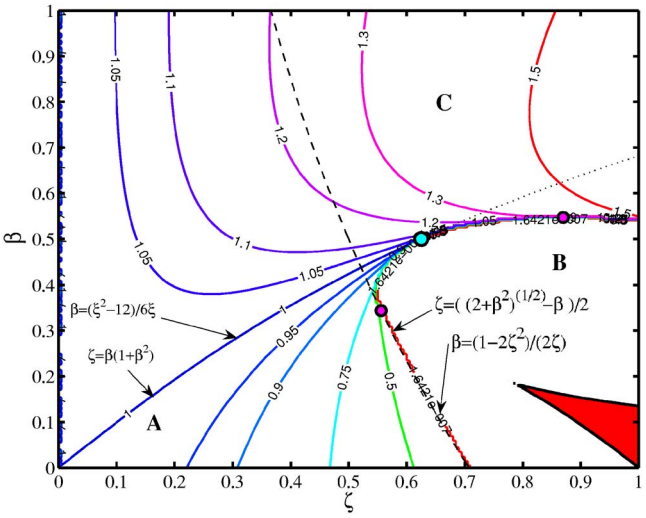

Fig. 6 Contours of the normalized excitation frequency corresponding to the maximum value of the amplitude of the frequency response function, ω_{max}/ω_n, as a function of ζ and β. Equations corresponding to $\omega_{max}/\omega_n=0$ (dashed line) and $\omega_{max}/\omega_n=1$ (dotted line) are shown in the figure. These equations are valid in the region A only. The function ξ is defined in Eq. (81).

driving frequency for which the amplitude of the frequency response function will reach a maximum value.

The value of ζ_{mL} can be obtained from the optimization problem (67) by constructing the Lagrangian

$$\mathcal{L}_2(\zeta,\beta)=\zeta+\gamma_2\mathcal{M}(\zeta,\beta) \tag{76}$$

where γ_2 is the Lagrange multiplier. Following a similar procedure, it can be shown that the optimal value of ζ is given by

$$\zeta_{mL}=\tfrac{1}{2}\sqrt{\sqrt{5}-1}=0.5559 \tag{77}$$

For this value of ζ, the value of β can be obtained as

$$\beta_{mL}=\tfrac{1}{2}\sqrt{2\sqrt{5}-4}=0.3436 \tag{78}$$

The point (ζ_{mL},β_{mL}) is shown by a dot in Fig. 5. From this plot, it can be observed that if $\zeta<\zeta_{mL}$, then there always exists a driving frequency for which the amplitude of the frequency response function will reach a maximum value. From the preceding discussions, we have the following fundamental results:

THEOREM 5.1. *The amplitude of the frequency response function of a nonviscously damped oscillator can reach a maximum value if* $\zeta<\frac{1}{2}\sqrt{\sqrt{5}-1}$ *or* $\beta>\frac{1}{2}\sqrt{3\sqrt{3}-4}$.

THEOREM 5.2. *If* $\zeta<\frac{1}{2}\sqrt{\sqrt{5}-1}$ *or* $\beta>\frac{1}{2}\sqrt{3\sqrt{3}-4}$, *then the amplitude of the frequency response function of a nonviscously damped oscillator reaches a maximum value when the driving frequency* $\omega=\omega_n(\sqrt{(1+2\zeta\beta+\beta^2)[2\cos(\theta/3)+1)/3-1]})/\beta$.

5.1.2 Parameter Relationships for $\omega_{max}=\omega_n$. The contour line $\omega_{max}/\omega_n=1$ in Fig. 5 is of special interest. For these particular parameter combinations, the maximum amplitude of the frequency response function of the damped system occurs *exactly* at the undamped natural frequency. This surprising fact occurs only in a nonviscously damped system and it is not possible for viscously damped systems. For a more detailed analysis, Fig. 6 again shows the contours of ω_{max}/ω_n when $\zeta\leqslant 1$ and $\beta\leqslant 1$.

In Fig. 6, when $\beta=0$, then ω_{max}/ω_n can be equal to 1 if and only if $\zeta=0$ (that is, when the system is undamped). The conditions for $\omega_{max}/\omega_n=1$ can be obtained by enforcing $x_{max}=1$. Thus, substituting $x=1$ in Eq. (49) and considering that $\zeta\neq 0$, we have

$$\beta+\beta^3-\zeta=0 \tag{79}$$

Solving this, the required condition can be given by

$$\zeta=\beta(1+\beta^2) \tag{80}$$

when β is known, or

$$\beta=(\xi^2-12)/6\xi \quad \text{where } \xi=\sqrt[3]{108\zeta+12\sqrt{12+81\zeta^2}} \tag{81}$$

when ζ is known. Equation (80) is plotted in Fig. 6. The same curve can also be obtained by plotting Eq. (81). One interesting fact emerging from Fig. 6 is that beyond certain values of ζ and β, the maximum dynamic response amplitude cannot occur at $\omega_{max}/\omega_n=1$. To obtain these limiting values, we substitute ζ from Eq. (80) into the condition of real solution given in Eq. (64). After some algebra, the resulting equation becomes

$$16\beta^{12}+72\beta^{10}+105\beta^8+45\beta^6-15\beta^4-9\beta^2+2=0 \tag{82}$$

The only positive real solution of the above equation is

$$\beta=1/2 \tag{83}$$

Substituting this value β in Eq. (80), one obtains

$$\zeta=5/8 \tag{84}$$

The point $(5/8,1/2)$ is shown in Fig. 6 by a dot. From this diagram, it is clear that ω_{max}/ω_n can be equal to one, if and only if $\zeta<5/8$ and $\beta<1/2$. When $x_{max}=1$, the maximum value of the amplitude of the frequency response function can be obtained from Eq. (44) as

$$|G|_{x_{max}=1}=\frac{\sqrt{1+\beta^2}}{2\zeta} \tag{85}$$

From this discussion, we have the following useful results:

THEOREM 5.3. *The maximum amplitude of the frequency response function (if it exists) of a nonviscously damped oscillator will occur below the undamped natural frequency if and only if* $\zeta<5/8$ *and* $\beta<1/2$.

THEOREM 5.4. *The maximum amplitude of the frequency response function (if it exists) of a nonviscously damped oscillator will occur above the undamped natural frequency if* $\zeta>5/8$ *or* $\zeta<\beta(1+\beta^2)$ *and* $\beta>1/2$ *or* $\beta>(\xi^2-12)/6\xi$.

Another curious feature of Fig. 6 is the flatness of ω_{max}/ω_n around the contour line 1. This implies that for a wide range of parameter combinations, it is possible to observe a damped resonance very close to the undamped natural frequency. For a viscously damped system, this can happen only if the damping is very small ($\zeta\lesssim 0.05$). But for a nonviscously damped system, this can happen even when ζ is as large as 0.6.

It was shown that the amplitude of the frequency response function cannot reach a maximum value for some combinations of ζ and β (the parameter region B in Figs. 5 and 6). Considering small values of ζ and β so that $\zeta\leqslant\zeta_{mL}$ and $\beta\leqslant\beta_{mL}$, we aim to derive a simple analytical expression for the existence of $|G|_{max}$. Because $x=\tilde{\omega}^2$, the condition for existence of the maximum amplitude of the frequency response function can be expressed as

$$x_{max}\geqslant 0 \tag{86}$$

Therefore, the critical condition can be obtained by substituting $x=0$ in Eq. (49) as

$$1-2\zeta\beta-2\zeta^2=0 \tag{87}$$

Solving this equation for ζ, the condition for existence of $|G|_{max}$ can be expressed by

$$\zeta<\tfrac{1}{2}(\sqrt{2+\beta^2}-\beta) \tag{88}$$

when

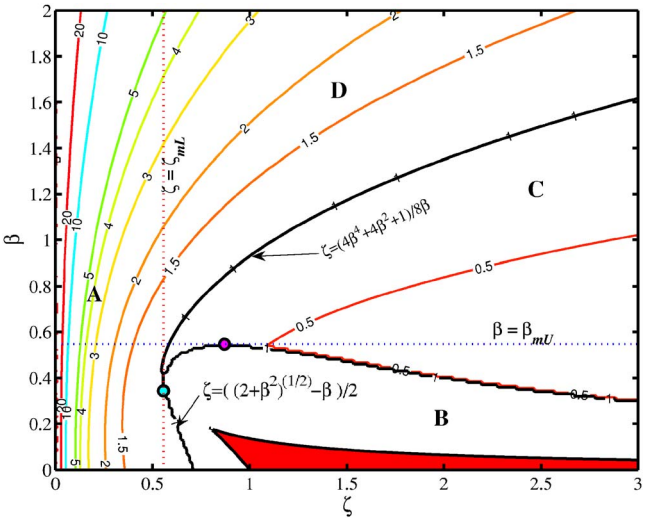

Fig. 7 Contours of the maximum amplitude of the normalized frequency response function $|G|_{max}$ as a function of ζ and β

$$\beta \leqslant \tfrac{1}{2}\sqrt{2\sqrt{5}-4} \tag{89}$$

For the special case when only viscous damping is present, substituting $\beta=0$ in Eq. (88), one obtains the required condition as $\zeta \leqslant 1/\sqrt{2}$, which is well known for viscously damped systems. This condition can alternatively be expressed in terms of ζ by solving Eq. (87) for β as

$$\beta < \frac{1-2\zeta^2}{2\zeta} \tag{90}$$

when

$$\zeta \leqslant \tfrac{1}{2}\sqrt{\sqrt{5}-1} \tag{91}$$

The validity of Eqs. (88) and (90) can be verified from Fig. 6. When $\zeta \leqslant \zeta_{mL}$ and $\beta \leqslant \beta_{mL}$, Eqs. (88) and (90) match perfectly with the zero line obtained from the expression of x_{max} in Eq. (58). Observe that these equations become invalid when $\zeta \geqslant \zeta_{mL}$ and $\beta \geqslant \beta_{mL}$. From this discussion, we have the following result:

THEOREM 5.5. *If* $\zeta \leqslant \frac{1}{2}\sqrt{\sqrt{5}-1}$ *and* $\beta \leqslant \frac{1}{2}\sqrt{2\sqrt{5}-4}$, *the amplitude of the frequency response function of a nonviscously damped oscillator can reach a maximum value if and only if* $\zeta < (\sqrt{2+\beta^2}-\beta)/2$ *or* $\beta < (1-2\zeta^2)/2\zeta$.

5.2 The Amplitude of the Maximum Dynamic Response. The maximum value of the amplitude of the frequency response function is a useful quantity because it can be related to the structural failure and design. Figure 7 shows the contours of the maximum amplitude of the normalized frequency response function $|G|_{max}$ as a function of ζ and β. The values of $|G|_{max}$ are calculated from Eq. (44) by substituting x_{max} from Eq. (58) in place of x. This diagram is divided into four regions for discussions. In region A, where $\zeta < \zeta_{mL}$, the amplitude of the frequency response function of the system will always have a maximum value. The values of $|G|_{max}$ are higher for smaller values of ζ, as expected. A useful fact to be noted is that for a fixed value of ζ, the value of $|G|_{max}$ is higher for higher values of β. This can also be verified from Fig. 4. This fact may have undesirable consequences, especially if β is large. In region B, the amplitude of the frequency response function does not have a maximum value. The shaded portion inside region B (shown before in Figs. 2 and 3) corresponds to the parameter region, where the system cannot have any oscillatory motions. Clearly, within this overdamped region, it is not possible for the dynamic response amplitude to reach a maximum value. In region C where $\beta > \beta_{mU}$, the amplitude of the frequency response function of the system will always have a maximum value, but the value of the maximum response is less than 1. In region D, observe that $\beta > \beta_{mU}$, but unlike region C, the value of the maximum response is more than 1. In general, for a fixed value of ζ, the values of $|G|_{max}$ increase with the increasing values of β. The numerical values of $|G|_{max}$ in regions C and D are, however, smaller compared to those in region A. From this discussion, we have the following general result:

THEOREM 5.6. *For a given value of* ζ, *the maximum amplitude of the frequency response function* (*if it exists*) *of a nonviscously damped oscillator increases with increasing values of* β.

The contour line "1" in Fig. 7 is of special interest because $|G|_{max} > 1$ implies that the maximum dynamic response amplitude is more than the static response. For the parameter combinations in the left side of the contour line 1, the amplitude of the maximum dynamic response is always greater than 1. In the the region to the right, the amplitude of the maximum dynamic response is less than the static response amplitude of the system. The exact parameter combinations for which $|G|_{max}$ is more than 1 is considered next.

Substituting x_{max} from Eq. (58) in the expression of $|G|^2$ in Eq. (44), we can obtain the expression of $|G|^2_{max}$. Equating the resulting expression to 1 and simplifying, we have

$$\begin{aligned}&[8\zeta^3\beta^3+(12\beta^2+12\beta^4)\zeta^2+(12\beta^3+6\beta+6\beta^5)\zeta+3\beta^2+1+\beta^6\\&\quad+3\beta^4][8\cos^3(\theta/3)-12\cos^2(\theta/3)]+18[8\zeta^2\beta^2+(-2\beta^5+4\beta\\&\quad+4\beta^3)\zeta-\beta^4-\beta^6]\cos(\theta/3)+32\zeta^3\beta^3+(48\beta^4+12\beta^2)\zeta^2\\&\quad+(-48\beta+6\beta^5-24\beta^3)\zeta+4+3\beta^4-5\beta^6+12\beta^2=0\end{aligned} \tag{92}$$

This is a cubic equation in $\cos(\theta/3)$ and it can be solved exactly to obtain

$$\cos(\theta/3) = \frac{1-\zeta\beta-\beta^2/2}{1+\beta^2+2\zeta\beta} \tag{93}$$

or

$$\cos(\theta/3) = \frac{\beta^2+2\zeta\beta+(1\pm 3\kappa)/4}{1+\beta^2+2\zeta\beta} \tag{94}$$

where

$$\kappa = \sqrt{4\beta^4+4\beta^2-8\zeta\beta+1} \tag{95}$$

Among the above three solutions, any one of the two solutions given in Eq. (94) turns out be more useful. In order to obtain the relationship between ζ and β so that $|G|_{max}=1$, it is required to relate the expression of $\cos(\theta/3)$ in Eq. (94) to the expression of $\cos(\theta)$ in Eq. (54). Using the identity

$$\cos(\theta) = 4\cos^3(\theta/3) - 3\cos(\theta/3) \tag{96}$$

and substituting the expression of $\cos(\theta)$ from Eq. (54) and $\cos(\theta/3)$ from Eq. (94), we have

$$\begin{aligned}&4(4\beta-\kappa\beta)\zeta^2+(2\kappa-4\beta^2\kappa-8\beta^4-2)\zeta-4\beta^3-\beta-2\beta^3\kappa-4\beta^5\\&\quad-\kappa\beta=0\end{aligned} \tag{97}$$

or

$$\kappa = -\frac{(8\beta^4+2)\zeta+4\beta^5+4\beta^3+\beta-16\zeta^2\beta}{4\zeta^2\beta+(4\beta^2-2)\zeta+2\beta^3+\beta} \tag{98}$$

Equating the right-hand sides of Eqs. (95) and (98) and simplifying we have

$$\begin{aligned}&16\zeta^4\beta^2+(14\beta-8\beta^5+24\beta^3)\zeta^3+(-4\beta^2-8\beta^4-2-16\beta^6)\zeta^2\\&\quad-(9\beta+14\beta^3+8\beta^7+12\beta^5)\zeta+1+5\beta^2+8\beta^4+4\beta^6=0\end{aligned} \tag{99}$$

The two real and positive solutions of ζ of the preceding equation are given by

$$\zeta = (\sqrt{2+\beta^2} - \beta)/2 \tag{100}$$

or

$$\zeta = (4\beta^4 + 4\beta^2 + 1)/8\beta \tag{101}$$

If the expression of $\cos(\theta)$ in Eq. (93) was used in place of that in Eq. (94), then one would obtain only the condition in Eq. (100). The expression of $\cos(\theta)$ in Eq. (94) was selected because it produces more general results. Interestingly, the condition given in Eq. (100) was also identified as the condition for the existence of the maximum value of the frequency response function in Eq. (88). The value of ζ given in Eqs. (100) and (101) are shown in Fig. 7. Equation (100) is valid when $\beta \leqslant \frac{1}{2}\sqrt{2\sqrt{5}-4}$ and Eq. (101) is valid when $\beta > \frac{1}{2}\sqrt{2\sqrt{5}-4}$. From this analysis, we have the following fundamental result:

THEOREM 5.7. *The maximum amplitude of the normalized frequency response function of a nonviscously damped oscillator will be more than 1 if and only if* $\zeta < (\sqrt{2+\beta^2}-\beta)/2$ *when* $\beta \leqslant \frac{1}{2}\sqrt{2\sqrt{5}-4}$ *and* $\zeta < (4\beta^4+4\beta^2+1)/8\beta$ *when* $\beta \geqslant \frac{1}{2}\sqrt{2\sqrt{5}-4}$.

From this result, one practical question that naturally arises is, What is the critical value of ζ below which the maximum amplitude of the normalized frequency response function will always be more than 1? To answer this question, we look for the minimum value of ζ given by Eq. (101). Differentiating Eq. (101) with respect to β, the optimal value can be obtained from

$$\frac{4\beta^2 + 12\beta^4 - 1}{8\beta^2} = 0 \tag{102}$$

The only real and positive solution of this equation is

$$\beta = \frac{1}{\sqrt{6}} \tag{103}$$

Substituting this value of β in Eq. (101), the optimal value of ζ can be obtained as

$$\zeta = 2\sqrt{6}/9 \tag{104}$$

From this discussion we have the following theorem:

THEOREM 5.8. *The maximum amplitude of the normalized frequency response function of a nonviscously damped oscillator will be more than 1 if* $\zeta < 2\sqrt{6}/9$.

The converse statement of Theorem 5.8 is, however, not always true. The value of $|G|_{\max}$ can be more than 1 even if $\zeta > 2\sqrt{6}/9$, as can be seen in region C in Fig. 7.

6 Simplified Analysis of the Frequency Response Function

Dynamic characteristics of the frequency response function of a nonviscously damped SDOF system have been elucidated in the previous section. The frequency at which the amplitude of the frequency response function reaches its maximum value can be obtained from Eq. (58). Although this is an exact expression, it is difficult to gain much physical insight due to its complexity. Here, we derive some simple expressions considering that ζ and β are small.

In Fig. 6, it was noted that for a wide range of values of ζ and β, the amplitude of the frequency response function reaches its maximum value when the normalized excitation frequency is close to 1. For this reason, we assume that

$$x_{\max} = 1 - \delta \tag{105}$$

Substituting this in place of x in Eq. (49) and simplifying, one obtains:

$$\beta^4\delta^3 + (-2\beta^4 + 2\beta^3\zeta - 2\beta^2)\delta^2 + (\beta^4 + 2\beta^2 - 4\beta^3\zeta - 4\zeta\beta + 1)\delta + 2\zeta\beta + 2\beta^3\zeta - 2\zeta^2 = 0 \tag{106}$$

This is a cubic equation in δ, which needs to be solved to obtain the frequency where $|G|^2$ reaches its maximum value. Since δ is expected to be small for small values of ζ and β, neglecting the coefficients associated with δ^2 and δ^3 in Eq. (106) and solving the resulting linear equation we obtain

$$\delta \approx \frac{2\zeta^2 - 2\zeta\beta(1+\beta^2)}{(1+\beta^2)(1+\beta^2-4\zeta\beta)} \tag{107}$$

Substituting δ in Eq. (105), the frequency corresponding to the maximum value of the amplitude of the frequency response function can be approximately obtained as

$$\tilde{\omega}_{\max} = \sqrt{x_{\max}} = \frac{\omega_{\max}}{\omega_n} \approx \sqrt{1 - \frac{2\zeta^2 - 2\zeta\beta(1+\beta^2)}{(1+\beta^2)(1+\beta^2-4\zeta\beta)}} \tag{108}$$

For the special case when only viscous damping is present, substituting $\beta=0$ in Eq. (108), one obtains $\tilde{\omega}_{\max} = \sqrt{1-2\zeta^2}$, which is well known for viscously damped systems.

Substituting $x = x_{\max}$ from (105) into the expression of $|G|^2$ in Eq. (44) and retaining only up to quadratic terms in δ, one has

$$|G|^2_{\max} \approx \frac{1+\beta^2-\beta^2\delta}{4\zeta^2 + (4\zeta\beta - 4\zeta^2)\delta + (\beta^2 + 1 - 4\zeta\beta)\delta^2} \tag{109}$$

Substituting δ from (107) into the preceding equation and retaining only up to cubic terms in β, one has

$$|G|_{\max} \approx \frac{1}{2\zeta}\sqrt{\frac{(1+\beta^2)}{(1+2\beta^2)}\frac{(1-4\zeta\beta+(3-2\zeta^2)\beta^2-6\beta^3\zeta)}{(1-2\zeta\beta-\zeta^2)}} \tag{110}$$

For the special case when only viscous damping is present, substituting $\beta=0$ in Eq. (110) results in the exact corresponding expression $|G|_{\max} = 1/(2\zeta\sqrt{1-\zeta^2})$, as given in Eq. (42). To verify the accuracy of the approximate formulas (108) and (110), we calculate the percentage error with respect to the exact solutions obtained in the previous section. The percentage error is calculated, for example, as

$$100 \times \frac{(\tilde{\omega}_{\max})_{\text{exact}} - (\tilde{\omega}_{\max})_{\text{approx}}}{(\tilde{\omega}_{\max})_{\text{exact}}} \tag{111}$$

Figures 8 and 9, respectively, show the contours of percentage errors arising due to the use of approximate Eqs. (108) and (110).

For $\tilde{\omega}_{\max}$ calculated from Eq. (108), the error is less than 2% when $\zeta, \beta \leqslant 0.5$. The error in the calculation of $|G|_{\max}$ from Eq.

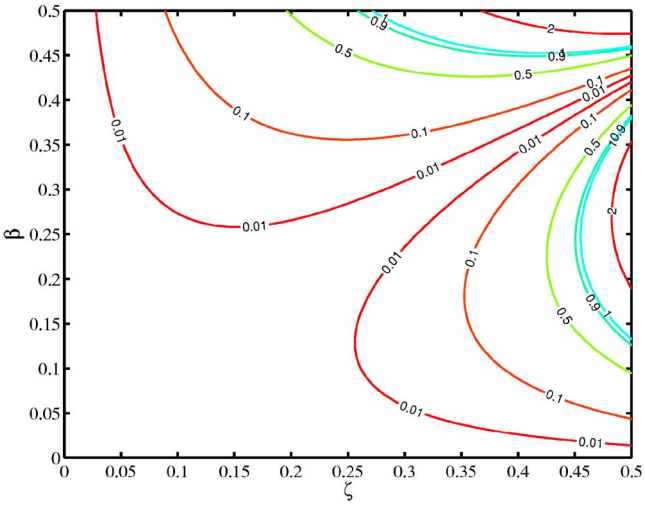

Fig. 8 Contours of percentage error in the approximate calculation of $\omega_{\max}/\omega_n$ from Eq. (108) as a function of ζ and β

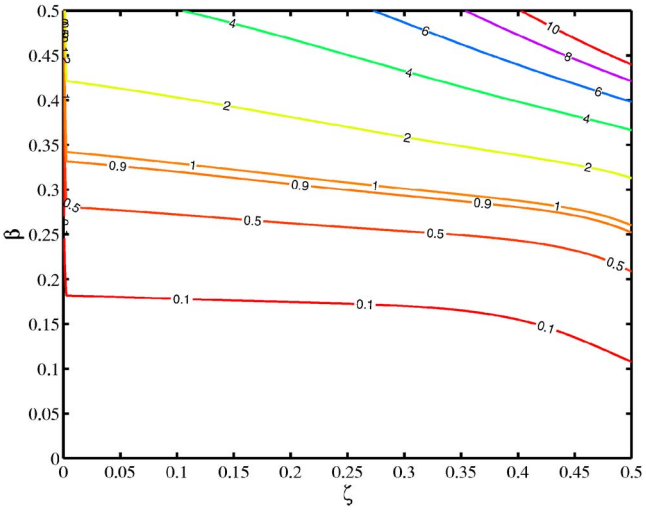

Fig. 9 Contours of percentage error in the approximate calculation of $|G|_{max}$ from Eq. (110) as a function of ζ and β

(110) is somewhat more. When $\zeta, \beta \approx 0.5$, the error is close to 10%. From Fig. 9, it can be observed that the error in the calculation of $|G|_{\max}$ increases with the increasing values of β, but it is relatively insensitive with respect to ζ.

The approximate expressions (108) and (110) will break down if $\zeta > \zeta_{mL}$ and $\beta > \beta_{mU}$. For such parameter values, it is not possible to extend a perturbation type method based on a viscous damped system, as proposed here. Nevertheless, if a system is moderately nonviscously damped (say $\beta < 0.5$), the dynamics can be explained using the proposed approximations (108) and (110).

7 Summary and Concluding Remarks

Dynamic response characteristics of a nonviscously damped linear single-degree-of-freedom oscillator have been discussed. The nonviscous damping force was expressed by a viscoelastic type exponentially fading memory kernel. It was shown that the dynamic response properties of the oscillator are governed by two nondimensional factors; namely, the viscous damping factor ζ and the nonviscous damping factor β. The system considered reduces to the classical viscously damped oscillator when the nonviscous damping factor is zero. Several fundamental properties that characterize the dynamic response of a nonviscously damped oscillator have been discovered. A nonviscously damped oscillator has three eigenvalues, one of which is always nonoscillating in nature. The conditions for the occurrence of the maximum value of the amplitude of the dynamic response were reviewed. The characteristics of the driving frequency corresponding to the maximum amplitude of the frequency response function and the value of the maximum response amplitude were discussed in detail. The main findings of the paper are:

1. A nonviscously damped oscillator will have oscillatory motions if $\zeta < 4/(3\sqrt{3})$ or $\beta > 1/(3\sqrt{3})$.
2. If $\beta < 1/(3\sqrt{3})$, the oscillator will have oscillatory motions if and only if $\zeta \notin [\zeta_L, \zeta_U]$. ζ_L and ζ_U given in Eqs. (26) and (27) are the lower and upper critical damping factors, respectively.
3. The amplitude of the frequency response function of a nonviscously damped oscillator can reach a maximum value if $\zeta < \frac{1}{2}\sqrt{\sqrt{5}-1}$ or $\beta > \frac{1}{2}\sqrt{3\sqrt{3}-4}$.
4. If $\zeta < \frac{1}{2}\sqrt{\sqrt{5}-1}$ or $\beta > \frac{1}{2}\sqrt{3\sqrt{3}-4}$, then the amplitude of the frequency response function of a nonviscously damped oscillator reaches a maximum value when the driving frequency $\omega = \omega_n\{\sqrt{(1+2\zeta\beta+\beta^2)[2\cos(\theta/3)+1]/3-1}\}/\beta$.
5. The maximum amplitude of the frequency response function (if it exists) of a nonviscously damped oscillator will occur below the undamped natural frequency if and only if $\zeta < 5/8$ and $\beta < 1/2$.
6. The maximum amplitude of the frequency response function (if it exists) of a nonviscously damped oscillator will occur above the undamped natural frequency if $\zeta > 5/8$ or $\zeta < \beta(1+\beta^2)$ and $\beta > 1/2$ or $\beta > (\xi^2 - 12)/6\xi$.
7. If $\zeta \leqslant \frac{1}{2}\sqrt{\sqrt{5}-1}$ and $\beta \leqslant \frac{1}{2}\sqrt{2\sqrt{5}-4}$, the amplitude of the frequency response function of a nonviscously damped oscillator can reach a maximum value if and only if $\zeta < (\sqrt{2+\beta^2} - \beta)/2$ or $\beta < (1-2\zeta^2)/2\zeta$.
8. For a given value of ζ, the maximum amplitude of the frequency response function (if it exists) of a nonviscously damped oscillator increases with increasing values of β.
9. The maximum amplitude of the normalized frequency response function of a nonviscously damped oscillator will be more than 1 if and only if $\zeta < (\sqrt{2+\beta^2} - \beta)/2$ when $\beta \leqslant \frac{1}{2}\sqrt{2\sqrt{5}-4}$ and $\zeta < (4\beta^4 + 4\beta^2 + 1)/8\beta$ when $\beta \geqslant \frac{1}{2}\sqrt{2\sqrt{5}-4}$.
10. The maximum amplitude of the normalized frequency response function of a nonviscously damped oscillator will be more than 1 if $\zeta < 2\sqrt{6}/9$.

Using these results, one can understand the nature of the dynamic response without actually solving the problem. These concepts will be particularly useful in dealing with multiple-degree-of-freedom systems. The studies reported in this paper show that the classical concepts based on viscously damped oscillators can be extended to nonviscously damped systems only under certain conditions. In general, if $\beta > \frac{1}{2}\sqrt{3\sqrt{3}-4}$, the dynamic response characteristics will be significantly different from a classical viscously damped oscillator. The results derived in this paper are expected to be valid for a proportionally damped multiple-degree-of-freedom system with a single exponential kernel. However, formal results are necessary in this direction. Further research is needed to extend these results to systems with multiple exponential kernels and nonproportional damping.

Acknowledgment

The author acknowledges the support of the Engineering and Physical Sciences Research Council (EPSRC) through the award of an advanced research fellowship, Grant No. GR/T03369/01.

References

[1] Woodhouse, J., 1998, "Linear Damping Models for Structural Vibration," J. Sound Vib., **215**(3), pp. 547–569.
[2] Bagley, R. L., and Torvik, P. J., 1983, "Fractional Calculus—a Different Approach to the Analysis of Viscoelastically Damped Structures," AIAA J., **21**(5), pp. 741–748.
[3] Torvik, P. J., and Bagley, R. L., 1987, "Fractional Derivatives in the Description of Damping: Materials and Phenomena," The Role of Damping in Vibration and Noise Control, ASME Report No. DE-5.
[4] Gaul, L., Klein, P., and Kemple, S., 1991, "Damping Description Involving Fractional Operators," Mech. Syst. Signal Process., **5**(2), pp. 81–88.
[5] Maia, N. M. M., Silva, J. M. M., and Ribeiro, A. M. R., 1998, "On a General Model for Damping," J. Sound Vib., **218**(5), pp. 749–767.
[6] Bland, D. R., 1960, *Theory of Linear Viscoelasticity*, Pergamon Press, London.
[7] Christensen, R. M., 1982, *Theory of Viscoelasticity*, 1st ed., Academic Press, New York (reprinted by Dover Publication Inc., 2003, 2nd ed.).
[8] Biot, M. A., 1955, "Variational Principles in Irreversible Thermodynamics With Application to Viscoelasticity," Phys. Rev., **97**(6), pp. 1463–1469.
[9] Muravyov, A., and Hutton, S. G., 1997, "Closed-Form Solutions and the Eigenvalue Problem for Vibration of Discrete Viscoelastic Systems," ASME J. Appl. Mech., **64**, pp. 684–691.
[10] Muravyov, A., and Hutton, S. G., 1998, "Free Vibration Response Characteristics of a Simple Elasto-hereditary System," ASME J. Vibr. Acoust., **120**(2), pp. 628–632.
[11] Palmeri, A., Ricciardelli, F., Luca, A. D., and Muscolino, G., 2003, "State Space Formulation for Linear Viscoelastic Dynamic Systems With Memory," J. Eng. Mech., **129**(7), pp. 715–724.
[12] Palmeri, A., Ricciardelli, F., Muscolino, G., and Luca, A. D., 2004, "Random

Vibration of Systems With Viscoelastic Memory," J. Eng. Mech., **130**(9), pp. 1052–1061.
[13] Wagner, N., and Adhikari, S., 2003, "Symmetric State-Space Formulation for a Class of Non-viscously Damped Systems," AIAA J., **41**(5), pp. 951–956.
[14] Adhikari, S., and Wagner, N., 2003, "Analysis of Asymmetric Non-viscously Damped Linear Dynamic Systems," ASME J. Appl. Mech., **70**(6), pp. 885–893.
[15] Cremer, L., and Heckl, M., 1973, *Structure-Borne Sound*, 2nd ed., Springer-Verlag, Berlin, Germany (translated by E. E. Ungar).
[16] Adhikari, S., and Woodhouse, J., 2001, "Identification of Damping: Part, 2, Non-viscous Damping," J. Sound Vib., **243**(1), pp.63–88.
[17] McTavish, D. J., and Hughes, P. C., 1993, "Modeling of Linear Viscoelastic Space Structures," ASME J. Vibr. Acoust., **115**, pp. 103–110.
[18] Adhikari, S., 2002, "Dynamics of Non-viscously Damped Linear Systems," J. Eng. Mech., **128**(3), pp. 328–339.
[19] Adhikari, S., 2005, "Qualitative Dynamic Characteristics of a Non-viscously Damped Oscillator," Proc. R. Soc. London, Ser. A, **461**,(2059), pp. 2269–2288.
[20] Adhikari, S., and Woodhouse, J., 2003, "Quantification of Non-viscous Damping in Discrete Linear Systems," J. Sound Vib., **260**(3), pp. 499–518.
[21] Abramowitz, M., and Stegun, I. A., 1965, *Handbook of Mathematical Functions, With Formulas, Graphs, and Mathematical Tables*, Dover Publications, New York.
[22] Muller, P., 2005, "Are the Eigensolutions of a 1-d.o.f. System With Viscoelastic Damping Oscillatory or Not?," J. Sound Vib., **285**(1–2), pp. 501–509.
[23] Vinokur, R., 2003, "The Relationship Between the Resonant and Natural Frequency for Non-viscous Systems," J. Sound Vib., **267**, pp. 187–189.
[24] Dickson, L. E., 1898, "A New Solution of the Cubic Equation," Am. Math. Monthly, **5**, pp. 38–39.

Analytical Solutions for Translational Motion of Spinning-Up Rigid Bodies Subject to Constant Body-Fixed Forces and Moments

Mohammad A. Ayoubi
Ph.D. Candidate
e-mail: maayoubi@purdue.edu

James M. Longuski
Professor
e-mail: longuski@purdue.edu

School of Aeronautics and Astronautics,
Purdue University,
West Lafayette, IN 47907-2023

The problem of a spinning, axisymmetric, or nearly axisymmetric rigid body subject to constant body-fixed forces and moments about three axes is considered. Approximate closed-form analytical solutions are derived for velocity and for the transverse displacement. The analytical solutions are valid when the excursion of the spin axis with respect to an inertially fixed direction is small (which is usually the case for spin-stabilized spacecraft and rockets). Numerical simulations confirm that the solutions are highly accurate when applied to typical motion of a spacecraft, such as the Galileo.
[DOI: 10.1115/1.2755110]

1 Introduction

In rigid-body dynamics, there is a rich history of analytical solutions, much of which is well represented in the treatise by Leimanis [1]. The analytical work on rocket and spacecraft problems goes back to Rosser [2] and continues to modern works on spacecraft dynamics [1,3–52]. The early dynamicists had no access to computers and devoted great effort into finding integrals of the motion and to reducing the dynamics problem to "quadrature integrals." The idea of a quadrature integral is to find the square area under a given curve or function. Once a problem has been reduced to quadratures, it is possible to tabulate its value over the range of integration. Such tabulation could be accomplished by simple numerical integrations that can be made arbitrarily accurate. Mathematical handbooks are replete with examples of famous quadrature integrals, such as Jacobian elliptic functions, Fresnel integrals, Bessel functions, and error functions.

One of the advantages of a closed-form analytical solution is to help scientists and engineers to perform parametric studies. Although it is straightforward to numerically solve the equations of motion governing a rigid body subject to moments and forces, it is not easy to determine how uncertainties in geometric parameters, in mass properties, and in related parameters affect the solution and the *final conditions*. Longuski and Kia [26] provide an example of such a study that is facilitated by the availability of an analytical solution for the motion of the angular momentum vector. (Their study took advantage of the fact that the final state of the angular momentum vector is known from the analytical solution, and hence, no numerical integration is required to determine perturbed final states due to change in a variety of parameters, such as the mass properties, the applied torques, and the initial conditions. When the time of the final state is long, the power of this approach is significant.) In addition, the displacement solution may be important during formation flying, operations near a shuttle or a space station, and in maneuver analysis.

In this paper, we use the results of Ayoubi and Longuski [50,51] to find the analytical solutions for the transverse velocity and displacement of a spinning rigid body. We assume that the body-fixed forces and moments, and mass properties are constant. Thus for axisymmetric or nearly axisymmetric rigid bodies, the spin rate increases linearly with time. In addition, it is assumed that the spin axis of the rigid body corresponds to either the maximum or minimum principal moment of inertia. We present approximate closed-form solutions for transverse velocity and displacement and outline the corresponding solution for axial velocity. The results are valid for axisymmetric, nearly axisymmetric, and under certain conditions, for asymmetric rigid bodies.

2 Euler's Equations of Motion

The motion of a rigid body is governed by Euler's equations of motion [53], which can be written as

$$\dot{\omega}_x(t) = \frac{M_x}{I_x} - \left[\frac{I_z - I_y}{I_x}\right]\omega_y\omega_z \tag{1}$$

$$\dot{\omega}_y(t) = \frac{M_y}{I_y} - \left[\frac{I_x - I_z}{I_y}\right]\omega_z\omega_x \tag{2}$$

$$\dot{\omega}_z(t) = \frac{M_z}{I_z} - \left[\frac{I_y - I_x}{I_z}\right]\omega_x\omega_y \tag{3}$$

where ω_x, ω_y, and ω_z are components of the absolute angular velocity of the rigid body in the body-fixed reference frame; M_x, M_y, and M_z are body-fixed moments, and I_x, I_y, and I_z are principal moments of inertia about the x-, y-, and z-axes of the body-fixed reference frame, respectively. We assume throughout that the body-fixed moments are constant and the body is spun up (or down) about the maximum or minimum moment of inertia axis. (The assumption of constant forces and constant moments is often reasonable in spacecraft applications because most thrusters operate in a bang-bang mode in which maximum thrust is achieved in a few tens of milliseconds and remains constant until shut down [54]. In order to develop a more sophisticated model, we can make use of the work of Longuski and Tsiotras [35] and Tsiotras and Longuski [36], which employs polynomial functions of time to represent the thrust.) For axisymmetric, nearly axisymmetric, or asymmetric rigid bodies where the product $\omega_x\omega_y$ is small enough, Eqs. (1)–(3) can be simplified as

$$\dot{\omega}_x(t) = \frac{M_x}{I_x} - \left[\frac{I_z - I_y}{I_x}\right]\omega_y\omega_z \tag{4}$$

Contributed by the Applied Mechanics Division of ASME for publication in the JOURNAL OF APPLIED MECHANICS. Manuscript received April 10, 2006; final manuscript received May 3, 2007; published online January 11, 2008. Review conducted by Oliver M. O'Reilly.

$$\dot{\omega}_y(t) = \frac{M_y}{I_y} - \left[\frac{I_x - I_z}{I_y}\right]\omega_z\omega_x \tag{5}$$

$$\dot{\omega}_z(t) \approx \frac{M_z}{I_z} \tag{6}$$

By integrating Eq. (6) and assuming that the axial moment, M_z, is constant, we obtain

$$\omega_z(t) \approx \left(\frac{M_z}{I_z}\right)t + \omega_{z0},\ \omega_{z0} \triangleq \omega_z(0) \tag{7}$$

which is, of course, exact for axisymmetric rigid bodies. For the case of asymmetric bodies, our assumption of $[(I_y - I_x)/I_z]\omega_x\omega_y$ being "small enough" is highly dependent on the application.

3 Kinematic Equations

By using a Type I: 3-1-2 Euler angle sequence [54], which relates the orientation of the body-fixed reference frame to the inertial reference frame, the kinematic equations can be written as follows:

$$\dot{\phi}_x = \omega_x \cos\phi_y + \omega_z \sin\phi_y \tag{8}$$

$$\dot{\phi}_y = \omega_y - (\omega_z \cos\phi_y - \omega_x \sin\phi_y)\tan\phi_x \tag{9}$$

$$\dot{\phi}_z = (\omega_z \cos\phi_y - \omega_x \sin\phi_y)\sec\phi_x \tag{10}$$

where ϕ_x, ϕ_y, and ϕ_z are the Eulerian angles. With the assumptions that ϕ_x and ϕ_y are small and that $\phi_y\omega_x$ is small compared to ω_z, Eqs. (8)–(10) can be simplified as

$$\dot{\phi}_x = \omega_x + \omega_z\phi_y \tag{11}$$

$$\dot{\phi}_y = \omega_y - \phi_x\omega_z \tag{12}$$

$$\dot{\phi}_z = \omega_z \tag{13}$$

After substituting Eq. (13) into Eq. (6) and integrating, we obtain

$$\phi_z = \frac{1}{2}\frac{M_z}{I_z}t^2 + \omega_{z0}t + \phi_{z0},\quad \phi_{z0} \triangleq \phi_z(0) \tag{14}$$

4 Inertial Acceleration Equation

In the presence of constant body-fixed forces f_x, f_y, and f_z, the rigid body will accelerate with respect to the inertial reference frame. The following equation relates the acceleration in the body-reference frame with respect to the inertial reference frame:

$$\begin{Bmatrix} \dot{v}_X(t) \\ \dot{v}_Y(t) \\ \dot{v}_Z(t) \end{Bmatrix} = [A]_{312}\begin{Bmatrix} \frac{f_x}{m} \\ \frac{f_y}{m} \\ \frac{f_z}{m} \end{Bmatrix} \tag{15}$$

where $[A]_{312}$ is the direction cosine matrix

$$[A]_{312} = \begin{bmatrix} c\phi_z c\phi_y - s\phi_z s\phi_x s\phi_y & -s\phi_z c\phi_x & c\phi_z s\phi_y + s\phi_z s\phi_x c\phi_y \\ s\phi_z c\phi_y + c\phi_z s\phi_x s\phi_y & c\phi_z c\phi_x & s\phi_z s\phi_y - c\phi_z s\phi_x c\phi_y \\ -c\phi_x s\phi_y & s\phi_x & c\phi_x c\phi_y \end{bmatrix} \tag{16}$$

When ϕ_x and ϕ_y are small, the direction cosine matrix can be simplified as

$$[A]_{312} \approx \begin{bmatrix} c\phi_z & -s\phi_z & \phi_y c\phi_z + \phi_x s\phi_z \\ s\phi_z & c\phi_z & \phi_y s\phi_z - \phi_x c\phi_z \\ -\phi_y & \phi_x & 1 \end{bmatrix} \tag{17}$$

By introducing the complex functions [1,5,25]

$$\phi = \phi_x(t) + i\phi_y(t) \tag{18}$$

$$v(t) = v_X(t) + iv_Y(t) \tag{19}$$

$$f = f_x + if_y \tag{20}$$

and using the first two rows of Eq. (15), the transverse acceleration can be written in the following compact form:

$$\dot{v}(t) = e^{i\phi_z(t)}\left[\frac{f}{m} - \frac{if_z}{m}\phi(t)\right] \tag{21}$$

and the last row of Eq. (15) gives

$$\dot{v}_Z(t) = \frac{f_z}{m} + \left(\frac{i}{2m}\right)[\bar{f}\phi(t) - f\bar{\phi}(t)] \tag{22}$$

Before integrating Eq. (21) and finding the transverse velocity solution, we need to know the closed-form solutions for $\phi_z(t)$ and $\phi(t)$, which are given in Ref. [44]. Because the closed-form solutions for the Euler angles are the basis of the transverse velocity solution, in Sec. 5 we provide a brief review of those results.

5 Closed-Form Analytical Solution for the Eulerian Angles

In this solution for the Eulerian angles, the body-fixed moments, M_x, M_y, and M_z are assumed constant. By substituting a new variable τ,

$$\tau(t) \triangleq \omega_z = \left(\frac{M_z}{I_z}\right)t + \omega_{z0},\quad \tau(0) \triangleq \omega_{z0} \tag{23}$$

into Eq. (13) and integrating with respect to τ, $\phi_z(\tau)$ can be obtained as

$$\phi_z(\tau) = \frac{\lambda}{2}(\tau^2 - \tau_0^2) + \phi_{z0} \tag{24}$$

where λ is defined as

$$\lambda \triangleq \frac{I_z}{M_z} \tag{25}$$

It can be shown that Eqs. (1) and (2) can be combined and written in the following complex form:

$$\phi'(\tau) + i\lambda\tau\phi(\tau) = \lambda\omega(\tau) \tag{26}$$

where the complex function $\omega(\tau)$ is defined as

$$\omega(\tau) = \omega_x(\tau) + i\omega_y(\tau) \tag{27}$$

Equation (26) is a first-order nonhomogeneous differential equation with a variable coefficient. It can be shown that the solution is given by Tsiotras and Longuski [33] as

$$\phi(\tau) = \phi(\tau_0)e^{-i\lambda(\tau^2-\tau_0^2)/2} + \lambda e^{(-i\lambda\tau^2/2)}I_\phi(\tau_0,\tau;\lambda,\rho) \tag{28}$$

where

$$I_\phi(\tau_0,\tau;\lambda,\rho) \triangleq \int_{\tau_0}^{\tau} e^{(i\lambda u^2/2)}\omega(u)du \tag{29}$$

$$I_\phi(\tau_0,\tau;\lambda,\rho) = k_1 I_{\phi 1}(\tau_0,\tau;\lambda,\rho) + k_2 I_{\phi 2}(\tau_0,\tau;\kappa,\rho) \tag{30}$$

$$k_1 \triangleq \frac{\sqrt{|k_x|} + \sqrt{|k_y|}}{2k},\quad k_2 \triangleq \frac{\sqrt{|k_x|} - \sqrt{|k_y|}}{2k} \tag{31}$$

$$k_x \triangleq \frac{I_z - I_y}{I_x}, \quad k_y \triangleq \frac{I_z - I_x}{I_y} \tag{32}$$

$$k \triangleq \sqrt{k_x k_y} \tag{33}$$

where k represents the mass properties of the rigid body and $I_{\phi 2}$ provides the contribution from an asymmetric body

$$I_{\phi 1}(\tau_0, \tau; \lambda, \rho) \triangleq \int_{\tau_0}^{\tau} e^{(i\lambda u^2/2)} \Omega(u) du \tag{34}$$

$$I_{\phi 2}(\tau_0, \tau; \kappa, \rho) \triangleq \int_{\tau_0}^{\tau} e^{(i\lambda u^2/2)} \bar{\Omega}(u) du \tag{35}$$

where the bar denotes complex conjugate. We see that the integrals $I_{\phi 1}$ and $I_{\phi 2}$ have $\Omega(u)$ in the integrand, which represents the solution for Euler's equations of motion

$$\Omega(u) = \Omega_x(u) + i\Omega_y(u) \tag{36}$$

$$\Omega_x(u) \triangleq \omega_x(u)\sqrt{|k_y|}, \quad \Omega_y(u) \triangleq \omega_y(u)\sqrt{|k_x|} \tag{37}$$

$$I_{\phi 1}(\tau_0, \tau; \lambda, \rho) = [\Omega(\tau_0) e^{(-i\rho\tau_0^2/2)} - F\bar{I}_{u0}(\tau_0; \rho)]\bar{I}_{u0}(\tau_0, \tau; -\mu) + FJ_{u0}(\tau_0, \tau; \mu, \rho) \tag{38}$$

$$I_{\phi 2}(\tau_0, \tau; \kappa, \rho) = [\bar{\Omega}(\tau_0) e^{(i\rho\tau_0^2/2)} - \bar{F}I_{u0}(\tau_0; \rho)]I_{u0}(\tau_0, \tau; \kappa) + \bar{F}\bar{J}_{u0}(\tau_0, \tau; -\kappa, \rho) \tag{39}$$

$$\rho \triangleq k\lambda, \quad \mu \triangleq \lambda + \rho = \lambda(1+k), \quad \kappa \triangleq \lambda - \rho = \lambda(1-k) \tag{40}$$

Here, we observe that $I_{\phi 1}$ and $I_{\phi 2}$ depend ultimately on the Fresnel integral

$$I_{u0}(\tau_0, \tau; \lambda) \triangleq \int_{\tau_0}^{\tau} e^{(i\lambda u^2/2)} du \tag{41}$$

$$F = F_x + iF_y \tag{42}$$

where F represents the constant transverse body-fixed torque

$$F_x \triangleq \left(\frac{M_x}{I_x}\right)\left(\frac{I_z}{M_z}\right)\sqrt{|k_y|} \tag{43}$$

$$F_y \triangleq \left(\frac{M_y}{I_y}\right)\left(\frac{I_z}{M_z}\right)\sqrt{|k_x|} \tag{44}$$

and where J_{u0} is an integral of the Fresnel integral

$$J_{u0}(\tau_0, \tau; \mu, \rho) \triangleq \int_{\tau_0}^{\tau} e^{(i\mu u^2/2)} \bar{I}_{u0}(u; \rho) du \tag{45}$$

which we analyze later. Now, having found closed-form solutions for the Eulerian angles, we proceed to find the transverse velocity solution in Sec. 6.

6 Transverse Velocity Solution

Before integrating Eq. (21), we will find it useful to replace the variable t with τ by multiplying both sides of Eq. (21) by $dt/d\tau$ as follows:

$$\frac{dv}{d\tau} = \frac{\lambda}{m} e^{i\phi_z(\tau)}[f - if_z\phi(\tau)] \tag{46}$$

After integration of both sides, we get

$$v(\tau) = v(\tau_0) + \frac{\lambda f}{m} T_{v11}(\tau_0, \tau; \lambda) - \frac{i\lambda f_z}{m} T_{v12}(\tau_0, \tau; \lambda) \tag{47}$$

where T_{v11} and T_{v12} are defined as

$$T_{v11}(\tau_0, \tau; \lambda) \triangleq \int_{\tau_0}^{\tau} e^{i\phi_z(u)} du \tag{48}$$

$$T_{v12}(\tau_0, \tau; \lambda) \triangleq \int_{\tau_0}^{\tau} e^{i\phi_z(u)} \phi(u) du \tag{49}$$

On the right-hand side of Eq. (47), the second and third terms represent the contribution of transverse and axial body-fixed forces on transverse velocity. In the case of spinning-up and spinning-down spacecraft maneuvers, when f_x or $f_y \neq 0$ and $f_z = 0$, the transverse velocity solution can be expressed very concisely in terms of Fresnel integrals Refs. [37,55,56]. The analytical solution for the thrusting spacecraft maneuver when $f_x = f_y = 0$ and $f_z \neq 0$ does not appear in the previous literature; we present the complete transverse velocity solution (for the general case of nonzero f_x, f_y, and f_z) in this section for the first time. The analytic solution for transverse velocity is complicated in the case of $f_z \neq 0$ and $f_x = f_y = 0$ because f_z is the only contributer to the acceleration, and the axial force must be accurately portrayed in its projection onto the inertial XY plane. Because of the dependency of the solution on the Eulerian angles and on the angular velocity solutions, the analytical solution for transverse velocity breaks down when the solutions for the Eulerian angles and angular velocities break down.

By substituting Eq. (24) into Eq. (48), T_{v11} can be written in the following form:

$$T_{v11}(\tau_0, \tau; \lambda) = e^{i(\phi_{z0} - \lambda\tau_0^2/2)} I_{u0}(\tau_0, \tau; \lambda) \tag{50}$$

where

$$I_{u0}(u; \lambda) = \sqrt{\frac{\pi}{|\lambda|}}\, \mathrm{sgn}(u) \tilde{E}\left(\sqrt{\frac{|\lambda|}{\pi}} u\right) \tag{51}$$

$$\tilde{E}\left(\sqrt{\frac{|\lambda|}{\pi}} u\right) = \begin{cases} E\left(\sqrt{\dfrac{|\lambda|}{\pi}} u\right) & \text{when} \quad \lambda < 0 \\ \bar{E}\left(\sqrt{\dfrac{|\lambda|}{\pi}} u\right) & \text{when} \quad \lambda \geq 0 \end{cases} \tag{52}$$

and

$$E(x) \triangleq \int_0^x e^{(-i\pi u^2/2)} du \tag{53}$$

is the complex Fresnel integral. The sgn(.) symbol in Eq. (51) represents the signum function, which is $\mathrm{sgn}(x) = 1$ for $x \geq 0$ and $\mathrm{sgn}(x) = -1$ for $x < 0$.

Substituting Eqs. (24) and (28) into Eq. (49) (after some algebra) provides

$$T_{v12}(\tau_0, \tau; \lambda) = \phi(\tau_0) e^{i\phi_{z0}}(\tau - \tau_0) + \lambda e^{i(\phi_{z0} - \lambda\tau_0^2/2)} T_{v21}(\tau_0, \tau; \lambda, \rho) \tag{54}$$

where

$$T_{v21}(\tau_0, \tau; \lambda, \rho) \triangleq \int_{\tau_0}^{\tau} I_{\phi}(\tau_0, u; \lambda, \rho) du \tag{55}$$

Substituting Eq. (30) into Eq. (55), yields

$$T_{v21}(\tau_0, \tau; \lambda, \rho) = k_1 T_{v31}(\tau_0, \tau; \lambda, \rho) + k_2 T_{v32}(\tau_0, \tau; \kappa, \rho) \tag{56}$$

where T_{v31} and T_{v32} are defined as

$$T_{v31}(\tau_0, \tau; \lambda, \rho) \triangleq \int_{\tau_0}^{\tau} I_{\phi 1}(\tau_0, u; \lambda, \rho) du \tag{57}$$

$$T_{v32}(\tau_0,\tau;\kappa,\rho) \triangleq \int_{\tau_0}^{\tau} I_{\phi 2}(\tau_0,u;\kappa,\rho)du \tag{58}$$

By integration by parts, we can show that T_{v31} and T_{v32} can be determined as

$$\begin{aligned} T_{v31}(\tau_0,\tau;\lambda,\rho) = {} & \pi I_{\phi 1}(\tau_0,\tau;\lambda,\rho) - \frac{F}{i\mu}[e^{i\mu\tau^2/2}\bar{I}_{u0}(\tau;\rho) \\ & - e^{i\mu\tau_0^2/2}\bar{I}_{u0}(\tau_0;\rho)] - (i\mu)^{-1}[\Omega_0 e^{-i\rho\tau_0^2/2} \\ & - F\bar{I}_{u0}(\tau_0;\rho)](e^{i\mu\tau^2/2} - e^{i\mu\tau_0^2/2}) + \frac{F}{i\mu}I_{u0}(\tau_0,\tau;\lambda) \end{aligned} \tag{59}$$

$$\begin{aligned} T_{v32}(\tau_0,\tau;\kappa,\rho) = {} & \pi I_{\phi 2}(\tau_0,\tau;\kappa,\rho) - \frac{\bar{F}}{i\kappa}[e^{i\kappa\tau^2/2}I_{u0}(\tau;\rho) \\ & - e^{i\kappa\tau_0^2/2}I_{u0}(\tau_0;\rho)] - (i\kappa)^{-1}[\bar{\Omega}_0 e^{i\rho\tau_0^2/2} - \bar{F}I_{u0}(\tau_0;\rho)] \\ & \times (e^{i\kappa\tau^2/2} - e^{i\kappa\tau_0^2/2}) + \frac{\bar{F}}{i\kappa}I_{u0}(\tau_0,\tau;\lambda) \end{aligned} \tag{60}$$

With T_{v31} and T_{v32}, the analytical closed-form transverse velocity solution is completed.

7 Transverse Displacement Solution

The displacement solution can be found by integrating the velocity equation, which is

$$v(\tau) = v(\tau_0) + \frac{\lambda f}{m}T_{v11}(\tau_0,\tau;\lambda) - \frac{i\lambda f_z}{m}T_{v12}(\tau_0,\tau;\lambda) \tag{61}$$

with respect to time. After integration, we obtain

$$\begin{aligned} d(\tau) = {} & d(\tau_0) + \lambda v(\tau_0)(\tau-\tau_0) + \frac{\lambda^2 f}{m}T_{d11}(\tau_0,\tau;\lambda) \\ & - \frac{i\lambda^2 f_z}{m}T_{d12}(\tau_0,\tau;\lambda) \end{aligned} \tag{62}$$

where

$$\begin{aligned} T_{d11}(\tau_0,\tau;\lambda,\rho) & \triangleq \int_{\tau_0}^{\tau} T_{v11}(\tau_0,u;\lambda)du \\ & = e^{i(\phi_{z0}-\lambda\tau_0^2/2)}\int_{\tau_0}^{\tau} Iu_0(\tau_0,u;\lambda)du \end{aligned} \tag{63}$$

$$\begin{aligned} T_{d12}(\tau_0,\tau;\lambda,\rho) & \triangleq \int_{\tau_0}^{\tau} T_{v12}(\tau_0,u;\lambda)du \\ & = \phi(\tau_0)e^{i\phi_{z0}}\frac{(\tau-\tau_0)^2}{2} + \lambda e^{i(\phi_{z0}-\lambda\tau_0^2/2)}T_{d22}(\tau_0,\tau;\lambda,\rho) \end{aligned} \tag{64}$$

$$\begin{aligned} T_{d22}(\tau_0,\tau;\lambda,\rho) & \triangleq \int_{\tau_0}^{\tau} T_{v21}(\tau_0,u;\lambda,\rho)du \\ & = k_1 T_{d31}(\tau_0,\tau;\lambda,\rho) + k_2 T_{d32}(\tau_0,\tau;\kappa,\rho) \end{aligned} \tag{65}$$

and

$$T_{d31}(\tau_0,\tau;\lambda,\rho) \triangleq \int_{\tau_0}^{\tau} T_{v31}(\tau_0,u;\lambda,\rho)du \tag{66}$$

$$T_{d32}(\tau_0,\tau;\kappa,\rho) \triangleq \int_{\tau_0}^{\tau} T_{v32}(\tau_0,u;\kappa,\rho)du \tag{67}$$

The contributions of the transverse forces and axial forces on transverse displacement are represented by the third and fourth terms on the right-hand side of Eq. (62), respectively. Like the velocity solution, both terms in Eq. (62) depend on the Eulerian angle and the angular velocity solutions so that the displacement analytical solution is valid when those solutions are valid. Equation (63) shows that the effect of transverse body-fixed forces on the transverse displacement can be written in terms of an integral of a Fresnel integral, resulting in a secular term. We are, of course, not surprised to see that the transverse displacement grows with time due to transverse force.

Using integration by parts, we can show that T_{d31} and T_{d32} can be determined as

$$\begin{aligned} T_{d31}(\tau_0,\tau;\lambda,\rho) = {} & [\Omega_0 e^{-i\rho\tau_0^2/2} - F\bar{I}_{u0}(\tau_0;\rho)]\Bigg[T_{d41}(\tau_0,\tau;\mu) \\ & - \frac{I_{u0}(\tau_0,\tau;\mu) - (\tau-\tau_0)e^{i\mu\tau_0^2/2}}{i\mu}\Bigg] \\ & + FT_{d42}(\tau_0,\tau;\mu,\rho) - \frac{F}{i\mu}[J_{u0}(\tau_0,\tau;\mu,\rho) - \bar{I}_{u0}(\tau_0;\rho) \\ & \times (\tau-\tau_0)e^{i\mu\tau_0^2/2}] - \frac{F}{i\mu}[-T_{d21}(\tau_0,\tau;\lambda) + I_{u0}(\tau_0;\lambda) \\ & \times (\tau-\tau_0)] \end{aligned} \tag{68}$$

and

$$\begin{aligned} T_{d32}(\tau_0,\tau;\kappa,\rho) = {} & [\bar{\Omega}_0 e^{i\rho\tau_0^2/2} - \bar{F}I_{u0}(\tau_0;\rho)]\Bigg[T_{d43}(\tau_0,\tau;\kappa) \\ & - \frac{I_{u0}(\tau_0,\tau;\kappa) - (\tau-\tau_0)e^{i\kappa\tau_0^2/2}}{i\mu}\Bigg] + \bar{F}T_{d44}(\tau_0,\tau;\kappa,\rho) \\ & - \frac{\bar{F}}{i\kappa}[J_{u0}(\tau_0,\tau;-\kappa,\rho) - I_{u0}(\tau_0;\rho)(\tau-\tau_0)e^{i\kappa\tau_0^2/2}] \\ & - \frac{\bar{F}}{i\kappa}[-T_{d21}(\tau_0,\tau;\lambda) + I_{u0}(\tau_0;\lambda)(\tau-\tau_0)] \end{aligned} \tag{69}$$

where

$$T_{d41}(\tau_0,\tau;\mu) \triangleq \int_{\tau_0}^{\tau} u\bar{I}_{u0}(\tau_0,u;-\mu)du \tag{70}$$

$$T_{d42}(\tau_0,\tau;\mu,\rho) \triangleq \int_{\tau_0}^{\tau} uJ_{u0}(\tau_0,u;\mu,\rho)du \tag{71}$$

$$T_{d43}(\tau_0,\tau;\kappa) \triangleq \int_{\tau_0}^{\tau} uI_{u0}(\tau_0,u;\kappa)du \tag{72}$$

$$T_{d44}(\tau_0,\tau;\kappa,\rho) \triangleq \int_{\tau_0}^{\tau} u\bar{J}_{u0}(\tau_0,u;-\kappa,\rho)du \tag{73}$$

After some manipulations, it can be shown that T_{d41}, T_{d42}, T_{d43}, and T_{d44} can be written in terms of our "elementary functions," I_{u0} and J_{u0}, as follows:

$$T_{d41}(\tau_0,\tau;\mu) = \frac{\tau^2}{2}I_{u0}(\tau_0,\tau;\mu) - \frac{\tau e^{i\mu\tau^2/2} - \tau_0 e^{i\mu\tau_0^2/2} - I_{u0}(\tau_0,\tau;\mu)}{2\mu i} \tag{74}$$

$$T_{d42}(\tau_0,\tau;\mu,\rho)=\frac{\tau^2}{2}J_{u0}(\tau;\mu,\rho)-\frac{\tau_0^2}{2}J_{u0}(\tau_0;\mu,\rho)+\frac{1}{2\mu i}J_{u0}(\tau_0,\tau;\mu,\rho)-\frac{1}{2\mu i}[\tau e^{i\mu\tau^2/2}\bar{I}_{u0}(\tau;\rho)-\tau_0 e^{i\mu\tau_0^2/2}\bar{I}_{u0}(\tau_0;\rho)]-\frac{1}{2\mu\lambda}(e^{i\lambda\tau^2/2}-e^{i\lambda\tau_0^2/2})-\frac{\tau^2-\tau_0^2}{2}J_{u0}(\tau_0;\mu,\rho) \tag{75}$$

$$T_{d43}(\tau_0,\tau;\kappa)=\frac{\tau^2}{2}I_{u0}(\tau_0,\tau;\kappa)-\frac{\tau e^{i\kappa\tau^2/2}-\tau_0 e^{i\kappa\tau_0^2/2}-I_{u0}(\tau_0,\tau;\kappa)}{2\kappa i} \tag{76}$$

$$T_{d44}(\tau_0,\tau;\kappa,\rho)=\frac{\tau^2}{2}\bar{J}_{u0}(\tau;-\kappa,\rho)-\frac{\tau_0^2}{2}\bar{J}_{u0}(\tau_0;-\kappa,\rho)+\frac{1}{2\kappa i}\bar{J}_{u0}(\tau_0,\tau;-\kappa,\rho)-\frac{1}{2\kappa i}[\tau e^{i\kappa\tau^2/2}I_{u0}(\tau;\rho)-\tau_0 e^{i\kappa\tau_0^2/2}I_{u0}(\tau_0;\rho)]-\frac{1}{2\kappa\lambda}(e^{i\lambda\tau^2/2}-e^{i\lambda\tau_0^2/2})-\frac{\tau^2-\tau_0^2}{2}\bar{J}_{u0}(\tau_0;-\kappa,\rho) \tag{77}$$

With T_{d41}, T_{d42}, T_{d43}, and T_{d44}, the displacement analytical closed-form solution is completed.

8 Closed-Form Analytical Solution for the Axial Velocity

In order to find the axial velocity solution, we need to integrate Eq. (22) with respect to time t. Let us multiply Eq. (22) by $dt/d\tau$, use Eq. (23), and then integrate it, which yields

$$v_Z(\tau)=v_Z(\tau_0)+\frac{\lambda f_z}{m}(\tau-\tau_0)-\frac{\lambda}{m}\,\mathrm{Im}\left[\int_{\tau_0}^{\tau}\bar{f}\phi(u)du\right] \tag{78}$$

where Im[.] denotes the imaginary part. If $f_z\neq 0$, the integral term, last term in Eq. (78), can be ignored in most applications. However if $f_z=0$, the last term in Eq. (78) can be determined by substituting and using Eqs. (28)–(45) in Eq. (78). Ayoubi [52] shows that the integral term has a finite limit. The complete closed-form solution contains about 100 terms; we refer the interested reader to Ref. [51] for more details.

9 Numerical Results

In this section, we show a few numerical results, concentrating on the accuracy of the transverse solution; we do not provide numerical details of the Eulerian angles and angular velocity solutions, which are already discussed extensively in the literature [32,33].

We compare our analytical solution to the exact solution. By "exact solution," we mean a highly accurate numerical integration of Eqs. (1)–(3), (8)–(11), (15), and (16). Because of the approximation of the $J_{u0}(\tau_0,\tau;\mu,\rho)$ function via two piecewise continuous functions (given in Appendix A) for small and large arguments, we recall that we have two analytical theories: the "low spin rate theory" and the "high spin rate theory." The low spin rate theory includes spin rates from 0 to 2.36 rpm, and the high spin rate theory covers spin rates higher than 2.36 rpm. We note that our approximation solution for J_{u0} is very accurate for all spin rates; it does not break down at intermediate spin rates. We employe the software package MATHEMATICA® ([57,58]) in this simulation to generate the exact solution. (We use the Bogacki–Shampine order-five method with local relative and absolute errors of order 10^{-14}.) The following mass properties and body-fixed forces and moments (inspired from the case of the Galileo spacecraft) are used during the simulation with all the initial conditions set to zero:

$$m=2000\ \text{kg},\quad I_x=2985,\quad I_y=2729,\quad I_z=4183\ \text{kg m}^2 \tag{79}$$

$$f_x=7.66,\quad f_y=-6.42,\quad f_z=10.0\ \text{N} \tag{80}$$

$$M_x=-1.253,\quad M_y=-1.494,\quad M_z=13.5\ \text{N m} \tag{81}$$

We will investigate the following case, where

$$\omega_z(0)=2.36,\quad \omega_z(t_f)=10\ \text{rpm} \tag{82}$$

with the rest of the initial conditions set to zero (i.e., $\omega_x(0)=\omega_y(0)=\phi_x(0)=\phi_y(0)=v_X(0)=v_Y(0)=v_Z(0)=0$).

The transverse velocity and displacement for low spin rate in the inertial frame are shown in Ref. [50]. As we noted in the development of the analytical solution for the Eulerian angles, $\phi_x(t)$ and $\phi_y(t)$, these angles must remain small throughout the motion for the theory to be valid. Thus, the initial values of ϕ_x and ϕ_y must be small and the effect of the transverse torques must be small as well. One way of insuring that the transverse torque remains small enough is to require that

$$\frac{\sqrt{M_x^2+M_y^2}}{I_z\omega_z^2}<\delta \tag{83}$$

where δ is a small positive constant(i.e., much less than unity), as discussed in the literature [30]. However, Eq. (83) is not necessary in the initial state of a spin-up maneuver starting from zero spin rate ($\omega_z(0)=0$). We note that in the zero spin rate case, the following inequality must be satisfied:

$$\frac{\sqrt{(M_x/I_x)^2+(M_y/I_y)^2}}{M_z/I_z}<\varepsilon \tag{84}$$

to prevent a large excursion of the spin axis in inertial space, where ε is a small positive constant (much smaller than unity). Equations (83) and (84) serve as rules of thumb for when our analytical solutions are valid. It is clear that the accuracy of the analytical solution for the transverse velocity and for the transverse displacement are dependent on the accuracy of the antecedent analytical solutions for the angular velocity and for the Eulerian angles. Since in our example (shown in Figs. 1–4), we have small values for ϕ_x and ϕ_y throughout the motion, the results of the analytical solutions for the transverse velocity and the transverse displacement are quite good. In this particular case, $\varepsilon=0.22$.

The associated error between the exact and analytical solution for the transverse velocity is shown in Fig. 3. We see that the velocity relative error is $<1\%$ (for most of the duration). Additional tests of the analytical solution are given in Ref. [50].

Of course, it is possible to choose initial and final spin rates, $\omega_z(0)$ and $\omega_z(t_f)$, such that a combination of the low spin rate and high spin rate theories is required. We have performed additional accuracy tests (not shown here) that demonstrate that the simple concatenation of the two theories provides results consistent with the accuracies we have seen in the two cases we have presented. Tests of the analytical solution for the axial velocity confirm that it is highly accurate for practical cases as shown in Ref. [51].

10 Conclusion

A complete, closed-form, approximate analytical solution has been found and outlined for the transverse and axial velocities and transverse displacement of a spinning-up rigid body subject to constant forces and torques about all three body axes. Also, we assume that mass properties are constant and the rigid body spins around its maximum or minimum principal moment-of-inertia

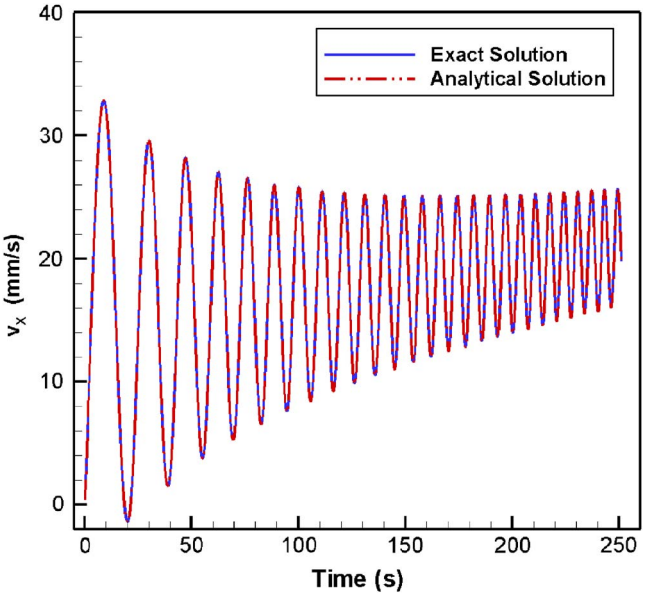

Fig. 1 Exact and analytical solutions for inertial velocity v_X at high spin rate

axis. We demonstrate that this solution is highly accurate when compared to the exact solution. Our analysis applies to axisymmetric, nearly axisymmetric, and (under special conditions) asymmetric rigid bodies. This behavior of the rigid body is fundamentally based on the Fresnel integral and related integrals. The numerical simulations are superior to the analytical solutions when the simulation time is small. However, when the maneuver duration is long, the analytical solutions provide quick results for final states, without the need for numerical integration. Applications of this analytical theory may include spacecraft onboard computations, probabilistic error modeling for mission-planning, development of new control concepts for spacecraft maneuvers, and maneuver analysis. This work complements the contributions of numerous authors in the literature.

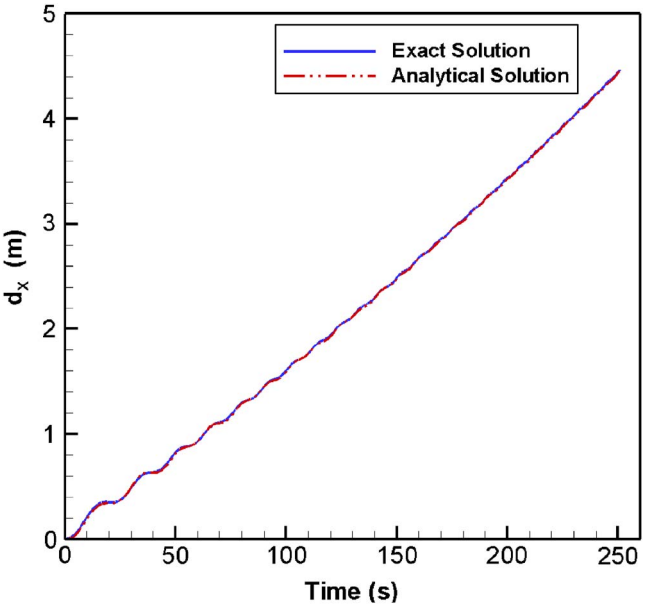

Fig. 2 Exact and analytical solutions for inertial displacements d_X at high spin rate

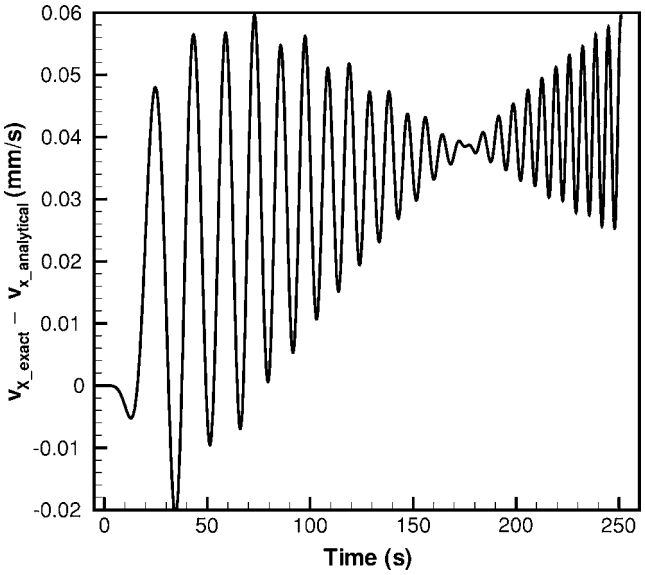

Fig. 3 Exact minus analytical solution of inertial velocity v_X at high spin rate

Appendix A: $J_{u0}(\tau_0, u; \mu, \rho)$ Function

In the definition of $J_{u0}(\tau_0, u; \mu, \rho)$, Eq. (45), it was shown [33,44] that J_{u0} can be approximated (see Table 1) as

$$J_{u0}(\tau_0, \tau; \mu, \rho) = \begin{cases} J_{u0s}(\tau; \mu, \rho), & \text{if } \tau \le \tau_s = \sqrt{8/|\rho|} \\ J_{u0s}(\tau_s; \mu, \rho) + J_{u0l}(\tau_s, \tau; \mu, \rho), & \text{otherwise} \end{cases} \tag{A1}$$

where, for $\tau \le \tau_s$

$$J_{u0s}(u; \mu, \rho) \triangleq \sqrt{\frac{\pi}{|\rho|}} \sum_{n=0}^{11} (a_n + ib_n) \left(\frac{|\rho|}{8} \right)^{n+(1/2)} I_u(\tau; \lambda, 2n+1) \tag{A2}$$

and for $\tau > \tau_s$ we have

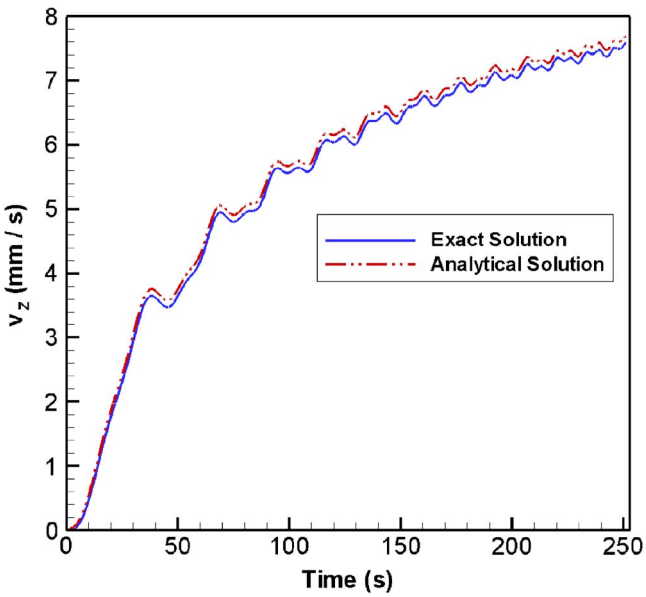

Fig. 4 Exact(solid line) and analytical (dashed line) solution of inertial axial velocity v_Z at high spin rate

Table 1 Boersma's numerical values of coefficients for the $J_{uo}(\tau;\mu,\rho)$ approximation [55]

i	a_i	b_i	c_i	d_i
0	1.595769140	−0.000000033	0.000000000	0.199471140
1	−0.000001702	4.255387524	−0.024933975	0.000000023
2	−6.808568854	−0.000092810	0.000003936	−0.009351341
3	−0.000576361	−7.780020400	0.005770956	0.000023006
4	6.920691902	−0.009520895	0.000689892	0.004851466
5	−0.016898657	5.075161298	−0.009497136	0.001903218
6	−3.050485660	−0.138341947	0.011948809	−0.017122914
7	−0.075752419	−1.363729124	−0.006748873	0.029064067
8	0.850663781	−0.403349276	0.000246420	−0.027928955
9	−0.025639041	0.702222016	0.002102967	0.016497308
10	−0.150230960	−0.216195929	−0.001217930	−0.005598515
11	0.034404779	0.019547031	0.000233939	0.000838386

$$J_{u0l}(\tau_s,\tau;\mu,\rho) \triangleq \sqrt{\frac{\pi}{|\rho|}}\frac{(1-i)}{2}\int_{\tau_s}^{\tau} e^{(i\mu\xi^2/2)}d\xi + \sqrt{\frac{\pi}{|\rho|}}\sum_{n=0}^{11}(c_n+id_n) \times\left(\frac{8}{|\rho|}\right)^{(n+(1/2))} I_d(\tau_s,\tau;\lambda,2n+1) \tag{A3}$$

See Appendixes B and C for more details on the $I_u(\tau;\lambda,n)$ and $I_d(\tau_s,\tau;\lambda,n)$ functions.

Appendix B: $I_u(u;\lambda,n)$ Function

In determining J_{u0s} in Appendix A, we introduced the function $I_u(\tau;\lambda,n)$, which is defined as

$$I_u(\tau_0,\tau;\lambda,n) \triangleq \int_{\tau_0}^{\tau} e^{(i\lambda u^2/2)}u^n du \tag{B1}$$

By using the integration by parts technique, a recursive formula can be found for $I_u(\tau;\lambda,n)$ as

$$I_u(\tau;\lambda,n) = \frac{-i\tau^{n-1}}{\lambda}e^{(i\lambda\tau^2/2)} + \frac{i(n-1)}{\lambda}I_u(\tau;\lambda,n-2) \quad (n\geq 2) \tag{B2}$$

$$I_u(\tau;\lambda,1) = \frac{-i}{\lambda}\left[e^{(i\lambda\tau^2/2)}-1\right] \tag{B3}$$

$$I_{u0}(\tau;\lambda) = \sqrt{\frac{\pi}{|\lambda|}}\,\mathrm{sgn}(\tau)\tilde{E}\left(\frac{\sqrt{|\lambda|}}{\pi}\tau\right) \tag{B4}$$

where

$$\tilde{E}\left(\frac{\sqrt{|\lambda|}}{\pi}\tau\right) = \begin{cases} E\left(\dfrac{\sqrt{|\lambda|}}{\pi}\tau\right) & \text{when} \quad \lambda<0 \\ \bar{E}\left(\dfrac{\sqrt{|\lambda|}}{\pi}\tau\right) & \text{when} \quad \lambda>0 \end{cases} \tag{B5}$$

and

$$E(x) \triangleq \int_0^x e^{(-i\pi u^2/2)}du \tag{B6}$$

is the complex Fresnel integral. The sgn(.) symbol in Eq. (B4) represents the signum function, which is $\mathrm{sgn}(x)=1$ for $x\geq 0$ and $\mathrm{sgn}(x)=-1$ for $x<0$.

$$I_u(\tau;0,n) = \frac{\tau^{n+1}}{n+1} \tag{B7}$$

$$I_{u0}(\tau;0) = \frac{\tau^2}{2} \tag{B8}$$

A recursive integral formula can be found as

$$\int_0^{\tau} I_u(\xi;\lambda,n)d\xi = \frac{-i}{\lambda}I_u(\tau;\lambda,n-1) + \frac{i(n-1)}{\lambda} \times\int_0^{\tau} I_u(\xi;\lambda,n-2)d\xi \quad (n\geq 2) \tag{B9}$$

$$\int_0^{\tau} I_{u0}(\xi;\lambda)d\xi = \sqrt{\frac{\pi}{|\lambda|}}\int_0^{\tau}\mathrm{sgn}(\xi)\tilde{E}\left(\frac{\sqrt{|\lambda|}}{\pi}\xi\right)d\xi \tag{B10}$$

$$\int_0^{\tau} I_u(\xi;\lambda,1)d\xi = \int_0^{\tau}\frac{-i}{\lambda}[e^{(i\lambda\xi^2/2)}-1]d\xi = \frac{-i}{\lambda}[\tau - I_{u0}(\tau;\lambda)] \tag{B11}$$

Appendix C: $I_d(u;\lambda,n)$ Function

In Eq. (A3), we introduced a new function $I_d(\tau_s,\tau;\lambda,n)$, which can be defined as

$$I_d(\tau_0,\tau;\lambda,n) \triangleq \int_{\tau_0}^{\tau}\frac{e^{(i\lambda u^2/2)}}{u^n}du \tag{C1}$$

We can show that

$$I_d(\tau;\lambda,n) = \begin{cases} \dfrac{e^{(i\lambda\tau^2/2)}}{(n-1)\tau^{(n-1)}} + \dfrac{i\lambda}{n-1}I_d(\tau;\lambda,n-2), & (n\geq 2;\lambda\neq 0) \\ \dfrac{1}{(n-1)\tau^{(n-1)}}, & (n\geq 2;\lambda=0) \end{cases} \tag{C2}$$

$$I_{d0}(\tau;\lambda) = \begin{cases} I_{u0}(\infty;\lambda) - I_{u0}(\tau;\lambda), & (\lambda\neq 0) \\ -\tau, & (\lambda=0) \end{cases} \tag{C3}$$

$$I_d(\tau;\lambda,1) = \frac{1}{2}E_i\left(\frac{|\lambda|\tau^2}{2}\right) \tag{C4}$$

where $E_i(\tau)$ is the exponential integral function and is defined as

$$E_i(\tau) \triangleq \int_{\tau}^{\infty}\frac{e^{i\xi}}{\xi}d\xi \tag{C5}$$

A recursive integral formula is given by

$$\int_{\tau_s}^{\tau} I_d(\xi;\lambda,n)d\xi = \frac{1}{n-1}[I_d(\tau_s,\tau;\lambda,n-1) + i\lambda\int_{\tau_s}^{\tau} I_d(\xi;\lambda,n-2)d\xi] \quad (n\geq 2) \tag{C6}$$

and

$$\int_{\tau_s}^{\tau} I_{d0}(\xi;\lambda)d\xi = I_{u0}(\infty;\lambda)(\tau-\tau_s) - \sqrt{\frac{\pi}{|\lambda|}}\int_{\tau_0}^{\tau}\mathrm{sgn}(\xi)\tilde{E}(\sqrt{|\lambda|/\pi}\xi)d\xi \tag{C7}$$

$$\int_{\tau_s}^{\tau} I_d(\xi;\lambda,1)d\xi = \tau I_d(\tau;\lambda,1) - \tau_s I_d(\tau_s;\lambda,1) + I_{u0}(\tau_s,\tau;\lambda) \tag{C8}$$

References

[1] Leimanis, E., 1965, *The General Problem of the Motion of Coupled Rigid Bodies About a Fixed Point*, Springer-Verlag, New York, Chap. 2.

[2] Rosser, J. B., Newton, R. R., and Gross, G. L., 1947, *Mathematical Theory of Rocket Flight*, McGraw-Hill, New York, pp. 49–262.

[3] Bödewadt, U. T., 1952, "Der Symmetrische Kreisel bei Zeitfester Drehkraft," Math. Zeit., **55**, pp. 310–320.

[4] Jarmolow, K., 1957, "Dynamics of a Spinning Rocket With Varying Inertia and Applied Moment," J. Appl. Phys., **28**(3), pp. 308–313.

[5] Davis, Jr., L., Follin, Jr., J. W., and Blitzer, L., 1958, *Exterior Ballistics of Rockets*, Van Nostrand, New York, Chap. 9.

[6] Buglia, J. J., Young, G. R., Timmons, J. D., and Brinkworth, H. S., 1961, "Analytical Method of Approximating the Motion of a Spinning Vehicle With Variable Mass and Inertia Properties Acted Upon by Several Disturbing Parameters," Langley Research Center, Langley Air Force Base, VA, NASA TR No. R-110.

[7] Martz, W., 1961, "Method for Approximating the Vacuum Motions of Spinning Symmetrical Bodies With Nonconstant Spin Rates," Langley Research Center, Langley Station, Hampton, VA, NASA TR No. R-115.

[8] Armstrong, R. S., 1965, "Errors Associated With Spinning-Up and Thrusting Symmetric Rigid Bodies," Jet Propulsion Laboratory, California Institute of Technology, Pasadena, Feb. Technical Report No. 32-644.

[9] Likins, P. W., 1967, "Attitude Stability Criteria for Dual-Spin Spacecraft," J. Spacecr. Rockets, **4**, pp. 1638–1643.

[10] Cochran, J. E., 1972, "Effects of Gravity-Gradient Torque on the Rotational Motion of a Triaxial Satellite in a Precessing Elliptic Orbit," Celest. Mech., **6**, pp. 127–150.

[11] Junkins, J. L., Jacobson, I. D., and Blanton, J. N., 1973, "A Nonlinear Oscillator Analog of Rigid Body Dynamics," Celest. Mech., **7**(4), pp. 398–407.

[12] Larson, V., and Likins, P. W., 1973, "Fuel-Optimal Angular Momentum Vector Control for Spinning and Dual-Spin Spacecraft," Astronaut. Acta, **18**, pp. 215–227.

[13] Morton, H. S., Junkins, J. L., and Blanton, J. N., 1974, "Analytical Solutions for Euler Parameters," Celest. Mech., **10**(4), pp. 287–301.

[14] Larson, V., and Likins, P. W., 1974, "Closed-Form Solutions for the State Equation for Dual-Spin and Spinning Spacecraft," J. Astronaut. Sci., **21**(5-6), pp. 244–251.

[15] Morton, H. S., Junkins, J. L., and Blanton, J. N., 1974, "Analytical Solutions for Euler Parameters," Celest. Mech., **10**(4), pp. 287–301.

[16] Kraige, L. G., and Junkins, J. L., 1976, "Perturbation Formulations for Satellite Attitude Dynamics," Celest. Mech., **13**(1), pp. 39–64.

[17] Kraige, L. G., and Skaar, S. B., 1977, "A Variation of Parameters Approach to the Arbitrary Torqued, Asymmetric Rigid Body Problem," J. Astronaut. Sci., **25**(3), pp. 207–226.

[18] Junkins, J. L., and Turner, J. D., 1980, "Optimal Continuous Torque Attitude Maneuvers," J. Guid. Control, **3**(4), pp. 210–217.

[19] Longuski, J. M., 1980, "Solution of Euler's Equations of Motion and Eulerian Angles for Near-Symmetric Rigid Bodies Subject to Constant Moments," AIAA/AAS Astrodynamics Conference, Danvers, MA, Aug. 11–13, AIAA Paper No. 80-1642.

[20] Longuski, J. M., 1981, "Galileo Maneuver Analysis," AAS/AIAA Astrodynamics Specialist Conference, Lake Tahoe, NV, Aug. 3–5, AAS Paper No. 81-137.

[21] Price, J. L., 1981, "An Economical Series Solution of Euler's Equations of Motion, With Application to Space-Probe Maneuvers," AAS/AIAA Astrodynamics Specialist Conference, Lake Tahoe, NV, Aug. 3–5, AAS Paper No. 81-105.

[22] Cochran, J. E., and Shu, P. H., 1982, "Attitude Motion of Asymmetric Dual-Spin Spacecraft," J. Guid. Control Dyn., **5**, pp. 37–42.

[23] Cochran, J. E., and Shu, P. H., 1983, "Attitude Motion of Spacecraft With Skewed Internal Angular Momenta," J. Astronaut. Sci., **31**, pp. 203–215.

[24] Klumpe, E. W., and Longuski, J. M., 1984, "Secular Solution for Delta-V During Spin Rate Change Maneuvers of Rigid Body Spacecraft," AIAA/AAS Astrodynamics Conference, Seattle, Aug., AIAA Paper No. 84-2011.

[25] Longuski, J. M., 1984, "On the Attitude Motion of a Self-Excited Rigid Body," J. Astronaut. Sci., **32**(4), pp. 463–473.

[26] Longuski, J. M., and Kia, T., 1984, "A Parametric Study of the Behavior of the Angular Momentum Vector During Spin Rate Changes of Rigid-Body Spacecraft," J. Guid. Control Dyn., **7**(3), pp. 295–300.

[27] Van der Ha, J. F., 1985, "Perturbation Solution of Attitude Motion Under Body-Fixed Torques," Acta Astronaut., **12**(10), pp. 861–869.

[28] Winfree, P. K., and Cochran, J. E., 1986, "Nonlinear Attitude Motion of a Dual-Spin Spacecraft Containing Spherical Dampers," J. Guid. Control Dyn., **9**(4), pp. 681–690.

[29] Kane, T. R., and Levinson, D. A., 1987, "Approximate Description of Attitude Motions of a Torque-Free, Nearly Axisymmetric Rigid Body," J. Astronaut. Sci., **35**, pp. 435–446.

[30] Longuski, J. M., Kia, T., and Breckenridge, W. G., 1989, "Annihilation of Angular Momentum Bias During Spinning-Up and Thrusting Maneuvers," J. Astronaut. Sci., **37**(4), pp. 433–450.

[31] Longuski, J. M., Campbell, R. S., and Klumpe, E. W., 1989, "Error Analysis for Pulsed Maneuvers of a Dual-Spin Spacecraft," AAS/AIAA Astrodynamics Specialist Conference, Stowe, VT, Aug. 7–10. AAS Paper 89-396.

[32] Longuski, J. M., 1991, "Real Solutions for the Attitude Motion of a Self-Excited Rigid Body," Acta Astronaut., **25**(3), pp. 131–140.

[33] Tsiotras, P., and Longuski, J. M., 1991, "A Complex Analytical Solution for the Attitude Motion of a Near-Symmetric Rigid Body Under Body-Fixed Torques," Celest. Mech. Dyn. Astron., **51**(3), pp. 281–301.

[34] Longuski, J. M., 1991, "Real Solutions for the Attitude Motion of a Self-Excited Rigid Body," Acta Astronaut., **25**(3), pp. 131–140.

[35] Longuski, J. M., and Tsiotras, P., 1993, "Analytical Solutions for a Spinning Rigid Bod Subject to Time-Varying Body-Fixed Torques—Part I: Constant Axial Torque," ASME J. Appl. Mech., **60**, pp. 970–975.

[36] Tsiotras, P., and Longuski, J. M., 1993, "Analytical Solutions for a Spinning Rigid Body Subject to Time-Varying Body-Fixed Torques—Part II: Time Varying Axial Torque," ASME J. Appl. Mech., **60**(4), pp. 976–981.

[37] Beck, R. A., and Longuski, J. M., 1994, "Analytical Solution for the Velocity of a Rigid Body During Spinning-Up Maneuvers," AIAA/AAS Astrodynamics Specialists Conference, Scottsdale, AZ, Aug. 1–3, AIAA Paper No. 94-3713.

[38] Randall, L. A., Longuski, J. M., and Beck, R. A., 1995, "Complex Analytic Solutions for a Spinning Rigid Body Subject to Constant Transverse Torques," AAS/AIAA Astrodynamics Specialists Conference, Halifax, Nova Scotia, Canada, Aug. 14–17, AAS Paper No. 95-373.

[39] Longuski, J. M., and Tsiotras, P., 1995, "Analytical Solutions of the Large Angle Problem in Rigid Body Attitude Dynamics," J. Astronaut. Sci., **43**(1), pp. 25–46.

[40] Tsiotras, P., and Longuski, J. M., 1996, "Analytical Solution of Euler's Equations of Motion for an Asymmetric Rigid Body," ASME J. Appl. Mech., **63**, pp. 149–155.

[41] Beck, R. A., and Longuski, J. M., 1997, "Annihilation of Transverse Velocity Bias During Spinning-Up Maneuvers," J. Guid. Control Dyn., **20**(3), pp. 416–421.

[42] Livneh, R., and Wie, B., 1997, "New Results for an Asymmetric Rigid Body With Constant Body-Fixed Torques," J. Guid. Control Dyn., **20**(2), pp. 873–881.

[43] Wie, B., 1998, *Space Vehicle Dynamics and Control*, AIAA, Washington, AIAA Education Series, pp. 352–365.

[44] Gick, R. A., 1999, "Analysis of the Motion of Spinning, Thrusting Spacecraft," Ph.D. thesis, School of Aeronautics and Astronautics, Purdue University, West Lafayette, pp. 17–18.

[45] Gick, R. A., Williams, M. H., and Longuski, J. M., 1999, "Floquet Approximation for a Nearly Axisymmetric Rigid Body With Constant Transverse Torque," J. Guid. Control Dyn., **22**(5), pp. 658–663.

[46] Gick, R. A., Williams, M. H., and Longuski, J. M., 2000, "Periodic Solutions for a Spinning Axisymmetric Rigid Body With Constant Principal Axis Torque," J. Guid. Control Dyn., **23**(5), pp. 781–788.

[47] Javorsek, II, D., and Longuski, J. M., 2000, "Velocity Pointing Errors Associated With Spinning Thrusting Spacecraft," J. Spacecr. Rockets, **37**(3), pp. 359–365.

[48] Sookgaew, J., and Eke, F. O., 2003, "Attitude Motions of a Spinning Rocket," AAS/AIAA Astrodynamics Specialists Conference, Big Sky, MT, Aug. 3–7, AAS Paper No. 03-580.

[49] Longuski, J. M., Gick, R. A., Ayoubi, M. A., and Randall, L., 2005, "Analytical Solutions for Thrusting, Spinning Spacecraft Subject to Constant Forces," J. Guid. Control Dyn., **28**(6), pp. 1301–1309.

[50] Ayoubi, M. A., and Longuski, J. M., 2005, "Velocity Solution for a Spinning-Up Rigid Body Subject to Constant Body-Fixed Moments and Forces," AAS/AIAA Astrodynamics Specialist Conference, Lake Tahoe, CA, Aug. 7–11. AAS Paper No. 05-261.

[51] Ayoubi, M. A., and Longuski, J. M., 2006, "Axial Velocity Solution for a Spinning-Up Rigid Body Subject to Constant Body-Fixed Forces and Moments," AIAA/AAS Astrodynamics Specialist Conference, Keystone, CO, Aug. 21–24, AIAA Paper No. 2006-6655.

[52] Ayoubi, M. A., 2007, "Analytical Theory for the Motion of Spinning Rigid Bodies," Ph.D. thesis, School of Aeronautics and Astronautics, Purdue University, West Lafayette, IN, Chaps. 3–6.

[53] Greenwood, D. T., 1988, *Principles of Dynamics*, 2 ed., Prentice-Hall, Englewood Cliffs, NJ, Chap. 8.

[54] Wertz, J. R., ed., 2000, *Spacecraft Attitude Determination and Control*, Reidel Publishing, Dordrecht, pp. 760–766.

[55] Boersma, J., 1960, "Computation of Fresnel Integrals," Math. Comput., **14**, p. 380.

[56] Abramowitz, M., and Stegun, I. A., 1972, *A Handbook of Mathematical Functions*, Dover Publications, New York.

[57] Wolfram, S., 1999, *The Mathematica Book*, Cambridge University Press, Cambridge, England, 4th Ed.

[58] Trott, M., 2006, *The Mathematica GuideBook for Symbolics*, Springer, New York.

Extended Fatigue Life by Shot Peening Process via Shakedown Analysis

Jehuda Tirosh[1]
Massachusetts Institute of Technology,
Cambridge MA, 02139

The goal of this work was to quantify the improvement in the fatigue limit of solid structures which have undergone shot peening (SP) by small rigid particles. The work was based on Melan's shakedown theorem for estimating the allowable safe stress amplitude (in a lower bound sense) of structures that otherwise might fail during fatigue loading by plastic strain accumulation (ratcheting). Aided by geometrical simplification (mainly by assuming that the residual craters of the peened surfaces are shallow and flat), the benefit of SP to increase fatigue limits of structures subjected to fluctuating loads was quantified and compared to experiments. As a by-product, the long-time accepted empirical formulas for decreasing fatigue limits due to an increase of the loading mean tensile stress (Gerber, 1874, Z Bayer Arch Ingenieur-Vereins, 6, pp. 101–110; Goodman, 1899, Mechanics Applied to Engineering, Longmans, Green, London) have received a theoretical justification from shakedown analysis. The suggested empiricism-free solution traces well Gerber and Goodman's empirical formulas in the positive mean stress regime of the applied load. It has a notable advantage that it also smoothly extends to the negative mean-stress regime (akin to the superimposed residual compressive stresses in a thin layer generated by the SP process) not covered hitherto by formulas. This shakedown analysis manifests the merit of shot peening processes by showing specifically the existence of larger range of fatigue-safe stress amplitudes (or equivalently, exhibiting a prolonged fatigue life) before disruption by ratcheting. Various fatigue experiments which were found in the open literature, are in a satisfactory agreement with the theoretical analysis. [DOI: 10.1115/1.2745357]

Keywords: shakedown condition, fatigue life-time, fatigue limit, shot peening, ball indentation, crater, inclusion model, lower bound, mean stress, residual stress, stress threshold, yielding

1 Introduction

The notion that the compressive component of residual stress can, under certain circumstances, defer premature mechanical failure, has been empirically recognized for more than a century. However, when fatigue loading was superimposed on the residual stresses, the time to failure, while empirically measurable, has not been theoretically predicted. For instance, the sleeved autofrettage procedure in barrel cannons [1], the overload stress cycle of cracked solid for delaying crack propagation [2], shot peening (SP) in surface treatments of machine parts for longer fatigue life (already encoded in military specifications [3]), are just a few of the applications benefited from imposed residual stresses. Due to cost considerations, SP is applied customarily only to critical mechanical parts (such as leaf springs, gears, connecting rods, etc.), largely in car and aircraft industries, where long fatigue lives are required.

It was the goal of this study to examine the capability of SP to increase fatigue limits (or alternatively, to prolong fatigue life) in a quantitative way. This is done by implementing the *lower bound of the shakedown theorem* (denote shortly as "shakedown analysis") originated by Melan in 1936 [4]. In recent years, assisted by this theory, researchers have been able to expand their understanding of several mechanical phenomena (e.g., Dvorak and Tarn [5], Ponter and co-workers [6,7], Kapoor and Johnson [8], Tirosh [9], and others, along with a refreshed theoretical guidelines by Polizzotto [10,11]).

The effect of SP is viewed here from *a crack-free approach*, which assumes that the structure has no initial cracks (besides the microstructural defects, which presumably do not grow by fatigue). This approach, originated historically by Gerber in 1874 [12] and followed by Goodman in 1899 [13], was widely practiced since that time and is still widely used in assessing decreases in fatigue limits as a result of an increase in the tensile mean stress. These well used empirical formulas have never been substantiated by theory. The present study is intended to provide a theoretical foundation to account for the effect of mean stress (both positive and negative) on fatigue limits affected by SP processes. Experimental background for the SP analysis presented here was provided by Al-Obaid [14] and by Hammond and Meguid [15]. Their empirical results are compared to validate the analysis, done in the analysis of [16].

The paper begins by outlining the basic assumptions and the material characterization. Next, the residual stress distribution near an impinged SP ball is solved. Assisted by the predefined "inclusion model," the magnitude of the residual stress is obtained. Further on, a fluctuating load between prescribed limits is superimposed on the residual stress and the associated expression for the shakedown condition is formulated. Finally, the pros and cons of the SP processes are viewed via comparison to several available experimental data.

2 Basic Assumptions and Definitions

Consider an elasto-plastic solid whose free surface undergoes shot peening by hard small particles (usually ceramics balls with

[1]On sabbatical leave, Faculty of Mechanical Engineering, Technion, Haifa, Israel.

Contributed by the Applied Mechanics Division of ASME for publication in the JOURNAL OF APPLIED MECHANICS. Manuscript received May 4, 2006; final manuscript received April 25, 2007; published online January 11, 2008. Review conducted by Jian Cao.

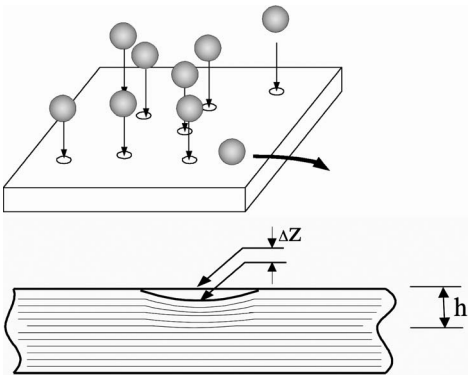

Fig. 1 Schematic view of shot-peening process and a single residual crater

diameter of about $2R_0 \approx 1$ [mm]) as shown in Fig. 1. The solid is affected by being plastically deformed in a relatively thin layer adjacent to the free surface. Each ball, after impacting and bouncing off the surface (assuming, for simplicity, in the normal direction), leaves on the surface a circular shallow "crater." The plastically affected zone beneath the crater, created by the indented ball, is customarily assessed numerically [17] and/or via the amount of the kinetic energy imparted to the solid by individual balls [18].

The basic assumptions in the development of the model are:

(i) The depth of the craters are small compared to the ball radius and are therefore considered flat.
(ii) The residual plastic strain beneath craters is elastically confined, being on the order of the elastic yield strain.
(iii) The residual plastic zone is hypothesized to have a penny-shaped configuration (of radius a and height h).
(iv) The effects of the impinging balls are considered as non-interactive.
(v) Multiple impacts of the balls and the changes of the material properties are excluded.

These assumptions define the so-called inclusion model of shot peening (Fig. 2) with which the model is derived.

3 Mechanical Behavior

The elasto-plastic engineering materials under consideration behave in a linear elastic manner up to yielding. That is,

$$\frac{\varepsilon}{\varepsilon_0} = \frac{\sigma}{\sigma_0} \quad \text{for } \sigma < \sigma_0$$
$$\varepsilon \to \varepsilon^p \quad \text{for } \sigma = \sigma_0 \tag{1}$$

where σ_0 is the yield stress in unidirectional tension, ε and ε^p are the effective strains defined in term of the second strain invariant as

$$\varepsilon = \frac{2}{\sqrt{3}}\sqrt{\frac{1}{2}\varepsilon_{ij}\varepsilon_{ij}} \tag{2}$$

and σ is the effective (von Mises) stress, related to ε (or ε^p) by the work equivalence, namely, $\sigma\varepsilon = \sigma_{ij}\varepsilon_{ij}$.

The true strain across the plastically deformed skin (h) is generated by the incremental indentation depth Δz of the ball (the decrement of Δz is considered positive). The in-plane plastic deformation is confined by the surrounding elastic matrix, so that the plastic strains are moderately small (of the order of the elastic strains). It is given by

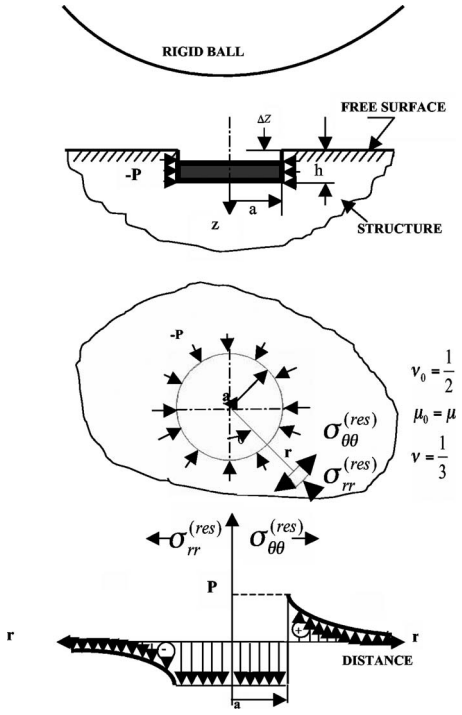

Fig. 2 The inclusion model used to simplify the theoretical shakedown analysis. The plastically deformed zone (incompressible inclusion) has a penny-shaped configuration, compressed by the elastic surrounding with a lateral pressure *p*. The residual stress distribution is shown beneath.

$$\varepsilon_z = \int_h^{h-\Delta z} \frac{dz}{z} = \ln\left(\frac{h-\Delta z}{h}\right) \simeq \frac{\Delta z}{h} + \frac{1}{2}\left(\frac{\Delta z}{h}\right)^2 - \cdots \quad \left(\text{for } \left|\frac{\Delta z}{h}\right| \ll 1\right) \tag{3}$$

Similarly, the other two plastic strain components, using (r, θ, z) coordinate system, are

$$\varepsilon_r = \varepsilon_\theta = \int_a^{a+\Delta a} \frac{dr}{r} = \ln\left(1 + \frac{\Delta a}{a}\right) \approx \frac{\Delta a}{a} \tag{4}$$

where a is the projected radius of the indent.

From the incompressibility condition of the plastically deformed volume beneath the crater, Eqs. (3) and (4) lead to the radial expansion of

$$\frac{\Delta a}{a} = \frac{1}{2}\frac{\Delta z}{h} \tag{5a}$$

From Eqs. (4) and (5a), it is readily seen that the effective plastic strain ε^p (defined in (2)) is reduced to

$$\varepsilon^p = |\varepsilon_z| = \frac{|\Delta z|}{h} = 2\frac{\Delta a}{a} \tag{5b}$$

A criterion of whether an indentation of depth Δz with imprint radius a will cause a fully plastic flow under the impinging balls was observed and formulated, for example, by Johnson [18] and Bower et al. [17]. It was shown that in order to generate a fully developed plastic flow under a semi-sphere indenter, a dimensionless parameter, say, A should exceed a certain value. It reads

$$A = \frac{\Delta z}{a}\frac{E}{\sigma_0} > 30 \tag{6}$$

where E denotes the elastic modulus of the indented material.

As a practical example, assume an indentation by a ball of radius $R_0=1$ mm into a material with relative strength of $\sigma_0/E \approx 10^{-3}$. If the included contact angle of the material/ball (2α) is about 10 deg, then the residual imprint radius is about $a \approx R_0\alpha$ (=0.1 mm). Therefore, the minimal indentation depth needed to satisfy Eq. (6) is of the order of few tenths of micrometers (somewhat larger than a typical grain sizes of common engineering materials). Such an amount of surface indentation, as measured, for example, by Hammond and Meguid [15], produces a significant in-plane compressive residual stress, the magnitude of which is addressed as follows.

4 Residual Stresses

4.1 The Source. Consider a single ball that impacts the top surface of a solid at a certain velocity and bounces back at a different velocity. The difference in the kinetic energy of the ball before and after impact is assumed to be the energy required to plastically deform a disklike volume of material under the traction-free trace of the ball. The elastic surrounding material which has been displaced by the impinging ball "attempts" to restore its initial position, whereas the plastically deformed disk (incompressible "inclusion") sustains a residual strain as expressed by Eq. (4). This physical situation causes an in-plane elastic residual compressive stress in the plastically deformed zone, the distribution of which is solved in the following development.

4.2 The Residual Stress Solution. The governing equations which express this physical situation (static self-equilibrium and compatibility) can classically be derived via an Airy stress function $\Phi(r,\theta)$ to a single bi-harmonic function, namely,

$$\nabla^4\Phi = 0 \quad \text{(with the pertinent boundary conditions)} \tag{7a}$$

where the stress components are defined in the (r,θ) plane as

$$\sigma_{rr} \triangleq \frac{\partial\Phi}{r\,\partial r} + \frac{\partial^2\Phi}{r^2\,\partial\theta^2}; \quad \sigma_{\theta\theta} \triangleq \frac{\partial^2\Phi}{\partial r^2}; \quad \sigma_{\theta r} \triangleq -\frac{\partial}{\partial r}\left(\frac{1}{r}\frac{\partial\Phi}{\partial\theta}\right) \tag{7b}$$

Due to the circular symmetry with respect to the angular direction (θ) of the SP affected zone, the general solution of Eq. (7*a*) has only one variable (r), which renders

$$\Phi = A\,\ln(\mathrm{r}) + Br^2 + Cr^2\ln(r) + D \tag{8}$$

The boundary conditions are (see Fig. 2):

(i) at $r=0$ the stresses are finite;
(ii) at $r=a$ the radial stress, $\sigma_{rr}^{(\mathrm{res})}(a)$, is the in-plane confining residual stress of magnitude p (pressurelike) imposed by the elastic surrounding;
(iii) at a remote distance from the crater (where $r \gg a$) the boundary of the plate is stress free, so that the radial stress is zero;
(iv) the value of the free constant (that is, D in Eq. (8)), is immaterial, since in the above potential function $\Phi(r)$, the "zero level" is arbitrary.

Based on these four boundary conditions, the solution of Eq. (8) via the definitions of Eq. (7*b*) is reduced to the following residual stresses:

$$\sigma_{rr}^{(\mathrm{res})} = \sigma_{\theta\theta}^{(\mathrm{res})} = 2B, \quad B = \frac{p}{2} \quad \text{along } 0 \le r \le a \tag{9a}$$

$$\sigma_{rr}^{(\mathrm{res})} = p/\rho^2, \quad \sigma_{\theta\theta}^{(\mathrm{res})} = -p/\rho^2$$

$$\text{where } \rho \triangleq r/a \quad \text{along } a < r \le \infty \tag{9b}$$

It is seen in (9*a*) that the residual compressive stress in the plastically deformed zone is under *a uniform hydrostatic state of* $p/2$. The magnitude p (as will be seen later) depends on the elastic modulus and the yield strength of the indented material.

Beyond the plastically deformed zone the radial stress $\sigma_{rr}^{(\mathrm{res})}$ continues to sustain compression with a rapid decay to zero at far distance as shown in Eq. (9*b*). The circumferential stress $\sigma_{\theta\theta}^{(\mathrm{res})}$ undergoes a (permissible) jump of $2p$ along the elastic-plastic interface as shown in Fig. 2. Outside the interface it becomes abruptly tensile stress.

The outcome is that after the shot-peening process *the mean residual stress inside the plastically deformed zone is uniformly compressive*. The expressions for plane stress and plane strain (respectively) are:

$$\sigma_m^{(0)} = \frac{1}{3}[\sigma_{rr}^{(\mathrm{res})} + \sigma_{\theta\theta}^{(\mathrm{res})} + (\approx 0)] = -\frac{2}{3}p \quad (0 \le r \le a) \tag{10}$$

$$\sigma_m^{(0)} = -p$$

From global equilibrium considerations it is clear that the radial stress component along the depth direction (z) *should* somewhere be changed to tension, as the line integral of the stress distribution (forces) and the first moment along any cross-sectional line between $0 \le z \le \infty$ in traction-free structure should sum to zero (see Fig. 6). Such results were practically tested (for example, by Al-Obaid [14]), showing that further down the structure, beyond a thin layer $(0 \le z \le h$, *for* $h \ll a)$ the compression turns sharply to tension, pending (slightly) on the impacting velocity of the rigid particles.

5 The Inclusion Model

5.1 The Plastic Thin Layer. To evaluate the magnitude p of the residual stress in Eq. (10), one can make use of the suggested penny-shaped inclusion model illustrated in Fig. 2. The top side of the inclusion is always traction free. Since the crater is considered shallow and flat, one may assume that the plastic layer underneath it is considerably thin with respect to the characteristic size of the crater (say, of the order of $h=10^1$ μm). This assumption leads to relatively light normal and shear stresses at the crater's bottom face. That is to say, the stress state of the inclusion model is close to plane stress condition although the overall structure is presumably under plane strain state. The following analysis considers both cases whenever this distinction is meaningful.

5.2 The In-Plane Pressure *p* Acting on the Inclusion. We consider a stress-free elastic structure with shear modulus μ embedded by a thin, incompressible, elastic deformable inclusion, with shear modulus μ_0. From here on, the properties with subscript "o" refer to the inclusion, such as the shear modulus μ_0 and the Poisson ratio ν_0. Otherwise the properties refer to the bulk solid. In the present situation the shear moduli are the same, $\mu = \mu_0$ but the Poisson ratios are different, i.e., $\nu \approx 1/3$ and $\nu_0 = 1/2$, respectively (to reflect incompressibility of the material presented by the inclusion).

The inclusion of radius a can be envisioned as if forced into penny-shaped cavity in the surface layer of the structure having a smaller space, say of a radius of $a-\Delta a$. This apparent geometrical "mismatch" of Δa is ultimately removed by the elastic adjustment of the expansion/contraction of the surrounding elastic solid in such a way that displacement continuity along their common border prevails all around. The remaining question is: What is the magnitude p of the interfacial radial pressure $\sigma_{rr}(a)$ needed to preserve this geometrical compatibility in terms of the initial mismatch Δa.

A general plane solution to this kind of problem is given by Muskhelishvili ([18]). With some algebra, it is shown that

$$p = \frac{4\mu_0\mu\delta}{2\mu_0 a + \mu(\chi_0 - 1)(a-\delta)}, \quad \delta \triangleq \Delta a \tag{11}$$

$$\chi_0 = 3 - 4\nu_0 \quad \text{or} \quad \chi_0 = \frac{3-\nu_0}{1+\nu_0}$$

for plane strain or plane stress, respectively.

If the actual indentation of a ball into the solid during SP is shallow with regard to the ball dimension, the geometrical mismatch is consequently small, say, $\Delta a/a \ll 1$. From elasticity relationships with Poisson ratio of $\nu=1/3$ and Young's modulus of $E \approx 8/3\mu$, Equation (11) gives the magnitude of the residual stress as

$$\frac{p}{\sigma_0} = -\frac{3}{8}\frac{E}{\sigma_0}\varepsilon^p \quad \text{for plane strain} \tag{12a}$$

and

$$\frac{p}{\sigma_0} = -\frac{9}{32}\frac{E}{\sigma_0}\varepsilon^p \quad \text{for plane stress} \tag{12b}$$

Since the disklike inclusion is confined to its plane by the elastic surrounding, the plastic strain is necessarily close to the limit elastic strain; namely, $1/\varepsilon^p \approx 1/\varepsilon_y \approx E/\sigma_0$. As a result of (12*a*) and (12*b*), the residual stress in $r \le a$ is in the range

$$\frac{9}{32} \le \left|\frac{p}{\sigma_0}\right| \le \frac{3}{8} \tag{13a}$$

If there is no interaction between the bombarding balls that impinge the whole surface, one can conclude from Eq. (13*a*) that after SP operation the solid is subjected to residual pressure of about

$$p \approx -\frac{1}{3}\sigma_0. \tag{13b}$$

This theoretical estimation of residual stress is on the lower end of experimentally measured values from post-SP solids [14,20], where the ratio p/σ_0 of about $-1/2$ is quoted rather than $-1/3$. However, one can see that the comparison becomes much closer when replacing the ideal rigid-plastic yield stress σ_0 by the ultimate tensile stress $\sigma_{\text{uts}}(\ge\sigma_0)$ in Eq. (13*a*). For example, with steel alloy (S48C) (where $\sigma_{\text{uts}}=630$ MPa) the measured residual compressive stresses, using X-ray diffraction techniques, vary near to $\sigma_{rr}^{(\text{res})} \approx \sigma_{\theta\theta}^{(\text{res})} \approx -200$ MPa (i.e., $p/\sigma_0 \approx -0.32$). Tests with aluminum 7075 (where $\sigma_{\text{uts}}=526$ MPa) the experimental residual stress were also $\sigma_{rr}^{(\text{res})} \approx \sigma_{\theta\theta}^{(\text{res})} \approx -200$ MPa (i.e., $p/\sigma_0 \approx -0.38$). Hence, the agreements with the prediction of Eq. (13*b*) are satisfactory. On the other hand, in regard to steel alloy 080M40, with experimental values of ($\sigma_{\text{uts}}=550$ MPa and $\sigma_{rr}^{(\text{res})} \approx \sigma_{\theta\theta}^{(\text{res})} \approx -440$ MPa), the ratio appears to be $p/\sigma_0 \approx -0.8$, which is considerably greater than anticipated.

6 In-Plane Fatigue Loading

During working conditions, the structure is assumed to undergo fatigue loading of all kinds, but primarily at relatively low stress levels (such as vibrations that result from rotating engines, considered as "high cycle fatigue"). If the shot-peened structure is subjected to "low cycle fatigue," the residual stress is presumably less important in light of the accompanying large scale plasticity. The following analysis stays general by including the whole spectrum of possible loadings. How is the SP effect quantified or (more precisely) what is the demarcation between the safe fluctuating stress amplitude for "infinite" lifetime and the unsafe stress amplitude at which the structure may eventually fail by ratcheting? The shakedown theorem is structured to give lower bound estimation to this question.

Elastic Solutions. Solutions for the elastic stress distribution caused by the (in-plane) remote fluctuating stress, $\sigma_\infty(t)$ inside the inclusion (with superscript "0") and outside it (with superscript "*e*") are solved rigorously by Muskhelishvili [19]. They are, respectively,

$$\sigma_{rr}^{(0)}(t) = \frac{\sigma_\infty(t)}{2}[\beta_0 - \delta_0\cos(2\theta)]$$

$$\sigma_{\theta\theta}^{(0)}(t) = \frac{\sigma_\infty(t)}{2}[\beta_0 - (6\gamma_0\rho^2 - \delta_0)\cos(2\theta)] \quad \rho \equiv (r/a) \le 1 \tag{14}$$

$$\tau_{r\theta}^{(0)}(t) = \frac{\sigma_\infty(t)}{2}(3\gamma_0\rho^2 - \delta_0)\sin(2\theta)$$

and

$$\sigma_{rr}^{(e)}(t) = \frac{\sigma_\infty(t)}{2}\{1 - \gamma\rho^{-2} - [1 - 2\beta\rho^{-2} - 3\delta\rho^{-4}]\cos(2\theta)\}$$

$$\sigma_{\theta\theta}^{(e)}(t) = \frac{\sigma_\infty(t)}{2}\{1 + \gamma\rho^{-2} + [1 - 3\delta\rho^{-4}]\cos(2\theta)\} \quad \rho \equiv (r/a) \ge 1 \tag{15}$$

$$\tau_{r\theta}^{(e)}(t) = \frac{\sigma_\infty(t)}{2}[1 + \beta\rho^{-2} + 3\delta\rho^{-4}]\sin(2\theta)$$

The parameters $\beta_o, \gamma_o, \delta_o$ in (14) and β, γ, δ in (15) depend on the four elastic constants of the two constituent materials $(\mu, \mu_0, \chi, \chi_0)$ as if they are virtually two different materials, according to

$$\gamma_0 = 0$$
$$\beta_0 = \frac{\mu_0(\chi+1)}{2\mu_0 + \mu(\chi_0 - 1)}, \quad \delta_0 = \frac{\mu_0(\chi+1)}{\mu + \mu_0\chi} \tag{16}$$

and

$$\gamma = \frac{\mu(\chi_0 - 1) - \mu_0(\chi - 1)}{2\mu_0 + \mu(\chi_0 - 1)}$$
$$\beta = -\frac{2(\mu_0 - \mu)}{\mu + \mu_0\chi}, \quad \delta = \frac{\mu_0 - \mu}{\mu + \mu_0\chi} \tag{17}$$

where

$$\chi = 3 - 4\nu \quad \chi_0 = 3 - 4\nu_0 \quad \text{for plane strain}$$
$$\chi = \frac{3-\nu}{1+\nu} \quad \chi_0 = \frac{3-\nu_0}{1+\nu_0} \quad \text{for plane stress} \tag{18}$$

The average fluctuating stress inside the inclusion is then

$$\sigma_m^{(0)}(t) = \frac{1}{3}\sigma_{ii}^{(0)}(t) = \frac{1}{3}(\sigma_{rr}^{(0)}(t) + \sigma_{\theta\theta}^{(0)}(t) + 0) \tag{19}$$

In view of (14) and (16), (19) is reduced to

$$\sigma_m^{(0)}(t) = \frac{\beta_0}{3}\sigma_\infty(t) \tag{20}$$

By substitution of the Poisson ratios $\nu=1/3$ and $\nu_0=1/2$ in β_0, the outcome is $\beta_0=9/8$.

A remarkable result that emerges from Eq. (20) is that the fluctuating average mean stress inside the inclusion is *independent of the positional coordinates* $(r \le a)$. This result is in agreement with Eshelby's well known "inclusion paradox" [21] stating that a remote load acting on an elastic solid (even in a 3D case) will always render a uniform stress inside an imbedded foreign inclusion.

7 Lower Bound by Shakedown Analysis

Melan's theorem [4] states that an elastic-plastic material subjected to a fluctuating load will respond to the load in an elastic way if the fluctuating *unbounded elastic stress* (*not* the actual elastic-plastic stress under the same boundary conditions) superimposed on a time-independent admissible residual stress field possessed by the structure, does not exceed the yield strength of the material.

In other words, the structure subjected to cyclic loading between prescribed limits will shakedown (i.e., will respond elastically without accumulation of strain) if the sum of the two stress distributions (the residual stress and the applied stress), $\sigma_{ij}^{(\mathrm{res})} + \sigma_{ij}^{(e)}(t)$, will not exceed yielding anywhere at all times. This means

$$F[\sigma_{ij}^{(\mathrm{res})} + \sigma_{ij}^{(e)}(t)] \leq \sigma_0 \quad \text{in } V, \text{ for any time } t \tag{21}$$

where $F(\cdots)$ is any applicable yield function in the volume V of the considered material. The equality sign in Eq. (21) produces the shakedown condition.

The shakedown condition is the locus of the lower bound solution for the greatest allowable fatigue-safe stress amplitudes for "infinite" life (called "fatigue limit," "endurance limit" or "fatigue threshold" σ_{th}) at all possible magnitudes of the elastic residual stresses existing in the solid.

Let us assign, for convenience, the instantaneous sum of the elastic stress and the residual stress as

$$\sigma_{ij}^{(\mathrm{sum})}(t) \equiv \sigma_{ij}^{(e)}(t) + \sigma_{ij}^{(\mathrm{res})} \tag{22}$$

By specifying a certain yield function $F(\cdots)$ to Eq. (21), the shakedown analysis is constructed via, say, von Mises yield criterion, by the following steps:

(i) Use the yield condition F$(\cdots)$, which is

$$F = \frac{1}{2}[(\sigma_{rr}^{(\mathrm{sum})} - \sigma_{\theta\theta}^{(\mathrm{sum})})^2 + (\sigma_{\theta\theta}^{(\mathrm{sum})} - \sigma_{zz}^{(\mathrm{sum})})^2 + (\sigma_{zz}^{(\mathrm{sum})} - \sigma_{rr}^{(\mathrm{sum})})^2] + 3\tau_{r\theta}^{(\mathrm{sum})2} = \sigma_0^2 \tag{23}$$

(ii) Use the elastic stress components, $\sigma_{ij}^{(e)}(t)$ from Eq. (15) and the residual stress components $\sigma_{ij}^{(\mathrm{res})}$ from Eq. (14) to specify the expression (22).

(iii) Substitute Eq. (22) into Eq. (23) to render a closed form expression (though lengthy) for the *shakedown condition*, written shortly in terms of its independent variables as

$$F\{\sigma_\infty^2, p^2, \theta, \rho\} = \sigma_0^2 \tag{24}$$

In order to satisfy Eq. (24), one has to search through the loaded structure for the *first yielding point*.

Due to linearity of the elastic stress fields (up to yielding) the location of this point does not vary at various stress amplitudes. It was found to be positioned always on the inclusion/matrix interface (at $\rho=1$, and $\theta=45$ deg). As a result, Eq. (24) is reduced to the following ellipselike expression in the stress space using the normalized stress amplitude $(\sigma_\infty(t)/\sigma_0)$ and the normalized residual stress (p/σ_0) as coordinates. It yields

$$K_{11}\left(\frac{\sigma_\infty(t)}{\sigma_0}\right)^2 + K_{12}\left(\frac{\sigma_\infty(t)}{\sigma_0}\right)\left(\frac{p}{\sigma_0}\right) + K_{22}\left(\frac{p}{\sigma_0}\right)^2 = 1 \tag{25}$$

The coefficients of the ellipse given in Eq. (25) are evaluated in plane strain case to be: $K_{11}=1$, $K_{12}=1$, $K_{22}=1$. In plane stress case they are $K_{11}=273/256$, $K_{12}=9/8$, $K_{22}=1$. These two ellipses are drawn for the whole range of elastic residual stresses in Fig. 3, using zero-tension and zero-compression loading histories. In the considered problem, the difference between plane strain and plane stress solutions is practically indistinguishable. The meaning of the shakedown condition of Eq. (25) is that the applied stress $\sigma_\infty(t)$ is fatigue safe when it falls inside (or on) the ellipses of Fig. 3. Stress amplitudes that are outside the ellipses are prone to fatigue failure by ratcheting.

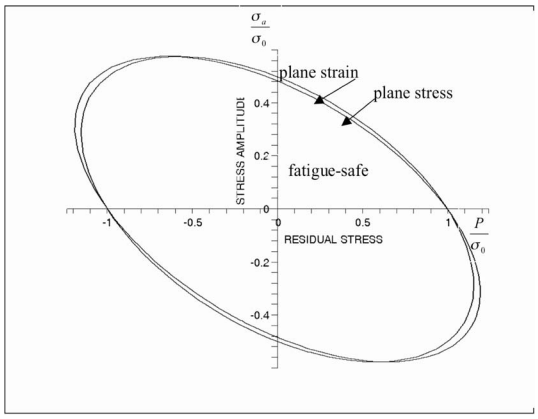

Fig. 3 The shakedown condition (solid curves) for zero-tension and zero-compression loading as a function of the magnitude of the residual stresses for plane stress and plane strain cases (akin to a thin surface layer of the structure and its bulk respectively). The difference in the present fatigue problem is considered negligible. The stress values inside the closed ellipses indicate fatigue-safe loading amplitudes. The stress values outside the ellipse indicate unsafe fatigue loading in the sense of being exposed to accumulation of plastic strains (ratcheting). The solid lines are the demarcation between safe and unsafe fatigue loading (shakedown conditions).

In classical fatigue experiments (i.e., laboratory fatigue tests) the fluctuating loads are prescribed between extreme amplitudes of $\sigma_{\infty\max}$ and $\sigma_{\infty\min}$ during harmonic time periods. It is customary to define a *time-independent average mean stress* to which the structure is continuously subjected as

$$\sigma_m = \frac{[\sigma_{\infty\max} + \sigma_{\infty\min}]}{2} \tag{26}$$

For fully reversed fatigue loading (namely, $R=-1$, where $R \equiv \sigma_{\infty\min}/\sigma_{\infty\max}$) the mean stress in the bulk structure is zero. However, if the structure has undergone SP beforehand, the hydrostatic residual pressure at the affected surface layer shifts the "zero-ground mean stress" to a negative value with a clear fatigue-limit advantage.

It is suggested herewith to consider the loading mean stress of Eq. (26) as an *enlarged definition of time-independent residual stress* acting throughout the bulk structure. Thus, (after replacing p by σ_m and naming the fluctuated stress amplitude $\sigma_\infty(t)$ by σ_a in Eq. (25)), *the shakedown condition provides admissible generality for fatigue analysis*. The final expression (plotted in Fig. 4(*a*)) is hence given by

$$K_{11}\left(\frac{\sigma_a}{\sigma_0}\right)^2 + K_{12}\left(\frac{\sigma_a}{\sigma_0}\right)\left(\frac{\sigma_m}{\sigma_0}\right) + K_{22}\left(\frac{\sigma_m}{\sigma_0}\right)^2 = 1 \tag{25'}$$

The experimental fatigue data added to Fig. 4(*a*) were collected from Dowling [22].

A good agreement is seen for positive mean stress with regard to the empirical formulas of Gerber [12] and Goodman [13] and the suggested shakedown curve. In the negative mean stress regime both empirical lines are clearly inappropriate, while the suggested theoretical curve appears in agreement with experiments. Presently, no other theoretical expression has yet been offered to describe how negative mean stress (in particular) affects the fatigue limit of structures.

8 Quantification of SP Merits

The stress amplitude of the fatigue limit is defined for practical purposes as the threshold stress amplitude σ_{th} at which the struc-

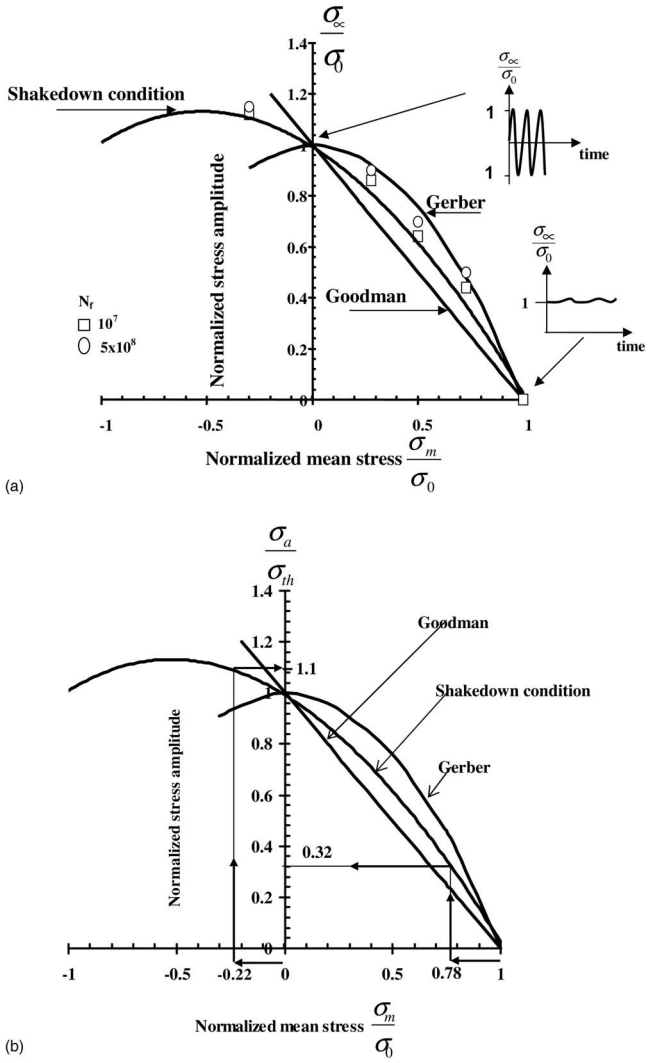

Fig. 4 (*a*) The anticipated deterioration/enhancement of the fatigue limit (in fully reversed fatigue cycles) by an increase/decrease of the mean stress (the SP affected layer is always under residual hydrostatic pressure and thus always reduce the mean stress in the layer). The comparison to "historic" experimental functions (Gerber's parabola, 1874, Goodman's line, 1899), is satisfactory merely along the positive side of the mean stress. The shakedown analysis solution seems to comply with experiments also in the negative side. The fatigue data were performed on 7075-T6 aluminum by Dowling [22] for infinite life (where the number of cycles are $N_f \geq 10^7$). (*b*) Schematic demonstration of the anticipated improvement in fatigue-limit achievable by SP operation, shown, as an example, at two extreme structural mean stress: $\sigma_m=0$ *and* $\sigma_m=\sigma_0$. The associated improvements in the fatigue limit are calculated to be increased by 10% and 32%, respectively.

ture can survive at least $N_f \geq 10^7$ cycles under a fully reversed cycles (that is at $\sigma_m=0$). Therefore, in order to quantify the advantage of SP in increasing the fatigue limit, it is convenient to normalize the stress amplitude in Eq. (25′) with respect to the fatigue limit at fully reversed cycles; namely, by replacing σ_0 by σ_{th} without any change otherwise, as shown in Fig. 4(*b*).

The plot indicates a sharp deterioration in the allowable stress amplitude (or alternatively diminishing fatigue life) when the mean tensile stress in the structure is increased. Inversely, *a significant improvement in fatigue limits is manifested when decreasing the loading mean stress*; i.e., *by adding compressive hydrostatic residual stress*. This primary merit of the SP process is examined as follows.

Consider structures undergoing fluctuating load with fully reversed cycles, $\sigma_{\infty\max}=-\sigma_{\infty\min}$. After applying the SP process, which causes residual compressive layer of $p \cong -\sigma_0/3$ (from (13*b*)), the mean stress in this layer is changed by

$$\Delta\sigma_m^{(0)} \cong -2p/3 \cong -0.22\sigma_0 \tag{27a}$$

The associated improvement in the fatigue limit is readily understood from Fig. 4(*b*). It shows that the stress amplitude of the fatigue limit is favorably increased by 10%, namely,

$$\Delta\sigma_\infty^{(0)} = 0.10\sigma_{\text{th}} \tag{27b}$$

On the other extreme, consider loading amplitude near $\sigma_m^{(0)}=\sigma_0$. In this case the structure will not shakedown, which means that it will fail (by ratcheting) for any added positive residual stress and/or for slightly higher stress amplitudes. However, when applying the SP process, the mean stress is reduced by

$$\Delta\sigma_m^{(0)} \cong \sigma_0 - 2p/3 \tag{27c}$$

and no fatigue failure is expected.

In such a situation, as exhibited in Fig. 4(*b*), the allowable stress amplitudes is consequently raised by 32%, since

$$\Delta\sigma_\infty^{(0)} = 0.32\sigma_{\text{th}} \text{ (when } \sigma_m = \sigma_0) \tag{27d}$$

and thus enables the prolonging of fatigue life.

The experimental S-N curve (stress versus number of cycles) of Hammond and Meguid [14] can now be replotted by superimposing on their pre-SP measurements the predicted fatigue-limit improvements. The results are compared to their actual post-SP measurements in Figs. 5(*a*) and 5(*b*) for two different materials.

9 Discussion

The pronounced benefit of SP process is to reduce (at the treated surface layer) the hazardous mean stress level of the fatigue loading. This reduction is a result of a favorable residual stress induced by the SP process. The associated improvement in the allowable fatigue limit amplitude with respect to non-shot-peened structures is at least 10% (when the loading mean stress is zero, i.e., $\sigma_m=0$) and up to 32% (when the loading mean stress is close to the yield stress, i.e., $\sigma_m=\sigma_0$), as seen in Fig. 4(*b*). The theoretical anticipation agrees relatively well with experimental data (see Figs. 5(*a*) and 5(*b*)).

The above benefit of SP processes is not complete without considering its down side. As mentioned, the core of the solid beneath the SP layer has inevitably (from static equilibrium consideration) a tensile in-plane residual stress as well. This tensile stress has an adverse effect on fatigue lifetime, the magnitude of which needs to be explored in each case. Since the layer that contains the compressive residual stress of SP processes was shown to be thin, the remaining cross-sectional area of the solid should be much thicker in order to "disperse" along a longer distance (and thus to lower) the detrimental effect of the residual tensile stress (see Fig. 6). Such a conclusion was evidenced in [14] and [20]. It becomes clear now that there is no beneficial reason, for instance, to shot peen *thin* sheets of metals.

Finally, another quantitative advantage of SP is worth mentioning. The fact that the compressive residual stress is concentrated along a thin layer adds a meaningful advantage regarding the *damage tolerant approach*. It is known that micro-cracks tend to propagate from the free surfaces, because (by fracture mechanics arguments) they have higher stress intensity factors (by about 12%) compared to micro-cracks of the same length inside the volume subjected to the same loads. The presence of the residual compressive stress at the surface layer is superimposed on the tensile fatigue stress and hence diminishes its harmful effect on driving cracks propagation. Therefore, SP processes enhance longer fatigue life *also* by delaying (or even arresting) elongation of cracks from free surfaces.

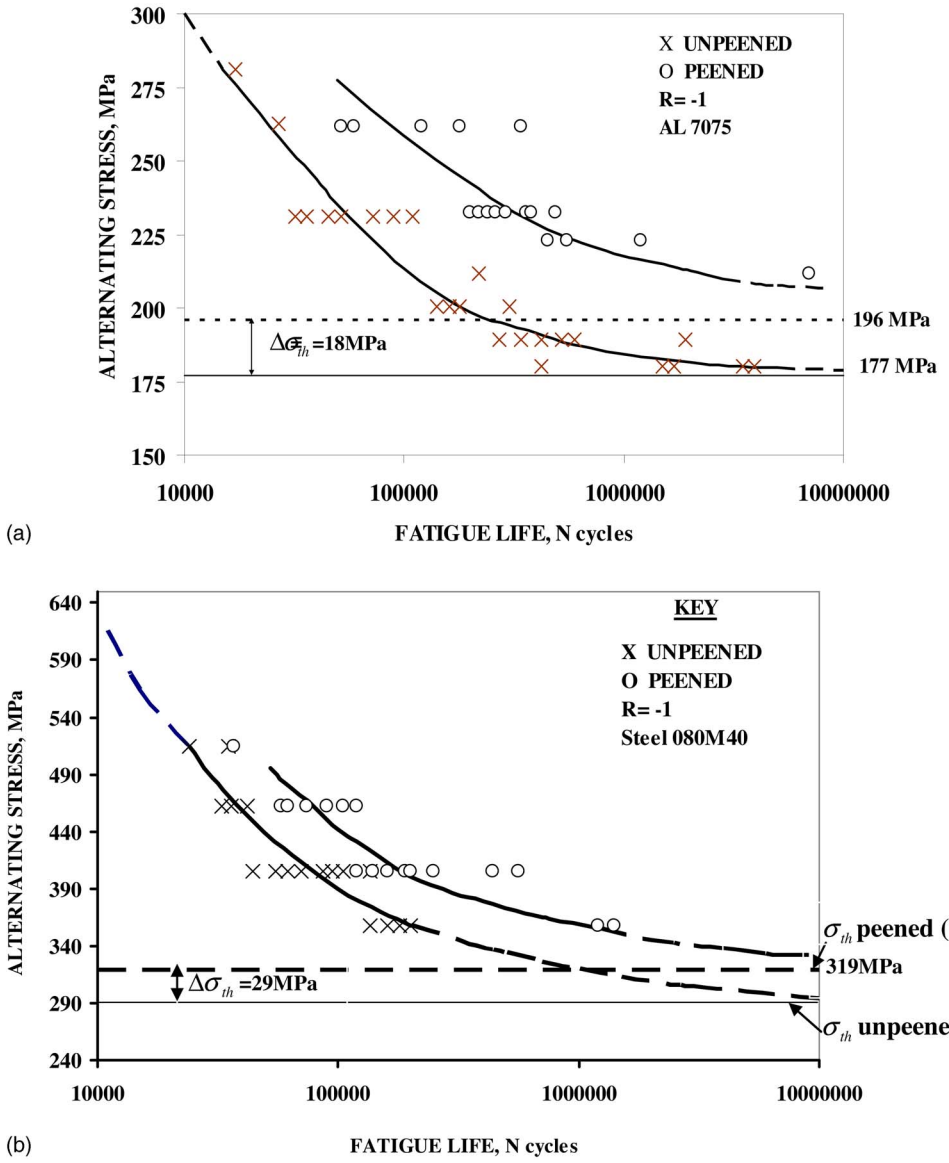

Fig. 5 (*a*) **Experimental fatigue data (taken from [15]) shows fatigue limit of about 177 MPa for the unpeened material (aluminum 7075). From shakedown analysis, the fatigue limit was anticipated to increase from 177 MPa to about 195 MPa after operating with SP. Data for post-SP measurements indicates that the prediction is satisfactory (but lower by about 5%) in agreement with the lower bound concept of Melan's theorem). (*b*) Fatigue data of pre-SP steel (080M-40) shows fatigue limit of 290 MPa. Shakedown analysis predicted an increase of fatigue limit from 290 MPa to 319 MPa after operating with SP. Test results (taken from [15]) are shown to be very close to the anticipated post-SP fatigue limit.**

10 Conclusions

(a) The theoretical shakedown analysis is shown to capture relatively well the influence of the mean loading stress on fatigue limits on both positive and negative sides of the diagram.

(b) The overall attribute of SP is to enhance the fatigue limit by adding negative residual mean stress into the surface layer of the structure.

(c) This favorable effect is lightly non-linear (as opposed to Goodman's line). The quantified improvement varies from 10% to 32% in the stress amplitude of the fatigue limit.

(d) The potential propagation of micro-cracks in the SP affected surface layer is delayed (or entirely arrested) by the residual compressive stress layer.

(e) The bulk core of the structure is unavoidably affected by self-equilibrated residual tensile stresses whose magnitude depends on the structure thickness. From this regard, the expected SP improvement of fatigue life is slightly worsened. Statistically, this overall view may be reflected by relatively large scatter of experimental fatigue data (as seen, for example, in Figs. 5(*a*) and 5(*b*)). Such considerations seemingly have passed unnoticed in the literature.

Acknowledgment

The author is indebted to Prof. L. Anand for fruitful discussions, to Prof. D. Parks for comprehensive lectures on Fatigue (MIT, Spring 2005) and to Prof. F. McClintock for celebrating with the author 40 years of past mentor/student relationship. The

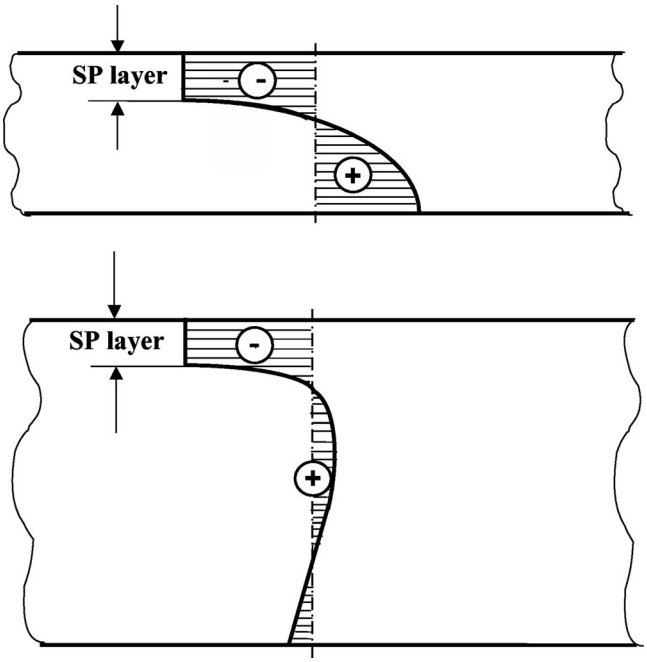

Fig. 6 A schematic view on the in-plane residual stress distribution along cross sections of thin and thick plates resulting from a shot-peening process. It is seen that the thicker the plate the lower is the magnitude of the (harmful) tensile stress, unavoidably arises beneath the SP top layer (to equilibrate the compressive stress generated in the SP layer). The sign "–" stands for compressive stress and "+" for the tensile stress. The associated bending moments (undesired in most cases) will also be less pronounced in thicker plates.

overall research was supported by funds for research promotion at the Technion via the National Academy of Science in Israel, SMOLER RESEARCH FUND and M. & C. Papo Research Fund. Special thanks go to Dr. L. Rubinski from the Metal-Forming Lab. in the Faculty of Mechanical Engineering for high quality technical assistance.

References

[1] Timoshenko, S., and Goodier, J. N., 1951, *Theory of Elasticity*, McGraw-Hill, New York.
[2] Broek, D., 1988, *The Practical Use of Fracture Mechanics*, Kluwer Academic, Dordrecht, The Netherlands.
[3] Anonymous, 1989, "*Shot Peening of Metal Parts*," Military Specification, MIL-S-13165C.
[4] Melan, E., 1936, "Theorie statisch unbestimmter Systeme aus idealplastischem Baustoff," Sitzungsbericht der Akademie der Wissenschaften (Wien) Abt. IIa, **145**, pp. 195–218.
[5] Dvorak, G. J., and Tarn, J. Q., 1975, "Fatigue and shakedown in metal matrix composite," in *Fatigue of Composite Materials, ASTM, STP 569*, ASTM, West Conshohocken, PA, pp. 145–168.
[6] Ponter, A. R. S, and Engelhardt, M., 2000, "Shakedown Limits for a General Yield Condition: Implementation and Application for a Von Mises Yield Condition," Eur. J. Mech. A/Solids, **19**, pp. 423–425.
[7] Ponter, A. R. S., and Karadeniz, S., 1985, "An Extended Shakedown Theory for Structures that Suffer Cyclic Thermal Loading. 1-Theory," ASME Trans. J. Appl. Mech., **52**, pp. 877–882.
[8] Kapoor, A., and Johnson, K. L., 1994, "Plastic Ratcheting as a Mechanism of Metallic Wear," Proc. R. Soc. London, Ser. A, **445**, pp. 367–381.
[9] Tirosh, J., 1998, "On the Shakedown Conditions for Dilute Reinforced Composite," J. Mech. Phys. Solids, **46**, pp. 167–185.
[10] Polizzotto, C., 1993, "On the Conditions to Prevent Plastic Shakedown of Structures. I. Theory," ASME Trans. J. Appl. Mech., **60**, pp. 15–19; 20–25.
[11] Polizzott, C., 1993, "A Study on Plastic Shakedown of Structures: I-Basic Properties," ASME Trans. J. Appl. Mech., **60**, pp. 318–323; 324–330.
[12] Gerber, H., 1874, "bestimungm der Zulassigen Spannungen in Eisenkonstructionen," Z Bayer Arch Ingenieur-Vereins, **6**, pp. 101–110.
[13] Goodman, J. M, 1899, *Mechanics Applied to Engineering*, Longmans, Green.
[14] Al-Obaid, Y. F., 1990, "A Rudamentary Analysis of Improving Fatigue Life of Metals by Shot-Peening," ASME Trans. J. Appl. Mech., **57**, pp. 307–312.
[15] Hammond, D. W., and Meguid, S. A., 1990, "Crack Propagation in the Presence of Shot-Peening Residual Stress," Eng. Fract. Mech., **37**(2), pp. 373–387.
[16] Tirosh, J., and Peles, S., 2001, "Bounds on the Fatigue Threshold in Metals," J. Mech. Phys. Solids, **49**, pp. 1301–1322.
[17] Bower, A. F., Fleck, N. A., Needleman, A., and Ogbonna, N., 1993, "Indentation of a Power Law Creeping Solid," Proc. R. Soc. London, Ser. A, **441**, pp. 97–124.
[18] Johnson, K. L., 1985, *Contact Mechanics*, Cambridge University Press, New York.
[19] Muskhelishvili, N. I., 1963, *Some Basic Problems of the Mathematical Theory of Elasticity*, P. Noordhoff Ltd., Groningen, The Netherlands.
[20] Kobayashi, M., Matzui, T., and Murakami, Y., 1998, "Mechanism of Creation of Compressive Residual Stress by Shot Peening," Int. J. Fatigue, **20**(5), pp. 351–357.
[21] Eshelby, J. D., 1957, "The Determination of the Elastic Field of an Ellipsoidal Inclusion," Proc. R. Soc. London, Ser. A, **A241**, pp. 376–386.
[22] Dowling, N. E., 1999, *Mechanical Behavior of Materials*, Prentice-Hall, Englewood Cliffs, NJ.

Parametric Instability of a Moving Particle on a Periodically Supported Infinitely Long String

A. V. Metrikine
Faculty of Civil Engineering and Geosciences,
Delft University of Technology,
P.O. Box 5048,
2600 GA Delft, The Netherlands

A new method is proposed of theoretical analysis of the dynamic instability of a moving object on a periodically supported, infinitely long elastic structure. To demonstrate this method, a simple example is considered of a moving particle on an elastically supported string. The equations are obtained that govern the system parameters that correspond to the boundaries separating stability and instability in the parameter space. These equations are in the form of the determinant of an infinite matrix and are analogous to Hill's infinite determinant. A parametric analysis of the instability zones is carried out in the plane of the normalized particle mass and particle velocity. The focus is placed on the effect of elasticity and viscosity of the supports. An analytical validation is presented of the numerically obtained instability zones. This is done using a simplified model of the string on the corresponding continuous foundation. [DOI: 10.1115/1.2745368]

1 Introduction

As an integral part of the development of high-speed railway lines, the moving load problem has been the subject of many research efforts [1]. Vibrations of the rails caused by train wheels as well as vibrations of the overhead power lines induced by current collectors were in the focus of these efforts. The vast majority of the studies assumed that if the elastic system (a rail or a contact wire) is sufficiently long and the load speed is constant the steady-state regime will be reached by the system after a sufficiently long time. This implies that the dynamic interaction between the moving load and elastic system was assumed to be dynamically stable.

The dynamic stability of a moving load is not guaranteed provided that the degrees of freedom of the load are accounted for, for example, if the load is modeled as a mass-spring system in the gravity field. The possibility of the dynamic instability of a load on an infinitely long homogeneous elastic system was first demonstrated in [2] and [3]. The underlying physics of this phenomenon was explored in [4]. The engineering relevance of this type of instability for railways on soft soil was addressed in [5].

The instability of a moving load on a periodically inhomogeneous elastic system was first shown in [6]. This type of instability is closely related to parametric resonance in dynamic systems, the parameters of which vary periodically in time. Indeed, the parameters of a periodically inhomogeneous elastic system at the contact point with a moving load vary periodically in time provided that the load velocity is constant. The period of this variation equals d/V, where d is the spatial period of inhomogeneity and V is the load velocity. Obviously, one can expect parametric resonance if one of the natural frequencies of the load on the elastic system equals $nd/2V$.

Because of the relative difficulty of mathematical analysis that is needed to find the instability zones for a moving load on a periodically inhomogeneous system, only a few particular models have been analyzed in the past. In the pioneering paper [6], an oscillator was considered on a series of simply supported beams. Using the known mode shapes of this series of beams, the problem was reduced to an infinite set of ordinary differential equations with periodic in time coefficients. This system was subsequently analyzed using Hill's method of infinite determinants [7,8]. In [9] and [10], a perturbation method was applied assuming that the inhomogeneity of the elastic system is small. In [11], the reaction of a periodically inhomogeneous overhead wire system to a moving pantograph was replaced by a spring, the stiffness of which varies in time periodically. To describe this stiffness, both the static and dynamic stiffness of the wire were used.

The methods of the stability analysis presented in [6–11] are not general. The method introduced in [6] requires the mode shapes of the elastic system be known in advance, which is normally impossible, since such guideways as railway tracks and overhead power lines are supported elastically. The method developed in [9,10] requires the parameter variation be small with respect to the mean value, which is not realistic either. The method proposed in [11] is approximate since it does not account for the dependence of the dynamic stiffness of the elastic system on its interaction with the load. Thus, to the knowledge of the author of this paper, no published account exists of a general method, which would allow study of the dynamic stability of a load on a periodically inhomogeneous system.

In this paper, a method is proposed that allows one to find the instability zones of a moving particle on a periodically supported string. The supports are discrete and not rigid. The adopted model represents simplistically the dynamic interaction of an overhead power line and the current collector of a train.

The proposed method can be straightforwardly extended in the future to cope with other periodically inhomogeneous structures and more complex load descriptions provided that the load and the elastic structure have only one contact point. In the case of multiple contact points, the extension is somewhat more cumbersome.

This paper is structured as follows. In Sec. 2, the governing equations are given and the idea of the proposed method is explained. In Secs. 3 and 4, the equations are obtained, which determine the system parameters corresponding to the boundaries of the instability zones. The method of numerical analysis of these equations is discussed in Sec. 5. In Sec. 6, a parametric analysis of the instability zones is presented. To explain qualitatively the position of the instability zones in the parameter space, a corresponding simplified model is studied analytically in Sec. 7. A short discussion of the engineering relevance of the obtained results concludes the paper.

Contributed by the Applied Mechanics Division of ASME for publication in the JOURNAL OF APPLIED MECHANICS. Manuscript received June 9, 2006; final manuscript received March 7, 2007; published online January 11, 2008. Review conducted by Oliver M. O'Reilly.

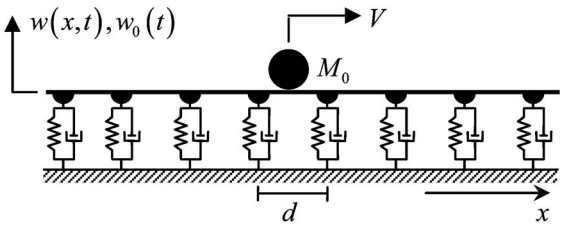

Fig. 1 Model

2 Equations of Motion

Referring to Fig. 1, we consider a particle that uniformly moves along a taut, periodically supported string. The linear dynamics of this system is governed by the following set of nondimensional equations

$$\partial_{\tau\tau} w - \partial_{\xi\xi} w = -M\delta(\xi - \alpha\tau) d_{\tau\tau} w_0$$

$$[\partial_\xi w]_{\xi=m} = (m_s d_{\tau\tau} + c_s d_\tau + k_s) w(m,\tau)$$

$$[w]_{\xi=m} = 0, \quad w_0(\tau) = w(\alpha\tau,\tau) \tag{1}$$

The first equation of this system governs the string dynamics under the moving particle. The second equation is the balance of vertical forces at the supported points of the string. The third equation ensures the string continuity, whereas the fourth equation states that the particle and the string are always in contact.

In Eqs. (1), $w(\xi,\tau)$ and $w_0(\tau)$ are the vertical displacements of the string and the moving mass, respectively; ξ and τ are the nondimensional coordinate and time; M and α are the nondimensional mass and speed of the particle; m_s, c_s, and k_s are the nondimensional mass, viscous damping coefficient, and stiffness of each support; $\xi=m$ is the position of the support number m, $m=0,\pm1,\pm2,\ldots$; $\partial_\tau=\partial/\partial\tau$, $\partial_\xi=\partial/\partial\xi$, $d_\tau=d/d\tau$, $\delta(\cdots)$ is the Dirac delta function, and the square brackets imply the following difference $[f(\xi)]_{\xi=m}=f(m+0)-f(m-0)$.

The relations between the nondimensional and original variables and parameters are given as

$$\tau = \frac{tc}{d}, \quad \xi = \frac{x}{d}$$

$$\alpha = \frac{V}{c}, \quad M = \frac{M_0}{d\rho A}$$

$$m_s = \frac{m_0}{d\rho A}, \quad k_s = \frac{k_0 d}{T}, \quad c_s = \frac{c_0 c}{T} \tag{2}$$

where d is the distance between two neighboring supports, c is the wave speed in the string ($c=\sqrt{T/\rho A}$), T and ρA are the tension and the mass per unit length of the string, M_0 and V are the mass and speed of the particle, and m_0, c_0, and k_0 are the mass, viscous damping coefficient, and stiffness of each support.

Note that no external vertical forces, which may act on the string and particle, are accounted for in the equations of motion. These forces do not influence the dynamic stability of the system in the linear approximation and, therefore, can be omitted as long as only the system stability is addressed.

It is obvious that if the moving particle is disturbed from its horizontal motion, it will excite waves in the string. The reaction of these waves will either decrease the energy of the transverse particle vibration or increase it. The latter option is possible thanks to the external energy source that must be present to maintain a constant speed of the particle along the string. If this option is realized, the system will be unstable. To find the boundaries of the instability domains in the space of system parameters, a relationship between these parameters has to be found that corresponds to a periodic in time transverse motion of the particle.

In this paper, we postulate that the period of the above motion should be either equal to or twice bigger than d/V, which is the period of variation of the string parameters under the particle. This postulate is justified by a clear analogy with vibrations of a mass on a spring with periodically varying in time stiffness, which is described by Hill's equation or Mathieu's equation. For these equations it is known that the boundaries of all instability zones correspond to the mass vibrations with the period that is equal to or twice bigger than the period of the stiffness variation. Note that if not the particle but a multi-degree-of-freedom oscillator would move on the string, periodic motions with other periods would also be possible.

Exploiting the postulated analogy, we represent the particle transverse motion with the periodicity $2d/V$ by the following Fourier series:

$$w_0(\tau) = \sum_{n=1}^{\infty} \{A_n \sin[\pi\alpha\tau(2n-1)] + B_n \cos[\pi\alpha\tau(2n-1)]\} \tag{3}$$

The form of this series directly follows from the Floquet theorem provided that it is applied to a single degree of freedom system [8].

Analogously, d/V-periodic motions can be represented as

$$w_0(\tau) = B_0 + \sum_{n=1}^{\infty} [A_n \sin(2\pi\alpha\tau n) + B_n \cos(2\pi\alpha\tau n)] \tag{4}$$

The above expression will be used in the next sections to obtain infinite determinants (analogous to Hill's determinants), using which the boundaries of the instability zones will be found.

3 $2d/V$-Periodic Boundaries

In this section, the instability zones whose boundaries correspond to $2d/V$-periodic motions are addressed. The analysis is based on finding the response of the string to the particle vibration described by Eq. (3) with the subsequent application of the condition of contact between the particle and the string.

For the analysis to follow, it is customary to rewrite Eq. (3) in the following complex form:

$$w_0(\tau) = \sum_{n=1}^{\infty} (C_n^+ e^{i\pi\alpha\tau(2n-1)} + C_n^- e^{-i\pi\alpha\tau(2n-1)}) \tag{5}$$

where

$$C_n^+ = \frac{B_n - iA_n}{2}, \quad C_n^- = \frac{B_n + iA_n}{2} \tag{6}$$

Substituting Eq. (5) into the governing equations, Eqs. (1), and applying integral Fourier transform over time that is defined as

$$w^{(\omega)}(\xi,\omega) = \int_{-\infty}^{\infty} w(\xi,\tau) \exp(i\omega\tau)\, d\tau \tag{7}$$

we obtain the following system of equations in the frequency domain:

$$\partial_{\xi\xi} w^{(\omega)} + w^{(\omega)}\omega^2 = -\left(\frac{M}{\alpha}\right) \exp(i\omega\xi/\alpha) \sum_{n=1}^{\infty} [\pi\alpha(2n-1)]^2 \times (C_n^+ e^{i\pi\xi(2n-1)} + C_n^- e^{-i\pi\xi(2n-1)}) \tag{8}$$

$$[\partial_\xi w^{(\omega)}]_{\xi=m} = (-m\omega^2 - i\omega c + k) w^{(\omega)}(m,\omega)$$

$$[w^{(\omega)}]_{\xi=m} = 0 \tag{9}$$

Note that the condition of contact between the moving particle and the string is not transformed to the frequency domain. This condition will be used later.

To find the solution of the system of equations (8) and (9), we will employ the so-called periodicity condition, which is often used for finding the steady-state response of periodically inhomogeneous guideways to a uniformly moving harmonic load (see [12–15]). It is natural to use this condition for solving Eqs. (8) and (9), because having assumed the periodicity of the particle vibration, we effectively represented the force imposed by the particle on the string as the superposition of harmonic loads.

The periodicity condition, which satisfies the system of equations (8) and (9), as can be readily checked by direct substitution, reads

$$w^{(\omega)}(\xi) = -w^{(\omega)}(\xi - m)\exp\left(\frac{\mathrm{i}\omega m}{\alpha}\right) \tag{10}$$

To obtain the solution to the problem governed by Eqs. (8) and (9) that satisfies the periodicity condition, the following steps will be undertaken. Firstly, the general solution to Eq. (8) will be written in the interval $0 \le \xi \le 1$. This solution will contain two unknown coefficients. Secondly, this solution will be "extended" to the interval $1 \le \xi \le 2$ by employing the periodicity condition. The solution in the latter interval will contain the same unknown coefficients. Finally, these coefficients will be found using the boundary conditions at $\xi = 1$, Eq. (9).

The general solution of Eq. (8) in the interval $0 \le \xi \le 1$ can be written as

$$w^{(\omega)} = D_1 e^{\mathrm{i}\omega\xi} + D_2 e^{-\mathrm{i}\omega\xi} + w_f^{(\omega)} \tag{11}$$

where

$$w_f^{(\omega)} = \sum_{n=1}^{\infty} e^{\mathrm{i}\omega\xi/\alpha}(E_n^+ e^{\mathrm{i}\pi\xi(2n-1)} + E_n^- e^{-\mathrm{i}\pi\xi(2n-1)}) \tag{12}$$

$$E_n^{\pm} = MZ_n^{\pm}C_n^{\pm}, \quad Z_n^{\pm} = \frac{[\pi\alpha(2n-1)]^2\alpha}{[\omega \pm \pi\alpha(2n-1)]^2 - \alpha^2\omega^2} \tag{13}$$

Using the periodicity condition this solution can be extended to the interval $1 \le \xi \le 2$ to give

$$w^{(\omega)} = -e^{\mathrm{i}\omega/\alpha}(D_1 e^{\mathrm{i}\omega(\xi-1)/\alpha} + D_2 e^{-\mathrm{i}\omega(\xi-1)/\alpha}) + w_f^{(\omega)}(\xi) \tag{14}$$

Now, using the boundary conditions at $\xi = 1$ given by Eq. (9), we can obtain the following system of two algebraic equations with respect to D_1 and D_2:

$$D_1 q + \frac{D_2}{q} = -p(D_1 + D_2)$$

$$-p(D_1 - D_2) - \left(D_1 q - \frac{D_2}{q}\right) = F\left(D_1 q + \frac{D_2}{q} - p\sum_{n=1}^{\infty}(E_n^+ + E_n^-)\right) \tag{15}$$

where

$$q = e^{\mathrm{i}\omega}, \quad p = e^{\mathrm{i}\omega/\alpha}, \quad F = \frac{-m_s\omega^2 - \mathrm{i}\omega c_s + k_s}{\mathrm{i}\omega} \tag{16}$$

The solution of this system can be written as

$$D_1 = \left(\frac{F}{\Delta_2}\right)\left(p + \frac{1}{q}\right)\sum_{n=1}^{\infty}(E_n^+ + E_n^-)$$

$$D_2 = -\left(\frac{F}{\Delta_2}\right)(q+p)\sum_{n=1}^{\infty}[E_n^+ + E_n^-]$$

$$\Delta_2 = 4\left[\cos\left(\frac{\omega}{\alpha}\right) + \cos(\omega) + \frac{\mathrm{i}F\sin(\omega)}{2}\right] \tag{17}$$

Thus, we found the string response in the frequency domain.

Applying the inverse Fourier transform to Eq. (11), the following expression is obtained, which governs the motion of the first span of the string ($0 \le \xi \le 1$) in the time domain:

$$w(\xi,\tau) = \frac{1}{2\pi}\int_{-\infty}^{\infty}\left[e^{-\mathrm{i}\omega\tau}\left(D_1 e^{\mathrm{i}\omega\xi} + D_2 e^{-\mathrm{i}\omega\xi} + \sum_{n=1}^{\infty} e^{\mathrm{i}\omega\xi/\alpha}(E_n^+ e^{\mathrm{i}\pi\xi(2n-1)} + E_n^- e^{-\mathrm{i}\pi\xi(2n-1)})\right)\right] d\omega \tag{18}$$

The displacement of the mass during the time interval $0 < \tau < 1/\alpha$ (when the mass moves over the first span) can be obtained from Eq. (18) using the condition of permanent contact between the particle and the string:

$$w_0(\tau) = w(\alpha\tau,\tau) = \frac{1}{2\pi}\int_{-\infty}^{\infty}\left(D_1 e^{-\mathrm{i}\omega(1-\alpha)\tau} + D_2 e^{-\mathrm{i}\omega(1+\alpha)\tau} + \sum_{n=1}^{\infty}(E_n^+ e^{\mathrm{i}\pi\alpha\tau(2n-1)} + E_n^- e^{-\mathrm{i}\pi\alpha\tau(2n-1)})\right) d\omega \tag{19}$$

Substituting into Eq. (19) the expression for the particle displacement, Eq. (6), and using expressions (13) and (17), we can rewrite Eq. (19) as

$$\begin{aligned}
&\sum_{n=1}^{\infty}\{A_n\sin[\pi\alpha\tau(2n-1)] + B_n\cos[\pi\alpha\tau(2n-1)]\} \\
&= \mathrm{i}\frac{M}{4\pi}\sum_{n=1}^{\infty}A_n\int_{-\infty}^{\infty}\left\{-Z_n^+ e^{\mathrm{i}\pi\alpha\tau(2n-1)} + Z_n^- e^{-\mathrm{i}\pi\alpha\tau(2n-1)} + \frac{F}{\Delta_2}(Z_n^- - Z_n^+)\left[\left(p+\frac{1}{q}\right)e^{-\mathrm{i}\omega(1-\alpha)\tau} - (q+p)e^{-\mathrm{i}\omega(1+\alpha)\tau}\right]\right\} d\omega \\
&+ \frac{M}{4\pi}\sum_{n=1}^{\infty}B_n\int_{-\infty}^{\infty}\left\{-Z_n^+ e^{\mathrm{i}\pi\alpha\tau(2n-1)} + Z_n^- e^{-\mathrm{i}\pi\alpha\tau(2n-1)} + \frac{F}{\Delta_2}(Z_n^- + Z_n^+)\left[\left(p+\frac{1}{q}\right)e^{-\mathrm{i}\omega(1-\alpha)\tau} - (q+p)e^{-\mathrm{i}\omega(1+\alpha)\tau}\right]\right\} d\omega
\end{aligned} \tag{20}$$

Note that both terms on the right-hand side should be real to comply with the real-valued left-hand side.

Our aim is to formulate an infinite set of homogeneous algebraic equations with respect to A_n and B_n, the determinant of which will be the direct analogy of Hill's infinite determinant. Such formulation is somewhat complicated by the explicit presence of time in the integrals. To circumvent this problem, we multiply Eq. (20) by $\sin[\pi\alpha\tau(2m-1)]$ and then integrate over the period of the vibration ($2\alpha\int_0^{1/\alpha}\cdots d\tau$). This yields

$$A_m = M\left(\sum_{n=1}^{\infty}A_n Q_{nm}^{(1)} + \sum_{n=1}^{\infty}B_n Q_{nm}^{(2)}\right) \tag{21}$$

where

$$Q_{nm}^{(1)} = \frac{\mathrm{i}\alpha}{2\pi}\int_{-\infty}^{\infty}\left\{-\frac{\mathrm{i}(Z_n^+ + Z_n^-)\delta_{mn}}{2\alpha} + \frac{F}{\Delta_2}(Z_n^- - Z_n^+)\times\left[\left(p+\frac{1}{q}\right)R_m^{(1)} - (q+p)R_m^{(2)}\right]\right\} d\omega \tag{22}$$

$$Q_{nm}^{(2)}=\frac{\alpha}{2\pi}\int_{-\infty}^{\infty}\left\{\frac{\mathrm{i}(Z_n^+-Z_n^-)\delta_{mn}}{(2\alpha)}+(F/\Delta_2)(Z_n^-+Z_n^+)\times\left[\left(p+\frac{1}{q}\right)R_m^{(1)}-(q+p)R_m^{(2)}\right]\right\}d\omega \tag{23}$$

$$R_m^{(1)}=\frac{-\pi\alpha(2m-1)}{(\omega-\alpha\omega)^2-[\pi\alpha(2m-1)]^2}(1+e^{-\mathrm{i}\omega(1-\alpha)/\alpha}) \tag{24}$$

$$R_m^{(2)}=\frac{-\pi\alpha(2m-1)}{(\omega+\alpha\omega)^2-[\pi\alpha(2m-1)]^2}(1+e^{-\mathrm{i}\omega(1+\alpha)/\alpha}) \tag{25}$$

and δ_{mn} is the Kronecker Delta.

Analogously, multiplication by $\cos[\pi\alpha\tau(2m-1)]$ followed by integration $2\alpha\int_0^{1/\alpha}\cdots d\tau$ reduces Eq. (20) to

$$B_m=\frac{M\alpha}{2\pi}\left(\sum_{n=1}^{\infty}A_nQ_{nm}^{(3)}+\sum_{n=1}^{\infty}B_nQ_{nm}^{(4)}\right) \tag{26}$$

where

$$Q_{nm}^{(3)}=\frac{\mathrm{i}\alpha}{2\pi}\int_{-\infty}^{\infty}\left\{-\frac{(Z_n^+-Z_n^-)\delta_{mn}}{2\alpha}+\frac{F}{\Delta_2}(Z_n^--Z_n^+)\times\left[\left(p+\frac{1}{q}\right)R_m^{(3)}-(q+p)R_m^{(4)}\right]\right\}d\omega \tag{27}$$

$$Q_{nm}^{(4)}=\frac{\alpha}{2\pi}\int_{-\infty}^{\infty}\left\{\frac{(Z_n^++Z_n^-)\delta_{mn}}{2\alpha}+\frac{F}{\Delta_2}(Z_n^-+Z_n^+)\times\left[\left(p+\frac{1}{q}\right)R_m^{(3)}-(q+p)R_m^{(4)}\right]\right\}d\omega \tag{28}$$

$$R_m^{(3)}=\frac{-\mathrm{i}\omega(1-\alpha)}{(\omega-\alpha\omega)^2-[\pi\alpha(2m-1)]^2}(1+e^{-\mathrm{i}\omega(1-\alpha)/\alpha}) \tag{29}$$

$$R_m^{(4)}=\frac{-\mathrm{i}\omega(1+\alpha)}{(\omega+\alpha\omega)^2-[\pi\alpha(2m-1)]^2}(1+e^{-\mathrm{i}\omega(1+\alpha)/\alpha}) \tag{30}$$

Equations (21) and (26) form an infinite set of homogeneous algebraic equations with respect to A_n and B_n, which can be written in the following matrix form:

$$\left(\boldsymbol{Q}^{(1)}-\frac{\boldsymbol{I}}{M}\right)\boldsymbol{A}+\boldsymbol{Q}^{(2)}\boldsymbol{B}=0$$

$$\boldsymbol{Q}^{(3)}\boldsymbol{A}+\left(\boldsymbol{Q}^{(4)}-\frac{\boldsymbol{I}}{M}\right)\boldsymbol{B}=0 \tag{31}$$

where the components of matrices $\boldsymbol{Q}$ are given by Eqs. (22), (23), (27), and (28), $\boldsymbol{I}$ is the identity matrix, $\boldsymbol{A}=\{A_1,A_2,A_3,\ldots\}^{\mathrm{T}}$, and $\boldsymbol{B}=\{B_1,B_2,B_3,\ldots\}^{\mathrm{T}}$. Note that all matrices in Eqs. (31) are real.

In order to guarantee a nontrivial solution of Eqs. (31), the determinant of this system of equations must vanish, e.g., the following equation must be satisfied:

$$\left|\boldsymbol{Q}_3-\boldsymbol{Q}_4\boldsymbol{Q}_2^{-1}\boldsymbol{Q}_1-\frac{1}{M^2}\boldsymbol{Q}_2^{-1}+\frac{1}{M}(\boldsymbol{Q}_4\boldsymbol{Q}_2^{-1}+\boldsymbol{Q}_2^{-1}\boldsymbol{Q}_1)\right|=0 \tag{32}$$

Equation (32) is an analog of the infinite Hill's determinant. The system parameters that satisfy this equation represent the boundaries separating stability and instability in the parameter space. The points of these boundaries correspond to the periodic motions of the particle with periods equal to $2d/V$.

4 d/V-Periodic Boundaries

The boundaries corresponding to d/V-periodic motions of the particle can be derived assuming the Fourier series representation for the particle deflection given by Eq. (4). Rewriting this equation as

$$w_0(\tau)=B_0+\sum_{n=1}^{\infty}\{C_n^+e^{2\mathrm{i}\pi\alpha\tau n}+C_n^-e^{-2\mathrm{i}\pi\alpha\tau n}\} \tag{33}$$

we can proceed along the same lines as in the previous section. The only difference to be noted is that the sign in the periodicity condition, Eq. (10), will change and this condition will take the form

$$w^{(\omega)}(\xi)=w^{(\omega)}(\xi-m)\exp\left(\frac{\mathrm{i}\omega m}{\alpha}\right) \tag{34}$$

The resulting infinite determinant has exactly the same shape as given by Eq. (32) and reads

$$\left|\boldsymbol{S}_3-\boldsymbol{S}_4\boldsymbol{S}_2^{-1}\boldsymbol{S}_1-\frac{1}{M^2}\boldsymbol{S}_2^{-1}+\frac{1}{M}(\boldsymbol{S}_4\boldsymbol{S}_2^{-1}+\boldsymbol{S}_2^{-1}\boldsymbol{S}_1)\right|=0 \tag{35}$$

where the components of $\boldsymbol{S}$ matrices are given as

$$S_{nm}^{(1)}=\frac{\mathrm{i}\alpha}{2\pi}\int_{-\infty}^{\infty}\left\{\frac{-\mathrm{i}(Y_n^++Y_n^-)\delta_{mn}}{2\alpha}+\frac{F}{\Delta_1}(Y_n^--Y_n^+)\times\left[\left(p-\frac{1}{q}\right)P_m^{(1)}+(q-p)P_m^{(2)}\right]\right\}d\omega \tag{36}$$

$$S_{nm}^{(2)}=\frac{\alpha}{2\pi}\int_{-\infty}^{\infty}\left\{\frac{\mathrm{i}(Y_n^+-Y_n^-)\delta_{mn}}{2\alpha}+\frac{F}{\Delta_1}(Y_n^-+Y_n^+)\times\left[\left(p-\frac{1}{q}\right)P_m^{(1)}+(q-p)P_m^{(2)}\right]\right\}d\omega \tag{37}$$

$$S_{nm}^{(3)}=\left(\frac{\mathrm{i}\alpha}{2\pi}\right)\int_{-\infty}^{\infty}\left\{\frac{-(Y_n^+-Y_n^-)\delta_{mn}}{2\alpha}+\frac{F}{\Delta_1}(Y_n^--Y_n^+)\times\left[\left(p-\frac{1}{q}\right)P_m^{(3)}+(q-p)P_m^{(4)}\right]\right\}d\omega \tag{38}$$

$$S_{nm}^{(4)}=\left(\frac{\alpha}{2\pi}\right)\int_{-\infty}^{\infty}\left\{\frac{(Y_n^++Y_n^-)\delta_m}{2\alpha}+\frac{F}{\Delta_1}(Y_n^-+Y_n^+)\times\left[\left(p-\frac{q}{1}\right)P_m^{(3)}+(q-p)P_m^{(4)}\right]\right\}d\omega \tag{39}$$

in which

$$P_m^{(1)}=\frac{-2\pi\alpha m}{(\omega-\alpha\omega)^2-(2\pi\alpha m)^2}(1-e^{-\mathrm{i}\omega(1-\alpha)/\alpha}) \tag{40}$$

$$P_m^{(2)}=\frac{-2\pi\alpha m}{(\omega+\alpha\omega)^2-(2\pi\alpha m)^2}(1-e^{-\mathrm{i}\omega(1+\alpha)/\alpha}) \tag{41}$$

$$P_m^{(3)}=\frac{-\mathrm{i}\omega(1-\alpha)}{(\omega-\alpha\omega)^2-(2\pi\alpha m)^2}(1-e^{-\mathrm{i}\omega(1-\alpha)/\alpha}) \tag{42}$$

$$P_m^{(4)}=\frac{-\mathrm{i}\omega(1-\alpha)}{(\omega+\alpha\omega)^2-(2\pi\alpha m)^2}(1-e^{-\mathrm{i}\omega(1+\alpha)/\alpha}) \tag{43}$$

$$Y_n^{\pm}=\frac{(2\pi\alpha n)^2\alpha}{(\omega\pm2\pi\alpha n)^2-\alpha^2\omega^2} \tag{44}$$

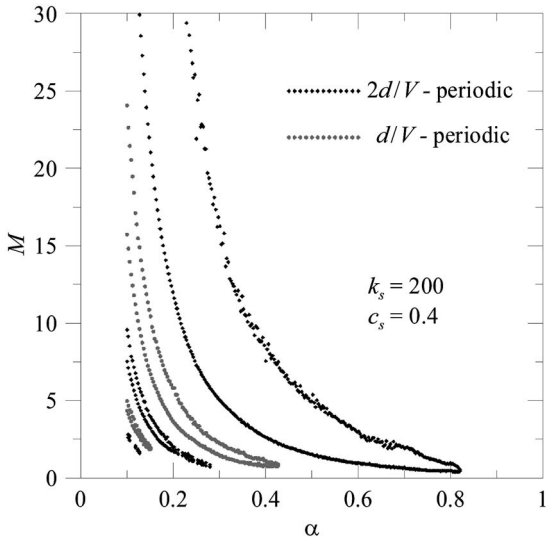

Fig. 2 Instability zones for stiff supports

$$\Delta_1 = 4\left(\cos(\omega/\alpha) - \cos(\omega) - \frac{iF\sin(\omega)}{2}\right) \tag{45}$$

The system parameters that satisfy Eq. (35) represent the boundaries separating stability and instability in the parameter space. The points of these boundaries correspond to the periodic motions of the particle with periods equal to d/V.

5 Method of Numerical Analysis

The system at hand is characterized by five dimensionless parameters, namely the particle mass M, its velocity α, and three parameters of the supports: m_s, c_s, and k_s. The instability zones will be analyzed in the plane $\{\alpha, M\}$ for a number of characteristic values of the support parameters. The procedure of finding the boundaries of the instability zones is as follows. Taking advantage of the fact that the mass M does not enter the $\boldsymbol{Q}$ and $\boldsymbol{S}$ matrices, these matrices are first calculated and stored for a number of values of α, keeping the support parameters unchanged. We varied α from 0.1 to 0.95 with the step 0.003. After having stored the values of the $\boldsymbol{Q}$ and $\boldsymbol{S}$ matrices, a loop with respect to M was organized, with the aim to find for each value of α those values of M that turn the determinants in Eqs. (32) and (35) to zero. Since these determinants are of infinite matrices, it is necessary to limit the number of matrix elements to be accounted for. Based on our analysis, the 15×15 matrices are sufficient to give relatively accurate estimations. However, to obtain smooth curves in the vicinity of the "tips" of the instability zones (see Fig. 2 in the next section), we used 25×25.

Numerical analysis of Eqs. (32)–(35) is somewhat complicated by the fact that each element of the matrices $\boldsymbol{Q}$ and $\boldsymbol{S}$ is an integral with infinite limits. These integrals have to be calculated many times to locate the boundaries of the instability zones. This procedure would be time expensive if the integrals would be calculated using a direct integration routine. Fast Fourier transform (FFT) is also not the best option, since the functions to be integrated have multiple peaks and the FFT analysis would require a substantial number of points to reach sufficient accuracy. Therefore, in this paper, the contour integration method [16] is employed. It is adequate and efficient to apply this method because all integrals in the matrices $\boldsymbol{Q}$ and $\boldsymbol{S}$ have exactly the same poles. Therefore, for every combination of the system parameters, one has to find the poles only once and then use them for calculation of all integrals. Our analysis showed that only zeroes of Δ_1 and Δ_2 contribute to the integration result, whereas zeroes of $Z_n^{\pm}$ and $Y_n^{\pm}$ do not. This is natural, since these are the zeroes of Δ_1 and Δ_2 that determine the frequencies of the waves, which the vibrating particle excites in the supported string.

To find complex zeroes of Δ_1 and Δ_2 the corresponding transcendental equations were solved numerically. A standard minimization routine was used to find the minimums of $|\Delta_{1,2}|$ from a guessed value, which was varied in the area $|\mathrm{Re}(\omega)| < 300$, $|\mathrm{Im}(\omega)| < 10$. To ensure that all roots in the chosen domain of the complex ω plane are found, the method of the argument [16,17] was applied. This method allows one to find the number of complex zeroes of a function within a chosen domain in a complex plane.

6 Parametric Analysis of Instability Zones

We first consider relatively stiff, slightly damped supports, which are characterized by the following dimensionless parameters: k_s=200, c_s=0.4, m_s=0.013. The boundaries of the corresponding instability zones are shown in Fig. 2 as dotted lines. The black diamonds mark the boundaries of the first, second, and third $2d/V$-periodic zones, whereas the gray circles mark the boundaries of the first and second d/V-periodic zones. Parametric resonance (the exponential increase of the amplitude of particle vibration in time) takes place if the system parameters belong to one of the areas within these boundaries.

Figure 2 shows five instability zones—these are all zones found using the numerical analysis. The higher-order zones do not exist in the chosen domain of parameters $0.1 < \alpha < 0.95$, $0 < M < 30$.

The effect of the stiffness of the supports can be analyzed using Fig. 3, which presents three plots corresponding to gradually decreasing stiffness. This figure clearly shows that the smaller the support stiffness the narrower the instability zones. If $k_s < 1$, the instability zones disappear from the parameter domain under consideration. This phenomenon can be understood by analogy with classical parametric resonance. Indeed, by decreasing the support stiffness we effectively reduce the modulation depth of the parameters variation under the moving particle. Obviously, this must reduce the size of the instability zones.

An important difference between the classical parametric resonance and the parametric resonance considered in this paper is related to the effect of damping. In the case of classical parametric resonance of an undamped system, the instability zones exist even if the parameter modulation is infinitesimal. In contrast, letting the viscosity in the spring supports vanish will not lead to extension of the instability zones in Figs. 2 and 3 towards the horizontal axis. In fact, the damping used to plot this figure is sufficiently small to represent the instability zones for zero damping.

To understand the fact that there is always a critical magnitude of the particle mass that must be exceeded to make parametric resonance possible, we have to go down to the physics of this phenomenon. As explained in [13], parametric resonance of a moving object on a periodically inhomogeneous elastic system occurs because of excitation of elastic waves by the moving object. As soon as the object starts to vibrate, every transition of the object through an inhomogeneity (a support, for example) is accompanied by excitation of a wave train with continuous spectrum. Thanks to the spatial periodicity of the elastic system and to the uniformity of the object motion, some frequencies of this spectrum correspond to waves, which are excited in phase at every transition. This leads to formation of a discrete spectrum of waves in the elastic system. These waves are of two distinct types, which are normally referred to as normal Doppler waves and anomalous Doppler waves [18]. In 1D systems, the phase velocity of the former waves is greater than the object velocity, while that of the latter is lower. Both types of waves have an effect on the energy of transverse vibrations of the object. The anomalous Doppler waves increase this energy, whereas the normal Doppler waves decrease it [4]. Dynamic instability (parametric resonance, in particular) occurs if the contribution of the anomalous Doppler waves is greater than that of the normal Doppler waves. On the

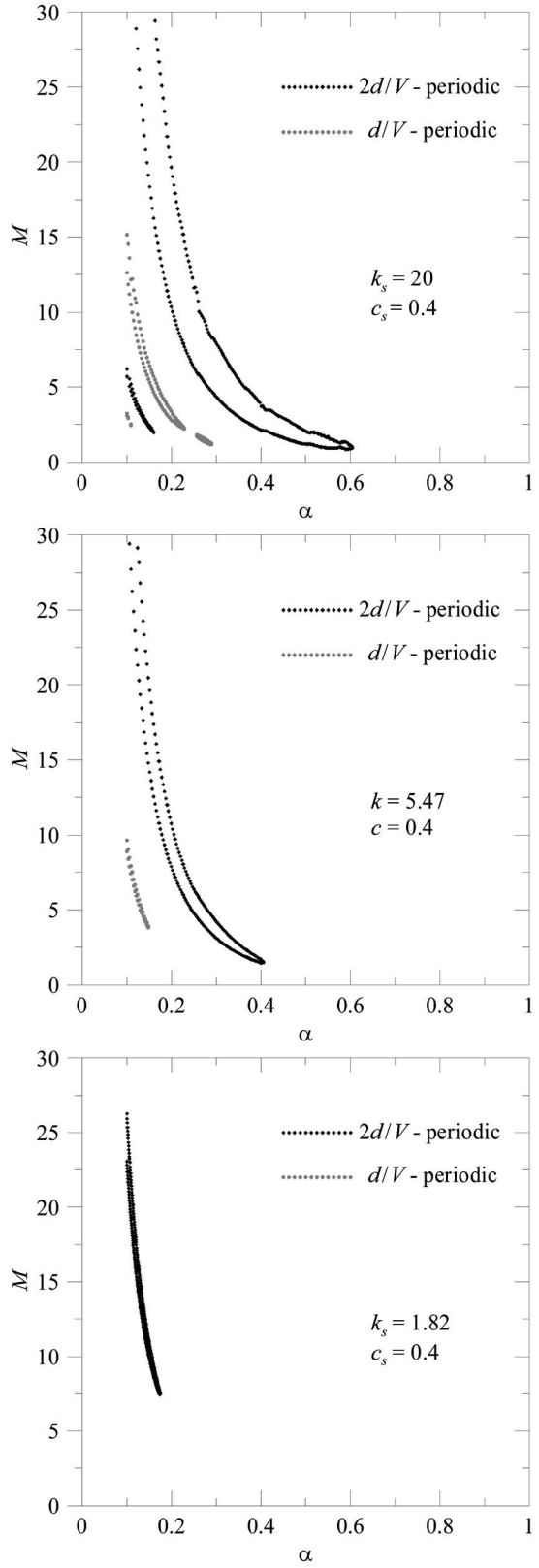

Fig. 3 Effect of the support stiffness

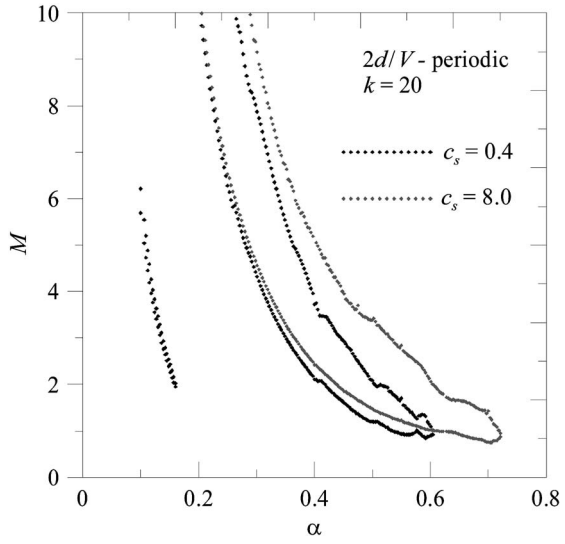

Fig. 4 Effect of the support viscosity

boundaries of instability zones these contributions are equal. In periodically inhomogeneous systems, the moving object excites both types of waves simultaneously, whatever is its velocity. The presence of the normal Doppler waves implies that there is always a certain amount of radiation damping. That is why, even in the absence of the viscous damping in the supports, a small-mass particle cannot experience instability. It is simply unable to excite powerful enough anomalous Doppler waves to overcome the radiation damping due to normal Doppler waves.

The effect of the increase of the viscous damping in the string supports is also worth demonstrating. This is shown in Fig. 4, in which only $2d/V$-periodic boundaries are shown for two values of the damping coefficient c_s.

A relatively small viscosity $c_s=0.4$ corresponds to two instability zones bounded by the black boundaries. The viscosity increase to $c_s=8$ removes the smaller instability zone but widens the main instability zone. The latter effect may be called destabilization by viscosity. It is not unexpectable since by increasing the viscosity, we not only increase the global energy dissipation in the system but also increase the energy of waves excited in the string when the particle passes the supports. In fact, by increasing the viscosity we increase the dynamic stiffness of the supports, which, in turn, increases the radiation energy. Given higher radiation energy, it is natural to expect a wider instability zone.

7 Analytical Assessment of Parameters Leading to Parametric Resonance

In this section, the position of the instability zones in $\{\alpha, M\}$-plane is explained qualitatively. To this end, the natural frequency Ω of the particle on the string is found analytically considering a "smeared" model for the string support. In this model, the inertia and damping of the supports are neglected and the discrete supports are replaced by a corresponding continuous elastic foundation with stiffness k_0/d. The natural frequency found using this model is then compared to the frequency d/V of the parameters variation under the moving mass of the original discretely supported string.

The system parameters leading to parametric resonance are assessed by analyzing the following equation:

$$2\Omega \approx \frac{2\pi n V}{d}, \quad n \in \mathbb{N} \tag{46}$$

Equation (46) is the classical condition of parametric resonance, which implies that the dynamic instability governed by this phenomenon may occur if the frequency of parameter variation multiplied by an integer approximately equals the doubled natural frequency of the system.

Free transverse vibrations of the moving mass on the continuously supported string are governed by the following equations

$$\partial_{\tau\tau} w - \partial_{\xi\xi} w + k_s w = -M\delta(\xi - \alpha\tau) d_{\tau\tau} w_0$$

$$w_0(\tau) = w(\alpha\tau, \tau) \tag{47}$$

where the same notations are used as in Eq. (1).

The fundamental solution to the operator $\partial_{\tau\tau} - \partial_{\xi\xi} + k_s$, according to [19], reads $J_0(\sqrt{k_s}\sqrt{\tau^2 - \xi^2})\mathrm{H}(\tau - |\xi|)/2$ where J_0 is the Bessel function of the first kind of zeroth order and H is the Heaviside function. Using this fundamental solution, the solution to the first equation of Eq. (47) can be written as

$$\begin{aligned} w(\xi, \tau) &= -\frac{M}{2}\int_0^\tau \int_{-\infty}^{\infty} \frac{d^2 w_0}{d\tilde{\tau}^2}\delta(\tilde{\xi} - \alpha\tilde{\tau}) \\ &\quad \times \mathrm{H}(\tau - \tilde{\tau} - |\xi - \tilde{\xi}|) J_0[\sqrt{k_s}\sqrt{(\tau - \tilde{\tau})^2 - (\xi - \tilde{\xi})^2}]\, d\tilde{\xi}\, d\tilde{\tau} \\ &= -\frac{M}{2}\int_0^\tau \frac{d^2 w_0}{d\tilde{\tau}^2} J_0[\sqrt{k_s}\sqrt{(\tau - \tilde{\tau})^2 - (\xi - \alpha\tilde{\tau})^2}] \\ &\quad \times \mathrm{H}(\tau - \tilde{\tau} - |\xi - \alpha\tilde{\tau}|)\, d\tilde{\tau} \end{aligned} \tag{48}$$

Substituting into this equation $\xi = \alpha\tau$ and using the condition of contact between the mass and the string (the second equation in Eq. (47)), we obtain the following integro-differential equation:

$$w_0(\tau) = -\frac{M}{2}\int_0^\tau \frac{d^2 w_0}{d\tilde{\tau}^2} J_0[\sqrt{k_s}\sqrt{1 - \alpha^2}(\tau - \tilde{\tau})]\, d\tilde{\tau} \tag{49}$$

This equation governs free transverse vibrations of the moving particle on the continuously supported string, taking no account of initial conditions (there is no need to account for those since we are interested in the natural frequency only).

The integral in Eq. (49) is of the convolution type. Therefore, the characteristic equation governing the eigenvalues of the particle transverse motion can be obtained by the direct application of the Laplace transform to Eq. (49). This gives

$$1 + \frac{(M/2)s^2}{\sqrt{s^2 + k_s(1 - \alpha^2)}} = 0 \tag{50}$$

where s is the Laplace variable. Replacing it by $\mathrm{i}\Omega$ and resolving Eq. (50) with respect to M, the following relationship is obtained between the mass M and the nondimensional natural frequency of the mass vibration:

$$M = \frac{2\sqrt{-\Omega^2 + k_s(1 - \alpha^2)}}{\Omega^2} \tag{51}$$

Substituting into this equation $\Omega = n\pi\alpha$, where Ω is given by Eq. (46), the following relation between α and M is obtained that may be expected to lead to parametric resonance:

$$M = \frac{2\sqrt{-(n\pi\alpha)^2 + k_s(1 - \alpha^2)}}{(n\pi\alpha)^2} \tag{52}$$

The curves corresponding to the main instability zone ($n = 1$) are shown in Fig. 5 as solid lines for two values of the support stiffness. For comparison, the corresponding boundaries of the instability zones found using the original model are also plotted as dotted lines.

We can see from Fig. 5 that the curves found analytically give the same trend of $M - \alpha$ dependence as the numerically found boundaries. The smaller the support stiffness, the better the simplistic analytical prediction. The major drawback of the analytically found prediction is that it suggests that instability can be expected at infinitesimal magnitudes of the mass. This drawback, however, is to be expected as the analytical model cannot capture the multimode dynamics of the system at low magnitudes of the particle mass.

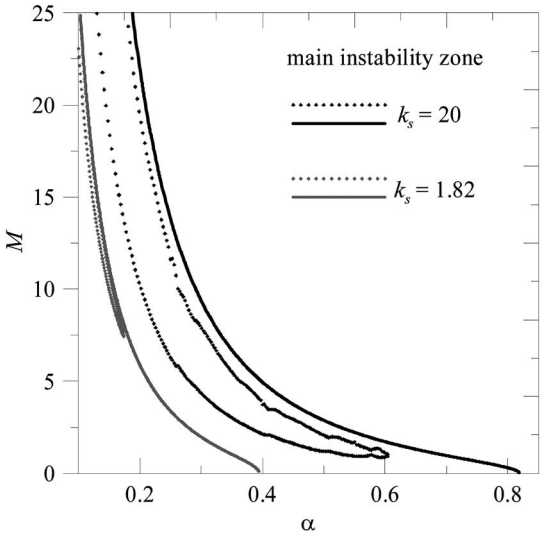

Fig. 5 Simplistic assessment of location of the main instability zone

8 Conclusions

In this paper, a new method has been presented of finding the boundaries of instability zones for an object that uniformly moves on a periodically supported structure. To demonstrate this method, a simple example has been considered of a particle moving on a string. The presented method can be straightforwardly applied to more complicated systems provided that the structure is one-dimensional and the moving object has only one contact point with the structure.

The model considered in this paper mimics simplistically the dynamic interaction of an overhead power line and the current collector of a train. The parameters of the supported string closely resemble those of a realistic overhead wire system suspended on the so-called rubber-damping hangers [20]. The wave speed in the contact wire discussed in [20] is about 95 m/s. This means that the main instability zone (40–70% of the wave speed) corresponds to the train speeds of 38–66 m/s, which belong to the operation range of modern high-speed trains.

The stiffness and viscosity of the current collector have been disregarded. Because of the latter, the obtained results cannot be applied directly in engineering practice. The mechanical properties of the current collector have a crucial effect on the system stability and can be tuned to ensure stability of current collection even in the case of relatively stiff hangers. This will be shown in a follow-up paper, in which both the multi-degree-of-freedom character of the current collectors as well as a multi-level character of modern overhead power lines will be accounted for.

References

[1] Frýba, L., 1999, *Vibrations of Solids and Structures Under Moving Loads*, Telford, London.

[2] Denisov, G. G., Kugusheva, E. K., and Novikov, V. V., 1985, "On the Problem of the Stability of One-Dimensional Unbounded Elastic Systems," J. Appl. Math. Mech., **49**(4), pp. 533–537.

[3] Bogacz, R., Novakowski, S., and Popp, K., 1986, "On the Stability of a Timoshenko Beam on an Elastic Foundation Under a Moving Spring-Mass System," Acta Mech., **61**, pp. 117–127.

[4] Metrikine, A. V., 1994, "Unstable Lateral Oscillations of an Object Moving Uniformly Along an Elastic Guide as a Result of Anomalous Doppler Effect," Acoust. Phys., **40**(1), pp. 85–89.

[5] Metrikine, A. V., and Popp, K., 1999, "Instability of Vibrations of an Oscillator Moving Along a Beam on an Elastic Half-Space," Eur. J. Mech. A/Solids, **18**(2), pp. 331–349.

[6] Chung, Y. I., and Genin, J., 1978, "Stability of a Vehicle on a Multispan Simply Supported Guideway," ASME J. Dyn. Syst., Meas., Control, **100**(4), pp. 326–332.

[7] Yakubovich, V. A., and Starzhinskii, V. M., 1975, *Linear Differential Equations With Periodic Coefficients*, IPST, Jerusalem, Israel.
[8] Nayfeh, A., and Mook, D. T., 1979, *Nonlinear Oscillations*, Wiley, New York.
[9] Vesnitskii, A. I., and Metrikine, A. V., 1993, "Parametric Instability in the Oscillations of a Body Moving Uniformly on a Periodically-Inhomogeneous Elastic System," J. Appl. Mech. Tech. Phys., **34**(2), pp. 266–271.
[10] Verichev, S. N., and Metrikine, A. V., 2003, "Instability of Vibrations of a Mass That Moves Along a Beam on a Periodically Inhomogeneous Foundation," J. Sound Vib., **260**(5), pp. 901–925.
[11] Wu, T. X., and Brennan, M. J., 1999, "Dynamic Stiffness of a Railway Overhead Wire System and its Effect on Pantograph-Catenary System Dynamics," J. Sound Vib. **219**(3), pp. 483–502.
[12] Vesnitskiy, A. I., and Metrikine, A. V., 1993, "Transition Radiation in a Periodically Non-Uniform Elastic Guide," Mech. Solids, **28**, pp. 158–162.
[13] Vesnitskiy, A. I., and Metrikine, A. V., 1996, "Transition Radiation in Mechanics," Phys. Usp., **166**, pp. 1043–1068.
[14] Belotserkovskiy, P. M., 1996, "On the Oscillations of Infinite Periodic Beams Subjected to a Moving Concentrated Force," J. Sound Vib., **193**, pp. 705–712.
[15] Sheng, X., Jones, C. J. C., and Thompson, D. J., 2005, "Responses of Infinite Periodic Structures to Moving or Stationary Harmonic Loads," J. Sound Vib., **282**(1–2), pp. 125–149.
[16] Fuchs, B. A., Shabat, B. V., and Berry, J., 1961–1964, *Functions of a Complex Variable and Some of Their Applications*, Pergamon, Oxford.
[17] Achenbach, J. D., 1990, *Wave Propagation in Elastic Solids*, North-Holland, Amsterdam.
[18] Ginzburg, V. L., 1979, *Theoretical Physics and Astrophysics*, Pergamon, Oxford.
[19] Vladimirov, V. S., 1979, *Generalized Functions in Mathematical Physics*, Mir, Moscow.
[20] Aboshi, M., and Kinoshita, H., 1998, "Current Collection Characteristics and Improvement Methods of High-Tension Overhead Catenary Systems," Electr. Eng. Jpn., **123**, pp. 67–76.

Flexural Resonant Frequencies of Thin Rectangular Cantilever Plates

Jason R. Looker
e-mail: jrlooker@ms.unimelb.edu.au

John E. Sader[1]
e-mail: jsader@unimelb.edu.au

Department of Mathematics and Statistics,
The University of Melbourne,
Parkville 3010 Victoria, Australia

Knowledge of the flexural vibration frequencies of thin rectangular cantilever plates forms the basis for numerous applications in sensing and instrumentation. Despite the seemingly simple nature of the problem, an accurate formula for the fundamental resonant frequency that is valid for all aspect ratios and Poisson's ratios is notably lacking in the literature. In this article, we present such a result using a variational and singular perturbation formulation. This yields a simple analytical formula that exhibits a maximum error of 2%. [DOI: 10.1115/1.2745377]

1 Introduction

Cantilever plates form the basis for numerous industrial and scientific applications ranging from their use in aerospace technologies [1] through the monitoring of biological processes such as DNA hybridization [2], mass measurements with attogram sensitivity [3], and the imaging of surfaces with atomic resolution [4]. Fundamental to many of these applications is the knowledge of the resonance characteristics of the cantilever. While classical beam theory can be used when the aspect ratio (length/width) is large, an accurate analytical formulation for arbitrary aspect ratio is lacking in the literature.

Classical exact solutions to the thin plate equations for rectangular plates are known for cases when all edges are free, simply supported or clamped, where Fourier analysis can be used [5,6]. However, the mixed boundary conditions of the cantilever problem precludes the use of such elementary techniques. As such, an exact analytical solution to the cantilever problem mimicking the simplicity of these classical results has proven elusive. Even approximate methods frequently rely on sophisticated and computationally intensive numerical schemes.

While a vast amount of work has appeared on the free vibration of rectangular plates, very few explicit approximate formulas exist. The first such formula appeared when Warburton [7] used characteristic beam vibration functions in conjunction with Rayleigh's method, to obtain a simple frequency expression for isotropic rectangular plates. This formula is valid for all modes of vibration and all of the classical boundary conditions (free, clamped or simply supported). Importantly, a dimensionless frequency parameter that depends on aspect ratio, Poisson's ratio, mode number, and the boundary conditions is used. However, for a cantilever, Warburton's frequency parameter is independent of aspect ratio and Poisson's ratio, and therefore cannot be uniformly valid for these quantities.

The accuracies of Warburton's formulas have also been shown to diminish if one or more free edges exist [7–10]. As such, this model is clearly of limited use for rectangular cantilevers. Warburton's research spawned two other papers that contain explicit formulas. Dickinson [9] extended Warburton's result to account for specially orthotropic plates and uniform direct in-plane forces. Kim and Dickinson [10] improved the accuracy of Dickinson's result by using three terms in the Rayleigh-Ritz method. However, for the scenarios considered, the increase in accuracy was less than 1%. Jänich [11] published another set of explicit formulas for the fundamental mode for 18 combinations of boundary conditions, including the cantilever. These formulas were derived using Rayleigh's method with simple trigonometric functions representing the deflection; it has since been shown that mode shapes are better approximated by beam functions [8]. As with the case for Warburton's formula, Jänich's frequency parameter is independent of aspect ratio for the cantilever case; the formulas are also only valid for a Poisson's ratio of 0.25. Thus, Jänich's formulas are of less practical value than those of Warburton, which we have already shown to be limited when applied to cantilevers.

There is clearly a need for an accurate, explicit, frequency expression for rectangular cantilever plates that is valid for arbitrary aspect ratio and Poisson's ratio. Reissner and Stein [1] developed such a model describing torsional vibration. In this paper, we develop Reissner's idea to encompass the flexural vibration of thin rectangular plates. However, unlike the torsional case, the flexural problem requires the use of advanced asymptotic techniques to handle the singular nature of the mixed boundary value problem. This in turn results in a simple analytical formula that is valid for all aspect ratios and Poisson's ratio, that exhibits a maximum error of $<2\%$ in comparison to rigorous finite element analysis of the governing thin plate equations. While we focus on the fundamental flexural mode of the cantilever due to its ubiquitous use in applications, we derive a general expression valid for all mode numbers whose deflection functions possess nodes approximately parallel to the clamped edge. The cantilever is composed of a linearly elastic homogeneous isotropic material of constant thickness. A schematic illustration of the cantilever geometry is given in Fig. 1.

2 Analysis

In this section we use the small-deflection theory of thin plates, the principle of least action [12] and the calculus of variations [13] to derive new governing equations that approximately describe the flexural vibrational modes for large but finite aspect ratio. To solve this system of equations we then employ a singular perturbation approach yielding a result that converges to the standard beam theory deflection function and frequency expression as the aspect ratio of the cantilever $A=L/b\to\infty$. In doing so, we also establish that the resulting next order correction to the beam frequency formula is $\mathcal{O}(1/A)$, a previously unknown result. Finally, we use this asymptotic expression together with the exact asymptotic solution for $A\to 0$ to derive a simple yet accurate analytical formula ($<2\%$ error) that is valid for arbitrary aspect ratio and Poisson's ratio.

2.1 Governing Equation $L/b\gg 1$. Since the thickness of the plate is small compared to its other linear dimensions and the

[1]Corresponding author.

Contributed by the Applied Mechanics Division of ASME for publication in the JOURNAL OF APPLIED MECHANICS. Manuscript received August 15, 2006; final manuscript received April 24, 2007; published online January 11, 2008. Review conducted by Oliver M. O'Reilly.

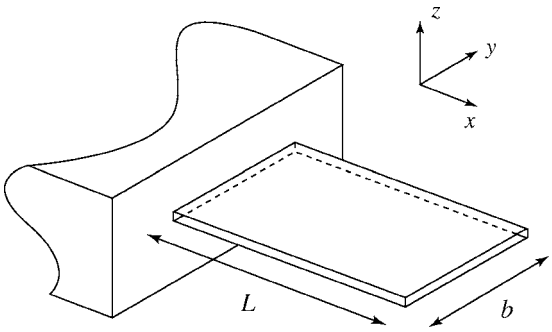

Fig. 1 Schematic of a thin rectangular cantilever plate with coordinate scheme shown whose origin is at the center-of-mass of the clamped edge. The thickness of the plate is *h* and is assumed to be much smaller than the plan view dimensions *L* and *b*.

deflection is assumed much smaller than the plate thickness, it is analyzed using classical small-deflection plate theory. The origin of the coordinate scheme is centered at the fixed end of the cantilever ($x=0$), so that $x \in [0,L]$ and $y \in [-b/2,b/2]$; see Fig. 1. We only consider deflections $w(x,y,t)$ perpendicular to its plane, i.e., in the z direction, where t is time.

We begin by formally expressing the deflection function as a series expansion in the y coordinate. Since we only consider flexural vibrations, the deflection function must be symmetric about the x axis and therefore an even function of y, i.e.,

$$w(x,y,t) = \sum_{n=0}^{N} w_{2n}(x,t) y^{2n} \tag{1}$$

The first two terms in this series are then retaining as a leading order approximation to the true deflection function

$$w(x,y,t) \approx w_0(x,t) + y^2 w_2(x,t) \tag{2}$$

The kinetic energy of the cantilever is given by

$$\mathrm{KE} = \frac{1}{2} h\rho \int \int_{\Omega} \left(\frac{\partial w}{\partial t} \right)^2 \mathrm{d}x\mathrm{d}y \tag{3}$$

where h is the thickness of the cantilever, ρ is its density, and $\Omega = [0,L] \times [-b/2,b/2]$ is the surface of the cantilever. The potential energy can be expressed as [14]

$$\mathrm{PE} = \frac{1}{2} D \int \int_{\Omega} \left[\left(\frac{\partial^2 w}{\partial x^2} + \frac{\partial^2 w}{\partial y^2} \right)^2 - 2(1-\nu) \left\{ \frac{\partial^2 w}{\partial x^2} \frac{\partial^2 w}{\partial y^2} - \left(\frac{\partial^2 w}{\partial x \partial y} \right)^2 \right\} \right] \mathrm{d}x\mathrm{d}y \tag{4}$$

where D is the flexural rigidity

$$D = \frac{Eh^3}{12(1-\nu^2)} \tag{5}$$

E is Young's modulus, and ν is Poisson's ratio. Recall that $\nu \in [0, \frac{1}{2}]$ for most materials. To complete the formulation, we use the action integral

$$\mathcal{A} = \int_0^T \mathrm{KE} - \mathrm{PE}\, \mathrm{d}t \tag{6}$$

where KE and PE are defined by Eqs. (3) and (4), and T is the period of vibration.

We first substitute Eq. (2) into $\mathcal{A}$ and perform the y integration. The governing equations and boundary conditions are then obtained by determining the necessary conditions on w_0 and w_2 such that $\mathcal{A}$ attains a minimum. This is achieved using the calculus of variations and results in two coupled fourth order linear homogeneous partial differential equations. To simplify these equations we introduce the following scaled variables:

$$\hat{x} = \frac{x}{L} \quad \hat{y} = \frac{y}{L} \quad \hat{t} = \sqrt{\frac{D}{h\rho}} \frac{t}{L^2} \quad \hat{w}_0 = w_0 \quad \hat{w}_2 = L^2 w_2 \tag{7}$$

The governing equations can then be reduced to ordinary differential equations by searching for solutions satisfying

$$\hat{w}_0(\hat{x},\hat{t}) = f(\hat{x}) e^{ik\hat{t}} \quad \text{and} \quad \hat{w}_2(\hat{x},\hat{t}) = g(\hat{x}) e^{ik\hat{t}} \tag{8}$$

where k is the scaled frequency parameter, or eigenvalue. The above transformations reduce the governing equations and boundary conditions to

$$\epsilon^2 \frac{\mathrm{d}^4 f}{\mathrm{d}x^4} + \frac{3\epsilon^4}{20} \frac{\mathrm{d}^4 g}{\mathrm{d}x^4} + 24\nu \frac{\mathrm{d}^2 f}{\mathrm{d}x^2} + \epsilon^2 (12\nu - 8) \frac{\mathrm{d}^2 g}{\mathrm{d}x^2} + 48g - \epsilon^2 k^2 f - \frac{3\epsilon^4}{20} k^2 g = 0 \tag{9}$$

$$\frac{\mathrm{d}^4 f}{\mathrm{d}x^4} + \frac{\epsilon^2}{12} \frac{\mathrm{d}^4 g}{\mathrm{d}x^4} + 2\nu \frac{\mathrm{d}^2 g}{\mathrm{d}x^2} - k^2 f - \frac{\epsilon^2}{12} k^2 g = 0 \tag{10}$$

$$f(0) = 0 \tag{11}$$

$$g(0) = 0 \tag{12}$$

$$\left. \frac{\mathrm{d}f}{\mathrm{d}x} \right|_{x=0} = 0 \tag{13}$$

$$\left. \frac{\mathrm{d}g}{\mathrm{d}x} \right|_{x=0} = 0 \tag{14}$$

$$\left. \left(\frac{\mathrm{d}^2 f}{\mathrm{d}x^2} + 2\nu g \right) \right|_{x=1} = 0 \tag{15}$$

$$\left. \frac{\mathrm{d}^2 g}{\mathrm{d}x^2} \right|_{x=1} = 0 \tag{16}$$

$$\left. \left(\frac{\mathrm{d}^3 f}{\mathrm{d}x^3} + \frac{\epsilon^2}{12} \frac{\mathrm{d}^3 g}{\mathrm{d}x^3} + 2\nu \frac{\mathrm{d}g}{\mathrm{d}x} \right) \right|_{x=1} = 0 \tag{17}$$

$$\left. \left(\frac{\epsilon^2}{15} \frac{\mathrm{d}^3 g}{\mathrm{d}x^3} + 8(\nu - 1) \frac{\mathrm{d}g}{\mathrm{d}x} \right) \right|_{x=1} = 0 \tag{18}$$

where $\epsilon = 1/A$ is a small parameter. Note that we have dropped the carets for convenience, thus *all variables shall henceforth refer to scaled quantities*. Equations (11)–(14) result from the cantilever being clamped at $x=0$, while Eqs. (15)–(18) are the free edge "natural" boundary conditions at the opposite end.

Observe from Eqs. (5), (7), and (8), that the plate flexural frequencies, ω_f, are related to k by

$$\omega_f = k \frac{h}{L^2} \sqrt{\frac{E}{12(1-\nu^2)\rho}} \tag{19}$$

2.2 Singular Perturbation Analysis. Our aim is to derive an asymptotic expression for the flexural frequencies for finite aspect ratio by solving Eqs. (9)–(18) for k. However, finding an exact analytical solution to this system poses a daunting task. Importantly, the mixed boundary valued nature of the clamped and free edge condition at $x=0$ induces a boundary layer in that region where rapid variations in the deflection function occur; see Fig. 2. This enables us to undertake a singular perturbation analysis of Eqs. (9)–(18), and in doing so obtain an asymptotic solution.

Define $f^{\mathrm{in}}(x)$ and $g^{\mathrm{in}}(x)$ to be the "inner" solutions to Eqs. (9) and (10) within the boundary layer that satisfy the boundary con-

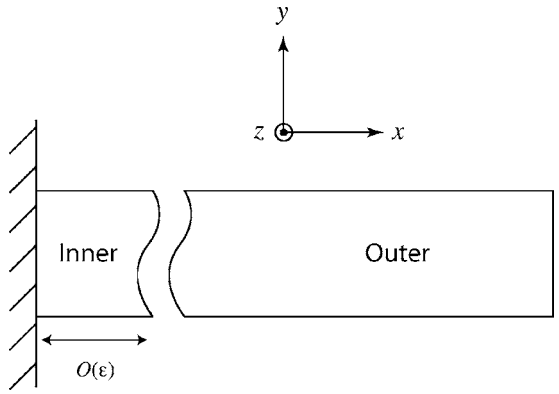

Fig. 2 Schematic of cantilever showing boundary layer ("inner" region) near the clamped end. The "outer" region is also shown.

ditions at $x=0$, and define $f^{\text{out}}(x)$ and $g^{\text{out}}(x)$ to be the "outer" solutions to Eqs. (9) and (10) that satisfy the boundary conditions at $x=1$. The limiting case $\epsilon=0$, which is equivalent to $A\to\infty$, generates the $\mathcal{O}(1)$ equations. It is well known that beam theory and plate theory become equivalent as $A\to\infty$. This implies that we must recover the beam theory result from these equations for our model to be mathematically consistent.

We propose the following asymptotic expansions:

$$f^{\text{out}}(x) \sim \sum_{i=0}^{\infty} f_i(x)\epsilon^i \quad \epsilon \to 0 \tag{20}$$

$$g^{\text{out}}(x) \sim \sum_{i=0}^{\infty} g_i(x)\epsilon^i \quad \epsilon \to 0 \tag{21}$$

$$k_n^2 \sim \sum_{i=0}^{\infty} u_i\epsilon^i \quad \epsilon \to 0 \tag{22}$$

where the functions $f_i(x)$ and $g_i(x)$ are independent of ϵ, $k=k_n$ is the nth eigenvalue of the system and the coefficients u_i depend on n. Substituting these expansions into Eqs. (9)–(18) and equating identical powers of ϵ generates a system of equations. Since we wish to obtain ω_f correct to $\mathcal{O}(\epsilon)$, we solve these equations for u_0 and u_1 only.

2.2.1 $\mathcal{O}(1)$ Solution. The $\mathcal{O}(1)$ equations are given by

$$\frac{d^4 f_0}{dx^4} - \beta^2 f_0 = 0 \tag{23}$$

$$g_0(x) = -\frac{\nu}{2}\frac{d^2 f_0}{dx^2} \tag{24}$$

subject to

$$\left.\frac{d^2 f_0}{dx^2}\right|_{x=1} = 0 \quad \left.\frac{d^3 f_0}{dx^3}\right|_{x=1} = 0 \tag{25}$$

where Eq. (24) was used in the derivation of Eqs. (23) and (25) and β is defined by

$$\beta^2 = \frac{u_0}{1-\nu^2} \tag{26}$$

Using the method of dominant balance, the boundary layer thickness can be shown to be $\mathcal{O}(\epsilon)$. Hence, within the boundary layer, $x=\mathcal{O}(\epsilon)$, and with our choice of length scale for y we obtain $y=\mathcal{O}(b/L)=\mathcal{O}(\epsilon)$. Therefore variations in the deflection function w with respect to x and y are comparable inside the boundary layer. Hence Eqs. (2) and (24) suggest the following rescalings:

$$f^{\text{in}}(x) = \epsilon^2 F(X) \tag{27}$$

$$g^{\text{in}}(x) = G(X) \tag{28}$$

where $F(X)$, $G(X)$ are $\mathcal{O}(1)$, and X is the inner variable defined by

$$X = \frac{x}{\epsilon} \tag{29}$$

This analysis indicates that $f^{\text{in}}(x)=0$ up to $\mathcal{O}(\epsilon^2)$.

Two additional boundary conditions on f_0 at $x=0$ are required to completely define the function throughout the interval [0,1]. The definition of the inner variable gives

$$f_0^{\text{in}}(x) = \mathcal{O}(\epsilon^2) \tag{30}$$

$$f_0^{\text{in}'}(x) = \mathcal{O}(\epsilon) \tag{31}$$

since $F(X)=\mathcal{O}(1)$. Equating like powers of ϵ in Eqs. (20), (30), and (31), and applying Van Dyke's matching rule [15] then gives

$$f_0(0) = 0 \tag{32}$$

$$f_0'(0) = 0 \tag{33}$$

Combining these results produces the final governing equation and boundary conditions for f_0,

$$\frac{d^4 f_0}{dx^4} - \beta^2 f_0 = 0 \tag{34}$$

$$f_0(0) = 0 \quad \left.\frac{df_0}{dx}\right|_{x=0} = 0 \tag{35}$$

$$\left.\frac{d^2 f_0}{dx^2}\right|_{x=1} = 0 \quad \left.\frac{d^3 f_0}{dx^3}\right|_{x=1} = 0 \tag{36}$$

Equations (34)–(36) are the classical beam equation and boundary conditions. It follows that f_0 must be the beam theory deflection function, given by

$$f_0(x) = C_1\sinh(\sqrt{\beta}x) + C_2\cosh(\sqrt{\beta}x) + C_3\sin(\sqrt{\beta}x) + C_4\cos(\sqrt{\beta}x)$$

where the $C_i \in \mathbb{R}$ are integration constants. It is well known that β must satisfy the following equation:

$$\beta = z_n^2$$

where z_n is the nth positive solution to

$$\cos z \cosh z + 1 = 0 \tag{37}$$

Solving Eq. (37) numerically gives $z_1=1.8751$, $z_2=4.6941$, $z_3=7.8548$, and $z_4=10.9955$. Equation (26) implies that u_0 is given by

$$u_0 = z_n^4(1-\nu^2) \tag{38}$$

Substituting $k_n=\sqrt{u_0}$ into Eq. (19) produces the $\mathcal{O}(1)$ flexural frequency,

$$\omega_f = h\sqrt{\frac{E}{12\rho}}\left(\frac{z_n}{L}\right)^2$$

This is the classical beam theory result as expected. Observe that the beam flexural frequency is independent of Poisson's ratio. Furthermore, it can be shown that the plate flexural frequencies are given exactly by the beam result for $\nu=0$, regardless of the aspect ratio A. Therefore we obtain

$$\lim_{A\to\infty} \omega_f = \omega_f^{\infty} = \omega_f|_{\nu=0} \tag{39}$$

where ω_f^{∞} represents the beam formula. It follows that the plate theory flexural frequency can be expressed as

$$\omega_f^2 = \omega_f^{\infty 2} + \mathcal{O}(\epsilon) \text{ as } \epsilon \to 0$$

2.2.2 $\mathcal{O}(\epsilon)$ Solution. We now seek the $\mathcal{O}(\epsilon)$ correction for ω_f and so u_1 must be calculated. It is easy to verify that the $\mathcal{O}(\epsilon)$ outer equations are given by

$$\frac{d^4 f_1}{dx^4} - \beta^2 f_1 = \frac{u_1}{1-\nu^2} f_0 \tag{40}$$

$$g_1(x) = -\frac{\nu}{2}\frac{d^2 f_1}{dx^2} \tag{41}$$

$$\left.\frac{d^2 f_1}{dx^2}\right|_{x=1} = 0 \quad \left.\frac{d^3 f_1}{dx^3}\right|_{x=1} = 0 \tag{42}$$

where β is defined by Eq. (26). It can be seen that u_1 must be determined before Eqs. (41) and (42) can be solved. This is achieved by making use of the Rayleigh quotient which connects the eigenvalues to the deflection function, enabling u_1 to be determined without directly solving Eqs. (40)–(42), as we shall discuss below.

Rayleigh's quotient can be obtained by equating the maximum kinetic and potential energies, and is expressed in the following scaled form:

$$k_n^2 = \frac{\int\int_\Omega \left[\left(\frac{\partial^2 w}{\partial x^2} + \frac{\partial^2 w}{\partial y^2}\right)^2 - 2(1-\nu)\left\{\frac{\partial^2 w}{\partial x^2}\frac{\partial^2 w}{\partial y^2} - \left(\frac{\partial^2 w}{\partial x \partial y}\right)^2\right\}\right] dx dy}{\int\int_\Omega w^2 dx dy} \tag{43}$$

where the independent variables have been scaled as in Sec. 2.1, and Ω here is the scaled plate surface. Substituting $w = f + y^2 g$ into Eq. (43) and performing the y integration, yields

$$k_n^2 = \frac{\int_0^1 (f'')^2 + \frac{\epsilon^4}{80}(g'')^2 + \frac{\epsilon^2}{6} f'' g'' + 4g^2 + 4\nu f'' g + \frac{\epsilon^2 \nu}{3} g g'' + \frac{2\epsilon^2(1-\nu)}{3}(g')^2 dx}{\int_0^1 f^2 + \frac{\epsilon^4}{80} g^2 + \frac{\epsilon^2}{6} f g dx} \tag{44}$$

The primes denote differentiation with respect to x. The $\mathcal{O}(\epsilon)$ correction for k_n^2 (and hence ω_f) can be obtained from Eq. (44) without solving the $\mathcal{O}(\epsilon)$ outer equations, Eqs. (40)–(42).

Since the equations for f and g exhibit boundary layer behavior, we split the range of integration into an inner and outer region and employ the "summing a split range of integration" method as described in Hinch [15]. In future we will refer to this method as SSRI. Let τ satisfy the relation

$$0 < \epsilon \ll \tau \ll 1$$

such that

$$\tau \to 0 \text{ as } \epsilon \to 0$$

We apply the method of SSRI to the numerator of Eq. (44). Define the following:

$$\mathrm{PE}_f = \int_0^1 (f'')^2 + \frac{\epsilon^4}{80}(g'')^2 + \frac{\epsilon^2}{6} f'' g'' + 4g^2 + 4\nu f'' g + \frac{\epsilon^2 \nu}{3} g g'' + \frac{2\epsilon^2(1-\nu)}{3}(g')^2 dx = \mathrm{PE}_f^{\mathrm{in}}(\epsilon,\tau) + \mathrm{PE}_f^{\mathrm{out}}(\epsilon,\tau) \tag{45}$$

where

$$\mathrm{PE}_f^{\mathrm{in}}(\epsilon,\tau) = \int_0^\tau (f'')^2 + \frac{\epsilon^4}{80}(g'')^2 + \frac{\epsilon^2}{6} f'' g'' + 4g^2 + 4\nu f'' g + \frac{\epsilon^2 \nu}{3} g g'' + \frac{2\epsilon^2(1-\nu)}{3}(g')^2 dx \tag{46}$$

$$\mathrm{PE}_f^{\mathrm{out}}(\epsilon,\tau) = \int_\tau^1 (f'')^2 + \frac{\epsilon^4}{80}(g'')^2 + \frac{\epsilon^2}{6} f'' g'' + 4g^2 + 4\nu f'' g + \frac{\epsilon^2 \nu}{3} g g'' + \frac{2\epsilon^2(1-\nu)}{3}(g')^2 dx \tag{47}$$

We first consider the integral $\mathrm{PE}_f^{\mathrm{in}}(\epsilon,\tau)$. Inside the boundary layer, the functions f and g obey Eqs. (27) and (28) with the inner variable satisfying $X = x/\epsilon$. Therefore

$$f^{\mathrm{in}''}(x) = F''(X) \tag{48}$$

$$g^{\mathrm{in}'}(x) = \frac{1}{\epsilon} G'(X) \tag{49}$$

$$g^{\mathrm{in}''}(x) = \frac{1}{\epsilon^2} G''(X) \tag{50}$$

where the primes denote differentiation with respect to X. Equations (48)–(50) and the change of variable, $x = \epsilon X$, then give

$$\mathrm{PE}_f^{\mathrm{in}}(\epsilon,\tau) = \epsilon \int_0^{\tau/\epsilon} (F'')^2 + \frac{1}{80}(G'')^2 + \frac{1}{6} F'' G'' + 4G^2 + 4\nu F'' G + \frac{\nu}{3} G G'' + \frac{2(1-\nu)}{3}(G')^2 dX = \epsilon \mathcal{I}_1^{\mathrm{in}}(\epsilon,\tau) + \mathcal{O}(\epsilon^2) \tag{51}$$

Turning our attention to $\mathrm{PE}_f^{\mathrm{out}}(\epsilon,\tau)$, recall that we are only interested in the $\mathcal{O}(\epsilon)$ correction to the eigenvalues, u_1. Hence we use the following expansions:

$$f^{\mathrm{out}}(x) = f_0(x) + f_1(x)\epsilon + \mathcal{O}(\epsilon^2) \tag{52}$$

$$g^{\text{out}}(x) = g_0(x) + g_1(x)\epsilon + \mathcal{O}(\epsilon^2)$$

These are simply the first two terms from Eqs. (20) and (21). Substituting Eq. (52) into PE_f^{out} produces

$$\begin{aligned}\text{PE}_f^{\text{out}}(\epsilon,\tau) &= \int_\tau^1 (f_0'')^2 + 4g_2^2 + 4\nu f_0'' g_2 \mathrm{d}x + \epsilon \int_\tau^1 2f_0'' f_1'' + 8g_2 g_3 \\ &\quad + 4\nu f_0'' g_3 + 4\nu f_1'' g_2 \mathrm{d}x + \mathcal{O}(\epsilon^2) \\ &= \mathcal{I}_0^{\text{out}}(\tau) + \epsilon \mathcal{I}_1^{\text{out}}(\tau) + \mathcal{O}(\epsilon^2) \end{aligned} \tag{53}$$

Substituting Eqs. (51) and (53) into Eq. (45) gives

$$\text{PE}_f = \mathcal{I}_0^{\text{out}}(\tau) + (\mathcal{I}_1^{\text{in}}(\epsilon,\tau) + \mathcal{I}_1^{\text{out}}(\tau))\epsilon + \mathcal{O}(\epsilon^2) \tag{54}$$

We now consider the denominator of Eq. (44). To begin we define

$$\text{KE}_f = \int_0^1 f^2 + \frac{\epsilon^4}{80} g^2 + \frac{\epsilon^2}{6} fg \mathrm{d}x \tag{55}$$

Observe that the integrand of KE_f does not contain any derivatives. We then expand f as

$$f(x) = f_0(x) + f_1(x)\epsilon + \mathcal{O}(\epsilon^2) \tag{56}$$

Since the inner solution for f is $\mathcal{O}(\epsilon^2)$ and the remaining terms in the integrand of KE_f are of $\mathcal{O}(\epsilon^2)$, the functions g^2 and fg will not contribute at $\mathcal{O}(\epsilon)$. These facts imply that we do not need to split the range of integration of KE_f. Thus

$$\text{KE}_f = \int_0^1 f_0^2 \mathrm{d}x + \epsilon \int_0^1 2f_0 f_1 \mathrm{d}x + \mathcal{O}(\epsilon^2) = \mathcal{J}_0 + \epsilon \mathcal{J}_1 + \mathcal{O}(\epsilon^2) \tag{57}$$

A geometric series expansion can now be used to give

$$\frac{1}{\text{KE}_f} = \frac{1}{\mathcal{J}_0} - \frac{\mathcal{J}_1}{\mathcal{J}_0^2}\epsilon + \mathcal{O}(\epsilon^2) \tag{58}$$

Substituting Eqs. (54) and (58) into Eq. (44) then gives

$$k_n^2 = \frac{\mathcal{I}_0^{\text{out}}(0)}{\mathcal{J}_0} + \frac{1}{\mathcal{J}_0}\left(\lim_{\epsilon\to 0} \mathcal{I}_1^{\text{in}}(\epsilon,\tau) + \mathcal{I}_1^{\text{out}}(0) - \frac{\mathcal{I}_0^{\text{out}}(0)\mathcal{J}_1}{\mathcal{J}_0}\right)\epsilon + \mathcal{O}(\epsilon^2) \tag{59}$$

where we have used the definition of τ and the continuity of $\mathcal{I}_0^{\text{out}}$ and $\mathcal{I}_1^{\text{out}}$ to substitute $\tau=0$. From this we recover the following expression for the $\mathcal{O}(\epsilon)$ correction for k_n^2:

$$u_1 = \frac{1}{\mathcal{J}_0}\left(\lim_{\epsilon\to 0} \mathcal{I}_1^{\text{in}}(\epsilon,\tau) + \mathcal{I}_1^{\text{out}}(0) - \frac{\mathcal{I}_0^{\text{out}}(0)\mathcal{J}_1}{\mathcal{J}_0}\right) \tag{60}$$

For our method to be self-consistent we must be able to prove that

$$u_0 = z_n^4(1-\nu^2) = \frac{\mathcal{I}_0^{\text{out}}(0)}{\mathcal{J}_0} \tag{61}$$

which can be shown to be true after a significant amount of algebraic manipulation. By employing Eq. (34), Eq. (36) and Eqs. (40)–(42), together with the additional boundary condition $f_1(0)=0$, and multiple integration by parts, we obtain the following simple expressions:

$$\mathcal{I}_0^{\text{out}}(0) = (1-\nu^2)\int_0^1 (f_0'')^2 \mathrm{d}x \tag{62}$$

$$\mathcal{I}_1^{\text{out}}(0) = -2(1-\nu^2) f_0''(0) f_1'(0) + z_n^4(1-\nu^2)\mathcal{J}_1 \tag{63}$$

Substituting Eqs. (61)–(63) into Eq. (60) yields the required expression for the $\mathcal{O}(\epsilon)$ correction for the eigenvalues,

$$u_1 = \frac{1}{\mathcal{J}_0}\left(\lim_{\epsilon\to 0} \mathcal{I}_1^{\text{in}}(\epsilon,\tau) - 2(1-\nu^2) f_0''(0) f_1'(0)\right) \tag{64}$$

Equation (64) contains two objects that are still unknown: $\lim_{\epsilon\to 0} \mathcal{I}_1^{\text{in}}(\epsilon,\tau)$ and $f_1'(0)$. The governing equation for f_1 is a fourth order inhomogeneous linear differential equation, where the inhomogeneous term is proportional to f_0. The inhomogeneous term makes its solution highly cumbersome therefore its avoidance is desirable. This is achieved by applying Van Dyke's matching rule [15] to $f_1'(x)$. Using the definition of the inner variable and Eq. (27), it can be shown that

$$f_1'(0) = \lim_{X\to\infty} F'(X) \tag{65}$$

To evaluate $\mathcal{I}_1^{\text{in}}$ and $f_1'(0)$, clearly we are required to determine the functions F and G, which necessitates solution of the inner equations.

Substituting Eqs. (27) and (28) into Eqs. (9) and (10) we obtain

$$\frac{\mathrm{d}^4 F}{\mathrm{d}X^4} + \frac{3}{20}\frac{\mathrm{d}^4 G}{\mathrm{d}X^4} + 24\nu\frac{\mathrm{d}^2 F}{\mathrm{d}X^2} + (12\nu - 8)\frac{\mathrm{d}^2 G}{\mathrm{d}X^2} + 48G = 0 \tag{66}$$

$$\frac{\mathrm{d}^4 F}{\mathrm{d}X^4} + \frac{1}{12}\frac{\mathrm{d}^4 G}{\mathrm{d}X^4} + 2\nu\frac{\mathrm{d}^2 G}{\mathrm{d}X^2} = 0 \tag{67}$$

subject to

$$F(0) = 0 \quad F'(0) = 0 \quad G(0) = 0 \quad G'(0) = 0 \tag{68}$$

where terms of $\mathcal{O}(\epsilon^4)$ have been ignored. Note that these equations are independent of the eigenvalues. Equations (66) and (67) can now be decoupled to produce

$$\frac{\mathrm{d}^6 G}{\mathrm{d}X^6} + \bar{\alpha}\frac{\mathrm{d}^4 G}{\mathrm{d}X^4} + \bar{\beta}\frac{\mathrm{d}^2 G}{\mathrm{d}X^2} = 0 \tag{69}$$

where F satisfies

$$\frac{\mathrm{d}^2 F}{\mathrm{d}X^2} = \frac{1}{24\nu}\left(-\frac{1}{15}\frac{\mathrm{d}^4 G}{\mathrm{d}X^4} + (8 - 10\nu)\frac{\mathrm{d}^2 G}{\mathrm{d}X^2} - 48G\right) \tag{70}$$

and $\bar{\alpha}$, $\bar{\beta}$ are given by

$$\bar{\alpha} = 120(\nu - 1) \quad \bar{\beta} = 720(1-\nu^2) \tag{71}$$

Equation (69) can be solved by elementary techniques. This produces an expression for G that contains six integration constants. All but two of these constants can be determined by applying the boundary conditions (Eq. (68)), and noting that for matching, G can have no exponentially growing terms. The remaining two constants can be found via Van Dyke's matching rule [15]. This completely specifies G up to an arbitrary constant,

$$G(X) = \frac{\nu z_n^2 C}{r_1 - r_2}[r_1(1 - \exp(-r_2 X)) - r_2(1 - \exp(-r_1 X))] \tag{72}$$

where r_1 and r_2 are defined by

$$\begin{aligned} r_1 &= \frac{1}{\sqrt{2}}\sqrt{-\bar{\alpha} + \sqrt{\bar{\alpha}^2 - 4\bar{\beta}}} \\ r_2 &= \frac{1}{\sqrt{2}}\sqrt{-\bar{\alpha} - \sqrt{\bar{\alpha}^2 - 4\bar{\beta}}} \end{aligned} \tag{73}$$

the z_n are given by Eq. (37), and C is the arbitrary constant. This is an eigenvalue problem and so C does not need to be determined.

The remaining inner function F can be determined by integrating Eq. (70) twice and then substituting in G and G''. The resulting two integration constants can be found by applying the inner boundary conditions for F. Therefore both F, G and any required derivatives are completely specified. This enables the integral $\mathcal{I}_1^{\text{in}}(\epsilon,\tau)$ and the boundary condition $f_1'(0)$ to be evaluated. Finally, evaluation of the remaining quantities in Eq. (64) produces the sought after $\mathcal{O}(\epsilon)$ correction for the eigenvalues,

$$u_1 = \frac{4z_n^4\nu^2\sqrt{1-\nu^2}(\sqrt{5}(1-\nu)+\sqrt{1-\nu^2})}{\sqrt{3}(\sqrt{5-5\nu-\sqrt{10}\sqrt{2-5\nu+3\nu^2}}+\sqrt{5-5\nu+\sqrt{10}\sqrt{2-5\nu+3\nu^2}})} \tag{74}$$

The eigenvalues can now be expressed in the following form:

$$k_n^2 = z_n^4(1-\nu^2)(1+\mathcal{F}(\nu)\epsilon)+\mathcal{O}(\epsilon^2) \text{ as } \epsilon\to 0$$

where

$$\mathcal{F}(\nu) = \frac{4\nu^2(\sqrt{5}(1-\nu)+\sqrt{1-\nu^2})}{\sqrt{3}\sqrt{1-\nu^2}(\sqrt{5-5\nu-\sqrt{10}\sqrt{2-5\nu+3\nu^2}}+\sqrt{5-5\nu+\sqrt{10}\sqrt{2-5\nu+3\nu^2}})} \tag{75}$$

which is simply $u_1/z_n^4(1-\nu^2)$. We will refer to this function as the $\mathcal{O}(\epsilon)$ correction function for ω_f. Earlier we noted that

$$\omega_f^2 = \omega_f^{\infty 2}+\mathcal{O}(\epsilon) \text{ as } \epsilon\to 0 \tag{76}$$

We can extend this classical beam theory result by substituting the new analytic expression for k_n^2 into Eq. (19). This gives

$$\omega_f^2 = \omega_f^{\infty 2}(1+\mathcal{F}(\nu)\epsilon)+\mathcal{O}(\epsilon^2) \quad \text{as } \epsilon\to 0 \tag{77}$$

Alternatively, we can approximate the flexural frequencies by

$$\omega_f = \omega_f^{\infty}\sqrt{1+\mathcal{F}(\nu)\frac{b}{L}} \tag{78}$$

This new result gives the leading order correction to the classical beam solution for large but finite aspect ratio A.

It can be shown that $\mathcal{F}(\nu)$ behaves like ν^2 to leading order. Note that $\mathcal{F}(0)=0$, and so our new analytic expression conforms to the earlier observation that $\omega_f=\omega_f^{\infty}$ for $\nu=0$. Also observe that $\mathcal{F}(\nu)$ is independent of the mode of vibration.

2.3 Uniformly Valid Expression for Arbitrary Aspect Ratio. We now derive an expression that is uniformly valid, regardless of the aspect ratio A and Poisson's ratio of the cantilever. To achieve this, we make use of the asymptotic solutions derived for small (see Appendix) and large aspect ratio A, and link these solutions using a Padé approximant [15].

The appropriate Padé approximant is given by

$$\left(\frac{\omega_f}{\omega_f^{\infty}}\right)^2 = \frac{a_0(b_0-a_0)+a_1b_0\epsilon}{b_0-a_0+a_1\epsilon} \tag{79}$$

Note that Eq. (79) satisfies

$$\left(\frac{\omega_f}{\omega_f^{\infty}}\right)^2 = a_0+a_1\epsilon+\mathcal{O}(\epsilon^2) \quad \text{as } \epsilon\to 0 \tag{80}$$

$$\lim_{\epsilon\to\infty}\left(\frac{\omega_f}{\omega_f^{\infty}}\right)^2 = b_0 \tag{81}$$

Comparing Eqs. (80) and (81) with Eq. (77) and the small aspect ratio limit from the Appendix determines the unknown coefficients a_0, a_1, and b_0. Equation (79) then yields the following uniformly valid analytical expression for the flexural frequencies:

$$\omega_f = \omega_f^{\infty}\sqrt{\frac{1+\mathcal{Z}(\nu)(b/L)}{1+(1-\nu^2)\mathcal{Z}(\nu)(b/L)}} \tag{82}$$

where

$$\mathcal{Z}(\nu) = \frac{\mathcal{F}(\nu)}{\nu^2} = \frac{4(\sqrt{5}(1-\nu)+\sqrt{1-\nu^2})}{\sqrt{3}\sqrt{1-\nu^2}(\sqrt{5-5\nu-\sqrt{10}\sqrt{2-5\nu+3\nu^2}}+\sqrt{5-5\nu+\sqrt{10}\sqrt{2-5\nu+3\nu^2}})} \tag{83}$$

and the beam theory flexural formula is given by

$$\omega_f^{\infty} = h\sqrt{\frac{E}{12\rho}}\left(\frac{z_n}{L}\right)^2 \tag{84}$$

It can be shown that $\mathcal{Z}(\nu)$ is weakly dependent on ν, and only varies by 10% for $\nu\in[0,0.5]$.

3 Results and Discussion

We now examine the accuracy of Eq. (82) by comparing it with rigorous numerical solutions obtained using a finite element (FE) analysis of the governing thin plate equation.[2] The number of elements in the FE method were refined systematically to ensure an accuracy greater than 0.1%. These numerical results cover a wide range of aspect ratios $0.02\leqslant A\leqslant 50$ and Poisson's ratio $0\leqslant\nu\leqslant 0.499$ and thus permit assessment of the global validity of Eq. (82).

It can be seen from Eq. (78) that the correction to the classical beam theory result is independent of mode number, and hence Eq.

[2]The finite element analysis was implemented using LUSAS, which is a trademark of, and is available from FEA Ltd., Forge House, 66 High St., Kingston Upon Thames, Surrey KT1 1HN, UK. Quadrilateral thin plate elements with linear interpolation were used throughout.

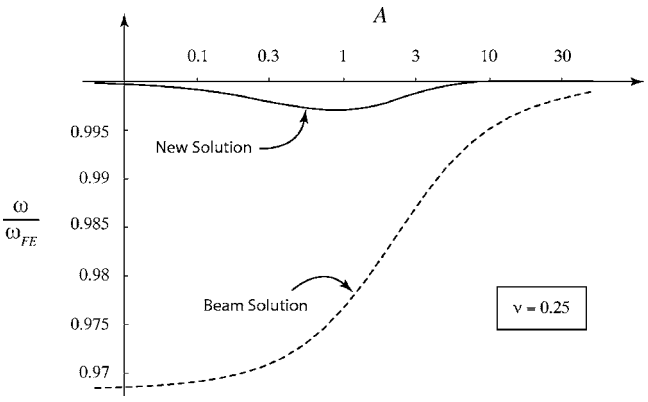

Fig. 3 Plot of the error in ω_f (Eq. (82)) with ω_f^∞ (Eq. (84)), when compared with finite element results ω_{FE} for the fundamental mode ($z_1=1.8751$). The solid line represents ω_f/ω_{FE} and the broken line represents $\omega_f^\infty/\omega_{FE}$.

(78) is equally valid for all modes of flexural vibration, subject to $A \gg 1$. Consequently Eq. (82), which is valid for all A, is also independent of mode number. However, for $0<A\ll 1$ it becomes increasingly difficult to distinguish the higher flexural modes from other modes of vibration. Therefore an assessment of the global validity of Eq. (82) for all A and mode numbers is not practically relevant. As a result we focus our assessment of the global validity of Eq. (82) on the fundamental flexural mode, which is also of greatest practical value in applications.

First, we note that Eq. (82) is exact in the limit of zero Poisson's ratio. Results illustrating the accuracy of standard beam theory and the new solution for Poisson's ratio greater than zero are given in Figs. 3 and 4. Note that as the aspect ratio $A\to\infty$ both approximate formulas converge to the required numerical result, as expected. However, as the aspect ratio A is reduced, the accuracy of the beam theory solution deteriorates significantly. This is due to the assumption inherent in beam theory that nonzero stresses exist only along the axis of the beam, which is clearly inadequate for finite aspect ratios. In contrast, note the superior accuracy exhibited by the new uniformly valid solution (Eq. (82)) for all aspect ratios. In particular, this solution converges to the required numerical result as $A\to 0$ and $A\to\infty$. In the intermediate regime where $A=\mathcal{O}(1)$, Eq. (82) exhibits its maximum error of 2%. Note that the error also increases with increasing Poisson's ratio, as expected, since the formula is exact for a Poisson's ratio

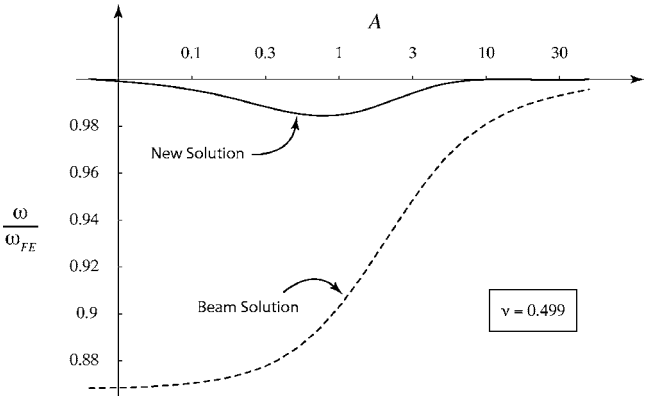

Fig. 4 Plot of the error in ω_f (Eq. (82)) with ω_f^∞ (Eq. (84)), when compared with finite element results ω_{FE} for the fundamental mode ($z_1=1.8751$). The solid line represents ω_f/ω_{FE} and the broken line represents $\omega_f^\infty/\omega_{FE}$.

of zero. Nonetheless, it presents a dramatic improvement on the classical beam result, which is in error by a factor of $\sqrt{1-\nu^2}$ as $A\to 0$.

The analysis presented here is derived under the assumption that the cantilever dynamics are not affected by any surrounding medium, such as fluid. It is well known that immersion in fluid can significantly affect the resonance characteristics of cantilever plates, and such effects should be taken into account when using the derived solution in practice [16,17].

4 Conclusion

A simple uniformly valid expression for the fundamental flexural vibration frequency of a thin rectangular cantilever plate has been presented. This was derived using an accurate variational approach based on an energy minimization principle and a singular perturbation solution. The resulting formula presents a significant improvement over the standard beam theory result, exhibiting a maximum error of $<2\%$. This formula is expected to be of value to the development and usage of applications that rely on the resonance characteristics of thin cantilever plates, such as required in the atomic force microscope.

Acknowledgment

This research was supported by the Particulate Fluids Processing Centre of the Australian Research Council and by the Australian Research Council Grants Scheme.

Appendix: The Limit $A\to 0$

To determine the limit $A\to 0$ ($\epsilon\to\infty$) we will consider the full dynamic plate equations [18],

$$D\nabla^4 w + h\rho\frac{\partial^2 w}{\partial t^2} = 0$$

where the differential operator ∇^4 can be expressed as

$$\nabla^4 = \frac{\partial^4}{\partial x^4} + 2\frac{\partial^4}{\partial x^2\partial y^2} + \frac{\partial^4}{\partial y^4}$$

The boundary conditions are

$$w = \frac{\partial w}{\partial x} = 0 \quad \text{at } x = 0$$

$$\frac{\partial^2 w}{\partial n^2} + \nu\frac{\partial^2 w}{\partial s^2} = 0 \quad \text{at free edge}$$

$$\frac{\partial^3 w}{\partial n^3} + (2-\nu)\frac{\partial^3 w}{\partial n\partial s^2} = 0 \quad \text{at free edge}$$

where n, s are the normal and tangential coordinates to the free edge.

In the limit as $A\to 0$, no deflection in the y direction is possible due the fact that the plate is infinitely narrow and clamped along $x=0$. Therefore

$$w(x,y,t) \to w(x,t) \quad \text{as } A\to 0$$

Because $A\to 0$, the edges $y=\pm(b/2)$ have a negligible effect and can also be ignored. These observations reduce the dynamic plate equations to

$$\frac{\partial^4 w}{\partial x^4} + \frac{h\rho}{D}\frac{\partial^2 w}{\partial t^2} = 0$$

$$w = \frac{\partial w}{\partial x} = 0 \quad \text{at } x = 0$$

$$\frac{\partial^2 w}{\partial x^2} = \frac{\partial^3 w}{\partial x^3} = 0 \quad \text{at } x = L$$

If we scale x by L and t by t_c we find that

$$t_c = \frac{L^2}{h}\sqrt{\frac{12(1-\nu^2)\rho}{E}}$$

This is precisely the same time scale that we use above. Searching for solutions of the form $w(x,t) = \bar{w}(x)e^{ikt}$, yields the following governing equations:

$$\frac{d^4\bar{w}}{dx^4} - k^2\bar{w} = 0$$

$$\bar{w} = \frac{d\bar{w}}{dx} = 0 \quad \text{at } x = 0$$

$$\frac{d^2\bar{w}}{dx^2} = \frac{d^3\bar{w}}{dx^3} = 0 \quad \text{at } x = 1$$

These governing equations are identically the classical beam equation and boundary conditions with the exception of the time scale, t_c. This implies that

$$\lim_{\epsilon\to\infty} k_{\text{plate}} = k_{\text{beam}}$$

We therefore obtain

$$\lim_{\epsilon\to\infty} \omega_f = \frac{1}{t_c}\lim_{\epsilon\to\infty} k_{\text{plate}} = \frac{k_{\text{beam}}}{t_c} = h\sqrt{\frac{E}{12\rho}}\left(\frac{z_n}{L}\right)^2 \frac{1}{\sqrt{1-\nu^2}} = \frac{\omega_f^\infty}{\sqrt{1-\nu^2}}$$

References

[1] Reissner, E., and Stein, M., 1951, "Torsion and Transverse Bending of Cantilever Plates," N.A.C.A. Technical Note 2369.

[2] Fritz, J., Baller, M. K., Lang, H. P., Rothuizen, H., Vettiger, P., Meyer, E., Guentherodt, H. J., Gerber, C., and Gimzewski, J. K., 2000, "Translating Biomolecular Recognition Into Nanomechanics," Science, **288**(5464), pp. 316–318.

[3] Ilic, B., Craighead, H. G., Krylov, S., Senaratne, W., Ober, C., and Neuzil, P., 2004, "Attogram Detection Using Nanoelectromechanical Oscillators," J. Appl. Phys., **95**(7), pp. 3694–3703.

[4] Giessibl, F. J., 1995, "Atomic-Resolution of the Silicon (111)-(7×7) Surface by Atomic-Force Microscopy," Science, **267**(5194), pp. 68–71.

[5] Levy, M., 1899, "Sur l'Équilibre Élastique d'Une Plaque Rectangulaire," C. R. Acad. Sci. Hebd Seances Acad. Sci. D, **129**, p. 535.

[6] Jaramillo, T. J., 1950, "Deflections and Moments Due to a Concentrated Load on a Cantilever Plate of Infinite Length," ASME J. Appl. Mech., **17**(1), pp. 67–72.

[7] Warburton, G. B., 1954, "The Vibration of Rectangular Plates," Proc. Inst. Mech. Eng., **168**, pp. 371–384.

[8] Leissa, A. W., 1973, "Free Vibration of Rectangular-Plates," J. Sound Vib., **31**(3), pp. 257–293.

[9] Dickinson, S. M., 1978, "Buckling and Frequency of Flexural Vibration of Rectangular Isotropic and Orthotropic Plates Using Rayleigh's Method," J. Sound Vib., **61**(1), pp. 1–8.

[10] Kim, C. S., and Dickinson, S. M., 1985, "Improved Approximate Expressions for the Natural Frequencies of Isotropic and Orthotropic Rectangular-Plates," J. Sound Vib., **103**(1), pp. 142–149.

[11] Jänich, R., 1962, "Die naherungsweise Berechnung der Eigenfrequenzen von rechteckigen Platten bei verschiedenen Randbedingungen," Die Bautechnik, (3), pp. 93–99.

[12] Feynman, R. P., Leighton, R. B., and Sands, M., 1963, *The Feynman Lectures on Physics*, Addison-Wesley, Reading, MA.

[13] Smirnov, V. I., 1964, *A Course of Higher Mathematics*, Vol. 4, Pergamon, Oxford.

[14] Timoshenko, S. P., and Woinowsky-Krieger, S., 1959, *Theory of Plates and Shells*, McGraw-Hill, New York.

[15] Hinch, E. J., 1991, *Perturbation Methods*, Cambridge University Press, Cambridge.

[16] Sader, J. E., 1998, "Frequency Response of Cantilever Beams Immersed in Viscous Fluids With Applications to the Atomic Force Microscope," J. Appl. Phys., **84**(1), pp. 64–76.

[17] Van Eysden, C. A., and Sader, J. E., 2007, "Frequency Response of Cantilever Beams Immersed in Viscous Fluids With Applications to the Atomic Force Microscope: Arbitrary Mode Order," J. Appl. Phys., **101**, p. 044908.

[18] Mansfield, E. H., 1964, *The Bending and Stretching of Plates*, Pergamon, Oxford.

Extended Stoney's Formula for a Film-Substrate Bilayer With the Effect of Interfacial Slip

Yin Zhang
State Key Laboratory of Nonlinear Mechanics (LNM),
Institute of Mechanics,
Chinese Academy of Sciences,
Beijing 100080, P.R.C.

The curvature-stress relation is studied for a film-substrate bilayer with the effect of interfacial slip and compared with that of an ideal interface without interfacial slip. The interfacial slip together with the dimensions, elastic and interfacial properties of the film and substrate layers can cause a significant deviation of curvature-stress relation from that with an ideal interface. The interfacial slip also results in the so-called free edge effect that the stress, constraint force, and curvature vary dramatically around the free edges. The constant curvature as predicted by Stoney's formula and the Timoshenko model of an ideal interface is no longer valid for a bilayer with a nonideal interface. The models with the assumption of an ideal interface can also lead to an erroneous evaluation on the true stress state inside a bilayer with a nonideal interface. The extended Stoney's formula incorporating the effects of both the layer dimensions and interfacial slip is presented. [DOI: 10.1115/1.2745387]

1 Introduction

Almost all solid-state electronic components have the basic structure of a substrate as a platform for supporting various thin film structures [1]. Stress is of a great concern for the reliability of those composite structures [1,2]. Because the material properties of film and substrate such as Young's modulus, lattice parameters, coefficients of thermal expansion can be different and residual stress can build up during fabrication and processing, the resultant stresses inside the film and substrate can be different and result in the deflection of the composite structure to relax stress [3]. The following Stoney's 1909 formula [4] serves the cornerstone of relating the surface stress inside the film to the curvature of a composite structure

$$\kappa_{St} = \frac{6f}{E_2 t_2^2} \tag{1}$$

κ_{St} is the curvature and f is the force per unit length inside the film (when the film is very thin, f is the surface stress [5]). t_2 is the substrate thickness and E_2 is the substrate effective Young's modulus. The applicability of the above Stoney's formula relies on several assumptions, which are well summarized by Freund et al. [6] as the following six: (1) both the film and substrate thicknesses are small compared to the lateral dimensions; (2) the film thickness is much less than the substrate thickness; (3) the substrate material is homogeneous, isotropic, and linearly elastic, and the film material is isotropic; (4) edge effect near the periphery of the substrate are inconsequential and all physical quantities are invariant under change in position parallel to the interface; (5) all stress components in the thickness direction vanish throughout the material; (6) the strains and rotations are infinitesimally small. Many models are developed to relax one or some of the above assumptions to extend Stoney's formula to a more generalized and realistic application, for example, by considering the effects of thin substrate [6–12], large deformation [6], nonisotropic stress [13], temperature gradient [14], stress gradient [7,15], residual axial force, boundary conditions, length [5,16], diffusion effect [17], and plastic deformation [18]. However, all the analyses above [5–18] assume an ideal interface, i.e., no interfacial slip. In those models, the condition of no interfacial slip is enforced either explicitly by imposing the compatibility/continuity condition at the interface [8,11,14] or implicitly by assuming one single strain/displacement variable for both film and substrate layers [5–7,9,10,12,13,15–18]. Compared with an ideal interface (also called perfectly bonded interface [19] or coherent interface [20]), a nonideal interface results in the interfacial shear and normal stresses, which are generally zero in an ideal interface. Therefore, the overall deflection/curvature of the composite and the stress distribution inside it can by significantly affected. An interfacial shear stress due to temperature gradient is shown to exist in an ideal interface of a film-substrate bilayer by Huang and Rosakis [14], and this interfacial shear stress vanishes when there is no temperature gradient. However, when there is no temperature gradient, the interfacial stresses (both normal and shear) of a nonideal interface still exist and have an influence on the stress distribution inside the layers [3,21–24].

Because the strains inside two solid phases separated by an interface can be independent [20], the continuity condition of strain/displacement across an interface is a strong one, which allows no interfacial slip. During the fabrication and processing of film-substrate layered structures, such as chemical vapor deposition, wafer bonding, sputtering, doping/diffusion, implantation, thermal annealing process, heteroepitaxial film growth, etc., defects like dislocation [25,26], twin [27], cavities [25,28] appear. Therefore, the interface may not be composed of 100% well-fused bonds [28–30]. The formation of amorphous layer and dangling bonds in some regions between the two phases [29–31] also result in the weakly bonded interface areas. All these above will reduce the overall interface adhesion for sure [30]. The stress distribution inside the film calculated from the ideal interface model has been shown to deviate significantly from the experimental observation of a Cu–Si composite with the size of several microns [23,24], which will also lead to a different deflection/curvature from that predicted by the ideal interface model.

The models of allowing interfacial slip are developed by Chen and Nelson [3] and Suhir [21,22], which are referred to as the shear-lag (S-L) model and lap-shear (L-S) model [24], respectively. Suhir's 1986 model gives a simple second order differential equation for the interfacial shear stress [21]. However, its drawback is noticed that the interfacial peeling stress (normal to the interface) cannot be self-equilibrated [32]. With the introduction of "compliant interface," Suhir's 1989 revised model [22] leads to a sixth order differential equation similar to that of Chen and

Contributed by the Applied Mechanics Division of ASME for publication in the JOURNAL OF APPLIED MECHANICS. Manuscript received September 6, 2006; final manuscript received March 19, 2007; published online January 11, 2008. Review conducted by Zhigang Suo.

Nelson [3]. The S-L model of Chen and Nelson is originally developed to study the stress distribution of two bonded joints. It assumes that there is an isotropic layer of finite thickness between the two joints, which plays the role of stress transfer between the two layers. This stress-transfer layer is extended to the concept of the interface layer [23,24] as observed by high resolution transmission electron microscopy (HRTEM) that the 1–2 nm thick amorphous layer present at the interface of two crystal material layers [23,24,28]. The S-L model is shown to be equivalent to the damaged interface (DI) model [33] by Tullini [34]. Müller and Saúl give an in-depth discussion on various mechanisms causing the damaged/nonideal interface [35]. The effect, called the boundary layer effect or free edge effect unique to composite and not observed in homogeneous solids [19] arises, which is that the interfacial shear stress can be large and vary dramatically around the free edges (the constraint force and deflection/curvature which are related to the interfacial shear stress also share the similar characteristics). The interfacial stress is responsible for the failure (delamination, cracking) of composite structures [1,2,19], while, the ideal interface model as shown later in this paper cannot predict such boundary layer effect. The boundary layer effect is incorporated in the functions of interfacial stresses and their detailed solution procedures are given in this paper. This paper focuses on the effect of the interfacial slip on the overall deflection/curvature of the bilayer composite. The relation between the curvature and interfacial stresses is established by relaxing the aforementioned second, fourth and fifth assumptions given by Freund et al. [6]. The first, third, and sixth assumptions are retained, therefore, a beam model and related linear stress-strain relations can be applied. For the bilayer with a nonideal interface, the following two major results are presented in this paper: (1) the curvatures of the film and substrate with a nonideal interface can significantly deviate from the curvature predicated by the model of the ideal interface; (2) unlike that the film and substrate with an ideal interface share a common constant curvature; the curvatures of the film and substrate with a nonideal interface are different in general and vary with the length. These two results have a significant impact on the interpretation of the experimental data of the curvature-based measurement.

2 Model Development

2.1 Strain Distribution due to Lattice Mismatch. The lattice mismatch induced deflection of a film-substrate composite fabricated by heteroepitaxial growth is analyzed as an example to demonstrate the effect of interfacial slip on curvature. The strains inside the film and substrate layers are first calculated by assuming no composite deflection. The composite deflection with the presence of this calculated strain distribution is then derived in the following two models with and without interfacial slip. The derivation approach of composite deflection presented here is general, which can be applied to the analysis of composite deflection induced by other mechanisms. The lattice mismatch induced strains inside the film and substrate have the following relations [17]:

$$\epsilon_f - \epsilon_s = \epsilon_m$$
$$E_1 t_1 \epsilon_f + E_2 t_2 \epsilon_s = 0 \tag{2}$$

ϵ_f and ϵ_s are the strains induced by lattice mismatch in the film and substrate, respectively. ϵ_m is the mismatch strain defined as $\epsilon_m = (a_s - a_f)/a_f$ [7] (a_f and a_s are the lattice parameters of the film and substrate, respectively). E_1 and E_2 are the effective Young's moduli of the film and substrate. When the composite is a plate structure and under biaxial stress loading, $E_1 = Y_1/(1-\nu_1)$ and $E_2 = Y_2/(1-\nu_2)$ are the biaxial moduli [7] (Y_1 and Y_2 are the Young's moduli of the film and substrate, respectively. ν_1 and ν_2 are their Poisson's ratios). When the composite plate bends to a cylindrical surface, $E_1 = Y_1/(1-\nu_1^2)$ and $E_2 = Y_2/(1-\nu_2^2)$ [36]. When the composite is a beam structure, $E_1 = Y_1$ and $E_2 = Y_2$. t_1 and t_2 as shown in Fig. 1(*a*) are the thickness of the film and substrate. The first equation in Eq. (2) is the compatibility condition and the second one is the Newton's third law. From Eq. (2), ϵ_f and ϵ_s are solved as follows:

$$\epsilon_f = \epsilon_m \frac{E_2 t_2}{E_1 t_1 + E_2 t_2}$$
$$\epsilon_s = -\epsilon_m \frac{E_1 t_1}{E_1 t_1 + E_2 t_2} \tag{3}$$

Clearly, ϵ_f and ϵ_s have the opposite signs, which implies that there is a bending moment inside the film-substrate bilayer and the bilayer must deflect. The following derivation is about how the bilayer accommodates this bending moment by deflecting with and without interfacial slip.

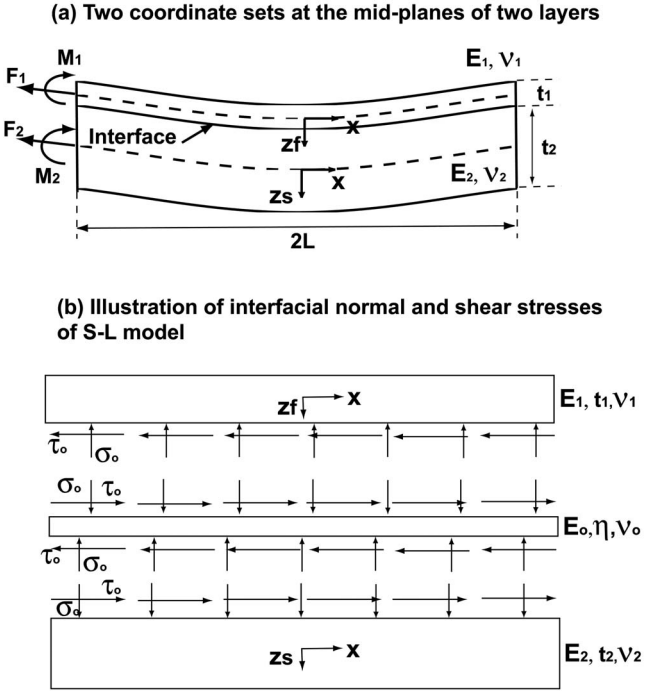

Fig. 1 (*a*) **Two coordinate systems at the mid-planes of two layers.** (*b*) **Illustration of interfacial normal stress (σ_o) and shear stress (τ_o) in the S-L model.**

2.2 Timoshenko Model. The Timoshenko model [8] is essentially a beam model. There is other method of solving this composite bending problem, such as elasticity approach [19]. Because the Timoshenko model uses the curvature as the unknown variable, it has the advantage that the curvature is directly solved.

The equilibrium requires the balance of both force and moment, which gives the following two equations:

$$F_1 + F_2 = 0 \tag{4}$$

and

$$M_1 + M_2 - F_1 \frac{t_1}{2} + F_2 \frac{t_2}{2} = 0 \tag{5}$$

F_1 and M_1 are the force and moment per unit width acting inside the film layer as shown in Fig. 1(*a*). F_2 and M_2 are those inside the substrate layer. From Eq. (4), the following equation is derived:

$$F_1 = P(x) = -F_2 \tag{6}$$

Substitute Eq. (6) into Eq. (5), it gives

$$\frac{P(x)(t_1+t_2)}{2} = M_1 + M_2 \tag{7}$$

The longitudinal normal strains of the two layers are expressed as the following:

$$\frac{du_1(x,z)}{dx} = \epsilon_f + \frac{P(x)}{E_1 t_1} + \frac{z}{\rho}$$

$$-\frac{t_1}{2} \leqslant z \leqslant \frac{t_1}{2}$$

$$\frac{du_2(x,z)}{dx} = \epsilon_s - \frac{P(x)}{E_2 t_2} + \frac{z}{\rho}$$

$$-\frac{t_2}{2} \leqslant z \leqslant \frac{t_2}{2} \tag{8}$$

$u_1(x,z)$ and $u_2(x,z)$ are the longitudinal displacements of the film and substrate, respectively. As shown in Fig. 1(*a*), two sets of coordinates are used in the Timoshenko model. z_f and z_s start from the midplanes of the film and substrate, respectively. $P(x)$ is the constraint force per unit width. ρ is the radius of curvature. Because curvature $\kappa = 1/\rho$, Eq. (8) assumes that the film and substrate share a common curvature [32].

The bending moment $(M_i, i=1,2)$ has the following relation with ρ:

$$M_i = \frac{E_i t_i^3}{12\rho} \tag{9}$$

Substitute Eq. (9) into Eq. (7), the following equation is obtained:

$$\frac{1}{\rho} = \frac{6P(x)(t_1+t_2)}{E_1 t_1^3 + E_2 t_2^3} \tag{10}$$

The compatibility condition at the interface requires that

$$\epsilon_f + \frac{P(x)}{E_1 t_1} + \frac{t_1}{2\rho} = \epsilon_s - \frac{P(x)}{E_2 t_2} - \frac{t_2}{2\rho} \tag{11}$$

Equation (11) physically indicates the continuity of strain at the interface, i.e., that there is no slip between the two layers. From Eq. (11), $P(x)$ is solved as a constant as follows:

$$P(x) = \frac{-\epsilon_m}{1/E_1 t_1 + 1/E_2 t_2 + 3(t_1+t_2)^2/(E_1 t_1^3 + E_2 t_2^3)} \tag{12}$$

Substitute this $P(x)$ of Eq. (12) into Eq. (10) and the curvature (κ_T) is solved also as a constant as the following:

$$\kappa_T = \frac{1}{\rho} = \frac{\kappa_{\mathrm{St}}\left(1 + \frac{t_1}{t_2}\right)}{1 + 4\frac{t_1 E_1}{t_2 E_2} + 6\frac{t_1^2 E_t}{t_2^2 E_2} + 4\frac{t_1^3 E_1}{t_2^3 E_2} + \frac{t_1^4 E_1^2}{t_2^4 E_2^2}} \tag{13}$$

κ_{St} is the Stoney's formula of Eq. (1) when f is set as $f = -\epsilon_m E_1 t_1$. The Timoshenko model is a free body diagram analysis with the introduction of constraint force $P(x)$. The curvature of Eq. (13) is exactly the same as that derived by Freund and Suresh [17] who use an energy approach. In Freund and Suresh's derivation [7], there is no constraint force assumed, but one displacement variable is used for both film and substrate layer (therefore, the continuity of displacement and strain at the interface is automatically satisfied), which is equivalent to the enforcement of no interfacial slip in Eq. (11). It is also noticed that $\lim_{t_1/t_2 \to 0} \kappa_T = \kappa_{\mathrm{St}}$ and the Timoshenko model in essence extends the Stoney formula by relaxing the aforementioned second assumption given by Freund et al. [6].

2.3 S-L Model. As the S-L model is demonstrated to fit the experimental observation much better than the L-S model [23,24], the S-L model is adopted here to study the interfacial slip effect. The S-L model is rather complex and here an outline of its derivation is given for reader to better understand. In the S-L model, an interfacial layer is assumed. The interfacial normal stress $(\sigma_o(x))$ and shear stress $(\tau_o(x))$ due to interfacial slip is illustrated in Fig. 1(*b*). With interfacial slip, the constraint condition of Eq. (11) is invalid. $\sigma_o(x)$ and $\tau_o(x)$ are related to the longitudinal and transverse displacements of the film and substrate layers, respectively. The presence of $\sigma_o(x)$ and $\tau_o(x)$ changes the equation of equilibrium of each layer as reflected in the following derivations. Because the longitudinal and transverse displacements of the film and substrate layers are not independent of each other, $\sigma_o(x)$ and $\tau_o(x)$ are not two independent variables, either. Therefore, the major effort in the following derivation is actually to decouple $\sigma_o(x)$ and $\tau_o(x)$ for the solution purpose, which also results in the two sixth order differential governing equations for $\sigma_o(x)$ and $\tau_o(x)$.

$\sigma_o(x)$ and $\tau_o(x)$ have the following expressions:

$$\sigma_o(x) = \frac{E_o}{\eta}[v_2(x) - v_1(x)] \tag{14}$$

$$\tau_o(x) = \frac{G_o}{\eta}\left[u_1\left(x, \frac{t_1}{2}\right) - u_2\left(x, -\frac{t_2}{2}\right)\right] \tag{15}$$

E_o, G_o are the Young's modulus and shear modulus of the interface layer, respectively. η is the thickness of the interface layer. In the S-L model, E_o, G_o, and η are fitting factors [23,24]. The actual varying parameters in the S-L model are E_o/η and G_o/η. $u_1(x, t_1/2)$ and $u_2(x, -t_2/2)$ are the longitudinal displacements of the film layer and substrate layer at the interface, respectively. $v_1(x)$ and $v_2(x)$ are the transverse displacements of the midplanes of the layers. The transverse displacement $(v_i(x))$ in the S-L model is independent of z. As indicated in Fig. 1(*b*) $\sigma_o(x)$ is perpendicular to the interface and the fifth assumption of the Stoney formula [6] is clearly violated. Also as shown later, the boundary conditions are used to find $\sigma_o(x)$ and $\tau_o(x)$ and the edge effects are thus incorporated into their solutions; $\sigma_o(x)$ and $\tau_o(x)$ are the functions of x and they vary along the direction parallel to the interface. The fourth assumption is also violated. The following derivation as the above Timoshenko model does not need the second assumption of very thin film thickness, either. As mentioned above, the interfacial normal and shear stresses do not exist in an ideal interface case. In Eq. (8) P is a normal constant constraint force parallel to the interface. In the model of a film-viscous layer-rigid substrate by Huang and Suo [37,38], the pressure that drives the flow of viscous layer also acts on the film in the direction perpendicular to the interface and the flow itself provides the shear stress (parallel to the interface) to the film layer, which resembles the functions of $\sigma_o(x)$ and $\tau_o(x)$. Although Huang and Suo assume that the no-slip boundary condition (at the viscous layer-rigid substrate interface) and the elastic film is bonded to the viscous layer [37,38], the flow of the viscous layer in fact causes the slip between the film and substrate.

In the S-L model, the equilibrium of moment is

$$\frac{dM_1(x)}{dx} - V_1(x) - \frac{t_1}{2}\tau_o(x) = 0$$

$$\frac{dM_2(x)}{dx} - V_2(x) - \frac{t_2}{2}\tau_o(x) = 0 \tag{16}$$

$M_1(x)$ and $M_2(x)$ are the moments acting in layer 1 and 2, respectively. V_i $(i=1,2)$ stands for the vertical shear force per unit width. The vertical force equilibrium requires

$$dV_1(x) + \sigma_o(x)dx = 0$$
$$dV_2(x) - \sigma_o(x)dx = 0 \tag{17}$$

Differentiating Eq. (16) and using Eq. (17), the following is derived:

$$\frac{d^2M_1(x)}{dx^2} + \sigma_o(x)dx - \frac{t_1}{2}\frac{d\tau_o(x)}{dx} = 0$$
$$\frac{d^2M_2(x)}{dx^2} - \sigma_o(x)dx - \frac{t_2}{2}\frac{d\tau_o(x)}{dx} = 0 \tag{18}$$

The moment and curvature radius have the following relation:

$$M_i(x) = \frac{D_i}{\rho_i(x)} = -D_i\frac{d^2v_i(x)}{dx^2} \tag{19}$$

Here ρ_i $(i=1,2)$ is the radius of curvature and $1/\rho_i(x) = -d^2v_i(x)/dx^2$, the minus sign is due to the coordinate system as shown in Fig. 1(*a*) [8,24,36]. It should be kept in mind that in general $d^2v_1(x)/dx^2 \neq d^2v_2(x)/dx^2$ for the composite with interfacial slip. D_i $(i=1,2)$ is the bending stiffness per unit width of layer i defined as $D_i = E_i t_i^3/12$. Substituting Eq. (19) into Eq. (18), the following is derived:

$$-D_1\frac{d^4v_1(x)}{dx^4} + \sigma_o(x) - \frac{t_1}{2}\frac{d\tau_o(x)}{dx} = 0$$
$$-D_2\frac{d^4v_2(x)}{dx^4} - \sigma_o(x) - \frac{t_2}{2}\frac{d\tau_o(x)}{dx} = 0 \tag{20}$$

Differentiating Eq. (14) four times and using the expressions of d^4v_1/dx^4 and d^4v_2/dx^4 derived from Eq. (20), the following is obtained:

$$\frac{d^4\sigma_o(x)}{dx^4} + \frac{E_o b}{\eta}\sigma_o(x) = \frac{E_o a}{\eta}\frac{d\tau_o(x)}{dx} \tag{21}$$

a and b are defined as follows:

$$a = \frac{1}{2}\left(\frac{t_1}{D_1} - \frac{t_2}{D_2}\right)$$
$$b = \frac{1}{D_1} + \frac{1}{D_2} \tag{22}$$

The longitudinal strains of the two layers in the S-L model have the following expressions:

$$\frac{du_1(x,z)}{dx} = \epsilon_f + \frac{P(x)}{E_1t_1} - z\frac{d^2v_1(x)}{dx^2} \quad -\frac{t_1}{2} \leqslant z \leqslant \frac{t_1}{2}$$
$$\frac{du_2(x,z)}{dx} = \epsilon_s - \frac{P(x)}{E_2t_2} - z\frac{d^2v_2(x)}{dx^2} \quad -\frac{t_2}{2} \leqslant z \leqslant \frac{t_2}{2} \tag{23}$$

$P(x)$ is also an unknown constraint axial force. At the interface, the longitudinal strains are as follows:

$$\frac{du_1\left(x,\frac{t_1}{2}\right)}{dx} = \epsilon_f + \frac{P(x)}{E_1t_1} - \frac{t_1}{2}\frac{d^2v_1(x)}{dx^2}$$
$$\frac{du_2\left(x,-\frac{t_2}{2}\right)}{dx} = \epsilon_s - \frac{P(x)}{E_2t_2} + \frac{t_2}{2}\frac{d^2v_2(x)}{dx^2} \tag{24}$$

Differentiating Eq. (15), gives

$$\frac{d\tau_o(x)}{dx} = \frac{G_o}{\eta}\left[\frac{du_1\left(x,\frac{t_1}{2}\right)}{dx} - \frac{du_2\left(x,-\frac{t_2}{2}\right)}{dx}\right] \tag{25}$$

Substituting Eq. (24) into Eq. (25), gives

$$\frac{d\tau_o(x)}{dx} = \frac{G_o}{\eta}\left[\left(\frac{t_1^2}{12D_1} + \frac{t_2^2}{12D_2}\right)P(x) - \frac{t_1}{2}\frac{d^2v_1(x)}{dx^2} - \frac{t_2}{2}\frac{d^2v_2(x)}{dx^2} - \Delta\right] \tag{26}$$

Here $\Delta = \epsilon_s - \epsilon_f$. Differentiating Eq. (26) twice and using both Eq. (20) and the fact of $dP(x)/dx = \tau_o(x)$, gives

$$\frac{d^3\tau_o(x)}{dx^3} - \frac{G_o c}{\eta}\frac{d\tau_o(x)}{dx} = -\frac{G_o a}{\eta}\sigma_o(x) \tag{27}$$

and $c = (t_1^2/D_1 + t_2^2/D_2)/3$. Differentiating Eq. (21) twice and using Eqs. (21) and (27) again, leads to

$$\frac{d^6\sigma_o(x)}{dx^6} - \frac{G_o c}{\eta}\frac{d^4\sigma_o(x)}{dx^4} + \frac{E_o b}{\eta}\frac{d^2\sigma_o(x)}{dx^2} - \frac{E_o G_o(bc - a^2)}{\eta^2}\sigma_o(x) = 0 \tag{28}$$

Equation (28) is the uncoupled governing equation of interfacial normal stress $\sigma_o(x)$. To derive the uncoupled governing equation of interfacial shear stress $\tau_o(x)$, Eq. (27) is differentiated four times and Eqs. (21) and (27) are used again. The seventh order differential equation is obtained as follows:

$$\frac{d^7\tau_o(x)}{dx^7} - \frac{G_o c}{\eta}\frac{d^5\tau_o(x)}{dx^5} + \frac{E_o b}{\eta}\frac{d^3\tau_o(x)}{dx^3} - \frac{G_o E_o(bc - a^2)}{\eta^2}\frac{d\tau_o(x)}{dx} = 0 \tag{29}$$

Integrate Eq. (29) once with the use of $\tau_o(0) = 0$ because the interfacial shear stress is an odd function [3,24], the following sixth order differential equation is derived

$$\frac{d^6\tau_o(x)}{dx^6} - \frac{G_o c}{\eta}\frac{d^4\tau_o(x)}{dx^4} + \frac{E_o b}{\eta}\frac{d^2\tau_o(x)}{dx^2} - \frac{E_o G_o(bc - a^2)}{\eta^2}\tau_o(x) = 0 \tag{30}$$

It must be emphasized that the two uncoupled Eqs. (28) and (30) are not independent of each other and they are related to each other by Eq. (21).

2.4 Solutions of $\sigma_o(x)$, $\tau_o(x)$, and Curvatures. $\sigma_o(x)$ of Eq. (28) has the following solution form [3,24]:

$$\sigma_o(x) = A_1\cosh(\beta_1 x) + A_2\sinh(\beta_1 x) + A_3\cosh(\beta_h x)\cos(\beta_v x) + A_4\sinh(\beta_h x)\cos(\beta_v x) + A_5\sinh(\beta_h x)\sin(\beta_v x) + A_6\cosh(\beta_h x)\sin(\beta_v x) \tag{31}$$

Here A_is $(i=1-6)$ are the unknown constants to be determined by the boundary conditions. β_1, β_h, and β_v are the eigenvalues solved from the characteristic equation of Eq. (28). The following parameters are defined to express the eigenvalues:

$$\Phi_0 = \frac{c}{3}\frac{G_o}{\eta} \quad \Phi_1 = \frac{b}{3}\frac{E_o}{\eta} - \frac{c^2}{9}\left(\frac{G_o}{\eta}\right)^2$$
$$\Phi_2 = \frac{1}{3}\left[c^3\left(\frac{G_o}{\eta}\right)^3 - \frac{27}{2}a^2\frac{E_o}{\eta}\frac{G_o}{\eta} + 9bc\frac{E_o}{\eta}\frac{G_o}{\eta} + \frac{R_1}{2\eta^6}\right]^{1/3} \tag{32}$$

R_1 is defined as follows:

$$R_1 = [4(3bE_o\eta^3 - c^2G_o^2\eta^2)^3 + (2c^3G_o^3\eta^3 - 27a^2E_oG_o\eta^4 + 18bcE_oG_o\eta^4)^2]^{1/2} \tag{33}$$

y_1, y_h, and y_v are defined as

$$y_1 = \Phi_0 - \frac{\Phi_1}{\Phi_2} + \Phi_2 \quad y_h = \Phi_0 + \frac{1}{2}\left(\frac{\Phi_1}{\Phi_2} - \Phi_2\right) \quad y_v = \frac{\sqrt{3}}{2}\left(\frac{\Phi_1}{\Phi_2} + \Phi_2\right) \tag{34}$$

Now β_1, β_h, and β_v are defined as

$$\beta_1 = \sqrt{y_1} \quad \beta_h = \sqrt{\frac{\sqrt{y_h^2 + y_v^2}}{1 + \tan^2\left[\frac{1}{2}\tan^{-1}(y_h/y_v)\right]}}$$
$$\beta_v = \beta_h \tan\left[\frac{1}{2}\tan^{-1}(y_v/y_h)\right] \tag{35}$$

The symmetry condition requires $\sigma_o(x)$ to be an even function [3,24], therefore Eq. (31) changes as follows:

$$\sigma_o(x) = A_1 \cosh(\beta_1 x) + A_3 \cosh(\beta_h x)\cos(\beta_v x) + A_5 \sinh(\beta_h x)\sin(\beta_v x) \tag{36}$$

The 3 boundary conditions for Eq. (36) are the following [3,24]:

$$\int_{-L}^{L} \sigma_o(x)dx = 0 \quad \frac{d^2\sigma_o(L)}{dx^2} = 0$$
$$\frac{d^4\sigma_o(L)}{dx^4} - \frac{E_o b}{\eta}\sigma_o(L) = -\frac{E_o a}{\eta}\frac{G_o \Delta}{\eta} \tag{37}$$

$-L \leqslant x \leqslant L$ and $2L$ is the beam length. Here the boundary conditions are expressed by σ_o and their physical meaning cannot easily be told. Physically, the first boundary condition above indicates that the vertical shear force is zero at the free edge. The second and third ones involve the fact that both the axial force and bending moment are zero at the free edges [3,24]. The 3 boundary conditions of Eq. (37) written in A_is are the following 3 equations:

$$\frac{\sinh(\beta_1 L)}{\beta_1}A_1 + \left[\frac{\beta_v}{\beta_h^2 + \beta_v^2}\cosh(\beta_h L)\sin(\beta_v L) + \frac{\beta_h}{\beta_h^2 + \beta_v^2}\sinh(\beta_h L)\cos(\beta_v L)\right]A_3 + \left[\frac{\beta_h}{\beta_h^2 + \beta_v^2}\cosh(\beta_h L)\sin(\beta_v L) - \frac{\beta_v}{\beta_h^2 + \beta_v^2}\sinh(\beta_h L)\cos(\beta_v L)\right]A_5 = 0 \tag{38}$$

$$\beta_1^2 \cosh(\beta_1 L)A_1 + [(\beta_h^2 - \beta_v^2)\cosh(\beta_h L)\cos(\beta_v L) - 2\beta_h\beta_v \sinh(\beta_h L)\sin(\beta_v L)]A_3 + [(\beta_h^2 - \beta_v^2)\sinh(\beta_h L)\sin(\beta_v L) + 2\beta_h\beta_v \cosh(\beta_h L)\cos(\beta_v L)]A_5 = 0 \tag{39}$$

$$\left[\left(\beta_1^4 + \frac{E_o b}{\eta}\right)\cosh(\beta_1 L)\right]A_1 + \left[(\beta_h^2 - \beta_v^2)^2 - 4\beta_h^2\beta_v^2 + \frac{E_o b}{\eta}\right)\cosh(\beta_h L)\cos(\beta_v L) - 4\beta_h\beta_v(\beta_h^2 - \beta_v^2)\sinh(\beta_h L)\sin(\beta_v L)\Big]A_3 + \left[(\beta_h^2 - \beta_v^2)^2 - 4\beta_h^2\beta_v^2 + \frac{E_o b}{\eta}\right)\sinh(\beta_h L)\sin(\beta_v L) + 4\beta_h\beta_v(\beta_h^2 - \beta_v^2)\cosh(\beta_h L)\cos(\beta_v L)\Big]A_5 = -\frac{E_o a}{\eta}\frac{G_o \Delta}{\eta} \tag{40}$$

The 3 boundary conditions above uniquely determine the values of A_1, A_2, and A_3.

For the solution of interfacial shear stress $\tau_o(x)$ of Eq. (30), the solution has the following form:

$$\tau_o(x) = C_1 \sinh(\beta_1 x) + C_2 \sinh(\beta_h x)\cos(\beta_v x) + C_3 \cosh(\beta_h x)\sin(\beta_v x) + C_4 \cosh(\beta_h x)\cos(\beta_v x) + C_5 \sinh(\beta_h x)\sin(\beta_v x) + C_6 \cosh(\beta_1 x) \tag{41}$$

Here C_is $(i=1-6)$ are the unknown constants to be determined by the boundary conditions. While, in order to keep $\tau_o(x)$ as an odd function [3,24], Eq. (41) changes to the following form:

$$\tau_o(x) = C_1 \sinh(\beta_1 x) + C_2 \sinh(\beta_h x)\cos(\beta_v x) + C_3 \cosh(\beta_h x)\sin(\beta_v x) \tag{42}$$

C_i $(i=1-3)$ are correlated to A_is via Eq. (21). C_is are expressed in A_is as

$$C_1 = \frac{1}{\beta_1}\frac{\eta}{E_o a}\left(\beta_1^4 + \frac{E_o b}{\eta}\right)A_1 \quad C_2 = \frac{\eta}{E_o a}(\gamma_1 A_3 - \gamma_2 A_5)$$
$$C_3 = \frac{\eta}{E_o a}(\gamma_1 A_5 + \gamma_2 A_3) \tag{43}$$

with the definition of γ_1 and γ_2 as

$$\gamma_1 = \beta_h\left[\frac{E_o b}{\eta(\beta_h^2 + \beta_v^2)} + \beta_h^2 - 3\beta_v^2\right]$$
$$\gamma_2 = \beta_v\left[\frac{E_o b}{\eta(\beta_h^2 + \beta_v^2)} + \beta_v^2 - 3\beta_h^2\right] \tag{44}$$

Once $\sigma_o(x)$ and $\tau_o(x)$ are solved, κ_f can be obtained as follows by integrating the first equation of Eq. (16):

$$\kappa_f = -\frac{d^2 v_1(x)}{dx^2} = -\frac{1}{D_1}\int_{-L}^{x}\int_{-L}^{x}\sigma_o(x)dxdx + \frac{t_1}{2D_1}\int_{-L}^{x}\tau_o(x)dx \tag{45}$$

During the derivation of Eq. (45), the facts that $M_1 = -D_1 d^2 v_1/dx^2$ in Eq. (19) and $dV_1/dx = -\sigma_o(x)$ in Eq. (17) are also used. Similarly, the curvature of the substrate is found by integrating the second equation of Eq. (16),

$$\kappa_s = -\frac{d^2 v_2(x)}{dx^2} = \frac{1}{D_2}\int_{-L}^{x}\int_{-L}^{x}\sigma_o(x)dxdx + \frac{t_2}{2D_2}\int_{-L}^{x}\tau_o(x)dx \tag{46}$$

Generally, $\kappa_f \neq \kappa_s$ in the S-L model in contrast to $\kappa_f = \kappa_s = \kappa_T$ of the Timoshenko model. A more dramatic case is demonstrated in the model of a (soft) film-viscous layer-rigid substrate [37,38] that the soft film is buckled with relatively large wave number and the rigid substrate remains flat. Also, the above curvatures of the film and substrate in the S-L model vary along the beam span in contrast to the constants of the Timoshenko model. Huang and Rosakis also summarize six assumptions for the applicability of the Stoney formula and their sixth is that "all surviving stress and curvature components are spatially constant over the plate system's surface, a situation which is often violated in practice" [14]. Clearly, here the interfacial slip is one of the mechanisms responsible for such violation. With the solution of $\tau_o(x)$ and $P(x) = \int_{-L}^{x}\tau_o dx$ [24], the strain/stress inside the film and substrate can also be evaluated via Eq. (23).

3 Results and Discussion

Here the film is germanium with $Y_1 = 105.08$ GPa, $\nu_1 = 0.26$, and $a_f = 0.56574$ nm; the substrate is silicon with $Y_2 = 150$ GPa, $\nu_2 = 0.17$, and $a_s = 0.54306$ nm [7]. $\epsilon_m \approx -4\%$. The interface layer is

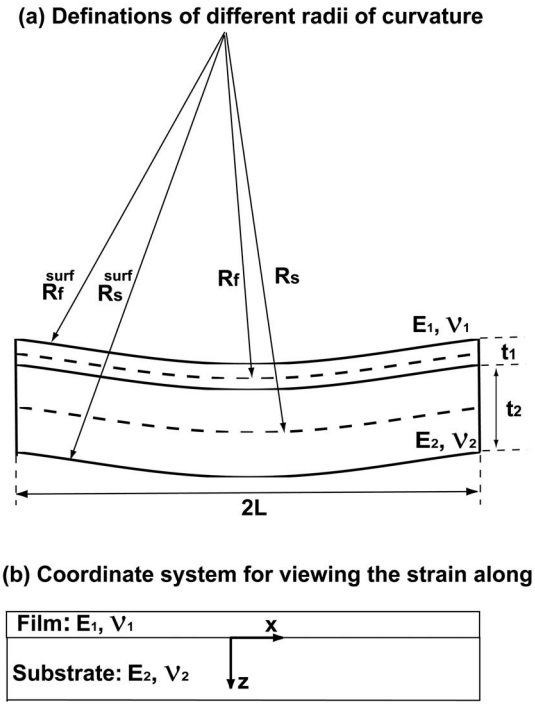

Fig. 2 (*a*) **The definitions of different radii of curvature.** R_f **and** R_s **are the radii of curvature of the mid-planes of film and substrate, respectively.** R_f^{surf} **and** R_s^{surf} **are the radii of curvature of the surfaces of film and substrate, respectively.** (*b*) **The coordinate system for viewing the strain along the thickness.**

assumed isotropic, so $G_o=E_o/2(1+\nu_o)$ [24]. ν_o is the Poisson's ratio of the interface layer and $\nu_o=0.2$ is assumed. The range of G_o/η taken in Murray and Noyan's paper is around $10^{17}-10^{21}$ Pa/m [24]. Here the relatively compliant interface layer parameters are taken in order to better demonstrate the effect of interfacial slip. Two cases of $E_o/\eta=2\times10^{16}$ Pa/m and 2×10^{17} Pa/m are studied comparatively. As noticed by Huang and Zhang [15], the experimentally measured radii of curvature are those of the surfaces, which are indicated by R_f^{surf} and R_s^{surf} in Fig. 2(*a*). The beam model of both the Timoshenko and S-L model actually describes the behavior of the midplanes of the two layers. The radii of curvature given by the two models are thus R_f and R_s as shown in Fig. 2(*a*). $R_f=R_f^{surf}+t_1/2$ and $R_s=R_s^{surf}-t_2/2$. As demonstrated later in this section, R_f and R_s have the order of 10^2-10^3 μm, the thickness (t_1 and t_2) is just $1-3$ μm. So the curvature difference between the model and experimental measurement is so little to be ignored. As mentioned above, two sets of coordinate system are used in both the Timoshenko and S-L models during the derivation. It may cause confusion when examining the strain across the thickness as shown later in Fig. 5. So here a new coordinate system located at the interface as shown in Fig. 2(*b*) is introduced for the result presentation purpose.

The curvatures of the film and substrate of the S-L model when $E_o/\eta=2\times10^{16}$ Pa/m and 2×10^{17} Pa/m are calculated from Eqs. (45) and (46). The curvatures of the Timoshenko model for the film and substrate are the same. As indicated in Eq. (13), the curvature of the Timoshenko model is a constant when the dimensions are fixed. In Fig. 3, the following dimensions are used: $t_1=t_2=2$ μm and $L=10$ μm. The uniform curvature of the Timoshenko model is calculated as $\kappa_T=14914.1$ m^{-1}. For the ideal interface case described by the Timoshenko model, the curvature can only be uniform without the presence of residual axial stress [16]. During the derivation above, the implicit assumption of no residual stress is applied. For the composite with ideal interface and no residual axial stress, its curvature is proved to be independent on the length [16]. As indicated in Eq. (13), κ_T of the Timoshenko model is independent of the beam length $2L$. However, the two curvatures of the S-L model in Eqs. (45) and (46) explicitly

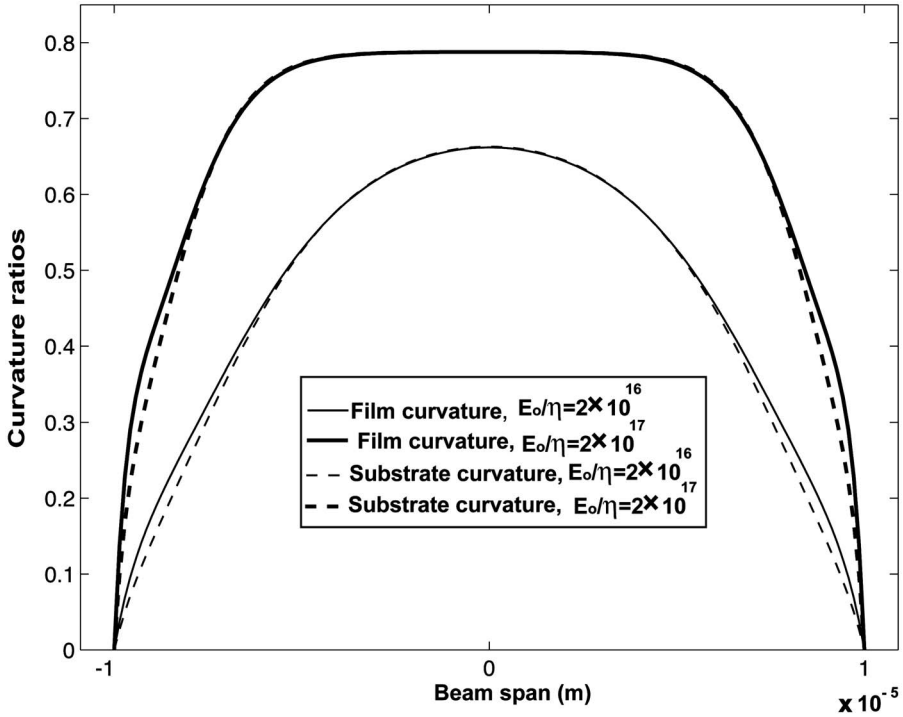

Fig. 3 The curvatures of film and substrate of the S-L model divided by κ_T**.** E_o/η **is taken as** 2×10^{16} **Pa/m and** 2×10^{17} **Pa/m, respectively. The thickness of film layer is** $t_1=2$ μ**m and the thickness of the substrate layer is** $t_2=2$ μ**m;** $L=10$ μ**m and** $\kappa_T=14914.1$ **m**$^{-1}$**.**

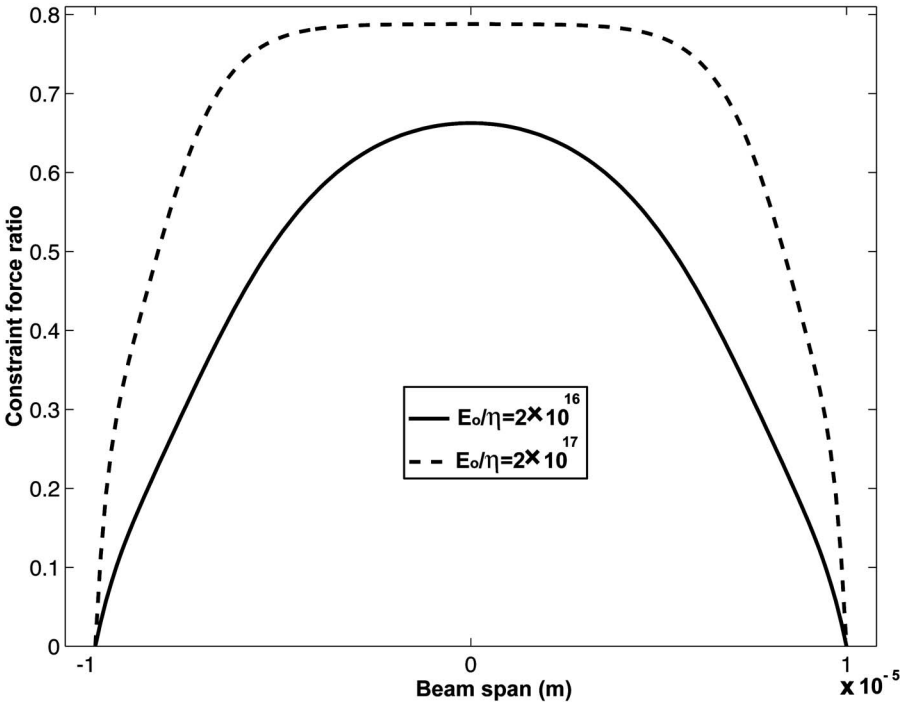

Fig. 4 The constraint forces per unit width of the S-L model with different E_o/ηs divided by that of the Timoshenko model (P_{timo}=1268.1 N m^{-1}). t_1=2 μm, t_2=2 μm, and L=10 μm.

depend on the length. During the derivation of the Timoshenko model, no boundary conditions are used. For the composite with ideal interface and no residual axial stress, its curvature is also proved to be independent on the boundary conditions [16]. The free-free boundary conditions in Eq. (37) are used for the solution of the interfacial stresses, therefore, the curvature of the S-L model is dependent on the boundary conditions. In Fig. 3, κ_f and κ_s are divided by κ_T for comparison reason. As shown in Fig. 3, there is little difference between κ_f and κ_s for both $E_o/\eta=2\times10^{16}$ Pa/m and 2×10^{17} Pa/m. The κ_f and κ_s of $E_o/\eta=2\times10^{17}$ Pa/m are larger than those of 2×10^{16} Pa/m, respectively.

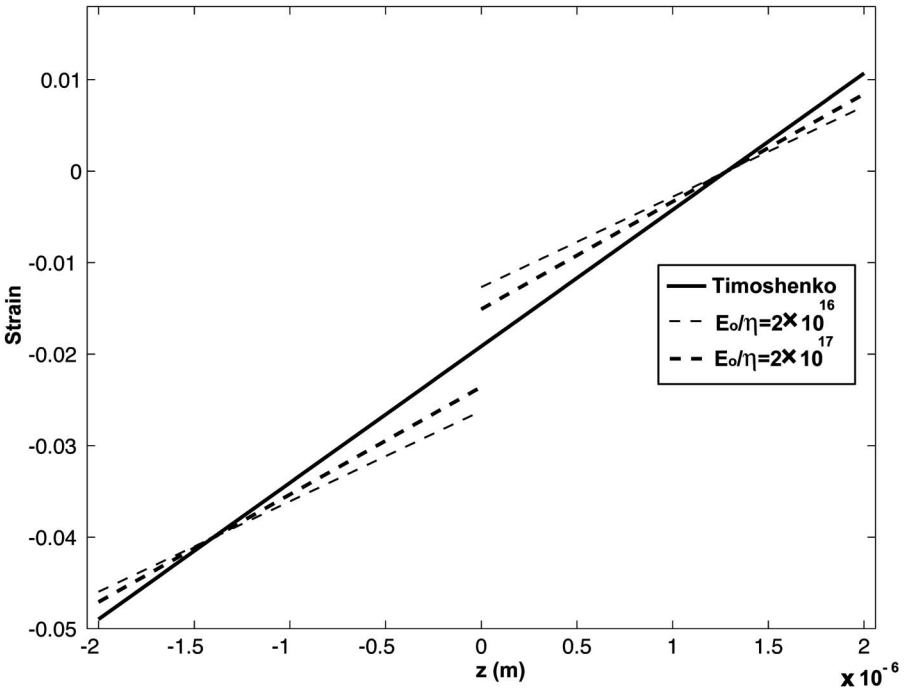

Fig. 5 The comparison of strains calculated by the Timoshenko model and S-L model with different E_o/ηs. t_1=2 μm, t_2=2 μm, and L=10 μm. The coordinate system is given in Fig. 2(*b*).

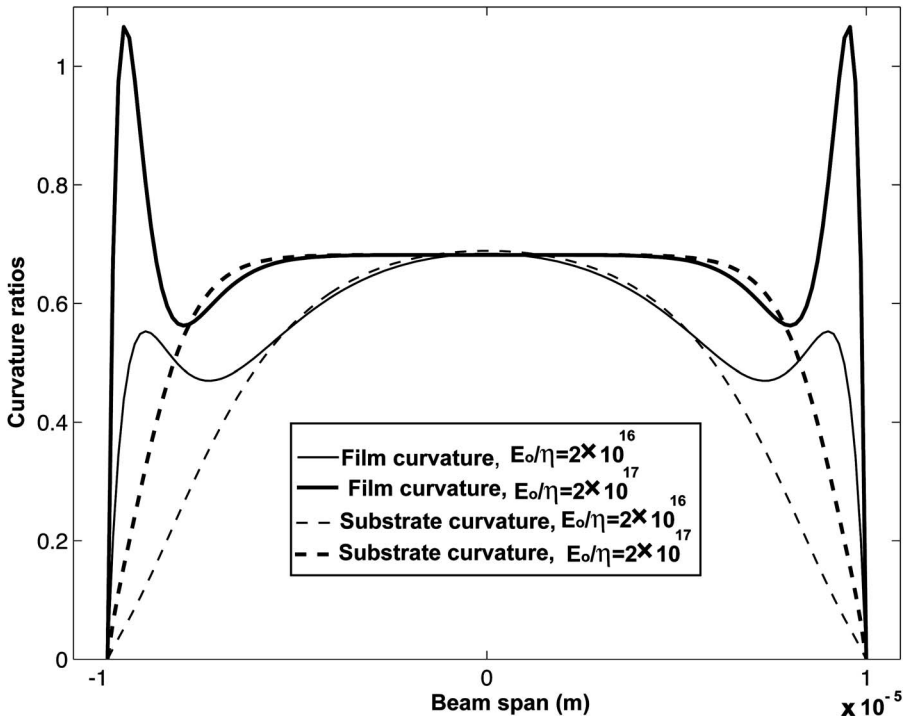

Fig. 6 The curvatures of film and substrate of the S-L model divided by κ_T. E_o/η is taken as 2×10^{16} Pa/m and 2×10^{17} Pa/m, respectively. $t_1=1$ μm, $t_2=3$ μm, $L=10$ μm, and $\kappa_T=9942$ m^{-1}.

The interface layer is less compliant with larger E_o/η. When E_o/η approaches infinity, it is the rigid interface of the Timoshenko model, which allows no interfacial slip. It is also noticed in Fig. 3 that the curvatures of the S-L model are nonuniform. Figure 4 examines how the interfacial slip can alter the constraint axial force. The dimensions in Fig. 4 are the same as those in Fig. 3. In the Timoshenko model, the constraint axial force per unit width in Eq. (12) is solved from the constraint condition of no interfacial slip as indicated in Eq. (11). The constraint force per unit width calculated from Eq. (12) is $P_{\text{timo}}=1268.1$ N m^{-1}. The constraint

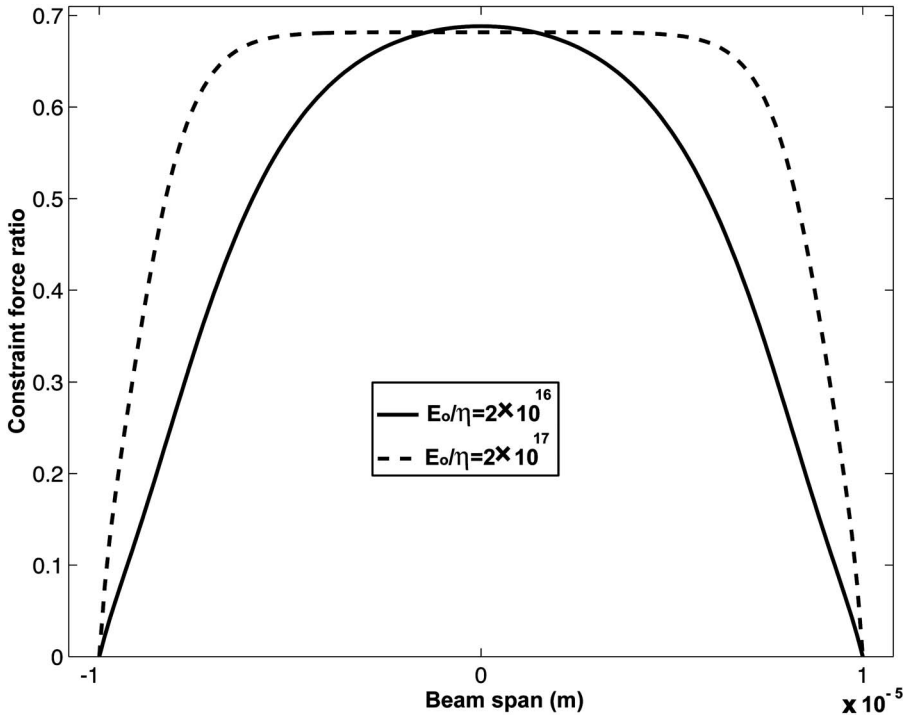

Fig. 7 The constraint forces per unit width of the S-L model with different E_o/ηs divided by that of the Timoshenko model ($P_{\text{timo}}=1721$ N m^{-1}). $t_1=1$ μm, $t_2=3$ μm, and $L=10$ μm.

axial force per unit width of the S-L model is $P(x)=\int_{-L}^{x}\tau_o dx$ [24]. In Fig. 4, $P(x)$ calculated for both $E_o/\eta=2\times10^{16}$ Pa/m and 2×10^{17} Pa/m is again divided by P_{timo} for comparison. Clearly, with the interfacial slip, the constraint force is smaller than that of the ideal interface case. It is also noticed that the constraint force of the S-L model varies with x and $E_o/\eta(G_o/\eta)$ with the fixed layers dimensions, while that of the Timoshenko model is a constant. Figure 5 shows the axial strains of the Timoshenko model and S-L model. The axial strain of the Timoshenko model is calculated from Eq. (8) and the S-L one is from Eq. (23). In Fig. 5, the strain of the Timoshenko model is continuous across the interface, which is also indicated by Eq. (11). The coordinate system in Fig. 5 as mentioned at the beginning of this section is the one shown in Fig. 2(*b*). The strains of the S-L models are discontinuous at the interface reflecting the fact of interfacial slip. The strain of $E_o/\eta=2\times10^{17}$ Pa/m is less "discontinuous" than that of $E_o/\eta=2\times10^{16}$ Pa/m. E_o/η as a fitting parameter physically indicates the effect of interfacial slip as reflected in Eq. (14). Larger E_o/η means smaller interfacial slip and for ideal interface $E_o/\eta=\infty$. As both the theoretical analysis and experiments show that the layers dimensions also have significant influence on the interfacial stresses (σ_o and τ_o) as those interfacial parameters (i.e., E_o, G_o, and η) [23,24], so the thickness of both the film and substrate is changed in Figs. 6 and 7 to show the effect of layer dimensions. In Figs. 6 and 7, $t_1=1$ μm, $t_2=3$ μm, and $L=10$ μm. For these dimensions, $\kappa_T=9942$ m^{-1} and $P_{\text{timo}}=1721$ N m^{-1}. The curvatures and constraint forces are also divided by these new κ_T and P_{timo}, respectively. In Fig. 6, the curvature difference between the film and substrate becomes significant around the free edges. The film curvatures of both $E_o/\eta=2\times10^{16}$ Pa/m and 2×10^{17} Pa/m in Figs. 6 experience much more dramatic variation around the free edges. The difference between κ_f and κ_s in both Figs. 3 and 6 is very little around the center. Compared with those in Fig. 4, the profiles of the film and substrate constraint forces in Fig. 7 do not have a dramatic change, just the gap (difference) around the bilayer center is smaller.

4 Concluding Remarks

The interfacial slip of non-ideal interface can significantly reduce the constraint force as compared with that of ideal interface. The curvature of the nonideal interface also varies with the structure length and differs from that of the ideal interface. Therefore, the evaluation of stress state inside the structure based on the measured curvature and the model of ideal interface can result in a serious error without properly evaluating the interface state. E_o/η and G_o/η are the fitting parameters in the S-L model to be varied to fit the experimental data. Once, the proper E_o/η and G_o/η are chosen, Eqs. (45) and (46) extend the Stoney's formula to the application of the composite with interfacial slip.

Acknowledgment

This work is supported by both the National Natural Science Foundation of China (NSFC, Grant No. 10502050) and the Scientific Research Foundation for the Returned Overseas Chinese Scholars, State Education Ministry of China.

References

[1] Hu, S. M., 1979, "Film-Edge-Induced Stress in Substrates," J. Appl. Phys., **50**, pp. 4661–4666.
[2] Hu, S. M., 1991, "Stress-Related Problems in Silicon Technology," J. Appl. Phys., **70**, pp. R53–R80.
[3] Chen, W. T., and Nelson, C. W., 1979, "Thermal Stress in Bonded Joints," IBM J. Res. Dev., **23**, pp. 179–188.
[4] Stoney, G. G., 1909, "The Tension of Metallic Films Deposited by Electrolysis," Proc. R. Soc. London, Ser. A, **82**, pp. 172–175.
[5] Zhang, Y., Ren, Q., and Zhao, Y., 2004, "Modelling Analysis of Surface Stress on a Rectangular Cantilever Beam," J. Phys. D, **37**, pp. 2140–2145.
[6] Freund, L. B., Floro, J. A., and Chason, E., 1999, "Extensions of the Stoney Formula for Substrate Curvature to Configurations With Thin Substrates or Large Deformation," Appl. Phys. Lett., **74**, pp. 1987–1989.
[7] Freund, L. B., and Suresh, S., 2003, *Thin Film Materials: Stress, Defect Formation and Surface Evolution*, Cambridge University Press, Cambridge, UK, Chaps. 2 and 6.
[8] Timoshenko, S., 1925, "Analysis of Bi-Metal Thermostats," J. Opt. Soc. Am., **11**, pp. 233–255.
[9] Brenner, A., and Senderoff, A., 1949, "Calculation of Stress in Electrodeposits From the Curvature of a Plate Strip," J. Res. Natl. Bur. Stand., **42**, pp. 105–123.
[10] Atkinson, A., 1995, "Macro-and Microstress Analysis in Sol-Gel Derived $Pb(Zr_xTi_{1-x})O_3$ Thin Films," Br. Ceram. Proc., **54**, pp. 1–7.
[11] Röll, K., 1976, "Analysis of Stress and Strain Distribution in Thin Films and Substrates," J. Appl. Phys., **47**, pp. 3224–3229.
[12] Hsueh, C. H., Lee, S., and Chuang, T. J., 2003, "An Alternative Method of Solving Multilayer Bending Problems," J. Appl. Mech., **70**, pp. 151–154.
[13] Blech, I. A., Blech, I., and Finot, M., 2005, "Determination of Thin-Film Stresses on Round Substrate," J. Appl. Phys., **97**, p. 113525.
[14] Huang, Y., and Rosakis, A. J., 2005, "Extension of Stoney's Formula to Non-Uniform Temperature Distributions in Thin Film/Substrate Systems. The Case of Radial Symmetry," J. Mech. Phys. Solids, **53**, pp. 2483–2500.
[15] Huang, S., and Zhang, X., 2006, "Extension of the Stoney Formula for Film-Substrate Systems With Gradient Stress for MEMS Applications," J. Micromech. Microeng., **16**, pp. 382–389.
[16] Zhang, Y., and Zhao, Y., 2006, "Applicability Range of Stoney's Formula and Modified Formulas for a Film/Substrate Bilayer," J. Appl. Phys., **99**, pp. 053513.
[17] Yang, F., and Li, J. C. M., 2003, "Diffusion-Induced Beam Bending in Hydrogen Sensors," J. Appl. Phys., **93**, pp. 9304–9309.
[18] Hu, Y. Y., and Huang, W. M., 2004, "Elastic and Elastic-Plastic Analysis of Multilayer Thin Films: Close-Form Solution," J. Appl. Phys., **96**, pp. 4154–4160.
[19] Wang, S. S., and Choi, I., 1982, "Boundary-Layer Effects in Composite Laminates," ASME J. Appl. Mech., **49**, pp. 541–548.
[20] Cammarata, R. C., Sieradzki, K., and Spaepen, F., 2000, "Simple Model for Interface Stresses With Application to Misfit Dislocation Generation in Epitaxial Thin Films," J. Appl. Phys., **87**, pp. 1227–1234.
[21] Suhir, E., 1986, "Stresses in Bi-Metal Thermostats," ASME J. Appl. Mech., **53**, pp. 657–660.
[22] Suhir, E., 1989, "Interfacial Stresses in Bi-Metal Thermostats," ASME J. Appl. Mech., **56**, pp. 595–600.
[23] Noyan, I. C., Murray, C. E., Chey, J. S., and Goldsmith, C. C., 2004, "Finite Size Effects in Stress Analysis of Interconnect Structures," Appl. Phys. Lett., **85**, pp. 724–726.
[24] Murray, C. E., and Noyan, I. C., 2002, "Finite Size Effects in Thin-Film Composites," Philos. Mag. A, **82**, pp. 3087–3117.
[25] Sagalowicz, L., Rudra, A., Kapon, E., Hammar, M., Salomonsson, F., Black, A., Jouneau, P. H., and Wipijewski, T., 2000, "Defects, Structure, and Chemistry of InP-GaAs Interfaces Obtained by Wafer Bonding," J. Appl. Phys., **87**, pp. 4135–4146.
[26] Liau, Z. L., 1997, "Strained Interface of Lattice-Mismatch Wafer Fusion," Phys. Rev. B, **55**, pp. 12899–12901.
[27] Zhang, X., Misra, A., Wang, H., Lima, A. L., Hundley, M. F., and Hoagland, R. G., 2005, "Effects of Deposition Parameters on Residual Stresses, Hardness and Electrical Resistivity of Nanoscale Twinned 330 Stainless Steel Thin Films," J. Appl. Phys., **97**, p. 094302.
[28] Jasinski, J., Liliental-Weber, Z., Estrada, S., and Hu, E., 2002, "Microstructure of GaAs/GaN Interfaces Produced by Direct Wafer Fusion," Appl. Phys. Lett., **81**, pp. 3152–3154.
[29] Shi, F., MacLaren, S., Xu, C., Cheng, K. Y., and Hsieh, K. C., 2003, "Hybrid-Integrated GaAs/GaAs and InP/GaAs Semiconductors Through Wafer Bonding Technology: Interface Adhesion and Mechanical Strength," J. Appl. Phys., **93**, pp. 5750–5756.
[30] Shi, F., Chang, K., Hsieh, K. C., Guido, L., and Hoke, B., 2004, "Interface Structure and Adhesion of Wafer-Bonded GaN/GaN and GaN/AlGaN Semiconductors," J. Appl. Phys., **95**, pp. 909–912.
[31] Okuno, Y., Uomi, K., Aoki, M., Taniwatari, T., Suzuki, M., and Kondow, M., 1995, "Anti-Phase Direct Bonding and its Application to the Fabrication of InP-Based 1.55 μm Wavelength Lasers on GaAs Substrates," Appl. Phys. Lett., **66**, pp. 451–453.
[32] Ru, C. Q., 2002, "Interfacial Thermal Stresses in Bimaterial Elastic Beams: Modified Beam Models Revisited," J. Electron. Packag., **124**, pp. 141–146.
[33] Benveniste, Y., 1984, "On the Effect of Debonding on the Overall Behavior of Composite Materials," Mech. Mater., **3**, pp. 349–358.
[34] Tullini, N., Savoia, M., and Horgan, C. O., 1997, "End Effects in the Multilayered Orthotropic Strips With Imperfect Bonding," Mech. Mater., **26**, pp. 23–34.
[35] Müller, P., and Saúl, A., 2004, "Elastic Effects on Surface Physics," Surf. Sci. Rep., **54**, pp. 157–258.
[36] Timoshenko, S. P., and Woinowsky-Krieger, S. P., 1959, *Theory of Plates and Shells*, 2nd ed., McGraw-Hill, New York.
[37] Huang, R., and Suo, Z., 2002, "Wrinkling of a Compressed Elastic Film on a Viscous Layer," J. Appl. Phys., **91**, pp. 1135–1142.
[38] Huang, R., and Suo, Z., 2002, "Instability of a Compressed Elastic Film on a Viscous Layer," Int. J. Solids Struct., **39**, pp. 1791–1802.

Temperature Rise in Polymeric Materials During High Rate Deformation

M. Garg

A. D. Mulliken

M. C. Boyce[1]
e-mail: mcboyce@mit.edu

Department of Mechanical Engineering,
Massachusetts Institute of Technology,
Cambridge, MA 02139-4307

Many polymeric materials undergo substantial plastic strain prior to failure. Much of this post yield deformation is dissipative and, at high strain rates, will result in a substantial temperature rise in the material. In this paper, an infrared (IR) detector system is constructed to measure the rise in temperature of a polymer during high strain rate compression testing. Temperature measurements were made using a high-speed mercury-cadmium-telluride (HgCdTe) single-element photovoltaic detector sensitive in the mid-infrared spectrum (6–12 μm), while mechanical deformation was accomplished in a split Hopkinson pressure bar (SHPB). Two representative polymers, an amorphous thermoplastic (polycarbonate (PC)) and a thermoset epoxy (EPON 862/W), were tested in uniaxial compression at strain rates greater than 1000 s^{-1} while simultaneously measuring the specimen temperature as a function of strain. For comparison purposes, analogous measurements were conducted on these materials tested at a strain rate of 0.5 s^{-1} on another test system. The data are further reduced to energy quantities revealing the dissipative versus storage character of the post yield work of deformation. The fraction of post yield work that is dissipative was found to be a strong function of strain for both polymers. Furthermore, a greater percentage of work is found to be dissipative at high rates of strain (>1000 s^{-1}) than at the lower rate of strain (0.5 s^{-1}) for both polymers; this is consistent with the need to overcome an additional energy barrier to yield at strain rates greater than 100 s^{-1} in these two polymers. The highly cross-linked thermoset polymer was found to store a greater percentage of the post yield work of deformation than the physically entangled thermoplastic. [DOI: 10.1115/1.2745388]

Keywords: split-Hopkinson, infrared, polymer, polycarbonate, epoxy, adiabatic

1 Introduction

[2]Polymers are increasingly used as integral component materials in products specifically designed to withstand high rates of loading. Applications span both commercial and military interests, ranging from protective shields for personnel and sensitive equipment, to windows and windshields for vehicles, or canopies for aircrafts and helicopters, see, e.g., [1]. During such loading events, many polymers are able to undergo substantial magnitudes of plastic strain prior to failure. Much of the post yield deformation is dissipative and, at high rates, will result in a significant temperature rise in the polymer. Depending on the temperature sensitivity of the mechanical behavior of the particular polymer, the temperature increase can result in substantive thermal softening of the polymer. While the post yield work in most metals is, to a large extent, dissipative in nature (e.g., [2]), a more complex situation exists for the case of polymeric materials. The mechanisms of yield and post yield deformation in polymers allow for significant energy storage to occur in addition to the dissipation (see, for instance [3–7]). The exact nature and evolution of the storage mechanisms are still subjects of investigation. Mechanical testing at very high rates of deformation provides adiabatic conditions and measurement of the temperature rise during high rate deformation provides data on the dissipative portion of the post yield work of deformation as a function of strain. Several investigators have made measurements of the temperature rise in a polymer during high rate compression testing in a SHPB using either thermocouples (e.g., [8,9]) or infrared measurement systems (e.g., [10–13]). However, the reported data are neither comprehensive nor consistent as evident in comparisons of measurements on the temperature rise in PC reported by different investigators. PC exhibits little variation in stress-strain behavior from one manufacturer to another, yet there is variability in the reported temperature measurement data; for example, Fig. 1 depicts data from three investigators where the Rittel [9] measurement used thermocouples, the Li and Lambros [12] and the Lerch et al. [13] measurements used IR systems. In this paper, we report on an IR-based experimental setup and procedure for measuring the temperature rise in polymeric samples during high rate deformation within a SHPB; the system builds directly on the previous work of other investigators in this area and adds refinements. The system is then utilized to measure the temperature rise in PC and in an epoxy (EPON 862/W) at strain rates greater than 1000 s^{-1} to true strains greater than 0.50; the data are then further reduced to energy quantities to understand the dissipative versus storage character of the post yield work of deformation.

2 Experimental Setup

The experimental apparatus used here consists of two parts: a split Hopkinson pressure bar (SHPB) for measuring the large deformation stress-strain behavior in uniaxial compression at strain rates of approximately 1000 s^{-1}, and an IR detector system for measuring surface temperature rise during deformation. A schematic of the experimental setup is shown in Fig. 2.

2.1 Split-Hopkinson Pressure Bar Setup. Uniaxial compression tests were performed on a SHPB test apparatus designed in cooperation with and built by Physics Applications, Inc., of Dayton, Ohio. The theory of SHPB testing has been well documented

[1]Corresponding author.

[2]Note that the dissipative versus stored aspects of work are also a topic of ongoing investigation even in the case of metals.

Contributed by the Applied Mechanics Division of ASME for publication in the JOURNAL OF APPLIED MECHANICS. Manuscript received September 18, 2006; final manuscript received February 16, 2007; published online January 11, 2008. Review conducted by Thomas W. Shield.

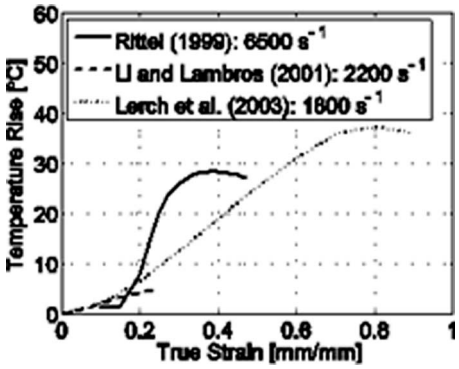

Fig. 1 Data on the temperature rise in polycarbonate during split Hopkinson bar compression as reported in the literature [9,12,13]

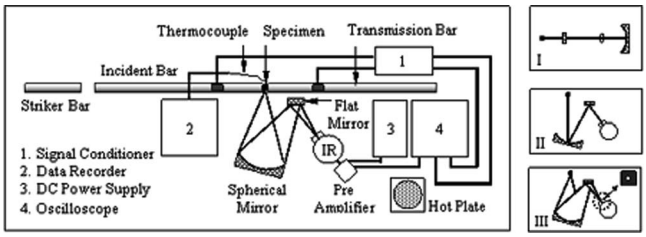

Fig. 2 Schematic of the IR calibration and test setup along with the SHPB apparatus (left). Schematics show alignment/focus procedures (right). I and II are vertical and rotational alignments with laser, respectively; III shows focusing with fiberoptic light.

(e.g., [14,15], and more recently [16]). In addition, issues unique to testing low-impedance, low yield strength materials are summarized in Chen et al. [17] and Gray and Blumenthal [18]. The particular apparatus used in this study consists of 19.0 mm diameter aluminum bars and is described in Mulliken and Boyce [19]. The polymer specimen dimensions were 6.0 mm in diameter and 3.4 mm in height. This geometry was chosen in an effort to keep the specimen height-to-diameter ratio close to 1:2,[3] and also to maximize the amount of radiation collected by the IR system. The specimens were lubricated and initially held in place by a small amount of petroleum jelly on the top and bottom surfaces; a high speed Cordin camera was used to verify the homogeneity of deformation during trial tests.

2.2 Infrared Imaging System Setup. As discussed in the Introduction, the temperature rise in polymers during SHPB compression testing has been measured by various researchers using thermocouples and IR detector techniques. Because of an order of magnitude difference in the SHPB test duration ($\sim$100 to $\sim$300 μs) and thermocouple response time (5–10 ms [20]), a high speed IR detector approach was preferred and adopted in this study.

2.2.1 Infrared Detector Assembly. Real time transient temperature measurements were performed using a high speed (response time $\sim$1 μs) IR radiation detector assembly. The assembly consists of a photovoltaic detector, preamplifier, dc power supply, and an oscilloscope. The photovoltaic detector consists of a single 250 μm$\times$250 μm HgCdTe element (Fermionics Corp., Simi Valley, CA) which is optimized for sensitivity in the mid-infrared spectrum (6–12 μm), corresponding to the range expected in our experiments. The detector is mounted behind a sapphire window and cooled to 77 K by filling the adjoining dewar with liquid nitrogen, which serves to minimize the electrical and thermal noise and maximizes the sensitivity of the detector. The signal from the photovoltaic element is further amplified through a dedicated low-noise, high-stability, rf dc-coupled preamplifier (Perry Amplifier, Brookline, MA), optimized in both gain and frequency input/output for the characteristics of the IR detector supplied. The preamplifier is powered by an Instek GPS-2303 multi-output regulated low-noise dc power supply. The power supply is configured to provide the necessary constant $\pm$12 V inputs to the preamplifier, while also preventing overload at excessive levels of current ($>$140 mA). Finally, the amplified signal is read into a Lecroy Waverunner® digital oscilloscope via high-impedance (1 MΩ) coupling.

[3]This particular aspect ratio helps to minimize wave attenuation in the wave signals while also negating the effects of radial and longitudinal inertia; see, for instance [17].

2.2.2 Imaging System. The imaging system used in the present study is a slight modification of that used by Zehnder and Rosakis [21], Hodowany et al. [22], and Li and Lambros [12]. In our system, the detector is stationary; a concave spherical mirror and a flat mirror focus the specimen radiation onto the detector, as shown in Fig. 2. The spherical mirror diameter and focal length are both 152 mm; the flat mirror has a diameter of 51 mm. Both mirrors are gold coated to enhance reflectivity ($\sim$97%) of the mid-infrared spectrum. The spherical mirror was placed 305 mm (radius of curvature) from the specimen surface; the flat mirror was placed at a distance of 178 mm from the spherical mirror. The detector was positioned 127 mm away from the flat mirror. The 305 mm gap was chosen to provide a 1:1 magnification of the image focused on the detector element.

The spherical mirror, the flat mirror, and the IR detector are mounted on stages which are adjustable in three mutually-perpendicular directions. In addition to translational degrees of freedom, both mirrors have rotational degrees of freedom about the horizontal and the vertical axes, parallel and perpendicular to the optical table, respectively.

2.2.3 Measurement and Data Reduction Issues

2.2.3.1 Radiation cone. The radiant flux E_{12} intercepted by the spherical mirror per unit area is given by $E_{12}=\varepsilon F_{12}\sigma T^4$, where ε, T, F_{12}, and σ are the emissivity, absolute temperature, shape factor, and Stephan-Boltzmann constant ($=5.67\times10^{-12}$ W/cm K^4), respectively. In order for E_{12} to be a function of temperature only, ε and F_{12} must be constants.

The emissivity is known to vary with the surface deformation and temperature of the specimen. Previous research on polycarbonate suggests that the effect of deformation on emissivity in this case is small [13,23], and the effect of T on ε is taken into account by calibration of the IR detector output prior to SHPB tests (e.g., [12,20]). To further suppress any changes and/or dependencies of ε, a thin layer of soot or black paint is often applied to the sample surface in order to provide an ε of $\sim$1 (e.g., [7,10,20]). However, unexpectedly, in this study, the use of black paint was found to be detrimental and actually degraded the temperature measurement as deformation progressed (see Appendix A); therefore, calibration and testing were conducted on uncoated specimens.

Next, the shape factor, F_{12}, must be determined. The shape factor is the fraction of radiation emitted from an area of the surface that gets intercepted by the mirror (and, in turn, reflected to the detector element). F_{12} depends on the geometry of the specimen, the SHPB apparatus, the mirror dimensions and the positioning of the mirror with respect to the specimen, as described in Appendix A. Depending on the particular test configuration and the strains imparted to the specimen, the cone of radiation picked up by the mirror can change with specimen deformation giving a shape factor that depends on strain. For our system, we have found this effect to be significant with F_{12} varying from approximately 0.06 at zero strain to 0.03 at an engineer-

ing strain of 0.5 (see Appendix A). To overcome the issues related to a dependence of F_{12} on strain, the spherical mirror is partially blocked using a nonreflective tape ($\varepsilon \sim 0.95$), during the calibration and the tests. This ensured that the effective area of the mirror collecting the radiation would be the same (shape factor ~ 0.03) during the calibration and over the entire duration of the test.

In addition, the transmission bar also displaces slightly during a test and, therefore, the incident bar blocks the focused point on the specimen surface at the later stages of the deformation; when this occurs, the effect on the temperature rise measurement is dramatic. However, providing an initial offset to the bar ensures that the IR detector is always focused on the specimen for the entire duration of the test and minimizes the effect. The optimal offset amount was found to be approximately one-half of the initial specimen height.

Other important factors that contribute to accurate temperature measurements using the IR system are the alignment/focusing of the imaging system and the calibration of the IR system. A similar approach as that used by others (e.g., [10,20,24,25]) was followed, performing alignment using visible light followed by calibration of the relationship between the IR measurement and the specimen temperature. The setup is detailed next.

2.2.3.2 Alignment and focus. For every test, the imaging system must be properly aligned and focused. Due to the very small element area ($250\ \mu m \times 250\ \mu m$), even slight misalignment or lack of focus causes the detector signal to severely diminish in magnitude. Though the entire optical setup is mounted on a vibration free optical table, the alignment and focusing steps must be repeated if a significant time has elapsed between tests and whenever a new material is examined.

Coarse alignment of the imaging system is accomplished with a HeNe diode laser that generates a focusable single line (Edmund Optics) when no specimen is in place. The laser is mounted behind the specimen location, located and aimed such that the beam passes through the center of the split Hopkinson bars. By adjusting the vertical degrees of freedom of the spherical mirror, flat mirror, and the IR detector, the laser beam is directed onto the center of the sapphire window located on the detector. This ensures that the system is properly aligned in the horizontal plane (see Fig. 2-I). Also, to ensure a 1:1 correspondence between the spot size on the specimen and the detector area, the locations of the components in the horizontal plane are adjusted such that the total optical path is approximately 610 mm.

For fine alignment, following [20], a mock specimen of black Teflon with a hole through the center (lateral surface) is placed between the incident and the transmission bars such that the through hole is aligned with the path of the laser beam in the horizontal plane. The beam exiting the specimen hole is adjusted to fall on the center of the spherical mirror, flat mirror, and finally on the IR detector by moving the bars (with the mock specimen in place) horizontally, or by fine adjustment of the translational degrees of freedom of the mirrors and the detector in the horizontal plane, see Fig. 2-II.

Finally, the alignment laser is replaced with a fiber optic light fitted with a focusing lens [10]. This light emits a conical beam (see Fig. 2-III), creating a silhouette image of the mock specimen on the outer face of the sapphire window. The sharpness of the image of the center hole is adjusted by moving the detector either forward or backward in the line of the projected image. Once the image of the center hole in the mock specimen is optimally focused on the face of the sapphire window, the housing is moved forward a known amount corresponding to the distance that the actual photovoltaic element is set back inside. Next, since the detector element can be seen behind the sapphire window with the help of the fiberoptic light, the laser beam through the hole is directed onto the center of the element by adjusting the horizontal tilt angles of the flat mirror. This ensures a complete fine alignment and focusing of a point on the specimen surface onto the detector element. A scriber is used to mark the center location of the specimen, initially aligned with the hole in the mock sample.

2.2.3.3 Calibration. For each set of tests on a material, calibration is required to relate the voltage change signal output from the IR detector assembly to the temperature change in the specimen. A schematic of the experimental setup configured for the calibration test is shown in Fig. 2. For calibration, another mock specimen is necessary, this time of identical material and geometry as the actual specimen to be tested. Here a *K*-type bare-wire thermocouple (Omega Engineering; CHAL-005) is embedded in the mock specimen on its lateral surface ~ 0.5 mm deep. The thermocouple is glued with a highly conductive room temperature epoxy (Omega Engineering). The mock specimen with embedded thermocouple is placed on a hot plate and heated below or close to T_g of the material so as not to deform the specimen. The temperature is monitored using an Omega RD8800 recorder which has a built-in cold-junction reference. Once at temperature near the T_g, the heated specimen is removed from the hot plate and quickly sandwiched between the SHPB at the aligned/focused position. As the specimen cools,[4] both the thermocouple temperature signal and the IR detector assembly signal (voltage) are recorded concurrently. Once the specimen reaches room temperature, the two data acquisition systems are stopped simultaneously. This calibration procedure is repeated 3–5 times. In the analysis of the calibration data, the IR signal and thermocouple temperature are aligned from their end points and plotted backwards, yielding a temperature rise versus voltage change curve. In the unlikely event of scattering among the various calibration curves, the curve which indicates the greatest voltage output by the detector for a given temperature rise is taken to be the most accurate. Calibration curves indicating an inferior voltage output for the same temperature rise correspond to imperfect placement of the calibration sample at the aligned/focused position.

3 Results and Discussion

The materials used in this study are Lexan® polycarbonate (a glassy thermoplastic; manufactured by GE plastics) and diglycidylbisphenol-F epoxy with curing agent W, type EPON 862/W (a thermoset; supplied by Wright Patterson Air Force Research Laboratory). Results are reported in terms of true stress versus true strain curves[5] and change in temperature versus true strain curves on tests conducted at strain rates of over 1000 s^{-1}. These data are further reduced to a set of post yield work W_{py}, stored energy U_{py}, and dissipated energy Q_{py} curves (all as a function of true strain). For comparison purposes, corresponding results are also presented for compression tests conducted on a servo-hydraulic Instron machine at a strain rate of 0.5 s^{-1} using the system and protocol similar to that reported in Arruda et al. [7] and briefly detailed in Appendix B for completeness.

3.1 Polycarbonate. Uniaxial compression true stress-true strain and temperature rise-true strain curves for PC at true strain rates of 3400 s^{-1} and 0.5 s^{-1} are shown in Fig. 3(*a*). For the high rate tests, three temperature curves are depicted to demonstrate the repeatability and reliability of the IR test system and protocol.

The true stress-strain results exhibit the characteristic features of polymer mechanical behavior including a rate-dependent yield

[4]Based on the finite element simulation and experimentation results of Macdougall [20] and Bjerke et al. [25], respectively, we assumed that heat is conducted through the highly conductive epoxy from the specimen to the thermocouple in an extremely short duration.

[5]For the high rate stress-strain data, dynamic equilibrium is reached just prior to the yield point; hence, the stress-strain curves are only valid after that point.

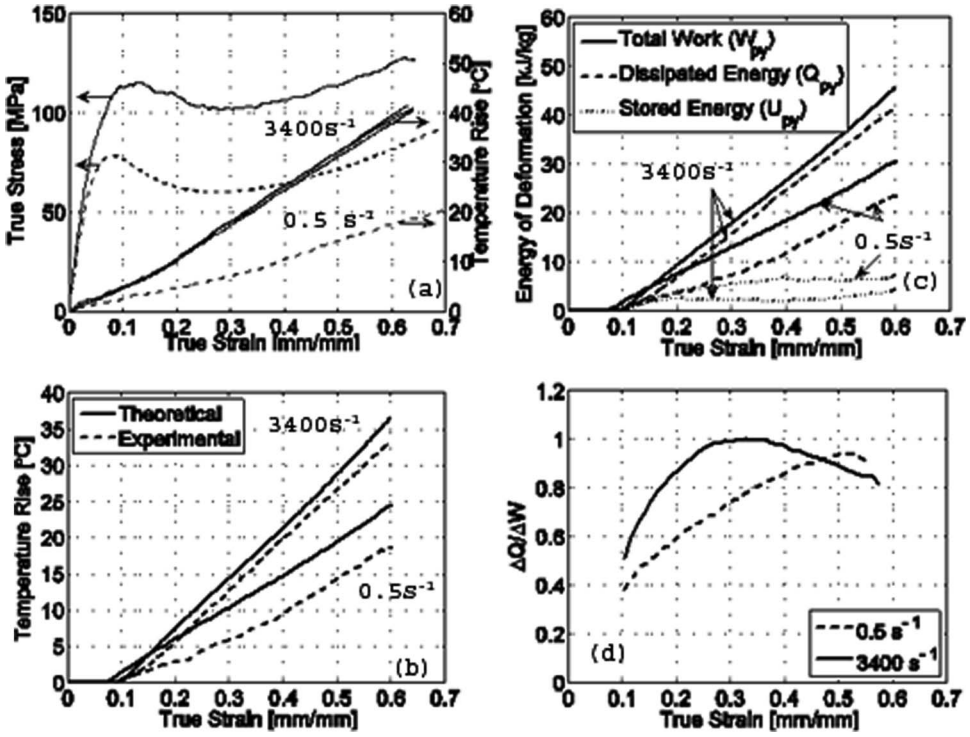

Fig. 3 (*a*) PC true-stress true-strain behavior and corresponding temperature rise under uniaxial compression at a true strain rate of 0.5 s^{-1} and 3400 s^{-1}. (*b*) Post-yield temperature rise as a function of true strain comparing experiment to an upper bound calculation which assumes 100% of the post-yield work to be dissipated for both the 0.5 s^{-1} and 3400 s^{-1} tests. (*c*) Post-yield work of deformation, dissipated energy (as computed based on the measured temperature rise) and stored energy; all as a function of true strain. (*d*) The fraction of incremental work dissipated (calculated over true strain increments of 0.01) as a function of true strain.

stress,[6] post-yield strain softening[7] up to moderate strains, followed by post-yield strain hardening. The corresponding temperature rise-strain curves exhibit a monotonic, nonlinear increase in temperature with increase in strain. At a strain of 0.60, the rise in temperature for the 3400 s^{-1} case is 39 °C compared with a rise of 20 °C for the 0.5 s^{-1} case. The higher temperature rise at 3400 s^{-1} is a reflection of the greater dissipation during deformation at the higher rate due to the dramatically higher yield stress (118 MPa) at 3400 s^{-1} compared to the yield stress (75 MPa) at 0.5 s^{-1} (note that the 0.5 s^{-1} conditions are nearly fully adiabatic). These data compare reasonably well with the Lerch et al. [13] data up to a strain of 0.65; note that the Lerch et al. [13] temperature results lie a little below those obtained here, but had been obtained at a slightly lower strain rate (1800 s^{-1}). We speculate that the plateauing of the temperature rise curve in the Lerch et al. [13] data (refer back to Fig. 1) after a strain of 0.70 is possibly due to either a reduction in the cone of radiation reflected at the larger strains and/or a calibration issue at the higher temperatures.

In order to better explore and understand the dissipative versus stored energy character of the post yield work of deformation, the stress-strain data and the temperature rise data are further reduced in two ways. First, the post yield work, W_{py}, as a function of strain is calculated (by integrating the stress-strain curve) and plotted in Fig. 3(*c*); W_{py} is then used to give an upper bound to the post yield temperature rise[8] as a function of strain in Fig. 3(*b*) where it is plotted together with the temperature data. Second, the measured temperature rise, ΔT, is used to calculate the dissipated energy via $Q_{py}=\rho c_p \Delta T$ as a function of strain and plotted in Fig. 3(*c*); the post yield stored energy U_{py} is then estimated by subtracting Q_{py} from W_{py} and also plotted in Fig. 3(*c*). For compression at a strain rate of 3400 s^{-1}, the stored energy curve reveals a significant level of energy storage after yield up to strains of 0.25; the energy storage then plateaus with a small monotonic increase beginning again at a strain of 0.45 (coinciding with the onset of significant strain hardening). Overall at this strain rate of 3400 s^{-1}, the post yield energy storage is quite small compared to the overall work of deformation as evidenced by the dissipation curve lying just beneath the work of deformation curve. To further identify the storage versus dissipative character of the work of deformation as a function of strain, we plot the ratio of the increment in dissipation over the increment in work, $\Delta Q_{py}/\Delta W_{py}$ (calculated over strain increments of 0.01) as a function of strain in Fig. 3(*d*). This clearly shows the significant storage character of post yield work up to a strain of 0.30, transitioning to nearly completely dissipative, then transitioning to exhibit additional storage at the highest strains.

For the case of deformation at a strain rate of 0.50 s^{-1}, the storage versus dissipative character of the work of deformation has a similar character as that observed at 3400 s^{-1}. However, a

[6]For experiments on the rate dependence of yield over a wide range in strain rate for PC, see for example [19,26,28–30]; [19,28,30] also present modeling of this rate dependence.

[7]We note that both the PC and the epoxy studied in this paper exhibit material strain softening under isothermal conditions (as observed in isothermal low rate compression tests which are not shown in this paper); the softening in the stress-strain curves in this paper contain contributions from both strain softening and from thermal softening.

[8]The upper bound to the temperature rise is computed via $\Delta T=W_{py}(\rho.c_p)$, where ρ is the material density and c_p is the specific heat at 25 °C; PC: $\rho=1200$ kg m^{-3}, $c_p=1250$ J kg^{-1} K^{-1}; Epon 862/W: $\rho=1005$ kg m^{-3}, $c_p=1500$ J kg^{-1} K^{-1}.

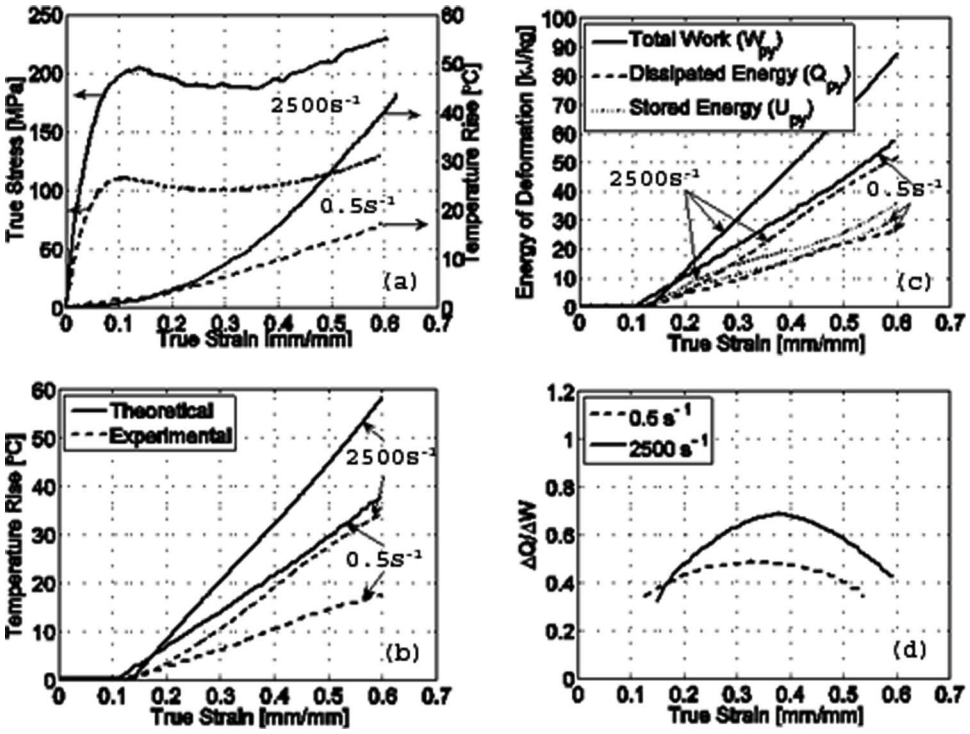

Fig. 4 (*a*) EPON 862/W true-stress true-strain behavior and corresponding temperature rise during uniaxial compression at a true strain rate of 0.5 s^{-1} and an average true strain rate of 2500 s^{-1}, respectively. (*b*) Comparison of temperature rise obtained experimentally and theoretically assuming 100% work is dissipated as thermal energy. (*c*) Post yield work of deformation, dissipated energy, and stored energy as a function of strain. (*d*) The fraction of incremental work dissipated (as calculated over true strain increments of 0.01) as a function of true strain.

significantly greater magnitude of energy is stored at 0.5 s^{-1} than at 3400 s^{-1}; this larger magnitude of energy storage combined with the smaller overall magnitude in work leads to a far greater percentage of work being stored during deformation at the 0.5 s^{-1} rate than the 3400 s^{-1} rate. The 0.50 s^{-1} data on energy storage versus dissipation are consistent with the deformation calorimetry data of Rudnev et al. [27] and Salamatina et al. [3]. These results regarding the different level of stored versus dissipated energy at the 3400 s^{-1} as compared to the 0.50 s^{-1} rates of deformation are also consistent with the transition in rate dependence of room temperature yield of PC as one transitions from strain rates less than 10 s^{-1} to rates greater than 100 s^{-1}, as discussed in Mulliken and Boyce [19,28,29] and Mulliken [30], where at the high rates an additional barrier to yield is encountered due to the need to activate local secondary molecular motions (β motions) in order to deform at high strain rates. The data of Fig. 3 show that this additional deformation mechanism encountered at the high strain rates is dissipative and also hinders the energy storage affiliated with the primary α motions of yield.

3.2 EPON 862/W Epoxy. A thermoset epoxy EPON 862/W was also tested at high (2500 s^{-1}) and moderate (0.5 s^{-1}) strain rates. The true stress versus true strain and the temperature rise versus true strain behaviors are shown in Fig. 4(*a*). Figures 4(*b*)–4(*d*) show the further reduction of these data into the corresponding upper bound to the temperature rise versus strain curve, the set of post-yield work curves, and the ratio of $\Delta Q_{py}/\Delta W_{py}$ versus strain curves. The tests were repeated at least three times at the same strain rate and the data were found to be consistent. The compressive stress-strain data exhibit the characteristic features of polymer stress-strain behavior as described earlier. The overall stress levels for this epoxy at the 0.50 s^{-1} and 2500 s^{-1} rates are observed to be greater than the corresponding levels in PC. The temperature rise is found to monotonically increase with strain in a nonlinear manner for both the 0.5 s^{-1} and the 2500 s^{-1} case. Despite the larger yield and post yield stress levels of the epoxy, the temperature rise magnitudes at any strain are comparable to the PC material.

The work related curves for EPON 862/W (Figs. 4(*c*) and 4(*d*)) reveal a greater percent of the post yield work of deformation to be stored in this epoxy when compared to the case of PC. This is consistent with the greater recovery of deformation upon unloading observed in this epoxy as compared to PC (see Table 1). We also note that the energy storage curves of 2500 s^{-1} and 0.5 s^{-1} are nearly coincident for this epoxy, suggesting that the energy storage mechanism in the epoxy is independent of strain rate. As in the PC material, the dramatic increase in strain rate at 2500 s^{-1} over that observed at 0.5 s^{-1} in this epoxy is found to be related to a need to activate local motions (tertiary γ motions for the case of EPON 862/W) at the high strain rates of deformation in order to yield the material [31] and are found here to be a dissipative event as evidenced by the increase in dissipation due to this increase in yield stress.

Table 1 Residual true strains after unloading from an imposed true strain of 0.62 (strain rate=0.5 s^{-1}) measured at different time periods after unloading

Material	$\varepsilon_{imposed}$	$\varepsilon_{unloaded}$ (t=0 s)	$\varepsilon_{unloaded}$ (t=15 min)	$\varepsilon_{unloaded}$ (t=1 h)
PC	0.62	0.49	0.49	0.49
EPON 862/W	0.62	0.40	0.38	0.38

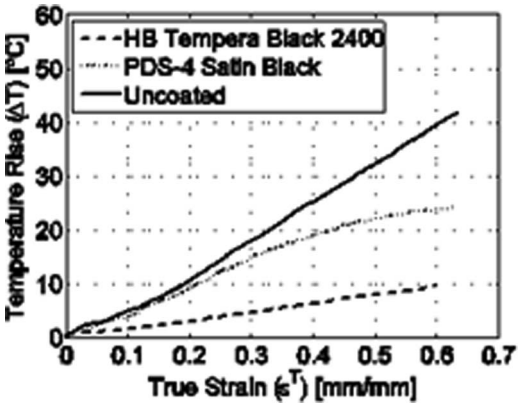

Fig. 5 Typical temperature rise curves showing the effect of black paint for the case of PC at strain rate of 3400 s^{-1}

4 Conclusions

A refined high-speed photovoltaic detector approach has been developed which is capable of measuring specimen surface temperature during high rate deformation within a split Hopkinson pressure bar. The IR detector was used to measure surface temperature during homogeneous uniaxial compression at true strain rates greater than 1000 s^{-1} in polycarbonate (PC) and EPON 862/W epoxy. The experimental data were validated by checking for repeatability, by comparing the data with quasistatic compression tests, and by comparing the data with the theoretical estimates of temperature rise as a function of strain. The data are further reduced to energy quantities revealing the dissipative versus storage character of the post yield work of deformation. The fraction of post yield work that is dissipative was found to be a strong function of strain for both polymers consistent with earlier deformation calorimetry data to moderate strains, for example [3,27]. Furthermore, a greater percentage of work is found to be dissipative at high rates of strain (>1000 s^{-1}) than at the lower rate of strain (0.5 s^{-1}) for both polymers; this is consistent with the need to overcome an additional energy barrier to yield at strain rates greater than 100 s^{-1} in these two polymers [19,28,31]. Although the various features of the compressive true stress-strain behavior in polycarbonate and EPON 862/W are similar, the highly cross-linked thermoset EPON 862/W was found to store a greater percentage of the post yield work of deformation than the physically entangled thermoplastic PC (consistent with the greater recovery of strain upon unloading observed in the EPON 862/W compared to that found in the PC). The measurement of temperature rise as a function of inelastic strain under adiabatic conditions provides important information to not only understand thermal softening issues in polymers, but also dissipative versus storage aspects of the post yield work of deformation which can guide constitutive model developments.

Acknowledgments

This research was funded by the AFOSR DURINT on Microstructure, Processing and Mechanical Performance of Polymer Nanocomposites (F49620-01-1-0447) and, in part, by the Office of Naval Research (N00014-04-10469). We acknowledge Dr. Sai Sarva for valuable discussions and assistance in the experimentation work. We also acknowledge the contributions of Dr. Jin Yi and Dr. Todd Bjerke during the initial phases of the setup of the infrared instrumentation.

Appendix A: Imaging System Issues

Surface Coating Issues. The use of a black coating to provide an emissivity of ~1.0 during infrared measurement was found to be unreliable during our very high rate tests. A comparison of calibrated temperature measurement as a function of axial strain on three specimens, one without and two with different types of black paint, are shown in Fig. 5; the cases with black paint, show a clear degradation in ability to measure the temperature as the strain increases. Therefore, we chose not to use any coating during high rate testing and, instead, to calibrate uncoated samples prior to each set of tests on a given material.

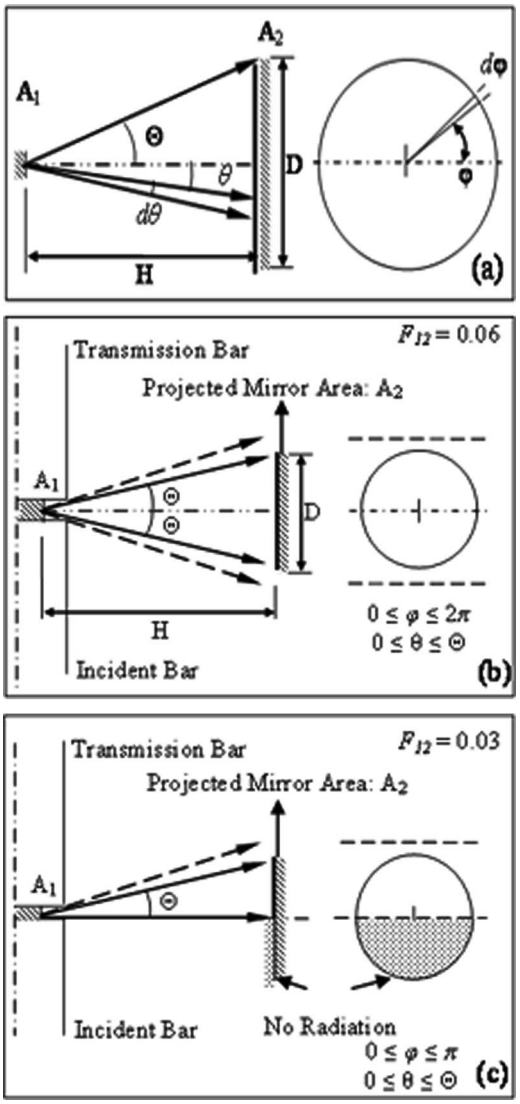

Fig. 6 Schematic in (*a*) shows the parameters used in estimating the shape factor; (*b*) shows the schematic of the initial setup before the specimen deforms and the corresponding cone of view; and (*c*) shows the setup once the specimen is subjected to 0.5 engineering strain during the test and the corresponding cone of view

IR Shape Factor. The shape factor, F_{12}, for use in relating the temperature to the radiation is defined as the fraction of radiation leaving an elemental surface of area A_1 that gets intercepted by the surface of area A_2. An estimate of F_{12} for the case of two parallel surfaces of area A_1 and A_2 (see Fig. 5(*a*)) separated by a distance H is given below, where the second surface is a disk of diameter D, and the elemental surface is small ($A_1 \ll A_2$) [32]. In the case of the imaging system used here, the area A_1 is on the surface of the specimen, and A_2 is the projected area of the spherical mirror, perpendicular to the line connecting A_1 and A_2 (see Fig. 6(*b*)).

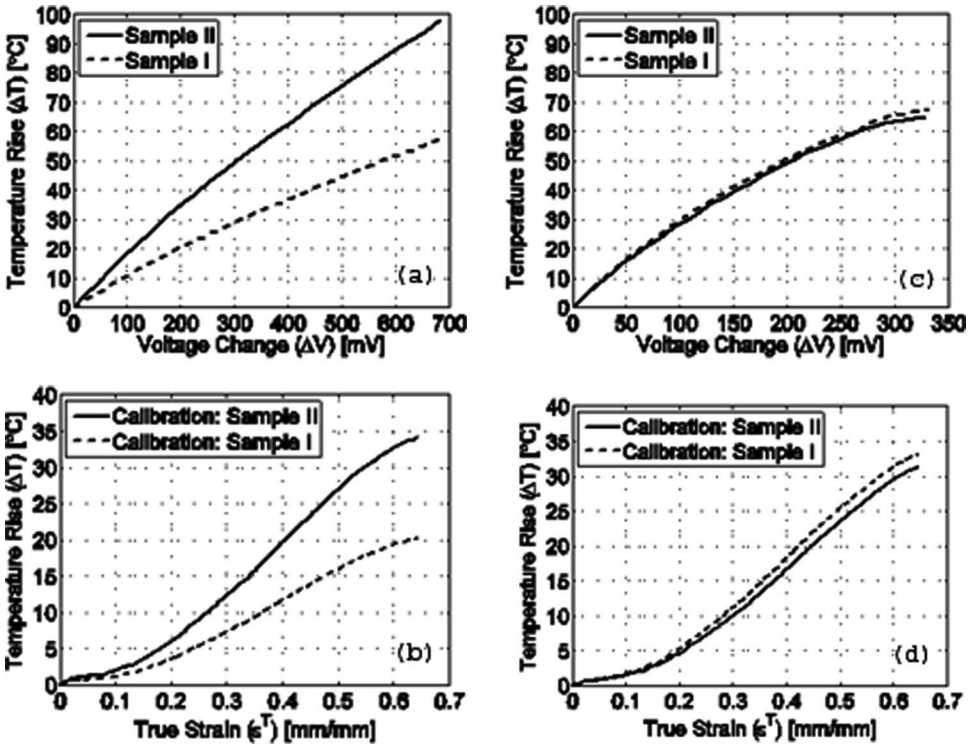

Fig. 7 Typical calibration curves (left) and corresponding temperature rise versus axial strain curves (right) showing the effect of shape factor on temperature measurements for epoxy samples compressed at a strain rate of 2500 s^{-1} before (*a*) and after partially (*b*) blocking the spherical mirror. Black paint was not applied to specimens (for case (*a*): the sample I F_{12} ~0.06; and the sample II F_{12}~0.03).

$$F_{12} = \frac{1}{\pi}\int_{\omega_{12}} \cos\theta d\omega = \frac{1}{\pi}\int_0^{2\pi}\int_0^{\Theta} \cos\theta \sin\theta d\theta d\phi = \sin^2\Theta = \frac{D^2}{D^2+4H^2} \tag{A1}$$

where

$$d\omega = \sin\theta d\theta d\phi \tag{A2}$$

In Eqs. (A1) and (A2), $d\omega$ is the differential solid angle subtended by elemental area dA_2 at an elemental area dA_1 and φ, θ, and Θ are the azimuthal angle, zenith angle, and the half of the angle subtended by the projected area A_2 at A_1, respectively. Substituting $D=152$ mm (spherical mirror diameter) and $H=305$ mm (radius of curvature of the mirror, or the distance of the mirror from the sample) in Eq. (A1), we get $F_{12}\approx 0.06$. Figure 6(*b*) shows at zero strain in the specimen, φ varies between 0 and 2π, which gives $F_{12}=0.06$, while Fig. 6(*c*) shows that at 0.5 engineering strain, φ varies between 0 and π, thus reducing the area of the mirror utilized to collect radiation by half, which gives $F_{12}=0.03$. Clearly, the schematics in Figs. 6(*b*) and 6(*c*) show how F_{12} varies between 0.03 and 0.06 as ($\pi \leqslant \varphi \leqslant 2\pi$) while the test is in progress.

To illustrate this effect further, Figs. 7(*a*) and 7(*b*) show the calibration curve obtained assuming $F_{12}\sim 0.06$ as compared to that using $F_{12}\sim 0.03$ and the effect of these two different calibration curves on the "measured" temperature rise as a function of strain. A calibration sample having diameter of 6.0 mm and height of 3.4 mm corresponded to the shape factor of 0.06 (sample I in Fig. 7(*a*)), while another calibration sample having diameter of 6.0 mm and height of 1.7 mm corresponded to the shape factor of 0.03 (sample II in Fig. 7(*a*)). To overcome the issues related to a dependence in shape factor on strain, the spherical mirror is partially blocked using a nonreflective tape ($\varepsilon\sim 0.95$), during the calibration and the tests. This ensured that the effective area of the mirror collecting the radiation would be the same (shape factor ~0.03) during the calibration and over the entire duration of the test. Figures 7(*c*) and 7(*d*) show how the taping of the spherical mirror results in a shape factor that does not depend on deformation. Partially blocking the mirror also results in lowering the amount of radiation collected which is directly proportional to the current produced by the IR detector; this is evident from voltage change values in the calibration curves of Figs. 7(*a*) and 7(*c*).

Note that in Fig. 6(*c*), the incident bar blocks the focal point on the specimen beyond 0.5 engineering strain (true strain of 0.69), which makes the temperature measurement beyond that point unreliable.

Appendix B: Brief Description of the Quasi-Static Mechanical Test and IR System

Quasi-static uniaxial compression tests ($0.5\ s^{-1}$) at ambient temperature were conducted on an Instron 1350 servo-hydraulic axial mechanical tester. The Instron actuator displacement was controlled to provide a constant true strain rate loading condition via a feedback loop using information from the extensometer to prescribe the motion of the actuator. The compression platens were designed to have a truncated conical shape where the conical feature ensures no blockage of radiation during deformation. Thin Teflon films were placed between specimen and the compression platens to achieve global homogeneous deformations. WD-40 lubricant was sprayed between Teflon films and platens to further enhance the homogeneous deformation. PC and epoxy specimens were machined as cubes with sides of 10.0 mm and 5.0 mm, respectively. These sample sizes provide nearly adiabatic conditions at a strain rate of $0.5\ s^{-1}$. All samples were painted with a black

acrylic spray paint[9] ($\varepsilon \sim 0.95$) an hour before the tests and were subjected to a maximum true strain of -0.62. During the test, true-stress and true-strain quantities were calculated from the load cell and extensometer output, respectively, while simultaneously specimen surface temperature was calculated directly by a Mikron MI-N5-H+Infraducer® with a spectral response range between 8 and 14 μm. This precalibrated infrared detector provides accurate temperature measurements based upon an input surface emissivity. The specimen was coated with black paint to maintain a constant emissivity with deformation (the integrity of the black coating with strain was found to be robust for these low deformation rates). The minimum spot size for this detector, achieved by placing the detector exactly 120 mm from the specimen, is 2.4 mm. The response time is 10 ms, and the accuracy is 0.6% of the measured value.

References

[1] Sands, J. M., Patel, P. J., Dehmer, P. G., Hsieh, A. J., and Boyce, M. C., 2004, "Protecting the Future Force: Transparent Materials Safeguard the Army's Vision," Advanced Materials and Processes Technology Information Analysis Center Quarterly, **8**(4), pp. 28–36.

[2] Bever, M. B., Holt, D. L., and Titchener, A. L., 1973, "The Stored Energy of Cold Work," *Progress in Materials Science*, Vol. 17, B. Chalmers, J. W. Christian, and T. B. Massalski, eds., Pergamon, New York, pp. 5–88.

[3] Salamatina, O., Rudnev, S., Voenniy, V., and Oleynik, E., 1992, "Heat and Stored Energy of Plastic Deformation of Solid Polymers and Heterogeneous Blends," J. Therm. Anal., **38**, pp. 1271–1281.

[4] Adams, G., and Farris, R., 1988, "Latent Energy of Deformation of Bisphenol A Polycarbonate," J. Polym. Sci., Part B: Polym. Phys., **26**, pp. 433–445.

[5] Chang, B., and Li, J., 1988, "Stored Energy of Cold Work in Polystyrene," Polym. Eng. Sci., **28**, pp. 1198–1202.

[6] Hasan, O. A., and Boyce, M. C., 1993, "Energy Storage During Inelastic Deformation of Glassy Polymers," Polymer, **34**, pp. 5085–5092.

[7] Arruda, E., Boyce, M. C., and Jayachandran, R., 1995, "Effects of Strain Rate, Temperature, and Thermomechanical Coupling on the Finite Strain Deformation of Glassy Polymers," Mech. Mater., **19**, pp. 193–212.

[8] Chou, S. C., Robertson, K. D., and Rainey, J. H., 1973, "The Effect of Strain rate and Heat Developed During Deformation on the Stress-Strain Curve of Plastics," Exp. Mech., **13**(3), pp. 422–432.

[9] Rittel, D., 1999, "On the Conversion of Plastic Work to Heat During High Strain Rate Deformation of Glassy Polymers," Mech. Mater., **31**, pp. 131–139.

[10] Trojanowski, A., Macdougall, D., and Harding, J., 1998, "An Improved Technique for the Experimental Measurement of Specimen Surface Temperature During Hopkinson-Bar Tests," Meas. Sci. Technol., **9**, pp. 12–19.

[11] Buckley, C. P., Harding, J., Hou, J. P., Ruiz, C., and Trojanowski, A., 2001, "Deformation of Thermosetting Resins at Impact Rates of Strain. Part I: Experimental Study," J. Mech. Phys. Solids, **49**, pp. 1517–1538.

[9]Unlike high rate tests, black paint coating was not observed to degrade at low rate tests.

[12] Li, Z., and Lambros, J., 2001, "Strain Rate Effects on the Thermomechanical Behavior of Polymers," Int. J. Solids Struct., **38**, pp. 3549–3562.

[13] Lerch, V., Gary, G., and Herve, P., 2003, "Thermomechanical Properties of Polycarbonate Under Dynamic Loading," J. Phys. IV, **110**, pp. 159–164.

[14] Davies, E., 1948, "A Critical Study of the Hopkinson Pressure Bar," Philos. Trans. R. Soc. London, Ser. A, **240**, pp. 375–457.

[15] Kolsky, H., 1949, "An Investigation Into the Mechanical Properties of Materials at Very High Rates of Loading," Proc. Phys. Soc. London, Sect. B, **62**, pp. 676–701.

[16] Gray III, G., 2000, "Classic Split-Hopkinson Bar Testing," *ASM Handbook*, Vol. 8, 12th ed., American Society for Metals, pp. 462–476.

[17] Chen, W., Zhang, B., and Forrestal, M., 1999, "A Split-Hopkinson Bar Technique for Low-Impedance Materials," Exp. Mech., **39**, pp. 81–85.

[18] Gray III, G., and Bluementhal, W., 2000, "Split-Hopkinson Pressure Bar Testing of Soft Materials," *ASM Handbook*, Vol. 8, 12th ed., American Society for Metals, pp. 488–496.

[19] Mulliken, A. D., and Boyce, M. C., 2006(a), "Mechanics of the Rate-Dependent Elastic-Plastic Deformation of Glassy Polymers From Low to High Strain Rates," Int. J. Solids Struct., **43**(5), pp. 1331–1356.

[20] Macdougall, D., 2000, "Determination of the Plastic Work Converted to Heat Using Radiometry," Exp. Mech., **40**(3), pp. 298–306.

[21] Zehnder, A. T., and Rosakis, A. J., 1991, "On the Temperature Distribution at the Vicinity of Dynamically Propagating Cracks in 4340 Steel," J. Mech. Phys. Solids, **39**(3), pp. 385–415.

[22] Hodowany, J., Ravichandran, G., Rosakis, A. J., and Rasakis, P., 2000, "Partition of Plastic Work Into Heat and Stored Energy in Metals," Exp. Mech., **40**(2), pp. 113–123.

[23] Bjerke, T., Li, Z., and Lambros, J., 2002, "Role of Plasticity in Heat Generation During High Rate Deformation and Fracture of Polycarbonate," Int. J. Plast., **18**, pp. 549–567.

[24] Kapoor, R., and Nemat-Nasser, N. S., 1998, "Determination of Temperature Rise During High Strain Rate Deformation," Mech. Mater., **27**, pp. 1–12.

[25] Bjerke, T., Li, Z., and Lambros, J., 2002, "Role of Plasticity in Heat Generation During High Rate Deformation and Fracture of Polycarbonate," Int. J. Plast., **18**, pp. 549–567.

[26] Moy, P., Weerasooriya, T., Hsieh, A., and Chen, W., 2003, "Strain Rate Response of a Polycarbonate Under Uniaxial Compression," *Proceedings of the SEM Annual Conference on Experimental Mechanics*, Society for Experimental Mechanics, Inc.

[27] Rudnev, S., Salamatina, O., Voenniy, V., and Oleynik, E., 1991, "Plastic Deformation Kinetics for Glassy Polymers and Blends," Colloid Polym. Sci., **269**, pp. 460–468.

[28] Mulliken, A. D., and Boyce, M. C., 2004, "Low to High Strain Rate Deformation of Amorphous Polymers," *Proceedings SEM X International Congress and Exposition on Experimental and Applied Mechanics*, Costa Mesa CA, 2004 (Society for Experimental Mechanics, Inc., 2004) Paper No. 197.

[29] Mulliken, A. D., Soong, S. Y., Boyce, M. C., and Cohen, R. E., 2006, "High-Rate Thermomechanical Behavior of Poly(Vinyl Chloride) and Plasticized Poly(Vinyl Chloride)," J. Phys. IV, **134**, pp. 217–223.

[30] Mulliken, A. D., 2006, "Mechanics of Amorphous Polymers and Polymer Nanocomposites During High Rate Deformation," Ph.D. thesis, Massachusetts Institute of Technology, Cambridge, MA.

[31] Garg, M., Boyce, M. C., and Cohen, R. E., 2007, "Rate Dependent Mechanical Behavior of Epon 862/W Epoxy and Epon 862/W-Nanoclay Nanocomposites," in preparation.

[32] Mills, A. F., 1999, *Heat Transfer*, 2nd ed., Prentice-Hall, NJ.

Solution for a Semi-Permeable Interface Crack in Elastic Dielectric/Piezoelectric Bimaterials

Q. Li

Y. H. Chen[1]
e-mail: yhchen2@mail.xjtu.edu.cn

School of Aerospace,
MOE Laboratory,
Xian Jiao-Tong University,
Xian, Shanxi 710049, P.R.C.

A semi-permeable interface crack in infinite elastic dielectric/piezoelectric bimaterials under combined electric and mechanical loading is studied by using the Stroh complex variable theory. Attention is focused on the influence induced from the permittivity of the medium inside the crack gap on the near-tip singularity and on the energy release rate (ERR). Thirty five kinds of such bimaterials are considered, which are constructed by five kinds of elastic dielectrics and seven kinds of piezoelectrics, respectively. Numerical results for the interface crack tip singularities are calculated. We demonstrate that, whatever the dielectric phase is much softer or much harder than the piezoelectric phase, the structure of the singular field near the semi-permeable interface crack tip in such bimaterials always consists of the singularity $r^{-1/2}$ *and a pair of oscillatory singularities* $r^{-1/2\pm i\varepsilon}$*. Calculated values of the oscillatory index* ε *for the 35 kinds of bimaterials are presented in tables, which are always within the range between 0.046 and 0.088. Energy analyses for five kinds of such bimaterials constructed by PZT-4 and the five kinds of elastic dielectrics are studied in more detail under four different cases: (i) the crack is electrically conducting, (ii) the crack gap is filled with air/vacuum, (iii) the crack gap is filled with silicon oil, and (iv) the crack is electrically impermeable. Detailed comparisons on the variable tendencies of the crack tip ERR against the applied electric field are given under some practical electromechanical loading levels. We conclude that the different values of the permittivity have no influence on the crack tip singularity but have significant influences on the crack tip ERR. We also conclude that the previous investigations under the impermeable crack model are incorrect since the results of the ERR for the impermeable crack show significant discrepancies from those for the semi-permeable crack, whereas the previous investigations under the conducting crack model may be accepted in a tolerant way since the results of the ERR show very small discrepancies from those for the semi-permeable crack, especially when the crack gap is filled with silicon oil. In all cases under consideration the curves of the ERR for silicon oil are more likely tending to those for the conducting crack rather than to those for air or vacuum. Finally, we conclude that the variable tendencies of the ERR against the applied electric field have an interesting load-dependent feature when the applied mechanical loading increases. This feature is due to the nonlinear relation between the normal electric displacement component and the applied electromechanical loadings from a quadratic equation.* [DOI: 10.1115/1.2745397]

Keywords: interface crack, elastic dielectric, piezoelectric, permittivity, the crack tip ERR, oscillatory singularity

1 Introduction

Manmade functional materials such as multiplayer piezoelectric ceramics, piezoelectric composites, and elastic dielectric/piezoelectric composites with enhanced electromechanical coupling properties have been developed in recent years. They combine strong piezoelectric ceramics with other compliant dielectrics (e.g., epoxy or polymer). These smart composites, e.g., PZT/polymer composites, have become attractive candidates for use in transducers and actuators for vibration control and and biomedical imaging applications. On the one hand, a basic theoretical framework for the design of piezocomposites with prescribed overall properties has been developed (see, e.g., [1–3] among many others) and a number of efforts have been carried out for interface cracks in dissimilar piezoelectric materials (see, e.g., [4–20] among many others). However, when an elastic dielectric and a piezoelectric material are bonded together along their interface, a high in-layer stress-electric field may produce on the interface due to the mechanical and electric mismatch properties of the two different kinds of materials. Interface cracking, sometimes called delamination or interlaminar cracking, as commonly seen in fiber reinforced composite laminates, should be considered as one of the most common failure type in elastic dielectric/piezoelectric composites. On the other hand, to the present authors' knowledge, a few of the analytical solutions for the interface crack problems in elastic dielectric/piezoelectric bimaterials were presented in the literature. It is noticed that such bimaterials should have two kinds of material mismatch properties along interface: the electric mismatch properties and the mechanical mismatch properties, although both of them should be coupled in the constitutive equations of piezoelectric materials. For example, their piezoelectric

[1]Corresponding author.

Contributed by the Applied Mechanics Division of ASME for publication in the JOURNAL OF APPLIED MECHANICS. Manuscript received October 30, 2006; final manuscript received February 4, 2007; published online January 11, 2008. Review conducted by Zhigang Suo.

phase has strong piezoelectricity and large permittivity (about 1000 times larger than air/vacuum), whereas their dielectric phase has a tiny piezoelectricity and much smaller permittivity (only about 4–10 times larger than air/vacuum). Moreover, such bimaterials should also have much stronger mechanical mismatch properties on interfaces than those for classical two-phase piezoelectric materials because the dielectric phase may be much softer (e.g., epoxy or polymer) or much harder (e.g., SiC or Al_2O_3) than the piezoelectric phase, whereas the differences in elastic moduli, piezoelectricity, and permittivity of two dissimilar piezoelectric materials, say, e.g., PZT-4/PZT-5H, are always relatively small. Recently, Ou and Chen [21] analyzed the interface crack problem in elastic dielectric/piezoelectric bimaterials based on the extended Stroh complex potential theory developed by Suo et al. [5]. However, their investigation was based on the electrically impermeable condition on the interface crack surfaces. As pointed out by many researchers in studying homogenous piezoelectric materials with cracks, this condition is physically incorrect and misleading (see, e.g., McMeeking [22–24]), whereas the electric boundary condition proposed by Parton and Kudryavtsev [25] and Hao and Shen [26] (called the semi-permeable crack or abbreviated as the PKHS crack) is more reasonable (see, e.g., [22–24,27–29] among many others). Therefore, the permittivity of the medium (e.g., air or vacuum, silicon oil, and NaCI solution, etc.) inside the interface crack gap in such bimaterials should receive special attention to clarify its influence on the crack tip singularity and the ERR in turn on the interface crack stability.

This paper has two goals. The first is to obtain an analytical solution accounting for the permittivity of the medium inside an interface crack gap in elastic dielectric/piezoelectric bimaterials and to study the influence of the permittivity on the crack tip singularity. The second is to provide some rich numerical results for the influence of different permittivties on the crack tip ERR under some practical loading levels. For convenience to use the Stroh theory (Suo et al. [5]), the elastic dielectric material with some permittivity is treated as a special transversely isotropic piezoelectric material with a tiny piezoelectricity and the distribution of the normal electric displacement component (NEDC) along the crack is assumed to be uniform as Xu and Rajapakse [29] did in homogeneous piezoelectrics. Thus, the problem can be deduced to a Hilbert problem. After obtaining the solution for the semi-permeable interface crack in infinite elastic dielectric/piezoelectric bimaterials, we present rich numerical results for the singular analysis at the interface crack tip for 35 types of such bimaterials constructed by the following five kinds of elastic dielectric materials: epoxy, polymer, Al_2O_3, SiC, and Si_3N_4 and by the following seven kinds of commercial piezoelectric ceramics: PZT-4, $BaTiO_3$, PZT-5H, PZT-6B, PZT-7A, P-7, and PZT-PIC 151, respectively. These results show that, unlike those for the impermeable crack model in dissimilar piezoelectric materials [17,18] which may either show oscillatory or show nonoscillatory singularities, the structure of the singular field near the semi-permeable interface crack tip in the present bimaterials always consists of the inverse square root singularity $r^{-1/2}$ and a pair of oscillatory singularities $r^{-1/2\pm i\varepsilon}$, which are similar to those in dissimilar elastic anisotropic materials and also similar to those of Beom and Atluri [15] or Beom [16] for a conducting or permeable interface crack between dissimilar piezoelectric ceramics. Calculated values of the oscillatory index ε for the 35 kinds of bimaterials are presented, which fall to the range between 0.046 and 0.088, whereas most of them are around 0.06 always much larger than those in 7 kinds of the ε class dissimilar piezoelectric materials reported by Ou [17]. Detailed comparisons and discussions on the crack tip ERR are performed by considering four different values of the permittivity of medium inside the interface crack gap: (i) the crack is electrically conducting (e.g., the gap filled with NaCI solution as did by Heyer et al. [30]), (ii) the gap filled with air/vacuum, (iii) the gap filled with silicon oil as did by Park and Sun [31,32], and (iv) the crack is electrically impermeable,

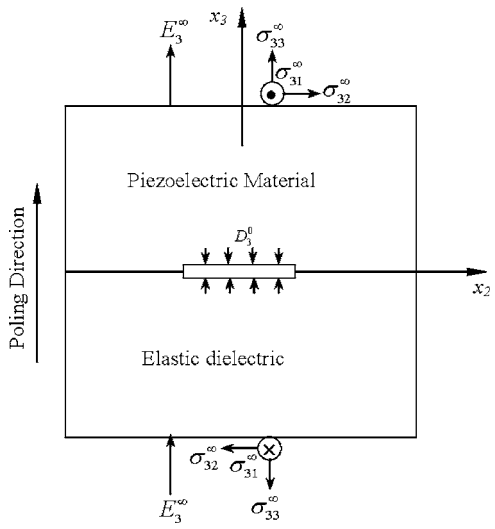

Fig. 1 A semi-permeable interface crack in elastic dielectric/piezoelectric bimaterial under the remote mechanical and electrical loadings

which are plotted in the figures. We conclude that the permittivity does not influence the crack tip singularity but influences the crack tip ERR significantly and in turn may influence the interface crack stability in such bimaterials under combined mechanical and electric loadings. We also conclude that, as McMeeking [22,23] pointed out in homogeneous piezoelectric materials, the previous investigations under the impermeable crack model are incorrect since the results of the ERR for the impermeable crack show significant discrepancies from those for the semi-permeable crack model, whereas the previous investigations under the conducting crack model may be accepted in a tolerant way since the results of the crack tip ERR show small discrepancies from those for the semi-permeable crack model, especially when the crack is filled with silicon oil. It is noticed that softer dielectrics such as epoxy and polymer (whose elastic moduli are much smaller than piezoelectric ceramics) yield larger discrepancies, whereas harder dielectrics such as Al_2O_3, SiC, and Si_3N_4 (whose elastic moduli are much larger than piezoelectric ceramics) yield smaller discrepancies. This reveals that the mechanical mismatch properties are more important than the electric mismatch properties in the present interface crack problem. In all figures under consideration the curves of the ERR for silicon oil are more likely tending to those for a conducting crack rather than to those for air or vacuum. Of great interest is that the variable tendencies of the crack tip ERR against the applied electric field have an interesting mechanical load-dependent feature. That is, the larger mechanical loading not only decreases the magnitude of the crack tip ERR, but also shifts the variable curves of the ERR when the applied electric field varies from -0.6 MV/m to $+0.6$ MV/m. As mentioned by Xu and Rajapakse [29], this feature is due to the nonlinear relation induced from a quadratic equation between the NEDC and the applied loadings. This finding provides a better understanding of the failure mechanism of the interface crack stability in elastic dielectric/piezoelectric bimaterials under practical loading levels.

2 Basic Formulations and Analytical Solutions

Consider an interface crack of length $2a$ lying along the interface between a elastic dielectric material and a transversely isotropic piezoelectric material under the generalized plane strain deformation as shown in Fig. 1. Let the remote uniform mechanical-electrical loading acting on the infinitely large bimaterial be denoted by σ_{32}^∞, σ_{33}^∞, σ_{31}^∞, and E_3^∞, respectively. The piezoelectric phase occupies the upper half space $x_3>0$ with the

Table 1 Material constants of 5 typical elastic dielectric materials

		Epoxy	Polymer	Al_2O_3	SiC	Si_3N_4
c_{11}	10^{10} N m^{-2}	0.80	0.386	47.0804	49.9391	41.7308
c_{12}	10^{10} N m^{-2}	0.44	0.257	14.4626	11.9433	17.8846
c_{13}	10^{10} N m^{-2}	0.44	0.257	14.4626	11.9433	17.8846
c_{33}	10^{10} N m^{-2}	0.80	0.386	47.0804	49.9391	41.7308
c_{44}	10^{10} N m^{-2}	0.18	0.064	16.3089	18.9979	11.9231
e_{13}	10^{-10} C m^{-2}	$-1.3275\approx 0$	$-1.3530\approx 0$	$-16.647\approx 0$	$-17.596\approx 0$	$-15.109\approx 0$
e_{33}	10^{-10} C m^{-2}	$1.1877\approx 0$	$0.8152\approx 0$	$22.029\approx 0$	$24.877\approx 0$	$17.124\approx 0$
e_{15}	10^{-10} C m^{-2}	$1.0531\approx 0$	$0.9069\approx 0$	$15.196\approx 0$	$16.402\approx 0$	$12.993\approx 0$
χ_{11}	10^{-10} C(V m)$^{-1}$	0.372	0.797	0.885	0.885	0.885
χ_{33}	10^{-10} C(V m)$^{-1}$	0.372	0.797	0.885	0.885	0.885

poling axis being perpendicular to the interface, whereas the isotropic elastic dielectric phase occupies the lower half space $x_3 < 0$. It is assumed that the crack is traction-free but filled with some medium with the permittivity ε_v so that the crack surfaces have an unknown normal electric displacement D_3^0 [29].

The present investigation starts from the semi-permeable crack or the PKHS crack model proposed firstly by Parton and Kudryavtsev [25] and then studied by Hao and Shen [26] and well-addressed more recently by McMeeking [22–24]. According to Fig. 1, the PKHS crack model is formulated by

$$D_3^+ = D_3^- \quad D_3^0(u_3^+ - u_3^-) = -\varepsilon_v(\phi^+ - \phi^-) \tag{1}$$

where the superscripts + and − refer to the upper and lower crack surfaces, respectively; u_3 is the displacement component normal to the crack surface; D_3^0 and ϕ is the unknown normal electrical displacement and the electrical potential along the crack surfaces, respectively; ε_v is the permittivity of the medium inside the interface crack gap. The value of ε_v for air or vacuum is $\varepsilon_v = \varepsilon_0 = 8.85 \times 10^{-12}$ C^2/N m^2.

All basic formulations for the extended Stroh's complex variable theory [5] are presented in the Appendix. In order to give an analytical solution, we assume that the NEDC along the interface crack is uniform [29].

Thus, using Viogt's notation, we can transform the constitutive relation of elastic dielectric material into the form of Eq. (A1) by letting the coefficients of Eq. (A1)

$$c_{13} = c_{12} \quad c_{33} = c_{11} \quad c_{44} = (c_{11} - c_{12})/2 \tag{2}$$

However, the elastic dielectric materials/piezoelectric bimaterials are constructed by two different kinds of solids with different constitutive equations, it is quite difficult to directly use the Stroh formulations of Suo et al. [5] to combine both kinds of constitutive equations in theoretical analyses. From the physical point of view, we know that the elastic dielectric material (the lower material in Fig. 1) always has a tiny piezoelectricity yielding some very small values of the mechanical-electric couple coefficients k_{33}, k_{31}, and k_{15} reduced from Eq. (A1). In general, commercial piezoelectric ceramics have some values of k_{33}, k_{31}, and k_{15} within the range between 0.5 and 0.7 in magnitude. Therefore, for dielectrics, as treated by Ou and Chen [21], we can approximately express these coefficients by the following values showing 10^{-10} smaller than those of commercial piezoelectric ceramics

$$k_{33} = d_{33}/\sqrt{\chi_{33}^{\sigma} s_{33}^{E}} = -0.3 \times 10^{-10} \tag{3a}$$

$$k_{31} = d_{31}/\sqrt{\chi_{33}^{\sigma} s_{11}^{E}} = 0.4 \times 10^{-10} \tag{3b}$$

$$k_{15} = d_{15}/\sqrt{\chi_{11}^{\sigma} s_{55}^{E}} = 0.5 \times 10^{-10} \tag{3c}$$

where d_{ij}, s_{ij}, χ_{ij} is the piezoelectric charge, elastic compliant, and dielectric constants of the material, respectively.

After doing so, we can treat the semi-permeable interface crack problem in elastic dielectric/piezoelectric bimaterials in the same way as those in two dissimilar piezoelectric materials by directly using the Stroh formulations [5,18].

Material constants of 5 elastic dielectrics are listed in Table 1 and those of 7 piezoelectric materials are listed in Table 2, respectively. It is seen from detailed comparisons between Table 1 and Table 2 that the material properties of the 5 elastic dielectric materials have quite different properties from those of the 7 piezoelectric materials due to the following three reasons. First, as we mentioned earlier, the piezoelectric coefficients of the elastic dielectric materials, say, the mechanical-electric coupling coefficients k_{33}, k_{31}, and k_{15} are extremely small but never zero (see Eqs. (3*a*)–(3*c*)). Second, we notice in Tables 1 and 2 that the permittivities of the 5 elastic dielectric materials, say χ_{11} and χ_{33}, are only 4–10 times larger than air/vacuum, which show the same order in magnitude as compared to silicon oil with 2.5 times larger

Table 2 Material constants of 7 typical piezoelectric ceramics

Material constant		PZT-4	PZT-5H	PZT-6B	PZT-7A	P-7	$BaTiO_3$	PZT-PIC 151
c_{11}	10^{10} N m^{-2}	13.9	12.6	16.8	14.8	13.0	15.0	11.0
c_{12}		7.78	5.50	6.00	7.62	8.30	6.60	6.3
c_{13}		7.43	5.30	6.00	7.42	8.30	6.60	6.4
c_{33}		11.3	11.7	16.3	13.1	11.9	14.6	10.0
c_{44}		2.56	3.53	2.71	2.54	2.50	4.4	2.0
e_{13}	C m^{-2}	−6.98	−6.50	−0.90	−2.10	−10.3	−4.35	−9.6
e_{33}		13.8	23.3	7.10	9.50	14.7	17.5	15.1
e_{15}		13.4	17.0	4.60	9.70	13.5	11.4	12.0
χ_{11}	10^{-10}	60.0	151	36.0	81.1	171	98.7	98.2
χ_{33}	C(V m)$^{-1}$	54.7	130	34.0	73.5	186	112	75.4

permittivity than air/vacuum, whereas the 7 piezoelectric materials have much larger permittivity than those of dielectrics. As pointed out by McMeeking [22–24], the permittivities of commercial piezoelectric materials have 1000 times larger than air/vacuum. Thirdly, we notice in Tables 1 and 2 that the elastic coefficients of epoxy and polymer (softer elastic dielectrics), say c_{11} and c_{33}, are much smaller than those of the 7 piezoelectric materials (at least 10 times smaller), e.g., the value of c_{11} for epoxy is merely 0.8×10^{10} N/m^2, 17.38 times smaller than PZT-4 (13.9×10^{10} N/m^2); in contrast, c_{11} and c_{33} of Al_2O_3, SiC, and Si_3N_4 (harder elastic dielectrics) are much larger than those of the 7 piezoelectric materials (about 3 times larger), e.g., the value of c_{11} for Al_2O_3 is 47.08×10^{10} N/m^2, 3.39 times larger than PZT-4. In this paper, we call the first and second differences mentioned above as the electric mismatch properties and call the third feature as the mechanical mismatch properties of the bimaterials, bearing in mind that all of them are coupled in the constitutive equations of piezoelectric materials. A question is, which one plays a more important role in singularity analysis and energy analysis for an interface crack in such bimaterials? This question needs to be well studied. Indeed, an interface crack in elastic dielectric/piezoelectric bimaterials may have quite different features from those in two dissimilar piezoelectric materials [15–18]. This is because the differences in the elastic, piezoelectric, and permittivity coefficients between two dissimilar piezoelectric materials are not so remarkable, whereas the differences in the elastic, piezoelectric and permittivity coefficients between an elastic dielectric and a piezoelectric are always remarkable. In other words, an elastic dielectric material and a piezoelectric material bonded along their interface not only have a large mismatch in the electric properties, but also have a large mismatch in the mechanical properties.

Here, the material properties of the transversely isotropic piezoelectric materials are always given by taking the x_3 axis to be the poling axis as shown in Fig. 1 and Table 2. In order to make comparisons, four electric boundary conditions on the crack surfaces are considered below: (i) the crack is electrically conducting (e.g., the gap filled with NaCI solution as did by Heyer et al. [30]), (ii) the gap filled with air/vacuum, (iii) the gap filled with silicon oil as did by Park and Sun [31,32], and (iv) the crack is insulating (impermeable crack). We see that cases (ii) and (iii) can be directly treated by using Eq. (1) without any difficulty, corresponding to $\varepsilon_v=\varepsilon_0=8.85\times10^{-12}$ C^2/Nm^2 in air or vacuum and $\varepsilon_v=2.5\varepsilon_0$ in silicon oil, respectively. However, cases (i) and (iv) are two limited cases of Eq. (1) corresponding to $\varepsilon_v\to\infty$ (the conducting crack) and $\varepsilon_v=0$ (the impermeable crack), respectively. Thus, some approximations should be made. Following Ou and Chen [21], we can use a much smaller value of the permittivity than air or vacuum, say $\varepsilon_v=10^{-8}\varepsilon_0$, to approximately treat the impermeable crack model, and use a much larger value than commercial piezoelectric materials, say $\varepsilon_v=10^{8}\varepsilon_0$, to approximately treat the conducting crack. The relative errors in calculating the crack tip ERR for these two extreme cases can be controlled within a relative error less than 0.1% by changing the value from $\varepsilon_v=10^{8}\varepsilon_0$ to $\varepsilon_v=10^{10}\varepsilon_0$ for case (i) and by changing the value from $\varepsilon_v=10^{-8}\varepsilon_0$ to $\varepsilon_v=10^{-10}\varepsilon_0$ for case (iv), respectively.

On the interface crack surfaces shown in Fig. 1, the generalized stresses $\mathbf{\Sigma}(x_2)=\mathbf{T^0}=(0,0,0,D_3^0)^T$ refer to the traction-free conditions and the uniform normal electric displacement along the semi-permeable interface crack, which yields a nonhomogenous Riemann-Hilbert problem as expressed in the following form:

$$\mathbf{g}^+(x_2)+\bar{\mathbf{H}}^{-1}\mathbf{H}\mathbf{g}^-(x_2)=\mathbf{K^0}+\mathbf{T^0}\quad |x_2|<a \tag{4}$$

where the material matrix $\mathbf{H}$, the unknown complex vector functions $\mathbf{g}(z)$ and the constant complex vector $\mathbf{K^0}$ are given by Eqs. (A25), (A26), and (A29) in the Appendix, respectively.

Without loss in generality, the homogeneous solution to Eq. (4) can be expressed in the following form [5]:

$$\mathbf{g}(z)=\mathbf{w}z^{-1/2+i\varepsilon_\alpha} \tag{5}$$

where $\mathbf{w}$ is a four-element column eigenvector and ε_α is a complex number, and both of them can be determined by an eigenvalue problem expressed in the following form:

$$\bar{\mathbf{H}}\mathbf{w}=e^{2\pi\varepsilon_\alpha}\mathbf{H}\mathbf{w} \tag{6}$$

By separating the matrix $\mathbf{H}$ into a real part denoted by $\mathbf{D}$ and an imaginary part denoted by $\mathbf{W}$, Eq. (6) can be rewritten as follows:

$$(\mathbf{D}^{-1}\mathbf{W}+i\eta\mathbf{I})\mathbf{w}=\mathbf{0} \tag{7}$$

where $\eta=-\tanh(\pi\varepsilon_\alpha)$, and the characteristic value problem Eq. (7) leads to the following characteristic equation:

$$\|\mathbf{D}^{-1}\mathbf{W}+i\eta\mathbf{I}\|=\eta^4+2b\eta^2+c=0 \tag{8}$$

where $\|\cdot\|$ denotes the determinant of a matrix and

$$b=\tfrac{1}{4}\mathrm{tr}[(\mathbf{D}^{-1}\mathbf{W})^2]\quad c=\|\mathbf{D}^{-1}\mathbf{W}\| \tag{9}$$

Ou [17] and Ou and Wu [18] have studied an impermeable interface crack in dissimilar piezoelectric materials. They have theoretically proven that $c=0$ for all combinations of the different transversely isotropic piezoelectric materials. They also found that: *the interface cracks in dissimilar piezoelectric materials have either oscillatory singularity with nonzero* ε *and vanishing* κ *or nonoscillatory singularity with nonzero* κ *and vanishing* ε. As is well known, the index ε controls the oscillatory singularity and the index κ controls the magnitude of the nonoscillatory singularity from the classical inverse square root singularity. However, Beom and Atluri [15] studied a conducting interface crack and Beom [16] studied a permeable crack in dissimilar piezoelectric materials and found that the crack tip always shows an oscillatory singularity. Our attention is focused on what happens for a semi-permeable interface crack in elastic dielectric/piezoelectric bimaterials to clarify whether the cracks in such bimaterials have the similar results as Ou and Wu [18] or as Beom and Atluri [16]. Solving the characteristic Eq. (8), we can denote the roots of ε_α corresponding to η_α ($\alpha=1,2,3,4$) as ε, $-\varepsilon$, $i\kappa$, and $-i\kappa$, respectively, where both ε and κ are well-known singularity parameters. It is noticed that there are two cases with the real number b in (8) and (9) less or larger than zero, respectively. If $b<0$, η is real such that

$$\varepsilon=\frac{1}{\pi}\tanh^{-1}\left[\frac{1}{\sqrt{2}}\sqrt{-\mathrm{tr}[(\mathbf{D}^{-1}\mathbf{W})^2]}\right]\quad \kappa=0 \tag{10}$$

In contrast, if $b>0$, η is a purely imaginary number, resulting in

$$\varepsilon=0\quad \kappa=\frac{1}{\pi}\tanh^{-1}\left[\frac{1}{\sqrt{2}}\sqrt{\mathrm{tr}[(\mathbf{D}^{-1}\mathbf{W})^2]}\right] \tag{11}$$

The associated linear independent eigenvector matrices $\mathbf{w}$ can be determined by Eq. (7). Thus, the four eigenpairs should have the following structures:

$$(\varepsilon,\mathbf{w}_1)\ \ (-\varepsilon,\mathbf{w}_2)\ \ (0,\mathbf{w}_3)\ \ (0,\mathbf{w}_4) \tag{12}$$

It can be noticed that $\mathbf{w}_1$ is complex and $\mathbf{w}_2=\bar{\mathbf{w}}_1$, but $\mathbf{w}_3$ and $\mathbf{w}_4$ are real. Suo et al. [5] have concluded that the eigenvectors $\mathbf{w}_\alpha$ ($\alpha=1,2,3,4$) in Eq. (A11) satisfy the certain orthogonal relations (A12) and (A13) related to the four distinct singularity parameters ε_α. In fact, Ting [33,34] has already found these relations. These relations have also been used by Deng and Meguid [10] for treating the conducting inclusion between two dissimilar piezoelectric materials.

Calculating numerical results of the singularity analysis at the interface crack tip are listed in Table 3 for 35 types of such bimaterials constructed by the 5 kinds of elastic dielectric materials: epoxy, polymer, Al_2O_3, SiC, and Si_3N_4 and the 7 kinds of commercial piezoelectric ceramics: PZT-4, $BaTiO_3$, PZT-5H, PZT-6B, PZT-7A, P-7, and PZT-PIC 151, respectively. We find from Table 3 that, unlike those of Ou [17] and Ou and Wu [18], the singular

Table 3 Oscillatory index ε with vanishing index κ for the semi-permeable interface crack in 35 kinds of elastic dielectric/piezoelectric bimaterials

$\kappa=0$,	$\varepsilon=$	Epoxy	Polymer	Al_2O_3	SiC	Si_3N_4
Piezoelectric material	PZT-4	0.0626	0.0500	0.0864	0.0884	0.0810
	$BaTiO_3$	0.0650	0.0509	0.0638	0.0655	0.0592
	PZT-5H	0.0630	0.0502	0.0856	0.0877	0.0802
	PZT-6B	0.0651	0.0510	0.0498	0.0510	0.0463
	PZT-7A	0.0639	0.0506	0.0553	0.0565	0.0520
	P-7	0.0629	0.0502	0.0579	0.0590	0.0547
	PZT-PIC 151	0.0608	0.0492	0.0861	0.0878	0.0817

parameters computed by Eq. (10) or (11) for the 35 kinds of elastic dielectric/piezoelectric bimaterials always show the oscillatory singularity with the nonzero oscillatory index ε, whereas the nonoscillatory index κ always vanishes. Moreover, the calculating values of ε for most of the 35 kinds of bimaterials are around 0.06, even though, in some cases, the maximum value of ε is 0.0884 for the PZT-4/SiC bimaterial and the minimum value of ε is 0.0463 for the Si_3N_4/PZT-6B bimaterial. It is found that the values of the oscillatory index ε of these 35 kinds of elastic dielectric/piezoelectric bimaterials are always much larger than those of the ε-class dissimilar piezoelectric materials. For example, the 7 kinds of the ε-class dissimilar piezoelectric materials reported by Ou [17] have some smaller values of ε as follows: $BaTiO_3$/PZT-5H with $\varepsilon=0.0130$; PZT-5H/PZT-6B with $\varepsilon=0.0219$; PZT-5H/PZT-7A with $\varepsilon=0.0069$; PZT6B/PZT-7A with $\varepsilon=0.0055$; PZT-6B/P-7 with $\varepsilon=0.0121$; PZT-4/PZT-PIC151 with $\varepsilon=0.0095$; PZT-6B/PZT-PIC151 with $\varepsilon=0.0134$, respectively. Obviously, this is because the mechanical mismatch properties for the 35 kinds of elastic dielectric/piezoelectric bimaterials are always much larger than the 7 kinds of dissimilar piezoelectric materials. In other words, the differences in elastic moduli between elastic dielectric and piezoelectric are always remarkable, whereas the differences between two dissimilar piezoelectric materials are not so.

Mathematically, all combinations of the elastic dielectric/piezoelectric bimaterials will lead to the double eigenvalue $\kappa=0$; hence some new orthogonal relations should be introduced to replace Eqs. (A12) and (A13). These results are similar to those in dissimilar elastic anisotropic materials, implying again that the mechanical mismatch properties are more important than the electric mismatch properties in elastic dielectric/piezoelectric bimaterials.

According to the characteristic Eq. (6), the associated eigenvectors satisfy

$$\bar{\mathbf{H}}\mathbf{w}_1 = e^{2\pi\varepsilon}\mathbf{H}\mathbf{w}_1 \quad \bar{\mathbf{H}}\mathbf{w}_2 = e^{-2\pi\varepsilon}\mathbf{H}\mathbf{w}_2 \quad \bar{\mathbf{H}}\mathbf{w}_3 = \mathbf{H}\mathbf{w}_3 \quad \bar{\mathbf{H}}\mathbf{w}_4 = \mathbf{H}\mathbf{w}_4 \tag{13}$$

After some manipulations, we demonstrate that $\mathbf{w}_\alpha$ would satisfy the following new orthogonal relations:

$$\begin{bmatrix} \mathbf{w}_1^T \\ \mathbf{w}_2^T \\ \mathbf{w}_3^T \\ \mathbf{w}_4^T \end{bmatrix} \mathbf{H}[\mathbf{w}_1, \mathbf{w}_2, \mathbf{w}_3, \mathbf{w}_4] = \begin{bmatrix} 0 & \mathbf{w}_1^T\mathbf{H}\mathbf{w}_2 & 0 & 0 \\ \mathbf{w}_2^T\mathbf{H}\mathbf{w}_1 & 0 & 0 & 0 \\ 0 & 0 & \mathbf{w}_3^T\mathbf{H}\mathbf{w}_3 & 0 \\ 0 & 0 & 0 & \mathbf{w}_4^T\mathbf{H}\mathbf{w}_4 \end{bmatrix} \tag{14}$$

which provide a powerful self-examination method to confirm the present numerical results.

It is obvious that the above orthogonal relations are different from those obtained by Ting [33,34] and Suo et al. [5]. It is convenient to display physical quantities in an eigenvector representation. The potential functions $\mathbf{g}(z)$ and constant vector $\mathbf{T}$ can be spanned by the eigenvector $\mathbf{w}_\alpha$ as

$$\mathbf{g}(z) = g_1(z)\mathbf{w}_1 + g_2(z)\mathbf{w}_2 + g_3(z)\mathbf{w}_3 + g_4(z)\mathbf{w}_4 \tag{15}$$

$$\mathbf{T} = \mathbf{K^0} + \mathbf{T^0} = t_1\mathbf{w}_1 + t_2\mathbf{w}_2 + t_3\mathbf{w}_3 + t_4\mathbf{w}_4 \tag{16}$$

Substituting Eqs. (15) and (16) into (4), we obtain the following decoupled Hilbert equations

$$g_\alpha^+(x_2) + e^{2\pi\varepsilon_\alpha} g_\alpha^-(x_2) = t_\alpha \quad (\alpha = 1,2,3,4) \tag{17}$$

The solution procedures follow those developed by England [35], yielding

$$g_\alpha(z) = \frac{t_\alpha}{1+e^{2\pi\varepsilon_\alpha}}\left[1 - \left(\frac{z-a}{z+a}\right)^{-i\varepsilon_\alpha}\frac{z-2i\varepsilon_\alpha a}{\sqrt{z^2-a^2}}\right] + \left(\frac{z-a}{z+a}\right)^{-i\varepsilon_\alpha}\frac{c_0^\alpha + c_1^\alpha z + \cdots + c_n^\alpha z^n}{\sqrt{z^2-a^2}} \tag{18}$$

By substituting Eqs. (18) and (16) into Eq. (15), the potential functions $\mathbf{g}(z)$ can be given as follows:

$$\mathbf{g}(z) = \mathbf{w}\left\langle\left\langle \frac{1}{1+e^{2\pi\varepsilon_\alpha}}\left[1 - \left(\frac{z-a}{z+a}\right)^{-i\varepsilon_\alpha}\frac{z-2i\varepsilon_\alpha a}{\sqrt{z^2-a^2}}\right]\right\rangle\right\rangle \mathbf{w}^{-1}(\mathbf{K^0}+\mathbf{T^0}) + \mathbf{w}\left\langle\left\langle\left(\frac{z-a}{z+a}\right)^{-i\varepsilon_\alpha}\right\rangle\right\rangle \frac{\mathbf{c}_0 + \mathbf{c}_1 z + \cdots + \mathbf{c}_n z^n}{\sqrt{z^2-a^2}} \tag{19}$$

where $\langle\langle\cdot\rangle\rangle$ indicates the diagonal matrix, in which each component varies according the Green index α, $\mathbf{c}_n=(c_n^1, c_n^2, c_n^3, c_n^4)^T$ being unknown constant vectors.

To find $\mathbf{c}_n$, we can take the limit as $z\to\infty$ in Eq. (19) and use the far-field uniform loading condition, and then obtain the following formulation:

$$\mathbf{c}_1 = \left\langle\left\langle \frac{1}{1+e^{2\pi\varepsilon_\alpha}}\right\rangle\right\rangle \mathbf{w}^{-1}(\mathbf{T}^\infty + \mathbf{K^0}) \quad \mathbf{c}_n = 0 \quad (n>1) \tag{20}$$

where $\mathbf{T}^\infty = \mathbf{B}\mathbf{f}'(\infty) + \bar{\mathbf{B}}\bar{\mathbf{f}}'(\infty) = (\sigma_{32}^\infty, \sigma_{33}^\infty, \sigma_{31}^\infty, D_3^\infty)^T$.

In deriving Eq. (20), the following relations have been used

$$\mathbf{w}^{-1}(\mathbf{I} + \bar{\mathbf{H}}^{-1}\mathbf{H})\mathbf{w} = \langle\langle 1 + e^{2\pi\varepsilon_\alpha}\rangle\rangle \tag{21}$$

It should be emphasized that the determination of the unknown constants $\mathbf{c}_0$ in Eq. (19) needs to use the single-valued condition of generalized displacement $\mathbf{\Delta u}$ (see Eq. (A4) in Appendix)

$$\oint_{L_c} \mathbf{\Delta u}(z)\mathrm{d}z = 0 \tag{22}$$

Combining Eqs. (A27), (19), and (22), we can obtain

$$\mathbf{c_0} = \left\langle\left\langle \frac{-2i\varepsilon_\alpha a}{1+e^{2\pi\varepsilon_\alpha}}\right\rangle\right\rangle \mathbf{w}^{-1}(\mathbf{T}^\infty + \mathbf{K^0}) \tag{23}$$

Thus, the full-generalized stress fields for the semi-permeable interface crack in elastic dielectric/piezoelectric bimaterials can be expressed as follows:

$$\mathbf{\Sigma}(z) = \mathbf{T^0} + \mathbf{w}\left\langle\left\langle\left(\frac{z-a}{z+a}\right)^{-i\varepsilon_\alpha}\frac{z-2i\varepsilon_\alpha a}{\sqrt{z^2-a^2}}\right\rangle\right\rangle\mathbf{w}^{-1}(\mathbf{T}^\infty - \mathbf{T^0}) \quad (24)$$

The jump of mechanical displacement and the drop of electric potential along the crack line ($-a \leqslant x_2 \leqslant a$) are given by integrating (A27) and considering (19)

$$\mathbf{\Delta u}(x_2) = \mathbf{H}\mathbf{w}\langle\langle\exp(-\pi\varepsilon_\alpha)(a-x_2)^{1/2-i\varepsilon_\alpha}(a+x_2)^{1/2+i\varepsilon_\alpha}\rangle\rangle\mathbf{w}^{-1}(\mathbf{T}^\infty - \mathbf{T^0}) \quad (25)$$

Since ε_α generally has a value much smaller than 1/2, varying around 0.06 for the 35 kinds of elastic dielectric/piezoelectric bimaterials (see Table 3), the jump of mechanical displacement and the drop of electric potential along the crack line ($-a \leqslant x_2 \leqslant a$) can be approximately obtained as

$$u_3^+ - u_3^- \approx \mathbf{H}_2\mathbf{w}\langle\langle\exp(-\pi\varepsilon_\alpha)\rangle\rangle\mathbf{w}^{-1}(\mathbf{T}^\infty - \mathbf{T^0})\sqrt{a^2-(x_2)^2} \quad (26)$$

$$\phi^+ - \phi^- \approx \mathbf{H}_4\mathbf{w}\langle\langle\exp(-\pi\varepsilon_\alpha)\rangle\rangle\mathbf{w}^{-1}(\mathbf{T}^\infty - \mathbf{T^0})\sqrt{a^2-(x_2)^2} \quad (27)$$

where $\mathbf{H}_2$ and $\mathbf{H}_4$ are the second and forth rows of $\mathbf{H}$, respectively.

By substituting Eqs. (26) and (27) into the semipermeable electric boundary condition (1), the normal component of electric displacement D_3^0 inside the crack can be derived by

$$D_3^0 = -\varepsilon_v\frac{\phi^+ - \phi^-}{u_3^+ - u_3^-} = -\varepsilon_v\frac{\mathbf{H}_2\mathbf{w}\langle\langle\exp(-\pi\varepsilon_\alpha)\rangle\rangle\mathbf{w}^{-1}(\mathbf{T}^\infty - \mathbf{T^0})}{\mathbf{H}_4\mathbf{w}\langle\langle\exp(-\pi\varepsilon_\alpha)\rangle\rangle\mathbf{w}^{-1}(\mathbf{T}^\infty - \mathbf{T^0})} \quad (28)$$

bearing in mind that Eq. (28) is a quadratic equation for unknown D_3^0 as mentioned by Xu and Rajapakse [29].

The emphasis here is focused on the distribution of the electromechanical fields near the crack tip. For this purpose, it is convenient to introduce the polar coordinates (r, θ) with the origin at the right crack tip. Thus, the singular generalized stress fields along the bonded interface near the crack tip can be derived as the polar coordinate system $(r, \theta) \to 0$

$$\mathbf{\Sigma}(r) = \frac{1}{\sqrt{2\pi r}}\mathbf{Y}(r^{-i\varepsilon_\alpha})(\mathbf{T}^\infty - \mathbf{T^0}) \quad (29)$$

where

$$\mathbf{Y}(r^{-i\varepsilon_\alpha}) = \mathbf{w}\left\langle\left\langle\sqrt{\pi a}\left(\frac{r}{2a}\right)^{-i\varepsilon_\alpha}(1-2i\varepsilon_\alpha)\right\rangle\right\rangle\mathbf{w}^{-1} \quad (30)$$

Since all combinations constructed from each pair of elastic dielectric material and transversely isotropic piezoelectric material considered in Table 3 lead to the same results, i.e., the first crack-tip oscillatory index ε does not vanish but the second parameter κ does always vanish, it can be concluded that the semi-permeable interface crack singularities in elastic dielectric/piezoelectric bimaterials are governed by the first parameter ε, regardless of the second parameter κ. This indicates that the structure of the singular field near the semi-permeable crack tip in such bimaterials consists of the inverse square root singularity $r^{-1/2}$ and a pair of oscillatory singularities $r^{-1/2\pm i\varepsilon}$. In other words, from the physical point of view, an interface crack under the semi-permeable electric boundary condition in such bimaterials always shows an oscillating singularity as those in dissimilar elastic anisotropic materials.

Thus, the vector of real-valued stress and electric displacement intensity factors, which uniquely characterize the singular fields at the semi-permeable interface crack tip can be defined as (Beom and Atluri [6])

$$\mathbf{K} = \lim_{r\to 0}\sqrt{2\pi r}\mathbf{Y}(r^{i\varepsilon_\alpha})\mathbf{\Sigma}(r) \quad (31)$$

where $\mathbf{K} = (K_{\mathrm{II}}, K_I, K_{\mathrm{III}}, K_D)^T$, the intensity factor $\mathbf{K}$ may be considered as an extension of the elastic version proposed by Wu [36] and Qu and Li [37].

Furthermore, the crack tip energy release rate (ERR) can be obtained by using the crack closure integral. With the right crack-tip extending by a small amount δa, the crack tip ERR can be expressed as

$$G = \lim_{\delta a\to 0}\frac{1}{2\delta a}\int_0^{\delta a}\{\sigma_{3i}(r)\Delta u_i(\delta a - r) + D_3(r)\Delta\phi(\delta a - r)\}\mathrm{d}r \quad (i = 1,2,3) \quad (32)$$

where

$$u_i(\delta a - r) = u_i(\delta a - r, \pi) - u_i(\delta a - r, -\pi)$$

and

$$\Delta\phi(\delta a - r) = \phi(\delta a - r, \pi) - \phi(\delta a - r, -\pi)$$

denote the jump of mechanical displacement and the drop of the electric potential jump across the interface crack, respectively.

Substituting the crack tip generalized stress field (29) and the jump of generalized displacement (25) across the crack into the closure integral (32) gives

$$G = \frac{a}{2}(\mathbf{T}^\infty - \mathbf{T^0})^T\mathbf{H}\mathbf{w} \ll \chi_\alpha \gg \mathbf{w}^{-1}(\mathbf{T}^\infty - \mathbf{T^0}) \quad (33)$$

where

$$\chi_\alpha = \frac{\left(-\frac{1}{2} + i\varepsilon_\alpha\right)\pi}{\sin\left[\left(-\frac{1}{2} + i\varepsilon_\alpha\right)\pi\right]}e^{-\pi\varepsilon_\alpha}(1 + 2i\varepsilon_\alpha).$$

In deriving Eq. (33), we have used the orthogonal relation described above in Eq. (14), and the identity

$$\int_0^1 t^q(1-t)^{-q}\mathrm{d}t = q\pi/\sin q\pi \quad |\mathrm{Re}(q)| < 1 \quad (34)$$

with $q = (-1/2 + i\varepsilon_\alpha)$.

3 Numerical Results and Discussions

This section deals with numerical results and discussions for interface cracks in 5 kinds of elastic dielectric/piezoelectric bimaterials constructed by PZT-4 and 5 kinds of elastic dielectrics whose material coefficients are listed in Table 1.

First, following Xu and Rajapakse [29], we focus our attention on the solution for the normal electric displacement D_3^0 along the interface crack obtained from Eq. (28) in the PZT-4/polymer bimaterial. It is noted that Eq. (28) is a quadratic equation of D_3^0. Generally speaking, there are two distinct roots, while only one of them is physically admissible for a given far-field electromechanical loading. Let root 1 (D_3^{01}) and root 2 (D_3^{02}) denote the two roots whose numerical results are listed in Table 4 under a uniform mechanical loading, $\sigma_{33}^\infty = 5$ MPa, and a varying electrical loading, $D_3^\infty = -0.4\times10^{-4}$ C/m^2, -0.2×10^{-4} C/m^2, 0, 0.2×10^{-4} C/m^2, and 0.4×10^{-4} C/m^2, for an interface crack of length 2 mm in the four kinds of electric boundary conditions along the crack surfaces with $\varepsilon_a = 10^8\varepsilon_0$, $\varepsilon_v = \varepsilon_0$, $\varepsilon_v = 2.5\varepsilon_0$, and $\varepsilon_v = 10^{-8}\varepsilon_0$, respectively. It can be seen from Table 4 that the five different values of the applied electrical loading in each case result identical values for the root 1 and quite different values for the root 2. As pointed out by Xu and Rajapakse [29], only D_3^{02} with a negative sign is reasonable since it has different values under varying electrical loadings, which mirrors the effect of the remote electrical loading,

Table 4 Normal electric displacement D_3^0 along the interface crack based on Eq. (28) for the PZT-4/polymer bimaterial under $\sigma_{33}^{\infty}=5$ MPa

$D_3^{\infty}(\mathrm{C/m^2})$		-0.4×10^{-4}	-0.2×10^{-4}	0	0.2×10^{-4}	0.4×10^{-4}
$\varepsilon_v=10^{-8}\varepsilon_0$	D_3^{01}	0.185	0.185	0.185	0.185	0.185
	D_3^{02}	-9.356×10^{-11}	-4.793×10^{-11}	-2.395×10^{-12}	4.304×10^{-11}	8.838×10^{-11}
$\varepsilon_v=\varepsilon_0$	D_3^{01}	4.387	4.387	4.387	4.387	4.387
	D_3^{02}	-3.932×10^{-4}	-2.017×10^{-4}	-1.009×10^{-5}	1.815×10^{-4}	3.731×10^{-4}
$\varepsilon_v=2.5\varepsilon_0$	D_3^{01}	10.690	10.690	10.690	10.690	10.690
	D_3^{02}	-4.0343×10^{-4}	-2.0689×10^{-4}	-1.0349×10^{-5}	1.8619×10^{-4}	3.8274×10^{-4}
$\varepsilon_v=10^8\varepsilon_0$	D_3^{01}	4.202×10^8	4.202×10^8	4.202×10^8	4.202×10^8	4.202×10^8
	D_3^{02}	-4.105×10^{-4}	-2.105×10^{-4}	-1.053×10^{-5}	1.895×10^{-4}	3.895×10^{-4}

whereas the value of D_3^{01} should be eliminated in every case [29]. Similar conclusions hold for the other 4 bimaterials, i.e., PZT-4/epoxy, PZT-4/Al_2O_3, PZT-4/SiC, and PZT-4/Si_3N_4, respectively. It should be emphasized that some nonlinear features in the subsequent calculations such as the crack tip ERR will occur due to the determination of D_3^{02}.

Second, we make a detailed energy analysis for the interface crack under the 4 kinds of electric boundary conditions from (i) to (iv). In order to provide some useful numerical results and to shorten the length of this paper, only 5 kinds of bimaterials: PZT-4/polymer, PZT-4/epoxy, PZT-4/Al_2O_3, PZT-4/SiC, and PZT-4/Si_3N_4 are considered below under some fixed mechanical loadings, say 1 MPa, 5 MPa, 10 MPa, and 20 MPa, respectively, and a varying electric field from −0.6 MV/m to 0.6 MV/m. Numerical results of the crack tip ERR are plotted in Figs. 2(*a*)–2(*d*), 3(*a*)–3(*d*), 4(*a*)–4(*d*), 5(*a*)–5(*d*), and 6(*a*)–6(*d*), respectively. It is seen in all figures that the discrepancies between the real black curves (referring to air or vacuum) and the imaginary curves (referring to the impermeable crack model) are always remarkable and the relative errors induced from the impermeable crack model can be over 100% or more. It is concluded that the crack tip ERR under the impermeable crack model, i.e., the case (iv) mentioned above, is incorrect as McMeeking [22–24] pointed out. Let us examine the results under other three cases (i), (ii), and (iii) in

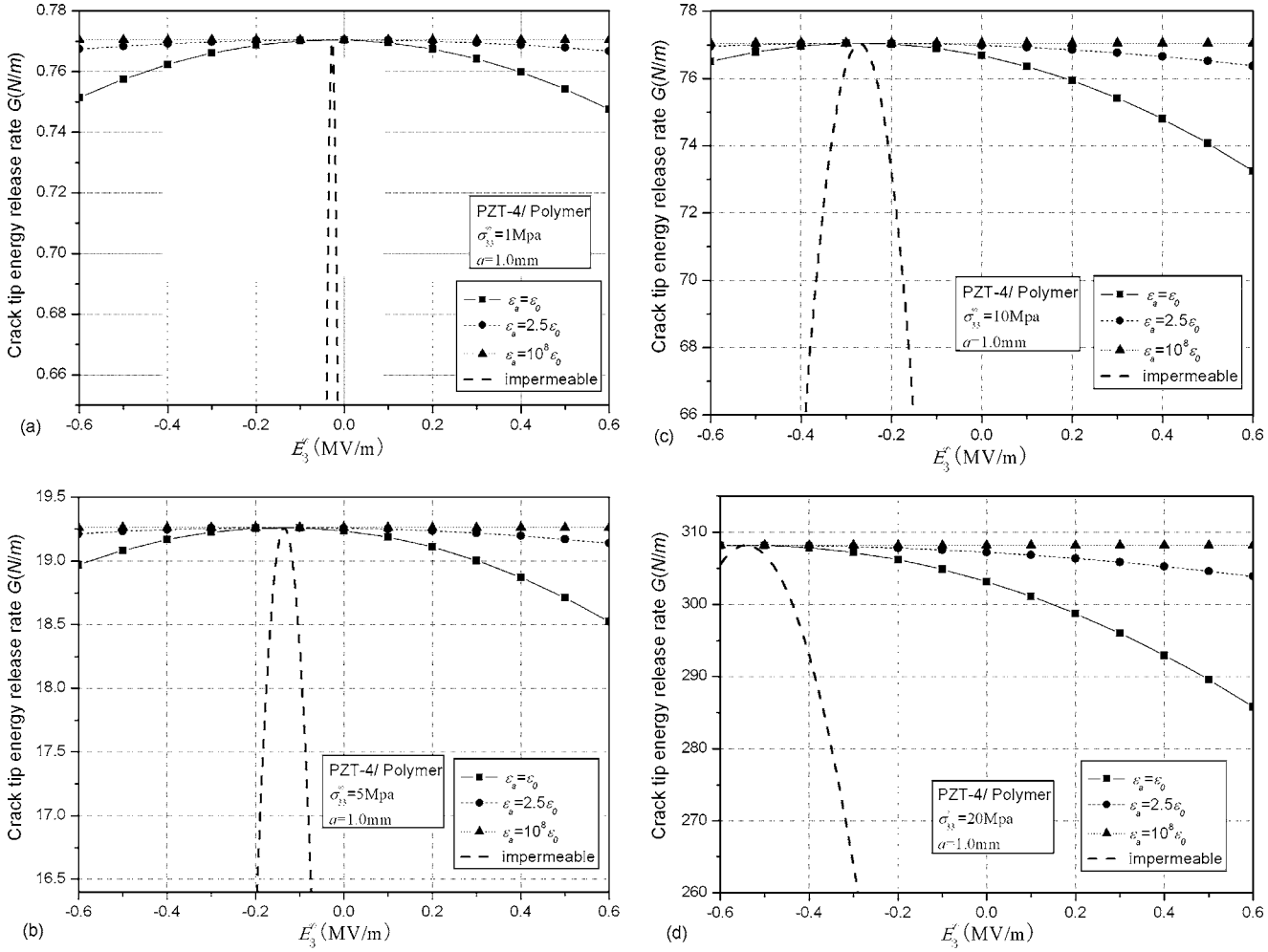

Fig. 2 The crack tip ERR for an interface crack in the PZT-4/polymer bimaterial against the applied electrical loading E_3^{∞} under (*a*) $\sigma_{33}^{\infty}=1$ MPa, (*b*) $\sigma_{33}^{\infty}=5$ MPa, (*c*) $\sigma_{33}^{\infty}=10$ MPa, (*d*) $\sigma_{33}^{\infty}=20$ MPa

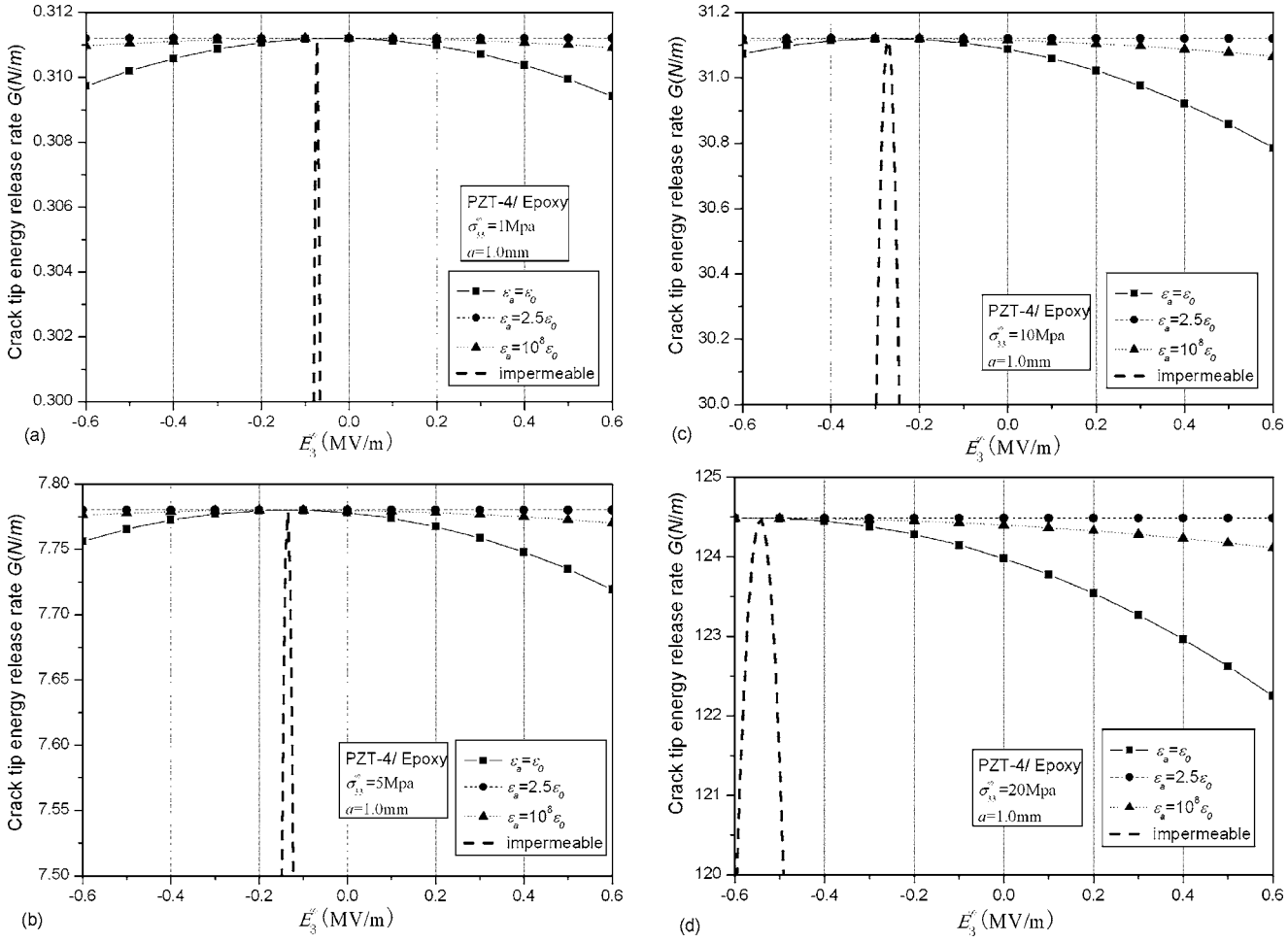

Fig. 3 The crack tip ERR for an interface crack in PZT-4/epoxy bimaterial against the applied electrical loading E_3^{∞} under (*a*) σ_{33}^{∞}=1 MPa, (*b*) σ_{33}^{∞}=5 MPa, (*c*) σ_{33}^{∞}=10 MPa, (*d*) σ_{33}^{∞}=20 MPa

detail. It is seen that under the relatively small mechanical loading, say 1 MPa, the maximum value of the crack tip ERR in Fig. 2(*a*) occurs nearly at the zero point of the applied electric field as many previous researchers found for a semipermeable crack in homogeneous cases. However, we will see that this is not always true when the mechanical loading becomes larger and larger. For example, when the mechanical loading becomes 5 MPa, the maximum value of the ERR shown in Fig. 2(*b*) does not occur at the zero point, rather, it occurs at a negative electric field, say about −0.15 MV/m, for the same crack in both air/vacuum and silicon oil. This is due to the nonlinear feature of the semi-permeable crack induced from the determination of D_3^{02}, i.e., the quadratic Eq. (28), as found by Xu and Rajapakse [29] and reviewed by Chen and Hasebe [38]. Moreover, under the 10 MPa mechanical loading as shown in Fig. 2(*c*), the maximum value of the ERR as the electric field varies occurs at about −0.3 MV/m for the same crack in both air/vacuum and silicon oil, far apart from the zero point of the electric field. It is also seen from Fig. 2(*d*) that, when the applied mechanical loading becomes much larger, say 20 MPa, the variable tendencies of the crack tip ERR against the electric field are quite different from those for the same crack subjected to the smaller mechanical loadings mentioned above. Indeed, as the electric field varies from −0.6 MV/m to 0.6 MV/m, the values of ERR for the crack in both air/vacuum and silicon oil always decrease. In other words, the maximum value occurs at −0.6 MV/m, far apart from those in Figs. 2(*b*) and 2(*c*) for the 10 MPa or 20 MPa mechanical loading. It is concluded that the larger the mechanical loading, the larger the discrepancy of the maximum value of ERR from the zero point of the applied electric field. That is, the larger mechanical loading not only decreases the magnitude of the crack tip ERR, but also shifts the variable curves of the crack tip ERR from the right side (referring to the positive electric field) to the left side (referring to the negative electric field). This load-dependent feature provides a better understanding of the failure mechanism of the interface crack stability in elastic dielectric/piezoelectric bimaterials when a large mechanical loading is preferred at infinity. That is, as the influence of the permittivity of the medium inside the crack gap depends on how large the crack opening is, the different levels of the applied mechanical loading yielding different levels of crack opening may change the relations between the failure mechanism and the applied electric field.

It is seen from Fig. 2(*a*) that when the applied mechanical loading is lower, say 1 MPa, and the applied electric field varies from −0.6 MV/m to 0.6 MV/m, the influence of the permittivity inside the crack gap on the crack tip ERR for a PZT-4/polymer bimaterial is very small. That is, the maximum relative error between the ERR values calculated from the conducting crack and those from the semi-permeable crack with air or vacuum is less than 3%. Of great interest is that the calculated values of the ERR with silicon oil are more likely tending to those for the conducting crack rather than to those with air or vacuum. Similar conclusions can be seen in Figs. 3(*a*), 4(*a*), 5(*a*), and 6(*a*) for other four bimaterials: PZT-4/epoxy, PZT-4/Al_2O_3, PZT-4/SiC, and PZT/Si_3N_4, respectively. However, when the applied mechanical loading becomes larger and larger, say 5 MPa, 10 MPa, or 20 MPa, the in-

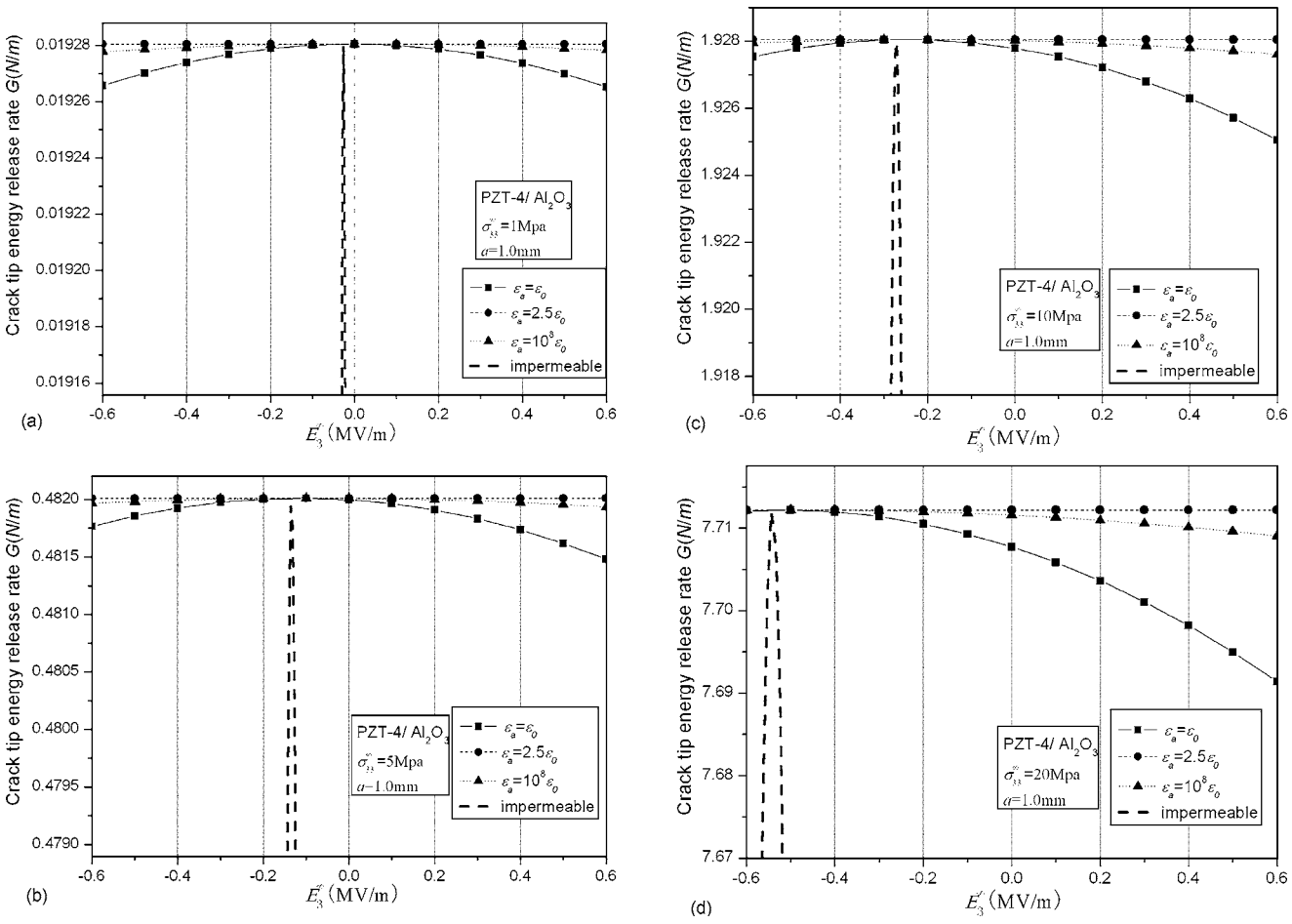

Fig. 4 The crack tip ERR for an interface crack in PZT-4/Al_2O_3 bimaterial against the applied electrical loading E_3^∞ under (*a*) σ_{33}^∞=1 MPa, (*b*) σ_{33}^∞=5 MPa, (*c*) σ_{33}^∞=10 MPa, (*d*) σ_{33}^∞=20 MPa

fluence of the permittivity on the crack tip ERR becomes larger and larger since the crack opening becomes larger and larger. It is seen from Figs. 2(*b*)–2(*d*) that the relative errors between the ERR values calculated from the conducting crack and those from the semi-permeable crack with air or vacuum can be larger than 3.9%, 5.2%, and 7.1%, respectively, whereas the curves of the ERR in silicon oil are still tending to those for the conducting crack rather than to those in air or vacuum. Similar conclusions can be seen in Figs. 3(*b*)–3(*d*) for PZT-4/epoxy bimaterial but the maximum relative error in Fig. 3(*d*) is merely 2.2%.

Let us see what happens for the bimaterials constructed by PZT-4 and some harder elastic dielectrics whose elastic moduli are much larger than commercial PZTs. Figures 4(*a*)–4(*d*), 5(*a*)–5(*d*), and 6(*a*)–6(*d*) show the curves of the crack tip ERR for the three kinds of bimaterials: PZT-4/Al_2O_3, PZT-4/SiC, and PZT-4/Si_3N_4, respectively. Of the most significance is that all relative errors between the ERR values calculated from the semi-permeable crack and those from the conducting crack are always less than 1% no matter how large the mechanical loading is within the range of practical interest. In other words, the harder elastic dielectric materials yield much smaller discrepancies of the crack tip ERR than softer dielectric materials such as polymer and epoxy!

Nevertheless, in all cases from Figs. 2(*a*)–2(*d*) to Figs. 6(*a*)–6(*d*) the conducting crack model always provides a good approximation of the semi-permeable crack in a tolerant way and the influences of the permittivity of the medium inside the interface crack gap could be entirely neglected in practical applications. In other words, whenever the elastic dielectric materials are softer or harder than PZTs, discrepancies in the crack tip ERR are less than 8% which is still within the tolerant range of engineering applications although the mechanical mismatch plays a more important role than the electric mismatch. Here, as mentioned above, we call the material mismatch on the interface from different mechanical properties of two dissimilar materials as the mechanical mismatch, whereas we call the material mismatch on the interface from different electric properties of two dissimilar materials as the electric mismatch, although both kinds of mismatch are coupled in constitutive equations of piezoelectric materials.

Therefore, the present investigation provides a positive note to Beom and Atluri [15] or Beom [16] who used the conducting or permeable crack model to treat interface cracks in dissimilar piezoelectric materials although they have not provided numerical results for certain combinations of dissimilar materials. As mentioned above, in all cases the influence of the permittivity of a medium inside a crack gap on the crack tip ERR against the applied electric field is significantly dependent on the level of the applied mechanical loading. The larger the mechanical loading, the larger the influence. The values of the crack-tip ERR in silicon oil are always more likely tending to those of a conducting crack rather than to those in air or vacuum. This is mainly because the permittivities of the 5 elastic dielectric materials are merely 4–10 times larger than air or vacuum, they have the same order in magnitude as that of silicon oil with permittivity 2.5 times larger than air.

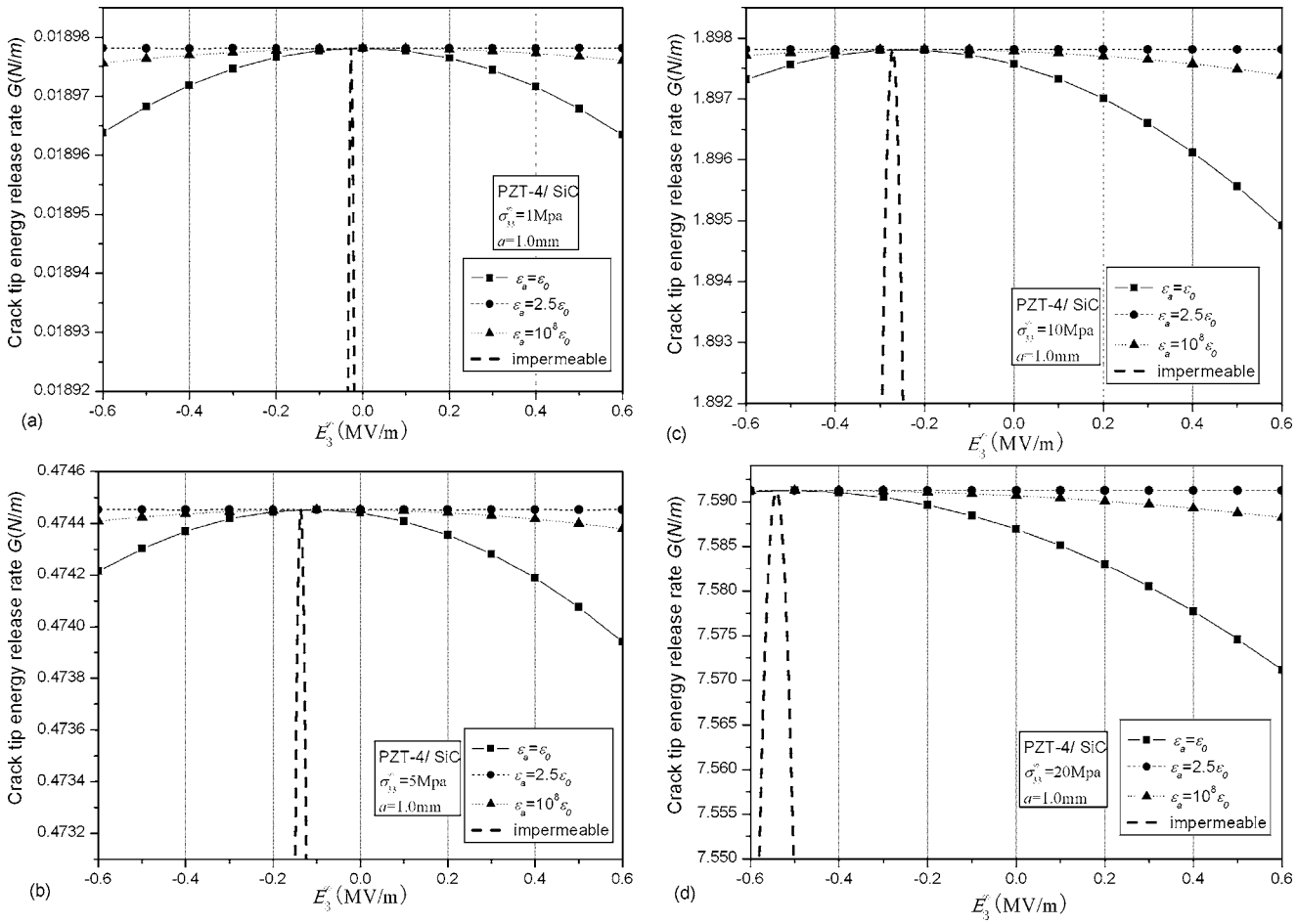

Fig. 5 The crack tip ERR for an interface crack in PZT-4/SiC bimaterial against the applied electrical loading E_3^∞ under (*a*) σ_{33}^∞ =1 MPa, (*b*) σ_{33}^∞=5 MPa, (*c*) σ_{33}^∞=10 MPa, (*d*) σ_{33}^∞=20 MPa

4 Conclusions

Based on the extended Stroh formalism, the solution for a semi-permeable interface crack problem in elastic dielectric/piezoelectric bimaterials is obtained. The influences induced from different permittivities of the medium inside the crack gap are studied in detail. Both softer dielectrics such as epoxy or polymer and harder dielectric such as Al_2O_3, SiC, and Si_3N_4 are considered by combining each of them with the 7 commercial piezoelectric ceramics: PZT-4, $BaTiO_3$, PZT-5H, PZT-6B, PZT-7A, P-7, respectively, and then 35 kinds of elastic dielectric/piezoelectric bimaterials are studied in detail. Two kinds of material mismatch properties are defined: the first is the mechanical mismatch properties accounting for the material mismatch induced from the different mechanical properties of the two dissimilar materials and the second is the electric mismatch properties induced from the different electric properties of the two dissimilar materials. Energy analyses reveal that in all bimaterials under consideration the discrepancies between the semi-permeable crack model and the impermeable crack model are always quite remarkable and the relative errors induced from the impermeable crack model can be over 100% or more. It is concluded that the crack tip ERR under the impermeable crack model in such bimaterials, i.e., the case (iv) mentioned above, is incorrect as McMeeking [22–24] pointed out in homogeneous cases. In the other three cases (i), (ii), and (iii) mentioned in the Introduction, the semi-permeable interface cracks in elastic dielectric/piezoelectric bimaterials are governed mainly by the mechanical mismatch although both kinds of material mismatch properties are coupled in constitutive equations of piezoelectric materials. That is, for harder dielectric/piezoelectric bimaterials the semi-permeable crack model yields nearly the same results as those of the conducting crack model with a relative error less than 1% even under a very large mechanical loading, say 20 MPa, whereas for softer dielectric/piezoelectric bimaterials the semi-permeable crack model yields relatively larger discrepancies from those of the conducting crack model. However, in all cases, the relative errors are always less than 8% under a very large mechanical loading, say 20 MPa, and under a varying electric field from −0.6 MV/m to +0.6 MV/m. This clearly reveals that the conducting interface crack model studied by Beom and Atluri [15] or the permeable crack model studied by Beom [16] does still provide a good approximation to the semi-permeable crack model in the elastic dielectric/piezoelectric bimaterials, whatever the elastic dielectrics are softer or harder. Of great interest is that the calculated values of the ERR with silicon oil are more likely tending to those for the conducting crack rather than to those with air or vacuum. The present investigation also reveals that the variable tendencies of the crack tip ERR against the applied electric field have an interesting load-dependent feature when the applied mechanical loading increases. This feature is due to the nonlinear relation between the NEDC and the applied electromechanical loadings from a quadratic equation. That is, the larger mechanical loading not only decreases the magnitude of the crack tip ERR, but also shifts the variable curves of the ERR when the applied electric field varies from −0.6 MV/m to +0.6 MV/m.

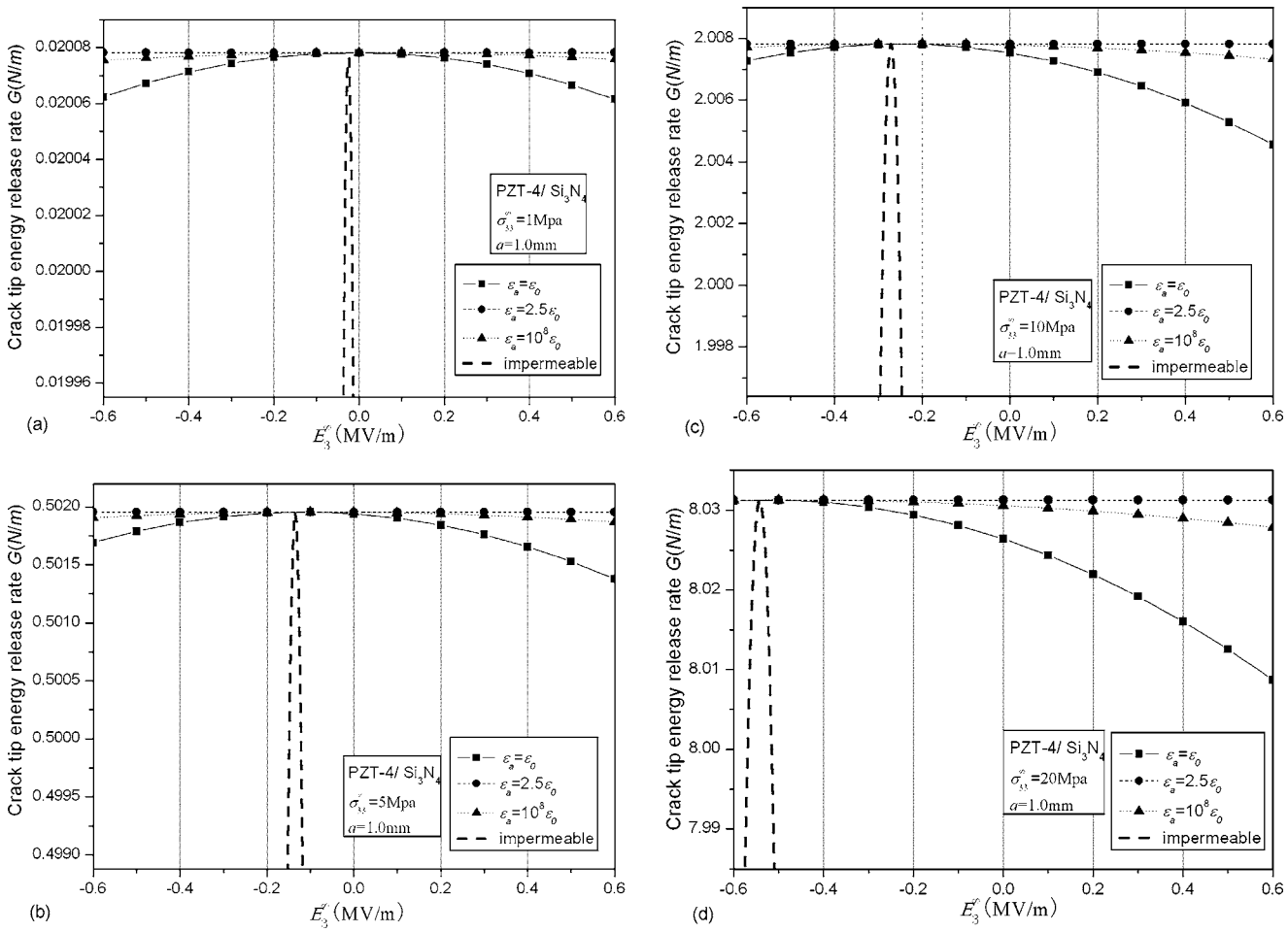

Fig. 6 The crack tip ERR for an interface crack in PZT-4/Si_3N_4 bimaterial against the applied electrical loading E_3^∞ under (*a*) σ_{33}^∞=1 MPa, (*b*) σ_{33}^∞=5 MPa, (*c*) σ_{33}^∞=10 MPa, (d) σ_{33}^∞=20 MPa

Acknowledgment

This work was supported by the National Science Foundation of China and by the Doctoral Research Foundation of the Chinese Ministry.

Appendix: The Extended Stroh's Formalism Developed by Suo et al. [5]

The complete set of basic equations for a linear piezoelectric solid is (see, Barnett and Lothe [39])

$$\begin{cases} \sigma_{ij} = C_{ijkl}u_{k,l} + e_{kij}\phi_{,k} \\ D_i = e_{ikl}u_{k,l} - \chi_{ik}\phi_{,k} \end{cases} \quad \text{Constitutive equations} \qquad \text{(A1)}$$

$$\begin{cases} \sigma_{ij,j} = 0 \\ D_{i,i} = 0 \end{cases} \quad \text{Equilibrium equations} \qquad \text{(A2)}$$

where σ_{ij}, u_i, D_i, and ϕ are separately the stress components, mechanical displacement components, electric displacement components, and electric potential; C_{ijkl}, e_{kij}, and χ_{ik} are the elastic, piezoelectric, and dielectric constants of the material, respectively.

The focus of this paper will be placed on two-dimensional, generalized plane strain problems where all stress and displacement components in a three-dimension space remain nonzero, but they depend on two coordinates, say, x_2, x_3 only. Assume that the field u_i and ϕ are

$$\mathbf{u} = \mathbf{a}f(z) \quad z = x_2 + px_3 \qquad \text{(A3)}$$

$$\mathbf{u} = [u_2, u_3, u_1, \phi]^T \quad \mathbf{a} = [a_1, a_2, a_3, a_4]^T \qquad \text{(A4)}$$

where the superscript T indicates transposition. Substituting Eqs. (A3) and (A4) into Eqs. (A1) and (A2), we obtain the following characteristic value problems:

$$\begin{cases} [C_{i2k2} + p(C_{i2k3} + C_{i3k2}) + p^2C_{i3k3}]a_k + [e_{2i2} + p(e_{3i2} + e_{2i3}) + p^2e_{3i3}]a_4 = 0 \\ [e_{2k2} + p(e_{2k3} + e_{3k2}) + p^2e_{3k3}]a_k - [\chi_{22} + p(\chi_{23} + \chi_{32}) + p^2\chi_{33}]a_4 = 0 \end{cases} \qquad \text{(A5)}$$

or we write them in a compact form [5]

$$[\mathbf{Q} + p(\mathbf{R} + \mathbf{R}^T) + p^2\mathbf{T}]\mathbf{a} = \mathbf{0} \tag{A6}$$

where $\mathbf{Q}$, $\mathbf{R}$, and $\mathbf{T}$ are 4×4 material matrices defined as

$$\mathbf{Q} = \begin{bmatrix} c_{i2k2} & e_{2i2} \\ e_{2k2} & -\chi_{22} \end{bmatrix} \quad \mathbf{R} = \begin{bmatrix} c_{i2k3} & e_{3i2} \\ e_{2k3} & -\chi_{23} \end{bmatrix} \quad \mathbf{T} = \begin{bmatrix} c_{i3k3} & e_{3i3} \\ e_{3k3} & -\chi_{33} \end{bmatrix} \tag{A7}$$

A nontrivial solution of the vector $\mathbf{a}$ requires that

$$\|\mathbf{Q} + p(\mathbf{R} + \mathbf{R}^T) + p^2\mathbf{T}\| = 0 \tag{A8}$$

where $\|\cdot\|$ denotes the determinant of a matrix. Solving the above characteristic equation, we obtain eight eigenvalues, forming four conjugate pairs,

$$p_{\alpha+4} = \bar{p}_\alpha \quad \mathbf{a}_{\alpha+4} = \bar{\mathbf{a}}_\alpha \quad (\alpha = 1,2,3,4) \tag{A9}$$

With an auxiliary vector $\mathbf{b}_\alpha$ introduced by Suo et al. [5] and defined as

$$\mathbf{b}_\alpha = (\mathbf{R}^T + p_\alpha\mathbf{T})\mathbf{a}_\alpha = -(1/p_\alpha)(\mathbf{Q} + p_\alpha\mathbf{R})\mathbf{a}_\alpha \tag{A10}$$

we can, obtain two 4×4 nonsingular material characteristic matrices $\mathbf{A}$ and $\mathbf{B}$, as follows:

$$\mathbf{A} = (\mathbf{a}_1,\mathbf{a}_2,\mathbf{a}_3,\mathbf{a}_4) \quad \mathbf{B} = (\mathbf{b}_1,\mathbf{b}_2,\mathbf{b}_3,\mathbf{b}_4) \tag{A11}$$

Applying a similar procedure to that of Ting [33,34] and Suo et al., [5], we can construct the important orthogonal relations between $\mathbf{A}$ and $\mathbf{B}$

$$\begin{aligned} \mathbf{A}^T\mathbf{B} + \mathbf{B}^T\mathbf{A} &= \mathbf{I} = \bar{\mathbf{A}}^T\bar{\mathbf{B}} + \bar{\mathbf{B}}^T\bar{\mathbf{A}} \\ \mathbf{A}^T\bar{\mathbf{B}} + \mathbf{B}^T\bar{\mathbf{A}} &= \mathbf{0} = \bar{\mathbf{B}}^T\mathbf{A} + \bar{\mathbf{A}}^T\mathbf{B} \end{aligned} \tag{A12}$$

as well as the closure relations

$$\begin{aligned} \mathbf{A}\mathbf{A}^T + \bar{\mathbf{A}}\bar{\mathbf{A}}^T &= \mathbf{0} = \mathbf{B}\mathbf{B}^T + \bar{\mathbf{B}}\bar{\mathbf{B}}^T \\ \mathbf{B}\mathbf{A}^T + \bar{\mathbf{B}}\bar{\mathbf{A}}^T &= \mathbf{I} = \mathbf{A}\mathbf{B}^T + \bar{\mathbf{A}}\bar{\mathbf{B}}^T \end{aligned} \tag{A13}$$

Thus, for a generalized plane strain deformation of a linear anisotropic piezoelectric solid, the general forms of the generalized displacement (mechanical displacement and electric potential) and the generalized stresses (mechanical stresses and electric displacement) can be expressed as

$$\mathbf{u} = [u_2,u_3,u_1,\phi]^T = 2\,\mathrm{Re}[\mathbf{A}\mathbf{f}(z)] \tag{A14a}$$

$$\mathbf{\Sigma} = [\sigma_{32},\sigma_{33},\sigma_{31},D_3]^T = 2\,\mathrm{Re}[\mathbf{B}\mathbf{f}'(z)] \tag{A14b}$$

$$\mathbf{\Lambda} = [\sigma_{22},\sigma_{23},\sigma_{21},D_2]^T = -2\,\mathrm{Re}[\mathbf{B}\mathbf{P}\mathbf{f}'(z)] \tag{A14c}$$

where Re denotes the real part of a complex argument; a prime ($'$) represents the derivative with respect to the variable of the associated function,

$$\mathbf{f}(z) = [f_1(z_1),f_2(z_2),f_3(z_3),f_4(z_4)]^T$$

$$z_\alpha = x_2 + p_\alpha x_3 \quad (\alpha = 1,2,3,4) \tag{A15}$$

and $\mathbf{P}$ is a diagonal matrix

$$\mathbf{P} = \mathrm{diag}[p_1,p_2,p_3,p_4] \tag{A16}$$

Representation (A14) is known as extended Stroh's formalism.

The continuity of the generalized stresses $\mathbf{\Sigma}(x_2)$ across the x_2 axis on both the bonded and cracked segments requires that

$$\mathbf{B}_1\mathbf{f}_1'^{+}(x_2) + \bar{\mathbf{B}}_1\bar{\mathbf{f}}_1'^{-}(x_2) = \mathbf{B}_2\mathbf{f}_2'^{-}(x_2) + \bar{\mathbf{B}}_2\bar{\mathbf{f}}_2'^{+}(x_2) \quad |x_2| < \infty \tag{A17}$$

Rearranging Eq. (A17), we can obtain

$$\mathbf{B}_1\mathbf{f}_1'^{+}(x_2) - \bar{\mathbf{B}}_2\bar{\mathbf{f}}_2'^{+}(x_2) = \mathbf{B}_2\mathbf{f}_2'^{-}(x_2) - \bar{\mathbf{B}}_1\bar{\mathbf{f}}_1'^{-}(x_2) \quad |x_2| < \infty \tag{A18}$$

Define a new analytical function as

$$\mathbf{\Psi}(z) = \begin{cases} \mathbf{B}_1\mathbf{f}_1'(z) - \bar{\mathbf{B}}_2\bar{\mathbf{f}}_2'(z) & x_3 > 0 \\ \mathbf{B}_2\mathbf{f}_2'(z) - \bar{\mathbf{B}}_1\bar{\mathbf{f}}_1'(z) & x_3 < 0 \end{cases} \tag{A19}$$

and reduce Eq. (A18) to

$$\mathbf{\Psi}^+(x_2) - \mathbf{\Psi}^-(x_2) = 0 \quad |x_2| < \infty \tag{A20}$$

The solution of Eq. (A20) is then given as follows (Muskhelishvili [40]):

$$\mathbf{\Psi}(z) = \mathbf{\Psi}(\infty) \tag{A21}$$

where

$$\mathbf{\Psi}(\infty) = \mathbf{B}_1\mathbf{f}_1'(\infty) - \bar{\mathbf{B}}_2\bar{\mathbf{f}}_2'(\infty) = \mathbf{B}_2\mathbf{f}_2'(\infty) - \bar{\mathbf{B}}_1\bar{\mathbf{f}}_1'(\infty) \tag{A22}$$

Define the jump of the generalized displacements across the interface crack

$$\mathbf{\Delta u}(x_2) = \mathbf{u}_1^+(x_2) - \mathbf{u}_2^-(x_2) \tag{A23}$$

Combining Eqs. (A14*a*), (A21), and (A23) yields

$$i\mathbf{\Delta u}'(x_2) = \mathbf{H}\mathbf{B}_1\mathbf{f}_1'^{+}(x_2) - \bar{\mathbf{H}}\mathbf{B}_2\mathbf{f}_2'^{-}(x_2) - (\bar{\mathbf{Y}}_2 - \bar{\mathbf{Y}}_1)\mathbf{\Psi}(\infty) \tag{A24}$$

where

$$\mathbf{H} = \mathbf{Y}_1 + \bar{\mathbf{Y}}_2 \quad \mathbf{Y}_1 = i\mathbf{A}_1\mathbf{B}_1^{-1} \quad \mathbf{Y}_2 = i\mathbf{A}_2\mathbf{B}_2^{-1} \tag{A25}$$

By defining

$$\mathbf{g}(z) = \begin{cases} \mathbf{B}_1\mathbf{f}_1'(z) & x_3 > 0 \\ \mathbf{H}^{-1}\bar{\mathbf{H}}\mathbf{B}_2\mathbf{f}_2'(z) + \mathbf{H}^{-1}(\bar{\mathbf{Y}}_2 - \bar{\mathbf{Y}}_1)\mathbf{\Psi}(\infty) & x_3 < 0 \end{cases} \tag{A26}$$

Eqs. (A24) and (A14*b*) can be expressed as

$$i\mathbf{\Delta u}'(x_2) = \mathbf{H}[\mathbf{g}^+(x_2) - \mathbf{g}^-(x_2)] \tag{A27}$$

$$\mathbf{\Sigma}(x_2) = \mathbf{g}^+(x_2) + \bar{\mathbf{H}}^{-1}\mathbf{H}\mathbf{g}^-(x_2) - \mathbf{K}^0 \tag{A28}$$

where

$$\mathbf{K}^0 = \bar{\mathbf{H}}^{-1}(\mathbf{Y}_2 + \bar{\mathbf{Y}}_2)\mathbf{\Psi}(\infty) \tag{A29}$$

References

[1] Harrison, W. B., McHenry, K. D., and Koepke, B. G., 1986, "Monolithic Multilayer Piezoelectric Ceramic Transducer," in *Proceedings of the IEEE Sixth International Symposium on Applied Ferromagnetics*, pp. 265–272.

[2] Shaulov, A. A., Smith, W. A., and Ting, R. Y., 1989, "Modified-Lead-Titanate/Polymer Composites for Hydrophone Applications," Ferroelectrics, **93**, pp. 177–182.

[3] Sevostianov, I., Levin, V., and Kachanov, M., 2001, "On the Modeling and Design of Piezocomposites With Prescribed Properties," Arch. Appl. Mech., **71**, pp. 733–747.

[4] Kuo, C. M., and Barnett, D. M., 1991, "Stress Singularities of Interface Cracks in Bonded Piezoelectric Half-Spaces," in *Modern Theory of Anisotropic Elasticity and Applications*, edited by J. J. Wu, T. C. T. Ting, and D. M. Barnett, SIAM Proceedings Series, SIAM, Philadelphia, PA, pp. 33–50.

[5] Suo, Z., Kuo, C. M., Barnett, D. M., and Willis, J. R., 1992, "Fracture Mechanics of Piezoelectric Ceramics, J. Mech. Phys. Solids, **40**, pp. 739–765.

[6] Beom, H. G., and Atluri, S. N., 1996, "Near-Tip and Intensity Factors for Interfacial Cracks in Dissimilar Anisotropic Piezoelectric Media," Int. J. Fract., **75**, pp. 163–183.

[7] Zhong, Z., and Meguid, S. A., 1997, "Interfacial Debonding of a Circular Inhomogeneity in Piezoelectric Materials," Int. J. Solids Struct., **34**, pp. 1965–1984.

[8] Qin, Q. H., and Yu, S. W., 1997, "An Arbitrarily-Oriented Plane Crack Terminating an Interface Between Dissimilar Piezoelectric Materials," Int. J. Solids Struct., **34**, pp. 581–590.

[9] Ru, C. Q., Mao, X., and Epstein, M., 1998, "Electric Field Induced Interfacial Cracking in Multilayer Electrostrictive Actuators," J. Mech. Phys. Solids, **46**, pp. 1301–1318.

[10] Deng, W., and Meguid, S. A., 1998, "Analysis of Conducting Rigid Inclusion at the Interface of Two Dissimilar Piezoelectric Materials," ASME J. Appl. Mech., **65**, pp. 76–84.

[11] Narita, K., and Shindo, Y., 1999, "Anti-Plane Shear Crack in a Piezoelectric Layer Bonded to Dissimilar Half Spaces," J. Mech. Phys. Solids, **42**, pp. 66–72.

[12] Ding, H. J., Chi, Y., and Guo, F., 1999, "Solutions for Transversely Isotropic

Piezoelectric Infinite Body, Semi-Infinite Body and Bimaterial Infinite Body Subjected to Uniform Ring Loading and Charges," Int. J. Solids Struct., **36**, pp. 2613–2631.
[13] Tian, W. Y., and Chen, Y. H., 2000, "Interaction Between an Interface Crack and Subinterface Microcracks in Metal/Piezoelectric Bimaterials," Int. J. Solids Struct., **37**, pp. 7743–7757.
[14] Ma, L. F., and Chen, Y. H., 2001, "Weight Functions for Interface Cracks in Dissimilar Anisotropic Piezoelectric Materials," Int. J. Fract., **110**, pp. 263–279.
[15] Beom, H. G., and Atluri, S. N., 2002, "Conducting Cracks in Dissimilar Piezoelectric Media," Int. J. Fract., **118**, pp. 285–301.
[16] Beom, H. G., 2003, "Permeable Cracks Between Two Dissimilar Piezoelectric Materials," Int. J. Solids Struct., **40**, pp. 6669–6679.
[17] Ou, Z. C., 2003, "Singularity Parameters ε and κ for Interface Cracks in Transversely Isotropic Piezoelectric Bimaterials," Int. J. Fract., **119**, pp. L41–L46.
[18] Ou, Z. C., and Wu, X. J., 2003, "On the Crack Tip Stress Singularity of Interfacial Cracks in Transversely Isotropic Piezoelectric Bimaterials," Int. J. Solids Struct., **40**, pp. 7499–7511.
[19] Li, Q., and Chen, Y. H., 2007, "Solution of a Semi-Permeable Interface Crack in Dissimilar Piezoelectric Materials," ASME J. Appl. Mech., **74**(4), pp. 833–844.
[20] Govorukha, V. B., Loboda, V. V., and Kamlah, M., 2006, "On the Influence of the Electric Permeability on an Interface Crack in a Piezoelectric Bimaterial Compound," Int. J. Solids Struct., **43**, pp. 1979–1990.
[21] Ou, Z. C., and Chen, Y. H., 2004, "Interface Crack Problem in Elastic Dielectric/Piezoelectric Bimaterials," Int. J. Fract., **130**, pp. 427–454.
[22] McMeeking, R. M., 1999, "Crack Tip Energy Release Rate for a Piezoelectric Compact Tension Specimen," Eng. Fract. Mech., **64**, pp. 217–244.
[23] McMeeking, R. M., 2001, "Towards a Fracture Mechanics for Brittle Piezoelectric and Dielectric Materials," Int. J. Fract., **108**, pp. 25–41.
[24] McMeeking, R. M., 2004, "The Energy Release Rate for a Griffith Crack in a Piezoelectric Material," Eng. Fract. Mech., **71**, pp. 1149–1163.
[25] Parton, V. Z., and Kudryavtsev, B. A., 1988, *Electromagnetoelasticity*, Gordon and Breach, New York.
[26] Hao, T. H., and Shen, Z. Y., 1994, "A New Electric Boundary Condition of Electric Fracture Mechanics and its Application," Eng. Fract. Mech., **47**, pp. 793–802.
[27] Dunn, M., 1994, "The Effects of Crack Face Boundary Conditions on the Fracture Mechanics of Piezoelectric Solids," Eng. Fract. Mech., **48**, pp. 25–39.
[28] Sosa, H., and Khutoryansky, N., 1996, "New Development Concerning Piezoelectric Materials With Defects," Int. J. Solids Struct., **33**, pp. 3399–3414.
[29] Xu, X. L., and Rajapakse, R. K. N. D., 2001, "On a Plane Crack in Piezoelectric Solids," Int. J. Solids Struct., **38**, pp. 7643–7658.
[30] Heyer, V., Schneider, G. A., Balke, H., Drescher, J., and Bahr, H. A., 1998, "A Fracture Criterion for Conducting Cracks in Homogeneously Poled Piezoelectric PZT-PIC 151 Ceramics," Acta Mater., **46**, pp. 6615–6622.
[31] Park, S. B., and Sun, C. T., 1995, "Fracture Criteria for Piezoelectric Ceramics," J. Am. Ceram. Soc., **78**, pp. 1475–1480.
[32] Park, S. B., and Sun, C. T., 1995, "Effect of Electric Fields on Fracture of Piezoelectric Ceramics," Int. J. Fract., **70**, pp. 203–216.
[33] Ting, T. C. T., 1986, "Explicit Solution and Invariance of the Singularities at an Interface Crack in Anisotropic Composites," Int. J. Solids Struct., **22**, pp. 965–983.
[34] Ting, T. C. T., 1990, "Interface Crack in Anisotropic Bimaterials," J. Mech. Phys. Solids, **38**, pp. 505–513.
[35] England, A. H., 1965, "A Crack Between Dissimilar Media," ASME J. Appl. Mech., **32**, pp. 400–402.
[36] Wu, K. C., 1990, "Stress Intensity Factors and Energy Release Rate for Interfacial Cracks Between Dissimilar Anisotropic Materials," ASME J. Appl. Mech., **57**, pp. 882–886.
[37] Qu, J. M., and Li, Q. Q., 1991, "Interfacial Dislocation and its Application to Interface Cracks in Anisotropic Bimaterials," J. Elast., **26**, pp. 169–195.
[38] Chen, Y. H., and Hasebe, N., 2005, "Current Understanding on Fracture Behaviors of Ferroelectric/Piezoelectric Materials," J. Intell. Mater. Syst. Struct., **16**, pp. 673–687.
[39] Barnett, D. M., and Lothe, J., 1975, "Dislocations and Line Charges in Anisotropic Piezoelectric Insulators," Phys. Status Solidi B, **67**, 105–111.
[40] Muskhelishvili, N. I., 1953, *Some Basic Problems of Mathematical Theory of Elasticity*, Noordhoof, Leyden.

A Time-Varying Stiffness Rotor Active Magnetic Bearings Under Combined Resonance

U. H. Hegazy[1]
Department of Mathematics,
Faculty of Science,
Al-Azhar University,
Gaza, Palestine
e-mail: uhijazy@yahoo.com

M. H. Eissa
Department of Engineering Mathematics,
Menoufia University,
Faculty of Electronic Engineering,
Menouf 32952, Egypt

Y. A. Amer
Department of Mathematics,
Faculty of Science,
Zagazig University,
Zagazig, Egypt

This paper is concerned with the nonlinear oscillations and dynamic behavior of a rigid disk-rotor supported by active magnetic bearings (AMB), without gyroscopic effects. The nonlinear equations of motion are derived considering a periodically time-varying stiffness. The method of multiple scales is applied to obtain four first-order differential equations that describe the modulation of the amplitudes and the phases of the vibrations in the horizontal and vertical directions. The stability and the steady-state response of the system at a combination resonance for various parameters are studied numerically, applying the frequency response function method. It is shown that the system exhibits many typical nonlinear behaviors, including multiple-valued solutions, jump phenomenon, hardening, and softening nonlinearity. A numerical simulation using a fourth-order Runge-Kutta algorithm is carried out, where different effects of the system parameters on the nonlinear response of the rotor are reported and compared to the results from the multiple scale analysis. Results are compared to available published work.
[DOI: 10.1115/1.2755118]

Keywords: active magnetic bearings, combined resonance, periodic time-varying stiffness

1 Introduction

Active magnetic bearings (AMBs) are being increasingly used in rotating machinery applications as an alternative to conventional mechanical bearings. The complicated nonlinear dynamics that characterize rotor-AMB systems emphasize the necessity to study their stability and nonlinearities to develop a better understanding of these systems. These nonlinearities necessarily introduce a whole range of phenomena that are not found in linear system [1], including jump phenomena, occurrence of multiple solutions, modulations, shift in natural frequencies, the generation of combination resonances, evidence of period-multiplying bifurcations, and chaotic motions.

In the literature, several investigations [2–6] have reported particular advantages of nonlinear systems with time-varying stiffness compared to those with constant stiffness. It is demonstrated that the stable region in the parametric space for variant stiffness systems is larger than the one for the invariant stiffness systems. Another advantage, from the control point of view, is that the stability and controllability in nonlinear systems with time-varying stiffness are better than those in nonlinear systems with the constant stiffness. Therefore, it is important for us to consider the influence of time-varying stiffness on the nonlinear dynamics of the rotor-AMB system, which will provide indications and directions of the design of the actuators and controllers in the rotor-AMB system.

There have been different studies conducted for the analysis of linear systems with time-varying stiffness. Typical mechanical examples of a piecewise linear system with time-varying coefficients appear in analyzing vibration of gear-pair systems [7–9]. The dynamic behavior of a piecewise nonlinear oscillator subject to a periodically time-varying, piecewise nonlinear stiffness is studied [10], with a comparison between time-varying and time-invariant systems. An adaptable vibration absorber with time-varying stiffness was designed and investigated [11], which showed that an optimization of the time-varying stiffness yielded improvements in root-mean-squared and peak displacements. It is well known that cracks may appear in rotating shafts due to the fatigue of the shaft material at sometime during the machine's life. There are a lot of papers dealing with rotordynamic systems in the presence of shaft cracks with time-varying stiffness. However, for cracks which periodically open and close in rotating shafts, known as "breathing" cracks, the formulation is much involved. The dynamic behavior of the Laval rotor or Jeffcott rotor was analyzed with the most simple crack model developed [12,13]. The simple model represents the breathing crack as a linear time-varying stiffness in the system, although for deeper cracks the nonlinearity of the stiffness plays an important role. The performance of optimal control methods on the response of a cracked rotor supported by AMBs was examined [14]. It was found that the introduction of a breathing crack alters the resulting vibration characteristics of the system and significantly complicates the design and analysis of the AMB controller. However, it was noted that in certain operating conditions, these vibration characteristics can be used to detect the presence of the crack. The vibrational response of a cracked rotating shaft subject to applied forces from AMBs was investigated [15,16]. A combination resonance was identified using the method of multiple scales and found that at this resonance, there is a proportional relationship between the amplitude of the response at the fundamental shaft frequency and the amplitude of the time-dependent stiffness introduced by the breathing crack. This relationship provides a mechanism to detect and quantify the presence of breathing cracks in rotating shafts.

One of the main challenging problems is to stabilize the rotor of the magnetic bearing systems and its controllability, which means the difficulty to get a stable spindle and controller. The model of a parametrically excited two-degree-of-freedom nonlinear system with quadratic and cubic nonlinearities was established [17] for the first time for a rotor-AMB system with eight-pole legs and time-varying stiffness. Furthermore, multipulse chaotic behavior was investigated [18], the asymptotic perturbation method was utilized [19], and the method of multiple scales was used [20] to

[1]Corresponding author.

Contributed by the Applied Mechanics Division of ASME for publication in the JOURNAL OF APPLIED MECHANICS. Manuscript received April 20, 2006; final manuscript received June 6, 2007; published online January 14, 2008. Review conducted by Marc P. Mignolet.

examine nonlinear oscillations and chaotic dynamics in the same rotor-AMB system. The results obtained indicate that the parametric excitation, or time-varying stiffness produced by the proportional derivative (PD) controller is considered to have significant influence on the responses of the rotor-AMB system.

The development of an AMB through theoretical and experimental investigations attracts a large number of scientists. The steady-state behavior of an auxiliary bearing/rotor system was studied [21]. A systematic control design for magnetic bearing systems subject to both input and state constraints was developed [22]. A simple nonlinear model for a radial AMB system was investigated, using a fully nonlinear force to displacement and the force to current characteristics. Important nonlinear phenomena was shown in Ref. [23]. The advantage of modern nonlinear dynamic tools is considered to study the steady-state response and stability of rotors with their auxiliary bearings [24]. Multiple solutions were obtained at resonance, and fractal boundaries separate stable and unstable regions. The approximate methods were used to examine the excitation parameters and geometric coupling to find the regimes of the nonlinear behavior of rotor motion in magnetic bearings, such as jumps and subharmonic motions [25]. Nonlinear oscillations and Hopf bifurcation in a rotor-AMB system were studied [26]. It was indicated that the steady-state solutions lose their stability at either saddle node bifurcation or Hopf bifurcation. Moreover, nonlinear oscillations, sadde-node, Hopf bifurcation, and the effects of control constants and unbalance on the nonlinear response of a rotor-AMB system were investigated at primary, internal, and superharmonic resonances [27,28]. The response of the system of a rigid rotor suspended by large air-gap AMBs was investigated subject to single parametric and harmonic excitation, using the perturbation method [29,30]. The effects of different parameters on the system behavior and stability were studied.

The present work examines the nonlinear response of a rotor-AMB system with quadratic and cubic nonlinearities and time-varying stiffness. The system is described by a two-degree-of-freedom nonlinear ordinary differential equations. The simultaneous primary and principal parametric resonance of the system is studied applying perturbation methods up to the second-order approximation. The frequency-response equation is numerically solved to obtain the steady-state solution, and the stability at the combined resonance case is determined by the eigenvalues of the corresponding Jacobian matrix. Rung–Kutta fourth-order method is applied to explore the nonlinear, dynamic behavior of the system. The time series solution of both modes of vibration is obtained at nonresonant case and combined resonance case. The effect of different parameters on the system behavior and its stability are investigated. Comparison to published work is reported.

2 Equations of Motion

The rotor-AMB system under investigation is a horizontal, uniform, symmetric shaft suspended by two identical radial AMBs at both ends. Each active magnetic bearing is assumed to have a stator of four pole pairs. The shaft is considered as one mass with two degrees of freedom in the horizontal and vertical directions, and assumed to be a rigid body in the AMBs. According to electromagnetic theory, the electromagnetic force F_i (shown in Fig. 1) produced by ith opposed pair of electromagnets is [17]

$$F_i = -\frac{1}{4}\mu_0 N^2 A\left[\frac{(I_0+I_i)^2}{(C_0+\delta_i)^2}-\frac{(I_0-I_i)^2}{(C_0-\delta_i)^2}\right]\cos\theta, \quad i=1,2,3,4 \tag{1}$$

where μ_0 is the permeability, A is the effective cross-sectional area of one electromagnet, N is the number of windings around the core, C_0 is the steady-state air gap between the stator and the shaft δ_i, and $i=1,2,3,4$ denote the radial displacements of the rotor in the i direction, θ is the corresponding half angle of the radial electromagnetic circuit, and 2α is the angle between the two radial

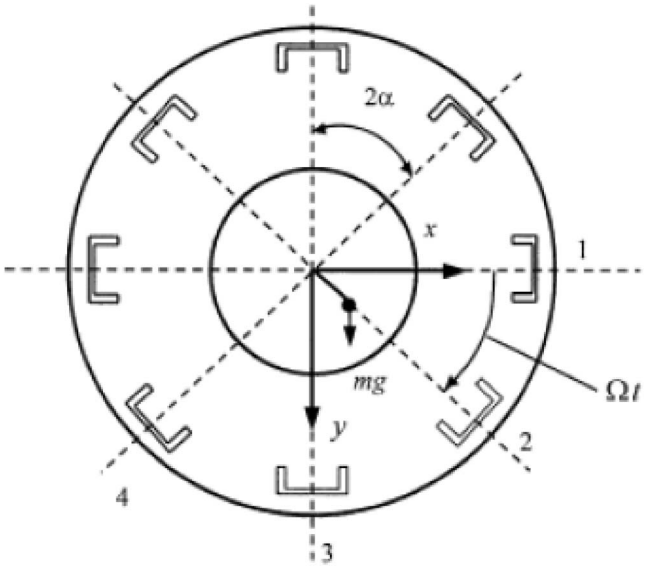

Fig. 1 Schematic for modeling magnetic forces acting on the rotor

electromagnets, I_0 is the bias current, and I_i is the control current in the i direction that is given by

$$I_1 = i_1, \quad I_i = i_0 + i_i, \quad i=2,3,4 \tag{2}$$

where i_0 is the static component of the control current i_i, and $i=1,2,3,4$ are the feedback components of the control current. Different control techniques have been used for magnetically supported rotors to achieve different goals, however the current proportional-derivative (PD) controller is considered

$$i_i = k_p\delta_i + k_d\dot{\delta}_i, \quad i=1,2,3,4 \tag{3}$$

where k_p is the proportional gain, k_d is the derivative gain, and $\dot{\delta}$ is the velocity in the direction of the displacement δ. Considering the Cartesian coordinates x and y, and knowing that $2\alpha=\pi/4$, the radial displacements of the rotor and the control current in the i direction can respectively be written as

$$\delta_1 = x, \quad I_1 = i_1$$

$$\delta_2 = x\cos\left(\frac{\pi}{4}\right)+y\sin\left(\frac{\pi}{4}\right), \quad I_2 = i_0+i_2$$

$$\delta_3 = y, \quad I_3 = i_0+i_3$$

$$\delta_4 = x\cos\left(\frac{3\pi}{4}\right)+y\sin\left(\frac{3\pi}{4}\right), \quad I_4 = i_0+i_4 \tag{4}$$

From the geometry of Fig. 1, the resultant electromagnetic forces in the horizontal and vertical directions are of the form

$$F_x = F_1 + F_2\cos\left(\frac{\pi}{4}\right)+F_4\cos\left(\frac{3\pi}{4}\right)$$

$$F_y = F_3 + F_2\sin\left(\frac{\pi}{4}\right)+F_4\sin\left(\frac{3\pi}{4}\right) \tag{5}$$

Substituting Eqs. (3) and (4) into Eq. (1), gives the resulting force as a nonlinear function of the control current and the rotor displacements x and y. For small vibration amplitudes, F_x and F_y are expanded about the (0,0) point using a Taylor series and is approximated up to third-order terms.

In our work, the proportional gain k_p is assumed to have the periodic from $k_p=k_0+k_1\cos\omega t+k_2\cos 2\omega t$, where ω is the fre-

quency of varying proportional gain. The resulting expressions for the electromagnetic force resultants in the horizontal and vertical directions are

$$F_x = -\bar{\alpha}_1 x - \bar{f}_{11} x \cos \omega t - \bar{f}_{12} x \cos 2\omega t + \bar{\alpha}_2 x^3 + \bar{\alpha}_3 x y^2 + \bar{\alpha}_4 x y + \bar{f}_{13} x y \cos \omega t + \bar{f}_{14} x y \cos 2\omega t + (\bar{\mu}_1 + 3\bar{\alpha}_5 x^2 + 3\bar{\alpha}_6 x\dot{x} + \bar{\alpha}_5 y^2 + 2\bar{\alpha}_6 y\dot{y})\dot{x} + (2\bar{\alpha}_5 x y + \bar{\alpha}_6 x\dot{y})\dot{y} + \bar{\alpha}_7 x\dot{y} + \bar{\alpha}_7 \dot{x} y \quad (6)$$

$$F_y = -\bar{\beta}_1 y - \bar{f}_{21} y \cos \omega t - \bar{f}_{22} y \cos 2\omega t + \bar{\beta}_2 y^3 + \bar{\beta}_3 x^2 y - \bar{\beta}_4 + \bar{\beta}_5 x^2 + \bar{\beta}_6 y^2 + \bar{f}_{23} x^2 \cos \omega t + \bar{f}_{24} x^2 \cos 2\omega t + \bar{f}_{25} y^2 \cos \omega t + \bar{f}_{26} y^2 \cos 2\omega t + (\bar{\mu}_1 + 3\bar{\alpha}_5 y^2 + 3\bar{\alpha}_6 y\dot{y} + \bar{\alpha}_5 x^2 + 2\bar{\alpha}_6 x\dot{x})\dot{y} + (2\bar{\alpha}_5 x y + \bar{\alpha}_6 \dot{x} y)\dot{x} + \bar{\alpha}_7 x\dot{x} + \bar{\beta}_7 y\dot{y} \quad (7)$$

where $a = (\mu_0 A N^2 I_0^2 / 4C_0^2) \cos \theta$ is the coefficient of the electromagnetic force.

$$\bar{\alpha}_1 = \frac{4a}{C_0 I_0}(2C_0 k_0 - 2I_0 - \gamma^2 I_0) \ (\mathrm{kg/s^2}),$$

$$\bar{\alpha}_2 = \frac{2a}{C_0^3 I_0^2}(6I_0^2 - 9C_0 I_0 k_0 + 3C_0^2 k_0^2 + 2\gamma^2 I_0^2) \ (\mathrm{kg/s^2 m^2})$$

$$\bar{\beta}_2 = \bar{\alpha}_3 = \bar{\beta}_3 = \frac{6a}{C_0^3 I_0^2}[C_0^2 k_0^2 - 3C_0 I_0 k_0 + 2(1+\gamma^2) I_0^2] \ (\mathrm{kg/s^2 m^2}),$$

$$\bar{\alpha}_4 = \frac{4\sqrt{2}\gamma a}{C_0^2 I_0}(2C_0 k_0 - 3I_0) \ (\mathrm{kg/s^2 m})$$

$$\bar{f}_{11} = \frac{8ak_1}{I_0}(\mathrm{kg/s^2}), \quad \bar{f}_{12} = \frac{8ak_2}{I_0} \ (\mathrm{kg/s^2}),$$

$$\bar{f}_{13} = \frac{8\sqrt{2}\gamma a k_1}{C_0 I_0} \ (\mathrm{kg/s^2 m}), \quad \bar{f}_{14} = \frac{8\sqrt{2}\gamma a k_2}{C_0 I_0} \ (\mathrm{kg/s^2 m})$$

$$\bar{\mu}_1 = -\frac{8ak_d}{I_0} \ (\mathrm{kg/m}), \quad \bar{\alpha}_5 = \frac{2ak_d}{C_0^2 I_0^2}(2C_0 k_0 - 3I_0) \ (\mathrm{kg/sm^2}),$$

$$\bar{\alpha}_6 = \frac{2ak_d^2}{C_0 I_0^2} \ (\mathrm{kg/m^2}), \quad \bar{\alpha}_7 = \frac{4\sqrt{2}\gamma a k_d}{C_0 I_0} \ (\mathrm{kg/sm})$$

$$\bar{\beta}_1 = \frac{8a}{C_0 I_0}[C_0 k_0 - (1+\gamma^2) I_0] \ (\mathrm{kg/s^2}), \quad \bar{\beta}_4 = 4a\gamma(1+\sqrt{2}),$$

$$\bar{\beta}_5 = \frac{2\sqrt{2}a\gamma}{C_0^2 I_0}(2C_0 k_0 - 3I_0) \ (\mathrm{kg/s^2 m})$$

$$\bar{\beta}_6 = \frac{2a\gamma}{C_0^2 I_0}[(2\sqrt{2}+4)C_0 k_0 - (3\sqrt{2}+6)I_0] \ (\mathrm{kg/s^2 m}),$$

$$\bar{\beta}_7 = \frac{4(2+\sqrt{2})a\gamma k_d}{C_0 I_0} \ (\mathrm{kg/sm})$$

$$\bar{f}_{21} = \frac{8ak_1}{I_0} \ (\mathrm{kg/s^2}), \quad \bar{f}_{22} = \frac{8ak_2}{I_0} \ (\mathrm{kg/s^2}),$$

$$\bar{f}_{23} = \frac{4\sqrt{2}\gamma a k_1}{C_0 I_0} \ (\mathrm{kg/s^2 m}), \quad \bar{f}_{24} = \frac{4\sqrt{2}\gamma a k_2}{C_0 I_0} \ (\mathrm{kg/s^2 m})$$

$$\bar{f}_{25} = \frac{4(\sqrt{2}+2)\gamma a k_1}{C_0 I_0} \ (\mathrm{kg/s^2 m}),$$

$$\bar{f}_{26} = \frac{4(\sqrt{2}+2)\gamma a k_2}{C_0 I_0} \ (\mathrm{kg/s^2 m}), \quad \gamma = \frac{i_0}{I_0} \quad (8)$$

In the work presented herein, the rotor is assumed to be a rigid body with two degrees of freedom, the weight of the rotor is considered. The equations of motion governing the unbalance of the model can be written as follows:

$$m\ddot{x} = F_x - c\dot{x} + me\Omega^2 \cos \Omega t, \quad m\ddot{y} = F_y - c\dot{y} + me\Omega^2 \sin \Omega t + mg \quad (9)$$

where m, e, c, and Ω are the mass, the eccentricity of the rotor, the damping coefficient, and the rotor speed, respectively. Setting $y = 0$ (steady-state motion) in Eq. (1), the weight of the rotor is therefore given by

$$mg = \frac{(1+\sqrt{2})\mu_0 A N^2}{4}\left[\frac{(I_0+i_0)^2}{C_0^2} - \frac{(I_0-i_0)^2}{C_0^2}\right]\cos\theta = 4(1+\sqrt{2})\frac{\mu_0 A N^2 I_0^2}{4C_0^2}\left(\frac{i_0}{I_0}\right)\cos\theta = 4(1+\sqrt{2})a\gamma \quad (10)$$

Substituting Eqs. (8), (9), and (12) into Eq. (11), introducing the nondimensional parameters $x = C_0\bar{x}$, $y = C_0\bar{y}$, $t = \sqrt{mC_0/a}\,\bar{t}$, $\omega = \sqrt{a/mC_0}\,\bar{\omega}$, $\Omega = \sqrt{a/mC_0}\,\bar{\Omega}$, letting $\bar{\mu} = c - \bar{\mu}_1$ and omitting the overbar for simplicity, the equations of motion governing the model in nondimensional form can be written as follows:

$$\ddot{x} + (\mu - 3\alpha_5 x^2 - 3\alpha_6 x\dot{x} - \alpha_5 y^2 - 2\alpha_6 y\dot{y})\dot{x} - (2\alpha_5 x y + \alpha_6 x\dot{y})\dot{y} + \omega_1^2 x - \alpha_7 \dot{x} y - \alpha_7 x\dot{y} - (\alpha_2 x^3 + \alpha_3 x y^2 + \alpha_4 x y) + (2x f_{11} - x y f_{13})\cos \omega t + (2x f_{12} - x y f_{14})\cos 2\omega t = F \cos \Omega t \quad (11)$$

$$\ddot{y} + (\mu - 3\alpha_5 y^2 - 3\alpha_6 \dot{y} y - \alpha_5 x^2 - 2\alpha_6 \dot{x} x)\dot{y} - (2\alpha_5 x y + \alpha_6 \dot{x} y)\dot{x} + \omega_2^2 y - \alpha_7 x\dot{x} - \beta_7 y\dot{y} - (\beta_2 y^3 + \beta_3 x^2 y + \beta_5 x^2 + \beta_6 y^2) - (x^2 f_{23} + y^2 f_{25} - 2y f_{21})\cos \omega t - (x^2 f_{24} + y^2 f_{26} - 2y f_{22})\cos 2\omega t = F \sin, \Omega t \quad (12)$$

where

$$\mu = \sqrt{\frac{C_0}{ma}}\bar{\mu}, \quad \alpha_5 = \sqrt{\frac{C_0^5}{ma}}\bar{\alpha}_5, \quad \alpha_6 = \frac{C_0^2}{m}\bar{\alpha}_6,$$

$$\alpha_7 = \sqrt{\frac{C_0^3}{ma}}\bar{\alpha}_7, \quad \beta_7 = \sqrt{\frac{C_0^3}{ma}}\bar{\beta}_7, \quad \omega_1^2 = \frac{C_0}{a}\bar{\alpha}_1$$

$$\alpha_2 = \frac{C_0^3}{a}\bar{\alpha}_2, \quad \alpha_3 = \frac{C_0^3}{a}\bar{\alpha}_3, \quad \alpha_4 = \frac{C_0^2}{a}\bar{\alpha}_4, \quad f_{11} = \frac{C_0}{2a}\bar{f}_{11},$$

$$f_{12} = \frac{C_0}{2a}\bar{f}_{12}, \quad f_{13} = \frac{C_0^2}{a}\bar{f}_{13}, \quad f_{14} = \frac{C_0^2}{a}\bar{f}_{14}$$

$$F = \frac{e\Omega^2}{C_0}, \quad \omega_2^2 = \frac{C_0}{a}\bar{\beta}_1, \quad \beta_2 = \frac{C_0^3}{a}\bar{\beta}_2, \quad \beta_3 = \frac{C_0^3}{a}\bar{\beta}_3,$$

$$\beta_5 = \frac{C_0^2}{a}\bar{\beta}_5, \quad \beta_6 = \frac{C_0^2}{a}\bar{\beta}_6, \quad f_{21} = \frac{C_0}{2a}\bar{f}_{21}$$

$$f_{22} = \frac{C_0}{2a}\bar{f}_{22}, \quad f_{23} = \frac{C_0^2}{a}\bar{f}_{23}, \quad f_{24} = \frac{C_0^2}{a}\bar{f}_{24}, \quad f_{25} = \frac{C_0^2}{a}\bar{f}_{25},$$

$$f_{26} = \frac{C_0^2}{a}\bar{f}_{26}$$

3 Perturbation Analysis

The method of multiple scales is applied to obtain a system of four first ordinary differential equations, which describe the time variation of the amplitudes and phases of the vibration in the horizontal and vertical directions. Introducing the small perturbation parameter ϵ, Eqs. (13) and (14) can be expressed as

$$\ddot{x} + \varepsilon(\mu - 3\alpha_5 x^2 - 3\alpha_6 x\dot{x} - \alpha_5 y^2 - 2\alpha_6 y\dot{y})\dot{x} - \varepsilon(2\alpha_5 xy + \alpha_6 x\dot{y})\dot{y} + \omega_1^2 x - \varepsilon\alpha_7 \dot{x}y - \varepsilon\alpha_7 x\dot{y} - \varepsilon(\alpha_2 x^3 + \alpha_3 xy^2 + \alpha_4 xy) + \varepsilon(2xf_{11} - xyf_{13})\cos\omega t + \varepsilon(2xf_{12} - xyf_{14})\cos 2\omega t = \varepsilon F\cos\Omega t \quad (13)$$

$$\ddot{y} + \varepsilon(\mu - 3\alpha_5 y^2 - 3\alpha_6 y\dot{y} - \alpha_5 x^2 - 2\alpha_6 x\dot{x})\dot{y} - \varepsilon(2\alpha_5 xy + \alpha_6 \dot{x}y)\dot{x} + \omega_2^2 y - \varepsilon\alpha_7 x\dot{x} - \varepsilon\beta_7 y\dot{y} - \varepsilon(\beta_2 y^3 + \beta_3 x^2 y + \beta_5 x^2 + \beta_6 y^2) - \varepsilon(x^2 f_{23} + y^2 f_{25} - 2yf_{21})\cos\omega t - \varepsilon(x^2 f_{24} + y^2 f_{26} - 2yf_{22})\cos 2\omega t = \varepsilon F\sin\Omega t \quad (14)$$

Equations (13) and (14) describe a two-degree-of-freedom nonlinear system with quadratic and cubic nonlinearities and time-varying stiffness. Approximate solutions of nonlinear Eqs. (15) and (16) are obtained using the method of multiple scales, assuming x, y in the form of

$$x(t,\varepsilon) = x_0(T_0,T_1) + \varepsilon x_1(T_0,T_1) + O(\varepsilon^2) \quad (15)$$

$$y(t,\varepsilon) = y_0(T_0,T_1) + \varepsilon y_1(T_0,T_1) + O(\varepsilon^2) \quad (16)$$

where $T_n = \varepsilon^n t$, T_0 is the fast time scale and T_1 is the slow time scale.

The time derivatives are

$$\frac{d}{dt} = D_0 + \varepsilon D_1, \quad \frac{d^2}{dt^2} = D_0^2 + 2\varepsilon D_0 D_1 + \varepsilon^2 D_1^2,$$

where

$$D_j = \frac{\partial}{\partial T_j}, \quad j = 0,1$$

Substituting for x, $\dot{x}$, $\ddot{x}$, and y, $\dot{y}$, $\ddot{y}$ in Eqs. (15) and (16), and then equating the coefficient of the same powers of ϵ gives

$$\varepsilon^0: (D_0^2 + \omega_1^2)x_0 = 0 \quad (17)$$

$$(D_0^2 + \omega_2^2)y_0 = 0 \quad (18)$$

$$\varepsilon^1: (D_0^2 + \omega_1^2)x_1 = -2D_0D_1x_0 - (\mu - 3\alpha_5 x_0^2 - 3\alpha_6 x_0 D_0 x_0 - \alpha_5 y_0^2 - 2\alpha_6 y_0 D_0 y_0)D_0 x_0 + (2\alpha_5 x_0 y_0 + \alpha_6 x_0 D_0 y_0)D_0 y_0 + \alpha_7 y_0 D_0 x_0 + \alpha_7 x_0 D_0 y_0 - 2f_{11}x_0\cos\omega t - 2f_{12}x_0\cos 2\omega t + \alpha_2 x_0^3 + \alpha_3 x_0 y_0^2 + \alpha_4 x_0 y_0 + f_{13}x_0 y_0\cos\omega t + f_{14}x_0 y_0\cos 2\omega t + F\cos\Omega t \quad (19)$$

$$(D_0^2 + \omega_2^2)y_1 = -2D_0D_1y_0 - (\mu - 3\alpha_5 y_0^2 - 3\alpha_6 y_0 D_0 y_0 - \alpha_5 x_0^2 - 2\alpha_6 x_0 D_0 x_0)D_0 y_0 + (2\alpha_5 x_0 y_0 + \alpha_6 y_0 D_0 x_0)D_0 x_0 + \alpha_7 x_0 D_0 x_0 + \beta_7 y_0 D_0 y_0 - 2f_{21}y_0\cos\omega t - 2f_{22}y_0\cos 2\omega t + \beta_2 y_0^3 + \beta_3 x_0^2 y_0 + \beta_5 x_0^2 + \beta_6 y_0^2 + (f_{23}x_0^2 + f_{25}y_0^2)\cos\omega t + (f_{24}x_0^2 + f_{26}y_0^2)\cos 2\omega t + F\sin\Omega t \quad (20)$$

The general solution of (17) and (18) can be expressed in the form

$$x_0(T_0,T_1) = A_0(T_1)\exp(i\omega_1 T_0) + \text{cc} \quad (21)$$

$$y_0(T_0,T_1) = B_0(T_1)\exp(i\omega_2 T_0) + \text{cc} \quad (22)$$

where A_0, B_0 are complex functions in T_1, which are defined in the next section (cc denotes a complex conjugate of the preceding term). Substituting (21) and (22) into (19) and (20), then the general solution of the resulted equations is given by

$$\begin{aligned} x_1(T_0,T_1) = {} & A_1(T_1)\exp(i\omega_1 T_0) + \frac{F}{2(\omega_1^2 - \Omega^2)}\exp(i\Omega T_0) - \frac{1}{8\omega_1^2}[(3i\alpha_5\omega_1 - 3\alpha_6\omega_1^2 + \alpha_2)A_0^3]\exp(3i\omega_1 T_0) + f_{11}A_0\left\{\frac{1}{\omega(2\omega_1+\omega)}\exp[i(\omega_1 + \omega)T_0] - \frac{1}{\omega(2\omega_1-\omega)}\exp[i(\omega_1-\omega)T_0]\right\} + f_{12}A_0\left[\frac{1}{4\omega(\omega_1+\omega)}\exp[i(\omega_1+2\omega)T_0] - \frac{1}{4\omega(\omega_1-\omega)}\exp[i(\omega_1-2\omega)T_0]\right] \\ & - \frac{1}{2}f_{13}A_0B_0\left\{\frac{1}{2(\omega_2+\omega)(\omega_2+2\omega_1+\omega)}\exp[i(\omega_1+\omega_2+\omega)T_0] + \frac{1}{2(\omega_2-\omega)(\omega_2+2\omega_1-\omega)}\exp[i(\omega_1+\omega_2-\omega)T_0]\right\} \\ & + \frac{1}{2}f_{13}A_0\bar{B}_0\left\{\frac{1}{2(\omega_2-\omega)(2\omega_1-\omega_2+\omega)}\exp[i(\omega_1-\omega_2+\omega)T_0] + \frac{1}{2(\omega_2+\omega)(2\omega_1-\omega_2-\omega)}\exp[i(\omega_1-\omega_2-\omega)T_0]\right\} \\ & - \frac{1}{2}f_{14}A_0B_0\left\{\frac{1}{2(\omega_2+2\omega)(\omega_2+2\omega_1+2\omega)}\exp[i(\omega_1+\omega_2+2\omega)T_0] + \frac{1}{2(\omega_2-2\omega)(\omega_2+2\omega_1-2\omega)}\exp[i(\omega_1+\omega_2-2\omega)T_0]\right\} + \frac{1}{2}f_{14}A_0\bar{B}_0\left\{\frac{1}{2(\omega_2-2\omega)(2\omega_1-\omega_2+2\omega)}\exp[i(\omega_1-\omega_2+2\omega)T_0] + \frac{1}{2(\omega_2+2\omega)(2\omega_1-\omega_2-2\omega)}\exp[i(\omega_1-\omega_2-2\omega)T_0]\right\} \\ & - \frac{1}{4\omega_2(\omega_1+\omega_2)}\{[i\alpha_5(\omega_1+2\omega_2) - \alpha_6\omega_2(\omega_2+2\omega_1) + \alpha_3]A_0B_0^2\}\exp[i(\omega_1+2\omega_2)T_0] \\ & + \frac{1}{4\omega_2(\omega_1-\omega_2)}\{[i\alpha_5(\omega_1-2\omega_2) + \alpha_6\omega_2(2\omega_1-\omega_2) + \alpha_3]A_0\bar{B}_0^2\}\exp[i(\omega_1-2\omega_2)T_0] - \frac{1}{\omega_2(2\omega_1+\omega_2)}\{[i\alpha_7(\omega_1+\omega_2) \\ & + \alpha_4]A_0B_0\}\exp[i(\omega_1+\omega_2)T_0] + \frac{1}{\omega_2(2\omega_1-\omega_2)}\{[i\alpha_7(\omega_1-\omega_2) + \alpha_4]A_0\bar{B}_0\}\exp[i(\omega_1-\omega_2)T_0] + \text{cc} \end{aligned} \quad (23)$$

$$y_1(T_0,T_1) = B_1(T_1)\exp(i\omega_2 T_0) - \frac{iF}{2(\omega_2^2-\Omega^2)}\exp(i\Omega T_0) - \frac{1}{8\omega_2^2}[(3i\alpha_5\omega_2 - 3\alpha_6\omega_2^2 + \beta_2)B_0^3]\exp(3i\omega_2 T_0) + \frac{1}{(\omega_2^2-4\omega_1^2)}[(\beta_5 - i\alpha_7\omega_1)A_0^2]\exp(2i\omega_1 T_0) + \frac{1}{(\omega_2^2-\omega^2)}[f_{23}A_0\bar{A}_0 + f_{25}B_0\bar{B}_0]\exp(i\omega T_0)\left[\frac{1}{(\omega_2^2-4\omega^2)}(f_{24}A_0\bar{A}_0 + f_{26}B_0\bar{B}_0)\right]\exp(2i\omega T_0) - \left[\frac{1}{3\omega_2^2}(i\alpha_7\omega_2+\beta_6)B_0^2\right]\exp(2i\omega_2 T_0) + f_{21}B_0\left\{\frac{1}{\omega(2\omega_2+\omega)}\exp[i(\omega_2+\omega)T_0] + \frac{1}{\omega(\omega-2\omega_2)}\exp[i(\omega_2-\omega)T_0]\right\} + f_{22}B_0\left\{\frac{1}{4\omega(\omega_2+\omega)}\exp[i(\omega_2+2\omega)T_0] + \frac{1}{4\omega(\omega-\omega_2)}\exp[i(\omega_2-2\omega)T_0]\right\} + \frac{1}{2}f_{23}A_0^2\left\{\frac{1}{\omega_2^2-(2\omega_1+\omega)^2}\exp[i(2\omega_1+\omega)T_0] + \frac{1}{\omega_2^2-(2\omega_1-\omega)^2}\exp[i(2\omega_1-\omega)T_0]\right\} - \frac{1}{2}f_{25}B_0^2\left\{\frac{1}{(\omega_2+\omega)(3\omega_2+\omega)}\exp[i(2\omega_2+\omega)T_0] + \frac{1}{(\omega-\omega_2)(\omega-3\omega_2)}\exp[i(2\omega_2-\omega)T_0]\right\} + \frac{1}{2}f_{24}A_0^2\left\{\frac{1}{\omega_2^2-4(\omega_1+\omega)^2}\exp[i(2\omega_1+2\omega)T_0] + \frac{1}{\omega_2^2-4(\omega_1-\omega)^2}\exp[i(2\omega_1-2\omega)T_0]\right\} - \frac{1}{2}f_{26}B_0^2\left\{\frac{1}{(2\omega+3\omega_2)(2\omega+\omega_2)}\exp[i(2\omega_2+2\omega)T_0] + \frac{1}{(2\omega-3\omega_2)(2\omega-\omega_2)}\exp[i(2\omega_2-2\omega)T_0]\right\} - \frac{1}{4\omega_1(\omega_2+\omega_1)}\{[i\alpha_5(\omega_2+2\omega_1) - \alpha_6\omega_1(\omega_1+2\omega_2)+\beta_3]B_0A_0^2\}\exp[i(\omega_2+2\omega_1)T_0] + \frac{1}{4\omega_1(\omega_2-\omega_1)}\{[i\alpha_5(\omega_2-2\omega_1) + \alpha_6\omega_1(2\omega_2-\omega_1)+\beta_3]B_0\bar{A}_0^2\}\exp[i(\omega_2-2\omega_1)T_0] + \frac{1}{\omega^2}(\beta_5A_0\bar{A}_0 + \beta_6B_0\bar{B}_0) + \text{cc} \tag{24}$$

where A_1, B_1 are complex functions in T_1, which are still arbitrary at this level of approximation. They can be determined by eliminating the secular terms at the next approximation.

4 Stability of the System

Here, we study simultaneous primary and principal parametric resonance as a combined resonance case, which has been confirmed numerically. Introducing the external detuning parameters σ_i, and $i=1,2,3,4$ as

$$\Omega = \omega_1 + \varepsilon\sigma_1, \quad \Omega = \omega_2 + \varepsilon\sigma_2 \tag{25}$$

$$\omega = 2\omega_1 + \varepsilon\sigma_3, \quad \omega = 2\omega_2 + \varepsilon\sigma_4 \tag{26}$$

and substituting (21), (22), (25), and (26) into (19) and (20), then eliminating secular terms yields the solvability conditions as

$$[(3i\alpha_5\omega_1 + 3\alpha_6\omega_1^2 + 3\alpha_2)A_0^2\bar{A} + (2i\alpha_5\omega_1 + 2\alpha_6\omega_2^2 + 2\alpha_3)A_0B_0\bar{B}_0 - 2i\omega_1A_0' - i\mu\omega_1A_0] + \{[i\alpha_5(2\omega_2-\omega_1) + \alpha_6\omega_2(2\omega_1-\omega_2) + \alpha_3]\bar{A}_0B_0^2\}\exp[i(\sigma_3-\sigma_4)T_1] - f_{11}\bar{A}_0\exp(i\sigma_3T_1) + \frac{1}{2}F\exp(i\sigma_1T_1) = 0 \tag{27}$$

$$[(3i\alpha_5\omega_2 + 3\alpha_6\omega_2^2 + 3\beta_2)B_0^2\bar{B} + (2i\alpha_5\omega_2 + 2\alpha_6\omega_1^2 + 2\beta_3)B_0A_0\bar{A}_0 - 2i\omega_2B_0' - i\mu\omega_2B_0] + \{[i\alpha_5(2\omega_1-\omega_2) + \alpha_6\omega_1(2\omega_2-\omega_1) + \beta_3]\bar{B}_0A_0^2\}\exp[i(\sigma_4-\sigma_3)T_1] - f_{21}\bar{B}_0\exp(i\sigma_4T_1) - \frac{i}{2}F\exp(i\sigma_2T_1) = 0 \tag{28}$$

Expressing A_0, B_0 in the polar forms $A_0=(1/2)a_1\exp(i\beta_1)$, $B_0=(1/2)a_2\exp(i\beta_2)$ and separating real and imaginary parts, we obtain the governing equations of the amplitudes α_i and phases γ_i

$$a_1' = -\frac{1}{2}\mu a_1 - (f_1\sin\gamma_3)a_1 + \frac{3}{8}\alpha_5a_1^3 + \frac{1}{4}\alpha_5a_1a_2^2 + (m_1\cos\gamma_4 + m_2\sin\gamma_4)a_1a_2^2 + F_1\sin\gamma_1 \tag{29}$$

$$a_1\gamma_1' = \sigma_1a_1 - (f_1\cos\gamma_3)a_1 + m_3a_1^3 + m_4a_1a_2^2 + (m_2\cos\gamma_4 - m_1\sin\gamma_4)a_1a_2^2 + F_1\cos\gamma_1 \tag{30}$$

$$a_2' = -\frac{1}{2}\mu a_2 - (f_2\sin\gamma_5)a_1 + \frac{3}{8}\alpha_5a_2^3 + \frac{1}{4}\alpha_5a_2a_1^2 + (n_1\cos\gamma_4 - n_2\sin\gamma_4)a_2a_1^2 - F_2\cos\gamma_2 \tag{31}$$

$$a_2\gamma_2' = \sigma_2a_2 - (f_2\sin\gamma_5)a_2 + n_3a_2^3 + n_4a_2a_1^2 + (n_2\cos\gamma_4 + n_1\sin\gamma_4)a_2a_1^2 + F_2\sin\gamma_2 \tag{32}$$

where $\gamma_i=\sigma_iT_1-2\beta_i$; $i=1,2$; $\gamma_3=\sigma_3T_1-2\beta_1$; $\gamma_4=(\sigma_3-\sigma_4)T_1+2(\beta_2-\beta_1)$; and $\gamma_5=\sigma_4T_1-2\beta_2$. $F_{1,2}$ and $f_{1,2}$ are defined in the Appendix. The steady-state solutions correspond to constant $a_{1,2}$ and $\gamma_{1,2}$; that is, $a_{1,2}'=0$ and $\gamma_{1,2}'=0$. Then Eqs. (29)–(32) can be reduced to a set of four nonlinear algebraic equations that is solved numerically to obtain the steady-state responses. We have following cases besides the trivial solution:

Case 1: $\mathbf{a_1=0}$ **and** $\mathbf{a_2\neq 0}$. Squaring Eqs. (31) and (32), then adding the squared results together gives the following frequency response equation:

$$\left(n_3^2 + \frac{9}{64}\alpha_5^2\right)a_2^6 + \left(2n_3\sigma_2 - \frac{3}{8}\mu\alpha_5\right)a_2^4 + \left(\sigma_2^2 + \frac{1}{4}\mu^2\right)a_2^2 - (F_2^2 + f_2^2a_2^2) = 0 \tag{33}$$

Case 2: $\mathbf{a_1\neq 0}$ **and** $\mathbf{a_2=0}$. Squaring Eqs. (29) and (30), then adding the squared results together gives the following frequency response equation:

$$\left(m_3^2+\frac{9}{64}\alpha_5^2\right)a_1^6+\left(2m_3\sigma_1-\frac{3}{8}\mu\alpha_5\right)a_1^4+\left(\sigma_1^2+\frac{1}{4}\mu^2\right)a_1^4 - (F_1-f_1a_1)^2=0 \tag{34}$$

Case 3: $\mathbf{a_1\neq 0}$ **and** $\mathbf{a_2\neq 0}$. Squaring Eqs. (29) and (30), then adding the squared results together, similarly to Eqs. (31) and (32) gives the following frequency response equations:

$$s_1a_1^6+s_2a_1^4+s_3a_1^2+s_4a_1-F_1^2=0 \tag{35}$$

$$s_5a_2^6+s_6a_2^4+s_7a_2^2+s_8a_2-F_2^2=0 \tag{36}$$

The coefficients s_i, $i=1,2,\ldots,8$ are defined in the Appendix.

To determine the stability of the fixed point solutions of Eqs. (29)–(32), we introduce the following forms:

$$A_0=\frac{1}{2}(p_1+iq_1)e^{i\sigma_1T_1},\quad B_0=\frac{1}{2}(p_2+iq_2)e^{i\sigma_2T_1}$$

$$\text{where}\quad p_{1,2},\ q_{1,2}\quad \text{are real}$$

Substitution the above forms of A_0 and B_0 into the linearized form of Eqs. (27) and (28), that is into

$$-i\omega_1(2A_0'+\mu A_0)-f_{11}\bar{A}_0\exp(i\sigma_3T_1)+\frac{1}{2}F\exp(i\sigma_1T_1)=0 \tag{37}$$

$$-i\omega_2(2B_0'+\mu B_0)-f_{21}\bar{B}_0\exp(i\sigma_4T_1)-\frac{i}{2}F\exp(i\sigma_2T_1)=0 \tag{38}$$

Then separating real and imaginary parts, gives the following equations:

$$p_1'+\frac{1}{2}\mu p_1-\Gamma_1q_1=0 \tag{39}$$

$$q_1'+\Gamma_1p_1+\Gamma_2q_1=0 \tag{40}$$

$$p_2'+\Gamma_4p_2+\Gamma_3q_2=0 \tag{41}$$

$$q_2'+\Gamma_3p_2+\frac{1}{2}\mu q_2=0 \tag{42}$$

where Γ_i $(i=1,2,3,4)$ are defined in the Appendix. The above system is a first-order autonomous ordinary differential equations; therefore, the stability of a particular fixed point with respect to an infinitesimal disturbance proportional to $e^{\lambda t}$ is determined by the eigenvalues of the Jacobian matrix of the right-hand sides of Eqs. (39)–(42). The zeros of the characteristic equation (the eigenequation) are given by

$$\lambda^4+l_1\lambda^3+l_2\lambda^2+l_3\lambda+l_4=0 \tag{43}$$

where l_i $(i=1,2,3,4)$ are constants, given in the Appendix. According to the Routh–Hurwitz criterion, the necessary and sufficient conditions for all the roots of Eq. (43) to possess negative real parts is that

$$l_1>0,\quad l_1l_2-l_3>0,\quad l_3(l_1l_2-l_3)-l_1^2l_4>0,\quad l_4>0$$

5 Frequency Response Curves

In this section, we investigate the steady-state response of the system at various parameters under combined resonance. The frequency response (Eqs. (33), (34), and (36)) are solved, and the stability is obtained from the eigenvalues of the corresponding Jacobian matrix. The results are shown in Figs. 2–4 as the amplitude $a_{1,2}$ against the detuning parameter $\sigma_{1,2}$, respectively. The stable and unstable branches of the plots are the solid and dashed lines, respectively.

5.1 Response Curves of Case 1: $\mathbf{a_1=0}$ **and** $\mathbf{a_2\neq 0}$**.** Considering Fig. 2(*a*) as basic case for comparison, it can be seen from Figs. 2(*a*) and 2(*b*) and Figs. 2(*a*)–2(*c*) that as the parametric excitation force amplitude f_{21} decreases and the natural frequency ω_2 increases, the branches of the response curves converge to each other, the region of unstable solutions and the amplitude decrease. The response curves in Fig. 2(*d*) are slowly converge to each other as the damping coefficient μ increases, while the amplitude decreases.

Figures 2(*e*)–2(*i*) illustrate the variation of steady-state amplitude as the nonlinear terms α_5, α_6, and β_2 are varied. Furthermore, Figs. 2(*g*) and 2(*h*) show several representative curves for the nonlinear term α_6. Comparing these curves shows that the nonlinearity effect (either hardening or softening nonlinearity) bends the frequency response curves to right when α_6 is negative and to left when α_6 is positive. This leads to a multivalued solutions and, hence, to jump phenomenon occurrence.

5.2 Response Curves of Case 2: $\mathbf{a_1\neq 0}$ **and** $\mathbf{a_2=0}$**.** The results of case 2 are shown in Fig. 3 as the amplitude a_1 against the detuning parameter σ_1. Figure 3(*c*) illustrates that as the external force amplitude F decreases the branches of the response curve converge to each other, the region of unstable solutions decreases. It can be seen from Figs. 3(*d*) and 3(*f*) that as the natural frequency ω_1 and nonlinear parameter α_2 increase, the steady-state amplitude decreases. Other parameters have similar effects as reported in case 1.

5.3 Response Curves of Case 3: $\mathbf{a_1\neq 0}$ **and** $\mathbf{a_2\neq 0}$**.** The curves in Fig. 4 are plotted as the amplitude a_2 against the detuning parameter σ_2. The nonlinear coefficient β_3, Fig. 4(*i*) and the natural frequency ω_1, Fig. 4(*j*), have trivial effect on the frequency response curves. Whereas other figures illustrate the same behavior of the remaining parameters, which was explained in two cases 1 and 2.

6 Numerical Solution

To verify analytic predictions, Eqs. (13) and (14) are numerically integrated using a fourth-order Runge–Kutta algorithm. A nonresonant system behavior is shown in Fig. 5. The behavior of the system under combined resonant conditions, Fig. 6, illustrates that the steady-state amplitude in the horizontal and vertical directions is increased to about 300% and 550%, respectively.

6.1 Effect of External Excitation Force Amplitude. Figure 7(*a*) illustrates that x and y amplitudes are monotonic, increasing functions in the external excitation amplitude force F.

6.2 Effect of Damping Coefficient. For positive values of the linear damping μ, the amplitudes of x and y are monotonic decreasing functions. This parameter can be used to control the system amplitude, as shown in Fig. 7(*b*), where more increase of μ leads to saturation phenomena. This behavior is in a good agreement with the response curves in Figs. 2(*d*), 3(*e*), and 4(*d*).

6.3 Effect of Nonlinear Coefficients. Figures 7(*c*)–7(*g*) show the effect of different nonlinear coefficients on the x and y amplitudes, which is summarized in Table 1.

Both effects of parameters in the frequency response results (Figs. 2–4) and the numerical solution results (Fig. 7) are in a good agreement.

6.4 Effect of Parametric Excitation Amplitudes. Figures 8(*a*) and 8(*e*) illustrate that as f_{11} and f_{21} increase, the x and y amplitudes increase, respectively, and more increase in f_{11} may lead to saturation phenomena. The results are in agreement with the frequency response curves in Figs. 3(*a*) and 3(*b*), 2(*a*) and 2(*b*), and 4(*a*) and 4(*b*), respectively. Table 2 summarizes the results in Fig. 8.

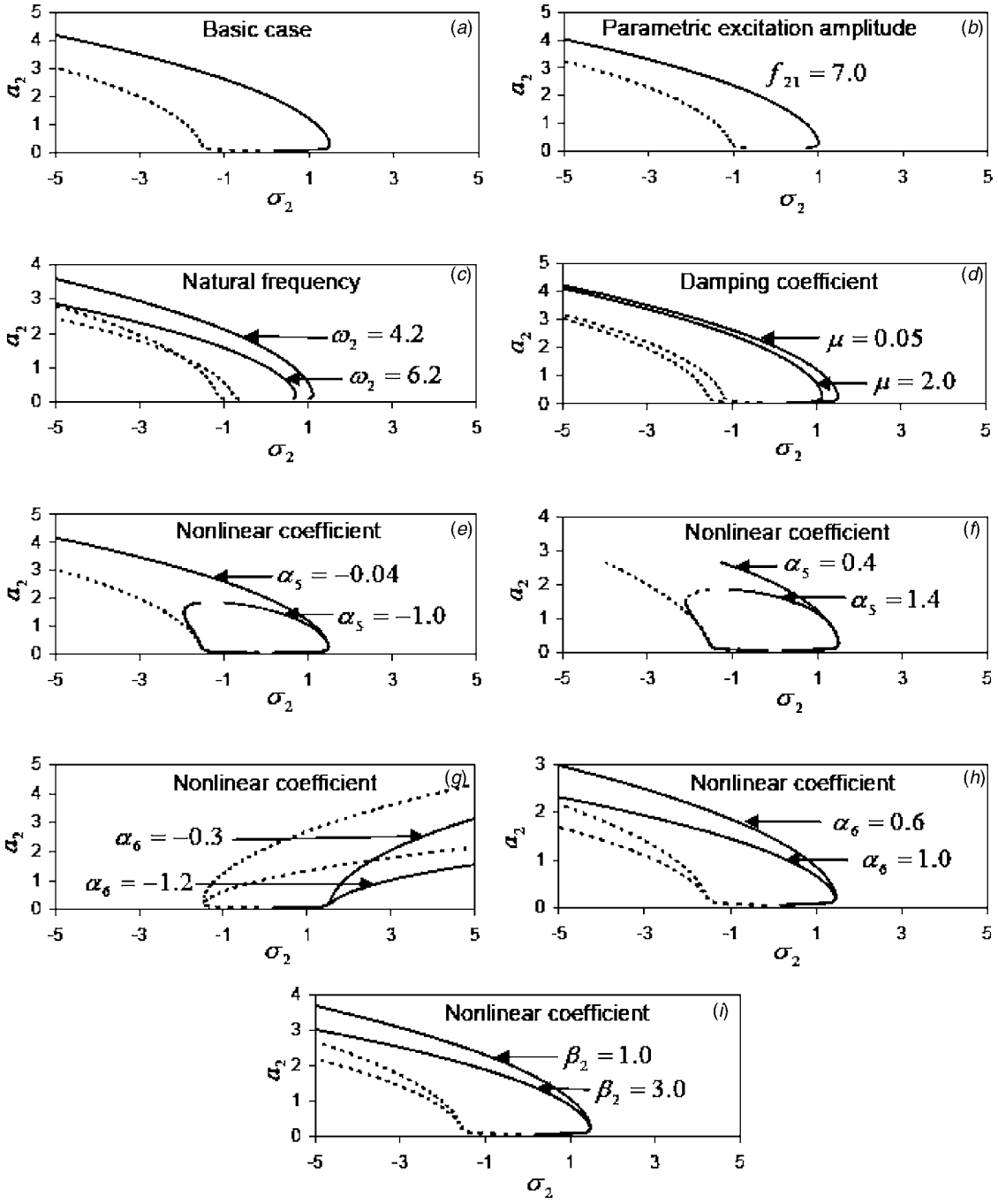

Fig. 2 Response curves of case 1: $a_1=0$, $a_2\neq 0$ at combined resonance condition. Basic case, physical coefficients: $F=0.5$, $f_{21}=10.0$, $\mu=0.5$, $\omega_2=3.2$, $\alpha_5=0.004$, $\alpha_6=0.3$, and $\beta_2=0.1$.

7 Conclusions

The nonlinear oscillations and dynamic response of a rigid rotor in active magnetic bearings (AMBs) with time-varying stiffness are investigated, and combined; simultaneous primary and principal parametric; and resonance condition has been considered. The method of multiple scales is applied to determine the combined resonance case and to study the system stability. The stability of the system and the effect of different parameters on system behavior have been studied under combined resonance, applying the frequency response equation method. They have been confirmed numerically. The presented results are expected to be useful in the design of rotor-AMB systems to suppress vibration. It may be concluded that:

1. The system has a variety of interesting phenomena such as multivalued solutions, jump, and softening and hardening nonlinearities, which is in agreement with Refs. [19,20].
2. The steady-state amplitudes in the horizontal and vertical directions are monotonic decreasing functions in the natural frequencies ω_1 and ω_2, respectively.
3. The steady-state amplitudes are monotonic increasing functions in the external force amplitude F, but more increase may lead to unstable behavior.
4. The steady-state amplitudes are monotonic decreasing functions in the damping coefficient μ, but more increase may lead to saturation phenomena.
5. The steady-state amplitude in the horizontal direction is a

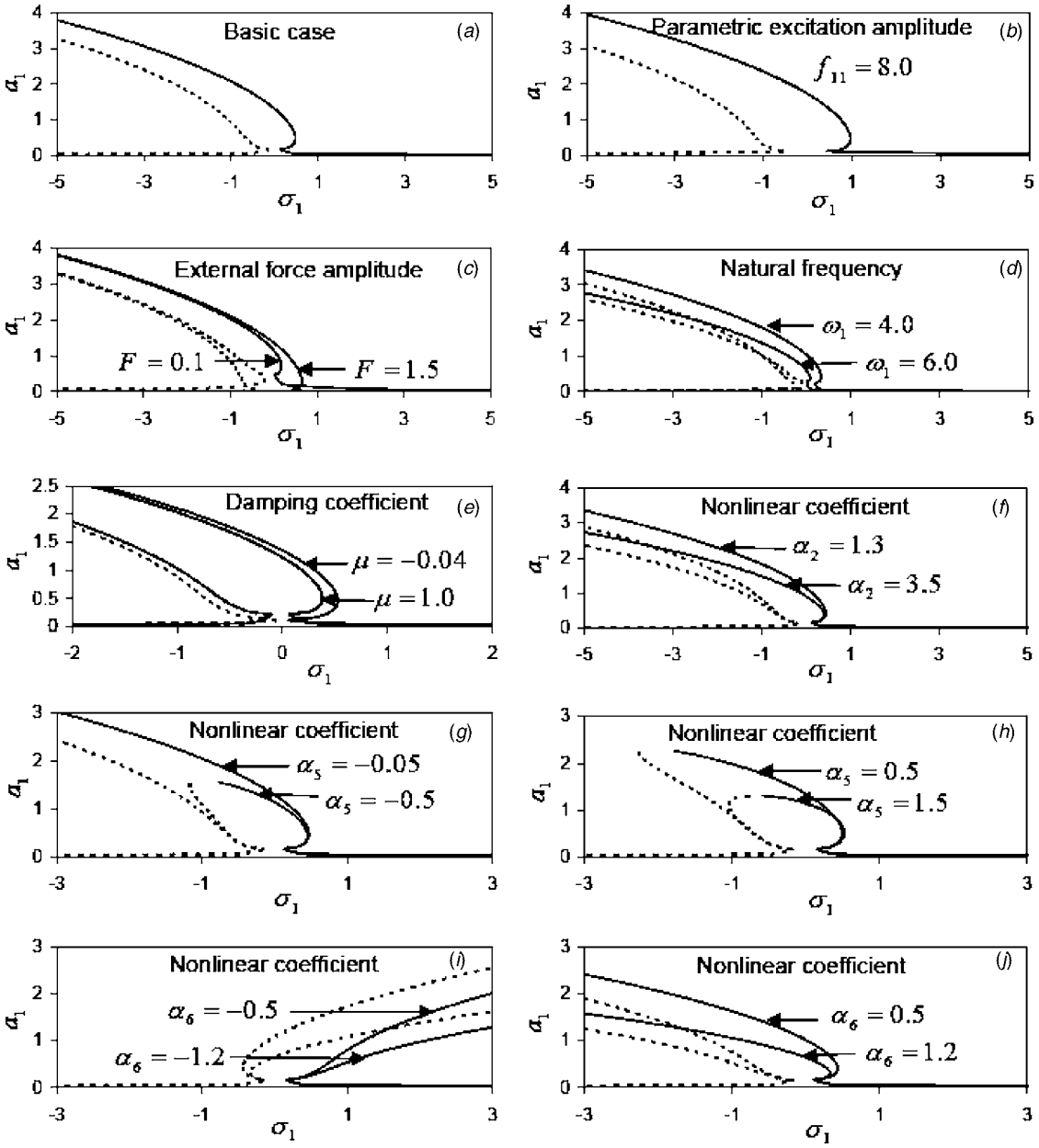

Fig. 3 Response curves of case 2: $a_1 \neq 0$, $a_2 = 0$ at combined resonance condition. Basic case, physical coefficients: $f_{11} = 5.0$, $\omega_1 = 3.2$, and $\alpha_2 = 0.3$, other coefficients have same values as those in Fig. 2(*a*).

monotonic increasing function in the nonlinear parameters α_3, α_4, β_2, β_3, whereas it is a monotonic decreasing function in the nonlinear parameters α_2.

6. The steady-state amplitude in the vertical direction is a monotonic increasing function in the nonlinear parameter β_5, whereas it is a monotonic decreasing function in the nonlinear parameters α_3, β_2, β_3, β_6.
7. The steady-state amplitude for the first mode is a monotonic increasing function in the parametric excitation amplitudes f_{11} and f_{13}, whereas it is a monotonic decreasing function in f_{12} and f_{14}. Further increase may lead to saturation phenomena.
8. For the second mode, the steady-state amplitude is a monotonic increasing function in the parametric excitation amplitudes f_{21}, f_{24}, f_{25}, whereas it is a monotonic decreasing function in f_{22}, f_{23}, and f_{26}.
9. The effect of parametric excitation is varied according to the type of resonance condition. For example, when simultaneous primary resonance is considered [20], the parametric excitation affects the shape of chaotic motion. Whereas, a combination resonance condition is sensitive to the magnitude of parametric excitation, which is in agreement with Refs. [15,16].
10. Stability and controllability in rotor-AMB systems with time-varying stiffness are better than those in the rotor-AMB systems with the constant stiffness [29,30].

Appendix

The coefficients of Eqs. (29)–(32)

$$m_1 = \frac{\alpha_5}{8\omega_1}(2\omega_2 - \omega_1), \quad m_2 = \frac{1}{8\omega_1}[\alpha_3 + \alpha_6\omega_2(2\omega_1 - \omega_2)],$$

$$m_3 = \frac{3}{8\omega_1}(\alpha_2 + \alpha_6\omega_1^2)$$

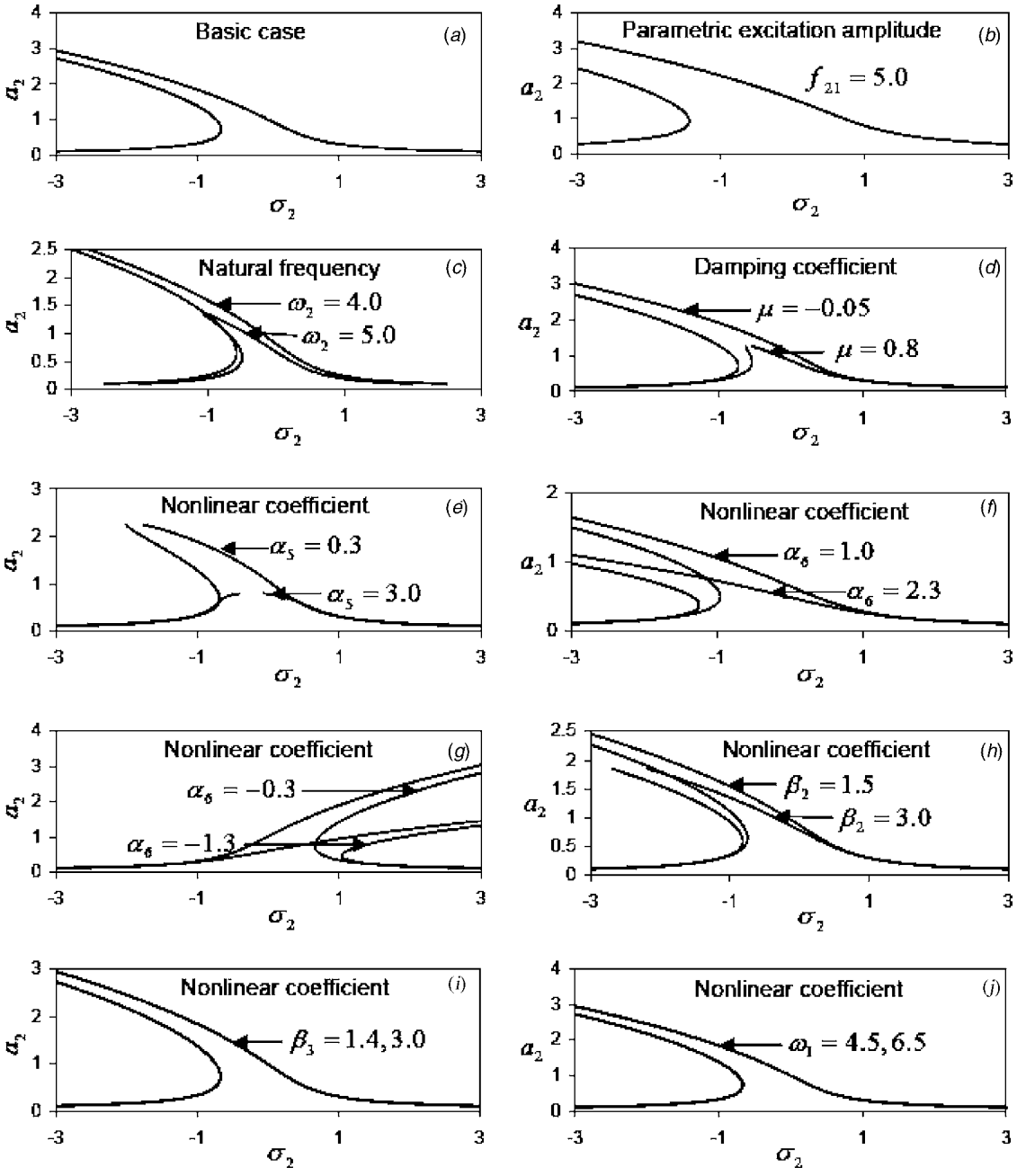

Fig. 4 Response curves of case 3: $a_1 \neq 0$, $a_2 \neq 0$ at combined resonance condition. Basic case, physical coefficients: $f_{21}=2.0$, $\omega_2=\omega_1=3.2$, and $\beta_2=0.1$, other coefficients have same values as those in Fig. 2(*a*).

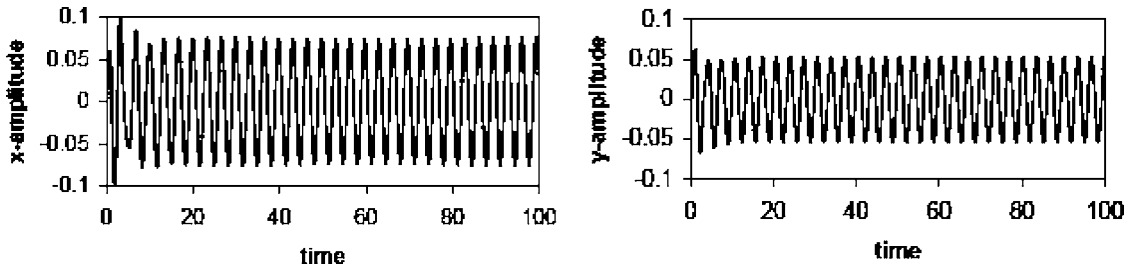

Fig. 5 Nonresonant time response solution, physical coefficients are: $F=0.5$, $\mu=0.5$, $\Omega=1.9$, $\omega=3.9$, $\omega_1=3.2$, $\omega_2=3.6$, f_{1i}, $i=1,2,3,4$ are 0.1, 0.1, 0.3, 0.4; f_{2i}, $i=1,2,\ldots,6$ are 0.1, 0.1, 0.15, 0.2, 0.25, 0.35; α_i, $i=2,3,\ldots,7$ are 0.3, 0.1, 0.01, 0.004, 0.3, 0.02, and β_i, $i=2,3,5,6,7$ are 0.1, 0.1, 0.01, 0.05, 0.01, respectively

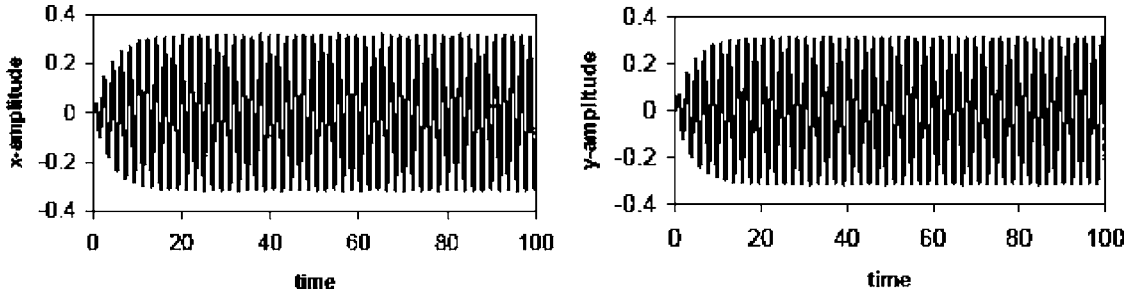

Fig. 6 Combined resonance solution: $\Omega=\omega_2=\omega_1$ and $\omega=2\omega_1$

$$m_4=\frac{1}{4\omega_1}(\alpha_3+\alpha_6\omega_2^2),\quad f_1=\frac{f_{11}}{2\omega_1},\quad F_1=\frac{F}{2\omega_1}$$

$$n_3=\frac{3}{8\omega_2}(\beta_2+\alpha_6\omega_2^2)$$

$$n_1=\frac{\alpha_5}{8\omega_2}(2\omega_1-\omega_2),\quad n_2=\frac{1}{8\omega_2}[\beta_3+\alpha_6\omega_1(2\omega_2-\omega_1)],$$

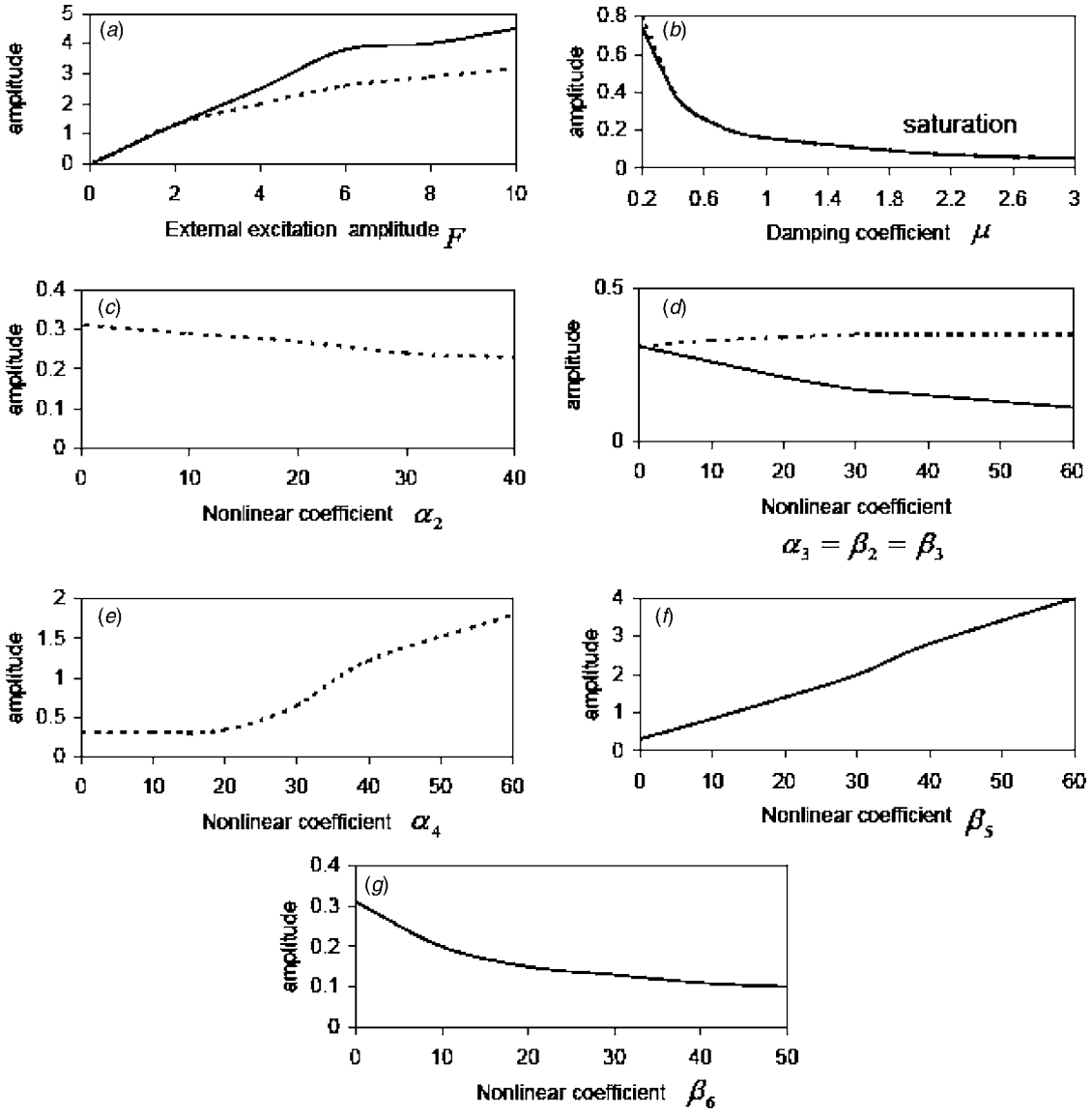

Fig. 7 Numerical solution under various values of the system parameters at combined resonance condition (dashed line is the *x* amplitude, solid line is the *y* amplitude)

Table 1 Effect of nonlinear coefficients. MI and MD denote that the amplitude is monotonic increasing, decreasing function in the nonlinear term, respectively.

Nonlinear parameter	x amplitude (dashed line)	y amplitude (solid line)
α_2, Fig. 7(c)	MD	Trivial effect
$\alpha_3=\beta_2=\beta_3$, Fig. 7(d)	MI	MD
α_4, Fig. 7(e)	MI	Trivial effect
β_5, Fig. 7(f)	Trivial effect	MI
β_6, Fig. 7(g)	Trivial effect	MD

Table 2 Effect of parametric excitation amplitudes

Parametric excitation	x amplitude	y amplitude
f_{12}; f_{13}; Figs. 8(a) and 8(c)	MI	Trivial effect
f_{12}, f_{14}; Figs. 8(b) and 8(d)	MD	Trivial effect
f_{21}, f_{24}, f_{25}; Figs. 8(e), 8(h), and 8(i)	Trivial effect	MI
f_{22}, f_{23}, f_{26}; Figs. 8(f), 8(g), and 8(j)	Trivial effect	MD

$$n_4 = \frac{1}{4\omega_2}(\beta_3 + \alpha_6\omega_1^2), \quad f_2 = \frac{f_{21}}{2\omega_2}, \quad F_2 = \frac{F}{2\omega_2}$$

The coefficients of Eq. (35)

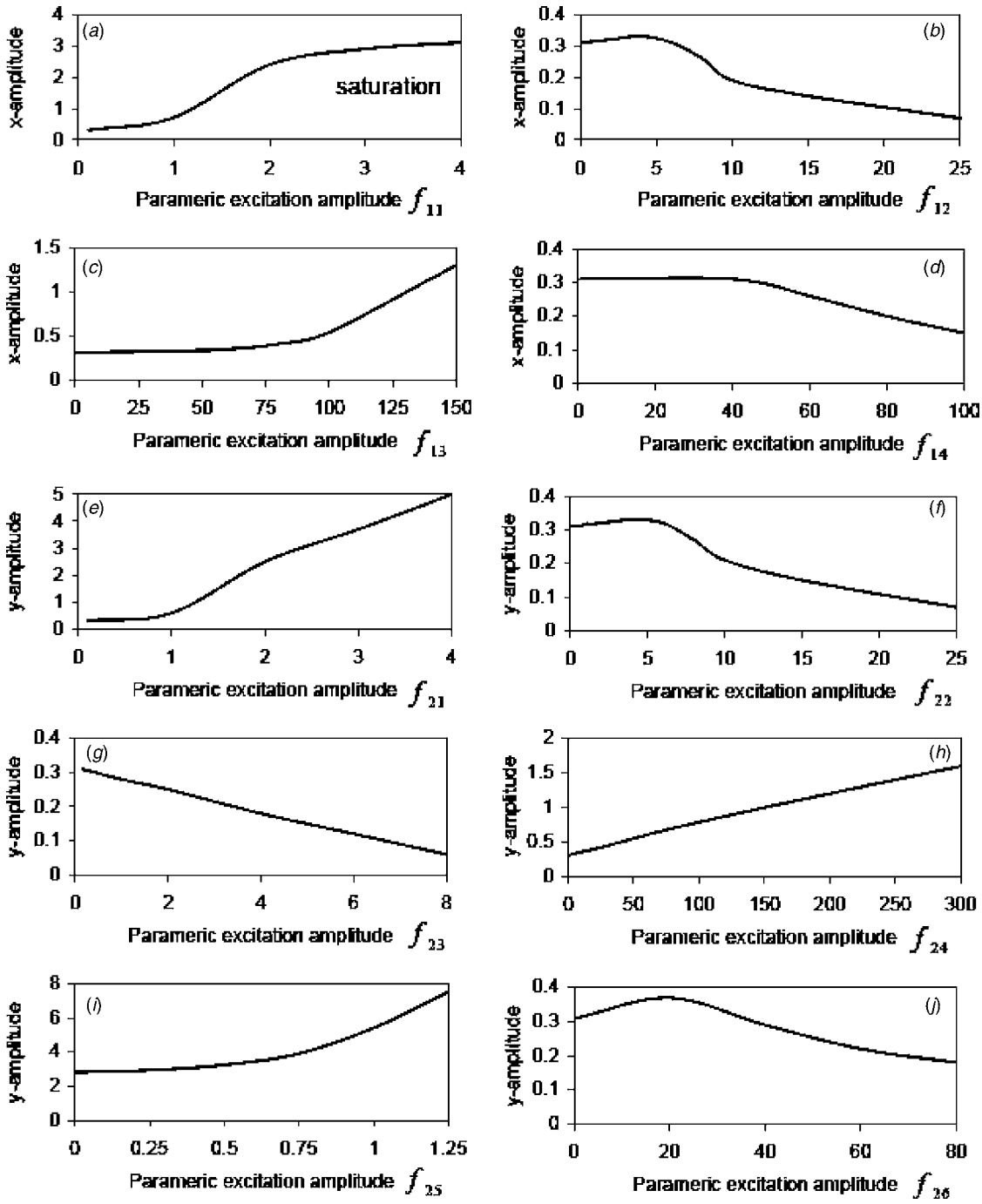

Fig. 8 Effect of parametric excitation amplitudes at combined resonance case

$$s_1 = \left(m_3^2 + \frac{9}{64}\alpha_5^2\right), \quad s_2 = \left[2m_3\sigma_1 - \frac{3}{8}\mu\alpha_5 + \left(2m_3m_4 + \frac{3}{16}\alpha_5^2\right)a_2^2\right]$$

$$s_3 = \left[\sigma_1^2 + \frac{1}{4}\mu^2 - f_1^2 + \left(m_4^2 - m_1^2 - m_2^2 + \frac{1}{16}\alpha_5^2\right)a_2^4 + (2m_4\sigma_1 + 2f_1m_2 - \mu\alpha_5)a_2^2\right]$$

$$s_4 = (-2f_1F_1 + 2F_1m_2a_2^2)$$

The coefficients of Eq. (36)

$$s_5 = \left(n_3^2 + \frac{9}{64}\alpha_5^2\right), \quad s_6 = \left[2n_3\sigma_2 - \frac{3}{8}\mu\alpha_5 + \left(2n_3n_4 + \frac{3}{16}\alpha_5^2\right)a_1^2\right]$$

$$s_7 = \left[\sigma_2^2 + \frac{1}{4}\mu^2 - f_2^2 + \left(n_4^2 - n_1^2 - n_2^2 + \frac{1}{16}\alpha_5^2\right)a_1^4 + (2n_4\sigma_2 - 2f_2n_2 - \mu\alpha_5)a_1^2\right], \quad s_8 = (-2F_2n_1a_1^2)$$

The coefficients of Eqs. (39)–(42)

$$\Gamma_1 = \left(\sigma_1 - \frac{f_{11}}{2\omega_1}\right), \quad \Gamma_2 = \left(\frac{1}{2}\mu + \frac{F}{2\omega_1 q_1}\right),$$

$$\Gamma_3 = \left(\sigma_2 - \frac{f_{21}}{2\omega_2}\right), \quad \Gamma_4 = \left(\frac{1}{2}\mu + \frac{F}{2\omega_2 p_1}\right)$$

The coefficients of Eq. (43)

$$l_1 = (\Gamma_2 + \Gamma_4), \quad l_2 = \left(\Gamma_1^2 - \Gamma_3^2 + \Gamma_2\Gamma_4 - \frac{1}{4}\mu^2\right)$$

$$l_3 = \left[\Gamma_1^2\left(\frac{1}{2}\mu + \Gamma_4\right) + \Gamma_3^2\left(\frac{1}{2}\mu - \Gamma_2\right) - \frac{1}{4}\mu^2(\Gamma_2 + \Gamma_4)\right]$$

$$l_4 = \frac{1}{2}\mu(\Gamma_3^2\Gamma_2 + \Gamma_1^2\Gamma_4) - \frac{1}{4}\mu^2\Gamma_2\Gamma_4 - \Gamma_1^2\Gamma_3^2$$

References

[1] El Naschie, M. S., 1992, *Stress Stability and Chaos in Structural Engineering: An Energy Approach*, McGraw-Hill, Singapore.

[2] Nayfeh, A. H., and Mook, D. T., 1995, *Nonlinear Oscillations*, Wiley, New York.

[3] Bajaj, A. K., 1987, "Bifurcations in a Parametrically Excited Nonlinear Oscillator," Int. J. Non-Linear Mech., **22**, pp. 47–59.

[4] Zhang, W., and Ye, M., 1994, "Local and Global Bifurcations of Valve Mechanism," Nonlinear Dyn., **6**, pp. 301–316.

[5] Ng, L., and Rand, R., 2002, "Nonlinear Effects on Coexistence Phenomenon in Parametric Excitation," Nonlinear Dyn., **33**, pp. 73–89.

[6] Wang, K. W., and Lai, J. S., 1996, "Parametric Control of Structural Vibrations via Adaptable Stiffness Dynamic Absorbers," ASME J. Vibr. Acoust., **118**, pp. 41–47.

[7] Kahraman, A., and Blankenship, G. W., 1997, "Experiments on Nonlinear Dynamic Behavior of an Oscillator With Clearance and Periodically Time-Varying Parameters," ASME J. Appl. Mech., **64**, pp. 217–226.

[8] Kahraman, A., and Blankenship, G. W., 1996, "Interactions Between Commensurate Parametric and Forcing Excitations in a System With Clearance," J. Sound Vib., **194**, pp. 317–336.

[9] Padmanabhan, C., and Singh, R., 1995, "Influence of a Mean Load on the Response of a Forced Nonlinear Hill's Oscillator," ASME Design Engineering, Technical Conf., Boston.

[10] Ma, O., and Kahraman, A., 2005, "Period-One Motions of a Mechanical Oscillator With Periodically Time-Varying, Piecewise-Nonlinear Stiffness," J. Sound Vib., **284**, pp. 893–914.

[11] Walsh, P. L., and Lamancusa, J. S., 1992, "A Variable Stiffness Vibration Absorber for Minimization of Transient Vibrations," J. Sound Vib., **152**(2), pp. 195–211.

[12] Gash, R., 1976, "The Dynamic Behavior of a Simple Rotor With Cross-Sectional Crack," *Vibrations in Rotating Machinery*, Institution of Mechanical Engineers, Cambridge, UK, pp. 123–128.

[13] Gash, R., 1993, "A Survey of the Dynamic Behavior of a Simple Rotating Shaft With a Transverse Crack," J. Sound Vib., **160**(2), pp. 313–332.

[14] Zhu, C., Robb, D. A., and Ewins, D. J., 2003, "The Dynamics of a Cracked Rotor With an Active Magnetic Bearing," J. Sound Vib., **265**(3), pp. 469–487.

[15] Quinn, D. D., Mani, G., Kasadra, M. E. F., Bash, T., Inman, D. J., and Krik, R. G., 2005, "Damage Detection of a Rotating Crack Shaft Using an Active Magnetic Bearing as a Force Actuator-Analysis and Experimental Verification," Mechatronics, **10**(6), pp. 640–646.

[16] Mani, G., Quin, D. D., and Kasadra, M., 2006, "Active Health Monitoring in a Rotating Crack Shaft Using Active Magnetic Bearings as Force Actuators," J. Sound Vib., **294**(3), pp. 454–465.

[17] Zhang, W., and Zu, J. W., 2003, "Nonlinear Dynamic Analysis for a Rotor-Active Magnetic Bearing System With Time-Varying Stiffness—Part I: Formulation and Local Bifurcation," *Proc. of 2003 ASME International Mechanical Engineering Congress and Exposition*, Washington, DC, Nov. 16–21, New York, ASME, New York, pp. 631–640.

[18] Zhang, W., Yao, M. H., and Zhan, X. P., 2005, "Multi-Pulse Chaotic Motions of a Rotor-Active Magnetic Bearing System With Time-Varying Stiffness," Chaos, Solitons Fractals, **27**, pp. 175–186.

[19] Zhang, W., and Zhan, X. P., 2005, "Periodic and Chaotic Motions of a Rotor-Active Magnetic Bearing With Quadratic and Cubic Terms and Time-Varying Stiffness," Nonlinear Dyn., **41**, pp. 331–359.

[20] Amer, Y. A., and Hegazy, U. H., 2007, "Resonance Behavior of a Rotor-Active Magnetic Bearing With Time-Varying Stiffness," Chaos, Solitons Fractals, **34**, pp. 1328–1345.

[21] Xie, H., and Folwers, G. T., 1994, "Steady-State Dynamic Behavior of an Auxiliary Bearing Supported Rotor System," ASME Winter Annual Meeting, Nov., Chicago, pp. 13–18.

[22] Hu, T., Lin, Z., Jiang, W., and Allaire, P. E., 2005, "Constrained Control Design for Magnetic Bearing Systems," ASME J. Dyn. Syst., Meas., Control, **127**, pp. 601–616.

[23] Steinschaden, N., and Springer, H., 1999, "Some Nonlinear Effects of Magnetic Bearings," *Proc. 1999 ASME Design Engineering Technical Conferences*, Sept. 12–15, Las Vegas, ASME, New York, pp. 1–9.

[24] Wang, X., and Noah, S., 1998, "Nonlinear Dynamics of a Magnetically Supported Rotor on Safety Auxiliary Bearing," ASME J. Vibr. Acoust., **120**, pp. 596–606.

[25] Chinta, M., and Palazzolo, A. B., 1998, "Stability and Bifurcation of Rotor Motion in a Magnetic Bearing," J. Sound Vib., **214**, pp. 793–803.

[26] Ji, J. C., Yu, L., and Leung, A. Y. T., 2000, "Bifurcation Behavior of a Rotor Supported by Active Magnetic Bearings," J. Sound Vib., **235**, pp. 133–151.

[27] Ji, J. C., and Hansen, C. H., 2001, "Non-linear Oscillations of a Rotor in Active Magnetic Bearings," J. Sound Vib., **240**, pp. 599–612.

[28] Ji, J. C., and Leung, A. Y. T., 2003, "Non-Linear Oscillations of a Rotor-Magnetic Bearing System Under Superharmonic Resonance Conditions," Int. J. Non-Linear Mech., **38**, pp. 829–835.

[29] Amer, Y. A., Eissa, M. H., Hegazy, U. H., and Sabbah, A. S., 2006, "Dynamic Behavior of an AMB/ Supported Rotor Subject to Parametric Excitation," ASME J. Vibr. Acoust., **128**, pp. 646–652.

[30] Eissa, M. H., Hegazy, U. H., and Amer, Y. A., 2007, "Dynamic Behavior of an AMB Supported Rotor Subject to Harmonic Excitation," Appl. Math. Model. (in press).

Response of a Helix Made of a Fractional Viscoelastic Material

M. Ostoja-Starzewski
Fellow ASME
Department of Mechanical Science and Engineering,
University of Illinois at Urbana-Champaign,
Urbana, IL 61801

H. Shahsavari
Department of Mechanical Engineering,
Massachusetts Institute of Technology,
Cambridge, MA 02139

Under investigation is the effective response of a helical strand (helix) made of a viscoelastic material governed by a constitutive relation with fractional-order (i.e., not integer-order) derivatives. The relation involves a 5-parameter model, which is well known to represent a real response much better than the conventional, integer-order models with the same number of parameters. We employ the correspondence principle of viscoelasticity to pass from the level of the strand's material to that of an effective, coupled axial-torsional response of the helix. The resulting fractional-order differential equation is more complex (i.e., it involves higher derivatives) than the constitutive equation governing the material per se. Also, the use of a fractional-order model results in more complexity of the helix' effective viscoelastic response than does an integer-order model with the same number of parameters. It is shown that shear deformations are more important than dilatational deformations. Lastly, a standard relaxation test is studied and an analytic solution is derived. [DOI: 10.1115/1.2745401]

1 Introduction

The term helix means a single helical strand or a bundle of such strands. In the latter case, such as a wire rope, there is a straight strand at the core, surrounded by several outer helical strands, Fig. 1. In the case of a bundle without the core strand, the outer helical strands are assumed to not collapse, and to not interact on their contact surfaces. Effectively, the loads they carry add up as in a parallel system.

The effective constitutive equations of the helix involve coupling of axial with torsional responses (e.g. [1])

$$\sigma = C_1\varepsilon + C_2\tau$$

$$\mu = C_3\varepsilon + C_4\tau \tag{1}$$

Here σ is the axial stress and μ is the couple-stress (moment per unit area), while ε and τ are the axial strain and angle of twist per unit length respectively. $C_1 \cdots C_4$ are the constitutive coefficients dependent on the material properties and the 3D geometry of the helix. They have been explicitly, and to a good approximation, derived analytically under certain assumptions in [2].

As is well known, the differential equation governing a conventional viscoelastic material (i being an integer, e.g. [3–5]) is

$$\sigma + \sum_{i=1}^{I} P_i \frac{d^i\sigma}{dt^i} = E_0\left(\varepsilon + \sum_{j=1}^{J} Q_j \frac{d^j\varepsilon}{dt^j}\right) \tag{2}$$

A more effective fit to experimental data with n and m being significantly smaller than any given I and J is offered by replacing the integer-order derivatives with fractional-order derivatives [6]

$$\sigma + \sum_{i=1}^{n} P_{\alpha_i} D^{\alpha_i}\sigma = E_0\left(\varepsilon + \sum_{j=1}^{m} Q_{\beta_j} D^{\beta_j}\varepsilon\right) \tag{3}$$

Let us note here that the model of type (3)—henceforth, called a *fractional viscoelastic* material—is more consistent with the molecular theories and experiments [4]. In (2) and (3), σ and ε stand for stress and strain, while P and Q are the relaxation and retardation times, respectively, and E_0 is the relaxed magnitude of elastic modulus (prolonged modulus of elasticity). Also, $\alpha_i (i = 1, 2, \ldots, n)$ and $\beta_j (j = 1, 2, \ldots, m)$ are the fractional parameters $(0 < \alpha_i, \beta_j < 1)$ and $D^{\alpha_i}\sigma$ and $D^{\beta_j}\varepsilon$ are the fractional-order derivatives defined as (see e.g. [7])

$$D^\alpha f(t) = \frac{\partial^\alpha}{\partial t^\alpha} f(t) = \frac{1}{\Gamma(1-\alpha)} \frac{\partial}{\partial t} \int_0^t \frac{f(\tau)}{(t-\tau)^\alpha} d\tau \quad 0 < \alpha < 1 \tag{4}$$

where Γ is the gamma function.

The integrodifferential operator in (4) is of a Caputo-type [6]. It has a fading memory because of the convolution with $t^{-\alpha}$. Here, if $\alpha = 1$ we say that the system has a perfect memory and if $\alpha = 0$ there is no memory [8]. For any value $0 < \alpha < 1$ the system has partial memory. The physical interpretation of this operator is interesting: Let us consider δ as a displacement of a simple rod under uniaxial loading. When $\alpha = 0$, $D^\alpha\delta = \delta$ and when $\alpha = 1$, $D^\alpha\delta = \dot{\delta}$. Thus, by multiplying a constant parameter by $D^\alpha\delta$, depending on the value of α, one may obtain either the elastic force (spring model) or the damping force (dashpot model). For any $0 < \alpha < 1$, the derived force is a combination of dashpot and spring models. In other words, the range $0 < \alpha < 1$ is a spectrum of a continuous change from spring to dashpot model.

Due to this property, the fractional model (3) is far more accurate than the model (2). For a wide range of macroscopically homogenous viscoelastic materials including say, elastomers, thermoplastics, and thermostiffening materials, the constitutive equation between stress and strain can be modeled only by using terms up to the first derivatives on the LHS and RHS of Eq. (3); this is called a *5-parameter model*. However, if one wants to model the same material with Eq. (2), many higher integer-order derivative terms on the LHS and RHS must be taken into account in order to achieve a comparable accuracy [9,10].

An interesting mathematical property of the fractional derivative is its Laplace transform [7]

$$L\langle D^\alpha f(t)\rangle = s^\alpha L\langle f(t)\rangle \quad l - 1 < \alpha < l \quad l \in \mathrm{N} \tag{5}$$

where

$$L\langle f(t)\rangle = \int_{-\infty}^{\infty} e^{-st} f(t) dt \tag{6}$$

The Caputo definition of a fractional-order derivative has been used in Eq. (4) because, in contradistinction to the Riemann-Liouville definition, it yields zero for a constant. This is why the initial conditions do not appear in Eq. (5).

Contributed by the Applied Mechanics Division of ASME for publication in the JOURNAL OF APPLIED MECHANICS. Manuscript received November 18, 2006; final manuscript received February 26, 2007; published online January 14, 2008. Review conducted by Robert M. McMeeking.

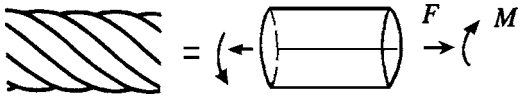

Fig. 1 A system of helical strands, showing a coupling of axial with torsional responses

2 Fractional-Order Equations Governing the Effective Helix' Response

Viscoelastic responses of a helix based on integer-order derivatives were studied in [2,3]. In this note we turn our attention to time dependent response of a helix by using the fractional approach. Considering the viscoelastic fractional-order differential equation (3) as a dilatational response of a material, its Laplace transform becomes

$$\underbrace{\left(1+\sum_{i=1}^{n} P_{\alpha_i} s^{\alpha_i}\right)}_{P(s)} \bar{\sigma}(s) = E_0 \underbrace{\left(1+\sum_{j=1}^{m} Q_{\beta_j} s^{\beta_j}\right)}_{Q(s)} \bar{\varepsilon}(s) \tag{7}$$

where the bar sign over σ and ε indicates the parameter in the Laplace transformed domain. $P(s)$ and $Q(s)$ are the coefficients of $\bar{\sigma}(s)$ and $\bar{\varepsilon}(s)$ for the assumed viscoelastic model, and unlike their counterparts in integer-order derivatives, they are no longer polynomials. Instead, they are expressions dependent on the fractional-order power of Laplace parameter. By recourse to the correspondence principle of viscoelasticity, and following a similar approach as that in the case of Eq. (2) in [2], it can be shown that one can recover Hooke's law in the transformed domain from Eq. (7) with the subsequent substitution for the transformed bulk modulus

$$3s\bar{K} = \frac{Q(s)}{P(s)} = \frac{\left(1+\sum_{i=1}^{n} P_{\alpha_i} s^{\alpha_i}\right)}{E_0\left(1+\sum_{j=1}^{m} Q_{\beta_j} s^{\beta_j}\right)} \tag{8}$$

An analogous formula can be derived for the shear response of isotropic materials. Unlike the case of integer-order derivatives, there is no constraint upon initial conditions of stress and strain in the bulk and shear behavior.

Previous experimental tests [10] indicate that most viscoelastic materials can be modeled sufficiently accurately by using only the first fractional derivative terms in each series of Eq. (3): $n=m=1$. We consider such a model for the bulk as well as the shear response of the fractional viscoelastic material making up the helical strand

$$\sigma(t) + PD^{\alpha}\sigma(t) = Q_0\varepsilon(t) + QD^{\alpha}\varepsilon(t) \tag{9}$$

$$S(t) + pD^{\beta}S(t) = q_0\gamma(t) + QD^{\beta}\gamma(t) \tag{10}$$

In the above, as discussed in detail in [8], the fractional-order derivatives on bulk stress (or shear stress) and bulk strain (or shear strain) are assumed to be the same. This reduces the number of parameters in the model from five to four. Considering the dilatational behavior, the Laplace transform of (9) is simply

$$\underbrace{\bar{\sigma}(s)(1+Ps^{\alpha})}_{P(s)} = \underbrace{(E_0+Qs^{\beta})\bar{\varepsilon}(s)}_{Q(s)} \tag{11}$$

so that the transformed modulus will be

$$3s\bar{K} = \frac{Q(s)}{P(s)} = \frac{E_0+Qs^{\beta}}{1+Ps^{\alpha}} \tag{12}$$

Analogous equations apply to the shear response of the helix. By using all these equations in the formulas (16)–(19) of [2], extensively rearranging the terms and applying the inverse Laplace transform to the fractional-order terms, the differential equations of the viscoelastic helix become

$$\Psi_{\sigma}\sigma = \Psi_{\varepsilon}\varepsilon + \Psi_{\tau}\tau \tag{13}$$

$$\Psi'_{\mu}\mu = \Psi'_{\varepsilon}\varepsilon + \Psi'_{\tau}\tau \tag{14}$$

The operators in (13) are

$$\Psi_{\sigma} = [c_0 + c_1D^{\alpha} + c_2D^{\beta} + c_3D^{\alpha+\beta} + c_4D^{2\alpha} + c_5D^{2\beta} + c_6D^{2\alpha+\beta} + c_7D^{\alpha+2\beta} + c_8D^{2\alpha+2\beta} + c_9D^{3\beta} + c_{10}D^{3\beta+\alpha} + c_{11}D^{3\beta+2\alpha}] \tag{15}$$

$$\Psi_{\varepsilon} = [h_0 + h_1D^{\alpha} + h_2D^{\beta} + h_3D^{\alpha+\beta} + h_4D^{2\alpha} + h_5D^{2\beta} + h_6D^{2\alpha+\beta} + h_7D^{\alpha+2\beta} + h_8D^{2\alpha+2\beta} + h_9D^{3\beta} + h_{10}D^{3\beta+\alpha} + h_{11}D^{3\beta+2\alpha}] \tag{16}$$

$$\Psi_{\tau} = [l_0 + l_1D^{\alpha} + l_2D^{\beta} + l_3D^{\alpha+\beta} + l_4D^{2\alpha} + l_5D^{2\beta} + l_6D^{2\alpha+\beta} + l_7D^{\alpha+2\beta} + l_8D^{2\alpha+2\beta} + l_9D^{3\beta} + l_{10}D^{3\beta+\alpha} + l_{11}D^{3\beta+2\alpha}] \tag{17}$$

The operators in (14) are very similar in form (and, therefore, not reproduced for the sake of brevity) but, certainly, have a different set of coefficients.

Several observations are in order here:

(i) Setting $\alpha=\beta=1$ in (9) and (10) converts the fractional model to an integer-order model of Zener type. The operators (15)–(17) reduce to

$$\Psi_{\sigma} = [g_0 + g_1D^1 + g_2D^2 + g_3D^3 + g_4D^4 + g_5D^5] \tag{18}$$

$$\Psi_{\varepsilon} = [e_0 + e_1D^1 + e_2D^2 + e_3D^3 + e_4D^4 + e_5D^5] \tag{19}$$

$$\Psi_{\tau} = [b_0 + b_1D^1 + b_2D^2 + b_3D^3 + b_4D^4 + b_5D^5] \tag{20}$$

which coincides with the results obtained in [2].

(ii) The operators (15)–(17) are asymmetric with respect to α and β; there are some extra terms that involve higher order derivatives of β (which was the fractional exponent for the shear response at the material level). This indicates that in the constitutive equations of viscoelastic helix, the effect of shear modulus is more pronounced than that of the bulk modulus. Such an effect does not arise in the integer-order models for the helix; operators in (18)–(20) involve six terms each.

(iii) Another interesting feature is that, even though the chosen fractional models at the material level are such that $0<\alpha, \beta<1$, the order of the fractional derivatives in the helix is definitely higher and can be, in general, greater than 1. Note that in real materials $0<\alpha, \beta<1$, as exemplified by $\alpha, \beta \cong 0.5$ for elastomers [7,8].

We postulate that the particular arrangement of the helix geometry through the bending constraint of 3D helical segments or other types of constraints such as the compatibility of axial-torsional deformations, explain the observations (ii) and (iii).

3 Relaxation Response of the Helix

In general, the advantage of having the governing differential equations of a viscoelastic helix (either integer or fractional type) is that one can simply study the macroscopic behavior of helices, for instance damped vibrations of such helical elements [11–14], or macroscopic creep/relaxation phenomena which we examine

here. The applications can range from cables used in suspension bridges or in prestressed concrete girders, to biological tissues which involve helical geometries.

Let us now focus on the governing equations (13) and (14) and the operators (15)–(18) to find the relaxation response of the helix. Since in the relaxation test the strains are constant with time, their fractional-order, Caputo-type derivatives become zero. Henceforth the operators (16) and (17) reduce to constants as

$$\Psi_\varepsilon = h_0 \tag{21a}$$

$$\Psi_\tau = l_0 \tag{21b}$$

while (15) remains unchanged. With this simplification, one can take the Laplace transform of Eq. (15) to find

$$\bar{\sigma}(s) = \frac{h_0 \varepsilon + l_0 \tau}{s\Psi(s)} \tag{22}$$

where $\Psi(s)$ is an algebraic operator

$$\Psi(s) = c_0 + c_1 s^\alpha + c_2 s^\beta + c_3 s^{\alpha+\beta} + c_4 s^{2\alpha} + c_5 s^{2\beta} + c_6 s^{2\alpha+\beta} + c_7 s^{\alpha+2\beta} + c_8 s^{2\alpha+2\beta} + c_9 s^{3\beta} + c_{10} s^{3\beta+\alpha} + c_{11} s^{3\beta+2\alpha} \tag{23}$$

The inverse transform of Eq. (22) exists, is real, continuous and causal, see the Appendix. Thus, the time dependent stress is given by (A8). In that equation, m is the smallest common denominator of the exponents of s in $\Psi(s)$. Note that the macroscopic relaxation response contains three terms. The first term is a constant independent of time; it is indeed the smallest possible value of $\sigma(t)$ (because the other two terms vanish as t approaches infinity). Note here that the structure of a 5-parameter fractional model (regardless of its fading memory) is similar to the integer-order Zener model. Hence, there is a spring (even though it might be weaker in the fractional case as opposed to integer case) parallel to the dashpot that prevents the total stress from approaching zero as time goes to infinity. Furthermore, the dashpot itself has a partial memory and can also behave like a spring. The second term is an integral that decreases with increasing time, while the last term is a sum of exponentially decaying sinusoidal functions. A similar expression can be found for the time dependent couple-stress $\mu(t)$ in relaxation.

In creep phenomena, the stress remains constant and strains increase in time. Therefore, Ψ_σ reduces to c_0 while Ψ_ε and Ψ_τ remain unchanged as a sum of fractional derivative operators. In this case, one cannot use either of Eqs. (13) or (14) to find the time dependent strains, but the coupled systems of Eqs. (13) and (14) have to be tackled. This again is possible analytically by making use of the Laplace transform and the reside theorem given in the Appendix. It turns out that, also in the creep test, there is a constant term in the solution, indicating that strains have an upper bound as time goes to infinity. As the resulting expressions are very lengthy, we do not show them.

4 Conclusions

The effective (along-the-axis) response of helices made of viscoelastic materials is far from trivial. In essence, the constitutive equations of helices are more complex than those of their constituents. The effect was brought out earlier for materials with integer-order derivatives [2] and, as shown here, is even stronger in the case of fractional-order derivatives. Overall, the effect is due to the 3D geometry of the helix.

More specifically, the influence of shear modulus of the fractional viscoelastic material is more complicated and dominant than that of its bulk modulus on the effective response of the helix. This observation is valid only when considering fractional-order derivatives for the helix material. In the special case of integer-order derivatives, one recovers the conventional differential equations. Note here that one cannot obtain the equations of the helix made of a fractional viscoelastic material by a direct generalization of those of the helix made of a conventional viscoelastic material.

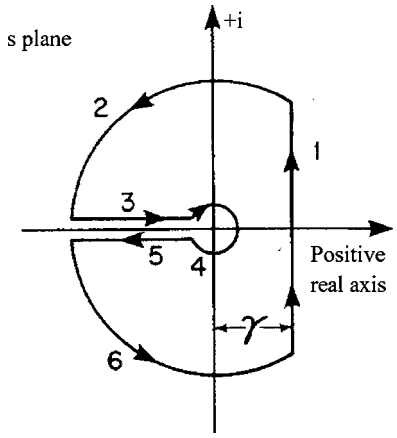

Fig. 2 Integration contour in the *s* plane, after [7]

The fractional-order equations governing the effective helix' response are employed to derive the explicit analytic solution in the standard relaxation test. In summary, the results of this paper provide guidance on equations and responses of 3D chiral fractional viscoelastic materials, similar to those on thermoelastic helices [15] which offered guidance on 3D chiral thermoelastic materials.

Acknowledgment

This work was made possible through support by the NSERC Fellowship while the second author was at McGill University.

Appendix

One can convert the fractional expression $\Psi(s)$ to a polynomial of integer order by

$$\Psi(s) = \sum_{J=1} b_j s^{j/m} = \sum_{J=1} b_j u^j = X(u) \tag{A1}$$

where $u = s^{1/m}$ and m is the smallest common denominator of the fractional exponents of s in $\Psi(s)$. Clearly, some of the coefficients b_j are zero, while any nonzero b_j corresponds to the coefficient of s in $\Psi(s)$ whose exponent becomes equal to j/m. The inverse transform of $\bar{\sigma}(s)$ exists and is real, continuous and causal when (i) $\bar{\sigma}(s)$ is analytic for $\mathrm{Re}(s) > 0$, (ii) $\bar{\sigma}(s)$ is real for s real and positive, (iii) $\bar{\sigma}(s)$ is of order $s^{-\gamma}$, where $\gamma > 1$, for $|s|$ large in the right half of the s-plane [13]. One can simply show that $\bar{\sigma}(s)$ satisfies all these three conditions. The inverse Laplace transform of (22) is then

$$L^{-1}[\bar{\sigma}(s)] = \frac{1}{2\pi i} \int_{\gamma - i\infty}^{\gamma + i\infty} e^{st} (\bar{\sigma}(s)) ds \tag{A2}$$

which can be evaluated by extending the line integral into a closed contour integration as in Fig. 2.

Next, we recall the residue theorem, which states that the integral along any closed contour, divided by $2\pi i$, is equal to the sum of the residues of poles of the integrand within that contour. In Fig. 2, the contour is divided into six segments with arrows which indicate the direction of integration. Note that, since the branch cut of $s^{1/m}$ is along the negative real axis of the s plane, segments 3–5 are required here. Using the residue theorem, we can write

$$\frac{1}{2\pi i}\int_1 e^{st}(\bar{\sigma}(s))ds = -\frac{1}{2\pi i}\sum_{k=2}^{6}\int_k e^{st}(\bar{\sigma}(s))ds + \sum_j b_j \quad \text{(A3)}$$

Equation (A2) is the left-hand side of Eq. (A3) when its limits are extended infinitely in the negative and positive imaginary directions of the s plane. To ensure the continuity of the closed contour, the radii of segments 2 and 6 are increased infinitely and consequently segments 3 and 5 are stretched to infinity on the negative real axis. It can be shown that the integrals along contours 2 and 6 are zero when the radius approaches infinity. The contour integral along the segment 4 can be obtained by using the following lemma (MacRobert [14]):

"If $\lim_{s\to a}\{(s-a)f(s)\}=k$, where k is a constant, then $\lim_{s\to a}\{\int f(s)ds\}=i(\theta_2-\theta_1)k$, the integral being taken for $s\to a$ and $r\to 0$ around an arc from θ_1 to θ_2 of the circle $|s-a|=r$."

It follows that

$$\lim_{s\to 0}\{s\bar{\sigma}(s)\} = \frac{h_0\varepsilon + l_0\tau}{c_0} \quad \text{(A4)}$$

so that, the contour integration along segment 4 becomes

$$\int_4 \bar{\sigma}(s)ds = -2\pi i\left(\frac{h_0\varepsilon + l_0\tau}{c_0}\right) \quad \text{(A5)}$$

where $(\theta_2-\theta_1)=-2\pi$ by convention. One can also show

$$\int_3 e^{st}(\bar{\sigma}(s))ds + \int_5 e^{st}(\bar{\sigma}(s))ds = -2i\ \mathrm{Im}\int_0^{\infty} e^{-rt}(\bar{\sigma}(re^{-i\pi}s))dr \quad \text{(A6)}$$

Using a conventional technique, the residues are then calculated as

$$b_j = \lim_{s\to\lambda_j^m}\{(s-\lambda_j^m)(\bar{\sigma}(s)e^{st})\} \quad \text{(A7)}$$

Here λ_j refers to the jth root of the integer polynomial $X(u)$. In view of Eqs. (A1) and (22), the roots of $X(u)$ correspond to the poles of $\bar{\sigma}(s)$ involving fractional exponents. Note that $s=0$ is not included within the closed contour of Fig. 2 and, therefore, its residue is not required.

Finally, by adding (A5)–(A7), Eq. (A3) becomes

$$\sigma(t) = \frac{h_0\varepsilon + l_0\tau}{c_0} + \frac{1}{\pi}\mathrm{Im}\left[\int_0^{\infty}\bar{\sigma}(re^{-i\pi})e^{-rt}dr\right] + (h_0\varepsilon + l_0\tau)\sum_j (s - \lambda_j^m)\frac{e^{\lambda_j^m t}}{\lambda_j^m\Psi(\lambda_j^m)} \quad \text{(A8)}$$

The summation in the last term is over the residues that are included within the closed contour in Fig. 2. The poles of Eq. (22) λ_j [those that make $\Psi(s)=0$] were found in the $s^{1/m}$ plane. As the Laplace transform is performed in the s plane, the poles λ_j should be transformed into λ_j^m so as to be on the s plane. That transformation, however, causes some of the original poles to be mapped onto Riemann surfaces not included within the closed contour of integration in the s plane. According to the residue theorem, the residues of such poles do not contribute to the solution. Thus, the summation over the index j in Eq. (A8) applies to those poles only that remain in the closed contour's plane after the transformation λ_j^m. The reside theorem in conjunction with fractional-order derivatives has been used in [7] in a slightly different way.

References

[1] Samras, R. K., Skop, R. A., and Milburn, D. A., 1974, "An Analysis of Coupled Extensional-Torsional Oscillations in Wire Rope," ASME J. Eng. Ind., **96**, pp. 1130–1135.

[2] Shahsavari, H., and Ostoja-Starzewski, M., 2005, "On Elastic and Viscoelastic Helices," Philos. Mag., **85**(33–35), pp. 4213–4230.

[3] Conway, T. A., and Costello, G. A., 1993, "Viscoelastic Response of a Strand," ASME J. Appl. Mech., **60**(2), pp. 534–540.

[4] Bagley, R. L., and Torvik, P. J., 1983, "A Theoretical Basis for the Application of Fractional Calculus to Viscoelasticity," J. Rheol., **27**(3), pp. 201–210.

[5] Bland, D. R., 1960, *Theory of Linear Viscoelasticity*, Pergamon, New York.

[6] Caputo, M., 1967, "Linear Models of Dissipation Whose Q is Almost Frequency Independent—Part II," Q. J. R. Astron. Soc., **13**, pp. 529–539.

[7] Bagley, R. L., and Torvik, P. T., 1983, "Fractional Calculus—A Different Approach to the Analysis of Viscoelastically Damped Structures," AIAA J., **21**(5), pp. 741–748.

[8] Baker, W. P., Eldred, L. B., and Palazotto, A., 1996, "Viscoelastic Material Response With a Fractional-Derivative Constitutive Model," AIAA J., **34**(3), pp. 596–600.

[9] Beda, T., and Chevalier, Y., 2004, "Identification of Viscoelastic Fractional Complex Modulus," AIAA J., **42**(7), pp. 1450–1456.

[10] Rossikhin, Y. A., and Shitikova, M. V., 2004, "Analysis of the Viscoelastic Rod Dynamics via Models Involving Fractional Derivatives or Operators of Two Different Orders," Shock Vib. Dig., **36**(1), pp. 3–26.

[11] Kilbas, A. A., Srivastava, H. M., and Trujillo, J. J., 2006, *Theory and Application of Fractional Differential Equations*, Elsevier, New York.

[12] Shahsavari, H., and Wihler, T. P., 2006, "Viscoelastodynamics of Helices," in preparation.

[13] Churchill, R. V., 1958, *Book of Operational Mathematics*, 2nd ed., McGraw-Hill, New York.

[14] MacRobert, T. M., 1962, *Functions of a Complex Variable*, 5th ed., Macmillan, New York.

[15] Ostoja-Starzewski, M., 2003, "Thermoelastic Waves in a Helix With Parabolic or Hyperbolic Heat Conduction," J. Therm. Stresses, **26**, pp. 1205–1219.

A Point Heat Source on the Surface of a Semi-Infinite Transversely Isotropic Piezothermoelastic Material

Peng-Fei Hou

Wei Luo

Department of Engineering Mechanics,
Hunan University,
Changsha 410082, P.R. China

Andrew Y. T. Leung
Department of Building and Construction,
City University of Hong Kong,
Hong Kong, SAR China

We use the compact harmonic general solutions of transversely isotropic piezothermoelastic materials to construct the three-dimensional Green's function of a steady point heat source on the surface of a semi-infinite transversely isotropic piezothermoelastic material by four newly introduced harmonic functions. All components of the coupled field are expressed in terms of elementary functions and are convenient to use. Numerical results for cadmium selenide are given graphically by contours.
[DOI: 10.1115/1.2745402]

1 Introduction

Green's functions or fundamental solutions play an important role in both applied and theoretical studies on the physics of solids. They are a basic building block of a lot of further works. For example, Green's functions can be used to construct many analytical solutions of practical problems when boundary conditions are imposed. They are essential in the boundary element method as well as the study of cracks, defects, and inclusions.

For purely elastic solids, Green's functions had been well investigated and a great deal of works can be found in the literature. For piezoelectric material with electromechanical coupling, Green's functions have also received much attention. For anisotropic piezoelectric material, Deeg [1], Wang [2], Benveniste [3], Chen [4], and Chen and Lin [5] expressed the Green's function of infinite material in the form of integral representation through the use of the transform techniques. Pan [6] derived the two-dimensional Green's functions of infinite, semi-infinite, and two-phase material by the complex function method, and Gao and Fan [7] also gave the two-dimensional Green's functions of semi-infinite material. Pan and Tonon [8] and Pan and Yuan [9] derived the solutions for the Green's functions of infinite and two-phase material.

With regards to the special case of transversely isotropic piezoelectric material, Sosa and Castro [10], Lee and Jiang [11], and Ding et al. [12–14] studied the two-dimensional Green's functions of infinite, semi-infinite, and two-phase material. Wang and Chen [15] and Wang and Zheng [16] obtained the Green's function for point loads acted on the surface of semi-infinite piezoelectric material. Dunn [17] gave an explicit solution for the Green' function of infinite piezoelectric material by taking Radon transform, coordinate transformation, and evaluation of residues in sequence. Later, Dunn and Wienecke [18,19] and Ding et al. [20,21] independently obtained the concise Green's functions of infinite and semi-infinite piezoelectric material in terms of elementary functions, which were employed to study the inclusion problem [22]. The thermal effects are not considered in all the above works. Piezoelectric ceramics and piezoelectric polymers, which are extensively utilized in smart structures and intelligent systems, all belong to pyroelectric materials. Rao and Sunar [23] pointed out that temperature variation in the piezoelectric material could affect the overall performance of a distributed control system. Therefore, in-depth investigation on electro-thermo-mechanical coupling behavior is significant.

Qin [24–27] further derived the two-dimensional Green's functions of anisotropic piezothermoelastic material with holes of various shapes. Chen [28] derived a compact three-dimensional general solution for transversely isotropic piezothermoelastic materials. In this general solution, all components of the piezothermoelastic field are expressed by four harmonic functions. Based on this general solution, Chen et al. [29] obtained the Green's function of transversely isotropic piezothermoelastic material with a penny-shaped crack.

In this paper, three-dimensional Green's function for a steady point heat source on the surface of a semi-infinite transversely isotropic piezothermoelastic material $z \geqslant 0$ is investigated. For completeness, the general solution of Chen [28] is described in Sec. 2. In Sec. 3, four new suitable harmonic functions are constructed in the form of elementary functions with undetermined constants by trial-and-error. The corresponding piezothermoelastic field can be obtained by substituting these functions into the general solution, and the undetermined constants can be obtained by the boundary conditions on the surface $z=0$ and the equilibrium conditions for a cylinder of $0 \leqslant z \leqslant a$ and $0 \leqslant r \leqslant b$, where a and b are arbitrary but should include the source point. Numerical examples are presented in Sec. 4. All stress, electric displacement components, and temperature increment are shown graphically by contours. Finally, the paper is concluded in Sec. 5.

2 General Solutions for Transversely Isotropic Piezothermoelastic Material

When the xy plane is parallel to the plane of isotropy in Cartesian coordinates (x,y,z), the constitutive relations of transversely isotropic piezothermoelastic materials are

$$\sigma_x = c_{11}\frac{\partial u}{\partial x} + c_{12}\frac{\partial v}{\partial y} + c_{13}\frac{\partial w}{\partial z} + e_{31}\frac{\partial \Phi}{\partial z} - \lambda_{11}\theta$$

$$\sigma_y = c_{12}\frac{\partial u}{\partial x} + c_{11}\frac{\partial v}{\partial y} + c_{13}\frac{\partial w}{\partial z} + e_{31}\frac{\partial \Phi}{\partial z} - \lambda_{11}\theta$$

$$\sigma_z = c_{13}\left(\frac{\partial u}{\partial x} + \frac{\partial v}{\partial y}\right) + c_{33}\frac{\partial w}{\partial z} + e_{33}\frac{\partial \Phi}{\partial z} - \lambda_{33}\theta$$

$$\tau_{yz} = c_{44}\left(\frac{\partial v}{\partial z} + \frac{\partial w}{\partial y}\right) + e_{15}\frac{\partial \Phi}{\partial y}$$

Contributed by the Applied Mechanics Division of ASME for publication in the JOURNAL OF APPLIED MECHANICS. Manuscript received November 19, 2006; final manuscript received March 9, 2007; published online January 14, 2008. Review conducted by Subrata Mukherjee.

$$\tau_{zx} = c_{44}\left(\frac{\partial u}{\partial z} + \frac{\partial w}{\partial x}\right) + e_{15}\frac{\partial \Phi}{\partial x}$$

$$\tau_{xy} = c_{66}\left(\frac{\partial u}{\partial y} + \frac{\partial v}{\partial x}\right) \tag{1a}$$

$$D_x = e_{15}\left(\frac{\partial u}{\partial z} + \frac{\partial w}{\partial x}\right) - \varepsilon_{11}\frac{\partial \Phi}{\partial x}$$

$$D_y = e_{15}\left(\frac{\partial v}{\partial z} + \frac{\partial w}{\partial y}\right) - \varepsilon_{11}\frac{\partial \Phi}{\partial y}$$

$$D_z = e_{31}\left(\frac{\partial u}{\partial x} + \frac{\partial v}{\partial y}\right) + e_{33}\frac{\partial w}{\partial z} - \varepsilon_{33}\frac{\partial \Phi}{\partial z} + p_3\theta \tag{1b}$$

where u, v, and w are components of the mechanical displacement in x, y, and z directions, respectively; σ_{ij} and D_i are the components of stress and electric displacement, respectively; Φ and θ are electric potential and temperature increment, respectively; c_{ij}, e_{ij}, ε_{ij}, λ_{ii}, and p_3 are elastic, piezoelectric, dielectric, thermal modules, and pyroelectric constants, respectively. The relation $c_{66} = (c_{11} - c_{12})/2$ holds for materials with transverse isotropy.

In the absence of body forces and free charges, the mechanical, electric and heat equilibrium equations are

$$\frac{\partial \sigma_x}{\partial x} + \frac{\partial \tau_{xy}}{\partial y} + \frac{\partial \tau_{zx}}{\partial z} = 0$$

$$\frac{\partial \tau_{xy}}{\partial x} + \frac{\partial \sigma_y}{\partial y} + \frac{\partial \tau_{yz}}{\partial z} = 0$$

$$\frac{\partial \tau_{zx}}{\partial x} + \frac{\partial \tau_{yz}}{\partial y} + \frac{\partial \sigma_z}{\partial z} = 0 \tag{2a}$$

$$\frac{\partial D_x}{\partial x} + \frac{\partial D_y}{\partial y} + \frac{\partial D_z}{\partial z} = 0 \tag{2b}$$

$$\beta_{11}\left(\frac{\partial^2 \theta}{\partial x^2} + \frac{\partial^2 \theta}{\partial y^2}\right) + \beta_{33}\frac{\partial^2 \theta}{\partial^2 z} = 0 \tag{2c}$$

where β_{ii} $(i=1,3)$ are coefficients of heat conduction.

Chen [28] derived a compact general solution to Eqs. (1) and (2) as follows:

$$U = \Lambda\left(i\psi_0 + \sum_{j=1}^{4} \psi_j\right)$$

$$w_m = \sum_{j=1}^{4} s_j k_{mj} \frac{\partial \psi_j}{\partial z_j}$$

$$\theta = k_{34}\frac{\partial^2 \psi_4}{\partial z_4^2} \tag{3a}$$

$$\sigma_1 = 2\sum_{j=1}^{4} (c_{66} - \omega_{1j}s_j^2)\frac{\partial^2 \psi_j}{\partial z_j^2} = -2\sum_{j=1}^{4} (c_{66} - \omega_{1j}s_j^2)\Delta\psi_j$$

$$\sigma_2 = 2c_{66}\Lambda^2\left(i\psi_0 + \sum_{j=1}^{4} \psi_j\right),$$

$$\sigma_{zm} = \sum_{j=1}^{4} \omega_{mj}\frac{\partial^2 \psi_j}{\partial z_j^2} = -\sum_{j=1}^{4} \omega_{mj}\Delta\psi_j$$

$$\tau_{zm} = \Lambda\left(s_0\rho_m i\frac{\partial \psi_0}{\partial z_0} + \sum_{j=1}^{4} s_j\omega_{mj}\frac{\partial \psi_j}{\partial z_j}\right) \quad (m=1,2) \tag{3b}$$

where the following notations for all components both in Cartesian coordinates (x,y,z) and cylindrical coordinates (r,ϕ,z) are introduced:

$$U = u + iv = e^{i\phi}(u_r + iu_\phi) \quad w_1 = w \quad w_2 = \Phi \tag{4a}$$

$$\sigma_1 = \sigma_x + \sigma_y = \sigma_r + \sigma_\phi$$

$$\sigma_2 = \sigma_x - \sigma_y + 2i\tau_{xy} = e^{2i\phi}(\sigma_r - \sigma_\phi + 2i\tau_{r\phi})$$

$$\tau_{z1} = \tau_{xz} + i\tau_{yz} = e^{i\phi}(\tau_{zr} + i\tau_{\phi z}) \quad \sigma_{z1} = \sigma_z$$

$$\tau_{z2} = D_x + iD_y = e^{i\phi}(D_r + iD_\phi) \quad \sigma_{z2} = D_z \tag{4b}$$

In addition, $z_j = s_j z$ $(j=0,1,2,3,4)$, $s_0 = \sqrt{c_{66}/c_{44}}$, $s_4 = \sqrt{\beta_{11}/\beta_{33}}$, and s_j $(j=1,2,3)$ satisfying $\mathrm{Re}(s_j) > 0$ are the three eigenvalues of the sixth degree polynomial listed in Appendix A. Functions ψ_j $(j=0,1,2,3,4)$ satisfy, respectively, the following harmonic equations:

$$\left(\Delta + \frac{\partial^2}{\partial z_j^2}\right)\psi_j = 0 \quad (j=0,1,2,3,4) \tag{5}$$

where

$$\Delta = \frac{\partial^2}{\partial x^2} + \frac{\partial^2}{\partial y^2} \text{ in coordinates } (x,y,z) \tag{6a}$$

$$\Delta = \frac{\partial^2}{\partial r^2} + \frac{\partial}{r\partial r} + \frac{\partial^2}{r^2\partial \phi^2} \text{ in coordinates } (r,\phi,z) \tag{6b}$$

In addition,

$$k_{1j} = \alpha_{1j}/s_j \; k_{2j} = \alpha_{2j}/s_j \; k_{3j} = \alpha_{3j} \tag{7a}$$

$$\omega_{1j} = c_{44}(1 + k_{1j}) + e_{15}k_{2j} = -c_{13} + (c_{33}k_{1j} + e_{33}k_{2j})s_j^2 - \lambda_{33}k_{3j}$$
$$= [c_{11} - (c_{13}k_{1j} + e_{31}k_{2j})s_j^2 + \lambda_{11}k_{3j}]/s_j^2$$

$$\omega_{2j} = e_{15}(1 + k_{1j}) - \varepsilon_{11}k_{2j} = -e_{31} + (e_{33}k_{1j} - \varepsilon_{33}k_{2j})s_j^2 + p_3k_{3j} \tag{7b}$$

$$\rho_1 = c_{44} \; \rho_2 = e_{15} \quad \Lambda = \frac{\partial}{\partial x} + i\frac{\partial}{\partial y} \tag{7c}$$

where α_{mj} $(m=1,2,3;\ j=1,2,3,4)$ are constants listed in Appendix A. It should be noted that the general solutions given in Eq. (3) are only valid for the case when the eigenvalues s_j $(j=1,2,3,4)$ are distinct.

For the nontorsional axisymmetric problem, $\psi_0 = 0$ and ψ_j $(j=1,2,3,4)$ are independent of ϕ, so that $u_\phi = 0$, $\tau_{\phi z} = \tau_{r\phi} = 0$, and $D_\phi = 0$. The general solution in cylindrical coordinates (r,ϕ,z) can be simplified to the following form:

$$u_r = \sum_{j=1}^{4} \frac{\partial \psi_j}{\partial r}$$

$$w_m = \sum_{j=1}^{4} s_j k_{mj} \frac{\partial \psi_j}{\partial z_j}$$

$$\theta = k_{34}\frac{\partial^2 \psi_4}{\partial z_4^2} \tag{8a}$$

$$\sigma_r = -2c_{66}\sum_{j=1}^{4} \frac{1}{r}\frac{\partial \psi_j}{\partial r} - \sum_{j=1}^{4} s_j^2\omega_{1j}\frac{\partial^2 \psi_j}{\partial z_j^2}$$

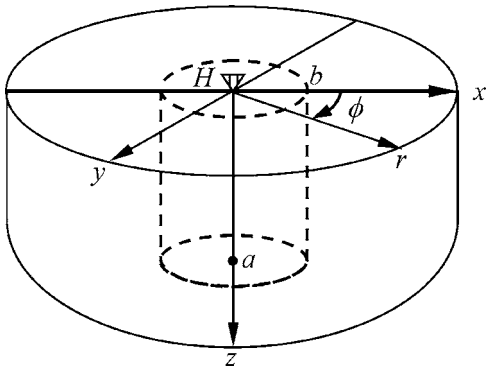

Fig. 1 A point heat source *H* on the surface of a semi-infinite piezothermoelastic material

$$\sigma_\phi = 2c_{66}\sum_{j=1}^{4}\frac{1}{r}\frac{\partial\psi_j}{\partial r} - \sum_{j=1}^{4}(s_j^2\omega_{1j} - 2c_{66})\frac{\partial^2\psi_j}{\partial z_j^2}$$

$$\sigma_z = \sum_{j=1}^{4}\omega_{1j}\frac{\partial^2\psi_j}{\partial z_j^2}$$

$$\tau_{zr} = \sum_{j=1}^{4}s_j\omega_{1j}\frac{\partial^2\psi_j}{\partial r\partial z_j} \tag{8b}$$

$$D_z = \sum_{j=1}^{4}\omega_{2j}\frac{\partial^2\psi_j}{\partial z_j^2}$$

$$D_r = \sum_{j=1}^{4}s_j\omega_{2j}\frac{\partial^2\psi_j}{\partial r\partial z_j} \tag{8c}$$

For the torsional axisymmetric problem, $\psi_j=0$ $(j=1,2,3,4)$ and ψ_0 is independent of ϕ, so that $u_r=u_z=0$, $\Phi=0$, $\theta=0$, $\sigma_r=\sigma_\phi=\sigma_z=\tau_{rz}=0$, and $D_r=D_z=0$. The general solution can be simplified to the following form:

$$u_\phi = -\frac{\partial\psi_0}{\partial r}$$

$$\tau_{r\phi} = 2c_{66}\left(\frac{1}{2}\frac{\partial^2}{\partial z_0^2} + \frac{\partial^2}{\partial r^2}\right)\psi_0 \tag{9a}$$

$$\tau_{\phi z} = s_0 c_{44}\frac{\partial^2\psi_0}{\partial r\partial z_0}$$

$$D_\phi = s_0 e_{15}\frac{\partial^2\psi_0}{\partial r\partial z_0} \tag{9b}$$

All of the above general solutions (3), (8), and (9) will be used in Sec. 3 and Appendix B.

3 A Point Heat Source on the Surface of a Semi-Infinite Transversely Isotropic Piezothermoelastic Material

Consider a semi-infinite transversely isotropic piezothermoelastic material $z\geqslant 0$ whose isotropic plane is perpendicular to the z axis (Fig. 1). A point heat source H is applied at the origin of the cylindrical coordinate (r,ϕ,z) and the surface $(z=0)$ is free and electro-thermally insolated. Based on the general solution (8), the coupled field in the semi-infinite piezothermoelastic material is derived in this section. This is a nontorsional axisymmetric problem. The boundary conditions on the surface $(z=0)$ are in the form of

$$\sigma_z = \tau_{zr} = 0 \quad D_z = 0 \quad \partial\theta/\partial z = 0 \tag{10}$$

Introducing the following harmonic functions:

$$\psi_0 = 0 \quad \psi_j = \mathcal{A}_j(z_j \ln R_j^* - R_j) \quad (j=1,2,3,4) \tag{11}$$

where $\mathcal{A}_j$ $(j=1,2,3,4)$ are constants to be determined, and

$$R_j^*(r,z) = R_j(r,z) + z_j \quad R_j(r,z) = \sqrt{r^2+z_j^2} \tag{12}$$

Substitution of Eq. (11) into Eq. (8) yields

$$u_r = -\sum_{j=1}^{4}\mathcal{A}_j\frac{r}{R_j^*} \quad w_m = \sum_{j=1}^{4}s_j k_{mj}\mathcal{A}_j \ln R_j^* \quad \theta = k_{34}\mathcal{A}_4\frac{1}{R_4} \tag{13a}$$

$$\sigma_r = 2c_{66}\sum_{j=1}^{4}\mathcal{A}_j\frac{1}{R_j^*} - \sum_{j=1}^{4}s_j^2\omega_{1j}\mathcal{A}_j\frac{1}{R_j}$$

$$\sigma_\phi = -2c_{66}\sum_{j=1}^{4}\mathcal{A}_j\frac{1}{R_j^*} - \sum_{j=1}^{4}(s_j^2\omega_{1j} - 2c_{66})\mathcal{A}_j\frac{1}{R_j}$$

$$\sigma_z = \sum_{j=1}^{4}\omega_{1j}\mathcal{A}_j\frac{1}{R_j}$$

$$\tau_{zr} = \sum_{j=1}^{4}s_j\omega_{1j}\mathcal{A}_j\frac{r}{R_j R_j^*} \tag{13b}$$

$$D_z = \sum_{j=1}^{4}\omega_{2j}\mathcal{A}_j\frac{1}{R_j}$$

$$D_r = \sum_{j=1}^{4}s_j\omega_{2j}\mathcal{A}_j\frac{r}{R_j R_j^*} \tag{13c}$$

Substitution of Eqs. (13*a*) into Eq. (10) give

$$\sum_{j=1}^{4}\omega_{mj}\mathcal{A}_j = 0 \quad (m=1,2) \tag{14}$$

$$\sum_{j=1}^{4}s_j\omega_{1j}\mathcal{A}_j = 0 \tag{15}$$

and $\partial\theta/\partial z=0$ is satisfied automatically.

When the mechanical, electric and thermal equilibriums for a cylinder of $0\leqslant z\leqslant a$ and $0\leqslant r\leqslant b$ are considered (Fig. 1), where a and b are arbitrary, and three additional equations can be obtained,

$$\int_0^{2\pi}\int_0^b \sigma_z(r,\phi,a)rdrd\phi + 2\pi b\int_0^a \tau_{zr}(b,\phi,z)dz = 0 \tag{16a}$$

$$\int_0^{2\pi}\int_0^b D_z(r,\phi,a)rdrd\phi + 2\pi b\int_0^a D_r(b,\phi,z)dz = 0 \tag{16b}$$

$$-\beta_{33}\int_0^{2\pi}\int_0^b \frac{\partial\theta}{\partial z}(r,\phi,a)rdrd\phi - 2\pi b\beta_{11}\int_0^a \frac{\partial\theta}{\partial r}(b,\phi,z)dz = H \tag{16c}$$

where β_{11} and β_{33} are coefficients of heat conduction along r and z axes, respectively.

Some useful integrals are listed below:

$$\int \frac{1}{R_j} r dr = R_j$$

$$\int \frac{r}{R_j R_j^*} dz = -\frac{1}{s_j} \frac{r}{R_j^*} \tag{17a}$$

$$\int \frac{\partial \theta}{\partial z} r dr = -s_4 k_{34} \mathcal{A}_4 \int \frac{z_4}{R_4^3} r dr = s_4 k_{34} \mathcal{A}_4 \frac{z_4}{R_4} \tag{17b}$$

$$\int \frac{\partial \theta}{\partial r} dz = -k_{34} \mathcal{A}_4 \int \frac{r}{R_4^3} dz = \frac{k_{34}}{s_4} \mathcal{A}_4 \frac{r}{R_4 R_4^*} \tag{17c}$$

Substituting Eqs. (13*b*) and (13*c*) into Eqs. (16*a*) and (16*b*) using integral (17*a*), one can obtain

$$\sum_{j=1}^{4} \omega_{mj} \mathcal{A}_j I_1 = 0 \quad (m = 1,2) \tag{18}$$

where

$$I_1 = [R_j(r,a)]_{r=0}^{r=b} - \left[\frac{b^2}{R_j^*(b,z)} \right]_{z=0}^{z=a} = b \tag{19}$$

By virtue of Eq. (19), Eq. (18) degenerates to Eq. (14).

Substituting Eq. (13*a*) into Eq. (16*c*) by using $s_4 = \sqrt{\beta_{11}/\beta_{33}}$ and integrals (17*b*) and (17*c*), one can obtain

$$-\mathcal{A}_4 I_2 = \frac{H}{2\pi k_{34} \sqrt{\beta_{11}\beta_{33}}} \tag{20}$$

where

$$I_2 = \left[\frac{s_4 a}{R_4(r,a)} \right]_{r=0}^{r=b} + \left[\frac{b^2}{R_4(b,z) R_4^*(b,z)} \right]_{z=0}^{z=a} = -1 \tag{21}$$

$\mathcal{A}_4$ can be determined by Eqs. (20) and (21) as follows:

$$\mathcal{A}_4 = \frac{H}{2\pi k_{34} \sqrt{\beta_{11}\beta_{33}}} \tag{22}$$

Thus, the coupled field in the semi-infinite transversely isotropic piezothermoelastic material is determined by Eqs. (13*a*), (14)–(16), (17*a*), and (18)–(22).

Consider the problems of point charge Q, concentrated forces P_x, P_y, P_z and concentrated moments M_x, M_y, M_z in the x, y, z direction, respectively, on the surface of a semi-infinite transversely isotropic piezothermoelastic material. One can find that the foundational Eqs. (1*a*) and (2*a*) are single-direction coupling, i.e., the thermal loading can change electroelastic fields, while on the contrary, the mechanical or electric loadings cannot change the thermal field ($\theta = 0$), so the corresponding solutions under electromechanical loadings degenerate to those when thermal effects are not considered, such as Ding et al. [30]. The corresponding solutions for all of the above cases are listed in Appendix B.

4 Numerical Results

The contours of temperature increment and all stress and electric displacement components in a semi-infinite transversely isotropic piezothermoelastic material induced by a point heat source H on the surface are evaluated numerically and plotted in Figs. 2–8. The material properties listed in Table 1 are taken from cadmium selenide [31].

In additions, the following nondimensional components are used in the Figures:

$$\vartheta = \frac{\theta}{T_0} \quad \sigma_k = \frac{\sigma_i}{c_{33}\alpha_r T_0} \quad \tau_{kl} = \frac{\tau_{ij}}{c_{33}\alpha_r T_0} \quad D_k = \frac{D_i}{\alpha_r T_0 \sqrt{c_{33}\varepsilon_{33}}}$$

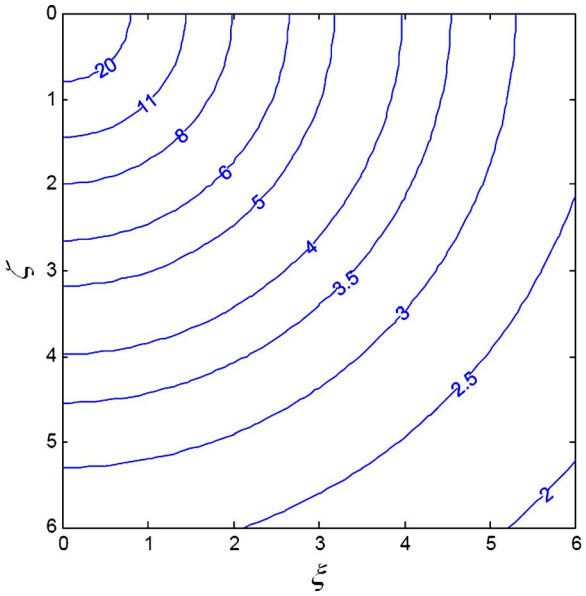

Fig. 2 Contour of nondimensional temperature increment $\vartheta \times 10^2$ under point heat source $\delta = 1$ acted at the origin

$$\xi = \frac{r}{r_1} \quad \zeta = \frac{z}{r_1} \quad (i,j = r,\phi,z;k,l = \xi,\mathrm{s},\zeta) \tag{23}$$

where r_1 is a nonzero dimension, α_r and T_0 are the thermal expansion coefficient and reference temperature, respectively.

In this case, Eq. (22) should be rewritten in following nondimensional form:

$$\mathcal{A}_4 = \frac{\delta}{2\pi s_4 k_{34}} \tag{24}$$

where δ is a nondimensional point heat source as follows:

$$\delta = \frac{H}{r_1 T_0 \beta_{33}} \tag{25}$$

Here let $\delta = 1$.

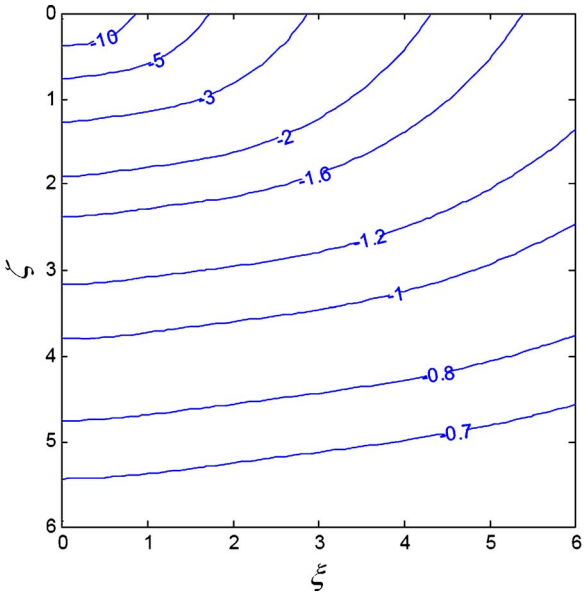

Fig. 3 Contour of nondimensional stress $\sigma_\xi \times 10^2$ under point heat source $\delta = 1$ acted at the origin

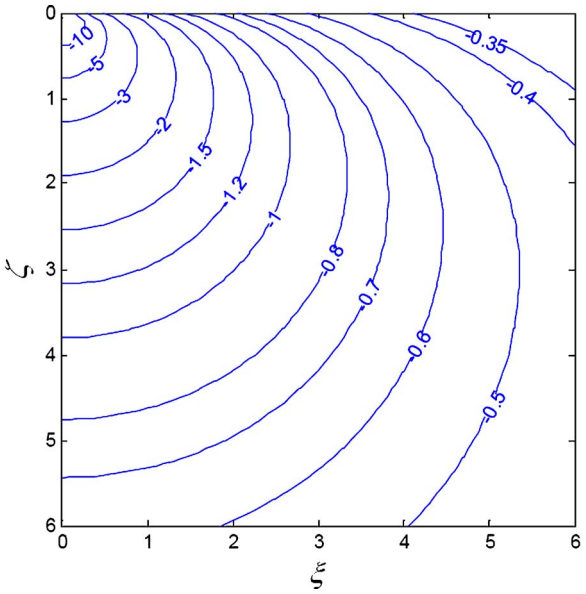

Fig. 4 Contour of nondimensional stress $\sigma_\varsigma \times 10^2$ under point heat source δ=1 acted at the origin

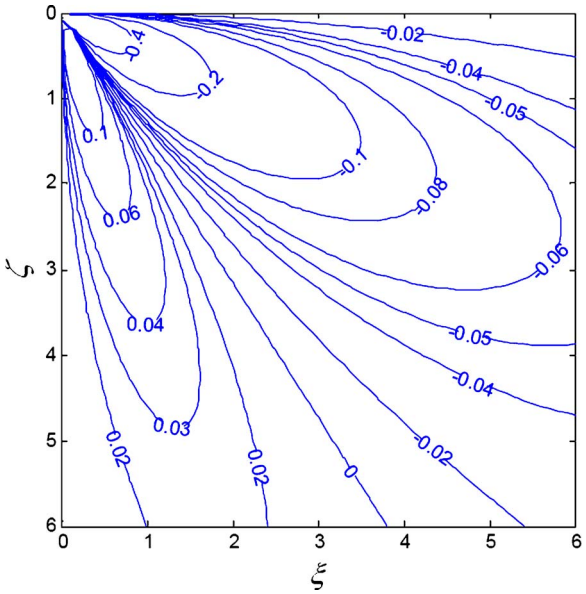

Fig. 6 Contour of nondimensional stress $\tau_{\zeta\xi} \times 10^2$ under point heat source δ=1 acted at the origin

On the basis of the contours plotted above, one can find all components are singular at origin at which the point heat source is located. In addition, following conclusions can be drawn:

(1) Figure 2 shows that the contour of temperature increment $\vartheta(\theta)$ is a normal circle. This is because the heat conduction coefficients β_{11} and β_{33} along the r and z axes, respectively, are equal for cadmium selenide.
(2) Figures 3 and 4 show that stresses $\sigma_\zeta(\sigma_z)$ and $\sigma_\varsigma(\sigma_\phi)$ are all negative in semi-infinite piezothermoelastic material.
(3) Figures 5 and 6 show that there are zero common tangents for stresses $\sigma_\zeta(\sigma_z)$ and $\tau_{zr}(\tau_{\zeta\xi})$, which are negative upon the zero common tangents and positive below them. One can also find that they tend to zero near the surface ζ=0 and satisfy the boundary condition.
(4) Figure 7 shows that there is a zero common tangent for electric displacement $D_\xi(D_r)$, which is positive upon the zero common tangent and negative below it. Figure 8 shows that electric displacement $D_\zeta(D_z)$ is all negative in the semi-infinite piezothermoelastic material. It is noted that although the expression in Eq. (13c) for electric displacements $D_\xi(D_r)$ and $D_\zeta(D_z)$ are similar to the expression in (13b) for stresses $\tau_{zr}(\tau_{\zeta\xi})$ and $\sigma_\zeta(\sigma_z)$, respectively, their distributions in Figs. 5–8 are much different.

5 Conclusions

By virtue of the compact general solution of Chen [28], four harmonic functions ψ_j (j=1,2,3,4) in Eq. (11) are constructed and the corresponding coupled field for a point heat source acted on the surface of a semi-infinite transversely isotropic piezothermoelastic material is derived. Because the obtained solution is in

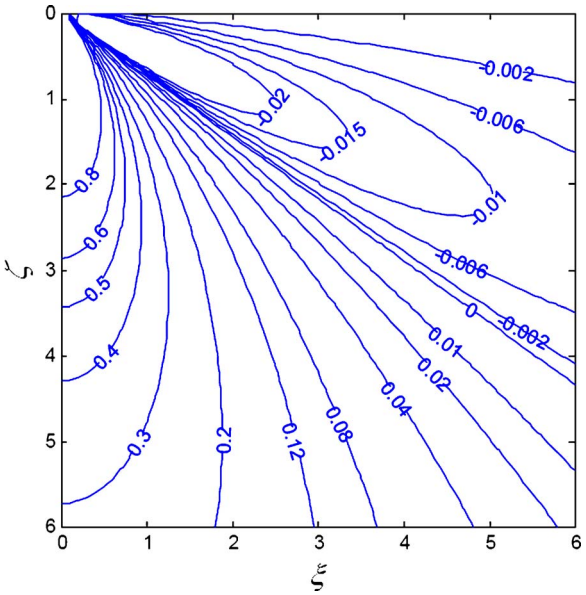

Fig. 5 Contour of nondimensional stress $\sigma_\zeta \times 10^2$ under point heat source δ=1 acted at the origin

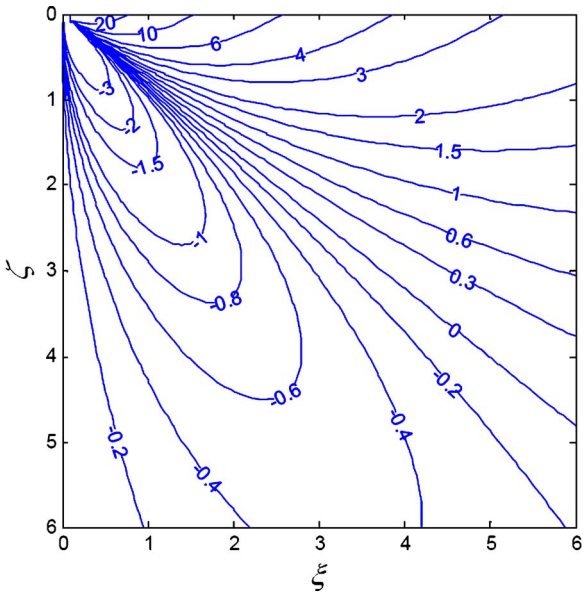

Fig. 7 Contour of nondimensional electric displacement $D_\xi \times 10^3$ under point heat source δ=1 acted at the origin

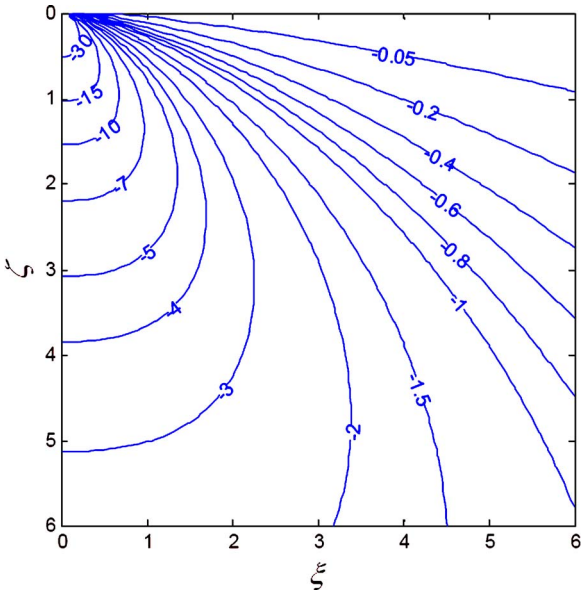

Fig. 8 Contour of nondimensional electric displacement $D_\xi \times 10^3$ under point heat source δ=1 acted at the origin

terms of elementary functions, it is very convenient to use. Typical numerical examples are presented. When the surface is under point charge, concentrated forces and concentrated moments, the corresponding solutions are listed in Appendix B.

Acknowledgment

The authors thankfully acknowledge the financial support from the National Natural Science Foundation of China (10472102), Special Foundation of the City University of Hong Kong (9610022), Outstanding Young Teacher Foundation in Hunan Province (521105236), National 985 Special Foundation of China, and the reviewer for his constructive comments, which lead to improvements of the earlier version of this article.

Appendix A

A.1 Eigenvalues in General Solution

The sixth degree polynomial to determine the three eigenvalues s_j $(j=1,2,3)$ is

$$a_0 s^6 - b_0 s^4 + c_0 s^2 - d_0 = 0 \tag{A1}$$

where

$$a_0 = c_{44}(e_{33}^2 + c_{33}\varepsilon_{33})$$

$$b_0 = c_{33}[c_{44}\varepsilon_{11} + (e_{15}+e_{31})^2] + \varepsilon_{33}[c_{11}c_{33} + c_{44}^2 - (c_{13}+c_{44})^2] + e_{33}[2c_{44}e_{15} + c_{11}e_{33} - 2(c_{13}+c_{44})(e_{15}+e_{31})]$$

$$c_0 = c_{44}[c_{11}\varepsilon_{33} + (e_{15}+e_{31})^2] + \varepsilon_{11}[c_{11}c_{33} + c_{44}^2 - (c_{13}+c_{44})^2] + e_{15}[2c_{11}e_{33} + c_{44}e_{15} - 2(c_{13}+c_{44})(e_{15}+e_{31})]$$

$$d_0 = c_{11}(e_{15}^2 + c_{44}\varepsilon_{11}) \tag{A2}$$

A.2 Constants α_{mj} in General Solution

α_{mj} $(m=1,2,3;\ j=1,2,3,4)$ in Eq. (7*a*) are defined as follows:

$$\alpha_{1j} = s_j\beta_{2j}/\beta_{1j}$$

$$\alpha_{2j} = s_j\beta_{3j}/\beta_{1j}$$

$$\alpha_{31} = \alpha_{32} = \alpha_{33} = 0$$

$$\alpha_{34} = \beta_{44}/\beta_{14} \tag{A3}$$

where

$$\beta_{mj} = a_m - b_m s_j^2 + c_m s_j^4 \quad (j=1,2,3)$$

$$\beta_{44} = a_0 s_4^6 - b_0 s_4^4 + c_0 s_4^2 - d_0 \tag{A4}$$

and

$$a_1 = -\lambda_{11}(c_{44}\varepsilon_{11} + e_{15}^2)$$

$$b_1 = (c_{13}+c_{44})(\lambda_{33}\varepsilon_{11} - p_3 e_{15}) + (e_{15}+e_{31})(\lambda_{33}e_{15} + p_3 c_{44}) - \lambda_{11}(c_{33}\varepsilon_{11} + c_{44}\varepsilon_{33} + 2e_{15}e_{33})$$

$$c_1 = (c_{13}+c_{44})(\lambda_{33}\varepsilon_{33} - p_3 e_3) + (e_{15}+e_{31})(\lambda_{33}e_{33} + p_3 c_{33}) - \lambda_{11}(e_{33}^2 + c_{33}\varepsilon_{33})$$

$$a_2 = c_{11}(\lambda_{33}\varepsilon_{11} - p_3 e_{15}) - \lambda_{11}[\varepsilon_{11}(c_{13}+c_{44}) + e_{15}(e_{15}+e_{31})]$$

$$b_2 = c_{44}(\lambda_{33}\varepsilon_{11} - p_3 e_{15}) + c_{11}(\lambda_{33}\varepsilon_{33} - p_3 e_{33}) - \lambda_{11}(c_{13}+c_{44}) + (e_{15}+e_{31})[p_3(c_{13}+c_{44}) + \lambda_{33}(e_{15}+e_{31}) - \lambda_{11}e_{33}]$$

$$c_2 = c_{44}(\lambda_{33}\varepsilon_{33} - p_3 e_{33})$$

$$a_3 = c_{11}(\lambda_{33}e_{15} + p_3 c_{44}) + \lambda_{11}(e_{31}c_{44} - e_{15}c_{13})$$

$$b_3 = p_3(c_{11} - c_{13}^2 - 2c_{13}c_{44}) + \lambda_{11}[c_{33}(e_{15}+e_{31}) - e_{33}(c_{13}+c_{44})] - \lambda_{33}[c_{13}(e_{15}+e_{31}) + c_{44}e_{31} - c_{11}e_{33}]$$

Table 1 Material properties of cadmium selenide [31]

Elastic constants ($\times 10^{10}$ N m^{-2})				
c_{11}	c_{12}	c_{13}	c_{33}	c_{44}
7.41	4.52	3.93	8.36	1.32
Thermal moduli ($\times 10^5$ N K^{-1} m^{-2})		Piezoelectric constant (C m^{-2})		
λ_{11}	λ_{33}	e_{31}	e_{33}	e_{15}
6.21	5.51	−0.16	0.347	−0.138

Dielectric constant ($\times 10^{-11}$ C^2 N^{-1} m^{-2})		Pyroelectric constant ($\times 10^{-6}$ C N^{-1})	Heat conduction coefficients (W K^{-1} m^{-1})		Thermal expansion coefficient ($\times 10^{-6}$ K^{-1})
ε_{11}	ε_{33}	p_3	β_{11}	β_{33}	α_γ
8.26	9.03	−2.94	9.0	9.0	4.4

$$c_3 = c_{44}(p_3 + \lambda_{33} e_{33}) \tag{A5}$$

a_0, b_0, c_0, and d_0 are defined in (A2).

Appendix B

B.1 Solution to the Problem of Combination of Concentrated Force P_z and Point Charge Q

This is still a nontorsional axisymmetric problem. Introduce the following harmonic functions;

$$\psi_0 = \psi_4 = 0 \quad \psi_j = \mathcal{B}_j \ln R_j^* \quad (j = 1,2,3) \tag{B1}$$

where R_j^* is defined in Eq. (12) and $\mathcal{B}_j$ $(j=1,2,3)$ are constants to be determined by

$$\sum_{j=1}^{3} s_j \omega_{1j} \mathcal{B}_j = 0$$

$$2\pi \sum_{j=1}^{3} \omega_{mj} \mathcal{B}_j = P_m \quad (m = 1,2) \tag{B2}$$

where

$$P_1 = P_z \quad P_2 = -Q$$

B.2 Solution to the Problem of Concentrated Force P_x

This is not an axisymmetic problem and the general solution (3*a*) should be used. Introducing the following harmonic functions:

$$\psi_0 = \frac{\mathcal{C}_0 r \sin\phi}{R_0^*} \quad \psi_j = \frac{\mathcal{C}_j r \cos\phi}{R_j^*} \quad (j = 1,2,3) \quad \psi_4 = 0 \tag{B4}$$

where R_j^* is defined in Eq. (12) and C_j $(j=0,1,2,3)$ are constants to be determined by

$$c_{44} s_0 \mathcal{C}_0 + \sum_{j=1}^{3} s_j \omega_{1j} \mathcal{C}_j = 0$$

$$\sum_{j=1}^{3} \omega_{mj} \mathcal{C}_j = 0 \ (m = 1,2)$$

$$-c_{44} s_0 \mathcal{C}_0 + \sum_{j=1}^{3} s_j \omega_{1j} \mathcal{C}_j = \frac{P_x}{\pi} \tag{B5}$$

The solution for concentrated force P_y is

$$\psi_0 = \frac{\mathcal{D}_0 r \cos\phi}{R_0^*} \quad \psi_j = \frac{\mathcal{D}_j r \sin\phi}{R_j^*} \ (j = 1,2,3) \quad \psi_4 = 0 \tag{B6}$$

where $\mathcal{D}_j$ $(j=0,1,2,3)$ are constants to be determined.

B.3 Solution to the Problem of Concentrated Moment M_y

This is not an axisymmetic problem and general solution (3) should be used. Introducing the following harmonic functions:

$$\psi_0 = \frac{\mathcal{E}_0 r \sin\phi}{R_0 R_0^*} \quad \psi_j = \frac{\mathcal{E}_j r \cos\phi}{R_j R_j^*} \quad (j = 1,2,3) \quad \psi_4 = 0 \tag{B7}$$

where R_j and R_j^* is defined in Eq. (12) and $\mathcal{E}_j$ $(j=0,1,2,3)$ are constants to be determined by

$$c_{44} s_0 \mathcal{E}_0 + 2\sum_{j=1}^{3} s_j \omega_{1j} \mathcal{E}_j = 0$$

$$-\rho_m s_0 \mathcal{E}_0 + \sum_{j=1}^{3} s_j \omega_{mj} \mathcal{E}_j = 0 \quad (m = 1,2)$$

$$2\pi \sum_{j=1}^{3} \omega_{1j} \mathcal{E}_j = M_y \tag{B8}$$

where ρ_m are defined in Eq. (7*c*)

The solution for concentrated moment M_x is

$$\psi_0 = \frac{\mathcal{F}_0 r \cos\phi}{R_0 R_0^*} \quad \psi_j = \frac{\mathcal{F}_j r \sin\phi}{R_j R_j^*} \quad (j = 1,2,3) \quad \psi_4 = 0 \tag{B9}$$

where $\mathcal{F}_j$ $(j=0,1,2,3)$ are constants to be determined.

B.4 Solution to the Problem of Concentrated Moment M_z

This is a torsional axisymmetric problem. Introducing the following harmonic functions:

$$\psi_0 = \frac{\mathcal{G}_0}{R_0} \quad \psi_j = 0 \quad (j = 1,2,3,4) \tag{B10}$$

where R_0 is defined in Eq. (12) and $\mathcal{G}_0$ is constant to be determined by

$$\mathcal{G}_0 = -\frac{M_z}{4\pi\sqrt{c_{44} c_{66}}} \tag{B11}$$

References

[1] Deeg, W. F., 1980, "The Analysis of Dislocation, Crack, and Inclusion Problem in Piezoelectric Solids," Ph.D. dissertation, Stanford University, Stanford, CA.

[2] Wang, B., 1992, "Three Dimensional Analysis of An Ellipsoidal Inclusion in a Piezoelectric Material," Int. J. Solids Struct., **29**, pp. 293–308.

[3] Benveniste, Y., 1992, "The Determination of The Elastic and Electric Fields in a Piezoelectric Inhomogeneity," J. Appl. Phys., **72**, pp. 1086–1095.

[4] Chen, T. Y., 1993, "Green's Functions and the Nonuniform Transformation Problem in a Piezoelectric Medium," Mech. Res. Commun., **20**, pp. 271–278.

[5] Chen, T. Y., and Lin, F. Z., 1993, "Numerical Evaluation of Derivatives of The Anisotropic Piezoelectric Green's Functions," Mech. Res. Commun., **20**, pp. 501–506.

[6] Pan, E. N., 1999, "A BEM Analysis of Fracture Mechanics in 2D Anisotropic Piezoelectric Solids," Eng. Anal. Boundary Elem., **23**, pp. 67–76.

[7] Gao, C. F., and Fan, W. X., 1998, "Green's Functions for The Plane Problem in a Half Infinite Piezoelectric Medium," Mech. Res. Commun., **25**, pp. 69–74.

[8] Pan, E., and Tonon, F., 2000, "Three-Dimensional Green's Functions in Anisotropic Piezoelectric Solids," Int. J. Solids Struct., **37**, pp. 943–958.

[9] Pan, E., and Yuan, F. G., 2000, "Three-Dimensional Green's Functions in Anisotropic Piezoelectric Bimaterials," Int. J. Eng. Sci., **38**, pp. 1939–1960.

[10] Sosa, H. A., and Castro, M. A., 1994, "On Concentrated Load at Boundary of a Piezoelectric Half-Plane," J. Mech. Phys. Solids, **42**, pp. 1105–1122.

[11] Lee, J. S., and Jiang, L. Z., 1994, "A Boundary Integral Formulation and 2D Fundamental Solution for Piezoelectric Media," Mech. Res. Commun., **22**, pp. 47–54.

[12] Ding, H. J., Wang, G. Q., and Chen, W. Q., 1997, "Fundamental Solution for Plane Problem of Piezoelectric Materials," Science in China, Sci. China, Ser. E: Technol. Sci., **40**, pp. 331–336.

[13] Ding, H. J., Wang, G. Q, and Chen, W. Q., 1998, "A Boundary Integral Formulation and 2D Fundamental Solutions for Piezoelectric Media," Comput. Methods Appl. Mech. Eng., **158**, pp. 65–80.

[14] Ding, H. J., Wang, G. Q., and Chen, W. Q., 1997, "Green's Functions for a Two-phase Infinite Piezoelectric Plane," Proc. R. Soc. London, Ser. A, **453**, pp. 2241–2257.

[15] Wang, Z. K., and Chen, G. C., 1994, "A General Solution and The Application of Space Axisymmetric Problem in Piezoelectric Materials," Appl. Math. Mech., **15**, pp. 615–626.

[16] Wang, Z. K., and Zheng, B. L., 1995, "The General Solution of Three-dimensional Problem in Piezoelectric Media," Int. J. Solids Struct., **31**, pp. 105–115.

[17] Dunn, M. L., 1994, "Electroelastic Green's Functions for Transversely Isotropic Piezoelectric Media and Their Application to The Solution of Inclusion and Inhomogeneity Problems," Int. J. Eng. Sci., **32**, pp. 119–131.

[18] Dunn, M. L., and Wienecke, H. A., 1996, "Green's Functions for Transversely Isotropic Piezoelectric Solids," Int. J. Solids Struct., **33**, pp. 4571–4581.

[19] Dunn, M. L., and Wienecke, H. A., 1999, "Half-Space Green's Functions For Transversely Isotropic Piezoelectric Solids," ASME J. Appl. Mech., **66**, pp. 675–679.

[20] Ding, H. J., Liang, J., and Chen, B., 1996, "Fundamental Solution for Transversely Isotropic Piezoelectric Media," Sci. China, Ser. E: Technol. Sci., **39**, pp. 766–775.
[21] Ding, H. J., Chen, B., and Liang, J., 1997, "On the Green's Functions for Two-Phase Transversely Isotropic Piezoelectric Media," Int. J. Solids Struct., **34**, pp. 3041–3057.
[22] Dunn, M. L., and Wienecke, H. A., 1997, "Inclusions and Inhomogeneities in Transversely Isotropic Piezoelectric Solids," Int. J. Solids Struct., **34**, pp. 3571–3582.
[23] Rao, S. S., and Sunar, M., 1993, "Analysis of Distributed Thermopiezoelectric Sensors and Actuators in Advanced Intelligent Structures," AIAA J., **31**, pp. 1280–1284.
[24] Qin, Q. H., 1998, "Thermoelectroelastic Green's Function for a Piezoelectric Plate Containing an Elliptic Hole," Mech. Mater., **30**, pp. 21–29.
[25] Qin, Q. H., 1999, "Green's Function for Thermopiezoelectric Materials with Holes of Various Shapes," Arch. Appl. Mech., **69**, pp. 406–418.
[26] Qin, Q. H., 1999, "Thermoelectroelastic Green's Function for Thermal Load inside or on the Boundary of an Elliptic Inclusion," Mech. Mater., **31**, pp. 611–626.
[27] Qin, Q. H., 2000, "Thermoelectroelastic Solution on Elliptic Inclusions and Its Application to Crack-inclusion Problems," Appl. Math. Model., **25**, pp. 1–23.
[28] Chen, W. Q., 2000, "On the General Solution for Piezothermoelasticity for Transverse Isotropy with Application," ASME J. Appl. Mech., **67**, pp. 705–711.
[29] Chen, W. Q., Lim, C. W., and Ding, H. J., 2005, "Point Temperature Solution for a Penny-shaped Crack in An Infinite Transversely Isotropic Thermo-Piezo-Elastic Medium," Eng. Anal. Boundary Elem., **29**, pp. 524–532.
[30] Ding, H. J., Hou, P. F., and Guo, F. L., 1999, "The Elastic and Electric Fields for Elliptical Hertzian Contact for Transversely Isotropic Piezoelectric Bodies," ASME J. Appl. Mech., **66**, pp. 560–562.
[31] Ashida, F., and Tauchert, T. R., 2001, "A General Plane-Stress Solution in Cylindrical Coordinates for a Piezothermoelastic Plate," Int. J. Solids Struct., **38**, pp. 4969–4985.

Free Convection and Mass Transfer Flow Near a Moving Vertical Porous Plate: An Analytical Solution

C. J. Toki[1]
Department of Ecology and Environment,
Technological Educational Institute of Ionian Islands,
Square of Kalvou,
29100 Zakynthos, Greece
e-mail: christina–toki@yahoo.com

An exact solution of the problem of the unsteady free convection and mass transfer flow near an infinite vertical porous plate, which moves with time-dependent velocity in a viscous and incompressible fluid, is presented here by the Laplace transform technique. All expressions of the new solutions of the present problem were obtained in closed forms with arbitrary Prandtl number (P_r), Schmidt number (S_c), thermal Grashof number (G_r), and mass Grashof number (G_m). Two applications of physical interest for porous or nonporous plate are discussed. Applying numerical values into the expressions of analytical solution, we was also discussed the vertical air flows—the usual phenomenon at plumes into the atmosphere. [DOI: 10.1115/1.2745411]

Keywords: free convection, heat transfer, mass transfer, porous plate, Laplace transforms

1 Introduction

Free convection flow involving coupled heat and mass transfer occurs frequently in nature. The driving forces for this flow arise due to the temperature and concentrations variations in the fluid. In atmospheric flows, for example, thermal convection resulting from heating of the earth by sunlight is affected by differences in water vapor concentration. Moreover, there are several engineering situations wherein combined heat and mass transport arise, viz. humidifiers, dehumidifiers, desert coolers, chemical reactors [1]. The usual way to study these phenomena is to consider a characteristic moving continuous surface.

Extensive research work has been published on free convection flow near vertical plate or surface with different boundary conditions [1,2]. The mass transfer effects on free convection flow past an impulsively started infinite vertical isothermal plate were first studied by Soundalgekar [3]. He gave an exact solution of this problem governed by coupled linear differential equations, using the Laplace transform technique. Then, free convection flow with mass transfer past a vertical moving plate has been studied by various authors [4–8].

Recently, the effects of the phenomenon of mass transfer on a free convection flow near an infinite vertical porous plate have been extensively studied by Takhar et al. [9], solving the problem numerically. Similar problems of the free convection with mass transfer have been also studied numerically by Sivasankaran et al. [10] and Alan et al. [11]. Hence, it appears that the analytical solution of this problem will be of greater interest.

The purpose of the present paper is to solve analytically the problem of the unsteady free convection flow of a viscous and incompressible fluid with the effects of mass transfer near an infinite vertical porous plate. Particularly, several flows due to an infinite, vertical, porous and moving plate (or surface) are considered under the action of the buoyancy forces, which arise from the combination of thermal and chemical species diffusion. A general exact solution for the partial differential equations governing these flows is obtained with the aid of the Laplace transform. Furthermore, this general result is applied for the most important cases of the flow where the motion of the porous plate has uniform velocity or acceleration. The case of the nonporous vertical plate is also discussed. During the course of discussions we consider the fluid as air in the presence of foreign species. The conclusions are finally presented.

The present results will be valuable useful for engineering, geophysical and environmental applications, especially for environmental boundary layer under the buoyancy effects [1,12].

2 Formulation of the Problem

Here the unsteady free convection and mass transfer flow of a viscous incompressible fluid near an infinite porous vertical plate (or surface) is considered. On this plate an arbitrary point has been chosen as the origin of a Cartesian coordinate system with the x' axis is along the plate in the upward direction and the y' axis normal to the plate (Fig. 1).

Initially, the plate and the fluid are at the same constant temperature T'_∞ and in stationary condition. Also, the species concentration C'_∞ is the same everywhere. Subsequently ($t' > 0$), this plate is assumed to be moving with a velocity $U_0 f(t')$ in its own plane along the x' axis; instantaneously the temperature of the plate and the concentration are raised to $T'_w (\neq T'_\infty)$ and $C'_w (\neq C'_\infty)$, respectively, which are hereafter regarded as constant.

In physical terms, we also assume for free convection flows that:

(i) All the physical properties of the fluid such as coefficient of viscosity (μ), coefficient of kinetic viscosity (ν), specific heat at constant pressure (c_P), thermal conductivity (κ), volumetric coefficient of thermal expansion (β_1^*), volumetric coefficient of expansion for concentration (β_2^*), chemical molecular diffusivity (D), etc., remain constant.
(ii) The influence of variations of density (ρ) (with temperature) and species concentration are considered only on the body force term, in accordance with the usual Boussinesq approximation [1,4].
(iii) In the energy equation, the term due to the viscous dissi-

[1]Permanent and corresponding address: Pediou Volis 32, Stavraki, 453 22, Ioannina, Greece.

Contributed by the Applied Mechanics Division of ASME for publication in the JOURNAL OF APPLIED MECHANICS. Manuscript received December 23, 2006; final manuscript received April 24, 2007; published online January 14, 2008. Review conducted by Nesreen Ghaddar.

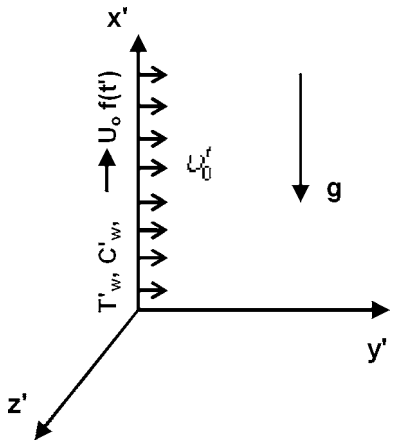

Fig. 1 A schematic of the problem and coordinate system

pation can be neglected in comparison with the conducting term [1,13]. This is a valid assumption, because of small velocities usually encountered in free convection flows [4].

(iv) In the energy equation and in the concentration equation, the thermal-diffusion (Soret) and diffusion-thermal (Dufour) effects can be ignored, because the level of concentration is usually assumed as very low in free convection flows [1,6].

(v) Under these assumptions, the physical variables are functions of the space coordinate y' and time t' only, since the flow of the fluid is assumed to be in the direction of the x' axis.

After all the above assumptions, it can be shown that the governing equations of the two-dimensional flow can be expressed as follows [4]:

Continuity equation (on integration form):

$$v' = \text{const.} = v'_0 \text{ (say)} \tag{1}$$

where v'_0 is the normal velocity of suction or injection at the wall according as $v'_0 < 0$ or $v'_0 > 0$, respectively; $v'_0 = 0$ represents the case of a nonpermeable wall.

Momentum equation:

$$\frac{\partial u'}{\partial t'} + v'_0 \frac{\partial u'}{\partial y'} = \nu \frac{\partial^2 u'}{\partial y'^2} + g\beta_1^*(T' - T'_\infty) + g\beta_2^*(C' - C'_\infty) \tag{2}$$

Energy equation:

$$\frac{\partial T'}{\partial t'} + v'_0 \frac{\partial T'}{\partial y'} = \frac{\kappa}{\rho c_P} \frac{\partial^2 T'}{\partial y'^2} \tag{3}$$

Concentration equation:

$$\frac{\partial C'}{\partial t'} + v'_0 \frac{\partial C'}{\partial y'} = D \frac{\partial^2 C'}{\partial y'^2} \tag{4}$$

Here u' is the velocity, T' is the temperature, C' is the species concentration, and g is the acceleration.

Assuming that no slipping occurs between the plate and the fluid, the initial and boundary conditions corresponding to the present problem are

$$u'(y',t') = 0 \; T'(y',t') = T'_\infty \; C'(y',t') = C'_\infty \quad \text{for } y' \geq 0 \text{ and } t' \leq 0 \tag{5a}$$

$$u'(0,t') = U_0 f(t') \; T'(0,t') = T'_w \; C'(0,t') = C'_w \quad \text{for } t' > 0 \tag{5b}$$

$$u'(\infty,t') \to 0 \; T'(\infty,t') \to T'_\infty \; C'(\infty,t') \to C'_\infty \quad \text{for } t' > 0 \tag{5c}$$

The above equations can be reduced to nondimensional forms by the introduction of the following dimensionless variables and parameters:

$$y = y' U_0/\nu \; t = t' U_0^2/\nu, \quad u = u'/U_0, \quad v_0 = v'_0/U_0 \tag{6a}$$

$$\theta = (T' - T'_\infty)/(T'_w - T'_\infty) \tag{6b}$$

$$C = (C' - C'_\infty)/(C'_w - C'_\infty) \tag{6c}$$

$$P_r = \mu c_P/\kappa \tag{6d}$$

$$S_c = \nu/D \tag{6e}$$

$$G_r = \nu g \beta_1^*(T'_w - T'_\infty)/U_0^3 \tag{6f}$$

$$G_m = \nu g \beta_2^*(C'_w - C'_\infty)/U_0^3 \tag{6g}$$

where G_r is the thermal Grashof number, G_m is the mass Grashof number, P_r is the Prandtl number, and S_c is the Schmidt number.

Using Eqs. (6), we obtain the nondimensional equations of the present problem

$$\frac{\partial^2 \theta}{\partial y^2} - v_0 P_r \frac{\partial \theta}{\partial y} - P_r \frac{\partial \theta}{\partial t} = 0 \quad \text{Energy equation} \tag{7a}$$

$$\frac{\partial^2 C}{\partial y^2} - v_0 S_c \frac{\partial C}{\partial y} - S_c \frac{\partial C}{\partial t} = 0 \quad \text{Concentration equation} \tag{7b}$$

$$\frac{\partial^2 u}{\partial y^2} - v_0 \frac{\partial u}{\partial y} - \frac{\partial u}{\partial t} = -G_r \theta - G_m C \quad \text{Momentum equation} \tag{7c}$$

The corresponding initial and boundary conditions of this system (7) of the differential equations are

$$u(y,t) = 0, \quad T(y,t) = 0, \quad C(y,t) = 0, \quad \text{for } y \geq 0 \text{ and } t \leq 0 \tag{8a}$$

$$u(0,t) = f(t), \quad T(0,t) = 1, \quad C(0,t) = 1, \quad \text{for } t > 0 \tag{8b}$$

$$u(\infty,t) \to 0, \quad T(\infty,t) \to 0, \quad C(\infty,t) \to 0, \quad \text{for } t > 0 \tag{8c}$$

The system (7) of differential equations, subject to the boundary conditions (8), includes the effects of free convection and mass transfer on the flows near a moving isothermal vertical porous plate.

3 Solution of the Problem

In order to obtain the analytical solution of the system (7) of differential equations, we shall use the Laplace transform technique.

Applying the Laplace transform (with respect to time t) to Eqs. (7) and (8), we get the solution of this system in the transform domain in the form

$$\bar{\theta}(y,s) = \frac{1}{s} e^{-ry} \tag{9}$$

$$\bar{C}(y,s) = \frac{1}{s} e^{-my} \tag{10}$$

$$\bar{u}(y,s) = \bar{f}(s) e^{-qy} + \bar{A}_r(y,P_r,s) + \bar{A}_m(y,S_c,s) \tag{11}$$

where

$$\bar{A}_r(y,P_r,s) = \frac{G_r}{s(r^2 + v_0 r - s)}(e^{-qy} - e^{-ry}) \text{ for } P_r \neq 1 \tag{12a}$$

$$\bar{A}_r(y,1,s) = \frac{yG_r}{s(v_0^2+4s)^{1/2}} e^{-qy} \text{ for } P_r = 1 \tag{12b}$$

$$\bar{A}_m(y,S_c,s) = \frac{G_m}{s(m^2+v_0 m-s)}(e^{-qy}-e^{-my}) \text{ for } S_c \neq 1 \tag{12c}$$

$$\bar{A}_m(y,1,s) = \frac{yG_m}{s(v_0^2+4s)^{1/2}} e^{-qy} \text{ for } S_c = 1 \tag{12d}$$

with the abbreviations

$$q \equiv \left(s+\frac{1}{4}v_0^2\right)^{1/2} - \frac{1}{2}v_0 \tag{13a}$$

$$r \equiv P_r^{1/2}\left(s+\frac{1}{4}v_0^2 P_r\right)^{1/2} - \frac{1}{2}v_0 P_r \tag{13b}$$

$$m \equiv S_c^{1/2}\left(s+\frac{1}{4}v_0^2 S_c\right)^{1/2} - \frac{1}{2}v_0 S_c \tag{13c}$$

Now, the exact solution of the system (7) can be obtained by taking the inverse transforms of Eqs. (9)–(11). So, the general solution of the present problem for the temperature $\theta(y,t)$, the species concentration $C(y,t)$ ant the velocity $u(y,t)$ for $t>0$ is in nondimensional form,

$$\theta(y,t) = \frac{1}{2}\operatorname{erfc}\left[\frac{1}{2}y(P_r/t)^{1/2} - \frac{1}{2}v_0(P_r t)^{1/2}\right] + \frac{1}{2}e^{P_r v_0 y}\operatorname{erfc}\left[\frac{1}{2}y(P_r/t)^{1/2} + \frac{1}{2}v_0(P_r t)^{1/2}\right] \tag{14a}$$

$$C(y,t) = \frac{1}{2}\operatorname{erfc}\left[\frac{1}{2}y(S_c/t)^{1/2} - \frac{1}{2}v_0(S_c t)^{1/2}\right] + \frac{1}{2}e^{S_c v_0 y}\operatorname{erfc}\left[\frac{1}{2}y(S_c/t)^{1/2} + \frac{1}{2}v_0(S_c t)^{1/2}\right] \tag{14b}$$

$$u(y,t) = \Phi(y,t) + A_r(y,P_r,t) + A_m(y,S_c,t) \tag{14c}$$

where

$$\Phi(y,t) = L^{-1}[\bar{f}(s)e^{-qy}] \tag{15}$$

$$A_r(y,P_r,t) = \frac{G_r P_r}{P_r-1} L^{-1}\left[\frac{1}{sr^2}(e^{-qy}-e^{-ry})\right] \tag{16a}$$

$$= \frac{G_r}{v_0^3 P_r(P_r-1)} L^{-1}\left\{(e^{-qy}-e^{-ry})\left[\frac{P_r^2 v_0^2}{r^3} - \frac{P_r v_0}{r^2} + \frac{1}{r} - \frac{1}{r+v_0 P_r}\right]\right\} \tag{16b}$$

$$= \frac{G_r}{v_0^2(P_r-1)}\left\{\exp\left(\frac{1}{2}yv_0 - \frac{1}{4}v_0^2 t\right)\sum_{\nu=2}^{3}\beta_\nu Ts_\nu\left(y,-\frac{1}{2}v_0 P_r{}^{1/2},\frac{1}{4}v_0^2(P_r-1),t\right) - \exp\left(\frac{1}{2}yv_0 P_r - \frac{1}{4}v_0^2 P_r t\right)\sum_{\nu=2}^{3}\beta_\nu Ts_\nu\left(yP_r^{1/2},-\frac{1}{2}v_0 P_r^{1/2},0,t\right)\right\} + \frac{G_r}{v_0^2 P_r(P_r-1)}\left[F\left(y,\frac{1}{2}v_0,t\right) - F\left(yP_r^{1/2},\frac{1}{2}v_0 P_r^{1/2},t\right)\right] \quad \text{for } P_r \neq 1 \tag{16c}$$

$$A_r(y,1,t) = \frac{yG_r}{2v_0}\left[\operatorname{erfc}\left(\frac{1}{2}y/t^{1/2} - \frac{1}{2}v_0 t^{1/2}\right) - e^{yv_0}\operatorname{erfc}\left(\frac{1}{2}y/t^{1/2} + \frac{1}{2}v_0 t^{1/2}\right)\right] \quad \text{for } P_r = 1 \tag{16d}$$

$$A_m(y,S_c,t) = \frac{G_m S_c}{S_c-1} L^{-1}\left[\frac{1}{sm^2}(e^{-qy}-e^{-my})\right] \tag{17a}$$

$$= \frac{G_m}{v_0^3 S_c(S_c-1)} L^{-1}\left\{(e^{-qy}-e^{-ry})\left[\frac{S_c^2 v_0^2}{m^3} - \frac{S_c v_0}{m^2} + \frac{1}{m} - \frac{1}{m+v_0 S_c}\right]\right\} \tag{17b}$$

$$= \frac{G_m}{v_0^2(S_c-1)}\left\{\exp\left(\frac{1}{2}yv_0 - \frac{1}{4}v_0^2 t\right)\sum_{\nu=2}^{3}\gamma_\nu Ts_\nu\left(y,-\frac{1}{2}v_0 S_c^{1/2},\frac{1}{4}v_0^2(S_c-1),t\right) - \exp\left(\frac{1}{2}yv_0 S_c - \frac{1}{4}v_0^2 S_c t\right)\sum_{\nu=2}^{3}\gamma_\nu Ts_\nu\left(yS_c^{1/2},-\frac{1}{2}v_0 S_c^{1/2},0,t\right)\right\} + \frac{G_m}{v_0^2 S_c(S_c-1)}\left[F\left(y,\frac{1}{2}v_0,t\right) - F\left(yS_c^{1/2},\frac{1}{2}v_0 S_c^{1/2},t\right)\right] \quad \text{for } S_c \neq 1 \tag{17c}$$

$$A_m(y,1,t) = \frac{yG_m}{2v_0}\left[\operatorname{erfc}\left(\frac{1}{2}y/t^{1/2} - \frac{1}{2}v_0 t^{1/2}\right) - e^{yv_0}\operatorname{erfc}\left(\frac{1}{2}y/t^{1/2} + \frac{1}{2}v_0 t^{1/2}\right)\right] \quad \text{for } S_c = 1 \tag{17d}$$

In the above expressions, the functions $Ts_j(\alpha,k,\lambda,t)$, $j=2,3$ are derived in Appendix A (see Eqs. (A3)), the coefficients β_j and γ_j, $j=2,3$ are given by

$$\beta_2 = -\frac{1}{P_r}, \quad \beta_3 = \frac{v_0}{P_r^{1/2}}, \quad \gamma_2 = -\frac{1}{S_c}, \quad \gamma_3 = \frac{v_0}{S_c^{1/2}} \tag{18}$$

and

$$F(z,b,t) = \frac{1}{2}\operatorname{erfc}\left(\frac{1}{2}z/t^{1/2} - bt^{1/2}\right) + \frac{1}{2}e^{2zb}\operatorname{erfc}\left(\frac{1}{2}z/t^{1/2} + bt^{1/2}\right) \tag{19}$$

The new expressions (14) are the general solution of the present problem. This general solution includes the effects of the heating (cf. term A_r), the diffusion (cf. term A_m), and the motion of the plate (cf. term $\Phi(y,t)$). Hereafter, we shall confine our moreover analysis primary to nondimensional velocity $u(y,t)$ for various types of $f(t)$, since the nondimensional temperature $\theta(y,t)$ and the nondimensional species concentration $C(y,t)$ are clearly described from the mathematical expressions (14*a*) and (14*b*), respectively.

4 Applications of the General Solution

In the present section the previous general result is applied to the two most important cases of flow: (i) the case of the motion of the plate with uniform velocity and (ii) the case of a single accelerated motion of the plate.

Case 1: Motion with uniform velocity. In this case the motion of plate corresponds to $f(t)=H(t)$ [with $H(t)$ the Heaviside unit function and $\bar{f}(s)=1/s$]. So, we observe that the solutions (14*a*) and (14*b*) for the temperature $\theta(y,t)$ and the species concentration $C(y,t)$, respectively, are unaffected and the solution (14*c*) for the velocity $u(y,t)$ for $t>0$ gives

$$u(y,t)=\frac{1}{2}\,\mathrm{erfc}\left(\frac{1}{2}y/t^{1/2}-\frac{1}{2}v_0t^{1/2}\right)+\frac{1}{2}e^{v_0y}\,\mathrm{erfc}\left(\frac{1}{2}y/t^{1/2}+\frac{1}{2}v_0t^{1/2}\right)+A_r(y,P_r,t)+A_m(y,S_c,t) \tag{20}$$

where the terms $A_r(y,P_r,t)$ and $A_m(y,S_c,t)$ are given from Eqs. (16) and (17), respectively, for various values of P_r and S_c.

Case 2: Accelerated motion. Consider now a single accelerated motion of the plate, which corresponds to $g(t)=tH(t)$ (with $\bar{g}(s)=1/s^2$). In this case, the solutions (14*a*) and (14*b*) are again unaffected and the solution (14*c*) for the velocity $u(y,t)$ for $t>0$ gives

$$u(y,t)=\frac{1}{2}(t-y/v_0)\mathrm{erfc}\left(\frac{1}{2}y/t^{1/2}-\frac{1}{2}v_0t^{1/2}\right)+\frac{1}{2}(t+y/v_0)e^{v_0y}\,\mathrm{erfc}\left(\frac{1}{2}y/t^{1/2}+\frac{1}{2}v_0t^{1/2}\right)+A_r(y,P_r,t)+A_m(y,S_c,t) \tag{21}$$

where the terms $A_r(y,P_r,t)$ and $A_m(y,S_c,t)$ are given again from Eqs. (16) and (17), respectively, for various values of P_r and S_c.

5 The Case of the Nonporous Vertical Plate

In this section we shall discuss a special case of the present problem considering the moving vertical plate as a nonporous plate. In this case suction or injection at the moving plate (or surface) is zero.

When the moving plate is a nonporous plate ($v_0=0$), we get reduced expressions of the general solution (14) for the temperature $\theta(y,t)$, the species concentration $C(y,t)$, and the velocity $u(y,t)$ for $t>0$, namely,

$$\theta(y,t)=\mathrm{erfc}\left[\frac{1}{2}y(P_r/t)^{1/2}\right] \tag{22a}$$

$$C(y,t)=\mathrm{erfc}\left[\frac{1}{2}y(S_c/t)^{1/2}\right] \tag{22b}$$

$$u(y,t)=\Phi^*(y,t)+A_r^*(y,P_r,t)+A_m^*(y,S_c,t) \tag{22c}$$

where

$$\Phi^*(y,t)=L^{-1}[\bar{f}(s)e^{-ys^{1/2}}] \tag{23}$$

$$A_r^*(y,P_r,t)=\frac{G_r}{P_r-1}L^{-1}[s^{-2}(e^{-ys^{1/2}}-e^{-yP_rs^{1/2}})] \tag{24a}$$

$$=\frac{G_r}{P_r-1}\left\{\left(t+\frac{1}{2}y^2\right)\mathrm{erfc}\left(\frac{1}{2}y/t^{1/2}\right)-y(t/\pi)^{1/2}e^{-y^2/4t}-\left(t+\frac{1}{2}y^2P_r\right)\mathrm{erfc}\left[\frac{1}{2}y(P_r/t)^{1/2}\right]+yP_r(t/\pi)^{1/2}e^{-y^2P_r/4t}\right\} \tag{24b}$$

$$A_r^*(y,1,t)=\frac{1}{2}yG_rL^{-1}[s^{-3/2}e^{-ys^{1/2}}]=yG_r(t/\pi)^{1/2}e^{-y^2/4t}-\frac{1}{2}y^2G_r\,\mathrm{erfc}\left(\frac{1}{2}y/t^{1/2}\right) \tag{24c}$$

$$A_m^*(y,S_c,t)=\frac{G_m}{S_c-1}L^{-1}[s^{-2}(e^{-ys^{1/2}}-e^{-yS_cs^{1/2}})] \tag{25a}$$

$$=\frac{G_m}{S_c-1}\left\{\left(t+\frac{1}{2}y^2\right)\mathrm{erfc}\left(\frac{1}{2}y/t^{1/2}\right)-y(t/\pi)^{1/2}e^{-y^2/4t}-\left(t+\frac{1}{2}y^2S_c\right)\mathrm{erfc}\left[\frac{1}{2}y(S_c/t)^{1/2}\right]+yS_c(t/\pi)^{1/2}e^{-y^2S_c/4t}\right\} \tag{25b}$$

$$A_m^*(y,1,t)=\frac{1}{2}yG_mL^{-1}[s^{-3/2}e^{-ys^{1/2}}]=yG_m(t/\pi)^{1/2}e^{-y^2/4t}-\frac{1}{2}y^2G_m\,\mathrm{erfc}\left(\frac{1}{2}y/t^{1/2}\right) \tag{25c}$$

Now, we consider the important cases of flow near a nonporous vertical moving plate: (i) the case of the motion of the plate with uniform velocity and (ii) the case of a single accelerated motion of the plate:

(i) For the case $f(t)=H(t)$ and $v_0=0$, the expressions (22*a*) and (22*b*) remain unaffected and the relation (22*c*) is reduced to

$$u(y,t)=\mathrm{erfc}\left(\frac{1}{2}y/t^{1/2}\right)+A_r^*(y,P_r,t)+A_m^*(y,S_c,t) \tag{26}$$

(ii) For the case $f(t)=tH(t)$ and $v_0=0$, the expressions (22*a*) and (22*b*) remain again in the same form. Then, instead of the solution (22*c*), we get the following analytical expression:

$$u(y,t)=\left(t+\frac{1}{2}y^2\right)\mathrm{erfc}\left(\frac{1}{2}y/t^{1/2}\right)-y(t/\pi)^{1/2}\exp(-y^2/4t)+A_r^*(y,P_r,t)+A_m^*(y,S_c,t) \tag{27}$$

The terms $A_r^*(y,P_r,t)$ and $A_m^*(y,S_c,t)$ of Eqs. (26) and (27) are given from Eqs. (24) and (25), respectively, for various values of P_r and S_c.

It should be pointed out here that my results of the case (i) (cf. Eq. (26)) are identical with those of Soundalgekar [3].

6 Discussion

An analytical solution for the problem of the unsteady free-convection flow with mass transfer near a moving porous vertical plate has been determined without any restrictions.

Expression (14) is the general solution of the present problem. The expressions (14*a*) and (14*b*) prescribe clearly the temperature $\theta(y,t)$ and the species concentration $C(y,t)$, respectively.

The velocity field was obtained by superposition of three terms (cf. Eq. (14*c*)). The first term $\Phi(y,t)$ depends on the motion of the plate. So, the previous result is applied to the two most important cases of the flow where the motion of the plate has uniform velocity or acceleration (cf. Eqs. (20) and (21)). The second term $A_r(y,P_r,t)$ expresses the effects of free convection currents due to the heating of the plate. The third term $A_m(y,S_c,t)$ expresses the effects of mass transfer on the flow due to the concentration level near to the plate.

The general solution which was exemplified in the previous sections can prove that its results satisfy the initial basic equations of the present problem.

Indeed, Eqs. (14) are exact solution of the system of differential Eqs. (7). First of all, it can be easily verified that the initial and boundary conditions by $\theta(y,t)$, $C(y,t)$, and $u(y,t)$. The verification of $\theta(y,t)$ and $C(y,t)$ given by (14*a*) and (14*b*) as solutions of (7*a*) and (7*b*), respectively, are straightforward, and are not done here.

We shall, however, show that Eq. (14*c*) represents the exact solution of Eq. (7*c*) for the motion of the plate with uniform

velocity or single acceleration (cf. Eqs. (20) and (21)). So, we observe that the left-hand side of Eq. (7*c*) can be reduced in the form

$$\frac{\partial^2 u(y,t)}{\partial y^2} - v_0 \frac{\partial u(y,t)}{\partial y} - \frac{\partial u(y,t)}{\partial t} = \left(\frac{\partial^2}{\partial y^2} - v_0 \frac{\partial}{\partial y} - \frac{\partial}{\partial t}\right)[\Phi(y,t) + A_r(y,P_r,t) + A_m(y,S_c,t)] \tag{28a}$$

$$= -G_r F\left(yP_r^{1/2}, \frac{1}{2}v_0 P_r^{1/2}, t\right) - G_m F\left(yS_c^{1/2}, \frac{1}{2}v_0 S_c^{1/2}, t\right) \tag{28b}$$

$$= -G_r\theta - G_m C \tag{28c}$$

Because it can be calculated the following expressions (cf. Appendix B) for both cases of the motion of the plate with uniform velocity or single acceleration and for any values of P_r and S_c,

$$\left(\frac{\partial^2}{\partial y^2} - v_0 \frac{\partial}{\partial y} - \frac{\partial}{\partial t}\right)\Phi(y,t) = 0 \tag{29a}$$

$$\left(\frac{\partial^2}{\partial y^2} - v_0 \frac{\partial}{\partial y} - \frac{\partial}{\partial t}\right)A_r(y,P_r,t) = -G_r F\left(yP_r^{1/2}, \frac{1}{2}v_0 P_r^{1/2}, t\right) \tag{29b}$$

$$\left(\frac{\partial^2}{\partial y^2} - v_0 \frac{\partial}{\partial y} - \frac{\partial}{\partial t}\right)A_m(y,S_c,t) = -G_m F\left(yS_c^{1/2}, \frac{1}{2}v_0 S_c^{1/2}, t\right) \tag{29c}$$

where the function $F(z,b,t)$ is given from Eq. (19).

Finally, from Eq. (28), it can be seen that Eq. (7*c*) is identically satisfied for both cases of the motion of the plate (cf. Sec. 4).

It should be pointed out here that the present solutions of the problem were obtained in closed forms with arbitrary Prandtl number (P_r) and Schmidt number (S_c). So, these solutions are ready for physical applications with $P_r = S_c$ or $P_r \neq S_c$.

The present solutions can be applied to an important class of flows in which the driving force for the flow is provided by combination of the thermal and chemical species diffusion effects. Examples of these applications are the flames and combustion, such as those related to furnaces, fires, chemical reactors, and engines, which are responsible for atmospheric pollution [1].

In order to get physical insight into the present problem, we give an example of evaluation of the numerical values of the velocity $u(y,t)$, the temperature $\theta(y,t)$ and the species concentration $C(y,t)$ for the case of air (P_r=0.71). The present results for air could be used as base for the study of plume flows into the atmosphere [12], which are responsible for atmospheric pollution [1].

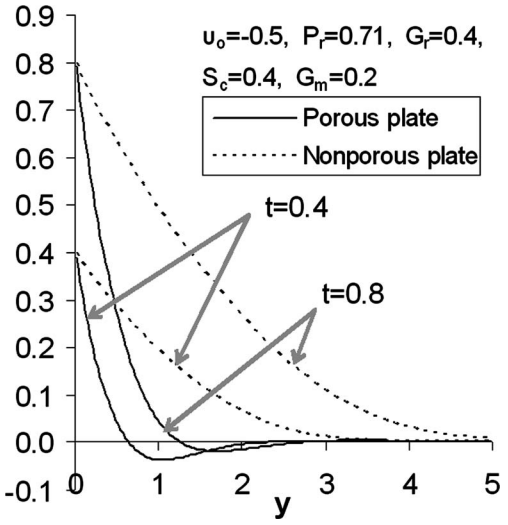

Fig. 3 Comparison of velocity profiles between the air flows near porous and nonporous vertical plates, which are moved with single acceleration

Numerical calculations in the present example have been carried out for different values of G_r and G_m and for fixed value of P_r (=0.71); the numerical values of the Schmidt number (S_c) are chosen such that they represent a reality in case of atmospheric air (cf., the numerical values of S_c, G_r and G_m on the work of Das et al. [6]).

Applying numerical values into the expressions of exact solutions (cf. Eqs. (20), (21), (26), and (27)) for the velocity, we get the velocity profiles of air flow near porous and nonporous vertical plates; Fig. 2 corresponds to the plates moving with uniform velocity and Fig. 3 to the plates, which are moved with single acceleration. We observe that the velocities near the porous plate are smaller than those of nonporous plate in both figures. In Fig. 2, the results are identical with those of Soundalgekar [3], since his exact solution of nonporous plate with uniform velocity is identical with Eq. (26).

The temperature profiles are derived from (14*a*) and (22*a*) and are shown in Fig. 4 for air. Similar, the species concentration profiles are evaluated from expressions (14*b*) and (22*b*) and these are plotted in Fig. 5. We observe that the temperatures and species concentration near the porous plate are smaller than those of non-

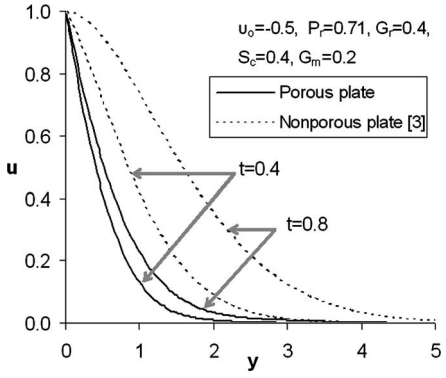

Fig. 2 Comparison of velocity profiles between the air flows near porous and nonporous vertical plates, which are moved with uniform velocity

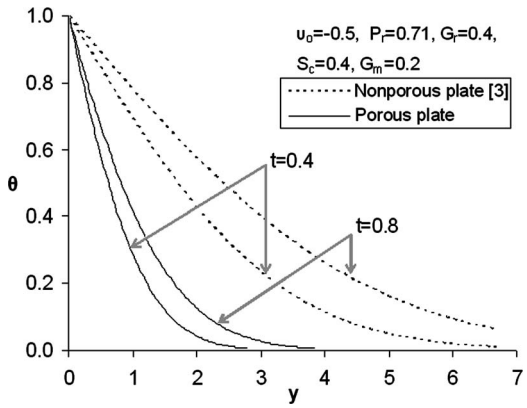

Fig. 4 Comparison of temperature profiles between the air flows near porous and nonporous vertical plates

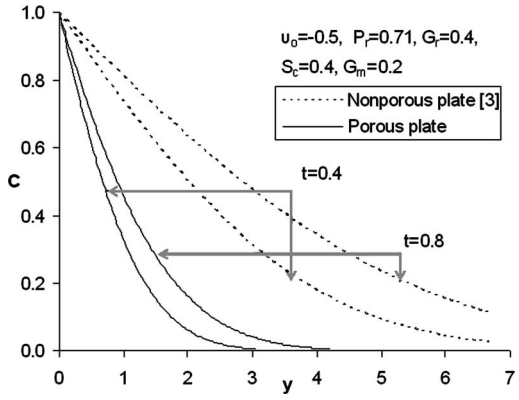

Fig. 5 Comparison of species concentration profiles between the air flows near porous and nonporous vertical plates

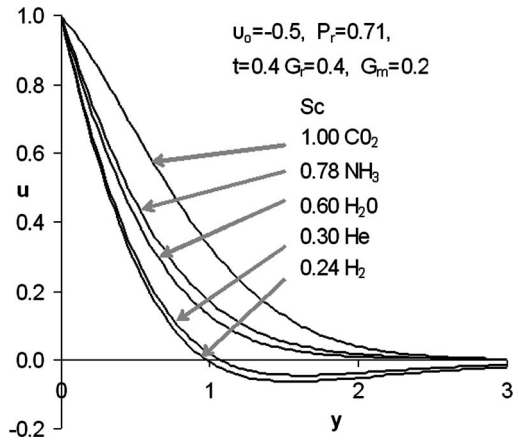

Fig. 6 Velocity profiles of the flow near a porous vertical plate for varying Schmidt number (S_c) at given P_r=0.71

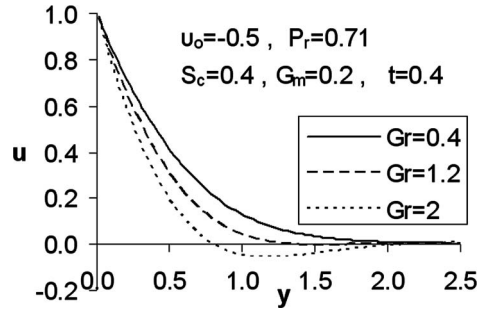

Fig. 7 Velocity profiles of the flow near a porous vertical plate for varying Grashof number (G_r) at given P_r=0.71

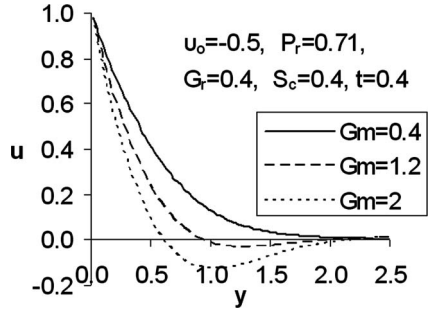

Fig. 8 Velocity profiles of the flow near a porous vertical plate for varying modified Grashof number (C_m) at given P_r=0.71

porous plate in both figures. In both Figs. 4 and 5, the results are identical with those of Soundalgekar [3], since his exact solutions of nonporous are identical with Eqs. (22*a*) and (22*b*).

For various values of Schmidt number (S_c) the velocity profiles of air flow near porous plate are shown on Fig. 6. The numerical values of S_c are chosen such that they represent a reality in case of air. These values of S_c are: 0.24 (H_2), 0.30 (He), 0.60 (H_2O), 0.78 (NH_3), and 1.00 (CO_2). It is seen from this figure that an increase in the Schmidt number leads to an increase in the velocity of air [10].

Moreover, for different values of the Grashof number (G_r) or of the modified Grashof number (C_m) the velocity profiles of air flow near porous plate are shown in Fig. 7 and Fig. 8, respectively. It is observed that increasing values of the G_r or C_m leads to a fall in the velocity for both cases.

7 Conclusions

(1) A general analytical solution for the problem of the unsteady free-convection flow with mass transfer near a moving porous vertical plate has been determined without any restrictions.
(2) It was proven that this general solution satisfies the initial basic equations of the present problem.
(3) The new analytical solution was discussed for the special case of the present problem considering the moving vertical plate as a nonporous plate. In this case of nonporous plate moving with uniform velocity, the present solution was found to be identical with the result of Soundalgekar [3].
(4) We study a physical example of evaluation of the numerical values of the velocity, the temperature and the species concentration for the case of air (P_r=0.71) near porous and nonporous plates. So, we deduce from the graphs that the velocities, temperatures, and species concentration near the porous plate are smaller than those of nonporous plate [3].
(5) To our knowledge, this work gives in close form the actual analytical solution of the free-convection flow with the mass transfer problem, which—besides engineering applications—is interested in the study of vertical air flows into the atmosphere.

Nomenclature

$A_m(y,S_c,t)$ = function due to the effects of mass transfer (cf. Eq. (16))
$A_r(y,P_r,t)$ = function due to the effects of the heating (cf. Eq. (17))
C = dimensionless species concentration in the fluid near the plate
C' = species concentration in the fluid near the plate
C'_∞ = species concentration in the fluid far away from the plate
C'_w = constant species concentration in the fluid at the plate
c_P = specific heat at constant pressure
D = chemical molecular diffusivity
$f(t')$ = nondimensional function of time
$F(z,b,t)$ = an abbreviating function (cf. Eq. (19))
g = acceleration due to gravity
G_r, G_m = thermal Grashof and mass Grashof numbers, respectively
P_r, S_c = Prandtl and Schmit numbers, respectively
t', t = time and dimensionless time, respectively
T' = temperature of the fluid near the plate
T'_∞ = temperature of the fluid far away from the plate
T'_w = constant temperature of the plate
$Ts_n(\alpha,k,\lambda,t)$ = function of the inverse Laplace transforms (cf. Eq. (A1))

u, v = dimensionless velocity components in the x', y' direction, respectively
u', v' = velocity components in the x', y' direction, respectively
U_0 = constant velocity of the plate
x = dimensionless coordinate along the plate in the upward direction
x' = space coordinate in the x' axis along the plate in the upward direction
y = dimensionless coordinate normal to the plate
y' = space coordinate in y' axis normal to the plate

Greek Symbols

β_j = constant coefficients for $j=2,3$ (cf. Eq. (18))
β_2^* = volumetric coefficient of expansion for concentration
β_1^* = volumetric coefficient of thermal expansion
γ_j = constant coefficients for $j=2,3$ (cf. Eq. (18))
θ = dimensionless temperature of the fluid near the plate
κ = thermal conductivity
μ = coefficient of viscosity
ν = coefficient of kinetic viscosity
ρ = density
v_0', v_0 = velocity and dimensionless velocity of suction or injection, respectively
$\Phi(y,t)$ = function due to the motion of the plate (cf. Eqs. (15), (B7), (B8))

Appendix A

Some inverse Laplace transforms used in the text:

The following functions are introduced. These were obtained from the inverse Laplace transforms, which used in the text and are not available in the literature of the extensive tables.

For $\mathrm{Re}(\alpha^2)>0$ we have [14]

$$T(\alpha,k,\lambda,t)\equiv Ts_1(\alpha,k,\lambda,t)=L^{-1}\left\{\frac{e^{-\alpha s^{1/2}}}{(s+\lambda)^{1/2}+k}\right\}$$
$$=\frac{e^{-\alpha^2/4t}}{(\pi t)^{1/2}}-\frac{k^3}{k^2+\lambda}e^{\alpha k+k^2t}\,\mathrm{erfc}\left(\frac{a}{2t^{1/2}}+kt^{1/2}\right)$$
$$-\frac{\lambda}{2(k+i\lambda^{1/2})}e^{-\lambda t-i\alpha\lambda^{1/2}}\,\mathrm{erfc}\left(\frac{a}{2t^{1/2}}-i(\lambda t)^{1/2}\right)$$
$$-\frac{\lambda}{2(k-i\lambda^{1/2})}e^{-\lambda t+i\alpha\lambda^{1/2}}\,\mathrm{erfc}\left(\frac{a}{2t^{1/2}}+i(\lambda t)^{1/2}\right)\quad t>0 \tag{A1}$$

This function can be given also by the useful form

$$T(\alpha,k,\lambda,t)=\frac{e^{-\alpha^2/4t}}{(\pi t)^{1/2}}-\frac{k^3}{k^2+\lambda}e^{\alpha k+k^2t}\,\mathrm{erfc}\left(\frac{a}{2t^{1/2}}+kt^{1/2}\right)$$
$$-\frac{\lambda^2}{\pi^{1/2}(k^2+\lambda)}e^{-\lambda t}\int_0^t\xi^{-1/2}e^{\lambda\xi-\alpha^2/4\xi}d\xi$$
$$-\frac{\alpha k\lambda}{2\pi^{1/2}(k^2+\lambda)}e^{-\lambda t}\int_0^t\xi^{-3/2}e^{\lambda\xi-\alpha^2/4\xi}d\xi\quad t>0 \tag{A2}$$

Subsequent simplifications and modifications of Eq. (A1) give other results for inverse Laplace transforms. So, differencing the function (A1) with respect to k, we get

$$Ts_{n+1}(\alpha,k,\lambda,t)=L^{-1}\left\{\frac{e^{-\alpha s^{1/2}}}{[(s+\lambda)^{1/2}+k]^{n+1}}\right\}=\frac{(-1)^n}{n!}\frac{\partial^n}{\partial k^n}T(\alpha,k,\lambda,t) \tag{A3a}$$

$$=Q_n(\alpha,k,\lambda,t)-U_{n+1}(\alpha,k,\lambda,t)\quad n=1,2,3,\ldots \tag{A3b}$$

The first term of Eq. (A3*b*) expresses the partial derivatives of the product $Qk^3/(k^2+\lambda)$, namely

$$Q_n(\alpha,k,\lambda,t)=\frac{(-1)^{n+1}}{n!}\left\{\frac{k^3}{k^2+\lambda}\frac{\partial^nQ}{\partial k^n}+\binom{n}{1}\frac{\partial}{\partial k}\left(\frac{k^3}{k^2+\lambda}\right)\frac{\partial^{n-1}Q}{\partial k^{n-1}}\right.$$
$$\left.+\cdots+Q\frac{\partial^n}{\partial k^n}\left(\frac{k^3}{k^2+\lambda}\right)\right\}\quad n=1,2,\ldots \tag{A3c}$$

with the abbreviation

$$Q\equiv e^{\alpha k+k^2t}\,\mathrm{erfc}\left(\frac{1}{2}\alpha t^{-1/2}+kt^{1/2}\right) \tag{A3d}$$

Special cases can be found by the calculations of the partial derivatives of $Q_n=Q_n(\alpha,k,\lambda,t)$ with $n=1,2$. So, we get [14]

$$Q_1=-2(t/\pi)^{1/2}K_0\exp(-\alpha^2/4t)+(\tau K_0+K_1)Q \tag{A4a}$$

$$Q_2=2(t/\pi)^{1/2}\left(\frac{1}{2}\tau K_0+K_1\right)\exp(-\alpha^2/4t)$$
$$-\left[\frac{1}{2}(2t+\tau^2)K_0+\tau K_1+\frac{1}{2}K_2\right]Q$$
$$=2(t/\pi)^{1/2}K_1\exp(-\alpha^2/4t)$$
$$-\left(tK_0+\frac{1}{2}\tau K_1+\frac{1}{2}K_2\right)Q-\frac{1}{2}\tau Q_1 \tag{A4b}$$

where

$$\tau\equiv 2kt+\alpha \tag{A5a}$$

$$K_n\equiv\frac{\partial^n}{\partial k^n}\left(\frac{k^3}{k^2+\lambda}\right)\quad n=0,1,2,\ \text{namely} \tag{A5b}$$

$$K_0\equiv\frac{k^3}{k^2+\lambda}\quad K_1\equiv\frac{k^2(k^2+3\lambda)}{(k^2+\lambda)^2} \tag{A5c}$$

$$K_2\equiv-\frac{2k\lambda}{(k^2+\lambda)^3}(k^2-3\lambda) \tag{A5d}$$

The second term of Eq. (A3*b*) is given by

$$U_{n+1}(\alpha,k,\lambda,t)=\frac{\lambda}{2(k+i\lambda^{1/2})^{n+1}}e^{-\lambda t-i\alpha\lambda^{1/2}}\,\mathrm{erfc}\left(\frac{a}{2t^{1/2}}-i(\lambda t)^{1/2}\right)$$
$$+\frac{\lambda}{2(k-i\lambda^{1/2})^{n+1}}e^{-\lambda t+i\alpha\lambda^{1/2}}\,\mathrm{erfc}\left(\frac{a}{2t^{1/2}}+i(\lambda t)^{1/2}\right)\quad n=1,2,3,\ldots \tag{A6a}$$

which is real for real values of α, k, and t, namely

(i) when $\lambda<0$,

$$U_{n+1}(\alpha,k,\lambda,t)=\frac{\lambda}{2(k-|\lambda|^{1/2})^{n+1}}e^{-\lambda t+\alpha|\lambda|^{1/2}}$$
$$\times\mathrm{erfc}\left(\frac{a}{2t^{1/2}}+(|\lambda|t)^{1/2}\right)$$
$$+\frac{\lambda}{2(k+|\lambda|^{1/2})^{n+1}}e^{-\lambda t-\alpha|\lambda|^{1/2}}$$
$$\times\mathrm{erfc}\left(\frac{a}{2t^{1/2}}-(|\lambda|t)^{1/2}\right)\quad n=1,2,3,\ldots \tag{A6b}$$

(ii) when $\lambda>0$,

$$U_{n+1}(\alpha,k,\lambda,t)=\frac{\lambda}{2(k^2+\lambda)^{(n+1)/2}}e^{-(\alpha^2/4t)}\times\sum_{\nu=0}^{\infty}\frac{(-1)^\nu}{\Gamma\left(\frac{1}{2}\nu+1\right)}(\lambda t+a^2/4t)^{\nu/2}\times\cos[(n+1)\varphi_1+\nu\varphi_2]\quad n=1,2,3,\ldots \tag{A6c}$$

where the angles $\varphi_{1,2}$ are defined by

$$\tan\varphi_1=\lambda^{1/2}/k\quad\tan\varphi_2=2\lambda^{1/2}t/\alpha\quad\text{with } 0\leqslant\varphi_{1,2}<\pi/2 \tag{A6d}$$

Equations (A6*a*)–(A6*d*) with $n=0$ give the corresponding expressions of the sum of last two terms in the left-hand side of Eq. (A1).

From the expression (A3*a*) we can find in the tables of Laplace transforms only the function $Ts_2(\alpha,k,0,t)$. The new expressions $Ts_n(\alpha,k,\lambda,t)$ with $n=2,3$ are used in the text.

We also use the general relation

$$\frac{\partial^2}{\partial\eta^2}Ts_n(\eta\gamma^{1/2},k,\lambda,t)=\gamma\frac{\partial}{\partial t}Ts_n(\eta\gamma^{1/2},k,\lambda,t),\quad\text{with }\eta\text{ real and }n=1,2,3,\ldots \tag{A7}$$

since we can readily prove (cf. Eq. (A1)) that

$$\frac{\partial^2}{\partial\eta^2}T(\eta\gamma^{1/2},k,\lambda,t)=\gamma\frac{\partial}{\partial t}T(\eta\gamma^{1/2},k,\lambda,t) \tag{A8a}$$

$$=\gamma\left\{\frac{1}{(\pi t)^{1/2}}\left(\frac{\eta^2\gamma}{4t^2}-\frac{\eta\gamma^{1/2}k+1}{2t}+k^2\right)\exp\left(-\frac{\eta^2\gamma}{4t}\right)-k^3\,\mathrm{erfc}\left[\frac{1}{2}\eta(\gamma/t)^{1/2}+kt^{1/2}\right]\exp(\eta\gamma^{1/2}k+k^2t)-\lambda T(\eta\gamma^{1/2},k,\lambda,t)\right\} \tag{A8b}$$

Appendix B

After extensive algebraic calculations, the following useful results can be shown for the present paper.

So, using Eqs. (16*c*) and Eq. (A7), we get

$$\left(\frac{\partial^2}{\partial y^2}-\upsilon_0\frac{\partial}{\partial y}-\frac{\partial}{\partial t}\right)A_r(y,P_r,t)=\frac{G_r}{\upsilon_0^2}\left(\frac{1}{P_r}W_2-\frac{\upsilon_0}{P_r^{1/2}}W_3\right)+\frac{G_r}{\upsilon_0^2P_r(P_r-1)}F(y,t)=-G_rF\left(yP_r^{1/2},\frac{1}{2}\upsilon_0P_r^{1/2},t\right) \tag{B1}$$

where

$$W_2\equiv\left(\frac{1}{4}\upsilon_0^2P_rT_{02}+\upsilon_0\frac{\partial T_{02}}{\partial y}+\frac{\partial T_{02}}{\partial t}\right)\exp\left(\frac{1}{2}y\upsilon_0P_r-\frac{1}{4}\upsilon_0^2P_rt\right)=\frac{yP_r^{1/2}}{2t}R \tag{B2}$$

$$W_3=\left(\frac{1}{4}\upsilon_0^2P_rT_{03}+\upsilon_0\frac{\partial T_{03}}{\partial y}+\frac{\partial T_{03}}{\partial t}\right)\exp\left(\frac{1}{2}y\upsilon_0P_r-\frac{1}{4}\upsilon_0^2P_rt\right)=R+\frac{1}{2}\upsilon_0P_r^{1/2}\,\mathrm{erfc}\left[\frac{1}{2}y(P_r/t)^{1/2}-\frac{1}{2}\upsilon_0(P_rt)^{1/2}\right] \tag{B3}$$

$$F(y,t)\equiv\left(\frac{\partial^2}{\partial y^2}-\upsilon_0\frac{\partial}{\partial y}-\frac{\partial}{\partial t}\right)\left[F\left(y,\frac{1}{2}\upsilon_0,t\right)-F\left(yP_r^{1/2},\frac{1}{2}\upsilon_0P_r^{1/2},t\right)\right]=-\frac{1}{2}\upsilon_0^2P_r(P_r-1)e^{\upsilon_0yP_r}\mathrm{erfc}\left[\frac{1}{2}y(P_r/t)^{1/2}+\frac{1}{2}\upsilon_0(P_rt)^{1/2}\right]+P_r^{1/2}(P_r-1)(\upsilon_0-y/2t)R \tag{B4}$$

with the abbreviations

$$T_{0\nu}\equiv Ts_\nu\left(yP_r^{1/2},-\frac{1}{2}\upsilon_0P_r^{1/2},0,t\right)\quad\nu=2,3 \tag{B5}$$

$$R\equiv(\pi t)^{-1/2}\exp\left(\frac{1}{2}y\upsilon_0P_r-\frac{1}{4}\upsilon_0^2P_rt-\frac{y^2}{4t}P_r\right) \tag{B6}$$

and the function $F(z,b,t)$ is given from Eq. (19).

We get also same final result (B1) with $P_r=1$, when we use directly the expression (16*d*) for $A_r(y,1,t)$.

Similarly, we have the result of Eq. (29*c*). The results of Eq. (29*a*) are obtained for two cases of $\Phi(y,t)$ (cf. Eqs. (20) and (21)), namely

$$\Phi=\frac{1}{2}\,\mathrm{erfc}\left(\frac{1}{2}y/t^{1/2}-\frac{1}{2}\upsilon_0t^{1/2}\right)+\frac{1}{2}e^{\upsilon_0y}\,\mathrm{erfc}\left(\frac{1}{2}y/t^{1/2}+\frac{1}{2}\upsilon_0t^{1/2}\right) \tag{B7}$$

or

$$\Phi=\frac{1}{2}(t-y/\upsilon_0)\,\mathrm{erfc}\left(\frac{1}{2}y/t^{1/2}-\frac{1}{2}\upsilon_0t^{1/2}\right)+\frac{1}{2}(t+y/\upsilon_0)e^{\upsilon_0y}\,\mathrm{erfc}\left(\frac{1}{2}y/t^{1/2}+\frac{1}{2}\upsilon_0t^{1/2}\right) \tag{B8}$$

References

[1] Gebhart, B., Jaluria, Y., Mahajan, R. L., and Sammakia, B., 1988, *Buoyancy-Induced Flows and Transport, Hemisphere*, New York, Chaps. 3, 6, 7, 8, 10, 12.

[2] Jaluria, Y., 1980, *Natural Convection Heat and Mass Transfer*, Pergamon, Oxford, UK.

[3] Soundalgekar, V. M., 1979, "Effects of Mass Transfer and Free Convection Currents on the Flow Past an Impulsively Started Vertical Plate," J. Appl. Mech., **46**, pp. 757–760.

[4] Hossain, M. A., and Mandal, A. C., 1985, "Mass Transfer Effects on the Unsteady Free Convection Flow Past an Accelerated Vertical Porous Plate," J. Phys. D, **18**, pp. L63–L69.

[5] Tokis, J. N., 1988, "Free Convection and Mass Transfer Effects on the Magnetohydrodynamic Flows Near a Moving Plate in a Rotating Medium," Astrophys. Space Sci., **98**, pp. 291–301.

[6] Das, U. N., Ray, S. N., and Soundalgekar, V. M., 1996, "Mass Transfer Effects on Flow Past an Impulsively Started Infinite Vertical Plate With Constant Mass Flux—An Exact Solution," Heat Mass Transfer, **31**, pp. 163–167.

[7] Muthucumaraswamy, R., 2003, "Effects of Chemical Reaction on Moving Isothermal Plate With Variable Mass Diffusion," Theor Appl. Mech., **30**(3), pp. 209–220.

[8] Ganesan, P., and Palani, G., 2003, "Natural Convection Effects on Impulsively Started Inclined Plate With Heat and Mass Transfer," Heat Mass Transfer, **39**, pp. 277–283.

[9] Takhar, H. S., Roy, S., and Nath, G., 2003, "Unsteady Free Convection Flow Over an Infinite Vertical Porous Plate Due to the Combined Effects of Thermal and Mass Diffusion, Magnetic Field and Hall Currents," Heat Mass Transfer, **39**, pp. 825–834.

[10] Sivasankaran, S., Bhuvaneswari, M., Kandaswamy, P., and Ramasami, E. K., 2006, "Lie Group Analysis of Natural Convection and Mass Transfer in an Inclined Porous Surface with Heat Generation," J. Appl. Math. Mech., **2**(1), pp. 34–40.

[11] Alan, M. S., Rahman, M. M., and Samadz, M. A., 2006, "Dufour and Soret Effects on Unsteady MHD Free Convection and Mass Transfer Flow Past a Vertical Porous Plate in a Porous Medium," Nonlinear Analysis: Modelling and Control, **11**(3), pp. 217–226.

[12] Eskinazi, S., 1975, *Fluid Mechanics and Thermodynamics of Our Environment*, Academic, New York, Chap. 10.

[13] Holman, J. P., 1972, *Heat Transfer*, McGraw-Hill, New York.

[14] Toki, C. J., and Tokis, J. N., 2007, "Exact Solutions for the Unsteady Free Convection Flows on a Porous Plate with Time-dependent Heating," Z. Angew. Math. Mech., **87**(1), pp. 4–13.

Boundary Perturbation Solution for Nearly Circular Holes and Rigid Inclusions in an Infinite Elastic Medium

Thushan C. Ekneligoda
e-mail: thushan@kth.se

Robert W. Zimmerman[1]
e-mail: robertzi@kth.se

Division of Engineering Geology
and Geophysics,
Royal Institute of Technology,
Stockholm 100 44, Sweden

The boundary perturbation method is used to solve the problem of a nearly circular rigid inclusion in a two-dimensional elastic medium subjected to hydrostatic stress at infinity. The solution is taken to the fourth order in the small parameter epsilon that quantifies the magnitude of the variation of the radius of the inclusion. This result is then used to find the effective bulk modulus of a body that contains a dilute concentration of such inclusions. The corresponding results for a cavity are obtained by setting the Muskhelishvili coefficient κ equal to -1, as specified by the Dundurs correspondence principle. The results for nearly circular pores can be expressed in terms of the pore compressibility. The pore compressibilities given by the perturbation solution are tested against numerical values obtained using the boundary element method, and are shown to have good accuracy over a substantial range of roughness values. [DOI: 10.1115/1.2745826]

Keywords: boundary perturbation, rigid inclusions, cavities, effective moduli

1 Introduction

Determination of the effective elastic moduli of a material containing inclusions or voids is a fundamental problem of mechanics that has relevance to materials science, geophysics, and biomechanics. Most such analyses have been based on the assumption that the inclusions are ellipsoidal, or special cases thereof, such as spherical, cylindrical, spheroidal, etc. [1,2]. In fact, the solution of the problem of an isolated ellipsoidal inclusion in an isotropic matrix is essentially given by the formulation of Eshelby [3]. In contrast, few analytical solutions are available for inclusions of non-ellipsoidal shape. In two dimensions, conformal mapping and the complex variable methods of Kolosov and Muskhelishvili can be used, in principle, to analyze inclusions of essentially any shape [4,5]. Nevertheless, these solutions are difficult to obtain, due in part to the fact that the conformal mapping function of the region inside or outside of a circle, to the region outside a pore or inclusion of arbitrary shape, is usually quite difficult to obtain [6,7], except for a few shapes, such as hypotrochoids [8,9] or quasi-polygons [10–12].

One method that can be used to develop approximate solutions to inclusion problems is the boundary perturbation approach. The basic ideas of the boundary perturbation approach were illustrated by van Dyke [13] in the context of fluid mechanics. Low and Chang [14] used this approach to study stresses around nearly circular pores. Wang and Chao [15] used the boundary perturbation method to solve the problem of a nearly circular inclusion in plane thermoelasticity. Similar studies were carried out by Parnes [16] and Gao [17].

Givoli and Elishakoff [18] used this approach to analyze a corrugated pore in an infinite region, under far-field loading, and found the solution up to terms of second order in the small parameter ε that quantified the amplitude of the corrugations. In the present work we extend this solution to fourth order in ε, and consider both the case of a pore and a rigid inclusion. We then use our solution for the corrugated pore to investigate the effect of small-scale roughness on the pore compressibility and the effective bulk modulus of a body containing a dilute concentration of such pores.

2 Problem Formulation for Infinite Region Containing a Rigid Inclusion

The solution of a two-dimensional isotropic elasticity problem can be represented in terms of the Airy stress function Φ, which satisfies the bi-harmonic equation $\nabla^2\nabla^2\Phi=0$. The general solution, neglecting those terms that do not correspond to a uniform stress at infinity, can be written in polar coordinates as [19,20]

$$\Phi = A_0 r^2 + A_1 \ln r + A_2\theta + \frac{A_3\cos\theta}{r} + \frac{A_4\sin\theta}{r} + \sum_{n=2}^{\infty}[A_{5,n}r^{-n+2}\cos n\theta + A_{6,n}r^{-n}\cos n\theta + A_{7,n}r^{-n+2}\sin n\theta + A_{8,n}r^{-n}\sin n\theta] \tag{1}$$

The stresses and displacements associated with this solution are given by

$$\tau_{rr} = 2A_0 + \frac{A_1}{r^2} - \frac{2A_3\cos\theta}{r^3} - \frac{2A_4\sin\theta}{r^3} - \sum_{n=2}^{\infty}[A_{5,n}(n+2)(n-1)r^{-n} + A_{6,n}n(n+1)r^{-n-2}]\cos n\theta - \sum_{n=2}^{\infty}[A_{7,n}(n+2)(n-1)r^{-n} + A_{8,n}n(n+1)r^{-n-2}]\sin n\theta \tag{2}$$

$$\tau_{\theta\theta} = 2A_0 - \frac{A_1}{r^2} + \frac{2A_3\cos\theta}{r^3} + \frac{2A_4\sin\theta}{r^3} + \sum_{n=2}^{\infty}[A_{5,n}(n-1)(n-2)r^{-n} + A_{6,n}n(n+1)r^{-n-2}]\cos n\theta + \sum_{n=2}^{\infty}[A_{7,n}(n-2)(n-1)r^{-n} + A_{8,n}n(n+1)r^{-n-2}]\sin n\theta \tag{3}$$

[1]Corresponding author.

Contributed by the Applied Mechanics Division of ASME for publication in the JOURNAL OF APPLIED MECHANICS. Manuscript received February 13, 2007; final manuscript received April 24, 2007; published online January 14, 2008. Review conducted by Martin Ostoja-Starzewski.

$$\tau_{r\theta}=\frac{A_2}{r^2}-\frac{2A_3\sin\theta}{r^3}+\frac{2A_4\cos\theta}{r^3}+\sum_{n=2}^{\infty}[A_{7,n}(n)(n-1)r^{-n}+A_{8,n}n(n+1)r^{-n-2}]\cos n\theta-\sum_{n=2}^{\infty}[A_{5,n}(n)(n-1)r^{-n}+A_{6,n}n(n+1)r^{-n-2}]\sin n\theta \tag{4}$$

$$2Gu_r=A_0(\kappa-1)r-\frac{A_1}{r}+\frac{A_3\cos\theta}{r^2}+\frac{A_4\sin\theta}{r^2}+\sum_{n=2}^{\infty}[A_{5,n}(\kappa+n-1)r^{-n+1}+A_{6,n}nr^{-n-1}]\cos n\theta+\sum_{n=2}^{\infty}[A_{7,n}(\kappa+n-1)r^{-n+1}+A_{8,n}nr^{-n-1}]\sin n\theta \tag{5}$$

$$2Gu_\theta=\frac{A_2}{r}+\frac{A_3\sin\theta}{r^2}-\frac{A_4\cos\theta}{r^2}+\sum_{n=2}^{\infty}[A_{7,n}(\kappa-n+1)r^{-n+1}-A_{8,n}nr^{-n-1}]\cos n\theta+\sum_{n=2}^{\infty}[-A_{5,n}(\kappa-n+1)r^{-n+1}+A_{6,n}nr^{-n-1}]\sin n\theta \tag{6}$$

where $(A_0,A_1,A_2,A_3,A_4,A_{5n},A_{6n},A_{7n},A_{8n})$ are constants, and (r,θ) are the usual polar coordinates.

For an infinite region containing a single inclusion, with hydrostatic stress p acting at infinity, (2) and (3) immediately show that $A_0=p/2$. The values of the other coefficients will depend on the shape and elastic properties of the inclusion. Jasiuk et al. [11] and Jasiuk [21] showed that the effective bulk modulus of a body containing a dilute concentration of these inclusions can be expressed solely in terms of the coefficient A_1, as follows:

$$\frac{K_{\text{eff}}}{K}=1+\frac{\kappa+1}{\kappa-1}A_1(\kappa,p=1)\frac{\pi}{A_{\text{inclusion}}}c \tag{7}$$

where K is the two-dimensional bulk modulus of the host material, κ is the Muskhelishvili parameter of the host material, which equals $3-4\nu$ for plane strain and $(3-\nu)/(1+\nu)$ for plane stress, ν is the three-dimensional Poisson ratio of the host material, c is area fraction of the inclusions, and A_1 is the coefficient of the log term in the Airy stress function for the case where the magnitude of the applied pressure is $p=1$. The essential explanation of this result is as follows. The two-dimensional bulk modulus can be related to the area change of the material, which can be calculated by integrating the radial displacement over a large circle centered on the inclusion. The A_0 term, which is independent of the inclusion, gives the area change that would occur in the absence of an inclusion. Most terms in (5) involve sin or cos, and thus their contributions to the area change integrate out to zero. Only the A_1 term gives a non-zero contribution to the excess area change due to the presence of the inclusion. A rigorous proof of (7) has been given in [21].

Dundurs [22] showed that the solution for a body containing a rigid inclusion could be transformed into the solution for the case in which the inclusion is a cavity, by setting $\kappa=-1$. Jasiuk [21] then showed that the effective bulk modulus of a body containing a dilute concentration of these cavities would be given by

$$\frac{K_{\text{eff}}}{K}=1+\frac{\kappa+1}{\kappa-1}A_1(\kappa=-1;p=1)\frac{\pi}{A_{\text{pore}}}c \tag{8}$$

where κ is set equal -1 to in the expression for A_1, but the actual value of κ of the host material is used when evaluating the term $(\kappa+1)/(\kappa-1)$.

We will exploit this correspondence in the present paper. Although we are ultimately mainly interested in the case of vacuous pores, when using the perturbation approach, the case of a rigid nearly circular inclusion is much easier to solve. This is because the boundary condition for the rigid inclusion is that the displacement vector must vanish, which directly implies that both components of the displacement, i.e., u_r and u_θ, must vanish along the boundary. On the the other hand, if the inclusion is a pore, the traction vector must vanish on the boundary. However, the normal and tangential components of the traction vector *on the actual non-circular boundary* are related to the stress components in the polar coordinate system in a very complicated manner [18]. Hence, the solution procedure for a rigid inclusion is substantially simpler than that for a pore. This simplification will allow us to find the solution to fourth-order in the perturbation parameter, as opposed to the second-order solution found by Givoli and Elishakoff [18].

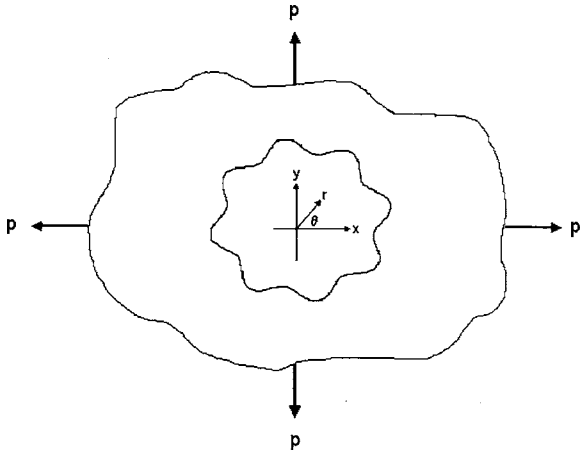

Fig. 1 Nearly circular corrugated inclusion subjected to far-field hydrostatic stress, shown for the case $m=8, \varepsilon=0.10$

3 General Solution for Rigid Inclusion

We start by considering a rigid circular disk of radius a, in an infinitely large plate subjected to a far-field hydrostatic stress of magnitude p. The Airy stress function for this problem is $\Phi=pr^2/2+(\kappa-1)pa^2\ln r/2$ [20], and the associated displacements and stresses are [23]

$$u_r=\frac{p(\kappa-1)r}{4G}-\frac{p(\kappa-1)a^2}{4Gr}\quad u_\theta=0 \tag{9}$$

$$\tau_{rr}=p+\frac{p(\kappa-1)a^2}{2r^2}\quad \tau_{\theta\theta}=p-\frac{p(\kappa-1)a^2}{2r^2}\quad \tau_{r\theta}=0 \tag{10}$$

Now consider a nearly circular inclusion that has a corrugated boundary described by

$$r=a(1+\varepsilon\sin m\theta), \tag{11}$$

where ε is a small parameter representing the amplitude of the corrugations, and m is an integer that represents the number of positive (or negative) bumps on the circumference of the circle. As an example, Fig. 1 shows the inclusion shape for $m=8$ and $\varepsilon=0.25$.

Following the standard procedure for a regular perturbation problem [13,18], we assume that the Airy stress function, the displacements and the stresses can each be expressed as perturbation series in the small parameter ε, i.e.,

$$\Phi(r,\theta)=\Phi^0(r,\theta)+\varepsilon\Phi^1(r,\theta)+\varepsilon^2\Phi^2(r,\theta)+\cdots \tag{12}$$

$$u_r(r,\theta)=u_r^0(r,\theta)+\varepsilon u_r^1(r,\theta)+\varepsilon^2 u_r^2(r,\theta)+\cdots \tag{13}$$

$$u_\theta(r,\theta) = u_\theta^0(r,\theta) + \varepsilon u_\theta^1(r,\theta) + \varepsilon^2 u_\theta(r,\theta) + \cdots \tag{14}$$

where the superscript n in Φ^n denotes the nth Airy function, and is not a power exponent. When $\varepsilon=0$, this solution must reduce to the solution for a circular inclusion, in which case we can say

$$\Phi^0(r,\theta) = \frac{pr^2}{2} + \frac{(\kappa-1)pa^2 \ln r}{2} \tag{15}$$

$$u_r^0(r,\theta) = \frac{p(\kappa-1)r}{4G} - \frac{p(\kappa-1)a^2}{4Gr} \quad u_\theta^0(r,\theta) = 0 \tag{16}$$

Each of the subsequent Airy functions will be of the form given by (1)–(6). As the far-field boundary conditions are already satisfied by the zeroth-order solution, the A_0 coefficient will vanish in all the higher-order Airy functions. The remaining coefficients in these functions are found by satisfying the boundary conditions at the interface between the matrix and the inclusion. These boundary conditions require that both displacement components vanish at the interface. Hence, for the purposes of deriving the solution, the stresses need not be considered any further.

Zero-displacement boundary conditions must be applied at the boundary of the inclusion, where $r \equiv r^* = a(1+\varepsilon \sin m\theta)$. But each function $u_r^n(r,\theta)$ is expressed naturally in terms of r and θ. In order to re-express the boundary conditions at $r=a$ instead of $r=a(1+\varepsilon \sin m\theta)$, the displacements are first expanded in a Taylor series about the value $r=a$, with $a\varepsilon \sin m\theta$ as the small variation in r. Following the procedure used in [18] for the stresses, we can say that

$$\begin{aligned} u_r^n(r^*,\theta) \equiv u_r^n(a + a\varepsilon \sin m\theta, \theta) &= u_r^n(a,\theta) \\ &+ a\varepsilon \sin m\theta \left.\frac{\partial u_r^n(r,\theta)}{\partial r}\right|_{r=a} \\ &+ \left.\frac{a^2\varepsilon^2 \sin^2 m\theta}{2}\frac{\partial^2 u_r^n(r,\theta)}{\partial^2 r}\right|_{r=a} \\ &+ \left.\frac{a^3\varepsilon^3 \sin^3 m\theta}{6}\frac{\partial^3 u_r^n(r,\theta)}{\partial^3 r}\right|_{r=a} + \cdots \end{aligned} \tag{17}$$

and similarly for $u_\theta^n(r^*,\theta)$. Applying this expansion to every term in (13), and then grouping terms according to ascending powers of ε, leads to

$$\begin{aligned} u_r(r^*,\theta) = 0 = u_r^0(a,\theta) &+ \left[a \sin m\theta \left.\frac{\partial u_r^0(r,\theta)}{\partial r}\right|_{r=a} + u_r^1(a,\theta)\right]\varepsilon \\ &+ \left[\left.\frac{a^2 \sin^2 m\theta}{2}\frac{\partial^2 u_r^0(r,\theta)}{\partial^2 r}\right|_{r=a} + a \sin m\theta \left.\frac{\partial u_r^1(r,\theta)}{\partial r}\right|_{r=a} \right. \\ &\left. + u_r^2(a,\theta)\right]\varepsilon^2 + \cdots \end{aligned} \tag{18}$$

and similarly for the tangential displacement,

$$\begin{aligned} u_\theta(r^*,\theta) = 0 = u_\theta^0(a,\theta) &+ \left[a \sin m\theta \left.\frac{\partial u_\theta^0(r,\theta)}{\partial r}\right|_{r=a} + u_\theta^1(a,\theta)\right]\varepsilon \\ &+ \left[\left.\frac{a^2 \sin^2 m\theta}{2}\frac{\partial^2 u_\theta^0(r,\theta)}{\partial^2 r}\right|_{r=a} + a \sin m\theta \left.\frac{\partial u_\theta^1(r,\theta)}{\partial r}\right|_{r=a} \right. \\ &\left. + u_\theta^2(a,\theta)\right]\varepsilon^2 + \cdots \end{aligned} \tag{19}$$

Requiring the no-displacement boundary condition to be satisfied at all orders of ε, the order-ε term in (18) yields

$$u_r^1(a,\theta) = -a \sin m\theta \left.\frac{\partial u_r^0(r,\theta)}{\partial r}\right|_{r=a} = -a \sin m\theta \left\{ \frac{p(\kappa-1)}{4G} + \left[\frac{p(\kappa-1)a^2}{4Gr^2}\right]_{r=a}\right\} = \frac{-p}{2G}(\kappa-1)a \sin m\theta \tag{20}$$

which serves as a boundary condition at $r=a$ for the as-yet unknown function $u_r^1(r,\theta)$. Likewise, the order-ε term in (19) yields

$$u_\theta^1(a,\theta) = -a \sin m\theta \left.\frac{\partial u_\theta^0(r,\theta)}{\partial r}\right|_{r=a} = -a \sin m\theta[0] = 0 \tag{21}$$

Examination of the general solution for Φ^1, as given by (1)–(6), shows that the only terms that yield a $\sin m\theta$ variation for $u_r^1(r,\theta)$ are those involving $A_{7,m}^1$ and $A_{8,m}^1$. Hence, the first-order displacement functions must have the form

$$2Gu_r^1(r,\theta) = \frac{A_{7,m}^1(\kappa+m-1)\sin m\theta}{r^{m-1}} + \frac{A_{8,m}^1 m \sin m\theta}{r^{m+1}} \tag{22}$$

$$2Gu_\theta^1(r,\theta) = \frac{A_{7,m}^1(\kappa-m+1)\cos m\theta}{r^{m-1}} - \frac{A_{8,m}^1 m \cos m\theta}{r^{m+1}} \tag{23}$$

Forcing these expressions to satisfy the boundary conditions (20) and (21) yields

$$\frac{A_{7,m}^1(\kappa+m-1)}{a^{m-1}} + \frac{A_{8,m}^1 m}{a^{m+1}} = -p(\kappa-1)a \tag{24}$$

$$\frac{A_{7,m}^1(\kappa-m-1)}{a^{m-1}} - \frac{A_{8,m}^1 m}{a^{m+1}} = 0 \tag{25}$$

the solution to which is

$$A_{7,m}^1 = \frac{-a^m p(\kappa-1)}{2\kappa} \tag{26}$$

$$A_{8,m}^1 = \frac{-a^{m+2}p(\kappa-1)(\kappa-m+1)}{2m\kappa} \tag{27}$$

Hence, the first-order displacement functions are

$$2Gu_r^1(r,\theta) = \frac{-p(\kappa-1)a^m}{2\kappa}\left[\frac{(\kappa+m-1)}{r^{m-1}} + \frac{(\kappa-m+1)a^2}{r^{m+1}}\right]\sin m\theta \tag{28}$$

$$2Gu_\theta^1(r,\theta) = \frac{-p(\kappa-1)a^m(\kappa-m+1)}{2\kappa}\left[\frac{1}{r^{m-1}} - \frac{a^2}{r^{m+1}}\right]\cos m\theta \tag{29}$$

Next, we set the coefficient of ε^2 to zero in expressions (18) and (19), to find the boundary conditions for $u_r^2(a,\theta)$ and $u_\theta^2(a,\theta)$. First, from the coefficient of ε^2 in (18), and using (16) for $u_r^0(r,\theta)$ and (28) for $u_r^1(r,\theta)$, we find

$$2Gu_r^2(a,\theta) = \frac{ap(k-1)[(\kappa-2)-2m(\kappa-1)]}{4\kappa}(1-\cos 2m\theta) \tag{30}$$

where we have used the identity $2\sin^2 m\theta = 1-\cos 2m\theta$ so as to express the boundary condition as a trigonometric series. Likewise, (16), (19), and (29) give

$$2Gu_\theta^2(a,\theta) = \frac{ap(\kappa-1)(\kappa-m+1)}{2\kappa}\sin 2m\theta \tag{31}$$

Hence, both $u_r^2(r,\theta)$ and $u_\theta^2(r,\theta)$ will consist of a term that is independent of θ, and a term that varies as $\cos 2m\theta$. Examination of the general solution (1)–(6) shows that the second-order displacement functions must therefore have the form

$$2Gu_r^2(r,\theta) = -\frac{A_1^2}{r} + [A_{5,2m}^2(\kappa + 2m - 1)r^{-2m+1} + 2A_{6,2m}^2 m r^{-2m-1}]\cos 2m\theta \tag{32}$$

$$2Gu_\theta^2(r,\theta) = [-A_{5,2m}^2(\kappa - 2m + 1)r^{-2m+1} + 2A_{6,2m}^2 m r^{-2m-1}]\sin 2m\theta \tag{33}$$

Requiring that the functions given by (32) and (33) satisfy the boundary conditions (30) and (31) leads to the following two equations for the $A_{i,2m}^2$ coefficients:

$$\frac{ap(\kappa-1)[(\kappa-2)-2m(\kappa-1)]}{4\kappa}(1-\cos 2m\theta) = -\frac{A_1^2}{a} + [A_{5,2m}^2(\kappa + 2m - 1)a^{-2m+1} + 2A_{6,2m}^2 m a^{-2m-1}]\cos 2m\theta \tag{34}$$

$$\frac{ap(\kappa-1)(\kappa-m+1)}{2\kappa}\sin 2m\theta = [-A_{5,2m}^2(\kappa - 2m + 1)a^{-2m+1} + 2A_{6,2m}^2 m a^{-2m-1}]\sin 2m\theta \tag{35}$$

Matching separately the coefficients of the constant term, the cosine term and the sine term yield the required three equations that allow us to solve for the three coefficients:

$$A_1^2 = \frac{-a^2 p(\kappa-1)[(\kappa-2)-2m(\kappa-1)]}{4\kappa} \tag{36}$$

$$A_{5,2m}^2 = \frac{a^{2m}p(\kappa-1)(2m-3)}{8\kappa} \tag{37}$$

$$A_{6,2m}^2 = \frac{a^{2m+2}p(\kappa-1)}{16m\kappa}[4(\kappa-m+1)+(2m-3)(\kappa-2m+1)] \tag{38}$$

The third-order and fourth-order solutions can be found by following this same methodology. Each of these solutions will have the form given by (5) and (6), but with only a small number of non-zero coefficients. These non-zero coefficients are given in the Appendix . We note here the pattern that only the even-order terms in the perturbation solution contain non-zero values of A_1, and so the expression for the effective bulk modulus will contain only even powers of ε. However, the even-order terms cannot be computed without having already computed all lower-order terms, so the odd terms must be computed, despite the fact that they do not contribute to the bulk modulus. The fact that the expression for the bulk modulus contains only even powers of ε could have been anticipated by noting that letting $\varepsilon \to -\varepsilon$ corresponds to rotating the cavity by one-half of a wavelength. As the far-field stress is isotropic, a rotation of the cavity cannot alter the bulk modulus, and so the expression for K_{eff} must be an even function of ε.

4 Effective Bulk Compressibility and Pore Compressibility

To be specific, we consider plane strain, in which case $(\kappa+1)/(\kappa-1)=2(1-\nu)/(1-2\nu)$. The expression for the effective bulk modulus given by Eq. (8) can then be written in terms of compressibility as follows:

$$\frac{C}{C_{\text{eff}}} = 1 + \frac{2(1-\nu)}{(1-2\nu)}A_1(\kappa=-1;p=1)\frac{\pi}{A_{\text{pore}}}\phi \tag{39}$$

where $C=1/K$ is the bulk compressibility of the host material, and we have replaced the inclusion area fraction c by the usual symbol for porosity ϕ. For small values of ϕ, equation (39) can be expanded as

$$C_{\text{eff}} = C - \frac{2(1-\nu)C}{(1-2\nu)}A_1(\kappa=-1;p=1)\frac{\pi}{A_{\text{pore}}}\phi \tag{40}$$

However, the effective compressibility can also be expressed in the present notation (exactly) as [24]

$$C_{\text{eff}} = C + \phi C_{\text{pc}} \tag{41}$$

where C_{pc} is the compressibility of the pore with respect to the far-field "confining" pressure. Comparison of (40) and (41) shows that the pore compressibility is given by

$$C_{\text{pc}} = \frac{-2(1-\nu)}{G}\frac{A_1(\kappa=-1;p=1)\pi}{A_{\text{pore}}} \tag{42}$$

The pore compressibility parameter is of great importance in petroleum engineering, but also provides a convenient means to discuss the effect of pores on the bulk modulus, as shown by (41).

An interesting qualitative implication of (42) is that, since the term $A_1(-1,1)$ does not depend on the elastic moduli, the pore compressibility is always proportional to $(1-\nu)/G$, with a dimensionless multiplicative factor that depends only on the shape of the pore. This result is consistent with the exact solutions found by Ekneligoda and Zimmerman [9] for a large family of pores having n-fold rotational symmetry, but we see now that it is completely general. Indeed, this fact can also be obtained from some of the recent results of Vigdergauz [25], if they are translated into the present terminology of "pore compressibility."

Returning to our corrugated pore, the pore area can easily be shown to be given by $A_{\text{pore}}=\pi a^2(1+\varepsilon^2/2)$. Hence, using (36) for $A_1(\kappa,p)$, we find, to second order in ε,

$$C_{pc} = \frac{2(1-\nu)}{G}\frac{[1+(4m-3)\varepsilon^2/2]}{(1+\varepsilon^2/2)} \tag{43}$$

The fourth-order perturbation solution yields

$$C_{pc} = \frac{2(1-\nu)}{G}\left[\frac{1+\varepsilon^2(4m-3)/2-\varepsilon^4 f}{(1+\varepsilon^2/2)}\right] \tag{44}$$

$$f = \left[\frac{3}{16} - \frac{1}{32}m(m+1)(2m+1) - \frac{(2m-3)}{8}\right] - \frac{1}{4}\left[\frac{A_{7,2m}^3(m-1)(m-2)}{a^m} + \frac{A_{8,2m}^3 m(m+1)}{a^{m+2}}\right] - \frac{m}{4}\left[\frac{A_{5,2m}^2 m(2m-1)(m-1)}{a^{2m}} + \frac{A_{6,2m}^2 m(2m+1)(m+1)}{a^{2m+1}}\right] \tag{45}$$

where the $A_{i,2m}^2$ coefficients are given in the Appendix .

5 Stress Concentration

The stress concentration at the boundary of a hole in a stressed body is of great engineering interest [4,14]. Givoli and Elishakoff [18] discussed the stress concentration at the boundary of holes described by Eq. (11), as given by their second-order perturbation solution. We have verified that the stresses obtained from our second-order solution agree with those found in [18]. However, as our main interest is in the pore compressibility and the effective bulk modulus, we will not pursue the issue of stress concentration any further.

6 Pore Compressibility of Corrugated Pore

We now compare the compressibilities predicted by our two-term and four-term perturbation solutions with the values obtained by boundary element calculations, and with some upper and lower bounds that can be derived. The boundary element calculations were performed using a code developed by Martel and Muller [26], which is a simplified version of the more general two-dimensional boundary element method code from Crouch and

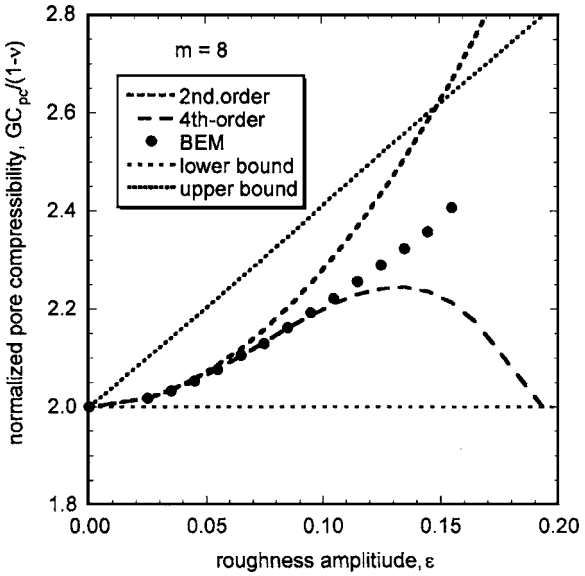

Fig. 2 Pore compressibility as a function of the roughness amplitude, for the case $m=8$

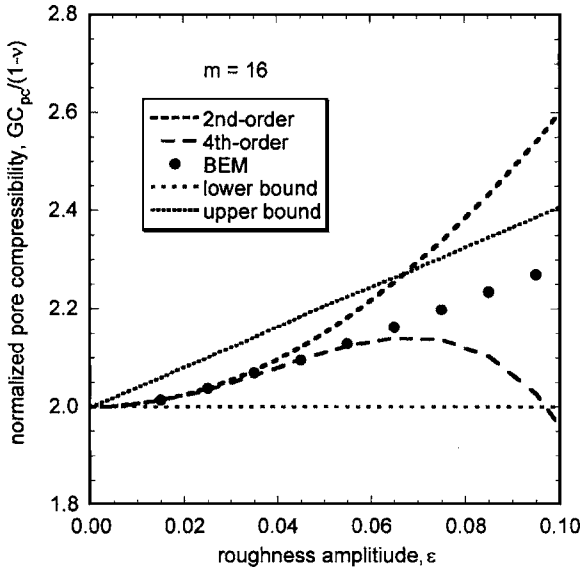

Fig. 3 Pore compressibility as a function of the roughness amplitude, for the case $m=16$

Starfield [27] that is based on the displacement discontinuity method. This code allows us to analyze the problem of a pore of specified shape in an infinite elastic region, with prescribed stresses at infinity, and requires discretization only of the pore boundary. Typically, about 300 boundary elements were needed to obtain a converged solution.

An upper bound on the pore compressibility parameter can be obtained by starting with the fact that if the actual pore is replaced by a pore defined by the smallest possible circumscribed circle, which has radius $a(1+\varepsilon)$, the overall bulk compressibility of the body cannot decrease, since removal of solid material cannot stiffen the body [28]. Considering a large body of area A containing only one pore, we can then say, from (41), that

$$C + \frac{A_{\text{pore}}}{A} C_{\text{pc}}(\text{pore}) \leq C + \frac{A_{\text{circumscribed circle}}}{A} C_{\text{pc}}(\text{circle}) \quad (46)$$

However, $C_{\text{pc}}(\text{circle}) = 2(1-\nu)/G$, $A_{\text{pore}} = \pi a^2(1+\varepsilon^2/2)$, and $A_{\text{circle}} = \pi a^2(1+\varepsilon)^2$, so we find that

$$C_{\text{pc}}(\text{pore}) \leq \frac{(1+\varepsilon)^2}{(1+\varepsilon^2/2)} \frac{2(1-\nu)}{G} \quad (47)$$

The Hashin-Shtrikman upper bound on the effective bulk modulus of a two-dimensional porous body [29] can be used to show that the pore compressibility of our irregular pore cannot be less than $2(1-\nu)/G$. This is equivalent to stating that no pore can be stiffer than a circular pore. A different lower bound on the compressibility of our irregular pore could be found by using an argument based on the largest possible inscribed circle, which has radius $a(1-\varepsilon)$. However, this lower bound would be lower than $2(1-\nu)/G$, and thus is not useful. Hence, the normalized compressibility of our corrugated pore is bounded as follows:

$$1 \leq \frac{GC_{\text{pc}}}{2(1-\nu)} \leq \frac{(1+\varepsilon)^2}{(1+\varepsilon^2/2)} \quad (48)$$

As we are, by definition, only interested in small values of ε, one can say roughly that the normalized pore compressibility must lie between 1 and $1+2\varepsilon$.

The two-term and four-term perturbation expressions are plotted in Figs. 2–4 as functions of ε, for the values $m=8$, 16, and 32. Also plotted are the upper and lower bounds, and the values computed using the boundary element method. As the influence of roughness on compressibility is of second order, the compressibility lies close to the lower bound for very small values of ε. However, as ε increases, the compressibility moves closer to the upper bound. Moreover, the difference between the exact value and the upper bound becomes smaller as the number of corrugations (m) increases. As the upper bound corresponds to the case in which the small bumps of solid material have been removed, this shows that, particularly as m increases, these small bumps provide no stiffness to the pore. Although one might think that this result could have been anticipated, we point out that the stress concentration increases drastically with m and ε [18], and it has been frequently asserted that the pore compressibility correlates with the stress concentration [30,31]. However, our results show that as m increases, the pore compressibility approaches an upper bound that is independent of m. Hence, this supposed correlation between pore compressibility and stress concentration, which had been inferred from the solutions for ellipsoidal and spheroidal pores, has no general validity whatsoever.

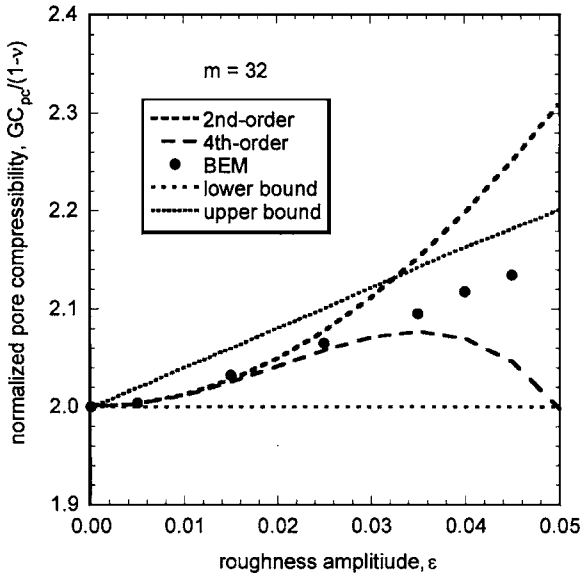

Fig. 4 Pore compressibility as a function of the roughness amplitude, for the case $m=32$

As expected, the two-term perturbation expression agrees closely with the numerical values for a certain range of ε, and then rapidly becomes unrealistically large, exceeding the upper bound. Using the compressibility predicted by the four-term solution extends the range of accuracy by about a factor of 2 in ε. For example, for $m=8$, the two-term solution is quite accurate until about $\varepsilon=0.07$, whereas the four-term solution is accurate until $\varepsilon=0.14$. The range of accuracy decreases as m increases, as was found by Givoli and Elishakoff [18] for the stress concentrations. Roughly, the four-term solution is accurate until a critical value of about $\varepsilon^*=1/m$, beyond which its accuracy deteriorates rapidly.

Although this may seem like a severe limitation on the usefulness of the perturbation approach, in practice it is not, as we now show. There are m sine waves of the corrugations along the circumference of the nominal circle, which has a circumference of $2\pi a$, and so the half-wavelength of each bump is $\pi a/m$. The change in radius that occurs over this half-wavelength is $2a\varepsilon$. If we make the reasonable assumption that the change in radius does not exceed the half-wavelength (otherwise, the corrugations would look like thin spikes), we find that ε is restricted to be less than $\pi/2m$. Thus, it seems that the range of accuracy of the pore compressibility predicted by our fourth-order perturbation solution probably covers most cases of practical interest.

7 Summary and Conclusions

The boundary perturbation method has been used to determine the displacements and stresses around a nearly circular rigid inclusion whose boundary is described by $r=a(1+\varepsilon \sin m\theta)$, and which is subjected to hydrostatic stress at infinity. The solution has been obtained up to the fourth order in ε. The corresponding solution of a cavity under hydrostatic loading was obtained using the Dundurs correspondence principle. It was verified that the second-order solution gives stress concentrations along the cavity boundary that agree with those obtained in [18].

From these solutions, we obtained expressions for the effective bulk modulus of a body that contains a dilute distribution of these inclusions (or cavities). For the case of a cavity, we also obtained the pore compressibility parameter C_{pc}. The pore compressibility of the corrugated circular pore exceeds that of a perfect circle by a term of order ε^2. This is in contrast to the stress concentration factor, which differs from those of a circle by a term of order ε. We conclude that small amounts of roughness have a negligible effect on the compressibility. In a sense, this follows directly from the bounds described in Sec. 6. However, the upper bound of the pore compressibility differs from the lower bound by a term of order ε, whereas the actual pore compressibility was found to deviate from the lower bound (i.e., the compressibility of a circle) by order ε^2. Hence, although roughness causes the pore compressibility to increase, the effect is much less than might have been inferred, for example, by taking the mean value of the upper and lower bounds.

Our results should be useful in attempts to estimate elastic properties of porous materials from images of the pore space [32], as they provide an estimate of the magnitude of roughness that can safely be ignored when analyzing the images. One encouraging implication of our results is that very high levels of magnification may not be needed. This is similar to what has been found when using image of pores to estimate the permeability of porous rocks, as small-scale roughness also has little effect on the hydraulic resistance in the laminar range [6].

APPENDIX

A The non-zero coefficients required for the first-order solution are

$$A^1_{7,m}=\frac{-a^m p(\kappa-1)}{\kappa} \tag{A1}$$

$$A^1_{8,m}=\frac{-a^{m+2} p(\kappa-1)(\kappa-m+1)}{\kappa m} \tag{A2}$$

The non-zero coefficients required for the second-order solution are

$$A^2_{5,2m}=\frac{a^{2m}(\kappa-1)(2m-3)}{8\kappa} \tag{A3}$$

$$A^2_{6,2m}=\frac{a^{2m+1}(\kappa-1)}{4\kappa m}\left[(\kappa-m+1)+\frac{(2m-3)(\kappa-2m+1)}{4}\right] \tag{A4}$$

$$A^2_1=\frac{-a^2 p(\kappa-1)[(\kappa-2)-2m(\kappa-1)]}{4\kappa} \tag{A5}$$

The non-zero coefficients required for the third-order solution are

$$A^3_{7,m}=\frac{-a^{m-1}G(T^3_{r,m}+T^3_{\theta,m})}{\kappa} \tag{A6}$$

$$A^3_{8,m}=a^{m+1}G\left[\frac{(\kappa+m-1)(T^3_{r,m}-T^3_{\theta,m})}{\kappa m}-\frac{2T^3_{r,m}}{m}\right] \tag{A7}$$

$$A^3_{7,3m}=\frac{-Ga^{3m-1}(T^3_{r,3m}+T^3_{\theta,3m})}{\kappa} \tag{A8}$$

$$A^3_{8,3m}=\frac{2a^{3m+1}G}{3m}\left[\frac{(\kappa+3m-1)(T^3_{r,3m}+T^3_{\theta,3m})}{2\kappa a^{3m-1}}-T^3_{r,3m}\right] \tag{A9}$$

$$T^3_{r,m}=\frac{1}{4G}\left[A^2_{5,2m}\frac{(\kappa+2m-1)(2m-1)}{a^{2m-1}}+A^2_{6,2m}\frac{2m(2m+1)}{a^{2m}}\right]+a(\kappa-1)\frac{3}{16G}\left\{1-\frac{1}{2\kappa}[m(m-1)(\kappa+m-1)+(m+1)(m+2)(\kappa-m+1)]\right\}+a\frac{(\kappa-1)}{8G}\left[\frac{(\kappa-2)-2m(\kappa-1)}{\kappa}\right] \tag{A10}$$

$$T^3_{\theta,3}=\frac{1}{4G}\left[-A^2_{5,2m}\frac{(\kappa-2m+1)(1-2m)}{a^{2m-1}}-A^2_{6,2m}\frac{2m(2m+1)}{a^{2m}}\right]+\frac{a}{16G\kappa}[(\kappa-1)(\kappa-m+1)(2m+1)] \tag{A11}$$

$$T^3_{r,3m}=-\frac{1}{4G}\left[A^2_{5,2m}\frac{(\kappa+2m-1)(2m-1)}{a^{2m-1}}+A^2_{6,2m}\frac{2m(2m+1)}{a^{2m}}\right]+a(\kappa-1)\frac{1}{16G}\left\{1-\frac{1}{\kappa}[m(m-1)(\kappa+m-1)+(m+1)(m+2)(\kappa-m+1)]\right\} \tag{A12}$$

$$T^3_{\theta,3m}=\frac{1}{4G}\left[A^2_{5,2m}\frac{(\kappa-2m+1)(1-2m)}{a^{2m-1}}+A^2_{6,2m}\frac{2m(2m+1)}{a^{2m}}\right]-\frac{a}{16G\kappa}\left[(\kappa-1)(\kappa-m+1)(2m+1)\right] \tag{A13}$$

The non-zero coefficients required for the fourth-order solution are

$$A^4_{5,2m}=\frac{Ga^{2m-1}(T^4_{\theta,2m}-T^4_{r,2m})}{\kappa} \tag{A14}$$

$$A^4_{6,2m} = \frac{Ga^{2m+1}}{2m}\left[-2T^4_{r,2m} + (T^4_{\theta,2m} - T^4_{r,2m})\frac{(\kappa - 2m + 1)}{\kappa}\right] \tag{A15}$$

$$A^4_{5,4m} = \frac{Ga^{4m-1}(T^5_{\theta,4m} - T^5_{r,4m})}{\kappa} \tag{A16}$$

$$A^4_{6,4m} = \frac{Ga^{4m+1}}{4m}\left[-2T^4_{r,4m} + \frac{(\kappa - 4m + 1)}{\kappa}(T^4_{\theta,4m} - T^4_{r,4m})\right] \tag{A17}$$

$$\begin{aligned} A^m_{15} = {} & \frac{-3a^2}{32G}(\kappa - 1)p + \frac{a^2}{64G}\left\{\frac{p(\kappa - 1)(m + 1)}{\kappa}[(m - 1)m(\kappa + m \right. \\ & \left. - 1) + (m + 2)(m + 3)(\kappa - m + 1)]\right\} \\ & + \frac{a^2 p(\kappa - 1)}{16G}\left[\frac{(\kappa - 2) - 2m(\kappa - 1)}{\kappa}\right] \\ & + \frac{a}{16G}\left[A^2_{5,2m}\frac{(\kappa + 2m - 1)(2m - 1)(2m)}{a^{2m-1}}\right. \\ & \left. + A^2_{6,2m}\frac{2m(2m + 1)(2m - 2)}{a^{2m+3}}\right] \\ & - \frac{a}{4G}\left[A^3_{7,2m}\frac{(\kappa + m - 1)(m - 1)}{a^{m-1}} + A^3_{8,m}\frac{m(m + 1)}{a^{m+1}}\right] \end{aligned} \tag{A18}$$

$$\begin{aligned} T^4_{r,2m} = {} & \frac{ap(\kappa - 1)}{16\kappa}[(\kappa - 2) - 2m(\kappa - 1)] \\ & + \frac{p(\kappa - 1)a}{8}\left\{\frac{ap(\kappa - 1)(m + 1)}{6}[(m - 1)m(\kappa + m - 1) + (m \right. \\ & \left. + 2)(m + 3)(\kappa - m + 1)] - 1\right\} - \frac{1}{4}\left[A^3_{7,m}\frac{(\kappa + m - 1)(m - 1)}{a^{m-1}} \right. \\ & \left. + A^3_{8,m}\frac{m(m + 1)}{a^{m+1}}\right] + \frac{1}{4}\left[A^3_{7,3m}\frac{(\kappa + 3m - 1)(3m - 1)}{a^{3m-1}} \right. \\ & \left. + A^3_{8,3m}\frac{3m(3m + 1)}{a^{3m+1}}\right] - \frac{a^2}{8}\left[A^3_{5,2m}\frac{(\kappa + 2m - 1)(2m - 1)2m}{a^{2m+1}} \right. \\ & \left. + A^3_{6,2m}\frac{2m(2m + 1)(2m + 2)}{a^{2m+3}}\right] \end{aligned} \tag{A19}$$

$$\begin{aligned} T^4_{r,4m} = {} & \frac{1}{32}\left\{p(\kappa - 1)a - \frac{ap(\kappa - 1)(m + 1)}{6\kappa}[(m - 1)m(\kappa + m - 1) \right. \\ & \left. + (m + 2)(m + 3)(\kappa - m + 1)]\right\} \\ & + \frac{1}{16}\left[A^2_{5,2m}\frac{(\kappa + 2m - 1)(2m - 1)(2m)}{a^{2m-1}} \right. \\ & \left. + A^2_{6,2m}\frac{2m(2m + 1)(2m - 2)}{2a^{2m-3}}\right] \\ & - a\left[A^3_{7,3m}\frac{(\kappa + 3m - 1)(3m - 1)}{a^{3m-1}} + A^3_{8,3m}\frac{3m(3m + 1)}{a^{3m+1}}\right] \end{aligned} \tag{A20}$$

$$\begin{aligned} T^4_{\theta,2m} = {} & -\frac{p(\kappa - 1)a(\kappa + m - 1)}{96G\kappa}[(1 - m)m(m + 1) + (m + 1)(m + 2) \\ & \times (m + 3)] - \frac{a^2}{8G}\left[A^3_{5,2m}\frac{(\kappa - 2m - 1)(1 - 2m)2m}{a^{2m+1}} \right. \\ & \left. + A^3_{8,m}\frac{2m(2m + 1)(2m + 2)}{a^{2m+3}}\right] \\ & - \frac{a}{4G}\left[A^3_{7,m}\frac{(\kappa - m - 1)(1 - m)}{a^m} + A^3_{8,m}\frac{m(m + 1)}{a^{m+2}}\right] \\ & + \frac{a}{4G}\left[A^3_{7,3m}\frac{(\kappa - 3m - 1)(1 - 3m)}{a^{3m}} + A^3_{8,3m}\frac{3m(3m + 1)}{a^{3m+2}}\right] \end{aligned} \tag{A21}$$

$$\begin{aligned} T^4_{\theta,4m} = {} & \frac{p(\kappa - 1)a(\kappa + m - 1)}{192G\kappa}[(1 - m)m(m + 1) + (m + 1)(m + 2) \\ & \times (m + 3)] + \frac{a^2}{16G}\left[A^3_{5,2m}\frac{(\kappa - 2m - 1)(1 - 2m)2m}{a^{2m+1}} \right. \\ & \left. + A^3_{6,m}\frac{2m(2m + 1)(2m + 2)}{a^{2m+3}}\right] \\ & - \frac{a}{4G}\left[A^3_{7,3m}\frac{(\kappa - 3m - 1)(1 - 3m)}{a^{3m}} + A^3_{8,3m}\frac{3m(3m + 1)}{a^{3m+2}}\right] \end{aligned} \tag{A22}$$

References

[1] Mura, T., 1987, *Micromechanics of Defects in Solids*, 2nd ed., Kluwer, Amsterdam.

[2] Nemat-Nasser, S., and Hori, M., 1999, *Micromechanics: Overall Properties of Heterogeneous Materials*, 2nd ed., North-Holland, Dordrecht, The Netherlands.

[3] Eshelby, J. D., 1957, "The Determination of the Elastic Field of an Ellipsoidal Inclusion, and Related Problems," Proc. R. Soc. London, Ser. A, **241**, pp. 376–396.

[4] Savin, G. N., 1961, *Stress Concentration Around Holes*, Pergamon, Oxford, UK.

[5] Muskhelishvili, N. I., 1963, *Some Basic Problems of the Mathematical Theory of Elasticity*, 2nd ed., Noordhoff, Groningen, The Netherlands.

[6] Sisavath, S., Jing, X. D., and Zimmerman, R. W., 2001, "Laminar Flow Through Irregularly-Shaped Pores in Sedimentary Rocks," Transp. Porous Media, **45**, pp. 41–62.

[7] Tsukrov, I., and Novak, J., 2004, "Effective Elastic Properties of Solids With Two-Dimensional Inclusions of Irregular Shapes," Int. J. Solids Struct., **41**, pp. 6905–6924.

[8] Zimmerman, R. W., 1986, "Compressibility of Two-Dimensional Cavities of Various Shapes," ASME J. Appl. Mech., **53**, pp. 500–504.

[9] Ekneligoda, T. C., and Zimmerman, R. W., 2006, "Compressibility of Two-Dimensional Pores Having n-Fold Axes of Symmetry," Proc. R. Soc. London, Ser. A, **462**, pp. 1933–1947.

[10] Chang, C. S., and Conway, H. D., 1968, "A Parametric Study of the Complex Variable Method for Analyzing the Stresses in an Infinite Plate Containing a Rigid Rectangular Inclusion," Int. J. Solids Struct., **4**, pp. 1057–1066.

[11] Jasiuk, I., Chen, J., and Thorpe, M. F., 1994, "Elastic Moduli of Two Dimensional Materials With Polygonal and Elliptical Holes," Appl. Mech. Rev., **47**(Supp 1), pp. 18–21.

[12] Kachanov, M., Tsukrov, I., and Shafiro, B., 1994, "Effective Moduli of Solids With Cavities of Various Shapes," Appl. Mech. Rev., **47**(Supp 1), pp. 152–174.

[13] van Dyke, M., 1975, *Perturbation Methods in Fluid Mechanics*, Parabolic Press, Stanford, CA.

[14] Low, E. F., and Chang, F. W., 1967, "Stress Concentrations Around Shaped Holes," J. Eng. Mech., **93**, pp. 33–44.

[15] Wang, C. H., and Chao, C. K., 2002, "On Perturbation Solutions for Nearly Circular Inclusion Problems in Plane Thermoelasticity," ASME J. Appl. Mech., **69**, pp. 36–44.

[16] Parnes, R., 1987, "The Boundary Perturbation Method in Elastostatics—Investigation of Higher-Order Effects and Accuracy of Solutions," J. Mec. Theor. Appl., **6**, pp. 295–314.

[17] Gao, H., 1990, "A Boundary Perturbation Analysis for Elastic Inclusions and Interfaces," Int. J. Solids Struct., **28**, pp. 703–725.

[18] Givoli, D., and Elishakoff, I. 1992, "Stress-Concentration at a Nearly Circular Hole With Uncertain Irregularities," ASME J. Appl. Mech., **59**, pp. S65-S71.

[19] Little, R. W., 1973, *Elasticity*, Prentice Hall, Englewood Cliffs, NJ.

[20] Barber, J. R., 1992, *Elasticity*, Kluwer, Dordrecht, The Netherlands.
[21] Jasiuk, I., 1995, Cavities vis-a-vis Rigid Inclusions: Elastic Moduli of Materials With Polygonal Inclusions," Int. J. Solids Struct., **32**, pp. 407–422.
[22] Dundurs, J., 1989, "Cavities vis-à-vis Rigid Inclusions and Some Related General Results in Plane Elasticity," ASME J. Appl. Mech., **56**, pp. 786–790.
[23] Goodier, J. N., 1933, "Concentration of Stress around Spherical and Cylindrical Inclusions and Flaws," Trans. ASME, **55**, pp. 39–44.
[24] Zimmerman, R. W., 1991, *Compressibility of Sandstones*, Elsevier, Amsterdam, The Netherlands.
[25] Vigdergauz, S., 2006, "Cross Relations Between the Planar Elastic Moduli of Perforated Structures," ASME J. Appl. Mech., **73**, pp. 163–166.
[26] Martel, S. J., and Muller, J. R., 2000, "A Two-Dimensional Boundary Element Method for Calculating Elastic Gravitational Stresses in Slopes," Pure Appl. Geophys., **157**, pp. 989–1007.
[27] Crouch, S. L., and Starfield, A. M., 1983, *Boundary Element Method in Solid Mechanics*, Allen and Unwin, London, UK.
[28] Gol'dshtein, R. V., and Entov, V. M. 1994, *Qualitative Methods in Continuum Mechanics*, Wiley, New York.
[29] Hashin, Z., 1983, "Analysis of Composite Materials – a Survey," ASME J. Appl. Mech., **50**, pp. 481–505.
[30] Warren, N., 1973, "Theoretical Calculation of the Compressibility of Porous Media," J. Geophys. Res., **78**, pp. 352–362.
[31] Rice, R. W., 1998, *Porosity of Ceramics*, Marcel Dekker, New York.
[32] Prokopiev, O., and Sevostianov, I., 2006, "On the Possibility of Approximation of Irregular Porous Microstructure by Isolated Spheroidal Pores," Int. J. Fract., **139**, pp. 129–136.

A Momentum Transfer Measurement Technique Between Contacting Free-Falling Bodies in the Presence of Adhesion

M. Benedetti[1]
Department of Materials Engineering and Industrial Technologies,
University of Trento,
38050 Trento, Italy
e-mail: matteo.benedetti@ing.unitn.it

D. Bortoluzzi
Department of Mechanical and Structural Engineering,
University of Trento,
38050 Trento, Italy

S. Vitale
Department of Physics,
University of Trento,
38050 Trento, Italy

The present paper is aimed at investigating the dynamics of release of objects in free-falling conditions typical of space applications. In the presence of surface interaction forces, a quick separation of the released from the constraining body will result in a momentum transfer, provided that the inertial forces exceed the maximum attractive force. The release conditions as well as the related parameters affecting the momentum acquired by the released body through the adhesion rupture play a fundamental role. Therefore, an analytical model has been set up to predict the imparted momentum in the case of conservative interaction forces. Furthermore, an experimental technique aimed at measuring the momentum transfer has been analyzed. Particular attention has been placed on the capability to accurately reproduce the stress status on the contact patch, on the noise sources affecting the measurement, and on the performances of a noise optimal-filtering technique in terms of achievable measurement resolution.
[DOI: 10.1115/1.2755104]

Keywords: momentum transfer measurement, impulse, surface forces, noise filtering

1 Introduction

The measurement of small impulses is relevant and necessary in various fields of science and engineering. Although the measurement of impulses of the order of several Newtons per second is common, there is an increasing demand for the measurement of impulses of the order of micro-Newtons per second in many industrial and research fields, such as space applications, process monitoring, and crash testing. For instance, in space propulsion studies, the exact knowledge of the impulse imparted by the thrusters to an orbiting satellite is needed for orbit maintenance, repositioning, and attitude control (e.g., [1–8]).

In the applications mentioned, the measured impulse is originated by a *noncontact force*, which may be electromagnetic or inertial (accelerated ions or gas molecules). The measurement of these kinds of impulses takes advantage of the fact that noncontact forces, although active between two bodies, are not affected by the way such bodies are constrained. Conversely, the present work deals with an application where the measurement of impulse concerns *contacting* bodies.

In the space environment, the precise release of bodies in outer space implies the contact with some kind of caging devices, which are deputed to the constraining of the object to be released during the launch phase. Therefore, the subsequent in-orbit release involves the sudden rupture of adhesive forces with consequent transfer of momentum. The breaking of adhesive junctions between contacting bodies, although of slight order of magnitude (from nano- up to milli-Newtons), can be promoted in space applications neither by environmental factors, such as the gravity field, nor by surface contamination caused by exposure to the atmosphere, nor by acoustic noise propagated by the air, nor by inertia forces due to ground microseismic movement. The unavoidable momentum transferred to the released body may cause too high residual velocities in comparison to the required release conditions. A meaningful example of these issues is given by the scientific space mission LISA (Laser Interferometer Space Antenna) [9]. The aim of this ESA NASA joint mission is the first in-flight revealing of gravitational waves, which will be detected by means of laser interferometer arms formed among three orbiting satellites. The sensing elements of the gravitational waves, constituting the end mirrors of the interferometer arms, will be cubic masses located within the satellites. During the experiment, the test masses will be set in free flight (see Fig. 1).

Unfortunately, the test masses need to be firmly secured to their housings as long as they are subjected to the Earth's gravity or to the spacecraft launch loads, in order to avoid any collision with the surrounding instruments. The constraining action against the launch loads is performed by the caging mechanism subsystem (CMSS), which applies large preloads on the filleted corners (see Fig. 2(*a*)) through four fingers [10]. A direct release to free-falling conditions would not be possible due to the unavoidable cold welding junctions arising at the mating surfaces between the test mass and the fingers. Once the spacecraft orbit is commissioned, the test mass is handed over to the grabbing positioning and release mechanism (GPRM), which has the function to grab the test mass and center it in the housing. This function is performed by applying a lower preload through dedicated surface pairs (Fig. 2(*b*)) that are thus preserved from strong cold welding and fretting phenomena because the test mass is no longer subject to high inertial loads. The last step is to retract the grabbing fingers and engage the test mass only through two small tips, which apply a minimum preload on a dedicated surface inside the test mass recess (see Fig. 2(*c*)). The release is carried out by quickly retracting the release tips.

After the release, only a limited (micro-Newton scale) force and torque authority is available on the test mass supplied by a capacitive actuation system [11,12]. It has been calculated that the residual velocity of the test mass must be $<5\ \mu$m/s; otherwise, the capacitive actuation will not be able to catch up and control the test mass in the available gaps. The release function constitutes a potential single-point failure of the mission because, if the test

[1]Corresponding author.

Contributed by the Applied Mechanics Division of ASME for publication in the JOURNAL OF APPLIED MECHANICS. Manuscript received December 21, 2005; final manuscript received June 1, 2007; published online January 16, 2008. Review conducted by Igor Mezic.

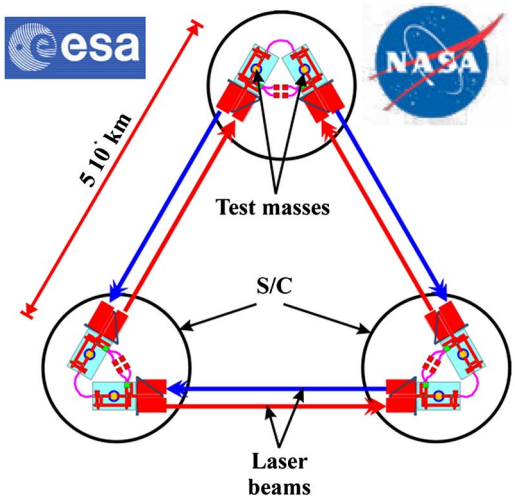

Fig. 1 Constellation of three orbiting satellites realizing the LISA experiment. Each satellite hosts two free-floating test masses, which are the end mirrors of laser interferometer arms.

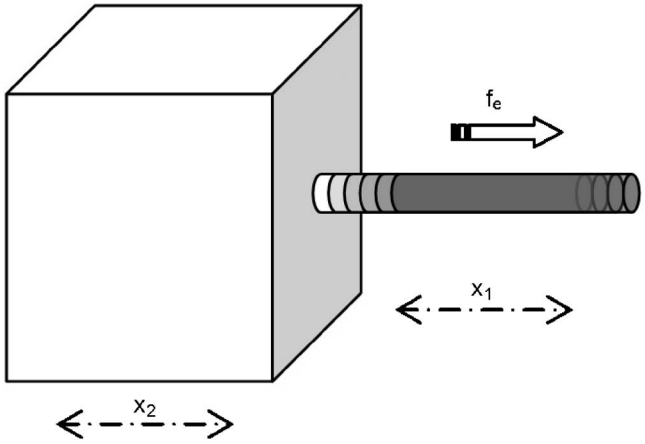

Fig. 3 Schematics of the system considered in the analysis of the release dynamics. Both the test mass (the cube on the right) and the plunger (the cylinder on the left) are considered pointlike particles. Only the motion along *x* is considered. The force f_e is applied to the plunger in order to pull it out of contact.

mass is not set in free floating conditions, neither scientific measurements nor a technology demonstration may be performed. It is now clear that the exact measurement of the momentum imparted to the test mass due to adhesive interactions plays a crucial role for the verification of compliance of both the release mechanism and procedure with the requirements for a successful release.

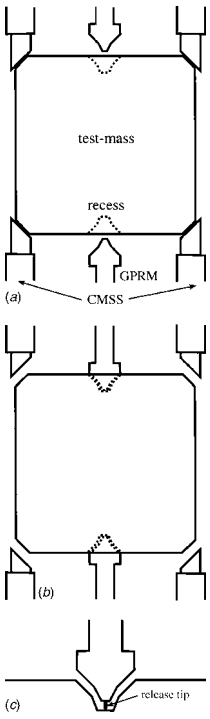

Fig. 2 Release procedure of the LISA test masses: (*a*) The caging mechanism subsystem (CMSS) constrains the test mass through four fingers before the launch of the satellite. (*b*) The test mass is handed over to grabbing positioning and release mechanism (GPRM), once the satellite has reached the orbit. (*c*) The grabbing finger is separated from the test mass by a release dedicated tip, which is in turn quickly separated from the test mass performing the final release.

The present paper is aimed at designing a ground-based laboratory experiment for the measurement of the momentum transfer during the release of a nominally free-falling physical body subjected to adhesive interactions. Accordingly, the main objectives of this paper are to (i) provide a critical assessment of the release conditions as well as the related parameters affecting the dynamics of the release, (ii) describe the obtained results in terms of their influence on the LISA scientific experiment, (iii) design an experiment representative of the in-orbit release for the measurement of the impulse imparted to the detached object, which shall be isolated from both the pervasive gravity field and the laboratory disturbances, (iv) discuss the main sources of noise disturbing the experiment, and (v) analyze the performances of a particular noise optimal-filtering technique in terms of achievable measurement resolution.

2 In-Flight Release Configuration

The considered configuration for the investigation of the in flight dynamics of the release of two objects interacting with a relative position-dependent force is schematized in Fig. 3. Body 1 represents the plunger performing the test mass release, whereas body 2 is the test mass (TM). The two bodies are initially at rest and in contact. From the point of view of their dynamic behavior, both objects are considered as point particles. A force f_e is applied to the plunger in order to separate it from the test mass. For the sake of simplicity, the entire discussion is just in one dimension, the x-axis, but it can be generalized to the three-dimensional case. x_1 and x_2 are the coordinate of the plunger and of the test mass, respectively, and r is the difference of their coordinates; $r=0$ represents the initial contact between the bodies.

In the literature, adhesive interactions, whatever their origin (van der Waals, electrostatics, Casimir, etc.), are treated as a position-dependent force [13,14]. Such an approach neglects nonconservative interactions that, in the context of the release of the test mass from the caging device, may contribute to the transferred momentum. The same approach, however, enables one to characterise the conservative part of the interacting force between the surface pairs. It is possible to associate a potential energy U to the adhesion force according to

$$f(r) = -\frac{\partial U}{\partial r} \tag{1}$$

where r is a separation coordinate that measures the relative motion of the surfaces in contact. The force $f(r)$ is then considered as

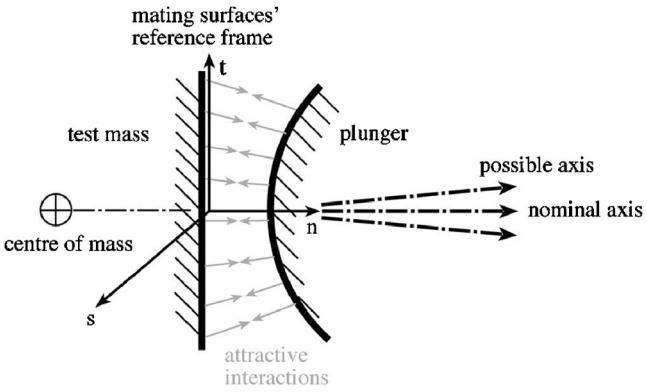

Fig. 4 In-flight release conditions of contacting free-floating bodies

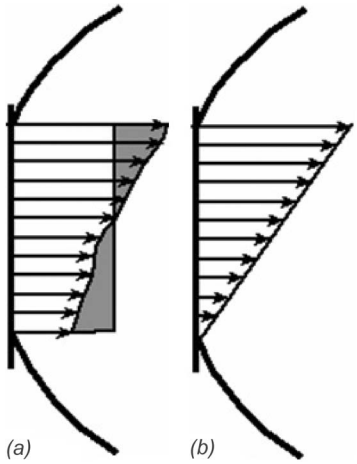

Fig. 6 (*a*) Possible adhesive pressure distribution with resultant momentum and (*b*) triangular adhesive pressure distribution

a well-defined function of r, though the specific shape may depend on the past history of the contact. *Nonconservative* interactions introduce more complex dependence of the transferred momentum on plunger motion. The experimental campaign, based on the measured technique described later in this paper, is expected to clarify how the actual adhesion phenomena deviate from the ideal conservative case presented.

The assumed initial status of the test mass and plunger system for the in-flight release foresees the two bodies in contact on a small surface, where the adhering forces are balanced by the Hertzian stresses. A local reference frame (see Fig. 4) is located at the center of the contact patch and defined by the normal (n) to the mating surfaces, a tangential axis (t) parallel to the gravity axis, and another tangential axis (s) defined by the cross product of the above unit vectors.

In the *nominal* conditions, the TM center of mass lies on the n-axis, which also coincides with the plunger translational axis. When the plunger is retracted, the test mass acquires momentum along n. The *actual* conditions are expected to differ from the nominal ones. If the TM center of mass does not lay on the plunger translational axis, due to axis misalignment and/or eccentric contact point, the adhesive force impulse also generates TM rotational momentum. Any TM center of mass misalignment with respect to the force affects the mechanical impedance of the test mass as seen by the force itself, as shown by the following formula:

$$\frac{\ddot{x}_P}{F} = \frac{1}{m} + \frac{e^2}{J} \tag{2}$$

where e is the misalignment, m the TM mass, J the TM moment of inertia around the center of mass, and P the contact point. A 1 mm misalignment results in a 0.28% increase of the mechanical impedance; therefore, such an effect is negligible. The impact on the adhesive force of a local relative rotation due to a center-of-mass misalignment will result in a different direction of plunger retraction. Figure 5 shows that, in the case of a spherical plunger

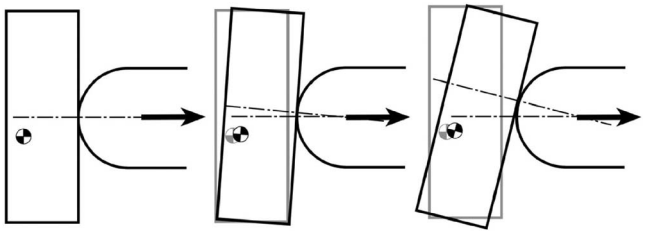

Fig. 5 Contact surface rotation due to center of mass misalignment during bodies separation

head, the contact point moves with respect to the plunger, but the different contact situation may be investigated by considering a retraction direction not aligned with the direction normal to the contact surface. A variable adhesive pressure distribution on the contact patch may cause some moment of the adhesive forces, as shown in gray in Fig. 6(a). A conservative asymmetry of the adhesive pressure is assumed with the triangular distribution shown in Fig. 6(b). In this case, the arm length of the force resultant would be $d/6$. Considering that the contact patch dimension is expected to be of the micrometer level, the actual center of mass misalignment (expected to be at least one order of magnitude larger) plays a dominant role in the angular momentum transfer. This means that the TM angular momentum transferred by the momentum of the adhesive force resultant is assumed negligible in the domain of the contact patch. Consequently, the transferred linear and angular momentum may be adequately described by a force impulse located at the actual position of the contact patch.

3 Dynamics of the Release

With the approximations enunciated in the preceding section, the dynamics of the system composed of the two point masses m_1 and m_2 is described by

$$m_1\ddot{x}_1 = -\frac{\partial U(|x_1 - x_2|)}{\partial x_1} + f_e$$

$$m_2\ddot{x}_2 = -\frac{\partial U(|x_1 - x_2|)}{\partial x_2} \tag{3}$$

The dynamics is easier to discuss if one switches to the "two-body" representation, using r and the coordinate of the center of mass as the dynamical coordinates

$$\ddot{r} = -\left(\frac{1}{m_1} + \frac{1}{m_2}\right)\frac{\partial U(|x_1 - x_2|)}{\partial x_1} + \frac{f_e}{m_1} \rightarrow \mu\ddot{r}$$

$$= -\frac{\partial U(r)}{\partial r} + \frac{m_2}{m_1 + m_2}f_e \tag{4}$$

$$(m_1 + m_2)\ddot{x}_{cm} = f_e \tag{5}$$

where the reduced mass is defined by

$$\mu = \frac{m_1 m_2}{m_1 + m_2} \tag{6}$$

and the coordinate of the center of mass

$$x_{cm} = \frac{m_1 x_1 + m_2 x_2}{m_1 + m_2} \tag{7}$$

The inverse transformation is

$$v_1 = v_{cm} + \frac{m_2}{m_1 + m_2}\dot{r}$$

$$v_2 = v_{cm} - \frac{m_1}{m_1 + m_2}\dot{r} \tag{8}$$

In the following, two limiting cases for the interaction force will be considered: (i) impulsive force of given total impulse and (ii) constant force until release.

3.1 Case 1: Impulsive Force of Given Total Impulse. If $f_e(t)$ consists of a pulse of duration $t_{\max}$ so short that the motion of both test mass and plunger may be neglected during the time of its action, then the problem reduces to that of a particle in a potential well ΔU with initial nonzero velocity. We call I the impulse of the force

$$I = \int_0^{t_{\max}} f(t)dt \tag{9}$$

Once the equivalent particle of Eq. (3) is well outside of the potential well, its effective kinetic energy is

$$\frac{1}{2}\mu\dot{r}^2 = \frac{1}{2}\mu\left(\frac{I}{m_1}\right)^2 - \Delta U \tag{10}$$

while the center of mass moves with velocity

$$v_{cm} = \frac{I}{m_1 + m_2} \tag{11}$$

From Eqs. (10) and (11), one gets the *TM release velocity*

$$v_2 = \frac{I}{m_1 + m_2} - \frac{m_1}{m_1 + m_2}\sqrt{\left(\frac{I}{m_1}\right)^2 - \frac{2}{\mu}\Delta U} \tag{12}$$

or the *TM kinetic energy at release*

$$\frac{1}{2}m_2 v_2^2 = \frac{1}{2}m_2\left(\frac{I}{m_1 + m_2}\right)^2\left\{1 - \sqrt{1 - \frac{2m_1^2}{\mu}\frac{\Delta U}{I^2}}\right\}^2 \tag{13}$$

Equation (12) can be expanded in series of the (small) parameter α

$$\alpha = \frac{2m_1^2}{\mu}\frac{\Delta U}{I^2} \tag{14}$$

as

$$\frac{1}{2}m_2 v_2^2 = \frac{1}{2}m_2\left(\frac{I}{m_1 + m_2}\right)^2\left\{\frac{\alpha^2}{4} + \frac{\alpha^3}{8}\cdots\right\} \tag{15}$$

Thus, if $\alpha \ll 1$, Eq. (15) gives

$$\frac{1}{2}m_2 v_2^2 = \frac{1}{2}\frac{m_1}{m_2}\frac{m_1 \Delta U^2}{I^2} = \frac{1}{4}\frac{m_1}{m_2}\frac{\Delta U^2}{T_o} \tag{16}$$

where on the right the kinetic energy T_o has been introduced

$$T_o = \frac{1}{2}\frac{I^2}{m_1} \tag{17}$$

that the free plunger would possess *if there was no adhesion at all*. It is worth noting that

$$\alpha = \frac{m_1 + m_2}{m_2}\frac{\Delta U}{T_o} \approx \frac{\Delta U}{T_o} \tag{18}$$

Thus, the condition for all this to hold is that $\Delta U \ll T_o$, a condition that should be easy to achieve just by design of the plunger actuator.

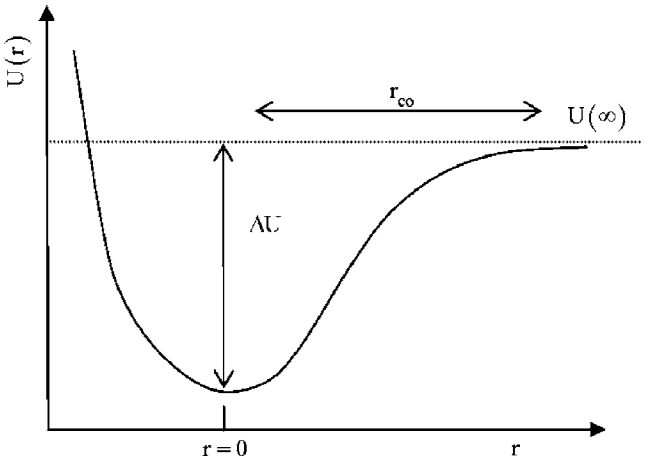

Fig. 7 The concept of the binding energy representing adhesion: when plunger and TM are at rest, *r* is taken as *r*=0 and *U* is at a minimum. The total binding energy is ΔU. In some of the calculations, we have to choose an arbitrary cutoff point where the force becomes negligible. The coordinate of this cutoff point is called r_{co}.

3.2 Case 2: A Constant Force Until Release. It is assumed that the plunger is actuated with a constant force $f_e = f_o$ until the separation reaches $r = r_{co}$ (see Fig. 7). At any time during the process, the kinetic energy of the equivalent particle in Eq. (4) is given by

$$\frac{1}{2}\mu\dot{r}^2 = -U(r) + \frac{m_2}{m_1 + m_2}f_o r \tag{19}$$

so that the final kinetic energy is

$$\frac{1}{2}\mu\dot{r}_{\text{fin}}^2 = -\Delta U + \frac{m_2}{m_1 + m_2}f_o r_{co} \tag{20}$$

Note that in Eq. (19) we have chosen $U(0)=0$. Meanwhile, the center of mass moves as

$$v_{cm} = \frac{f_o}{m_1 + m_2}t \tag{21}$$

with $t=0$ when the force is turned. In order to calculate the value of v_{cm} when r has reached r_{co}, it is necessary to know then how long it takes to do so. This can be bounded as follow. One can rewrite Eq. (19) as

$$\dot{r} = \sqrt{\frac{2}{\mu}\left[\frac{m_2}{m_1 + m_2}f_o r - U(r)\right]} \tag{22}$$

and then

$$\int_0^{r_{co}} \frac{1}{\sqrt{\frac{2}{\mu}\left[\frac{m_2}{m_1 + m_2}f_o r - U(r)\right]}}dr = t_{co} \tag{23}$$

where t_{co} is the unknown time to be found out. Equation (23) assumes the form

$$\sqrt{\frac{2m_1 r_{co}}{f_o}}\frac{1}{2}\int_0^1 \frac{1}{\sqrt{\left[x - \frac{U(r)}{m_2/(m_1 + m_2)f_o r_{co}}\right]}}dx$$

$$= t_o\frac{1}{2}\int_0^1 \frac{1}{\sqrt{[x - z(x)]}}dx = t_{co} \tag{24}$$

once the following items have been defined:

$$x = \frac{r}{r_{co}}, \quad t_o = \sqrt{\frac{2m_1 r_{co}}{f_o}} \quad \text{and} \quad z(x) = \frac{U(xr_{co})}{m_2/(m_1+m_2) f_o r_{co}} \tag{25}$$

It should be noted that t_o is the time the "free" plunger would take to reach r_{co} and, as r_{co} is of order <1 μm, i.e., the force is impulsive in any case. Now, the following considerations can be drawn:

- As $U(r)$ is a never decreasing function of r, so is z of $x: \partial U/\partial r, dz/dx \geq 0$
- One defines $T_o = f_o r_{co}$, which, as before, is the kinetic energy the plunger would acquire if there were no test mass or no adhesion. It is assumed, and checked later that this can be done, that $T_o \gg \Delta U$ in which case $z(x) \ll 1$
- In order to pull the plunger away, the force must overcome the maximum adhesion force with some substantial margin. Thus, $(\partial U/\partial r)_{\max} \ll f_e$. One defines

$$\gamma = \frac{(m_1+m_2)}{m_2 f_o}\left(\frac{\partial U}{\partial r}\right)_{\max} \tag{26}$$

γ is expected to be a small number, probably <0.01. As a consequence,

$$z(x) = \int_0^x \frac{dz}{dx'} dx' \leq \gamma x \tag{27}$$

and

$$\frac{1}{\sqrt{[x - z(x)]}} \leq \frac{1}{\sqrt{1-\gamma}} \frac{1}{\sqrt{x}} \tag{28}$$

Considering all this, one gets

$$t_{co} \leq \frac{1}{\sqrt{1-\gamma}} t_o \approx \left(1 + \frac{\gamma}{2}\right) t_o \tag{29}$$

If γ is entirely neglected, then the test mass moves with velocity

$$v_2 = v_{cm}(t_{co}) - \frac{m_1}{m_1+m_2}\dot{r}_{\text{fin}} = \frac{f_o}{(m_1+m_2)}\sqrt{\frac{2m_1 r_{co}}{f_o}} - \frac{m_1}{m_1+m_2}\sqrt{\frac{2}{\mu}\left(\frac{m_2}{m_1+m_2} f_o r_{co} - \Delta U\right)} \tag{30}$$

and has then a kinetic energy

$$\frac{1}{2} m_2 v_2^2 = \frac{m_2 m_1 T_o}{(m_1+m_2)^2}\left\{1 - \sqrt{\left(1 - \frac{(m_1+m_2)\Delta U}{m_2 T_o}\right)}\right\}^2 \tag{31}$$

By defining again $\alpha = [(m_1+m_2)\Delta U]/m_2 T_o$ a small number, one gets the same result as in Eq. (16)

$$\frac{1}{2} m_2 v_2^2 \approx \frac{1}{4}\frac{m_1}{m_2}\frac{\Delta U^2}{T_o} \tag{32}$$

4 Dynamical Requirements for the LISA Test Mass Release

The leading constraint determining the successful release of the LISA test mass is that the kinetic energy imparted to the test mass by the release device is less than the maximum kinetic energy that can be taken out of the test mass by the electrostatic suspension system. This energy has been estimated to be $T_{\max} \approx 2.5 \times 10^{-11}$ J [9], corresponding to a maximum linear momentum equal to about 1×10^{-5} kg·m/s in the case of a 2 kg heavy TM. From Eqs. (16) and (32), it can be calculated that the depth of the adhesion potential energy well ΔU must be less than

$$\Delta U \leq 2\sqrt{\frac{m_2}{m_1} T_0 T_{\max}} \tag{33}$$

As discussed in Sec. 2.2, the force applied to the plunger must overcome the maximum adhesion force with some substantial margin

$$\left(\frac{\partial U}{\partial r}\right)_{\max} \ll f_e \tag{34}$$

Moreover, in order Eq. (33) to be valid, it must be guaranteed that

$$\Delta U \ll \frac{m_2}{m_1+m_2} T_0 \tag{35}$$

It is worth noting that all the requirements defined in Eqs. (33)–(35) involve the depth of the energy well ΔU and the maximum adhesion force. The leading requirement for ΔU and T_o depends on the specific adopted solution and may be stated either by Eq. (33) or Eq. (35). The most interesting quantity appears to be ΔU in Eqs. (16) and (32). In a measurement where the plunger is quickly pulled away, one can use the result of Eq. (16) or Eq. (32) to derive that the transferred momentum is

$$\frac{p^2}{2m_2} \approx \frac{1}{4}\frac{m_1}{m_2}\frac{\Delta U^2}{T_0} \rightarrow p = \frac{\Delta U}{\sqrt{2} v_0} \tag{36}$$

where v_0 is the plunger velocity corresponding to the kinetic energy T_0. The transferred momentum is thus independent of the mass value and is a direct measure of ΔU provided that v_0 is reasonably well known. Noteworthy, v_0 can be modulated to some extent to increase the sensitivity and test the model. This result is of particular practical interest because it implies that, under the aforementioned assumptions, the transferred momentum can be estimated on the basis of the knowledge of the sole interaction potential energy ΔU, which can be measured with common experimental techniques, such as nanoindenters, atomic force microscopes, and surface force apparatuses (see, for example, [13,14]). If, however, the release is also affected by nonconservative interactions (such as friction or cold welding phenomena [15,16] acting between the contacting bodies), then such an energetic approach is no longer valid and the momentum transfer has to be directly measured. This issue will be discussed in the following section.

5 Measurement of the Momentum Transfer

5.1 Conceptual Measurement Configuration. The precise measurements of impulses performed by other authors [1–8] were critical, mainly for two reasons. First, the force impulse needs to be entirely converted into momentum; therefore, any other force acting in the same direction on the body subjected to the impulse must be minimized. Second, the momentum must be identified by the measurement of the resulting motion of the body that is affected by noise sources and by the unavoidable constraining forces.

5.1.1 Suspension System. The conversion of impulse into momentum may be guaranteed by a suspension system that minimizes the risk of any *impulsive* constraining force in the direction of the impulse to be measured. Constraining forces acting on longer time scales let the body develop a detectable motion from which the impulse may be identified. Suspension systems based on a simple pendulum [1], linear rail [1], and torsion pendulum [1,3–7] have been adopted to provide a weakly constrained axis, for the measurement of the steady and impulsive force exerted by thrusters for spacecraft applications. In the aforementioned applications, the presence of a single weakly constrained degree of freedom does not limit the measurement, as long as the impulsive force is a noncontact force and reasonably aligned with the "soft" axis. On the contrary, the impulsive force due to adhesion rupture is influenced by the complete three-axial stress status at the con-

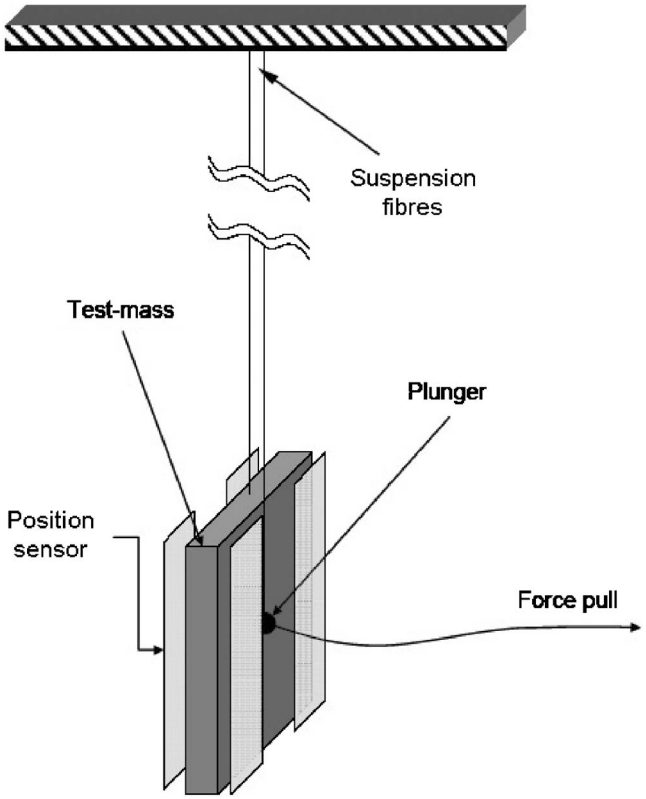

Fig. 8 The concept of the momentum transfer measurement configuration: two pendulums with nominally equal lengths representing the TM and the plunger, respectively. A position sensor detects the motion of the TM due to the momentum transferred upon pulling the plunger away. The suspension of the pendulum is only conceptual.

tact patch that depends on how *both* contacting bodies are constrained to the ground. This means that the body subjected to the adhesive impulse (i.e., the body to be released) needs to be weakly constrained not only in the direction along which the plunger is retracted, but also along the orthogonal directions.

Neglecting, for the moment, the stiff constraint along the vertical direction, many different solutions provide a suitable inertial isolation along two axes, and their macroscopic dynamics may be approximated by that of a low-damped simple pendulum, characterized in the small-displacement range by a length equal to the radius of curvature of the center of mass trajectory (for instance, Roberts linkage [17], Scott–Russel linkage [18]). On the basis of these considerations, the conceptual model of the simple pendulum has been chosen for the inertial isolation system in order to investigate the possible performance of the transferred momentum measurement experiment. As long as the pendulum length is compatible with the typical height of a laboratory ceiling (i.e., meter scale), the preferred practical implementation is the simple pendulum characterized by easily determinable dynamic properties (quality factor and length) and still providing good isolation from gravity and microseismic noise. Accordingly, the basic concept of the measuring apparatus, illustrated in Fig. 8, is to suspend both the test mass and the release plunger from two pendulums. A position sensor detects the weakly damped oscillation of the test mass due to the momentum transferred on pulling the plunger away. Larger pendulum lengths (i.e., tens of meters scale) are still achievable in a laboratory environment through the adoption of inertial isolations based on the aforementioned mechanisms. The drawback, however, is a much more difficult practical realization and a more complex dynamical behavior.

5.1.2 Identification of the Transferred Momentum. The identification of the momentum through the measurement of the resulting motion of the suspended body may focus, in principle, on the measurement of its velocity at the instant after the impulse application [3]. However, exact velocity measurements are hindered by background noise, electromagnetic interference, and structural harmonics [1]. An alternative technique, valid when the impulse width is much smaller than the oscillator period, measures the transferred momentum through the maximum displacement of the suspended body [1,5,7], which is approximately proportional to the impulse. This solution has given good results but is still affected by the noise superimposed on the few samples needed to identify the equilibrium position and the maximum displacement. A more complex approach is also presented in Ref. [3], where, after the identification of the damped oscillator characteristic parameters (resonant frequency, damping ratio, and suspended mass), the force impulse is obtained by fitting the measured motion with the typical damped oscillator response, and the noise effect is somehow averaged on the whole data set. Another technique focuses on the time-resolved motion [7], allowing the applied impulsive force to be reconstructed as a function of the time, with no restriction on the impulse widths as compared to the oscillator period. This method, however, is sensible to the noise present in the readout signal and accurate filtering is necessary prior to data processing.

In the present application, we propose to process the time-resolved motion of the damped oscillator through an optimal filter in order to measure the transferred momentum. Qualitatively, the role of the optimal filter is to extract the momentum from the data stream by enhancing the expected signal and averaging the noise, giving a decreasing weight to the samples as they lose information on the quantity and become dominated by noise. Details will be clarified in Sec. 5.4.

5.2 Measurement Basic Requirements. The initial conditions for the experiment, foresee the test mass and the plunger set into contact as shown in Fig. 8. In such a configuration, however, the stress status on the contact patch may be, in principle, far different in the ground experiment from the in-flight conditions. The in-flight release takes place with an unconstrained test mass, and, for equilibrium, shear stress at the contact patch is allowed neither along the t-axis nor along the s-axis. In the ground experiment (see Fig. 9), both the test mass mock-up and the plunger mock-up need to be suspended with some constraining stiffness to ground, named K_n, K_t and K_s. There are two main reasons for keeping the constraining stiffness to the lowest possible value, which will be addressed in the following sections.

5.2.1 Stress Status at the Contact Patch. In the ground-based experiment, the approach of the plunger mock-up to the test mass mock-up must be performed by actuating some suspending points, named in Fig. 9, N_1, S_1, and T_1. Because of the constraining stiffness, any positioning error of the suspending points with respect to the zero contact load between the two bodies causes preloading of the contact patch, both in compression (point N_1 moved forward after contact) and shear (points S_1 and T_1 moved forward after contact). Particular attention is paid to the stress status on the contact patch, because the interface surfaces undergo tribological conditions that may originate cold welding phenomena [15,16]. This occurs by bonding of the contacting bodies, whose separation involves the fracture of the bonding junction. Since all stress components acting on the junction contribute to its fracture (predictable by an appropriate three-axial failure criterion), the presence of shear stress in the ground-based experiment may help the rupture of adhesion and leads to an underestimation of the impulse occurred at the separation in comparison to the in-flight conditions.

In the proposed setup, owing to the pendulum suspension, both K_n and K_s stiffness are low enough so that a positioning error of the suspending point along n and s-axes induces a negligible pre-

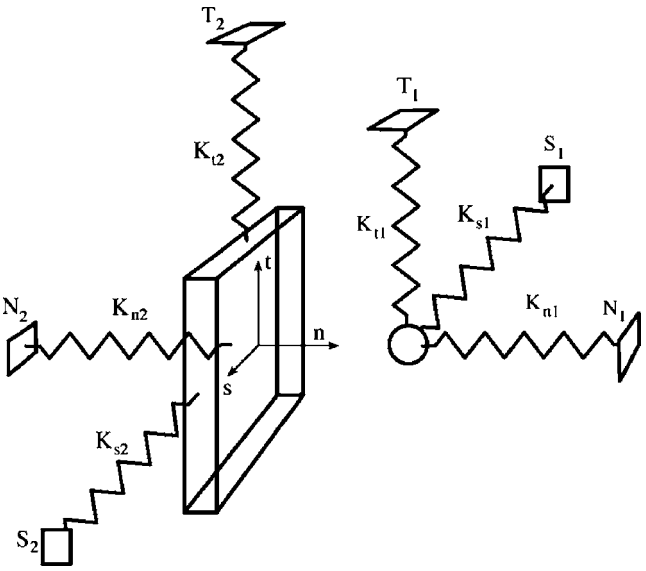

Fig. 9 Schematic representation of the ground-based experiment of the release of two initially contacting bodies. The *K* coefficients are the constraining stiffness components. The suffixes 1 and 2 refer to the suspending points of the two objects.

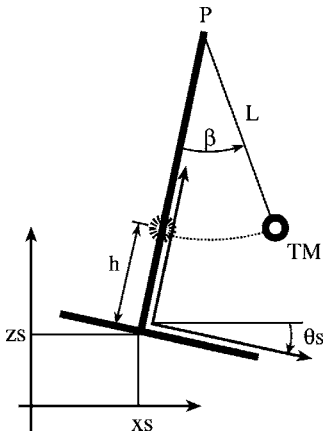

Fig. 11 Schematic illustration of the TM suspension, showing the meaning of the quantities used in the dynamical analysis of the measurement apparatus

loading force on the contact patch. On the contrary, a positioning error along the *t*-axis may originate shear stress. A worst-case situation is exemplarily illustrated in Fig. 10, where it is assumed that the surface topography of the TM (schematically depicted as a step in Fig. 10(*a*)) is able to bear the plunger weight once in contact with the TM, so that the suspension fiber becomes unloaded (Fig. 10(*b*)). During the following release, the gravity, which is not present in flight conditions, contributes to the fracture of the adhesive junction.

The risk of a gravity-aided adhesion rupture is first limited by adopting a very light plunger mock-up, that is represented by a millimeter-order diameter sphere. Second, the tension on the plunger mock-up suspending wire is measured by a load cell in order to monitor any variation of the vertical force with respect to the weight during the approach to the test mass mock-up.

5.2.2 Force Impulse Direction. In the nominal ground experiment setup, the momentum transfer takes place along the *n*-axis of the TM mock up, along which the constraining stiffness K_n is designed to be small enough to let the body develop easily measurable oscillations. However, the topological conditions of the contact area (surface roughness and curvature) as well as misalignments of the direction of plunger retraction could make the release direction noncoincident with the normal to the TM mating surface, both in flight and ground experiment environment. In the ground experiment, this would result in a momentum transfer not only along the test mass mock up *n*-axis, but also along the *s*- and *t*-axes. If the constraining stiffness K_s and K_t are not low enough, the following oscillations along the *s*- and *t*-axes would be too small to be detectable, and the components of the acquired momentum would not be measured.

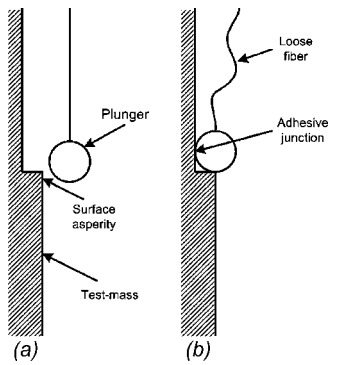

Fig. 10 Possible gravity-aided detachment. The gravity force introduces in the contact patch shear stresses responsible for the rupture of cold welding phenomena.

In the simple pendulum suspension setup, the problem arises along the *t*-axis. Any component of force impulse acting along this axis is not detected by the TM mock-up oscillations. However, if the plunger mock-up is subjected to a force pull component along the *t*-axis, then this is measured by the load cell that monitors the tension on the suspending fiber.

5.2.3 Microseismic Related Kinetic Energy. In the two-particle scheme, the adhered plunger constitutes a body bound in a force potential well. If we want to avoid that the momentum transfer is obscured by other phenomena related to the ground environment, we need to make sure that the force noise acting on the TM and the plunger (e.g., seismic noise) does not induce on the plunger, a kinetic energy, relative to the TM, sufficient to overcome the binding energy ΔU. Consequently, the suspension system shall provide sufficient isolation from the noise sources acting in the laboratory environment. This issue will be addressed in the following.

5.3 Experimental System Description. The experiment is basically aimed at measuring the transferred momentum between two suspended adhered bodies through the detection of the free oscillations of one of the two, after a sudden retraction of the other one. Both bodies are suspended by a thin fiber and the expected range of oscillation, compared to the suspending fiber length, is such that their dynamics may be approximated by that of a linearized simple pendulum. Each pendulum (the suspended TM is represented in Fig. 11) is characterized by the fiber length *L* and the suspended body height from ground *h*, and is subjected to the horizontal, vertical, and tilt microseismic motion of the ground (*xs*, *zs*, and θs, respectively).

In the development of a high-performance isolation system from ground vibration, considerable investigation has been focused on the characterization of the dissipative phenomena that damp the free oscillation of the suspended system. The damping of a suspension system is usually quantified by the quality factor *Q*, defined as the ratio between the total energy stored in the oscillator and the energy loss per cycle. Different damping mechanisms may take place in a suspension system, such as viscous forces, intrinsic loss of the materials, and stick and slip losses at

the joints [18]. A viscous force is proportional to the velocity, and its magnitude per unit displacement shows a linear dependence on the frequency, whereas the material and joint losses, often termed structural damping, are frequency independent over many decades of frequency. The presence of such dissipative phenomena may be identified by observing the frequency dependence of the Q factor: viscous damping gives rise to a linear relation between Q factor and frequency, whereas in the presence of structural damping, the Q factor displays a quadratic dependence on the frequency. As long as a reasonable Q factor is achieved (e.g., of the order of 10^4, which is commonly guaranteed by gravitational pendulums), the role of damping in the proposed application of the pendulum suspension is not critical. Typical transfer functions from applied force to oscillator displacement show nearly identical behavior with the aforementioned damping models. We have then chosen to adopt a viscous damping model in which the viscous constant is expressed as a function of the Q-factor.

5.3.1 Dynamics of the System. The equations of motion of the suspended TM (Fig. 11) have been written as functions of the total impulse imparted Po and the ground microseismic noise $xs(t)$, $zs(t)$, and $\theta s(t)$. In the hypothesis of small displacements and rotations, they have been linearized with respect to the variables $xs(t)$, $\theta s(t)$, and $\beta(t)$, while the dependence on $zs(t)$ becomes of higher order and is therefore neglected. The TM x displacement projected onto the ground frame (see Fig. 11), where it is actually measured, is expressed in the frequency domain as the outcome of a linear system where the inputs are represented by the Fourier transform of the microseismic motion $X_s(\omega)$ and $\Theta_s(\omega)$, and the magnitude Po of the ideal impulse

$$X(\omega) = H_{Po}(\omega)Po + H_{Xs}(\omega)X_s(\omega) + H_{\Theta_s}(\omega)\Theta_s(\omega) \tag{37}$$

The transfer functions are the following:

$$H_{Po}(\omega) = \frac{1}{m_{TM}} \frac{Q}{\left(\frac{g}{L_{TM}} - \omega^2\right)Q + i\omega\sqrt{\frac{g}{L_{TM}}}}$$

$$H_{Xs}(\omega) = \frac{Q\omega^2}{\left(\frac{g}{L_{TM}} - \omega^2\right)Q + i\omega\sqrt{\frac{g}{L_{TM}}}}$$

$$H_{\Theta s}(\omega) = L_{TM} \frac{\left(\frac{g}{L_{TM}} + \frac{h}{L_{TM}}\omega^2\right)Q + i\omega\sqrt{\frac{g}{L_{TM}}}}{\left(\frac{g}{L_{TM}} - \omega^2\right)Q + i\omega\sqrt{\frac{g}{L_{TM}}}} \tag{38}$$

In Fig. 12(a), the Bode plot of the impulse to displacement transfer function is shown, for a 0.01 kg TM and two different pendulum lengths (1 m and 10 m) having Q factor equal to 10^4. It constitutes the typical simple oscillator dynamical response, with resonant frequency equal to $(1/2\pi)\sqrt{g/L_{TM}}$ (around 500 mHz and 160 mHz for 1 m and 10 m length, respectively). It is characterized at frequencies below resonance by a nearly constant magnitude $L_{TM}/m_{TM}g$ equal to the inverse of the stiffness and above resonance by the $1/f^2$ decay of a nearly free-falling body.

A longer pendulum length has the advantage of a lower static stiffness and a wider free-falling-like bandwidth, which origin larger oscillations under the same given impulse. In Fig. 12(b), the Bode plot of the seismic horizontal displacement to the pendulum displacement is shown. The pendulum constitutes a seismic noise filter at frequencies below resonance, while the noise components, having larger frequencies, bypass the suspension and directly enter the TM displacement readout signal. In Fig. 12(c), the Bode plot of the seismic tilt to pendulum displacement is shown. The plot shows an inverted behavior with respect to the latter case, as it filters the tilt noise components only *above* resonance, where

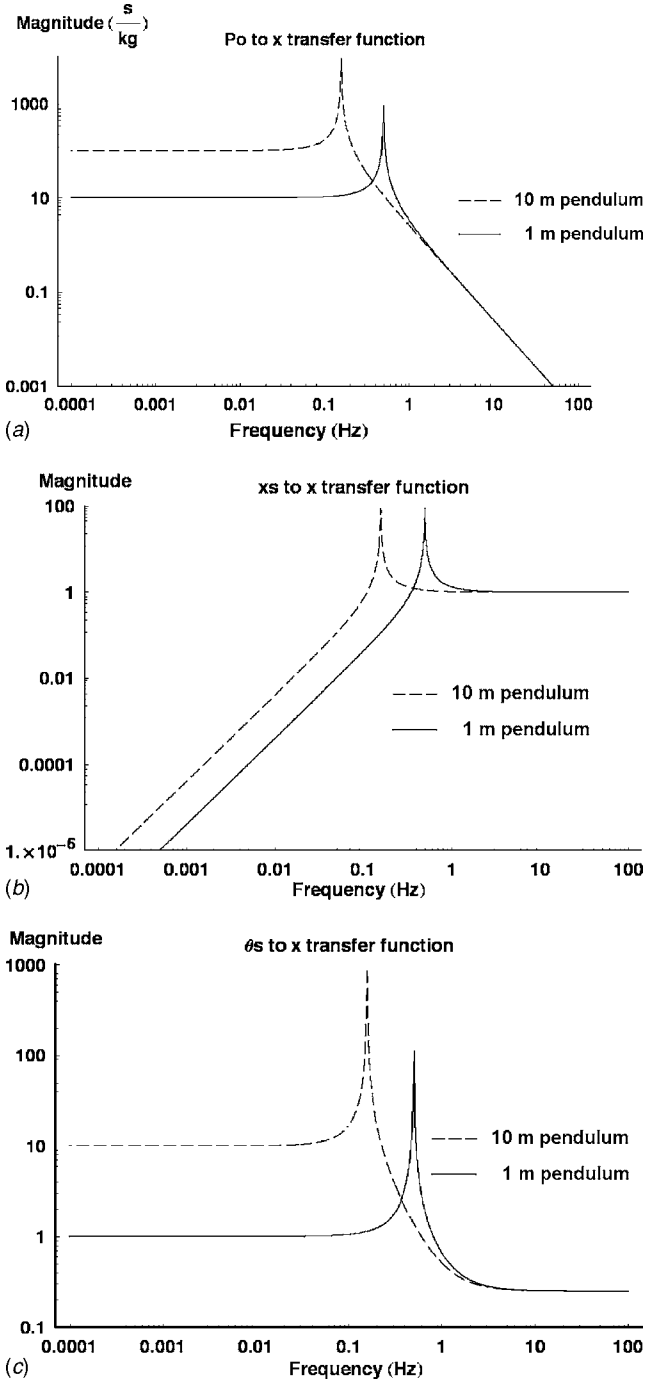

Fig. 12 Bode plot of (*a*) impulse, (*b*) seismic horizontal displacement, and (*c*) seismic tilt to pendulum displacement transfer function for two different pendulum lengths: 1 m and 10 m. The values of the parameters used in the calculation are summarized in Table 1.

the transfer function magnitude tends asintotically to h, the TM height from the ground. At low frequency, the transfer function magnitude tends to L_{TM}, showing that a long pendulum guarantees a worse rejection capability of the tilt noise than a short one.

The transfer functions here described give conflicting requirements on the design of the pendulum suspension. On one hand, the need to constrain the TM as least as possible and to filter the low-frequency horizontal seismic noise suggests to adopt a long pendulum. On the other hand, this choice increases the low-

Table 1 Values of parameters used in the calculations

Parameter	Symbol	Value
TM mass	M	0.01 kg
Pendulum length	L	1 m
TM distance from the ground	h	0.25 m
Gravity acceleration	g	9.807 m s^{-2}
Resonant angular frequency	$\omega_0=\sqrt{g/L}$	3.13 rad/s
Quality factor	Q	10^4
Horizontal acceleration seismic noise PSD	$S_{A,\text{seism}}$	4×10^{-13} m^2 s^{-4}/Hz
Tilt angular velocity seismic noise PSD	$S_{\dot{\theta},\text{seism}}$	2.5×10^{-17} rad^2 s^{-2}/Hz
Position sensor noise PSD	S_n	10^{-18} m^2/Hz

frequency tilt noise injected in the suspended body. A critical assessment of the optimal pendulum length will be discussed in the following.

5.3.2 Characterization of Microseismic and Readout Noise. The position readout noise as well as the microseismic horizontal displacement and tilt constitute the major sources of physical disturbance superimposed on the TM free oscillations. Therefore, a noise model has been elaborated to evaluate the resolution of the transferred momentum measurement. As a first cut to the problem, the noise model has been kept as simple as possible, in order to have a total noise at the readout signal whose power spectral density (PSD) may be described by functions that still allow for analytical manipulation in the optimal filtering technique. Typical measured horizontal and tilt noise PSDs have been reviewed, and considering that most of their effect is concentrated in a narrow range around resonance, the following noise model has been considered suitable (see Table 1):

1. Both horizontal and tilt noise have been considered zero-mean stationary and Gaussian stochastic processes.
2. The horizontal displacement noise PSD is assumed constant in acceleration, whereas the tilt noise PSD is assumed constant in velocity.
3. The two noise sources have been considered uncorrelated.

The model of the noise present in the TM x-displacement readout signal is completed (see Fig. 13) by adding a zero-mean stationary

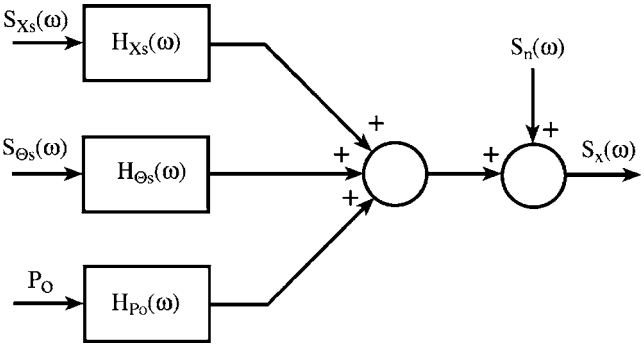

Fig. 13 Scheme of the model of the noise present in the TM *x*-displacement readout signal expressed by Eq. (39). *H* indicates the transfer functions, $S_{Xs}(\omega)$ is the horizontal displacement seismic noise PSD, $S_{\Theta s}(\omega)$ is the tilt seismic noise PSD, *Po* is the transferred impulse, and $S_n(w)$ is the position sensor noise PSD.

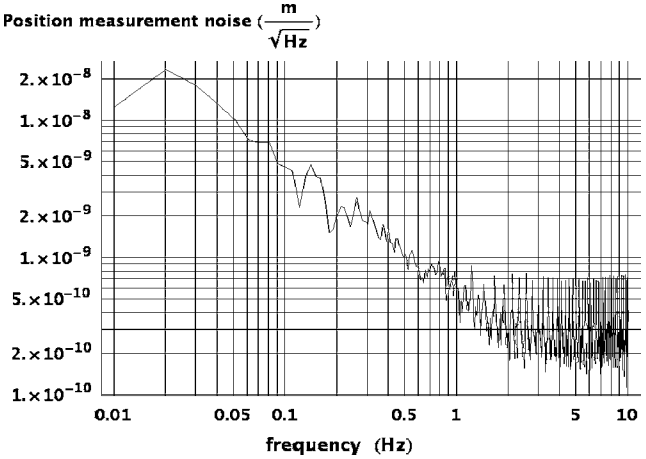

Fig. 14 Spectral density of the measurement noise of the laser interferometer used to monitor the position of a TM mock-up suspended inside a vacuum chamber

Gaussian white noise of the sensor $S_n(\omega)$. By means of the transfer functions from seismic noise to TM displacement (Eqs. (38)), the PSD of the total noise can be calculated

$$S_x(\omega)=|H_{Xs}(\omega)|^2S_{Xs}(\omega)+|H_{\Theta s}(\omega)|^2S_{\Theta s}(\omega)+S_n(\omega) \qquad (39)$$

The PSDs of the horizontal and tilt noise as well as of the readout noise has been measured using an experimental apparatus, set up in the laboratories of the University of Trento (Italy) according to the specifications elucidated above. Specifically, such an apparatus consists of a vacuum chamber in which a prismatic $18\times18\times5$ mm^3 Al TM mock-up is suspended by means of 1 m long pendulum. The TM position along the x direction is monitored by a laser interferometer, which is rigidly mounted on an optical window fixed to the vacuum chamber and detects the TM through an optical viewport. Further information thereabout can be found in Ref. [19]. This preliminary setup is intended to give experimental validation of an analytical model of the noise affecting the momentum measurement. To this purpose, the readout noise of the laser interferometer has been evaluated by measuring the position with respect to the measuring device of a mirror rigidly mounted inside the vacuum chamber. The spectral density of the position readout noise, plotted in Fig. 14, has been obtained by signal detrending, averaging ten time windows, and by applying the Hemming windowing. It can be noted that the spectral density is equal to $\sim10^{-9}$ m/$\sqrt{\text{Hz}}$ around the 0.465 Hz resonant frequency of the pendulum, where most of its effect is concentrated. The readout noise PSD has then been assumed constant and equal to 10^{-18} m^2/Hz. Furthermore, the laser interferometer has been used to measure the free oscillation of the TM mock-up over a long time scale (10 h). In Fig. 15, the spectral density of the position readout, obtained by averaging ten time windows and by applying the Hemming windowing, is compared to that predicted by Eq. (39) using the PSD values indicated in Table 1. It is worthnoting that the adopted noise model accurately reproduces the experimental data; in addition, the PSDs of horizontal and tilt seismic noise reported in Table 1 are in very good agreement with the literature (e.g., see Refs. [20–23]).

Figure 16 depicts the PSD of the TM position noise expressed by Eq. (39) using the data indicated in Table 1 for two pendulum lengths. Noteworthy, the low-frequency noise is dominated by the tilt contribution, and this effect is enhanced by the adoption of a longer pendulum. The limited dissipation originates a narrowband peak at the resonance, above which the TM becomes sensitive to

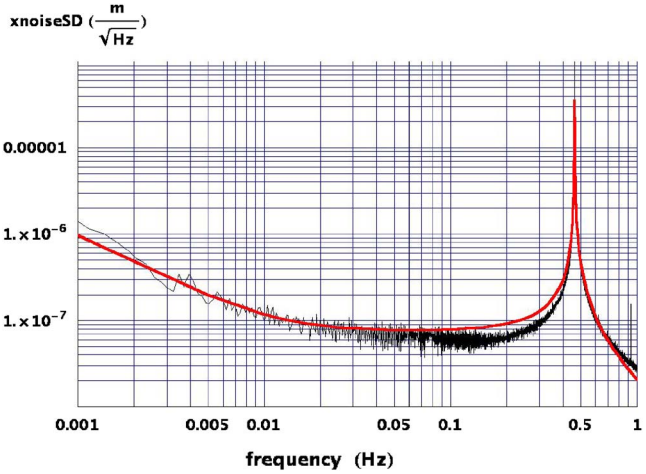

Fig. 15 Spectral density of the TM position noise deduced from the free oscillations of a TM mock-up suspended inside a vacuum chamber. The red (smooth) line corresponds to the TM noise model expressed by Eq. (39), where the values of the parameters used in the calculation are summarized in Table 1.

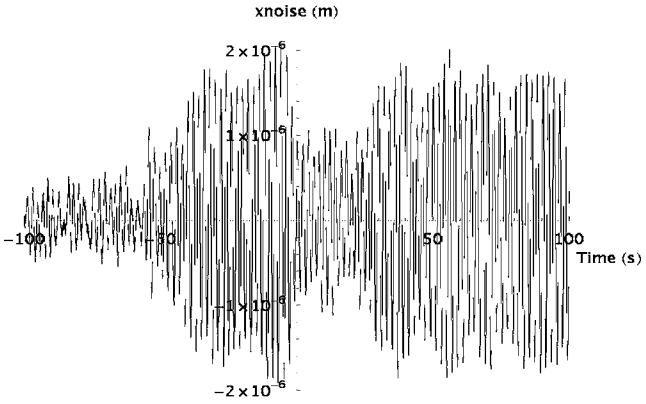

Fig. 17 Position read-out noise data modeled using the PSD displayed by Fig. 15. The values of the parameters used in the calculation are summarized in Table 1.

horizontal seismic noise. Being such a noise PSD constant in acceleration, its effect on the TM displacement is attenuated like $1/f^4$ and the resulting high-frequency noise quickly tends to the sensor noise. We adopt as a baseline a 1 m length pendulum: a brief discussion will be presented in the following on the choice of an optimal length. Starting from the PSD shown in Fig. 16, a sampled noise has been generated in order to build a realistic sampled data stream for the following optimal filter investigation. Data have been generated for 200 s at 500 Hz sampling frequency, in order to resolve a wide frequency band of the noise PSD. The sampled noise is shown in Fig. 17.

5.3.3 Microseismic Noise and Kinetic Energy of the Suspended Bodies. One condition in order for the momentum transfer not to be obscured by other phenomena is that the seismic noise does not induce on the plunger an effective kinetic energy sufficient to overcome the binding energy ΔU. This kinetic energy can be calculated from the relative velocity root mean square (rms) fluctuation. The horizontal seismic acceleration and seismic tilt angular velocity PSD are transferred to that of the relative velocity of TM and plunger according to

$$S_V = S_{A,\mathrm{seism}}\left|\frac{-igQ_{TM}+\sqrt{\frac{g}{L_{TM}}}L_{TM}\omega}{\omega\left[gQ_{TM}+L_{TM}\omega\left(i\sqrt{\frac{g}{L_{TM}}}-Q_{TM}\right)\right]}-\frac{-igQ_{pl}+\sqrt{\frac{g}{L_{TM}}}L_{pl}\omega}{\omega\left[gQ_{pl}+L_{pl}\omega\left(i\sqrt{\frac{g}{L_{pl}}}-Q_{pl}\right)\right]}\right|^2 + S_{\dot{\theta},\mathrm{seism}}\left|\frac{(h+L_{TM})\left(gQ_{TM}+i\sqrt{\frac{g}{L_{TM}}}L_{TM}\omega\right)}{gQ_{TM}+L_{TM}\omega\left(i\sqrt{\frac{g}{L_{TM}}}-Q_{TM}\omega\right)}-\frac{(h+L_{pl})\left(gQ_{pl}+i\sqrt{\frac{g}{L_{pl}}}L_{pl}\omega\right)}{gQ_{pl}+L_{pl}\omega\left(i\sqrt{\frac{g}{L_{pl}}}-Q_{pl}\omega\right)}\right|^2 \tag{40}$$

where the subscripts *TM* and *pl* indicate the length L and quality factors Q of the TM and plunger pendulums, respectively. The rms velocity is given by:

$$\langle v^2\rangle = \frac{1}{2\pi}\int_{-\infty}^{\infty} S_V(\omega)\mathrm{d}\omega \tag{41}$$

The preceding integral can be easily treated by considering the linear expansion in the difference $\delta L = L_{TM} - L_{pl}$, which is assumed to be made small and by assuming the worst case, where one of the two quality factors is much larger than the other. Moreover, as $S_{A,\mathrm{seism}}$ and $S_{\dot{\theta},\mathrm{seism}}$ are reasonably smooth functions around the resonant angular frequency $\omega_0 = \sqrt{g/L}$, one can approximate it with a constant and then get

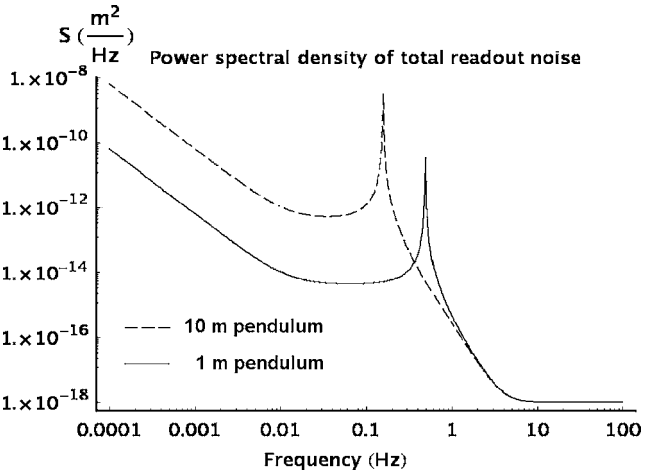

Fig. 16 PSD of the total readout noise simulated in Sec. 5.3.2 for two different pendulum lengths: 1 m and 10 m. The values of the parameters used in the calculation are summarized in Table 1.

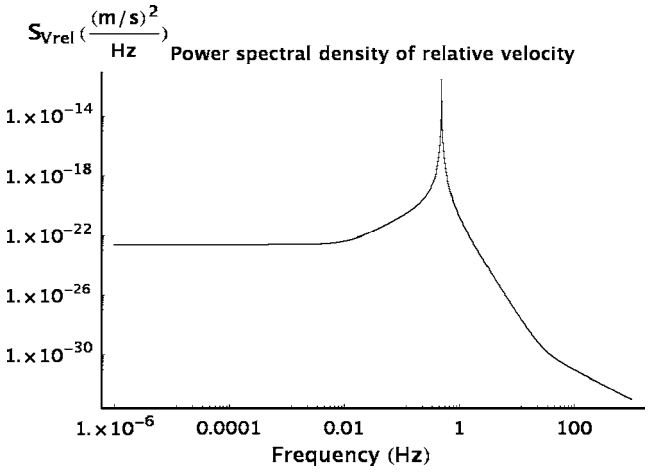

Fig. 18 Power spectral density of relative velocity of TM and plunger resulting from the seismic noise modelled in Sec. 5.3.2. The values of the parameters used in the calculation are summarized in Table 1.

$$\langle v^2\rangle = S_{A,\text{seism}}\frac{Q_{\max}^2}{2}\sqrt{\frac{L}{g}}\left(L+\frac{\delta L}{L}\right)+S_{\dot{\theta},\text{seism}}\frac{Q_{\max}^2}{2}\left[\sqrt{\frac{g}{L}}(h+L)^2 + g\sqrt{\frac{L}{g}}(h+L)(h+3L)\frac{\delta L}{L^2}\right] \quad (42)$$

where $Q_{\max}$ is the largest of the quality factors.

Substituting the realistic horizontal seismic acceleration and seismic tilt PSDs into Eq. (42) and assuming a difference of the pendulums' lengths of 1 mm, one obtains the PSD of relative velocity, depicted in Fig. 18, whose rms value is about 1×10^{-12} m^2/s^2. Assuming a plunger mass of $\sim$10 mg, a kinetic energy of about 2×10^{-17} J is obtained, i.e., well below the value of $T_{\max}\approx2.5\times10^{-11}$ J, set as an upper limit for ΔU.

5.4 Noise Optimal-Filter. Different techniques have been adopted in the literature to extract the applied impulse from the measured free oscillation of the suspended system. The more recent developments [7] have investigated the possibility of resolving the force function and measuring the applied impulse for long impulse widths. Accordingly, typical impulse widths expected in the present application are three orders of magnitude smaller than the oscillator period (milliseconds against seconds); therefore, the perfect impulse approximation seems reasonable. The effort is then focused on the possibility of exploiting the availability of the time-resolved motion of the oscillator to increase the measurement resolution of the transferred momentum.

In this section, we show that the standard Wiener–Kolmogorov filter (WKF) theory of optimal estimation (e.g., [24,25]) can be applied to assess the momentum transferred by an impulsive force to a harmonic oscillator. We assume that a harmonic oscillator of mass m, resonant angular frequency ω_0, and quality factor Q is subject to a force of total impulse P_0. The readout of the position x of the oscillator (in one dimension) is affected, as discussed in the preceding section, by a stationary and Gaussian noise with PSD $S_x(\omega)$. The momentum transferred from the force to the mass is measured from the motion of the oscillator as detected by the readout, which is given by

$$x(t) = As(t) + n(t) \quad (43)$$

where $s(t)$ is the response signal of the system to a unit impulse (known), A is the signal amplitude, function of the unknown impulse, and $n(t)$ is the noise. We now look for an optimal estimator of the signal amplitude from a linear combination of the data $x(t)$

$$\hat{A}(T) = \int_0^T h(t')x(T-t')dt' \quad (44)$$

where the "filter" function $h(t)$ has to be chosen such that $\hat{A}$ is an unbiased estimator

$$\langle\hat{A}\rangle = A \quad (45)$$

and that its variance $\sigma_{\hat{A}}^2 \equiv \langle\hat{A}^2\rangle - \langle\hat{A}\rangle^2$ is minimal. Consequently, $h(t)$ obeys the integral equations

$$\int_0^T h(t')s(T-t')dt' = 1 \quad (46)$$

in order to fulfill the condition expressed by Eq. (45), and

$$\int_0^T h(t'')R(t'-t'')\mathrm{d}t'' + \frac{\lambda}{2}s(T-t') = 0 \quad \text{for} \quad 0\le t\le T \quad (47)$$

according to the condition of minimal variance with the constrained imposed by Eq. (46). R is the autocorrelation of the stochastic noise $n(t)$, and λ is the Lagrange multiplier corresponding to the constrain expressed by Eq. (46). If the observation time T is large enough, one may assume that the data are available over the whole time scale. Thus, taking $T=0$, Eqs. (46) and (47) become

$$\int_{-\infty}^{\infty} h(t')s(-t')dt' = 1 \quad (48)$$

$$\int_{-\infty}^{\infty} h(t'')R(t'-t'')dt'' + \frac{\lambda}{2}s(-t') = 0 \quad \text{for} \quad -\infty\le t\le\infty \quad (49)$$

whose Fourier transforms are

$$\frac{1}{2\pi}\int_{-\infty}^{\infty} h(\omega)s(\omega)d\omega = 1 \quad (50)$$

$$h(\omega)S_x(\omega) + \frac{\lambda}{2}s^*(\omega) = 0 \quad (51)$$

where $s^*(\omega)$ is the conjugate Fourier transform of the signal. From Eqs. (50) and (51), one finally gets the filter function $h(\omega)$

$$h(\omega) = \frac{s^*(\omega)}{S_x(\omega)}\left[\frac{1}{2\pi}\int_{-\infty}^{\infty}\frac{|s(\omega)|^2}{S_x(\omega)}d\omega\right]^{-1} \quad (52)$$

The corresponding variance $\sigma_{\hat{A}}^2$ is equal to

$$\sigma_{\hat{A}}^2 = \left[\frac{1}{2\pi}\int_{-\infty}^{\infty}\frac{|s(\omega)|^2}{S_x(\omega)}d\omega\right]^{-1} \quad (53)$$

Now, applying this filter to a harmonic oscillator, the minimum detectable value of the transferred momentum is given by

$$\sigma_{P_0} = \left[\frac{1}{2\pi}\int_{-\infty}^{\infty}\frac{\frac{1}{m^2}\frac{1}{(\omega_0^2-\omega^2)^2+\omega^2\omega_0^2/Q^2}}{S_x(\omega)}\mathrm{d}\omega\right]^{-1/2} \quad (54)$$

Assuming as a first approximation that the readout noise has a white PSD, the preceding equation yields

$$\sigma_{P_0,\text{white}} = \sqrt{\frac{2S_x m^2\omega_0^3}{Q}} \quad (55)$$

Notably, the measurement precision of the transferred momentum is inversely proportional to the TM mass, suggesting the employment of a light mock-up of the TM. Moreover, the measurement

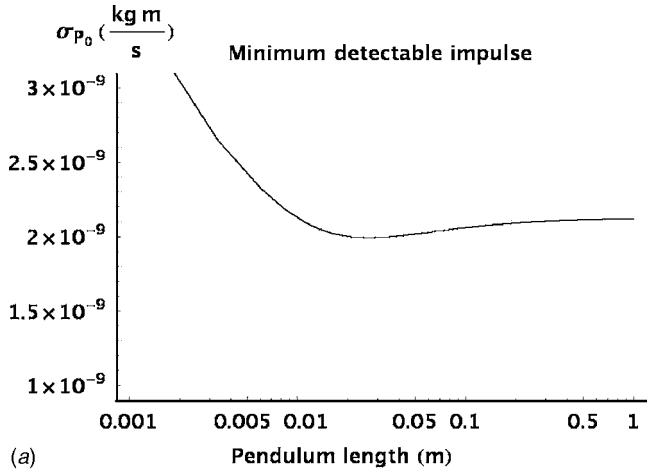

(*a*)

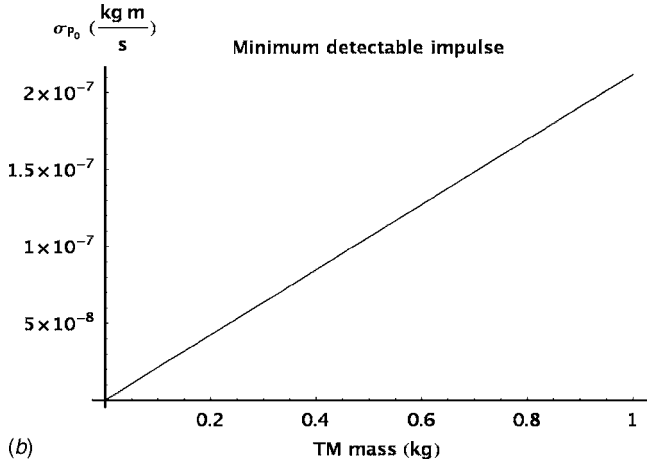

(*b*)

Fig. 19 (*a*) Variation of the minimum impulse detectable using a Wiener–Kolmogorov (WK) linear filter with the pendulum length. (*b*) Variation of the minimum impulse detectable using a WK linear filter with the TM mass. The values of the parameters used in the calculation are summarized in Table 1.

precision increases with decreasing resonant frequencies, i.e., increasing pendulum lengths. However, it should be reminded that large pendulum lengths tend to exacerbate the seismic noise on the TM, as illustrated in Fig. 16. Therefore, substituting the realistic PSD of readout noise derived in the preceding section into Eq. (54) and plotting the measurement resolution as a function of the pendulum length, one observes the existence of an optimal pendulum length (see Fig. 19(*a*)). This value represents the tradeoff between higher measurement sensibility of longer pendulums and lower noise disturbance of shorter ones. Long pendulums are however preferable because their resolution is maintained good and less affected by variations in the noise spectra. This is mainly because, given an impulse, they develop large oscillations anyway. Expectedly, plotting the minimum detectable value of the transferred momentum as a function of the TM mass, a proportional correlation is observed, as shown in Fig. 19(*b*). Remarkably, as illustrated in Figs. 19(*a*) and 19(*b*), a 0.01 kg heavy TM mock-up suspended on 1 m long pendulum will give a measurement resolution of about 2×10^{-9} kg m/s, i.e., 0.2% of the maximum linear momentum allowed in the LISA TM release.

We now test the ability of the filter function $h(t)$, defined by Eq. (46), to estimate the impulse imparted to a harmonic oscillator in the presence of the realistic readout noise modeled in Sec. 5.3.2. Let us assume that the TM is subjected at the instant $t=0$ to an impulse P_0 equal to 10^{-5} kg m/s. The resulting position readout is depicted in Fig. 20 and has been obtained by superimposing the

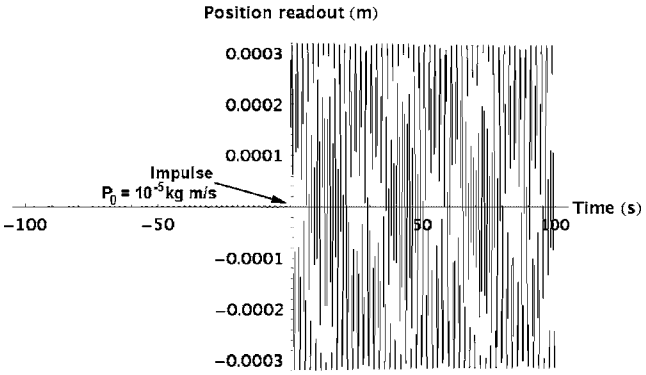

Fig. 20 Simulation of position readout data in the presence of seismic noise modeled in Sec. 5.3.2 in the case of application of an impulse equal to 10^{-5} kg m/s at the instant $t=0$. The values of the parameters used in the calculation are summarized in Table 1.

readout noise depicted in Fig. 17 on the response signal of the system to the impulse P_0 applied at the instant $t=0$. In order to extract the imparted impulse, one can build the filter function considering the response of the system to a unitary impulse (equal to its transfer function), according to the following expression:

$$h(\omega) = \frac{1}{m}\frac{1}{\dfrac{(\omega_0^2-\omega^2)-i\omega(\omega_0/Q)}{S_x(\omega)}}\sigma_{P_0}^2 \tag{56}$$

The advantage of the proposed technique for the momentum measurement is shown by Eq. (56). The instrument calibration consists of the calculation of the filtering function that is characterized by physical quantities, which may be easily measured: suspended mass, resonant frequency, and Q factor. The total noise at the readout $S_x(\omega)$ may be measured through a static experiment, in which no impulse is applied to the pendulum, as described in Sec. 5.3.2. Moreover, no signal prefiltering is needed to denoise the signal prior to processing, avoiding critical choices of filtering techniques and threshold settings.

The inverse Fourier transform of the function $h(\omega)$ is exactly the filter function $h(t)$, which is plotted in Fig. 21. Since the oscillation amplitude of the pendulum is proportional to the imparted impulse, the application of the filter function to the readout data of Fig. 20 gives the estimation of the imparted impulse. Figure 22 displays the dependence of the impulse estimation relative error on the integration time T defined in Eq. (46) for the estima-

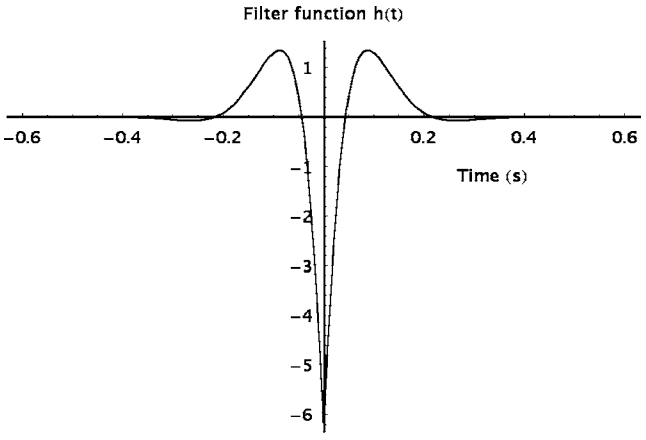

Fig. 21 WK filter function used in the estimation of the transferred momentum based on the position data shown in Fig. 20

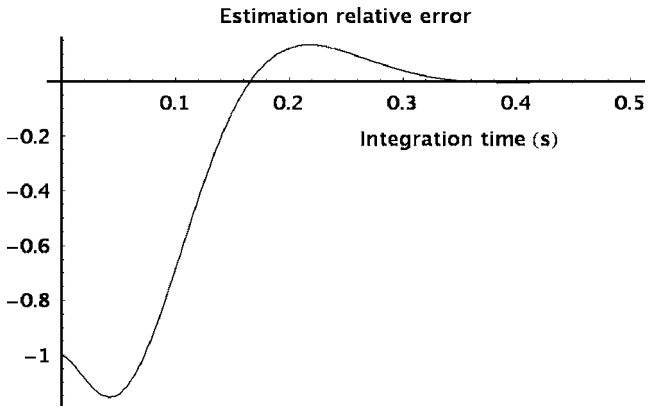

Fig. 22 Variation of the relative error in the estimation of the transferred momentum with the integration time, using the filter function illustrated in Fig. 21

tion of the unknown signal amplitude. It can be noted that the relative error drastically sinks for integration times longer than 0.4 s, corresponding to about five periods of the dominant pole of the function $h(\omega)$. In particular, a 200 s integration time yields an estimation of P_0 equal to 9.9988×10^{-6} kg m/s, i.e., $\sim 0.1\%$ relative error.

6 Conclusions

The present paper is focused on the measurement of the momentum transfer occurred when two free-falling bodies, interacting with surface forces, are impulsively separated in order to investigate the dynamics of release of objects in the absence of gravity. In particular, the release conditions as well as the related parameters, influencing the momentum acquired by the released body through adhesion rupture, have been extensively discussed. The dynamics of the release has been first analytically studied under the assumptions that only conservative forces act between the contacting objects. In this case, the knowledge of the only adhesion potential energy is sufficient to predict the impulse imparted to the test mass in the case of a quick retraction of the releasing device. On the contrary, a ground-based experiment is necessary if the contact is affected by additional nonconservative interaction phenomena, such as cold welding and sliding. Therefore, a measuring technique based on two pendulums, suspending the separating bodies, has been analyzed with particular attention on the capability to accurately reproduce the stress status on the contact patch, on the noise sources affecting the measurement and on the performances of a noise optimal-filtering technique in terms of achievable measurement resolution.

References

[1] Haag, T. W., 1991, "Thrust Stand for High Power Electric Propulsion Devices," Rev. Sci. Instrum., **62**, pp. 1186–1191.
[2] Jamison, J. A., Ketsdever, A. D., and Muntz, E. P., 2002, "Gas Dynamic Calibration of a Nano-Newton Thrust Stand," Rev. Sci. Instrum., **73**, pp. 3629–3637.
[3] Cubbin, E. A., Ziemer, J. K., Choueiri, E. Y., and Jahn, R. G., 1997, "Pulsed Thrust Measurements Using Laser Interferometry," Rev. Sci. Instrum., **68**, pp. 2339–2346.
[4] Merkowitz, S. M., Maghami, P. G., Sharma, A., Willis, W. D., and Zakrzwski, C. M., 2002, "A μN Thrust-Stand for LISA," Class. Quantum Grav., **19**, pp. 1745–1750.
[5] Gamero-Castaño, M., 2003, "A Torsional Balance for the Characterization of Micro-Newton Thrusters," Rev. Sci. Instrum., **74**, pp. 4509–4514.
[6] Selden, N. P., and Ketsdever, A. D., 2003, "Comparison of Force Balance Calibration Techniques for the Nano-Newton Range," Rev. Sci. Instrum., **74**, pp. 5249–5254.
[7] D'Souza, B. C., and Ketsdever, A. D., 2005, "Investigation of Time-Dependent Forces on a Nano-Newton-Second Impulse Balance," Rev. Sci. Instrum., **76**, p. 015105.
[8] Zhang, K. L., Chou, S. K., and Ang, S. S., 2005, "Development of a Low-Temperature Co-Fired Ceramic Solid Propellant Microthruster," J. Micromech. Microeng., **15**, pp. 944–952.
[9] Vitale, S., 2002, "LISA and its In-Flight Test Precursor SMART-2," Nucl. Phys. B, **110**, pp. 209–216.
[10] Biserni, M., Radaelli, P., Lesci, G., and Teti, D., 2006, "Caging Mechanism for LISA Pathfinder," *Proc. of 6th International LISA Symposium*, June 16–23, Goddard Space Flight Center, Greenbelt, MD.
[11] Benedetti, M., Bortoluzzi, D., Da Lio, M., and Fontanari, V., 2004, "The Role of Adhesion and Sub-Newton Pull-Off Forces on the Release of the Proof Mass for the LISA Test-Flight Package Experiment," *Proc. of the 4th AIMETA International Tribology Conference*, Rome, Sept. 14–17.
[12] Benedetti, M., Bortoluzzi, D., Da Lio, M., and Fontanari, V., 2006, "The Influence of Adhesion and Sub-Newton Pull-Off Forces on the Release of Objects in Outer Space," ASME J. Tribol., **128**, pp. 828–840.
[13] Bhushan, B., 2003, "Adhesion and Stiction: Mechanisms, Measurement Techniques, and Methods for Reduction," J. Vac. Sci. Technol. B, **21**, pp. 2262–2296.
[14] Israelachvili, J. N., 1999, "Surface Forces and Microrheology of Molecularly Thin Liquid Films," 2nd ed., *Handbook of Micro/Nanotribology*, B. Bhushan, ed., CRC Press, Boca Raton, pp. 267–319.
[15] Gilbreath, W. P., 1967, "Definition and Evaluation of Parameters Which Influence the Adhesion of Metals," *Adhesion or Cold Welding of Materials in Space Environments*, ASTM, Philadelphia, STP 431, pp. 128–148.
[16] Maugis, D., and Pollock, H. M., 1984, "Surface Forces, Deformation and Adherence at Metal Microcontacts," Acta Metall., **32**, pp. 1323–1334.
[17] Biral, F., Bortoluzzi, D., and Da Lio, M., 2005, "Dynamical Optimization of a Roberts Linkage-Based Inertial Sensor for Ground Testing of a Scientific Space Mission Critical Phase," Proceedings of the Multibody Dynamics 2005 ECCOMAS Thematic Conference, J. M. Goicolea, J. Cuadrado, C. García, Orden, eds., Madrid, June 21–24.
[18] Winterflood, J., and Blair, D. G., 1996, "A Long-Period Conical Pendulum for Vibration Isolation," Phys. Lett. A, **222**, pp. 141–147.
[19] Bortoluzzi, D., Baglivo, L., Benedetti, M., Biral, F., Bosetti, P., Cavalleri, A., Cristofolini, I., Da Lio, M., De Cecco, M., Dolesi, R., Fontanari, V., Lapolla, M., Oboe, R., Radaelli, P., Weber, J. W., and Vitale, S., 2006, "Test-Mass Release Phase Ground Testing for the LISA Pathfinder Mission," *Laser Interferometer Space Antenna, 6th International LISA Symposium*, American Institute of Physics, New York, **873**, pp. 556–560.
[20] McNamara, D. E., and Buland, R. P., 2004, "Ambient Noise Levels in the Continental United States," Bull. Seismol. Soc. Am., **94**, pp. 1517–1527.
[21] Acernese, F., et al., 2004, "Properties of Seismic Noise at Virgo Site," Class. Quantum Grav., **21**, pp. S433–S440.
[22] Hoffmann, H., Winterflood, J., Cheng, Y., and Blair, D. G., 2002, "Cross-Correlation Studies With Seismic Noise," Class. Quantum Grav., **19**, pp. 1709–1716.
[23] Hueller, M., 2004, "Geodesic Motion of LISA Test Masses: Development and Testing of Drag-Free Position Sensors," Ph.D. thesis, University of Trento, Italy.
[24] Papoulis, A., 1984, *Probability, Random Variables, and Stochastic Processes*, 2nd ed., McGraw-Hill, New York.
[25] Pollock, D. S. G., 2003, "Improved Frequency Selective Filters," Comput. Stat. Data Anal., **42**, pp. 279–297.

A Reciprocity Relation Couples Newtonian and Eshelbian Mechanics

G. Herrmann[1]
Stanford University,
Ortstrasse 7,
CH-7270 Davos Platz, Switzerland

R. Kienzler
Department of Production Engineering,
University of Bremen,
Am Biologischen Garten 2,
D-28359 Bremen, Germany
e-mail: rkienzler@uni-bremen.de

By considering a stressed elastic body subjected sequentially to a material displacement of a defect and the application of a physical force, the authors have succeeded in arriving at a novel type of coupling of Newtonian and Eshelbian mechanics by means of a reciprocity theorem analogous to that of Maxwell. This reciprocity relation is more involved than those in strictly physical or strictly material space. An order of magnitude analysis was required to obtain consistent relations. Several illustrative examples are worked out, and suggestions for some experiments, which in their evaluations would make use of the new expressions, are offered. [DOI: 10.1115/1.2755140]

Introduction

Since the introduction of the notion of a "force" on a singularity or a defect by Eshelby more than a half century ago, the area *configurational mechanics* or *mechanics in material space* or *Eshelbian mechanic*s, based on this notion, has experienced a broad development and growth, particularly during the past decade. This is evidenced by the publication of numerous journal papers, several books [1–3], and volumes of conference proceedings [4,5].

Whereas the usual or standard or *Newtonian mechanics* is concerned with equilibrium and motion of bodies with mass in a space, now specifically called *physical space* in which Newton's laws are applicable, configurational mechanics deals with objects that may or may not have mass, such as dislocations, cracks, inclusions, cavities, and nonhomogeneities, which, under suitable conditions, can move or be displaced within the deformable material body in which they find themselves. Thus, the notion of the Eshelby force can be somewhat generalized and is now often referred to as *material force*, by contrast to a *physical* (or Newtonian) *force* relevant in *mechanics in physical space*.

A material force is always defined as the negative gradient of the total energy of the system with respect to the position of the defect in the material. Far-reaching analogies (correspondence or duality) exist between mechanics in physical space and mechanics in material space as illustrated by numerous examples in [2].

Recognizing the usefulness of reciprocity theorems of Maxwell and Betti in Newtonian mechanics of linearly elastic bodies, the present authors have successfully attempted to establish analogous theorems in mechanics in material space [6]. Illustrations of these novel reciprocity theorems will be presented in [7].

The purpose of the present contribution consists in advancing two novel theorems in mixed, i. e., physical-material formulation. Thus, the terms "force" and "displacement," in the sequel, have to always be specified as being either physical or material. The development begins by considering a linearly elastic body in static equilibrium under the action of arbitrary applied surface tractions and body forces and containing an arbitrary number of defects and nonhomogeneities. Attention is focused on a point defect that can be displaced in the material and on an additional concentrated physical force, which can be applied at a different point of the body.

It turns out that in material space the material displacement of a defect plays the role of physical force application. In physical space, work is done by the applied physical force (cause) in a physical displacement (effect), whereas in material space work is done by the material forces (effect) in the applied material displacements (cause).

The analysis in the two mixed spaces carried out in the first section is more involved than the corresponding analysis in strictly physical or strictly material space and even requires an order-of-magnitude estimation in order to propose a consistent formulation of a reciprocity theorem analogous to that of Maxwell (cf., [8]). The augmented intricacy is a result of the fact that the physical displacement of the point of application of the force is different, depending on whether the defect has been displaced or not. This difference happens to be of the same order as the displacement of the point of application of the force due to the material displacement of the defect. A second relation analogous to Betti's theorem (cf., [9]) likewise contains not two, but three interrelated influence coefficients.

The subsequent section deals with three different versions of a simple, one-dimensional specific example to illustrate the validity of the purposed theorems. The final section contains several suggestions of possible experiments in which the novel theorems could be advantageously applied.

Formulation of the General Problem

Consider a linearly elastic body of arbitrary shape suitably supported and subjected to an arbitrary set of surface tractions and body forces that maintain static equilibrium and that induce a state of stress in the body. We focus our attention on a concentrated defect at point 1 and a physical concentrated force $\boldsymbol{F}$ that will be applied at point 2 (cf., Fig. 1). The body may contain an arbitrary set of various other defects and inhomogeneities. The physical state of stress is in turn accompanied by some distribution of material forces. Next, we contemplate a sequence of two operations A called $A1$ and $A2$.

In $A1$, we displace, within the material, the defect 1 by some small amount $\boldsymbol{\lambda}$. This changes the material force $\boldsymbol{B}_{10}$, effective there before, by some amount $\boldsymbol{B}_{11}^{A}$ such that the total material force $\boldsymbol{B}_1$, at 1 is now

$$\boldsymbol{B}_1 = \boldsymbol{B}_{10} + \boldsymbol{B}_{11}^{A} \tag{1}$$

Another consequence of the material displacement $\boldsymbol{\lambda}$ is that point 2, which has originally been displaced due to the state of stress by an amount $\boldsymbol{u}_{20}$ from the unstressed state, is now displaced additionally by an amount $\boldsymbol{u}_{21}^{A}$. Here and in the sequel, the first subscript indicates the location of the "effect" and the second the location of the "cause."

[1]Deceased, January 7, 2007.

Contributed by the Applied Mechanics Division of ASME for publication in the JOURNAL OF APPLIED MECHANICS. Manuscript received October 30, 2006; final manuscript received May 10, 2007; published online January 16, 2008. Review conducted by Zhigang Suo.

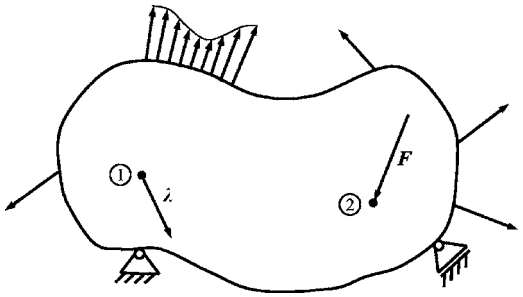

Fig. 1 Elastic body under arbitrary load with, especially, a concentrated defect at point 1 and a concentrated physical force at point 2

The work done on the body in the operation $A1$ is

$$W^{01} = \boldsymbol{\lambda} \cdot \boldsymbol{B}_{10} + \tfrac{1}{2}\boldsymbol{\lambda} \cdot \boldsymbol{B}^A_{11} \tag{2}$$

where the dot indicates a scalar product. The first term on the right recognizes the existence of $\boldsymbol{B}_{10}$ before $\boldsymbol{\lambda}$ was applied and the factor $1/2$ of the second term implies a linear relationship between the applied $\boldsymbol{\lambda}$ and the material force $\boldsymbol{B}^A_{11}$ induced by $\boldsymbol{\lambda}$. Such a relationship should be valid for small $\boldsymbol{\lambda}$.

In operation $A2$, we apply additionally the physical force $\boldsymbol{F}$ at point 2. This changes the physical stress distribution and the material forces throughout the whole body. $\boldsymbol{B}_1$ at point 1 will now be

$$\boldsymbol{B}_1 = \boldsymbol{B}_{10} + \boldsymbol{B}^A_{11} + \boldsymbol{B}^A_{12} \tag{3}$$

and the physical displacement at point 2 will now be

$$\boldsymbol{u}_2 = \boldsymbol{u}_{20} + \boldsymbol{u}^A_{21} + \boldsymbol{u}^A_{22} \tag{4}$$

The work done in $A2$ concerns only $\boldsymbol{F}$ because the defect at 1 has not been displaced in the material. (It has been displaced in physical space, but no work has been done.)

Thus, the work done on the body in the two parts of operation A, namely $A1$ and $A2$, is

$$W^A = \boldsymbol{\lambda} \cdot \boldsymbol{B}_{10} + \tfrac{1}{2}\boldsymbol{\lambda} \cdot \boldsymbol{B}^A_{11} + \tfrac{1}{2}\boldsymbol{F} \cdot \boldsymbol{u}^A_{22} \tag{5}$$

Next, we consider a sequence of two operations B consisting of $B1$ and $B2$ in which we apply the physical force $\boldsymbol{F}$ first and the material displacement $\boldsymbol{\lambda}$ second.

Application of $\boldsymbol{F}$ at 2 changes the material force $\boldsymbol{B}_{10}$ at 1 by an amount, say, $\boldsymbol{B}^B_{12}$, such that

$$\boldsymbol{B}_1 = \boldsymbol{B}_{10} + \boldsymbol{B}^B_{12} \tag{6}$$

and the physical displacement 2, proportional to $\boldsymbol{F}$, shall be called $\boldsymbol{u}^B_{22}$. The total physical displacement at 2 is now

$$\boldsymbol{u}_2 = \boldsymbol{u}_{20} + \boldsymbol{u}^B_{22} \tag{7}$$

and the work on the system is

$$W^{02} = \tfrac{1}{2}\boldsymbol{F} \cdot \boldsymbol{u}^B_{22} \tag{8}$$

In the second part $B2$ of the operation B, the point 1 is additionally displaced in the material by an amount $\boldsymbol{\lambda}$. This changes the material force at 1 by an amount, say, $\boldsymbol{B}^B_{11}$ and the physical displacement at 2 by an amount, say, $\boldsymbol{u}^B_{21}$. Thus, the total resulting material force at 1 is now

$$\boldsymbol{B}_1 = \boldsymbol{B}_{10} + \boldsymbol{B}^B_{12} + \boldsymbol{B}^B_{11} \tag{9}$$

and the total physical displacement at 2 is

$$\boldsymbol{u}_2 = \boldsymbol{u}_{20} + \boldsymbol{u}^B_{22} + \boldsymbol{u}^B_{21}. \tag{10}$$

The work done on the system in operation B is then

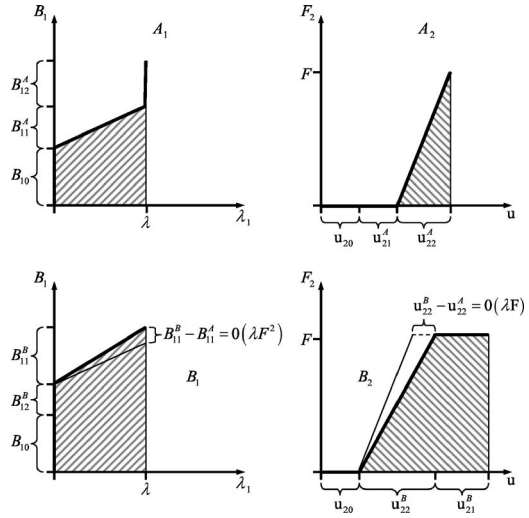

Fig. 2 Graphical illustration of the operations *A*1, *A*2, *B*1, and *B*2

$$W^B = \tfrac{1}{2}\boldsymbol{F} \cdot \boldsymbol{u}^B_{22} + \boldsymbol{\lambda} \cdot (\boldsymbol{B}_{10} + \boldsymbol{B}^B_{12}) + \tfrac{1}{2}\boldsymbol{\lambda} \cdot \boldsymbol{B}^B_{11} + \boldsymbol{F} \cdot \boldsymbol{u}^B_{21}. \tag{11}$$

It is argued now that the work done on the system in operations A and B should be the same, regardless of the sequencing, because, in the final state, the elastic stored energy in the body is the same and equal to the external work. Thus,

$$W^A = W^B$$

i.e.,

$$-\boldsymbol{\lambda} \cdot \left[\boldsymbol{B}^B_{12} + \tfrac{1}{2}(\boldsymbol{B}^B_{11} - \boldsymbol{B}^A_{11})\right] = \boldsymbol{F} \cdot \left[\boldsymbol{u}^B_{21} + \tfrac{1}{2}(\boldsymbol{u}^B_{22} - \boldsymbol{u}^A_{22})\right] \tag{12}$$

The various contributions to expression (12) are illustrated also graphically in Fig. 2

Order of Magnitude Estimates

We wish to examine now whether all terms in the relation $W^A = W^B$ above are of the same order or not. We recall [2] that the original material force B_{10} is of the order of the square of some originally applied forces F_0, which induced the physical state of stress, i.e.,

$$B_{10} = 0(F_0^2) \tag{13a}$$

where $0()$ indicates "order of…". The proportionality factor would characterize the "strength" of the defect, e.g., the length of a crack, the magnitude of the Burgers vector of a dislocation, the diameter of a cavity, the difference in stiffness of inclusion and bulk material, the jump in stiffness at a phase transition, etc. The change in the material force B^A_{11} due to a material displacement is proportional to the magnitude of the translation since linearity is implied. Thus,

$$B^A_{11} = 0(\lambda F_0^2) \tag{13b}$$

If, in addition, a physical force is applied, then the change of the material force would be

$$B^A_{12} = 0(\lambda F^2) \tag{13c}$$

In operation B, first the physical force is applied, changing the material force by an amount

$$B^B_{12} = 0(F^2) \tag{13d}$$

and the additional material translation λ causes

$$B^B_{11} = 0(\lambda F^2) \tag{13e}$$

On the displacement side at 2, we have the following estimates. Because of linearity the displacement in the initial state is

$$u_{20} = 0(F_0) \tag{14a}$$

Because of the material translation, the stiffness of the body is changed, resulting in a physical displacement of the amount

$$u_{21}^{A} = 0(\lambda F_0) \tag{14b}$$

An additional force would change the displacement to

$$u_{22}^{A} = 0(\lambda F) \tag{14c}$$

After applying first the physical force, the initial displacement is changed proportional to the applied force. Thus,

$$u_{22}^{B} = 0(F) \tag{14d}$$

Let us assume that the factor of proportionality would be β, i.e., $u_{22}^{B} = \beta F$. It may be mentioned that $u_{22}^{A} = \beta F + 0(\lambda F)$, i.e., the terms not involving λ are equal. Finally, an additional material translation of defect 1 causes a change in the physical displacement at 2 to the amount of

$$u_{21}^{B} = 0(\lambda F) \tag{14e}$$

We note, that the terms $\boldsymbol{\lambda} \cdot \boldsymbol{B}_{12}^{B}$, $\boldsymbol{F} \cdot \boldsymbol{u}_{21}^{B}$, and $\boldsymbol{F} \cdot 1/2(\boldsymbol{u}_{22}^{B} - \boldsymbol{u}_{22}^{A})$ are of the same order of magnitude $0(\lambda F^2)$, whereas the term $\boldsymbol{\lambda} \cdot (1/2) \times (\boldsymbol{B}_{11}^{B} - \boldsymbol{B}_{11}^{A})$ is of the order $0(\lambda^2 F^2)$ and can thus be omitted in further developments (see the graphical illustration in Fig. 2).

The reciprocity relation between an applied material defect displacement $\boldsymbol{\lambda}$ and a physical force $\boldsymbol{F}$ application is thus

$$-\boldsymbol{\lambda} \cdot \boldsymbol{B}_{12}^{B} = \boldsymbol{F} \cdot \left[\boldsymbol{u}_{21}^{B} + \tfrac{1}{2}(\boldsymbol{u}_{22}^{B} - \boldsymbol{u}_{22}^{A}) \right] \tag{15}$$

It is thus recognized that reciprocity in mixed (and coupled) physical-material space is more involved than in pure physical [8] or pure material space [6] because the difference in the work of the force $\boldsymbol{F}$ in the physical displacement of its point of application before and after application of the material displacement of a defect at some other point of the body is of the same order as the work done by the force in the physical displacement produced by the defect displacement $\boldsymbol{\lambda}$.

To establish a relation in physical-material space analogous to Betti's theorem, we have to consider the scalar version of the relation analogous to Maxwell's theorem. Let the component of $\boldsymbol{B}_{12}^{B}$ parallel to $\boldsymbol{\lambda}$ be called B_{12}^{BP} and the components of $\boldsymbol{u}_{2i}$ ($i = 1, 2$) parallel to $\boldsymbol{F}$ be called u_{2i}^{P}. Thus the scalar version of (15) is

$$-\lambda B_{12}^{BP} = F\left[u_{21}^{BP} + \tfrac{1}{2}(u_{22}^{BP} - u_{22}^{AP}) \right] \tag{16}$$

where F and λ are the magnitudes of $\boldsymbol{F}$ and $\boldsymbol{\lambda}$, respectively. Because of linearity, we have

$$-B_{12}^{BP} = \beta_{12} F \tag{17}$$

and

$$u_{21}^{BP} = \delta_{21}\lambda; \quad \tfrac{1}{2}(u_{22}^{BP} - u_{22}^{AP}) = \eta_{22}\lambda \tag{18}$$

where β_{12}, δ_{21}, and η_{22} are influence coefficients.

Hence,

$$\beta_{12} = \delta_{21} + \eta_{22} \tag{19}$$

which represents the physical-material (or Newtonian–Eshelbian) version of Betti's theorem [9].

It is noteworthy that in this novel mixed formulation, Betti's theorem acquires an additional term η_{22}, by contrast to classical Betti's theorem (in physical space) and the proposed version in strictly material space [6]. Thus, the coupling of physical and material space through reciprocity turns out to be more intricate than one might have expected.

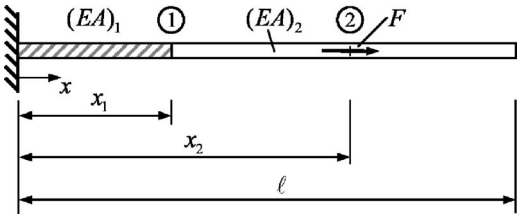

Fig. 3 Elastic bar with a jump in stiffness at 1 and a point force at 2

Illustration of the Mixed Reciprocity Relation for a Nonhomogeneous Bar

Absence of Initial Stress. We consider an elastic bar of length ℓ, built-in at left end and free at the other (cf. Fig. 3). The bar possesses the following stiffnesses:

$$\begin{aligned} &(EA)_1 \quad 0 \le x < x_1 \\ &(EA)_2 \quad x_1 < x \le \ell \end{aligned} \tag{20}$$

where E is Young's modulus and A the cross-sectional area. The jump in the compliance $C = 1/EA$ at point 1 ($x = x_1$) is designated as $[C]$

$$[C] = \frac{1}{(EA)_1} - \frac{1}{(EA)_2} \tag{21}$$

Application of an axial force F shall take place at point 2 ($x = x_2$).

Generally, the material force B acting at a jump in stiffness of a bar is, in the absence of distributed axial forces, given by [2]

$$B = -\tfrac{1}{2} N^2 [C] \tag{22}$$

where N is the tension/compression force at the point of the discontinuity. Initially, there is no applied force and, thus, the physical stress in the bar is zero and

$$B_{10} = 0, \quad u_{20} = 0 \tag{23}$$

where u is the axial physical displacement.

In an operation $A1$, the jump $[C]$ is displaced by an amount λ and afterward

$$B_{11}^{A} = 0 \quad u_{21}^{A} = 0 \tag{24}$$

The subsequent operation $A2$, with the application of F, leads to

$$B_{12}^{A} = -\tfrac{1}{2} F^2 [C] \tag{25}$$

and

$$\begin{aligned} u_{22}^{A} &= F\left(\frac{x_1 + \lambda}{(EA)_1} + \frac{x_2 - x_1 - \lambda}{(EA)_2} \right) \\ &= F\left(\frac{x_1}{(EA)_1} + \frac{x_2 - x_1}{(EA)_2} \right) + \lambda F[C] \\ &= u^F + \lambda F[C] \end{aligned} \tag{26}$$

In operation $B1$, application of F first, results in

$$B_{12}^{B} = -\tfrac{1}{2} F^2 [C] \tag{27}$$

$$u_{22}^{B} = F\left(\frac{x_1}{(EA)_1} + \frac{x_2 - x_1}{(EA)_2} \right) = u^F \tag{28}$$

Operation $B2$, which follows with the application of λ, leads to

$$B_{11}^{B} = 0 \quad u_{21}^{B} = \lambda F[C] \tag{29}$$

Substitution into the reciprocity relation yields

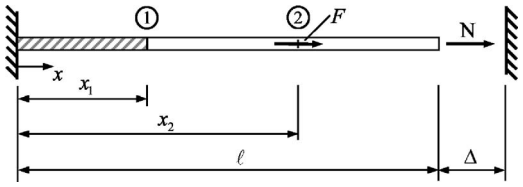

Fig. 4 Elastic bar prestressed by *N* to close the gap Δ

$$-\lambda\left(-\tfrac{1}{2}F^2[C]\right) = F\left[\lambda F[C] + \tfrac{1}{2}(u^F - u^F - \lambda F[C])\right] \quad (30)$$

which is an identity and verifies the validity of the reciprocity relation (16). The Betti version (19) of the reciprocity theorem is readily verified by substitution.

Load-Controlled Initial Stress. We again consider an elastic bar sketched in Fig. 3. but now, by contrast to the previous problem, an axial force N_0 is applied initially at the right end.

As in the general case we consider two operations $A1$ and $A2$, as well as two operations $B1$ and $B2$. The various material forces at point 1 and physical displacements at point 2 are, in this particular example, calculated to be

$$B_{10} = -\tfrac{1}{2}N_0^2[C]; \quad (31a)$$

$$B_{11}^A = 0 \quad (31b)$$

$$B_{11}^B = 0 \quad (31c)$$

$$B_{12}^B = -\tfrac{1}{2}(N_0+F)^2[C] + \tfrac{1}{2}N_0^2[C] = -F\left(N_0 + \tfrac{1}{2}F\right)[C] \quad (31d)$$

$$u_{20} = N_0\left(\frac{x_1}{(EA)_1} + \frac{x_2-x_1}{(EA)_2} + \frac{\ell-x_2}{(EA)_2}\right), \quad (32a)$$

$$u_{21}^A = N_0\lambda[C] \quad (32b)$$

$$u_{22}^A = u^F + F\lambda[C] \quad (32c)$$

where

$$u^F = F\left(\frac{x_1}{(EA)_1} + \frac{x_2-x_1}{(EA)_2}\right) \quad (32d)$$

$$u_{22}^B = u^F \quad (32e)$$

$$u_{21}^B = (N_0+F)\lambda[C] \quad (32f)$$

Substitution into the reciprocity relation leads indeed to an identity and thus verifies the validity of the proposed reciprocity relation.

Displacement-Controlled Initial Stress. In order to also validate the order-of-magnitude estimation, we consider the same bar as previously, but now it is subjected to a displacement controlled initial stress. The bar of original unstressed length ℓ is displaced at the free end by an amount $\Delta(\Delta \ll x_1, x_2, \ell)$ (cf. Fig. 4).

This induces an axial force N_0: the relationship between Δ and N_0 is

$$\Delta = N_0\left(\frac{x_1}{(EA)_1} + \frac{x_2-x_1}{(EA)_2} + \frac{\ell-x_2}{(EA)_2}\right) = N_0\gamma \quad (33)$$

with

$$\gamma = \frac{x_1}{(EA)_1} + \frac{x_2-x_1}{(EA)_2} + \frac{\ell-x_2}{(EA)_2} \quad (34)$$

Because of fixed grip conditions, the displacement Δ has to be the same after application of the material displacement λ at point 1 and the physical force F at point 2. This leads to

$$(F+N_{\lambda F})\frac{x_1+\lambda}{(EA)_1} + (F+N_{\lambda F})\frac{x_2-x_1-\lambda}{(EA)_2} + N_{\lambda F}\frac{\ell-x_2}{E_2A_2} = \Delta \quad (35)$$

where $N_{\lambda F}$ is the axial force at the right end of the bar. Furthermore,

$$N_{\lambda F}(\gamma + \lambda[C]) + F(\gamma_1 + \lambda[C]) = \Delta = N_0\gamma \quad (36)$$

with

$$\gamma_1 = \frac{x_1}{(EA)_1} + \frac{x_2-x_1}{(EA)_2} \quad (37)$$

It follows that

$$N_{\lambda F} = \frac{N_0 - F\left(\dfrac{\gamma_1}{\gamma} + \dfrac{\lambda[C]}{\gamma}\right)}{1 + \dfrac{\lambda[C]}{\gamma}} \quad (38)$$

An expansion in powers of λ leads to

$$N_{\lambda F} = N_0 - F\frac{\gamma_1}{\gamma} - \frac{\lambda[C]}{\gamma}\left[N_0 + F\left(1-\frac{\gamma_1}{\gamma}\right)\right] + 0(\lambda^2) \quad (39)$$

The axial force at cross section 1 after application of λ and F is

$$N_{\lambda F} + F \quad (40)$$

Thus,

$$N_{\lambda F}^1 = \left[N_0 + F\left(1-\frac{\gamma_1}{\gamma}\right)\right]\left(1-\frac{\lambda[C]}{\gamma}\right) \quad (41)$$

The axial force is called N_λ^1, if only λ is applied with $F=0$ in the above expression, N_F^1 if only F is applied with $\lambda=0$ above, and N_0^1 if neither λ nor F is applied.

The displacement of cross section 2, where F is applied and after application of λ and F, is

$$\delta_{\lambda F} = N_{\lambda F}^1\left(\frac{x_1+\lambda}{E_1A_1} + \frac{x_2-x_1-\lambda}{E_2A_2}\right) \quad (42)$$

or, after substitution

$$\delta_{\lambda F} = \left[N_0 + F\left(1-\frac{\gamma_1}{\gamma}\right)\right]\left(1-\frac{\lambda[C]}{\gamma}\right)(\gamma_1 + \lambda[C]) \quad (43)$$

Expansion in powers of λ leads to

$$\delta_{\lambda F} = \gamma_1\left[N_0 + F\left(1-\frac{\gamma_1}{\gamma}\right)\right] + \lambda[C]\left[N_0\left(1-\frac{\gamma_1}{\gamma}\right) + F\left(1-\frac{\gamma_1}{\gamma}\right)^2\right] + 0(\lambda^2) \quad (44)$$

The various displacements δ_λ, δ_F, and δ_0 if only λ is applied, if only F is applied, and if neither λ nor F is applied, respectively, can be obtained as special case of the above expression by setting $F=0$ or $\lambda=0$ or $F=\lambda=0$, respectively.

Next, we have to evaluate the various displacements to obtain

$$u_{21}^A = \delta_\lambda - \delta_0 = \lambda[C]N_0\left(1-\frac{\gamma_1}{\gamma}\right) \quad (45a)$$

$$u_{22}^A = \delta_{\lambda F} - \delta_\lambda = F\gamma_1\left(1-\frac{\gamma_1}{\gamma}\right) + \lambda[C]F\left(1-\frac{\gamma_1}{\gamma}\right)^2 \quad (45b)$$

$$u_{22}^B = \delta_F - \delta_0 = F\gamma_1\left(1-\frac{\gamma_1}{\gamma}\right) \quad (45c)$$

$$u_{21}^B = \delta_{\lambda F} - \delta_F = \lambda[C]\left(1-\frac{\gamma_1}{\gamma}\right)\left[N_0 + F\left(1-\frac{\gamma_1}{\gamma}\right)^2\right] \quad (45d)$$

The various material forces, in turn, are calculated to be

$$B_{10} = -\tfrac{1}{2}[C]N_0^2 \tag{46a}$$

$$B_{11}^A = -\frac{1}{2}[C]\{(N_\lambda^1)^2 - (N_0^1)^2\} = \frac{\lambda[C]^2}{\gamma}N_0^2 \tag{46b}$$

$$B_{12}^A = -\frac{1}{2}[C]\{(N_{\lambda F}^1)^2 - (N_\lambda^1)^2\} = -[C]F\left(1-\frac{\gamma_1}{\gamma}\right)\left[N_0 + \frac{1}{2}F\left(1-\frac{\gamma_1}{\gamma}\right)\right]\left(1-2\frac{\lambda[C]}{\gamma}\right) \tag{46c}$$

$$B_{12}^B = -\frac{1}{2}[C]\{(N_F^1)^2 - (N_0^1)^2\} = -[C]F\left(1-\frac{\gamma_1}{\gamma}\right)\left[N_0 + \frac{1}{2}F\left(1-\frac{\gamma_1}{\gamma}\right)\right] \tag{46d}$$

$$B_{11}^B = -\frac{1}{2}[C]\{(N_{\lambda F}^1)^2 - (N_F^1)^2\} = -\frac{\lambda[C]^2}{\gamma}\left[N_0 + F\left(1-\frac{\gamma_1}{\gamma}\right)\right]^2 \tag{46e}$$

Substitution into the general reciprocity relation (16) indeed results in an identity. This confirms the general order-of-magnitude analysis carried out in a previous section and validates (16).

Suggestions for Possible Experimental Applications of Reciprocity Relations

One can think of at least three possible practical applications of the mixed (physical-material) reciprocity relation

$$-\lambda B_{12}^B = F\left[u_{21}^B + \tfrac{1}{2}(u_{22}^B - u_{22}^A)\right] \tag{47}$$

We return to the first illustrative example above of a bar with no initial load or physical displacement (Fig. 3).

(a) The right-hand side of the reciprocity relation divided by λ can be evaluated by elementary means of standard strength-of-materials theory and will yield the material force B_{12}^B at cross section 1 without any knowledge of mechanics in material space, i.e.,

$$B_{12}^B = -\frac{F}{\lambda}\left(\lambda F[C] + \frac{1}{2}u^F - \frac{1}{2}u^F - \frac{1}{2}\lambda F[C]\right)$$

or

$$B_{12}^B = -\tfrac{1}{2}F^2[C] \tag{48}$$

If $[C]$ is interpreted as the jump in compliance at the interface of two phases of the same material and if a critical value of B_{12}^B exists, which induces a motion of this interface, then the above relation, for given $[C]$ can be used to determine a critical force F at which the phase interface starts moving.

(b) In a second possible experiment, the problem consists of determining the unknown magnitude of the jump in the compliance in a two-phase material, as sketched in Fig. 5(*a*).

For this purpose, two barlike samples are cut out of the bulk material. The two samples that differ by the location of the phase boundary, which is λ apart, are built in at one end, and a force F is applied at the free end to each sample as indicated in Fig. 5(*b*).

The end displacements of the two samples will be different and are labeled u_{22}^A and u_{22}^B. Substitution into the reciprocity relation and noting that here $u_{21}^B = 0$, we obtain

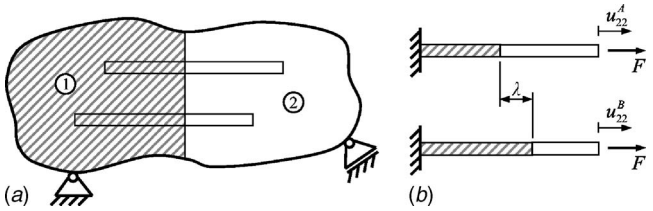

Fig. 5 Two-phase material (*a*) and loaded samples (*b*)

$$-\lambda\left(-\tfrac{1}{2}F^2[C]\right) = F\tfrac{1}{2}(u_{22}^B - u_{22}^A)$$

or

$$[C] = \frac{1}{F\lambda}(u_{22}^B - u_{22}^A) \tag{49}$$

which solves the problem posed.

(c) A third formulation of a possible experiment might concern the problem of the (slow) material displacement of the phase boundary as a function of time $\lambda(t)$ for given compliance jump $[C]$ and given applied load F. The elongation of the sample as a function of time $\Delta(t)$ will be

$$\Delta(t) = u_{22}^B(t) - u_{22}^A(0) \tag{50}$$

and from the reciprocity relation, we obtain

$$\lambda(t) = \frac{\Delta(t)}{F[C]} \tag{51}$$

To achieve an actual motion of the phase boundary, the sample might be subjected to a high temperature by placing it into a furnace, which might prevent a direct measurement of the position of the phase boundary.

Concluding Remarks

The developments presented above have demonstrated that a novel type of coupling can be established between Newtonian (physical) and Eshelbian (material) mechanics by means of reciprocity relations. The quantities that connect the two areas are, of course, energy and work. The new unifying theorems allowed us to suggest several experiments that might be useful under some circumstances.

Acknowledgment

The support by the Research in Pairs Programme of the Mathematisches Forschungsinstitut Oberwolfach is gratefully acknowledged. Thanks are also due to Dipl.-Ing. R. Schröder for carefully drawing the figures.

References

[1] Maugin, G. A., 1993, *Material Inhomogeneities in Elasticity*, Chapman & Hall, London.
[2] Kienzler, R., and Herrmann, G., 2000, *Mechanics in Material Space*, Springer, Berlin.
[3] Gurtin, M. E., 2000, *Configurational Forces as Basic Concepts of Continuum Physics*, Springer, New York.
[4] Kienzler, R., and Maugin, G. A., eds., 2001, *Configurational Mechanics of Materials*, (CISM Courses and Lectures No. 427), Springer, Vienna.
[5] Steinmann, P., and Maugin, G. A., eds., 2005, *Mechanics of Material Forces*, (Advances in Mechanics and Mathematics, Vol. 11), Springer, New York.
[6] Herrmann, G., and Kienzler, R., 2007, "Reciprocity Relations in Eshelbian Mechanics," Mech. Res. Commun., **34**, pp. 338–343.
[7] Kienzler, R., and Herrmann, G., 2007, "Nonlinear and Linearized Reciprocity Relations in Structural Configurational Mechanics," Acta Mech., DOI: 10.1007/s00707-007-0457-5.
[8] Barber, J. R., 1992, *Elasticity*, Kluwer, Dordrecht.
[9] Marguerre, K., 1962, "Elasticity, Basic Concepts," *Handbook of Engineering Mechanics*, W. Flügge, ed., McGraw-Hill, New York, Chap. 33, pp. 3–26.

A Dynamic Model of the Deformation of a Diamond Mesh Cod-End of a Trawl Net

F. G. O'Neill
FRS Marine Laboratory,
375 Victoria Road,
Aberdeen, AB11 9DB, Scotland

R. D. Neilson
Centre for Applied Dynamics Research,
School of Engineering and Physical Sciences,
University of Aberdeen,
Kings College,
Aberdeen, AB24 3UE, UK

A dynamic model of a diamond mesh cod-end subject to harmonic forcing is developed. The partial differential equations governing the displacements of the cod-end and the tension in the twine are first derived and then analyzed using the harmonic balance method by substituting a harmonic series for the dependent variables and the forcing term. A closed-form solution is derived for the case of rigid-body motion, where there is no deformation of the cod-end geometry, along with the conditions for the forcing under which this motion occurs. A pressure loading, which varies linearly over a portion of the cod-end and varies harmonically with time, is then introduced as a first representation of the loading on the cod-end that results from the pressure and acceleration forces on the catch due to surge motion of the towing vessel. The resulting sets of equations for the static and the first and second harmonic terms are solved numerically in a sequential manner, and the results presented for a number of cases. These results show that, due to the nonlinearity of the system, the oscillatory motion of the cod-end is asymmetric, and that the deformation of the net and the amplitude of oscillation increases as the region over which the forcing is applied increases. The model is the basis for a more complete coupled catch/cod-end model. [DOI: 10.1115/1.2755153]

Keywords: trawl, cod-end, dynamic model, harmonic balance, nonlinearity

1 Introduction

In recent decades, there has been increasing international concern about diminishing fish stocks. The depletion of stocks has, in the past, demonstrated both the biological and socioeconomic effects of overfishing. The collapse of the North Sea herring fishery in the 1970s resulted in a ban on all herring fishing in 1977 which was not lifted until 1983. The failure of the South American anchovy fishery and the Newfoundland cod fishery are other such situations and more recently fishery scientists have been predicting the collapse of the North Sea cod fishery [1].

Trawl nets are responsible for a large proportion of the world's catch. Depending on design, they can be operated by one or two boats and can be towed over the seabed or at any depth in midwater. As described by Galbraith et al. [2] trawls are basically funnel shaped, with their sides extended in front to form wings to guide fish into the mouth of the net (Fig. 1). Wardle [3] discusses the behavior of fish on encountering trawl fishing gear and describes how, on entering the mouth of a net, many fish will turn and swim forward, holding station, matching the speed of the net. As they become exhausted, there is a change in behavior and they turn again and seek a clear visual path back through the net to the cod-end.

The cod-end is the rearmost part of a trawl net. It is where the catch accumulates and where most fish escapes take place. Over the last 30 years, it has been the subject of intensive research, primarily, to ensure the release of juvenile target and nontarget species. The bulk of this research has been concerned with the experimental testing, at sea, of new designs of the trawl cod-end. There have also been efforts to develop predictive methods based on an understanding of the underlying physical and biological mechanism that govern fish escape from the cod-end. Herrmann [4,5] and Herrmann and O'Neill [6] present a predictive model of fish selection in the cod-end. The model these authors present requires information on the cod-end geometry, the fish behavior, the escape process, the fish population structure, and the fish morphology. The cod-end geometry is determined by the interaction of the water flow, the catch size, and the design and physical characteristics of the netting.

A number of models of netting deformation have been developed in recent years. Those of Hu et al. [7], Lee et al. [8], Takagi et al. [9], Le Dret et al. [10], Priour [11], Bessonneau and Marichal [12], and Niedzwiedz and Hopp [13] are numerical in nature and can model general three-dimensional deformations. General theories of networks formed by two families of twines can be found in Steigmann and Pipkin [14], Rivlin [15], and Kuznetsov [16,17]. A more specific model was developed by O'Neill [18], who derives and solves the steady-state differential equations governing the geometry of an axisymmetric diamond mesh cod-end. O'Neill [19,20] extends this model by accounting for netting made from different mesh shapes, twine extension, and the mesh resistance to opening that arises due to twine bending stiffness. Although the approach of O'Neill is limited to axisymmetric cod-ends, it lends itself readily to dimensional analysis, permitting the identification of significant terms. It also allows the derivation of some analytic solutions with which it is possible to validate numerical methodologies [21].

The importance of understanding the dynamic movement of the cod-end has been highlighted by O'Neill et al. [22], who investigate sea-state-induced vessel motion and fish selection in the cod-end and who demonstrate that there is a relationship between the dynamics of the cod-end and fish escape. These authors identify the following three categories of longitudinal periodic cod-end motion:

1. no deformation of the netting and no relative displacement of the catch
2. small deformation of the netting and recurring catch displacement at the free surface facing the flow
3. large (often asymmetric) deformation of the netting and considerable catch displacement

Contributed by the Applied Mechanics Division of ASME for publication in the JOURNAL OF APPLIED MECHANICS. Manuscript received November 30, 2006; final manuscript May 8, 2007; published online January 16, 2008. Review conducted by Oliver M. O'Reilly.

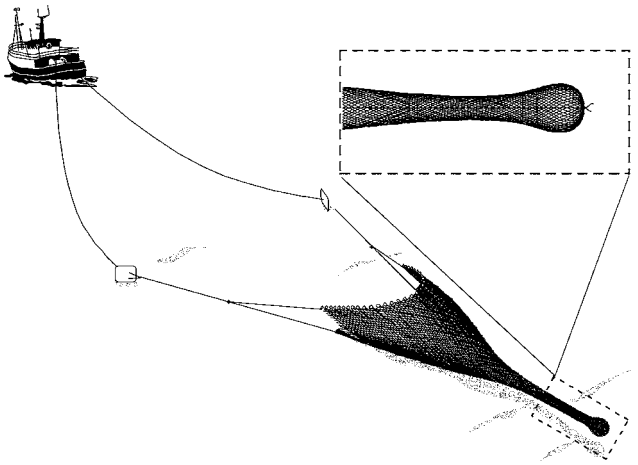

Fig. 1 A cod-end and its position on a demersal trawl

In this paper, we derive the equations governing the dynamic deformation of a trawl cod-end by considering the dynamic force balance that acts on a mesh element of the netting surface in the limit as the mesh size tends to zero. In the same way as O'Neill [18], we permit only axisymmetric deformations and assume that the netting twines are always under tension. Although these conditions are restrictive, they cover two of the three categories of motion identified in [22] above.

2 Deriving Governing Equations

Following the approach of [18], we consider a cod-end of circular cross section, N meshes around and P meshes long and of mesh size M. We restrict attention to a strip of meshes running the length of the cod-end and determine from these meshes a profile or outline of the cod-end (Fig. 2) by considering the force balance on one of these meshes in the limit as $M \to 0$ (Fig. 3). If we assume that the meshes under examination are bisected by the plane $z=0$, that the x-axis is the axis of symmetry, and that y is the distance the nodes of these meshes are from the axis of symmetry, then we can show that the force balance on a mesh element is

$$2\tau^{+}\begin{pmatrix}\cos\phi^{+}\cos\theta^{+}\\ \cos\phi^{+}\sin\theta^{+}\\ 0\end{pmatrix}-2\tau^{-}\begin{pmatrix}\cos\phi^{-}\cos\theta^{-}\\ \cos\phi^{-}\sin\theta^{-}\\ 0\end{pmatrix}-4\tau\begin{pmatrix}0\\ \sin\beta\sin\phi\\ 0\end{pmatrix}+\Delta\Sigma\begin{pmatrix}V\cos\theta-S\sin\theta\\ V\sin\theta+S\cos\theta\\ 0\end{pmatrix}=2\rho\Delta s\frac{\partial^2}{\partial t^2}\begin{pmatrix}x\\ y\\ 0\end{pmatrix} \tag{1}$$

where τ is the tension in a mesh bar, ϕ is half the angle between two adjacent mesh bars, θ is the angle the plane (they define) makes with the plane $y=0$, $\beta=\pi/N$, is half the angle made by the intersection of the radial lines through two nodes of a mesh either side of the plane $z=0$, $\Delta\Sigma$ is the area of a mesh element and equal to $2\pi yM\cos\phi/N$, ρ is the density per unit length of the netting twine, V and S are the tangential and normal components of the surface force acting per unit area of netting, and Δs is the incremental distance along the netting twine. Thus, s is the distance along the twine and follows a zigzag path, and accordingly Δs for a mesh element is equal to M.

On defining $T=2N\tau$, dividing the above expression by Δs and taking the limit as $\Delta s\to 0$, $M\to 0$, $N\to\infty$, and NM remains constant, the x- and y-component equations of the force balance become

$$\frac{\partial(T\cos\phi\cos\theta)}{\partial s}+2\pi y(V\cos\theta-S\sin\theta)\cos\phi=2N\rho\frac{\partial^2 x}{\partial t^2} \tag{2}$$

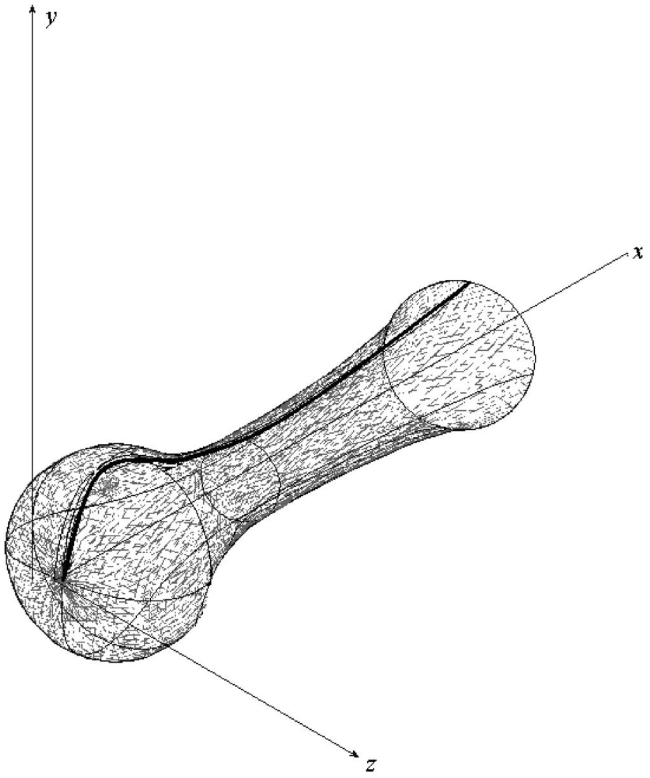

Fig. 2 Coordinate system and the strip of meshes under consideration

$$\frac{\partial(T\cos\phi\sin\theta)}{\partial s}-T\frac{\sin^2\phi}{y}+2\pi y(V\sin\theta+S\cos\theta)\cos\phi=2N\rho\frac{\partial^2 y}{\partial t^2} \tag{3}$$

We also have the following relationships between x, y, and s:

$$\cos^2\phi=1-\frac{4\pi^2y^2}{N^2M^2}=\left(\frac{\partial x}{\partial s}\right)^2+\left(\frac{\partial y}{\partial s}\right)^2 \tag{4}$$

which, on differentiating, yields

$$-\frac{4\pi^2y}{N^2M^2}\frac{\partial y}{\partial s}=\frac{\partial^2x}{\partial s^2}\frac{\partial x}{\partial s}+\frac{\partial^2y}{\partial s^2}\frac{\partial y}{\partial s} \tag{5}$$

Because

$$\tan\theta=\frac{\partial y}{\partial x}$$

we have

$$\cos\phi\cos\theta=\frac{\partial x}{\partial s}\quad\cos\phi\sin\theta=\frac{\partial y}{\partial s}\quad\frac{\sin^2\phi}{y}=\frac{4\pi^2y}{N^2M^2}$$

Substituting these identities into Eqs. (2) and (3) gives

$$T\frac{\partial^2x}{\partial s^2}+\frac{\partial T}{\partial s}\frac{\partial x}{\partial s}+2\pi y\frac{\partial x}{\partial s}V-2\pi y\frac{\partial y}{\partial s}S=2N\rho\frac{\partial^2x}{\partial t^2} \tag{6}$$

$$T\frac{\partial^2y}{\partial s^2}+\frac{\partial T}{\partial s}\frac{\partial y}{\partial s}-T\frac{4\pi^2y}{N^2M^2}+2\pi y\frac{\partial y}{\partial s}V+2\pi y\frac{\partial x}{\partial s}S=2N\rho\frac{\partial^2y}{\partial t^2} \tag{7}$$

which when inserted into (5) gives

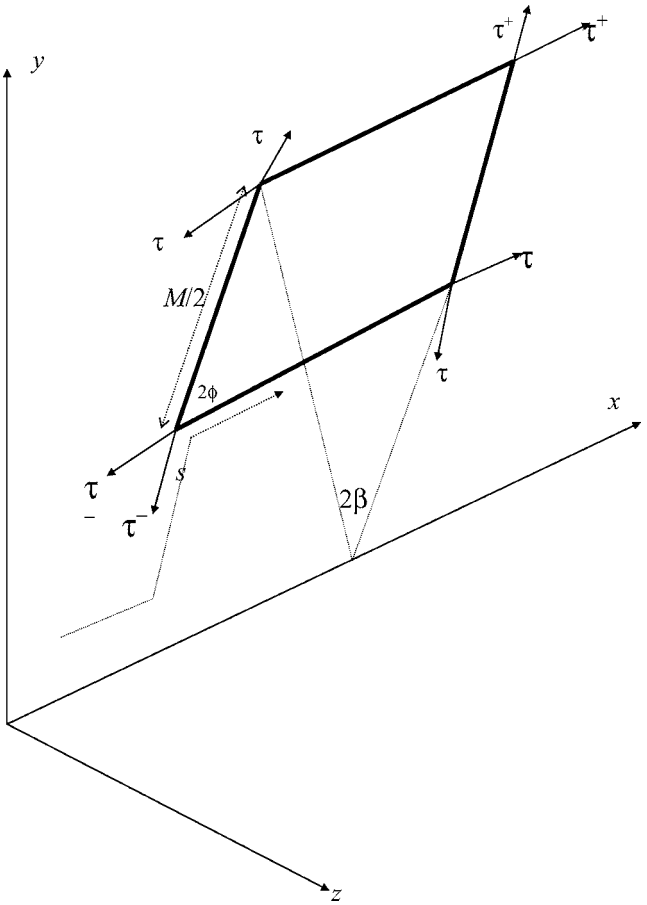

Fig. 3 Coordinate system and the tensile forces acting on one of the meshes on the strip under consideration

$$\frac{\partial T}{\partial s} - T\frac{8\pi^2 y}{N^2M^2 - 4\pi^2y^2}\frac{\partial y}{\partial s} + 2\pi y V(s,t) = \frac{2\rho N^3M^2}{N^2M^2 - 4\pi^2y^2}\left(\frac{\partial x}{\partial s}\frac{\partial^2 x}{\partial t^2} + \frac{\partial y}{\partial s}\frac{\partial^2 y}{\partial t^2}\right) \tag{8}$$

Grouping Eqs. (4), (7), and (8), we can define the following set of equations:

$$\frac{\partial T}{\partial s} - T\frac{8\pi^2 y}{N^2M^2 - 4\pi^2y^2}\frac{\partial y}{\partial s} + 2\pi y V(s,t) = \frac{2\rho N^3M^2}{N^2M^2 - 4\pi^2y^2}\left(\frac{\partial x}{\partial s}\frac{\partial^2 x}{\partial t^2} + \frac{\partial y}{\partial s}\frac{\partial^2 y}{\partial t^2}\right) \tag{9}$$

$$T\frac{\partial^2 y}{\partial s^2} + \frac{\partial T}{\partial s}\frac{\partial y}{\partial s} - T\frac{4\pi^2 y}{N^2M^2} + 2\pi y\frac{\partial y}{\partial s}V + 2\pi y\frac{\partial x}{\partial s}S = 2N\rho\frac{\partial^2 y}{\partial t^2} \tag{10}$$

$$\left(\frac{\partial x}{\partial s}\right)^2 + \left(\frac{\partial y}{\partial s}\right)^2 + \frac{4\pi^2y^2}{N^2M^2} = 1 \tag{11}$$

which govern the dynamic motion of a diamond mesh cod-end for given $V(s,t)$ and $S(s,t)$ and four prescribed boundary conditions.

3 Scaling and Nondimensionalistion

If we introduce the following scalings:

$$y = NMy', \quad x = NMx', \quad s = NMs', \quad S = S_0S', \quad V = S_0V', \quad T = N^2M^2S_0T', \quad t = \frac{t'}{\omega}$$

where S_0 is representative of the forces acting per unit area on the cod-end netting and ω is the fundamental angular frequency of the forcing variable, we get

$$(1 - 4\pi^2y^2)\frac{\partial T}{\partial s} - T8\pi^2 y\frac{\partial y}{\partial s} + 2\pi y(1 - 4\pi^2y^2)V(s,t) = \frac{\omega^2}{\omega_n^2}\left(\frac{\partial x}{\partial s}\frac{\partial^2 x}{\partial t^2} + \frac{\partial y}{\partial s}\frac{\partial^2 y}{\partial t^2}\right) \tag{12}$$

$$T\frac{\partial^2 y}{\partial s^2} + \frac{\partial T}{\partial s}\frac{\partial y}{\partial s} - T4\pi^2 y + 2\pi y\frac{\partial y}{\partial s}V + 2\pi y\frac{\partial x}{\partial s}S = \frac{\omega^2}{\omega_n^2}\frac{\partial^2 y}{\partial t^2} \tag{13}$$

$$\left(\frac{\partial x}{\partial s}\right)^2 + \left(\frac{\partial y}{\partial s}\right)^2 + 4\pi^2y^2 = 1 \tag{14}$$

where, for clarity, the dashed subscripts are suppressed and where $\omega_n = \sqrt{S_0/2\rho N}$ is representative of the natural angular frequency of the system.

Typically, $S_0 \sim 0.5c_d\rho_w U^2 \sim 1250\ \mathrm{Nm}^{-2}$ [23], $\rho \sim 0.02\ \mathrm{kgm}^{-1}$, and $N \sim 100$, giving a natural angular period ~ 0.05 s. Furthermore, it is established in [22] that, by comparing the average period of longitudinal cod-end pulsing to the most important cyclic components of the tension in the trawl warps and of the linear accelerations of the fishing vessel, the pulsing of the cod-end is a response to sea-state-induced vessel motion. Hence, the period of the forcing function will generally be >5 s, implying that the term $\omega^2/\omega_n^2 \sim 0.0001$. Accordingly, in most situations we can neglect the inertial terms associated with the acceleration of the netting. The inertia of the catch will however be important, and although it is not explicit in the present formulation, it (and also damping terms) can be introduced via the surface forces per unit area, V and S.

4 Periodic Solutions

Given that the cod-end dynamics are driven by sea-state-induced vessel motion, we look for periodic solutions of the following form:

$$x = \sum_k x_k(s)e^{ikt}, \quad y = \sum_k y_k(s)e^{ikt}, \quad T = \sum_k T_k(s)e^{ikt}$$

where the x_k, y_k, and T_k are all complex functions of s, $k = 0, 1 \ldots \infty$ and where we assume we can express the surface forces as

$$S = \sum_k S_k(s)e^{ikt}, \quad V = \sum_k V_k(s)e^{ikt}$$

The governing equations then become

$$\sum_k \frac{dT_k}{ds}e^{ikt} - 4\pi^2\sum_{klm}\left(y_ky_l\frac{dT_m}{ds} + 2y_kT_l\frac{dy_m}{ds}\right)e^{i(k+l+m)t} + 2\pi\sum_{kl} y_kV_le^{i(k+l)t} - 8\pi^3\sum_{klmp} y_ky_ly_mV_pe^{i(k+l+m+p)t} = -\frac{\omega^2}{\omega_n^2}\sum_{kl} k^2\left(x_k\frac{dx_l}{ds} + y_k\frac{dy_l}{ds}\right)e^{i(k+l)t}$$

$$\sum_{kl}\left(T_k\frac{d^2y_l}{ds^2}+\frac{dT_k}{ds}\frac{dy_l}{ds}-4\pi^2T_ky_l\right)e^{i(k+l)t}+2\pi\sum_{klm}\left(y_k\frac{dx_l}{ds}S_m+y_k\frac{dy_l}{ds}V_m\right)e^{i(k+l+m)t}=-\frac{\omega^2}{\omega_n^2}\sum_k k^2y_ke^{ikt}$$

$$\sum_{kl}\left(\frac{dx_k}{ds}\frac{dx_l}{ds}+\frac{dy_k}{ds}\frac{dy_l}{ds}+4\pi^2y_ky_l\right)e^{i(k+l)t}=1$$

where the summations are single, double, etc., according to the number of subscripts under the summation sign and where the summation range is from 0 to ∞.

We can choose the relevant harmonic components by identifying the products whose subscripts sum to 0, 1, 2, etc. This is effectively a harmonic balance procedure. We present the first three sets of equations here.

1. The equations governing the zero harmonic solutions, i.e., the static case, are

$\underline{k+l+m+p=0}$

$$\frac{dT_0}{ds}-T_0\frac{8\pi^2y_0}{1-4\pi^2y_0^2}\frac{dy_0}{ds}+2\pi y_0V_0=0$$

$$T_0\frac{d^2y_0}{ds^2}+\frac{dT_0}{ds}\frac{dy_0}{ds}-T_04\pi^2y_0+2\pi y_0S_0\frac{dx_0}{ds}+2\pi y_0V_0\frac{dy_0}{ds}=0$$

$$\left(\frac{dx_0}{ds}\right)^2+\left(\frac{dy_0}{ds}\right)^2+4\pi^2y_0^2=1$$

These can be shown to be identical to the steady-state equations of [18], where x_0, y_0, and T_0 are the corresponding steady-state solutions.

2. The equations governing the first harmonic solutions are

$\underline{k+l+m+p=1}$

$$\frac{dT_1}{ds}-4\pi^2\left(2y_0y_1\frac{dT_0}{ds}+y_0^2\frac{dT_1}{ds}+2y_0T_0\frac{dy_1}{ds}+2y_0T_1\frac{dy_0}{ds}+2y_1T_0\frac{dy_0}{ds}\right)+2\pi(y_0V_1+y_1V_0)-8\pi^3(y_0^3V_1+3y_0^2y_1V_0)=-\frac{\omega^2}{\omega_n^2}\left(x_0\frac{dx_1}{ds}+x_1\frac{dx_0}{ds}+y_0\frac{dy_1}{ds}+y_1\frac{dy_0}{ds}\right)$$

$$T_0\frac{d^2y_1}{ds^2}+T_1\frac{d^2y_0}{ds^2}+\frac{dT_0}{ds}\frac{dy_1}{ds}+\frac{dT_1}{ds}\frac{dy_0}{ds}-T_04\pi^2y_1-T_14\pi^2y_0+2\pi y_0S_0\frac{dx_1}{ds}+2\pi y_0S_1\frac{dx_0}{ds}+2\pi y_1S_0\frac{dx_0}{ds}+2\pi y_0V_0\frac{dy_1}{ds}+2\pi y_0V_1\frac{dy_0}{ds}+2\pi y_1V_0\frac{dy_0}{ds}=-\frac{\omega^2}{\omega_n^2}y_1$$

$$\frac{dx_0}{ds}\frac{dx_1}{ds}+\frac{dy_0}{ds}\frac{dy_1}{ds}+4\pi^2y_0y_1=0$$

3. And, those governing the second harmonics are

$\underline{k+l+m+p=2}$

$$\frac{dT_2}{ds}-4\pi^2\left(y_0^2\frac{dT_2}{ds}+2y_0y_1\frac{dT_1}{ds}+2y_0y_2\frac{dT_0}{ds}+y_1^2\frac{dT_0}{ds}\right)-8\pi^2\left(y_0T_0\frac{dy_2}{ds}+y_0T_2\frac{dy_0}{ds}+y_2T_0\frac{dy_0}{ds}+y_1T_1\frac{dy_0}{ds}+y_1T_0\frac{dy_1}{ds}+y_0T_1\frac{dy_1}{ds}\right)+2\pi(V_0y_2+V_1y_1+V_2y_0)-8\pi^3(y_0^3V_2+3y_0^2y_2V_0+3y_0^2y_1V_1+3y_0y_1^2V_0)=-4\frac{\omega^2}{\omega_n^2}\left(x_0\frac{dx_2}{ds}+x_1\frac{dx_1}{ds}+x_2\frac{dx_0}{ds}+y_0\frac{dy_2}{ds}+y_1\frac{dy_1}{ds}+y_2\frac{dy_0}{ds}\right)$$

$$T_0\frac{d^2y_2}{ds^2}+T_1\frac{d^2y_1}{ds^2}+T_2\frac{d^2y_0}{ds^2}+\frac{dT_0}{ds}\frac{dy_2}{ds}+\frac{dT_1}{ds}\frac{dy_1}{ds}+\frac{dT_2}{ds}\frac{dy_0}{ds}-4\pi^2(T_0y_2+T_1y_1+T_2y_0)+2\pi\left(y_0S_1\frac{dx_1}{ds}+y_1S_1\frac{dx_0}{ds}+y_1S_0\frac{dx_1}{ds}+y_0S_0\frac{dx_2}{ds}+y_0S_2\frac{dx_0}{ds}+y_2S_0\frac{dx_0}{ds}+y_0V_1\frac{dy_1}{ds}+y_1V_1\frac{dy_0}{ds}+y_1V_0\frac{dy_1}{ds}+y_0V_0\frac{dy_2}{ds}+y_0V_2\frac{dy_0}{ds}+y_2V_0\frac{dy_0}{ds}\right)=-\frac{4\omega^2}{\omega_n^2}y_2$$

$$\left(\frac{dx_1}{ds}\right)^2+2\frac{dx_0}{ds}\frac{dx_2}{ds}+\left(\frac{dy_1}{ds}\right)^2+2\frac{dy_0}{ds}\frac{dy_2}{ds}+4\pi^2(y_1^2+2y_0y_2)=0$$

Category 1 Motion. The first category of longitudinal periodic cod-end motion identified in [22] had no deformation of the netting and no relative displacement of the catch. It was, in effect, a periodic rigid-body motion along the x-axis. A general periodic solution to this problem, for the case where $\omega^2/\omega_n^2\ll 1$, has the form

$$x=x_0(s)+\sum_{k=1}^{\infty}x_ke^{ikt}\quad y=y_0(s),\quad T=\sum_k T_k(s)e^{ikt}$$

where the x_k are constant for $k>0$, the 0 subscript denotes the steady-state solution. Substituting these expressions into the equations governing the first and second harmonic components gives

$\underline{k+l+m+p=1}$

$$\frac{dT_1}{ds}-T_1\frac{8\pi^2y_0}{1-4\pi^2y_0^2}\frac{dy_0}{ds}+2\pi y_0V_1=0$$

$$T_1\frac{d^2y_0}{ds^2}+\frac{dT_1}{ds}\frac{dy_0}{ds}-T_14\pi^2y_0+2\pi y_0S_1\frac{dx_0}{ds}+2\pi y_0V_1\frac{dy_0}{ds}=0$$

and

$\underline{k+l+m+p=2}$

$$\frac{dT_2}{ds}-T_2\frac{8\pi^2y_0}{1-4\pi^2y_0^2}\frac{dy_0}{ds}+2\pi y_0V_2=0$$

$$T_2\frac{d^2y_0}{ds^2}+\frac{dT_2}{ds}\frac{dy_0}{ds}-T_24\pi^2y_0+2\pi y_0S_2\frac{dx_0}{ds}+2\pi y_0V_2\frac{dy_0}{ds}=0$$

In effect, these expressions are the steady-state equations when the applied forces are V_1 and S_1 and V_2 and S_2, respectively. They will only have the same y_0 solution when the expressions for T_1 and T_2, V_1 and V_2 and S_1 and S_2 are identical to those for T_0, V_0,

and S_0, respectively to within a multiplicative constant.

Thus, these results indicate that for category 1 type motion the applied surface forces must be such that

$$S = S_0(s)\left(1 + \sum_{k=1}^{\infty} \lambda_k e^{ikt}\right), \quad V = V_0(s)\left(1 + \sum_{k=1}^{\infty} \lambda_k e^{ikt}\right)$$

The resulting twine tension will be

$$T = T_0(s)\left(1 + \sum_{k=1}^{\infty} \lambda_k e^{ikt}\right)$$

Indeed, we can easily show that $x(s,t)=x_0(s)+f(t)$, $y(s,t)=y_0(s)$ and $T(s,t)=T_0(s)g(t)$ are general solutions of Eqs. (12)–(14) when $V(s,t)=V_0(s)g(t)$, $S(s,t)=S_0(s)g(t)$, and $\omega^2/\omega_n^2 \ll 1$ and where the exact form of f and g are determined by the forcing and/or boundary conditions (the case where the pressure forces are not dependent on s is a particular example of this type of motion).

Category 2 Motion. The second category of motion identified in [22] had small deformation of the netting and recurring catch displacement at the free surface facing the flow. A complete analysis of this problem would require the inclusion of the inertial effect of the catch and is beyond the scope of this paper. Instead, we investigate the cod-end dynamics that are associated with periodically varying surface forces. O'Neill and O'Donoghue [24] demonstrate that the most important hydrodynamic forces acting on the cod-end netting are the pressure forces acting in the region of the catch, and hence, we consider the case where $\omega^2/\omega_n^2 \ll 1$, $V(s,t)=0$ and specify $S(s,t)$ in the region of the catch and set it to zero elsewhere.

The appropriate form of the harmonic sets of equations are

$\underline{k+l+m+p=0}$

$$\frac{dT_0}{ds} - T_0 \frac{8\pi^2 y_0}{1-4\pi^2 y_0^2}\frac{dy_0}{ds} = 0$$

$$T_0\frac{d^2y_0}{ds^2} + \frac{dT_0}{ds}\frac{dy_0}{ds} - T_0 4\pi^2 y_0 + 2\pi y_0 S_0 \frac{dx_0}{ds} = 0$$

$$\left(\frac{dx_0}{ds}\right)^2 + \left(\frac{dy_0}{ds}\right)^2 + 4\pi^2 y_0^2 = 1$$

$\underline{k+l+m+p=1}$

$$\frac{dT_1}{ds} - 4\pi^2\left(2y_0y_1\frac{dT_0}{ds} + y_0^2\frac{dT_1}{ds} + 2y_0T_0\frac{dy_1}{ds} + 2y_0T_1\frac{dy_0}{ds} + 2y_1T_0\frac{dy_0}{ds}\right) = 0$$

$$T_0\frac{d^2y_1}{ds^2} + T_1\frac{d^2y_0}{ds^2} + \frac{dT_0}{ds}\frac{dy_1}{ds} + \frac{dT_1}{ds}\frac{dy_0}{ds} - T_0 4\pi^2 y_1 - T_1 4\pi^2 y_0 + 2\pi y_0 S_0\frac{dx_1}{ds} + 2\pi y_0 S_1\frac{dx_0}{ds} + 2\pi y_1 S_0\frac{dx_0}{ds} = 0$$

$$\frac{dx_0}{ds}\frac{dx_1}{ds} + \frac{dy_0}{ds}\frac{dy_1}{ds} + 4\pi^2 y_0 y_1 = 0$$

and

$\underline{k+l+m+p=2}$

$$\frac{dT_2}{ds} - 4\pi^2\left(y_0^2\frac{dT_2}{ds} + 2y_0y_1\frac{dT_1}{ds} + 2y_0y_2\frac{dT_0}{ds} + y_1^2\frac{dT_0}{ds}\right) - 8\pi^2\left(y_0T_0\frac{dy_2}{ds} + y_0T_2\frac{dy_0}{ds} + y_2T_0\frac{dy_0}{ds} + y_1T_1\frac{dy_0}{ds} + y_1T_0\frac{dy_1}{ds} + y_0T_1\frac{dy_1}{ds}\right) = 0$$

$$T_0\frac{d^2y_2}{ds^2} + T_1\frac{d^2y_1}{ds^2} + T_2\frac{d^2y_0}{ds^2} + \frac{dT_0}{ds}\frac{dy_2}{ds} + \frac{dT_1}{ds}\frac{dy_1}{ds} + \frac{dT_2}{ds}\frac{dy_0}{ds} - 4\pi^2(T_0y_2 + T_1y_1 + T_2y_0) + 2\pi\left(y_0S_1\frac{dx_1}{ds} + y_1S_1\frac{dx_0}{ds} + y_1S_0\frac{dx_1}{ds} + y_0S_0\frac{dx_2}{ds} + y_0S_2\frac{dx_0}{ds} + y_2S_0\frac{dx_0}{ds}\right) = 0$$

$$\left(\frac{dx_1}{ds}\right)^2 + 2\frac{dx_0}{ds}\frac{dx_2}{ds} + \left(\frac{dy_1}{ds}\right)^2 + 2\frac{dy_0}{ds}\frac{dy_2}{ds} + 4\pi^2(y_1^2 + 2y_0y_2) = 0$$

Although these equations were generated by a harmonic balance approach, the form of the equations allows solution in a manner similar to a perturbation expansion, namely, solution of the static (zero-harmonic) problem and substitution of this into the equations for the first harmonic, followed by solution of this set of equations and substitution into the next and so on.

A FORTRAN program was written to solve the sets of equations. First, an iterative finite difference scheme using central differences solved the steady state equations. Then the first and second harmonic equations were solved successively using the NAG routine D02HAF, which uses a Runge–Kutta–Merson method and a Newton iteration in a shooting and matching technique. In Fig. 4, we present the results for the deformed shape of the cod-end for the case, where

$$S(s,t) = \begin{cases} 1 + 0.25\dfrac{s}{s_c}e^{i\omega t} & s \le s_c \\ 0 & s > s_c \end{cases}$$

for three different values of s_c of 0.2, 0.4, and 0.6. This loading can be viewed as a first approximation to the pressure and inertial loading applied to the cod-end by the catch during surge motion of the towing vessel. Boundary conditions of

$$x(s)|_{s=0} = 0$$

$$y(s)|_{s=0} = 0$$

$$\left.\frac{dy(s)}{ds}\right|_{s=0} = 1$$

$$y(s)|_{s=1} = 0.05$$

were used for the analysis. The first three boundary conditions provide location of the net in space and a constraint of continuity of slope across the axis of symmetry of the cod-end. The fourth boundary condition places a constraint on the opening of the neck of the cod-end ensuring that it remains open at a fixed radius. Although these boundary conditions are used conveniently for the solution, the results are plotted in terms of the motion of the cod-end relative to the open end of the cod-end, which is assumed fixed in the axial direction.

5 Results

The deformed shape of the cod-end is plotted for the static case and for the maximum and minimum openings of the mesh of the cod-end at the face of the catch, s_c in Fig. 4.

The results show a clear trend of increased deformed region of the cod-end, in both the axial and radial directions, with greater s_c.

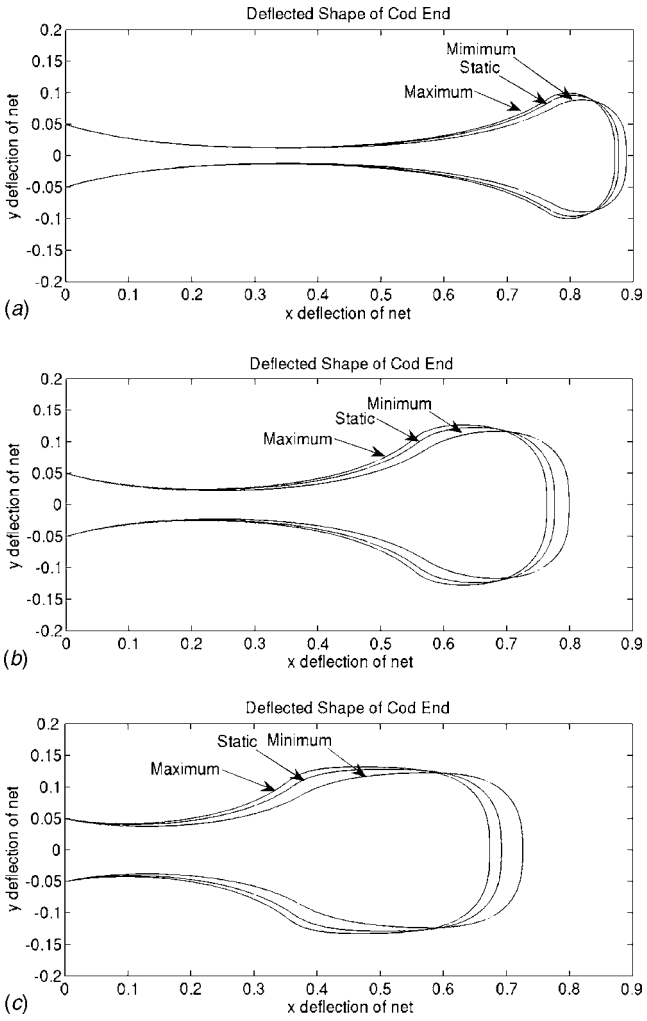

Fig. 4 Deflected shape of the cod-end for (*a*) s_c=0.2, (*b*) s_c =0.4, and (*c*) s_c=0.6

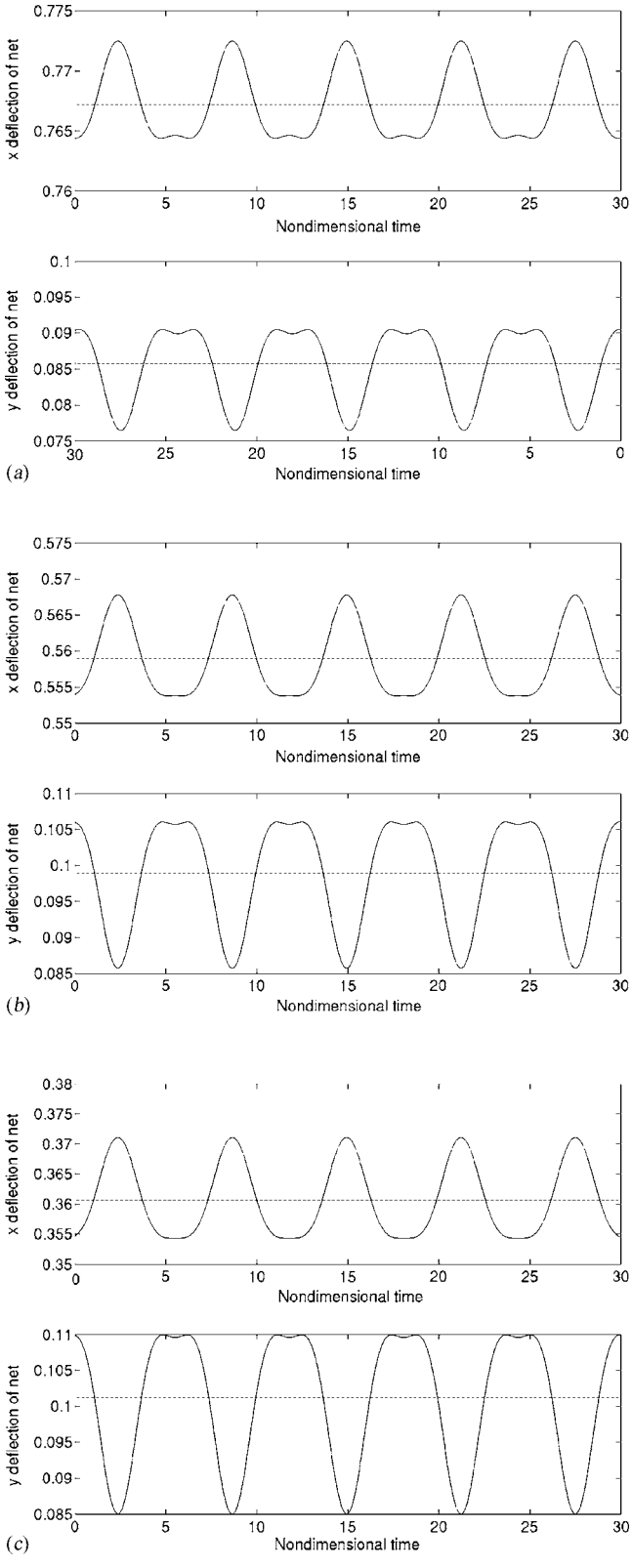

Fig. 5 Time history of the cod-end at the catch face for (*a*) s_c=0.2, (*b*) s_c=0.4, and (*c*) s_c=0.6

A trend of increasing diameter of the narrowest portion of the neck of the cod-end, with increasing extent of the catch, is also apparent. For the case of s_c=0.6, the cod-end has a section of near-constant radial deflection extending over ~20% of its length in the static case. It is noteworthy that the oscillatory motion is not symmetric around the static deformed shape. This is most apparent in the axial deflection of the cod-end. This asymmetry is a result of the second harmonic term, which arises in the analysis from the nonlinearity present in the system, and, in particular, the products of the first harmonic terms, which appear in the set of equations for "$k+l+m+p=2$." This asymmetry is also very apparent from the time histories of the x and y motions plotted for the face of the catch. These are presented in Figs. 5(a)–5(c) and show that the cod-end spends an appreciable part of the cycle of motion (~60%) at the larger deformations in the y directions. Referring to Fig. 6, which depicts the spatial orbits and the geometry of the mesh at the catch face, it is clear that this implies that the mesh is at its most open (in the lateral direction) for a substantial portion of the motion.

6 Discussion

The results presented are for a simplified case where the effect of the catch has been modeled as a pressure loading that varies linearly over a portion of the cod-end and varies harmonically with time. Although the analysis has been limited to the first two harmonic terms, it is possible to extend the analysis to higher-order harmonics. Because the sets of equations are solved sequentially, the second harmonic term will remain as it is and the solution for the third harmonic will introduce a component that is again symmetric about the static deformed shape, and thus, the asymmetry of the net motion (which was noted earlier) will not

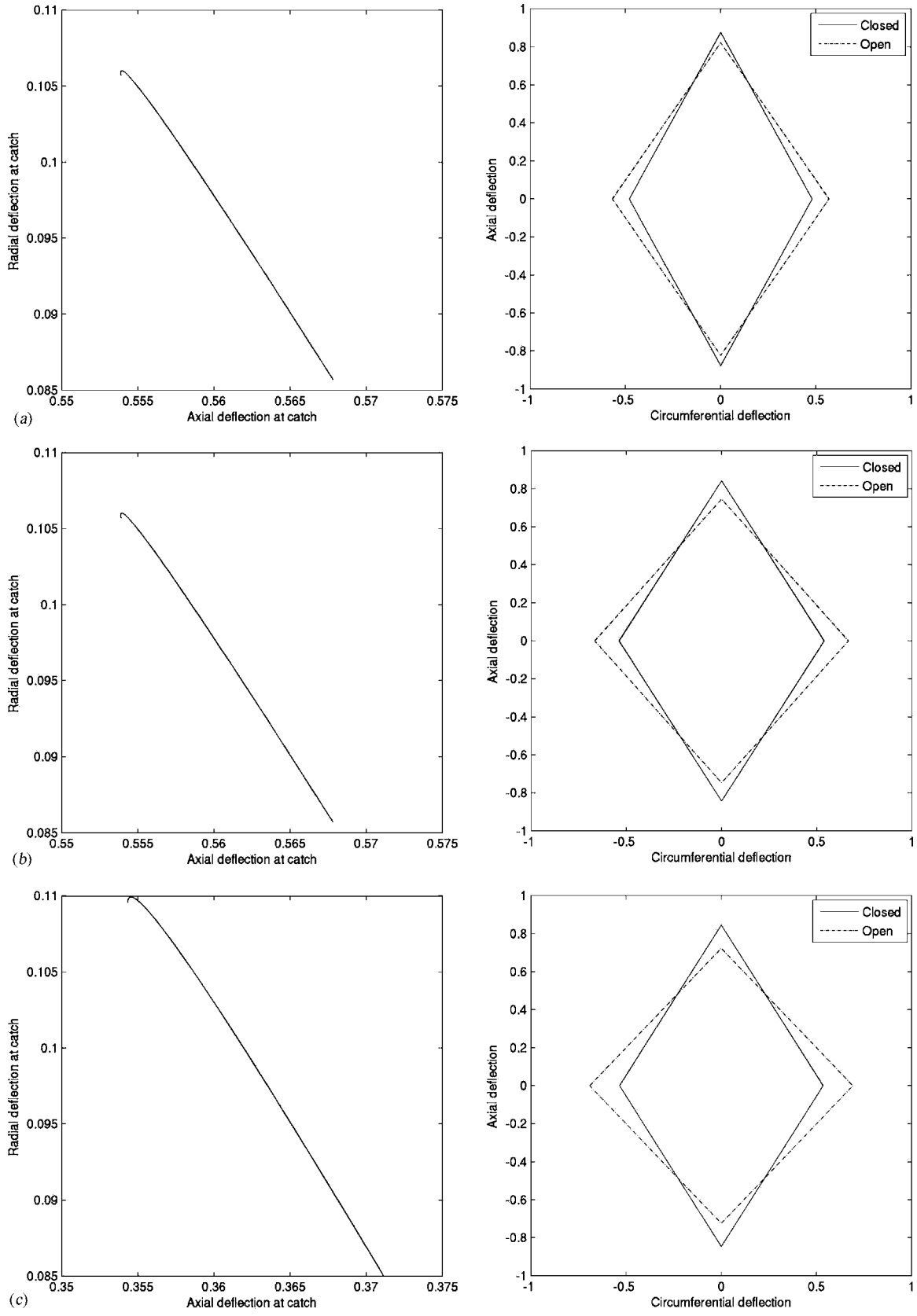

Fig. 6 Orbits and mesh opening at the catch face for (*a*) s_c=0.2, (*b*) s_c=0.4, and (*c*) s_c=0.6

increase further. Changes in the asymmetry will occur by increasing the analysis to the fourth order. Typically in such expansions, the size of the terms reduces with higher order.

The case examined here is very useful as it confirms the existence of the type 1 and 2 motions proposed in [22] and demonstrates that they can be elicited from the system. In [22], a direct

link is established between sea-state-induced vessel motion and cod-end selection. They identify a number of hydrodynamic and behavioral mechanisms, which may explain their results. Here, we have shown that by applying a harmonic load to the netting the lateral mesh opening ahead of the catch is greater than that of the corresponding static case for ~60% of the time (Fig. 5), raising the possibility of a mechanical explanation for the results of [22].

In reality, the loading on the netting is much more complex than the description we have used here. This arises from the interaction of the catch dynamics, the hydrodynamics, and the netting dynamics and will include terms to represent the catch inertia and damping terms. If these effects are included, then the effective natural frequency of the coupled catch/cod-end system will be lower and the assumption that $\omega^2/\omega_n^2 \ll 1$ may no longer hold. Consequently, other nonlinear effects (e.g., multiple coexisting solutions) may result and, although the constraint on symmetry of the cod-end on which the current model is based precludes spatial chaos (type 3 motion as described in [22]), temporal chaotic motion may exist. This will be a topic for further research.

7 Conclusions

A dynamic model of a diamond mesh cod-end subjected to harmonic forcing has been presented. By solving the resulting system of equations by the harmonic balance method, it has been shown that:

- The cod-end can exhibit rigid body motion (type 1 motion as described by in [22]) under harmonic excitation due to surge motion if the forces on the cod-end are proportional to the static loading and vary harmonically.
- The cod-end can exhibit oscillatory deformations (type 2 motion as described in [22]) under harmonic excitation due to surge motion where the pressure on the cod-end varies linearly over a portion of the cod-end and varies harmonically with time. This is a first approximation to the inertial and drag loading of the catch.
- Due to the nonlinearities in the governing equations, even harmonic terms arise in the solution and introduce asymmetry in the motion of the deformed cod-end even when the excitation is simple harmonic.
- With increasing region over which the forcing is applied, the amplitude of the oscillation increases.

The work forms the basis for a more complete model of the cod-end, which includes the inertia of the catch and consequently may introduce further nonlinear phenomena for example multiple coexisting solutions and potentially chaotic motion.

Nomenclature

i = $\sqrt{-1}$
k = summation index
l = summation index
m = summation index
M = mesh size
N = number of meshes around the cod-end
p = summation index
P = number of meshes along the cod-end
s = coordinate along the netting twine
S = normal component of the surface force acting per unit area of netting
s_c = extent of the pressure loading along the cod-end
S_k = shape function of the kth harmonic of the normal component of the surface force acting per unit area of netting
t = time
T = tension in the cod-end
T_k = shape function of the kth harmonic of the tension in the cod-end
V = tangential component of the surface force acting per unit area of netting
V_k = shape function of the kth harmonic of the tangential component of the surface force acting per unit area of netting
x = coordinate
x_k = shape function of the kth harmonic of motion in the x direction
y = coordinate
y_k = shape function of the kth harmonic of motion in the y direction
β = half the angle made by the intersection of the radial lines through two nodes of a mesh either side of the plane $z=0$
$\Delta\Sigma$ = area of a mesh element
Δs = incremental distance along the netting twine
ϕ = half the angle between two adjacent mesh bars
ρ = density per unit length of the netting twine
θ = angle the plane two adjacent mesh bars define makes with the plane $y=0$
τ = tension in a mesh bar

References

[1] Cook, R. M., Sinclair, A., and Stefansson, G., 1997, "Potential Collapse of North Sea Cod Stocks," Nature (London), **385**, pp. 521–522.
[2] Galbraith, R. D., Rice, A., and Strange, E. S., 2004, "An Introduction to Commercial Fishing Gear and Methods Used in Scotland," Scottish Fisheries Information Pamphlet No. 25.
[3] Wardle, C. S., 1986, "Fish Behaviour and Fishing Gear," *The Behaviour of Teleost Fishes*, Pritcher, T. J. ed., Croom Helm, London, pp. 463–495.
[4] Herrmann, B., 2005, "Effect of Catch Size and Shape on the Selectivity of Diamond Mesh Cod-Ends—I. Model Development," Fish. Res., **71**, pp. 1–13.
[5] Herrmann, B., 2005, "Effect of Catch Size and Shape on the Selectivity of Diamond Mesh Cod-Ends—II. Theoretical Study of Haddock Selection," Fish. Res., **71**, pp. 15–26.
[6] Herrmann, B., and O'Neill, F. G., 2006, "Theoretical Study of the Influence of Twine Thickness on Haddock Selectivity in Diamond Mesh Cod-Ends," Fish. Res., **80**, pp. 221–229.
[7] Hu, F., Shiode, D., Wan, R., and Tokai, T., 2006, "Accuracy Evaluation of Numerical Simulation of Mid-Water Trawl Nets," *Contributions on the Theory of Fishing Gears and Related Marine Systems*, Lee, Chun-Woo, ed., Busan, Korea, Vol. 4.
[8] Lee, C-W., Lee, J-H., Cha, B-J., Kim, H-Y., and Lee, J-H., 2005, "Physical Modeling for Underwater Flexible Systems Dynamic Simulation," Ocean Eng., **32**, pp. 331–347.
[9] Takagi, T., Shimizu, T., Suzuki, K., Hiraishi, T., and Katsutaro, Y., 2004, "Validity and Layout of 'NaLa': A Net Configuration and Loading Analysis System," Fish. Res., **66**, pp. 235–243.
[10] Le Dret, H., Priour, D., Lewandowski, R., and Chagneau, F., 2004, "Numerical Simulation of a Cod End Net—Part 1: Equilibrium in a Uniform Flow," J. Elast., **76**(2), pp. 139–162.
[11] Priour, D., 1999, "Calculation of Net Shapes by the Finite Element Method With Triangular Elements," Commun. Numer. Methods Eng., **15**(10), pp. 755–763.
[12] Bessonneau, J. S., and Marichal, D., 1998, "Study of the Dynamics of Submerged Supple Nets," Ocean Eng., **27**(7), pp. 563–583.
[13] Niedzwiedz, G., and Hopp, M., 1998, "Rope and Net Calculations Applied to Problems in Marine Engineering and Fisheries Research," Archive of Fishery and Marine Research, **46**, pp. 125–138.
[14] Steigmann, D. J., and Pipkin, A. C., 1991, "Equilibrium of Elastic Nets," Philos. Trans. R. Soc. London, Ser. A, **335**, pp. 419–454.
[15] Rivlin, R. S., 1959, "The Deformation of a Membrane Formed by Inextensible Cords," Arch. Ration. Mech. Anal., **2**, pp. 447–476.
[16] Kuznetsov, E. N., 1986, "Kinetoelastostatics of Axisymmetric Nets," ASME J. Appl. Mech., **53**, pp. 891–896.
[17] Kuznetsov, E. N., 1991, *Underconstrained Structural Systems*, Springer-Verlag, New York.
[18] O'Neill, F. G., 1997, "Differential Equations Governing the Geometry of a Diamond Mesh Cod-End of a Trawl Net," ASME J. Appl. Mech., **64**(7), pp. 7–14.
[19] O'Neill, F. G., 1999, "Axissymmetrical Trawl Cod-Ends Made From Netting of Generalized Mesh Shape," IMA J. Appl. Math., **62**, pp. 245–262.

[20] O'Neill, F. G., 2004, "The Influence of Bending Stiffness on the Deformation of Axisymmetric Networks," 23rd International Conference on Offshore Mechanics and Artic Engineering.
[21] O'Neill, F. G., 1998, "Mathematical Model of Trawl Cod-End Geometry," Ph.D. thesis, University of Aberdeen, Scotland.
[22] O'Neill, F. G., McKay, S., Ward, J. N., Strickland, A., Kynoch, R. J., and Zuur, A., 2003, "An Investigation of the Relationship Between Sea State Induced Vessel Motion and Cod-End Selection," Fish. Res., **60**, pp. 107–130.
[23] O'Neill, F. G., Knudsen, L. H., Wileman, D. A., and McKay, S. J., 2005, "Cod-End Drag as a Function of Catch Size and Towing Speed," Fish. Res., **72**, pp. 163–171.
[24] O'Neill, F. G., and O'Donoghue, T., 1997, "The Fluid Dynamic Loading on Catch and the Geometry of Trawl Cod-Ends," Proc. R. Soc. London, Ser. A, **453**, pp. 1631–1648.

A General Reduced Representation of One-Dimensional Frictional Interfaces

Michael Guthrie

Daniel Kammer

Department of Engineering Physics,
University of Wisconsin,
Madison, WI 53706

A physically-motivated, reduced representation of a general one-dimensional frictional interface is developed. Friction is introduced into the system as a state variable and is modeled by nonlinear springs of large but finite stiffness. The set of equations for the interface is reduced in a procedure similar to Guyan reduction by assuming that the system must deform in its quasistatic displacement shapes. The result of this reduction is that the degrees of freedom internal to the interface are removed from the analysis and only the boundary degrees of freedom are retained. The reduced system is then specialized to the case of a bar on a frictional surface. For this problem, a second reduction is made by noting that the time derivative of the friction force on the stuck block nearest the slip zone is much greater than the time derivatives of the friction forces elsewhere. Therefore only the friction force on the stuck block nearest the slip zone needs to be updated at each time step. The reduced representation developed in this paper is compared with a formulation from the literature and it is seen that the two match very closely and that the reduced representation is far less computationally intensive.
[DOI: 10.1115/1.2745375]

Introduction

It has been estimated that damping due to relative motion in frictional joints accounts for up to 90% of the total structural damping in many large built-up structures [1]. In most structures, this damping occurs due to microslip, or slip of only a small portion of the interfaces between contacting sections of the joints. When an interface undergoes microslip, the natural modes and frequencies of the structure near the interface are dependent upon the amplitude of the applied forcing and so the problem is nonlinear; consequently, damping due to microslip in joints has not been systematically incorporated into contemporary structural dynamics simulation. Instead, damping due to microslip in joints has traditionally been incorporated through linear damping models (e.g., modal or Rayleigh damping) with parameters chosen to match experimental results [2]. However, the growing need for predictive structural dynamics simulation has necessitated physically motivated joint models that do not need to be fit to experimental data [3]. Perhaps the most obvious method of incorporating joints into structural finite element models is to mesh the joints finely enough that all relevant joint behavior is captured. Unfortunately, due to the tremendous difference between the time scales intrinsic to the joint dynamics and the larger structure's dynamics, this method results in extremely small elements in the joint and prohibitively small time steps [4]. A great deal of literature has focused on incorporating the effects of frictional contacts into finite element models (e.g., [5–8]). A significant portion of this literature has attempted to derive reduced order models capable of efficiently incorporating the constitutive response of joints into a larger structural model. Among these are parallel-series Iwan models, Menq's receptance method, and series-series Iwan models.

One of the earliest efforts to devise constitutive models of joints was the work of Iwan, which considered parallel and series arrangements of springs and sliders (Fig. 1) [9,10]. Iwan proposed a continuum of series elements arranged in parallel with break-free forces ϕ given by a two parameter, band-limited probability density function in Ref. [9]. He applied this model to actual experimental data taken from a jointed structure by choosing the two parameters defining the break-free force distribution in order to match the experimental data as closely as possible. The resulting model matched the experimental data fairly well.

Iwan's parallel-series model has been improved by Segalman using observations regarding the relationship between frictional energy dissipation and forcing amplitude made by Goodman in Ref. [11]. Goodman conjectured that any system of elastic components held together by a normal load, and perturbed by an oscillatory tangential load, dissipates energy at a rate proportional to the forcing amplitude to the third power if the area of the slip zone increases linearly with the forcing amplitude. However, experiments have shown that real joints exhibit energy dissipation proportional to the 2.5th–2.9th power of the forcing amplitude, with the departure from Goodman's hypothesis possibly being due to the inaccuracy of the Coulomb friction model [12]. Segalman has used these energy dissipation considerations in Refs. [4,12–14] to devise more appropriate probability density functions $\rho(\phi)$ for the break-free force ϕ of the sliders in Iwan's parallel-series model. In Ref. [12], Segalman showed that for a parallel-series Iwan model undergoing microslip, energy dissipation is proportional to the third power of the forcing amplitude if $\rho(\phi)$ is nonsingular near $\phi=0$, while energy dissipation is proportional to the $(3+\chi)$th power of the forcing amplitude with $-1<\chi<0$ if $\rho(\phi)=\phi^{\chi}$ near $\phi=0$. Thus the experimentally observed relationship between energy dissipation and forcing amplitude can be accounted for by choosing $\rho(\phi)$ to have a weak singularity at $\phi=0$. Segalman refined this model in Ref. [14] by choosing a more complicated form of $\rho(\phi)$ defined by four parameters, which are chosen to match either experimental data or data from a finely meshed finite element model of the joint.

In addition to Segalman, a number of other researchers have built upon Iwan's parallel-series model. Song et al. developed a model of a jointed beam structure using parallel-series Iwan elements in Ref. [15]. This model uses the same two parameter band-limited distribution function for the slider strengths that Iwan used in Ref. [9], but in this work the parameters are chosen to fit experimental data using a neural network. Deshmukh et al. [16] considered a discrete parallel-series Iwan model in which each of the sliders was allowed to have mass. They proposed a collocation

Contributed by the Applied Mechanics Division of ASME for publication in the JOURNAL OF APPLIED MECHANICS. Manuscript received August 7, 2006; final manuscript received February 15, 2007; published online January 16, 2008. Review conducted by Antoinette Maniatty.

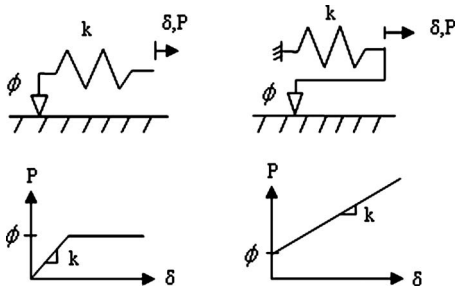

Fig. 1 Series (left) and parallel (right) Iwan elements and their associated force-displacement relations

procedure for fitting the stiffness and break-free force of each of the Iwan elements to experimentally observed softening curves and studied the convergence behavior of the model with increasing numbers of elements. Levine and White [17] deduced Iwan parameters for a model of the joints between the Cassini spacecraft and the Huygens probe by examining shifts in frequency response as excitation amplitude was increased. The primary limitation of all of these parallel-series Iwan models is that they are empirical and do not model the actual interface physics taking place. Because of this, model parameters must be chosen to fit experimental data or results from a finely meshed finite element model and so the method is not predictive.

Another approach to incorporating frictional contacts into structural models is the receptance method developed by Menq in Refs. [18–20]. The first step in this approach is to solve the linear problem posed by the structure with its frictional contacts removed. The reaction forces at the contacts are then approximated using Fourier series and the receptances of the linear finite element model are used to find the displacements induced by these reaction forces. Menq [18] developed this method for single point frictional contacts and as a result, the method did not match experimental data well for high normal loads (i.e., the microslip regime). In order to rectify this, Menq [19] extended the receptance method to incorporate distributed friction by considering the contact to be a flexible bar resting on a surface. Menq [20] observed that the distributed contact model agreed much more closely with experimental data than did the single point contact model. The primary drawback of the receptance approach is that for real frictional contacts that are more complicated than the simplified single point contact considered in Ref. [18] and the bar contact considered in Ref. [19], there is no straightforward way to determine "effective" properties of the simplified contacts that will accurately represent the more complicated real contacts.

A third approach to modeling frictional interfaces is the series arrangement of series Iwan elements. Despite being a more natural model of interface behavior than the parallel-series Iwan model, the series-series model has not received as much attention in the literature. Menq [19] appears to be one of the first to consider such a model as part of his effort to incorporate distributed contact into his receptance approach. Deshmukh et al. [21] considered a discrete series-parallel-series Iwan model of a bar on a surface and used the collocation procedure proposed in Ref. [16] to choose model parameters that fit a theoretical prediction of the frictional shear stress distribution obtained from shear-lag theory. Quinn and Segalman considered a series-series Iwan model of a massless bar on a surface in Ref. [22] and showed that this model can reproduce the experimentally observed power-law relationship between energy dissipation and forcing amplitude if the spatial distribution of slider break-free forces is chosen appropriately. Quinn had previously considered a discrete model of a bar with mass on a surface in Ref. [23] and obtained numerical results for this system by integrating the equations of motion. Quinn and Segalman [22] compared the theoretical predictions of the massless series-series Iwan model from Ref. [22] with the numerical results from a model like the one presented by Quinn in Ref. [23] and concluded that, for small forcing frequencies and amplitudes, the dynamics within the bar has very little effect on its response.

The work presented in this paper develops a physically-motivated, reduced representation of a general one-dimensional frictional interface. Friction is introduced into the system as a state variable and is modeled by nonlinear springs of large but finite stiffness. This state-space implementation of friction allows for the reduction of the system of equations describing the interface in a procedure similar to Guyan reduction [24]. In this procedure, the system is assumed to deform only in its quasistatic displacement shapes. The result of this reduction is that the degrees of freedom (dof) internal to the interface are removed from the analysis and only the boundary dof are retained. After developing this reduced representation of general one-dimensional frictional interfaces, this paper specializes the result to the case of a bar on a frictional surface that was considered in Refs. [22,23]. For this problem, a second reduction is made by noting that the time derivative of the friction force on the stuck block nearest the slip zone is much greater than the time derivatives of the friction forces elsewhere, which can therefore be neglected. The result is a reduced representation of a bar on a frictional surface that could perhaps be incorporated into a larger structural model. Although this paper only discusses the specialization of the formulation developed here to the problem of a bar on a frictional surface, this formulation is general and can be specialized to any one-dimensional problem.

The approach developed in this paper offers several advantages over those from the literature that were previously discussed. First, it requires far less computational expense than other formulations. Secondly, the approach developed here is physically motivated and so model parameters have direct physical interpretation. This could allow for truly predictive simulation. Finally, this approach is more systematic than other methods in that it could potentially be developed from the same finite element approach used to create the larger structural model.

Development of Full System Equations

Consider a general one-dimensional structure with N nodes, each with a single dof x_i, where $i=1,\ldots,N$. Let the structure have mass and stiffness matrices M and K, respectively, and allow Coulomb friction to act between some or all of the nodes and ground. Denote the coefficient of friction by μ and the normal load on the ith node by q_i. Now let

$$[v_1 \ \cdots \ v_N]^T \equiv [\dot{x}_1 \ \cdots \ \dot{x}_N]^T$$

where an overdot denotes differentiation with respect to time. Partition x and v into an a-set containing the boundary dof and a d-set containing the internal dof such that

$$x \equiv \begin{bmatrix} x_a \\ x_d \end{bmatrix} \text{ and } v \equiv \begin{bmatrix} v_a \\ v_d \end{bmatrix}$$

Denote the numbers of dof in the a-set and d-set as N_a and N_d, respectively. Let the a-set dof be loaded by some external applied load $F_a(t)$ and assume that the d-set dof are not subjected to any external load. Then the governing equation for this system is

$$M\ddot{x} + Kx = \begin{bmatrix} F_a(t) \\ 0_{N_d,1} \end{bmatrix} - \begin{bmatrix} G_a \\ G_d \end{bmatrix} \equiv F(t) - G \tag{1}$$

where $0_{z,y}$ denotes a z by y zero matrix and G_a and G_d denote the friction forces on the a-set and d-set, respectively. The positive direction for each friction force G_i is taken to be opposite the positive direction for the corresponding x_i.

In order for Eq. (1) to be of any use, the friction forces G must be defined. In this paper, friction is incorporated into Eq. (1) by making each frictional force a state variable and by using the constitutive law illustrated in Fig. 2. The "frictional stiffness" k_f is chosen to be much larger than k. Note that Segalman has observed

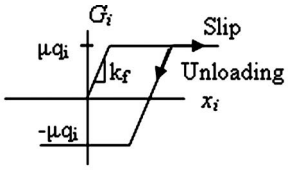

$$\dot{G}_i = \begin{cases} 0 & \text{if } |G_i| \geq \mu q_i \text{ and } \operatorname{sgn}(G_i) = \operatorname{sgn}(\dot{x}_i) \\ k_f & \text{otherwise} \end{cases}$$

Fig. 2 Graphical (l) and mathematical (r) representations of friction law

that a similar equation governs the slider displacement, and hence the friction force, in the single dof spring-slider system considered in Ref. [13]. Also note that this approach to modeling friction is equivalent to connecting each of the nodes to ground through a series Iwan element. It is convenient to write the constitutive law from Fig. 2 as

$$\dot{G} = Av \tag{2}$$

where

$$A = \begin{bmatrix} a_1 & 0 & \cdots & 0 \\ 0 & a_2 & \ddots & \vdots \\ \vdots & \ddots & \ddots & 0 \\ 0 & \cdots & 0 & a_N \end{bmatrix}$$

and

$$a_i = \begin{cases} 0 & \text{if } |G_i| \geqslant \mu q_i \text{ and } \operatorname{sgn}(G_i) = \operatorname{sgn}(\dot{x}_i) \\ k_f & \text{otherwise} \end{cases}$$

Development of Reduced Representation

The system defined by Eqs. (1) and (2) is a system in the $3N$ state variables x, v, and G. This system can be reduced from $3N$ to $3N_a+N_d$ state variables using a procedure similar to Guyan reduction [24] if it is assumed that the structure deforms in the shapes that it takes if all the d-set dof are massless and the a-set dof are given unit displacements. The use of these quasistatic displacement shapes is motivated by Quinn and Segalman [22]. In that work, the continuum problem posed by a flexible bar resting on a surface with Coulomb friction and subjected to a periodic load is discussed and it is stated that a closed form solution to this problem exists only when inertial effects are neglected. A discrete formulation of the problem is then considered and it is seen that, for forcing amplitudes much smaller than the force required to induce full slip and forcing frequencies much smaller than the fundamental frequency of the bar, the energy dissipation per forcing cycle predicted by the discrete model that includes mass differs very little from the theoretical prediction that does not include mass. Thus it seems a reasonable assumption to say that, for small forcing frequencies and amplitudes, the bar deforms in its quasistatic displacement shape. Extension of this logic suggests that, for small forcing frequencies and amplitudes, a general one-dimensional structure will deform in its quasistatic displacement shapes.

To find the quasistatic displacement shapes, consider the d-set partition of Eq. (1) and ignore mass effects,

$$K_{da}x_a + K_{dd}x_d = -G_d \tag{3}$$

where, for example, K_{da} denotes the d-set rows and a-set columns of K. Equation (3) can be solved for x_d,

$$x_d = -K_{dd}^{-1}G_d - K_{dd}^{-1}K_{da}x_a \tag{4}$$

This expression for x_d can be differentiated and the friction law from Eq. (2) can be applied to produce

$$v_d = -(K_{dd}+A_{dd})^{-1}K_{da}v_a \tag{5}$$

The displacement and velocity of the structure, x and v, can now be written in terms of the displacement and velocity of the a-set, x_a and v_a, as follows:

$$x = T_1x_a - \Psi \text{ and } v = T_2v_a \tag{6}$$

where

$$T_1 \equiv \begin{bmatrix} I_{N_a} \\ -K_{dd}^{-1}K_{da} \end{bmatrix} \quad \Psi \equiv \begin{bmatrix} 0_{N_a,1} \\ K_{dd}^{-1}G_d \end{bmatrix} \quad T_2 \equiv \begin{bmatrix} I_{N_a} \\ -(K_{dd}+A_{dd})^{-1}K_{da} \end{bmatrix}$$

and I_z denotes a $z \times z$ identity matrix. Note that this reduction is different than Guyan reduction in that the position and velocity must be represented using different transformations.

Substituting the transformations of Eq. (6) into Eq. (1) and premultiplying the entire equation by T_2^T results in

$$T_2^TMT_2\dot{v}_a + T_2^TK(T_1x_a - \Psi) = T_2^T(F-G)$$

or

$$M_{\text{eff}}\dot{v}_a + K_{\text{eff}}x_a - K_{ad}K_{dd}^{-1}G_d = F_a - G_a \tag{7}$$

where

$$M_{\text{eff}} \equiv T_2^TMT_2 \text{ and } K_{\text{eff}} \equiv K_{aa} - K_{ad}K_{dd}^{-1}K_{da}$$

It should be noted here that M_{eff} varies with time due to its dependence on the matrix A_{dd}, which depends upon which nodes are slipping and which are sticking.

Using Eq. (7) it is possible to track the a-set dof without knowing the d-set dof. However, integration of Eq. (7) does require knowledge of the friction forces G at each time step, so it is necessary to have an equation that gives the derivatives of these friction forces in terms of the a-set dof. Such an equation can be found by substituting v from Eq. (6) into the friction law from Eq. (2),

$$\dot{G} = \begin{bmatrix} A_{aa} \\ -A_{dd}(K_{dd}+A_{dd})^{-1}K_{da} \end{bmatrix} v_a \tag{8}$$

By collecting Eqs. (7) and (8), one obtains the equations of the reduced system

$$\tilde{M}\frac{d}{dt}\begin{bmatrix} v_a \\ x_a \\ G_a \\ G_d \end{bmatrix} + \tilde{K}\begin{bmatrix} v_a \\ x_a \\ G_a \\ G_d \end{bmatrix} = \begin{bmatrix} F_a \\ 0_{N_a,1} \\ 0_{N_a,1} \\ 0_{N_d,1} \end{bmatrix} = \begin{bmatrix} F_a \\ 0_{2N_a+N_d,1} \end{bmatrix} \tag{9}$$

where

$$\tilde{K} \equiv \begin{bmatrix} 0_{N_a,N_a} & K_{\text{eff}} & I_{N_a} & -K_{ad}K_{dd}^{-1} \\ -I_{N_a} & & & \\ -A_{aa} & & 0_{2N_a+N_d,2N_a+N_d} & \\ A_{dd}(K_{dd}+A_{dd})^{-1}K_{da} & & & \end{bmatrix},$$

$$\tilde{M} \equiv \begin{bmatrix} M_{\text{eff}} & 0_{N_a,2N_a+N_d} \\ 0_{2N_a+N_d,N_a} & I_{2N_a+N_d} \end{bmatrix}$$

This system has $3N_a+N_d$ state equations as opposed to the full system which has $3N$.

Specialization to a Bar on a Surface

All of the preceding analysis applies to general one-dimensional structures with Coulomb friction. However, further reduction of the problem can be discussed within the context of a specific structure and loading scenario. Toward this end, consider a flexible bar of stiffness EA/L and uniformly distributed mass M_b (Fig. 3). The bar is fixed at its left end and is subjected to an arbitrary normal load distribution. Let the bottom surface of the

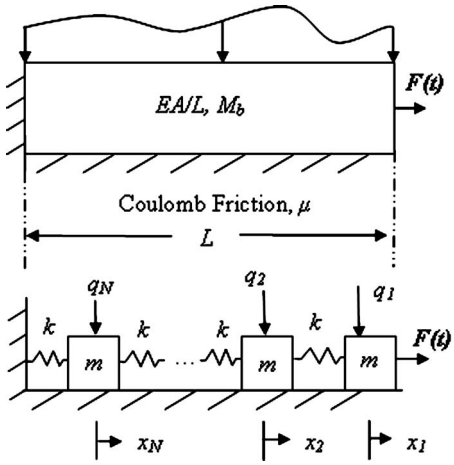

Fig. 3 Flexible bar on a surface (top) and its discrete representation (bottom)

bar experience Coulomb friction and let the right end be loaded by some periodic applied force. This system can be discretized by splitting the bar into N rigid blocks of mass $m \equiv M_b/N$ that are connected by springs of stiffness $k \equiv NEA/L$ and are subjected to normal loads in accordance with the normal load distribution. This system can be described by Eqs. (1) and (2) with $[x_a|x_d^T] = [x_1|x_2 \cdots x_N]$,

$$M = mI_N \quad \text{and} \quad K = k\begin{bmatrix} 1 & -1 & 0 & \cdots & \cdots & 0 \\ -1 & 2 & -1 & 0 & & \vdots \\ 0 & -1 & 2 & -1 & \ddots & \vdots \\ \vdots & \ddots & \ddots & \ddots & \ddots & 0 \\ \vdots & & 0 & -1 & 2 & -1 \\ 0 & \cdots & \cdots & 0 & -1 & 2 \end{bmatrix}$$

Reduction in the size of Eq. (9) can be accomplished for this example if one notes that, at each time step, the derivatives of the friction forces on all but one of the blocks are negligible. To see this, note that at any given time, there will be a region of slipping blocks near the applied load and the remainder of the blocks will be stuck. Call this region of slipping blocks the slip zone and denote the stuck block nearest the slip zone as the sth block. Now note that the derivatives of the friction forces on the slipping blocks are identically zero. In addition, the derivatives of the friction forces in the stick zone are given by $\dot{G}_i = k_f v_i$ where $i = s, \ldots, N$. Equation (5) can be rearranged and specialized to this example to get the following equation for the velocities of the d-set blocks:

$$(A_{dd} + K_{dd})v_d = k\begin{bmatrix} v_a \\ 0_{N_d-1,1} \end{bmatrix} \tag{10}$$

The velocities of the blocks in the stick zone are given by the $(s-1)$th through N_d^{th} rows of Eq. (10) for $s \neq 1$,

$$\left([0_{N_d-s+2,s-2} \quad k_f I_{N_d-s+2}] + k\begin{bmatrix} 0_{1,s-3} & -1 \\ 0_{N_d-s+1,s-3} & 0_{N_d-s+1,1} \end{bmatrix} \begin{bmatrix} 2 & -1 & 0 & \cdots & 0 \\ -1 & 2 & -1 & \ddots & \vdots \\ 0 & \ddots & \ddots & \ddots & 0 \\ \vdots & \ddots & -1 & 2 & -1 \\ 0 & \cdots & 0 & -1 & 2 \end{bmatrix} \right) \begin{bmatrix} v_2 \\ \vdots \\ v_{s-1} \\ - - - \\ v_s \\ \vdots \\ v_N \end{bmatrix} = 0_{N_d-s+2,1}$$

Note that it is not a contradiction for a stuck block to have nonzero velocity because friction has been modeled by nonlinear springs of large but finite stiffness k_f. Also note that it is assumed here that $s \neq 1$, and that for the special case where $s=1$ one can proceed similarly. By moving the term involving v_{s-1} to the right-hand side, the previous equation can be rewritten as

$$B\begin{bmatrix} v_s \\ \vdots \\ v_N \end{bmatrix} = \begin{bmatrix} v_{s-1} \\ 0 \\ \vdots \\ 0 \end{bmatrix} \tag{11}$$

where

$$B \equiv \begin{bmatrix} \beta+2 & -1 & 0 & \cdots & 0 \\ -1 & \beta+2 & -1 & \ddots & \vdots \\ 0 & \ddots & \ddots & \ddots & 0 \\ \vdots & \ddots & -1 & \beta+2 & -1 \\ 0 & \cdots & 0 & -1 & \beta+2 \end{bmatrix} \quad \text{and} \quad \beta \equiv \frac{k_f}{k}$$

Equation (11) can be used to find the velocities of the stuck blocks if the matrix B can be inverted. The inverse of B can be approximated as

$$\tilde{B}^{-1} \equiv \begin{bmatrix} b & b^2 & b^3 & \cdots & b^{N_d-s+1} & b^{N_d-s+2} \\ b^2 & b & b^2 & \ddots & & b^{N_d-s+1} \\ b^3 & b^2 & b & b^2 & \ddots & \vdots \\ \vdots & \ddots & b^2 & \ddots & \ddots & b^3 \\ b^{N_d-s+1} & & \ddots & \ddots & \ddots & b^2 \\ b^{N_d-s+2} & b^{N_d-s+1} & \cdots & b^3 & b^2 & b \end{bmatrix} \tag{12}$$

where

$$b \equiv (\beta+2)^{-1}$$

It is easily confirmed that

$$B\tilde{B}^{-1} = I + O(b^2)$$

If k_f is chosen to be much larger than k so that b is small, $\tilde{B}^{-1}$ is a good approximation of B^{-1}. From Eqs. (11) and (12), it is seen that

$$[v_s \ \cdots \ v_N]^T = [b \ b^2 \ \cdots \ b^{N_d-s+2}]^T v_{s-1} \tag{13}$$

and thus the derivatives of the friction forces on the blocks in the stick zone are

$$[\dot{G}_s \ \cdots \ \dot{G}_N]^T = k_f[b \ b^2 \ \cdots \ b^{N_d-s+2}]^T v_{s-1} \tag{14}$$

It is seen that the derivative of the friction force on the second stuck block is smaller than that on the first stuck block by a factor of b, the derivative of the friction force on the third stuck block is smaller than that on the first stuck block by a factor of b^2, etc. Thus, if k_f is chosen to be much larger than k so that b is small, it is reasonable to say that the only nonzero friction derivative is $\dot{G}_s$ (i.e., $\dot{G}_i = 0 \forall i \neq s$). Note that this is consistent with Menq's observation in Ref. [19] that as the stiffness of his elastoplastic layer approached infinity, the frictional shear distribution over his bar approached a step function.

For the sth block, the friction law from Eq. (2) produces

$$\dot{G}_s = k_f v_s \tag{15}$$

and, differentiating Eq. (4),

$$v_s = \begin{cases} v_a & \text{if } s = 1 \\ -(K_{dd}^{-1})_{\tilde{s}} \dot{G}_d - (K_{dd}^{-1})_{\tilde{s}} K_{da} v_a & \text{if } s \neq 1 \end{cases}$$

where the notation $(K_{dd}^{-1})_{\tilde{s}}$ denotes the $\tilde{s}$th row of K_{dd}^{-1} and $\tilde{s} = s - 1$. Because $\dot{G}_i = 0 \forall i \neq s$, this simplifies to

$$v_s = \begin{cases} v_a & \text{if } s = 1 \\ -(K_{dd}^{-1})_{\tilde{s},\tilde{s}} \dot{G}_s - (K_{dd}^{-1})_{\tilde{s}} K_{da} v_a & \text{if } s \neq 1 \end{cases} \tag{16}$$

where the notation $(K_{dd}^{-1})_{\tilde{s},\tilde{s}}$ denotes the $\tilde{s}$th, $\tilde{s}$th entry of K_{dd}^{-1}. Substituting Eq. (16) into Eq. (15) and solving for $\dot{G}_s$ shows that

$$\dot{G}_s = \begin{cases} k_f v_a & \text{if } s = 1 \\ -(1 + k_f (K_{dd}^{-1})_{\tilde{s},\tilde{s}})^{-1} k_f (K_{dd}^{-1})_{\tilde{s}} K_{da} v_a & \text{if } s \neq 1 \end{cases} \tag{17}$$

Thus, instead of integrating Eq. (9), one can simply update the a-set variables using

$$\begin{bmatrix} M_{\text{eff}} & 0 \\ 0 & 1 \end{bmatrix} \frac{d}{dt} \begin{bmatrix} v_a \\ x_a \end{bmatrix} + \begin{bmatrix} 0 & K_{\text{eff}} \\ -1 & 0 \end{bmatrix} \begin{bmatrix} v_a \\ x_a \end{bmatrix} = \begin{bmatrix} F_a(t) + K_{ad} K_{dd}^{-1} G_d - G_1 \\ 0 \end{bmatrix} \tag{18}$$

and then find the stuck block nearest the slip zone and update its friction force using Eq. (17). Thus the general system of $3N_a + N_d$ state equations expressed in Eq. (9) has been reduced for this particular example to a system of only three state equations.

In order to integrate Eqs. (17) and (18), one must find the stuck block nearest the slip zone, or the sth block, at each time step. The expression for matrix A listed in Eq. (2) indicates that in order to determine whether or not a given d-set block is stuck, the sign of its velocity must be checked. However, this requirement can be avoided because it can be shown that if the d-set blocks are moving, they must be moving in phase with the a-set block (i.e., $\text{sgn}(v_i) = \text{sgn}(v_a)$ for $i = 2, 3, \ldots, N$). Therefore, the coefficients a_i in Eq. (2) can be rewritten as

$$a_i = \begin{cases} 0 & \text{if } |G_i| \geqslant \mu q_i \text{ and } \text{sgn}(G_i) = \text{sgn}(v_a) \\ k_f & \text{otherwise} \end{cases} \tag{19}$$

Thus it is not necessary to determine the velocities of the d-set blocks in order to find the sth block while integrating Eqs. (17) and (18). Instead, the conditions indicated in Eq. (19) can be checked in order to determine whether or not a given block is stuck. An efficient algorithm for finding the sth block has been developed but is not discussed here.

A final issue that must be discussed in relation to the problem of Fig. 3 is the computation of M_{eff}. Using Eqs. (6) and (7), it can be shown that for this specific problem,

$$M_{\text{eff}} \equiv m(1 + K_{ad}[K_{dd} + A_{dd}]^{-1}[K_{dd} + A_{dd}]^{-1} K_{da})$$

Note that the total mass lumped at the a-set block, M_{eff}, depends upon how much of the interface is slipping due to its dependence on the matrix A_{dd}. According to the expression above, it is necessary to invert the matrix $(K_{dd} + A_{dd})$ at every time step in order to compute M_{eff}. However, this time consuming requirement can be loosened by noting that the ith block cannot slip unless all the blocks to its right, or the 1st through $(i-1)$th blocks, slip. Therefore, there are only N possible values of the matrix A_{dd},

$$A_{dd} \in \bigcup_{s=2}^{N+1} \begin{bmatrix} 0_{s-2,s-2} & 0_{s-2,N-s+1} \\ 0_{N-s+1,s-2} & k_f I_{N-s+1} \end{bmatrix} \tag{20}$$

where $s = 2$ and $s = N+1$ correspond to the entire d-set sticking and slipping, respectively. Prior to integrating Eq. (18), the value of M_{eff} for each value of s can be computed by letting A_{dd} assume each of the values listed in Eq. (20). Then, while integrating Eq. (18), one can retrieve the appropriate value of M_{eff} based upon the value of s. The initial computation of the various values of M_{eff} can be very costly from a computational standpoint for large N because this process requires inversion of N matrices of size $N - 1 \times N - 1$. However, the computational cost of this process can be greatly reduced if, instead of evaluating M_{eff} at each of the N admissible values of s, one only evaluates M_{eff} at p admissible values of s, where $p \ll N$. To visualize this procedure, imagine plotting the value of M_{eff} for $s = 2, 3, \ldots, N+1$ in order to obtain an M_{eff} vs s curve. Then by only evaluating M_{eff} at p admissible values of s, one is sampling the M_{eff} vs s curve at p values of s. To evaluate M_{eff} at values of s other than the p sampling points, one simply linearly interpolates the M_{eff} vs s curve between the sampling points. The number of points p required to obtain accurate values of M_{eff} at intermediate values of s depends upon the nature of the M_{eff} vs s curve. For the computational example problem considered later in this paper in which the density and normal load distribution are both uniform, the M_{eff} vs s curve is nearly linear and $p = 2$ is sufficient. More complicated scenarios, such as a nonuniform normal load or a nonuniform density, may destroy the linearity of the M_{eff} vs s curve and necessitate larger values of p. This matter will be the subject of future work.

Although this paper only discusses the specialization of Eq. (9) to the problem of a bar on a frictional surface, the approach presented here can be used to specialize Eq. (9) to any one-dimensional problem. Thus, a reduction similar to the one used to produce Eq. (17) can be performed in order to obtain an equation for the time derivative(s) of the friction force(s) on the edge(s) of the slip zone(s) in a more complicated problem. In addition, an approach similar to the one presented above can be used to estimate M_{eff} based upon the slip state of the structure.

Comparison of Formulations

In order to gauge the merit of the approach derived in this paper, it was compared to the formulation derived by Quinn in Ref. [25]. In that work, Quinn considered the system of Fig. 3. He noted that the discontinuity in the Coulomb friction model at zero velocity leads to numerical difficulties when integrating the equations of this system and developed a regularization of Coulomb friction that avoids these problems. This regularization is continuous at zero velocity but approaches the traditional Coulomb friction model as a smoothing parameter ε approaches zero. Quinn observed that by modeling friction using this regularization, the equations describing the system of Fig. 3 can be integrated using time steps 2–3 orders of magnitude larger than those required if the traditional Coulomb friction model is used.

The model presented by Quinn in Ref. [25] was chosen for comparison because it is, in a sense, the starting point for the proposed reduction procedure. The model of the system from Fig. 3 proposed by Quinn and the model expressed in Eqs. (1) and (2) differ only in the friction law used. Therefore, by comparing with

Table 1 Total execution time (s) for 25, 50, 100, 250, and 1000 block systems

	25 blocks	50 blocks	100 blocks	250 blocks	1000 blocks
Quinn	18	65	258	1917	51313
Reduced	3.6	7	16	43	381

the work of Quinn, one can see the effect that the proposed reduction has on both the results and the computational cost of the analysis.

Before proceeding with a comparison to Quinn's formulation, Eq. (17) must be modified slightly to avoid numerical difficulties,

$$\dot{G}_s = \begin{cases} k_f v_a + c\dot{v}_a & \text{if } s = 1 \\ -(1 + k_f(K_{dd}^{-1})_{\bar{s},\bar{s}})^{-1} k_f (K_{dd}^{-1})_{\bar{s}} K_{da} v_a & \text{if } s \neq 1 \end{cases} \tag{21}$$

When the entire bar is stuck ($s=1$), it can be seen that if $c=0$, then the very large stiffness in the first row of Eq. (18) results in spurious high frequency content that obscures numerical results. However, this problem does not arise if critical viscous damping is applied to the system by choosing

$$c = 2\sqrt{(K_{\text{eff}} + k_f) M_{\text{eff}}} \approx 2\sqrt{k_f m}$$

The need for such a damping term occurs when friction, which is modeled as a very stiff spring, acts at a node possessing mass. Thus it is unnecessary for this term to be included in $\dot{G}_s$ for $s \neq 1$ because the mass associated with the d-set has been relocated to the a-set through the proposed reduction procedure. It should also be noted that if no friction acts on the a-set, this problem does not arise and the damping term in Eq. (21) is unnecessary.

Equations (18) and (21) were used to simulate the system of Fig. 3 and the results were compared with those predicted by Quinn's formulation. For both formulations, the overall mass and stiffness of the bar were given unit value so that $m=1/N$ and $k=N$. In addition, the normal load was made uniform and the total friction force the bar could resist was taken to be unity, so that $\mu q = 1/N$ for each block. The applied forcing was $F(t)=F \sin \omega t$ with $F=\omega=0.25$. Note that with the overall mass, stiffness, and frictional capacity of the bar being unity, $F=1$ corresponds to the load that will induce full slip of the interface and $\omega=1$ corresponds to forcing at the natural frequency of a single dof representation of the bar. Both formulations were implemented for $N=25$, 50, 100, 250, and 1000.

For the reduced formulation, the friction spring stiffness was $k_f=100k$ (i.e., $\beta=100$). The equations were integrated over 3.1 cycles of the applied forcing using a 4th order Runge-Kutta integration scheme with $\Delta t = 0.5(25/N) \times 10^{-2}$ and the energy dissipation per cycle was computed during the 3rd cycle. For Quinn's formulation, the friction regularization parameter was taken to be $\varepsilon = 10\omega\Delta t$, just as in Ref. [25]. The equations were integrated over 3.1 cycles of the applied forcing using a 4th order Runge-Kutta algorithm with $\Delta t = (25/N) \times 10^{-2}$ and the energy dissipation per cycle was computed during the 3rd cycle. It should be noted that the reduced formulation requires a timestep that is half the size of the one required by Quinn's formulation due to the high frequency content introduced by the stiff frictional springs used in the reduced model. However, the computational results show that, despite its time step requirements, the reduced formulation is still much faster than Quinn's formulation. Also note that if no friction forces act on the a-set, the time step requirements for the reduced formulation are not as stringent for reasons explained in relation to Eq. (21). The total execution time for the two formulations is shown in Table 1 and the energy dissipation per cycle computed by the two formulations is given in Table 2.

The results in Table 1 indicate that for this example, the reduced formulation provides a drastic reduction in computational expense when compared with Quinn's formulation. For example, when $N=1000$, the reduced formulation is over 134 times faster than Quinn's formulation and offers this computational efficiency despite requiring twice as many time steps.

In addition to being much more efficient, the reduced formulation appears to be just as accurate as Quinn's formulation. Table 2 shows that when N is increased from 250 to 1000, the predictions of energy dissipation per cycle from the reduced formulation and Quinn's formulation change by 0.28% and 0.03%, respectively, so it appears that both predictions are nearly converged for $N=1000$. The difference between the computed values of energy dissipation per cycle from the two formulations for $N=1000$ is 0.39%.

Figure 4 shows the position of the first block in the 250 and 1000 block systems as predicted by Quinn's formulation and the reduced formulation. All of theses predictions agree very closely and it is difficult to distinguish one from another in Fig. 4. However, by examining the inset of this plot in Fig. 5 it can be seen that, for $N=250$, the reduced formulation predicts a peak displacement roughly 2.6% higher than that predicted by Quinn's formulation and that, for $N=1000$, this difference is reduced to 0.3%. Figure 6 shows the velocity of the first block in the 1000 block system as predicted by each of the two formulations. Again, it is difficult to distinguish between the two predictions so it is necessary to examine the inset of this plot in Fig. 7, where it is seen that the transition from stick to slip excites high frequency dynamics that decrease in frequency as the slip zone gains mass and becomes more flexible. Figure 7 shows that Quinn's formulation predicts response at several different frequencies, while the reduced formulation is only capable of representing response at a single frequency. However, because the high-frequency dynamics is unimportant with respect to energy dissipation, the predictions of the two formulations are very close. The unimportance of the high-frequency dynamics is expected and was a key assumption made in the development of the reduced formulation.

Figure 8 shows the energy dissipation per cycle predicted by the reduced formulation at several different values of forcing amplitude. In addition, a least squares fit to this data is plotted in Fig. 8. By considering a quasistatic continuum model of this problem, Quinn and Segalman [22] showed that the energy dissipation per cycle should vary with the cube of the forcing amplitude. As can be seen in Fig. 8, the relationship between energy dissipation per cycle and forcing amplitude predicted by the reduced formulation is in very close agreement with the cubic relationship predicted by Quinn and Segalman [22].

Table 2 Energy dissipation per cycle for 25, 50, 100, 250, and 1000 block systems

	25 blocks	50 blocks	100 blocks	250 blocks	1000 blocks
Quinn	0.01052827	0.01062863	0.01051746	0.01047247	0.01046909
Reduced	0.01106833	0.01048365	0.01035432	0.01039909	0.01042853

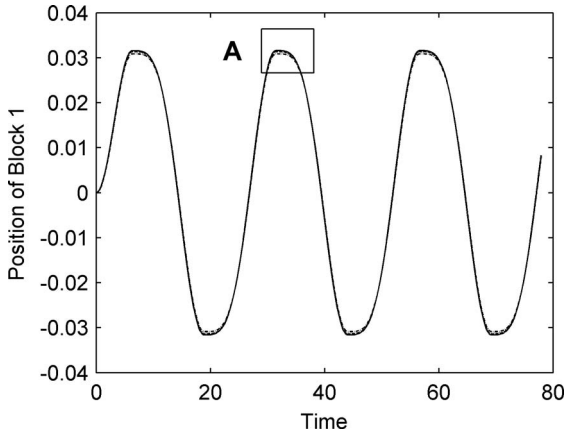

Fig. 4 Position of block 1 in 250 and 1000 block systems as predicted by the reduced formulation and Quinn's formulation

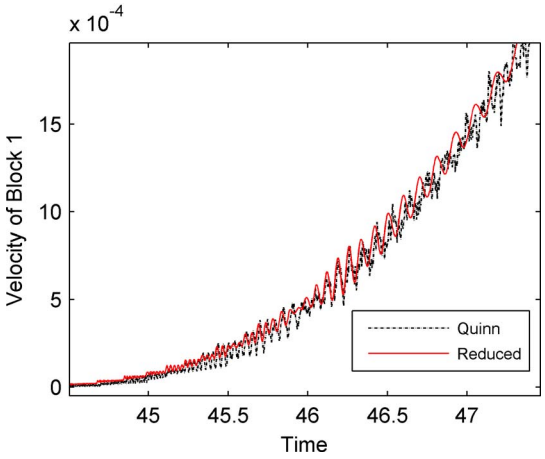

Fig. 7 Inset B of Fig. 6

Conclusion

A physically-motivated, reduced representation of a general one-dimensional frictional interface has been developed. Friction was introduced into the system as a state variable and was modeled by nonlinear springs of large but finite stiffness. This state-space implementation of friction allowed for the reduction of the system of equations describing the interface in a procedure similar to Guyan reduction. In this procedure, the system was assumed to deform only in its quasistatic displacement shapes. The result of this reduction was that the degrees of freedom internal to the interface were removed from the analysis and only the boundary degrees of freedom were retained. After developing this reduced representation of general one-dimensional frictional interfaces, this paper specialized the result to the case of a bar on a frictional surface that was considered in Refs. [22,23]. For this problem, a second reduction was made by noting that the time derivative of the friction force on the stuck block nearest the slip zone is much greater than the time derivatives of the friction forces elsewhere, which can therefore be neglected. The result was a reduced representation of a bar on a frictional surface that could perhaps be incorporated into a larger structural model. In addition to developing this reduced representation, this paper also discussed computationally efficient methods of approximating the effective mass at each timestep and performing required checks on the velocities of internal blocks. Finally, the reduced representation of a bar on a surface developed in this paper was compared with the formulation from Quinn [25] and it was seen that the two match very closely and that the reduced representation is far less computationally intensive.

The equations of the reduced representation can be thought of as describing a superelement that is capable of incorporating the effect of general one-dimensional frictional interfaces into larger structural models. This superelement approach offers several benefits over the other methods previously discussed here. First, it is computationally efficient. For the example problem considered in this paper, it was seen that the reduced representation is up to 134 times faster than Quinn's formulation. Secondly, the superelement

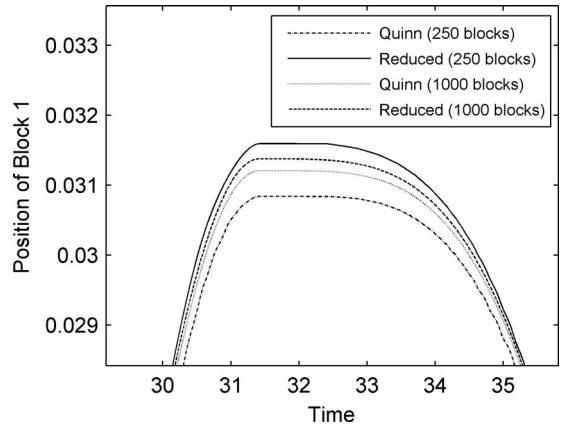

Fig. 5 Inset A of Fig. 4

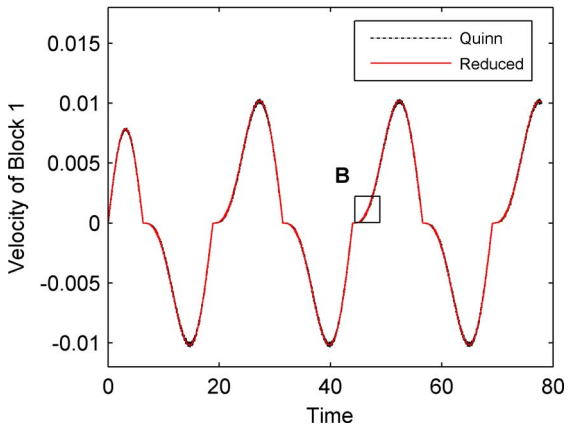

Fig. 6 Velocity of block 1 in 1000 block system as predicted by the reduced formulation and Quinn's formulation

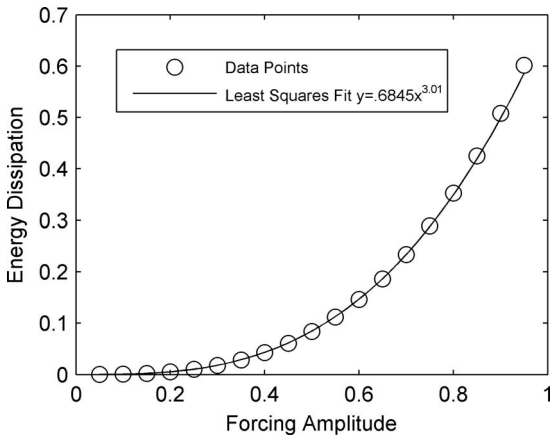

Fig. 8 Energy dissipation versus forcing amplitude from reduced formulation for $N=250$

approach is physically motivated and so model parameters have direct physical interpretation. This could allow for truly predictive simulation. Finally, the superelement approach is more systematic than other methods in that it could potentially be developed from the same finite element approach used to create the larger structural model. Future work will attempt to extend the approach of this paper in order to develop two and three-dimensional finite element based superelements that can incorporate the effect of general frictional contacts into large structural finite element models in a physically motivated manner without excessive computational burden.

Acknowledgment

The authors would like to thank the 3M Science and Technology Fellowship Program and Sandia National Laboratory for their support of this work.

References

[1] Beards, C. F., 1992, "Damping in Structural Joints," Shock Vib. Dig., **24**, pp. 3–7.
[2] Dohner, J. L., 2000, "A Reduced Order, One Dimensional Model of Joint Response," Sandia National Laboratories, Technical Report No. SAND2000-2753C.
[3] Dohner, J. L., 2001, "On the Development of Methodologies for Constructing Predictive Models of Structures With Joints and Interfaces," Sandia National Laboratories, Technical Report No. SAND2001-0003P.
[4] Segalman, D. J., Paez, T., Smallwood, D., Sumali, and A., Urbina, A., 2003, "Status and Integrated Road-Map for Joints Modeling Research," Sandia National Laboratories, Technical Report No. SAND2003-0897.
[5] Oden, J. C., and Martins, J. A. C., 1985, "Models and Computational Methods for Dynamic Friction Phenomena," Comput. Methods Appl. Mech. Eng., **52**, pp. 527–634.
[6] Bauchau, O. A., 1999, "On the Modeling of Friction and Rolling in Flexible Multibody Systems," Multibody Syst. Dyn., **3**, pp. 209–239.
[7] Bauchau, O. A., Rodriguez, J., and Bottasso, C. L., 2001, "Modeling of Unilateral Contact Conditions With Application to Aerospace Systems Involving Backlash, Freeplay, and Friction," Mech. Res. Commun., **28**, pp. 571–599.
[8] Bauchau, O. A., and Ju, C., 2006, "Modeling Friction Phenomena in Flexible Multibody Dynamics," Comput. Methods Appl. Mech. Eng., **195**, pp. 6909–6924.
[9] Iwan, W. D., 1966, "A Distributed-Element Model for Hysteresis and Its Steady-State Dynamic Response," J. Appl. Mech., **33**, pp. 893–900.
[10] Iwan, W. D., 1967, "On A Class of Models for the Yielding Behavior of Continuous and Composite Systems," J. Appl. Mech., **89**, pp. 612–617.
[11] Goodman, L. E., 1959, "A Review of Progress in Analysis of Interfacial Slip Damping," Structural Damping, papers presented at a colloquium on structural damping held at ASME annual meeting in Atlantic City, NJ, Jerome E. Ruzincka ed., December, pp. 35–48.
[12] Segalman, D. J., 2001, "An Initial Overview of Iwan Modeling for Mechanical Joints," Sandia National Laboratories, Technical Report No. SAND2001-0811.
[13] Segalman, D. J., 1999, "Observations on Simulation of Joint Friction," Proceedings of the 1999 ASME Design Engineering Technical Conferences, DETC99-VIB-8188.
[14] Segalman, D. J., 2002, "A Four-Parameter Iwan Model for Lap-Type Joints," Technical Report No. SAND2002-3828, Sandia National Laboratories.
[15] Song, Y., Hartwigsen, C. J., McFarland, D. M., Vakakis, A. F., and Bergman, L. A., 2004, "Simulation of Dynamics of Beam Structures With Bolted Joints Using Adjusted Iwan Beam Elements," J. Sound Vib., **273**, pp. 249–276.
[16] Deshmukh, D. V., Berger, E. J., Mackin, T. J., and Inglis, H., 2005, "Convergence Behaviors of Reduced-Order Models For Frictional Contacts," J. Vibr. Acoust., **127**, pp. 370–381.
[17] Levine, M. B., and White, C., 2001, "Microdynamic Analyses for Establishing Nanometric Stability Requirements of Jointed Precision Space Structures," *Proceedings of the 2001 International Modal Analysis Conference*, pp. 1395–1401.
[18] Menq, C.-H., and Griffin, J. H., 1985, "A Comparison of Transient and Steady State Finite Element Analyses of the Forced Response of a Frictionally Damped Beam," J. Vibr. Acoust., **107**, pp. 19–25.
[19] Menq, C.-H., Bielak, J., and Griffin, J. H., 1986, "The Influence of Microslip on Vibratory Response, Part I: A New Microslip Model," J. Sound Vib., **107**(2), pp. 279–293.
[20] Menq, C.-H., Bielak, J., and Griffin, J. H., 1986, "The Influence of Microslip on Vibratory Response, Part II: A Comparison With Experimental Results," J. Sound Vib., **107**(2), pp. 295–307.
[21] Deshmukh, D. V., and Berger, E. J., 2005, "Dynamic Analysis of a Series Iwan Model Derived From a Continuous Frictional Interface," *Proceedings of the 2005 ASME International Design Engineering Technical Conferences*, Long Beach, CA, September 24–28, ASME, New York, DETC2005-85328, pp. 1943–1953.
[22] Quinn, D. D., and Segalman, D. J., 2005, "Using Series-Series Iwan-Type Models for Understanding Joint Dynamics," J. Appl. Mech., **72**, pp. 666–673.
[23] Quinn, D. D., 2001, "Distributed Friction and Microslip in Mechanical Joints With Varying Degrees-of-Freedom," *Proceedings of the 2001 ASME Design Engineering Technical Conferences*, Pittsburgh, PA, September 9–12, ASME, New York, DETC2001/VIB-21514.
[24] Guyan, R. J., 1965, "Reduction of Stiffness and Mass Matrices," AIAA J., **3**(5), p. 380.
[25] Quinn, D. D., 2004, "A New Regularization of Coulomb Friction," J. Vibr. Acoust., **126**, pp. 391–397.

Constitutive Modeling of the Stress-Stretch Behavior of Two-Dimensional Triangulated Macromolecular Networks Containing Folded Domains

M. Arslan

M. C. Boyce[1]
e-mail: mcboyce@mit.edu

Department of Mechanical Engineering,
Massachusetts Institute of Technology,
Cambridge, MA 02139

H. J. Qi
Department of Mechanical Engineering,
University of Colorado,
Boulder, CO

C. Ortiz
Materials Science and Engineering,
Massachusetts Institute of Technology,
Cambridge, MA 02139

The mechanical behavior of the red blood cell membrane is governed by the lipid bilayer which resists changes in surface area and the underlying spectrin network which resists changes in shape. The constituent spectrin chains of the network consist of a series of domains along the chain, which exhibit noncovalent interactions. Upon sufficient extension of a chain, each folded domain undergoes mechanically-induced unfolding after reaching a chain force between 10 and 35 pN. Individual spectrin chains within the network experience their first unfolding event at different levels of macroscopic strain depending on the macroscopic loading conditions and the orientation of each constituent chain with respect to the macroscopic loading. A microstructurally-informed continuum level constitutive model is developed which tracks individual chain deformation behavior as well as the overall macroscopic network stress-strain behavior. Using the introduced continuum approach and statistical mechanics based models of the chain force-extension behavior together with a transition state model of domain unfolding; a constitutive model for the membrane stress-stretch behavior is constructed. Uniaxial tension and simple shear behaviors of the membrane are simulated incorporating the unfolding of the individual chains. A Taylor averaging approach is used as a first approximation to account for the irregularities in the spectrin network which result in a near plateau-like force behavior with increasing stretch. [DOI: 10.1115/1.2745373]

1 Introduction

Many protein molecules have multidomain structures which result in a force-extension behavior with a characteristic sawtooth pattern due to stretch-induced unfolding of domains along the molecular chain (Fig. 1). During a displacement controlled extension test, the force increases in a nonlinear manner with stretch until reaching a peak, whereupon there is a drop in the force, followed by a nonlinear rise to a peak, followed by a drop, and so on [1–5]. Upon reaching a rate-dependent peak force, a domain will unfold, releasing an additional chain length which increases the configurational space available to accommodate the overall extended chain length. Due to the entropic nature of the single molecule extension behavior, the increase in configurational space results in the observed drop in force and the increased compliance after the force drop.

Single molecule force-spectroscopy has been used to quantify the force-extension behavior and corresponding mechanically-induced unfolding of domains along the spectrin molecule [4,5]. Rief et al. [4] noted that the peak unfolding force is approximately 30 pN when a long chain spectrin molecule is stretched at a rate of 0.3 μm/s and also identified rate dependence to the peak unfolding force. Law et al. observed spectrin unfolding to occur at forces ranging between ~10 and ~37 pN during the extension of short (3–4 repeat units) strands of spectrin at extension rates of 1 μm/s [4,5].

In this paper, a microstructurally-informed continuum level constitutive model which accounts for the triangulated molecular network structure is developed which tracks individual chain deformation behavior as well as the overall macroscopic network stress-strain behavior [6]. The force-extension behavior of individual chains is modeled using a statistical mechanics representation of the long chain molecule together with an Eyring-type transition state model [7] to capture the rate dependence of domain unfolding. The chain constitutive model taken together with the network representation determines the effect of individual chain unfolding events on the overall network stress-strain behavior.

2 Membrane Structure of a Red Blood Cell

The mechanical properties of the red blood cell membrane are governed by the lipid bilayer, which resists changes in the membrane surface area of the red blood cell, and the spectrin network, which resists surface shearing of the membrane. The surface area stiffness (~500 dyn/cm) is much greater than the surface shear stiffness (~0.01 dyn/cm). Hence this membrane is a two-dimensional analog to a rubbery solid where a rubber exhibits a high bulk modulus (~1 GPa) and a low shear modulus (~1 MPa). The distinct physical origins of the mechanical behavior of the surface area and that of the surface shear together with the high contrast in these properties enables separate modeling of the shear behavior from that of the surface area behavior. Indeed, in most instances, it is sufficient to approximate the surface area as remaining constant. Phenomenological neo-Hookean hyperelastic-type constitutive models have been proposed and used in early work by Skalak et al. [8] and Evans [9], and higher-order hyperelastic models in recent work by Suresh and coworkers [10,11]. A microstructurally-informed continuum level model of the large deformation behavior of the spectrin network has recently been developed by Arslan and Boyce in [6]. The

[1]Corresponding author.

Contributed by the Applied Mechanics Division of ASME for publication in the JOURNAL OF APPLIED MECHANICS. Manuscript received June 24, 2006; final manuscript received March 2, 2007; published online February 6, 2008. Review conducted by Ellen M. Arruda.

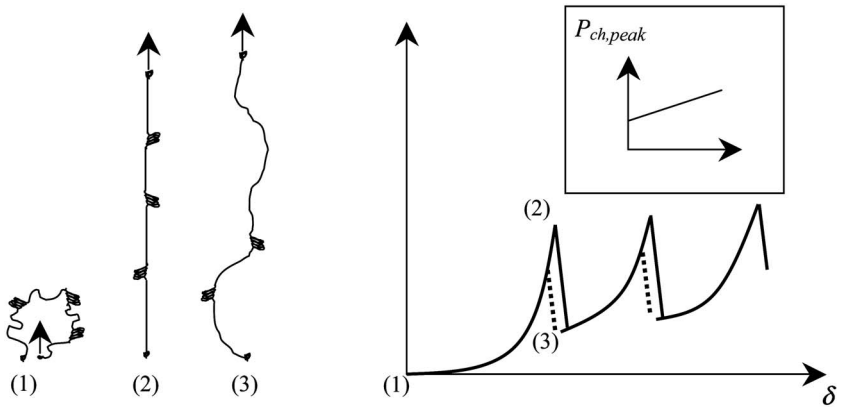

Fig. 1 Schematics of the stages of unfolding of a single chain under mechanical loading. (1) Corresponds to the undeformed chain, with a nonzero end-to-end distance, (2) corresponds to the nearly fully extended chain when the force reaches a value that will unfold a domain; a domain then begins to unfold as the force drops, and (3) corresponds to the chain after one domain has unfolded and the chain force starts increasing nonlinearly with monotonic stretching again. The dashed lines showing another level of force drop correspond to a lower extension rate. The inset of the plot shows how the peak force of unfolding changes with extension rate (Schematic adapted from [1]).

Arslan and Boyce model predicts the membrane stress-strain behavior based on the force-extension behavior of the constituent chains and the triangulated network geometry. Arslan and Boyce also identified the roles of both chain rotation and chain stretching to the nonlinear stress-strain behavior of the network by examining networks with linear chain behavior in comparison to networks with nonlinear chain behavior. In this paper, the Arslan and Boyce constitutive model for the spectrin network is enhanced to take into account the unfolding behavior of the constituent chains.

3 Constitutive Model

In recent years, several investigations have adopted and extended the framework of statistical mechanics based models for rubber elasticity (e.g., Flory [12], Treloar [13], Boyce and Arruda [14]) to develop microstructurally-motivated models of biological materials (e.g., Bischoff et al. [15,16], Bergstrom and Boyce [17], Holzapfel [18], Qi, et al. [19,20], Arslan and Boyce [6,21], Kuhl, et al. [22]). Our constitutive model for the general membrane stress-stretch behavior of the spectrin network follows this successful methodology [6]. Indeed, a recent review paper [23] highlights the need and the trend for models of the behavior of the various molecular networks of biological cells to properly account for the translation of the macroscopic strain to the constituent elements of these networks. The Arslan and Boyce model for the finite deformation of triangulated networks is reviewed and extended below in terms of (1) identification of the networked microstructure and the mapping of macroscopic deformation onto the corresponding network representative volume element (RVE); (2) description of the force-extension behavior of the RVE constituent chains together with a transition-state unfolding criterion; and (3) construction of a strain energy density function for the network and its corresponding macroscopic stress-stretch behavior.

3.1 Network Idealization, Representative Volume Element, and Deformation. The spectrin network of the red blood cell is found to possess a triangulated network as shown in the micrographs of spread cell membranes (e.g., [24,25]). We note that the "spread" state of the membrane is a highly biaxially stretched state; the triangulated network structure is in tact under these large deformations showing the robustness of the crosslink sites to mechanical deformation. Hence, as in [6], we idealize the microstructure to be perfectly triangulated as shown in Fig. 2. A unit equilateral triangle is identified as the RVE (Fig. 2(*c*)). Voronoi tessellation is used to assess the area affiliated with the RVE (Fig. 2(*a*)). Therefore the chain density of the network is found to be $\upsilon = 3/2A_{\text{triangle}}$. A schematic of the undeformed RVE is given in Fig. 2(*c*), where r_o is the initial chain end-to-end distance and ϕ_A, ϕ_B, and ϕ_C represent the orientation of the constituent chains with respect to the one-direction. In the proposed microstructurally-informed model, the change in length (the stretching of the chains) and orientation (the rotation of the chains) of the chains can be tracked with macroscopic deformation as demonstrated and discussed in Arslan and Boyce [6].

An arbitrary macroscopic deformation is mapped onto the unit cell equilateral triangle RVE. The membrane deformation gradient $\mathbf{F}_{2D}$ is defined in the 1–2 frame as

$$\mathbf{F}_{2D} = \frac{\partial \mathbf{x}}{\partial \mathbf{X}} = \begin{bmatrix} F_{11} & F_{12} \\ F_{21} & F_{22} \end{bmatrix}$$

where $\mathbf{x}$ is the deformed position of a material point and $\mathbf{X}$ is the reference position. The RVE is subjected to an arbitrary deformation gradient giving the stretch of constituent network chains A, B, C in terms of the macroscopic deformation gradient. The simplicity of the unit cell triangle RVE provides a unique, kinematically-determined mapping of the macroscopic deformation gradient to the microscopic network deformation. Denoting the current end-to-end distance of each chain as $r_i (i=A,B,C)$, the axial stretch of each chain in the network is, $\lambda_i = r_i / r_o (i=A,B,C)$ and can be expressed in terms of an arbitrary deformation gradient as demonstrated by Arslan and Boyce [6]:

$$\lambda_A = (F_{11}^2 + F_{21}^2)^{1/2}$$

$$\lambda_B = \frac{1}{2}((F_{11} - F_{12}\sqrt{3})^2 + (F_{21} - F_{22}\sqrt{3})^2)^{1/2} \tag{1}$$

$$\lambda_C = \frac{1}{2}((F_{11} + F_{12}\sqrt{3})^2 + (F_{21} + F_{22}\sqrt{3})^2)^{1/2}$$

3.2 Force-Extension Behavior of Constituent Chains. The mechanical behavior of the constituent chains (the spectrin molecules of the triangulated skeletal network of the red blood cell are long chain molecules containing many repeat units along the length of chain between crosslink sites) of the RVE (A,B,C) is

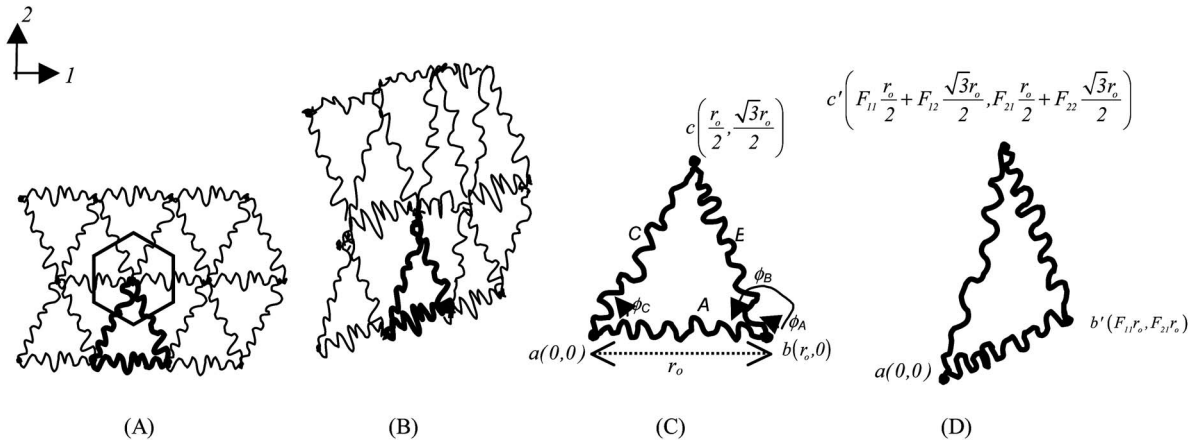

Fig. 2 Schematic of an area of the triangulated network in (*a*) the undeformed state, also depicting Voronoi tessellation (the superposed hexagon) to identify the area of the RVE, and (*b*) an arbitrary deformed state. Schematic of the isolated (*c*) undeformed representative volume element, and (*d*) the RVE when subjected to an arbitrary loading condition.

modeled using the non-Gaussian Freely Jointed Chain (FJC) model (e.g., Treloar [13]).[2] The chain force-extension expression is given by

$$P_{\text{ch}} = \frac{Nk_b\theta}{L_c}\beta \tag{2}$$

with corresponding chain strain energy,

$$\mathcal{U}_{\text{ch}} = k_b\theta N\left(\frac{r}{L_c}\beta + \ln\left(\frac{\beta}{\sinh\beta}\right)\right) \tag{3}$$

where N is the number of Kuhn segments along the chain, k_b is Boltzmann's constant, θ is the absolute temperature, $L_c=Nl$ is the contour length of the chain, l is the Kuhn segment length, r is the chain end-to-end distance, and β is the inverse Langevin function. The Langevin function is defined as $L(\beta)=\coth(\beta)-(1/\beta)$, with the inverse, $\beta=L^{-1}(r/L_C)$.

To incorporate unfolding of a folded domain in the microstructurally-informed model [6], we utilize a transition state model.

Following transition state theory, a domain can be modeled as being in one of two states: the folded state, or the unfolded state. To transfer from the folded state to the unfolded state, an energy barrier of ΔG has to be overcome. Following Rief et al. [26] and Qi et al. [20], we use the Bell [27] adaptation of the Eyring model [7]: the energy barrier to translate from one state to the other is reduced by the applied chain force, P_{ch}, multiplied by the width of the activation barrier, x_u, giving a frequency of unfolding, ω,

$$\omega(P_{\text{ch}}) = \omega_o \exp\left(\frac{-(\Delta G - P_{\text{ch}}x_u)}{k_B\theta}\right) = \alpha\exp\left(\frac{P_{\text{ch}}x_u}{k_B\theta}\right) \tag{4}$$

where k_B is Boltzmann's constant, θ is absolute temperature, and α is a lumped parameter, $\alpha=\omega_o\exp(-\Delta G/k_B\theta)$. α and x_u are then obtained from the data of peak unfolding force as a function of the strain rate. For completeness, we note that the energy barrier to unfolding depends on the particular folded domain through its molecular geometry and the nature of intermolecular interactions; the axial chain force will map to a combination of shear and normal intermolecular stresses within the domain. Hence, the unfolding of a domain will be due to some combination of normal and shear separation and will depend on how the domain is being loaded. In a long chain molecule with many domains in series, the domain most favorably oriented to unfold (i.e., the domain which will unfold at the lowest axial chain force) will be the domain to unfold; therefore, the experimentally observed unfolding force at a given rate of extension is repeatable and the effect of the chain force on lowering the energy barrier is effectively captured by Eq. (4).

After a folded domain unfolds, additional chain length is released from the fold and the contour length increases leading to an increase in the available configurational space (implying higher entropy), and a corresponding drop in the chain force. This behavior of a repeating sequence of a force rise with extension to a peak followed by a load drop, gives rise to a "sawtooth pattern" (Fig. 1). Rief et al. [4] have tested the force-extension behavior of long chain spectrin molecules at different extension rates, observing unfolding to occur at an average of ~27 pN at 0.08 μm/s and ~32 pN at 0.80 μm/s.

Prior to unfolding, the number of the effective rigid links along the chain is $N_{(t=0)}=n-m_{(t=0)}(q-1)$, where n is the total number of rigid Kuhn links, m is the number of folded domains, and q is the effective number of links of length l in a folded domain [19]. When a domain unfolds, the number of folded domains decreases by 1, giving $m_{(t=t_1)}=m_{(t=0)}-1$. After one domain unfolds, the effective number of rigid links at $t=t_1$, $N_{(t=t_1)}$ is updated according to $N_{(t=t_1)}=n-m_{(t=t_1)}(q-1)$. The contour length,$L_c$, of the molecule increases, giving a new contour length of $L_{c(t=t_1)}=N_{(t=t_1)}l$, where l is the length of the rigid links. The summary of the formulation of the procedure for force-extension with unfolding is given in Appendix A.

3.3 Strain Energy Density of the RVE. To determine the behavior of the network, the strain energy of the RVE, $\mathcal{U}$, is calculated by the summation of the strain energy in each chain. The strain energy density, $\mathcal{U}^*$ is given by

$$\mathcal{U}^* = \frac{1}{2A_{\text{triangle}}}(\mathcal{U}_A + \mathcal{U}_B + \mathcal{U}_C) \tag{5}$$

where A_{triangle} is the area of the RVE. Thus, the strain energy density is given by

$$\mathcal{U}^*_{\text{NGC}} = \frac{\upsilon}{3}\left\{k_b\theta N\sum_{i=A,B,C}\left[\frac{\lambda_i r_o}{L_c}\beta_1 + \ln\left(\frac{\beta_i}{\sinh\beta_i}\right) - \left(\frac{r_o}{L_c}\beta_o + \ln\left(\frac{\beta_o}{\sinh\beta_o}\right)\right)\right]\right\} \tag{6}$$

where υ is the chain density $(=3/2A_{\text{triangle}})$ given earlier, r_o is the

[2]We note here that these flexible molecular chains can be alternatively represented using the worm-like chain (WLC) model. Qi et al. [20] have found WLC and FJC models to give quite similar results. Therefore, we only present FJC here.

Table 1 Spectrin properties

Model parameters	Spectrin network
Initial end-to-end distance, r_o (nm)	75
Persistence length, l (nm)	10.25
Initial contour length (nm), L_o	180
Increase in contour length due to unfolding, ΔL (nm)	28.8
Activation barrier width, x_u (nm)	1.7
α ($\times 10^{-6}$ s^{-1})	6.0

initial end-to-end distance of a chain (i.e., the initial chain length or distance between cross-links), $\lambda_i (i=A,B,C)$ are the constituent chain stretches defined earlier as a function of the macroscopic deformation gradient, and $\beta_i = L^{-1}(\lambda_i r_o / L_c)$.

The Cauchy stress is determined by proper differentiation of the strain energy density function (Appendix B) and is given by

$$\mathbf{T} = \left[\frac{\partial U_A^*}{\partial \lambda_A} * \frac{\partial \lambda_A}{\partial \mathbf{F}_{2D}} + \frac{\partial U_B^*}{\partial \lambda_B} * \frac{\partial \lambda_B}{\partial \mathbf{F}_{2D}} + \frac{\partial U_C^*}{\partial \lambda_C} * \frac{\partial \lambda_C}{\partial \mathbf{F}_{2D}} \right] \mathbf{F}_{2D}^T + h\mathbf{I} \quad (7)$$

Here h is the additional equibiaxial membrane stress (due to the preservation of area constraint) required to satisfy equilibrium. The $(\partial \lambda_i / \partial \mathbf{F})$ terms are independent of chain constitutive behavior and obtained by direct differentiation of the kinematically specified relationships (Eq. (1)) connecting the stretch of each chain to the macroscopic deformation.

3.4 Material Properties. The network and chain properties for r_o, l, and L_o are found as discussed in Arslan and Boyce [6] and are given in Table 1. As discussed in [6], the initial elastic stiffness of the model with these properties captures the experimentally reported modulus for the skeletal spectrin network (as measured, for example, using cell aspiration tests). The unfolding properties consist of x_u, α, and ΔL. These properties are determined from fitting the model to the AFM data of Rief et al. [4,26] as given in [19] and therefore capture the experimentally observed dependence of unfolding force on the extension rate.

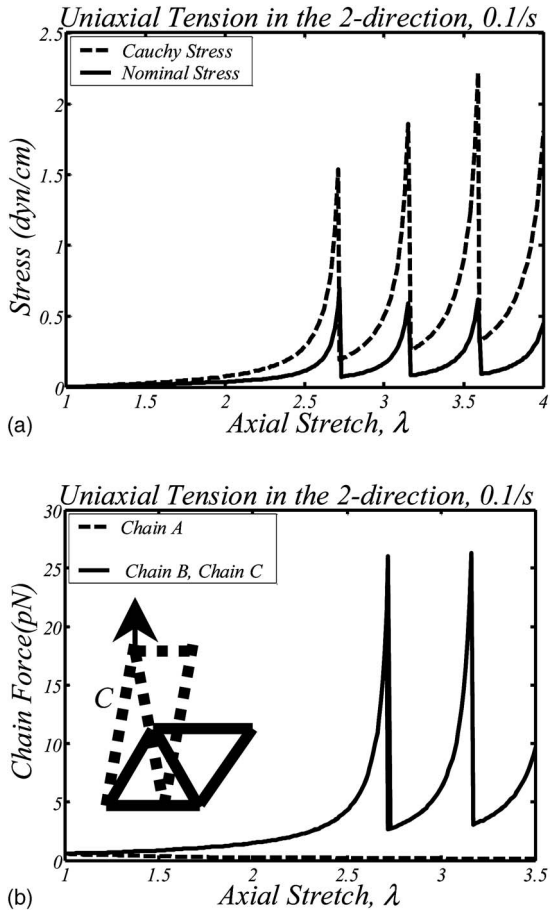

Fig. 3 (*a*) Stress-stretch behavior of the membrane under uniaxial tension in the two-direction at a strain rate of 0.1/s where Cauchy and nominal stress are compared, (*b*) constituent chain force-extension behaviors in the RVE during uniaxial tension in the two-direction

4 Results

4.1 Uniaxial Tension. Figure 3(*a*) shows the Cauchy (true) and nominal stress versus stretch behavior of the network when subjected to uniaxial tension in the two-direction. The nominal stress curve has a plateau-like peak stress region where successive unfolding events occur at a nominal peak unfolding stress of 0.5 dyn/cm. The first unfolding event happens at a stretch of $\lambda = 2.75$. In terms of the Cauchy (true) stress, the unfolding stress increases with each unfolding event due to the decrease in load-bearing area as the membrane is stretched. Once an unfolding event occurs in a constituent chain, the macroscopic stress drops due to the force drop in the chain(s). After the stress drop, the stress increases in a nonlinear manner with further extension, but now with a lower stiffness because of the increase in the compliance of the constituent chains which have experienced an unfolding event.

Figure 3(*b*) shows the constituent chain behavior during tensile stretching. Chains B and C are observed to extend and exhibit a sawtooth force-extension behavior. Chain A does not contribute to the unfolding events since it is only compressed under this applied macroscopic stretch.

Figure 4(*a*) shows the uniaxial stress versus macroscopic stretch for tension applied in different directions ranging from $\theta = 0$ deg to 30 deg. Because of the symmetry, 60 deg loading gives the same stress response as the 0 deg loading, likewise, 90 deg loading gives the same response as 30 deg loading. 0 deg loading reflects uniaxial tension in the one-direction and 90 deg loading reflects uniaxial tension in the two-direction. The sixfold symmetry of the undeformed microstructure results in isotropy of the very initial modulus. A nearly direction-independent behavior is shown to be retained up to rather large stretches ($\lambda = 2.2$), showing the isotropic robustness of the triangulated microstructure. However, at very large stretch values the developing anisotropy begins to manifest itself. The first unfolding event occurs at a smaller macroscopic stretch when uniaxial tension is applied at 0 deg than in the 30 deg case. This shows that the number of unfolding events and the degree of deformation is dependent on the loading direction as the sixfold symmetry condition does not hold at larger stretches due to the developing microstructural anisotropy as captured naturally in the microstructurally-informed constitutive model. In actual networks, there exists some irregularities in the network structure which may lead to ongoing load and deformation redistribution within the network (and isotropy to larger stretches) as macroscopic stretching increases, especially when unfolding begins to occur in some chains.

In order to achieve a stress-stretch curve that represents the red blood cell membrane behavior more accurately, a Taylor averaging approach [30] is used. As a first approximation, to account for a slightly irregular triangulated network, we "average" the behavior of constituent unit triangles inclined at 0 deg, 10 deg, 20 deg, and 30 deg with the one-direction. It is assumed that each con-

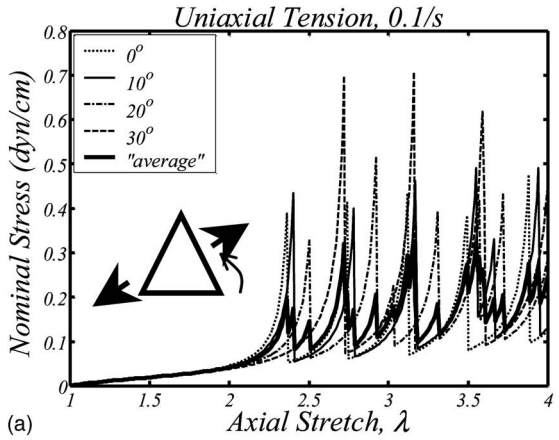

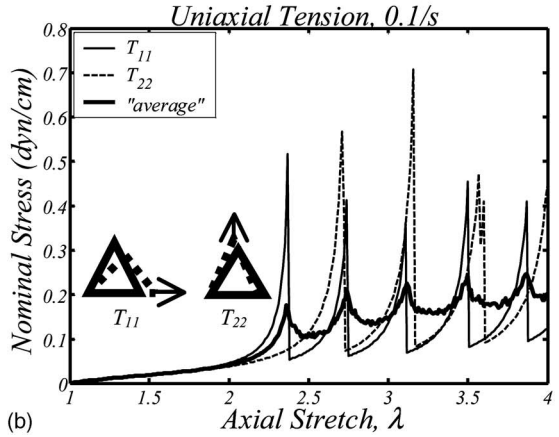

Fig. 4 Stress-stretch behavior of the membrane under uniaxial tension (*a*) in a range from 0 deg to 30 deg loading, depicting the mean stress; (*b*) in the 11- and the 22-directions, the "average" curve depicting the macroscopic composite stress behavior

stituent triangle experiences the same deformation gradient, $\mathbf{F}$.[3] Based on this assumption, the individual Cauchy stress, $\mathbf{T}$, of each constituent triangle is calculated as described earlier and the macroscopic composite stress is calculated by taking a volume average of the stress from all constituent triangles. The "average" curve in Fig. 4(*a*) depicts the mean of the stress response for directions: 0 deg, 10 deg, 20 deg, and 30 deg. The dramatic sawtooth response obtained for a perfectly triangulated structure is observed to smooth out to a behavior with lower peaks and lower drops. In order to achieve an even more precise and smoothened stress-stretch response, the macroscopic composite stress was ascertained by calculating the average response for a network comprised of unit triangles whose orientation varied in 1 deg intervals; see the "average" curve shown in Figure 4(*b*). The numerous distributed orientations of the chains in the network result in a plateau-like force behavior in contrast to the "sawtooth" pattern of the perfectly triangulated network. This plateau corresponds to simultaneous chain stretching and domain unfolding events taking place in different chains in the rather irregular network. The unfolding peaks and drops are contained within a stress band of mild-fluctuations. This plateau-like behavior gives compliance to

[3]We recognize that the Taylor approach does not capture the ongoing interplay of local load and deformation redistributions on the network chains that an actual irregular structure experiences, but feel this first approach to averaging illustrates the basic influence of a more complex triangulated network structure on the overall macroscopic stress-strain behavior.

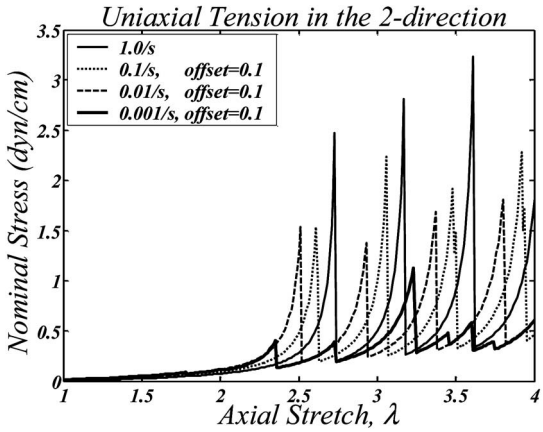

Fig. 5 The strain-rate dependence of the nominal stress-stretch behavior of the membrane under uniaxial tension in the two-direction

the network that enables large scale deformations at nearly constant stresses.

Figure 5 shows the strain-rate dependence of the stress-stretch behavior under large stretches for strain rates from I/s to as low as $0.001/s$. When the strain-rate decreases, the stretch at which the unfolding occurs drops, the peak stress decreases, and the stress drop decreases. The decrease in the peak stresses and the stress drops also leads to a plateau-like stress level at very low strain rates which limits and controls the level of force required for large deformations.

The initial end-to-end distance $r_o=75$ nm implies a pretension in the network [6,20]. Figure 6 compares the effect of two different initial end-to-end distances (75 nm, 125 nm) on the uniaxial tensile response of the network. When the initial end-to-end distance is taken to be 125 nm (an initial chain end-to-end distance close to the initial contour length of the chain), the areal chain density decreases which would normally be associated with a decrease in modulus. However, the fact that $r_o=125$ nm is close to the contour length gives an increase in the initial modulus and a decrease in the extensibility of the network; the unfolding events are found to initiate at much lower stretch levels. Hence we can see that network pretension strongly influences the overall mechanical behavior.

4.2 Simple Shear. Figure 7(*a*) shows the shear stress versus nominal shear strain, $\tan\gamma$, behavior of the network at a shear rate of 0.1 rad/s. We note that the curves of shear stress in the 12- and

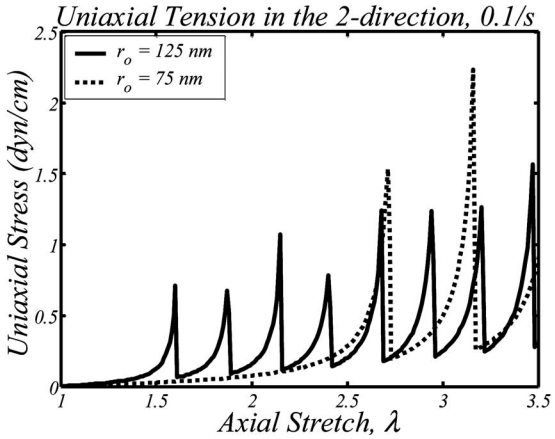

Fig. 6 Effect of pretension on the uniaxial stress-stretch behavior

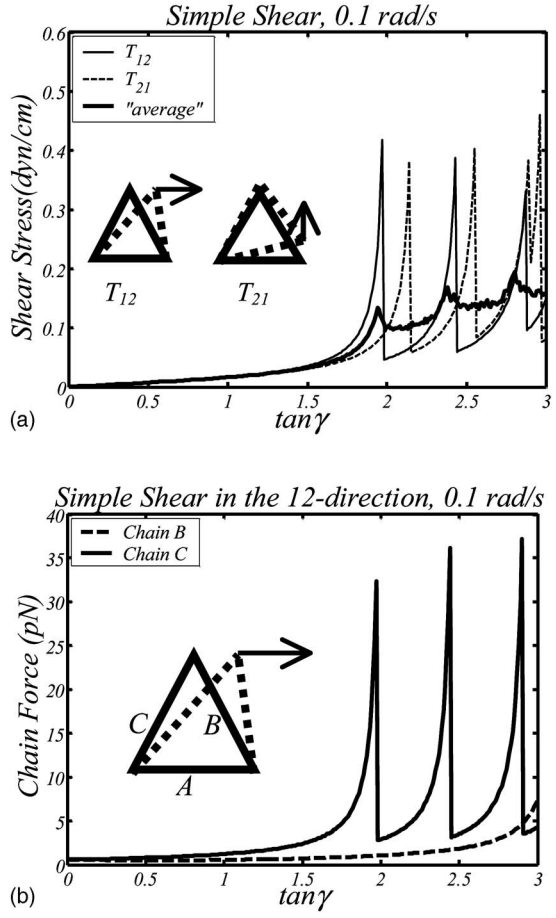

Fig. 7 (*a*) Stress-stretch behavior of the membrane under simple shear in the 12-direction and in the 21-direction, the "average" curve depicting the macroscopic composite stress behavior; (*b*) chain force-extension behavior in the RVE under simple shear in the 12-direction

the 21-direction are nearly coincident upto a shear strain of $\tan\gamma=1.5$, demonstrating the robustness of this triangulated microstructure in providing isotropic mechanical behavior to relatively large strains. At a shear rate of 0.1 rad/s, when shear is applied in the 12-direction, the first unfolding happens at $\tan\gamma=1.97$, while for shear in the 21-direction, the first unfolding occurs at $\tan\gamma=2.2$. The shear strains at which the network experiences initial unfolding is very close for shearing in different directions. Figure 7(*a*) also shows the macroscopic composite shear stress versus stretch behavior calculated following the Taylor averaging approach as discussed in the case of uniaxial tension where we average over 1 deg increments between 0 deg and 30 deg. The averaging is seen to result in the plateau-like behavior once a critical unfolding stress is reached.

Figure 7(*b*) shows the chain force versus macroscopic stretch for shearing in the 12-direction. When shear is applied in the 12-direction, only chains B and C deform, stretching and rotating with the deformation. Chain B compresses until it makes an angle of $\theta_B=90$ deg with the 1-direction, it then extends. This delayed extension results in chain C initiating the unfolding in the overall RVE. Therefore, the shear stress-shear strain plot shows an initial unfolding behavior which is identical to chain C's unfolding behavior.

5 Summary

The mechanical behavior of the red blood cell membrane is governed by the lipid bilayer which resists changes in surface area and the underlying spectrin network which resists changes in shape. The constituent chains of the spectrin network consist of a series of domains along the chain, which exhibit noncovalent interactions. Unfolding of these folded domains can be triggered by the application of large deformation to the macromolecular network, depending on the extension rate and also the statistical distribution of the strength of the internal bonds of the module. The force-extension behavior of a single modular macromolecule exhibits a "sawtooth" pattern due to unfolding giving a sequence of force rise to a peak followed by a load drop, rise to a peak and drop, etc. A microstructurally informed continuum level constitutive model which tracks individual chain deformation behavior as well as the overall macroscopic network stress-strain behavior is developed by Arslan and Boyce [6]. In this paper, using the introduced continuum approach together with single molecule force-extension behavior and a transition state model of unfolding, large deformation behavior of two-dimensional triangulated networks of biomacromolecules is studied. Uniaxial tension and simple shear behaviors of the membrane are simulated incorporating the unfolding of the individual chains. The constituent chains of the representative volume element (RVE) of the idealized network do not unfold at the same time since the stretch (and force) in each chain is different depending on the macroscopic deformation. The triangulated network provides a more realistic approach to modeling the spectrin network than the "four chain" network representation [20] of macromolecular membranes since it directly accounts for the network geometry. The triangulated structure is found to be rather robustly isotropic in mechanical behavior to very large stretches. However, the individual chain deformations evolve much differently and each molecule unfolds at different stretch levels during a macroscopic deformation which amplifies the effect of developing anisotropy on the mechanical response of the network. In actual networks, there exists some irregularities in the network structure which may provide additional robustness to isotropy as macroscopic stretching increases since the load and deformation will redistribute amongst the network molecules. In order to account for the irregularities in the spectrin network structure, a Taylor model approach is used as a first approximation for averaging, whereby the same deformation gradient is applied to RVEs with different initial orientations and the resulting stress is the volume average of the stress on each RVE. It is found that the distribution in the orientations of RVEs result in a rather plateau-like stress-stretch response after reaching a critical stress level that initiates the first unfolding event; the plateau is due to the multitude of unfolding events occurring at different stretch levels balanced by ongoing force increases in other chains. The plateau controls the level of stress required for the deformation of the red blood cell membrane. Therefore, the averaging approach gives a first approximation of the stress-strain response of the red blood cell membrane accounting for aspects of distributions in the network structure. The effect of the strain rate on the mechanical response is also investigated in this paper. When the strain rate is as low as 0.001/s, the stress peaks and drops become less apparent due to the decrease in the critical stress level needed to initiate unfolding as the rate is reduced; the predicted network rate dependence is strongly dependent on the rate-dependence of single molecule unfolding for which there is currently limited data [4,5].

Acknowledgment

This research was supported by the U.S. Army through the Institute for Soldier Nanotechnologies, under Contract No. DAAD-19-02-D0002 with the U.S. Army Research Office.

Appendix A: Procedure for Force-Extension With Unfolding

The Monte Carlo algorithm used to model the random unfolding events can be summarized as follows:

1. A chain is subject to a stretch and its force at that stretch is determined using the FJC model of Eq. (2);
2. The unfolding frequency is calculated using Eq. (4);
3. The probability of unfolding a domain is calculated according to $dp = m_t \omega \Delta t$, where m_t is the number of folded domains in the chain at time t;
4. The domains are sampled to determine their unfolding status;
5. If unfolding occurs, the contour length L_0 of the chain is updated and the force on that chain is recomputed using its new, updated structural parameters;
6. The steps are repeated where the macroscopic stretch is incrementally increased in each step.

Rief et al. [26] and Qi et al. [20] applied the Monte Carlo simulation algorithm to various molecules including dextran and spectrin to model the single molecule unfolding.

Appendix B: Formulation of Macroscopic Membrane Stress-Strain Relationship

$\mathcal{U}^*$, the strain energy density function, is defined to be a function of $\boldsymbol{F}$, the membrane deformation gradient and the number of effective rigid links along the chain, N,

$$\mathcal{U}^* = \mathcal{U}^*(\boldsymbol{F}, N) \tag{B1}$$

Following the approach taken by Holzapfel [28], Qi and Boyce [20,29], from the Second Law of Thermodynamics, the Clausius-Planck inequality for an isothermal process is written as

$$\boldsymbol{T}_o \cdot \dot{\boldsymbol{F}} - \dot{\mathcal{U}}^* \geq 0 \tag{B2}$$

where, $\boldsymbol{T}_o$ is the first Piola Kirchhoff stress.

Following (B1), the derivative of the strain energy density function gives

$$\dot{\mathcal{U}}^* = \frac{\partial \mathcal{U}^*}{\partial \boldsymbol{F}} \cdot \dot{\boldsymbol{F}} + \frac{\partial \mathcal{U}^*}{\partial N} \dot{N} \tag{B3}$$

Using (B3) and rearranging (B2),

$$\left(\boldsymbol{T}_o - \frac{\partial \mathcal{U}^*}{\partial \boldsymbol{F}} \right) \cdot \dot{\boldsymbol{F}} - \frac{\partial \mathcal{U}^*}{\partial N} \dot{N} \geq 0 \tag{B4}$$

For an arbitrary deformation,

$$\boldsymbol{T}_o = \frac{\partial \mathcal{U}^*}{\partial \boldsymbol{F}}, \tag{B5}$$

and

$$-\frac{\partial \mathcal{U}^*}{\partial N} \dot{N} \geq 0 \tag{B6}$$

For an incompressible material, Eq. (B5) gives the first Piola Kirchhoff stress and the Cauchy stress is then found to be

$$\boldsymbol{T} = \frac{\partial \mathcal{U}^*}{\partial \boldsymbol{F}} \boldsymbol{F}^T - p\boldsymbol{I}$$

Inequality (B6) shows that unfolding a domain is a dissipative process.

References

[1] Rief, M., Gautel, M., Oesterhelt, F., Fernandez, J. M., and Gaub, H. E., 1997, "Reversible Unfolding of Individual Titin Immunoglobulin Domains by AFM," Science, **276**, pp. 1109–1112.

[2] Oberhauser, A. F., Marszalek, P. E., Erickson, H. P., and Fernandez, J. M., 1998, "The Molecular Elasticity of the Extracellular Matrix Protein Tenascin," Nature (London), **393**, pp. 181–185.

[3] Fisher, T. E., Oberhauser, A. F., Carrion-Vazquez, M., Marszalek, P. E., and Fernandez, J. M., 1999, "The Study of Protein Mechanics With the Atomic Force Microscope," TIBS, **24**, pp. 379–384.

[4] Rief, M., Pascual, J., Saraste, M., and Gaub, H. E., 1999, "Single Molecule Force Spectroscopy of Spectrin Repeats: Low Unfolding Forces in Helix Bundles," J. Mol. Biol., **286**, pp. 553–561.

[5] Law, R., Carl, P., Harper, S., Dalhaimer, P., Speicher, D., and Discher, D. E., 2003, "Cooperativity in Forced Unfolding of Tandem Spectrin Repeats," Biophys. J., **84**, pp. 533–544.

[6] Arslan, M., and Boyce, M. C., 2005, "Constitutive Modeling of the Finite Deformation Behavior of Membranes Possessing a Triangulated Network Microstructure," J. Appl. Mech., **73**, pp. 536–543.

[7] Eyring, H., 1936, "Viscosity, Plasticity and Diffusion as Examples of Absolute Reaction Rates," J. Chem. Phys., **4**, pp. 283–291.

[8] Evans, E. A., 1973, "A New Material Concept for the Red Cell Membrane," Biophys. J., **13**, pp. 926–940.

[9] Skalak, R., Tozeren, A., Zarda, R. P., and Chien, S., 1973, "Strain Energy Function of Red Blood Cell Membranes," Biophys. J., **13**, pp. 245–264.

[10] Dao, M., Lim, C. T., and Suresh, S., 2003, "Mechanics of the Human Red Blood Cell Deformed by Optical Tweezers," J. Mech. Phys. Solids, **51**, pp. 2259–2280.

[11] Mills, J. P., Qie, L., Dao, M., Lim, C. T., and Suresh, S., 2004, "Nonlinear Elastic and Viscoelastic Deformation of the Human Red Blood Cell With Optical Tweezers," Mech. Chem. Biosyst., **1**, pp. 169–180.

[12] Flory, P. J., 1953, *Principles of Polymer Chemistry*, Cornell University Press, Ithaca, NY.

[13] Treloar, L. R. G., 1958, *The Physics of Rubber Elasticity*, Clarendon, Oxford.

[14] Boyce, M. C., and Arruda, E. M., 2000, "Constitutive Models of Rubber Elasticity: A Review," Rubber Chem. Technol., **73**, pp. 504–523.

[15] Bischoff, J. E., Arruda, E. M., and Grosh, K., 2002, "Orthotropic Hyperelasticity in Terms of an Arbitrary Molecular Chain Model," J. Appl. Mech., **69**, pp. 198–201.

[16] Bischoff, J. E., Arruda, E. M., and Grosh, K., 2002, "A Microstructurally Based Orthotropic Hyperelastic Constitutive Law," J. Appl. Mech., **69**, pp. 570–579.

[17] Bergstrom, J., and Boyce, M. C., 2001, "Deformation of Elastomeric Networks: Relation Between Molecular Level Deformation and Classical Statistical Mechanics Models of Rubber Elasticity," Macromolecules, **34**(3), pp. 614–626.

[18] Holzapfel, G. A., 2002, "Structural and Numerical Models for the (Visco)elastic Response of Arterial Walls With Residual Stresses," *Biomechanics of Soft Tissue in Cardiovascular Systems* (CISM Courses and Lectures, International Centre for Mechanical Sciences), G. A. Holzapfel and R. W. Ogden, eds., Springer-Verlag, Wien.

[19] Qi, H. J., Ortiz, C., and Boyce, M. C., 2005, "Protein Forced Unfolding and its Effect on the Finite Deformation Stress-Strain Behavior of Biomacromolecular Solids," Mater. Res. Soc. Symp. Proc., **874**, pp. L.4.3.1–L.4.3.6.

[20] Qi, H. J., Ortiz, C., and Boyce, M. C., 2006, "Constitutive Model for the Stress-Strain Behavior of Biomacromolecular Networks Containing Folded Domains," ASME J. Eng. Mater. Technol., **128**, pp. 509–518.

[21] Arslan, M., Boyce, M. C., Qi, H. J., and Ortiz, C., 2005, "Constitutive Modeling of the Stress-Stretch Behavior of Biological Membranes Containing Folded Domains," Mater. Res. Soc. Symp. Proc., **898**, pp. L14-05.

[22] Kuhl, E., Garikipati, K., Arruda, E. M., and Grosh, K., 2005, "Remodeling of Biological Tissue: Mechanically Induced Reorientation of a Transversely Isotropic Chain Network," J. Mech. Phys. Solids, **53**(7), pp. 1552–1573.

[23] Bausch, A. R., and Kroy, K., 2006, "A Bottom-Up Approach to Cell Mechanics," Nat. Phys., **2**, pp. 231–238.

[24] Liu, S., Derick, L. H., and Palek, J., 1987, "Visualization of the Hexagonal Lattice in the Erythrocyte Membrane Skeleton," J. Cell Biol., **104**, pp. 527–536.

[25] Byers, T. J., and Branton, D., 1985, "Visualization of the Protein Associations in the Erythrocyte Membrane Skeleton," Proc. Natl. Acad. Sci. U.S.A., **82**, pp. 6153–6157.

[26] Rief, M., Fernandez, J. M., and Gaub, H. E., 1998, "Elastically Coupled Two-Level Systems as a Model for Biopolymer Extensibility," Phys. Rev. Lett., **81**, pp. 4764–4767.

[27] Bell, G. I., 1978, "Models for the Specific Adhesion of Cells to Cells," Science, **200**, pp. 618–627.

[28] Holzapfel, G. A., 2000, *Nonlinear Solid Mechanics: A Continuum Approach for Engineering*, Wiley, New York.

[29] Qi, H. J., and Boyce, M. C., 2004, "Constitutive Model for Stretch-Induced Softening of the Stress-Stretch Behavior of Elastomeric Materials," J. Mech. Phys. Solids, **52**, pp. 2187–2205.

[30] Taylor, G. I., 1938, "Plastic Strain in Metals," J. Inst. Met., **62**, pp. 307–324.

Bryan Eisenhower
Student
Department of Mechanical and Environmental Engineering,
University of California,
Santa Barbara, CA

Gregory Hagen
Senior Researcher

Andrzej Banaszuk

United Technologies Research Center,
411 Silver Lane,
East Hartford, CT 06108

Igor Mezić
Professor
Department of Mechanical and Environmental Engineering,
University of California,
Santa Barbara, CA

Passive Control of Limit Cycle Oscillations in a Thermoacoustic System Using Asymmetry

In this paper we investigate oscillations of a dynamical system containing passive dynamics driven by a positive feedback and how spatial characteristics (i.e., symmetry) affect the amplitude and stability of its nominal limit cycling response. The physical motivation of this problem is thermoacoustic dynamics in a gas turbine combustor. The spatial domain is periodic (passive annular acoustics) which are driven by heat released from a combustion process, and with sufficient driving through this nonlinear feedback a limit cycle is produced which is exhibited by a traveling acoustic wave around this annulus. We show that this response can be controlled passively by spatial perturbation in the symmetry of acoustic parameters. We find the critical parameter values that affect this oscillation, study the bifurcation properties, and subsequently use harmonic balance and temporal averaging to characterize periodic solutions and their stability. In all of these cases, we carry a parameter associated with the spatial symmetry of the acoustics and investigate how this symmetry affects the system response. The contribution of this paper is a unique analysis of a particular physical phenomena, as well as illustrating the equivalence of different nonlinear analysis tools for this analysis.
[DOI: 10.1115/1.2745399]

1 Introduction

Thermoacoustic instabilities in gas turbines develop when acoustics in a combustor couple with an unsteady heat-release in a positive feedback loop. Thermoacoustic modeling and control is well-studied for axially extended combustion chambers, as in [1–4], where the acoustic to heat-release coupling is dominated by longitudinal acoustic modes. Because different instability regimes occur at different operating conditions, recent attention has focused on thermoacoustic modeling in combustion chambers with annular, or cylindrical geometries [5–9].

Control of thermoacoustic oscillations is a rich field due to the complexity of the dynamics as well as the prominence of both land and air-based jet engines. These high-energy devices operate in a wide range of operating conditions, all of which are highly nonlinear due to turbulence, combustion, and other extreme conditions. The oscillations lead to compromised performance, high noise levels, or catastrophic engine damage. Current control means (see [10]) include avoiding operating conditions which exhibit large oscillations, and introduction of additional dissipation including acoustic dampers or resonators [11], or in some cases active feedback control [12–14]. The first option is detrimental in terms of marketing/engine use while redesign using dampers and resonators takes time and adds weight. Active control is challenging due to actuator limitations including harsh conditions, high temporal frequencies, and the limited amount of control authority a finite number of actuators offers.

With these limitations in mind, any approach that opens the operating envelope, and does not add weight or significant complexity and redesign is a valuable solution. In this paper we study such a solution; introducing precise spatial variations (asymmetry) in a specific mean property of the dynamics which directly affects the amplitude of limit cycle oscillations.

Approaches to analyze thermoacoustic oscillations are abundant, ranging from complex CFD simulation to reduced order analysis. The reduced order analysis often includes spatial approximation of the first principle dynamics resulting in a system of ordinary differential equations. This spatial approximation can be performed many ways including an *elementwise* approach or by a modal decomposition. If a modal approach is used, the model is often of very low order (since the thermoacoustic instability is typically tied predominantly to one or two acoustic modes) while if the element approach is used, the ODE system will result in numerous coupled oscillators. We mention this here because although our approximation in this study is modal, resulting in two coupled modes (oscillators), the tools used here align with those used in to study synchronized aspects of multiple coupled oscillators.

The organization of this paper is as follows: we begin by developing a reduced model of the dynamics starting with first principles. The equilibrium of this model is then investigated using numerical bifurcation analysis tools. Following this, the periodic equilibria are determined using two methods, averaging, and harmonic balance. The results of these two methods are compared and the limit cycle properties are investigated using both approaches illustrating that altering the symmetry in a specific parameter always reduces the limit cycle amplitude and eventually stabilizes the system. It is also shown that the oscillations during this imposed asymmetry remain stable.

2 Modeling

In this section we briefly describe the thermoacoustic model used in the current analysis. In an annular combustion system, flow passes down the length of an annulus, and is eventually mixed with fuel. When this mixture reaches a series of flames distributed around this annulus, it reacts/combusts. This combustion process both reacts to the acoustics (i.e., how the acoustics bring the fuel mixture to the flame), while at the same time it drives the acoustics with its heat release. Figure 1 presents a schematic of the annular combustor and feedback interconnection between the acoustics and heat release.

The fundamental structure and justification of all assumptions of the transport equations for this system is available in the works of Culick (e.g. [15]). The transport equations are

Contributed by Applied Mechanics Division of ASME for publication in the JOURNAL OF APPLIED MECHANICS. Manuscript received November 6, 2006; final manuscript received February 15, 2007; published online February 6, 2008. Review conducted by Robert M. McMeeking.

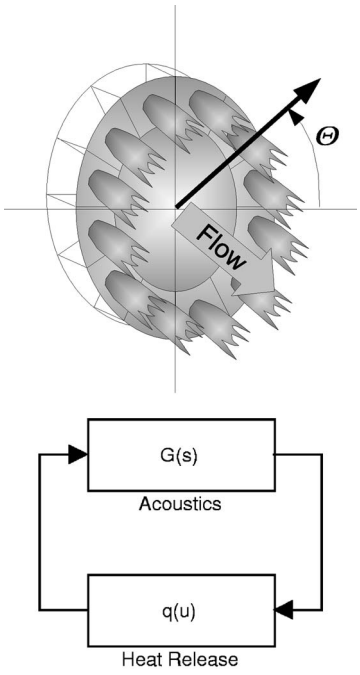

Fig. 1 Schematic of the annular domain with the first pair of Fourier modes

$$\frac{\partial \rho}{\partial t} + \nabla \cdot (u\rho) = 0 \tag{1}$$

$$\rho \frac{\partial u}{\partial t} + \rho u \cdot \nabla u = -\nabla p \tag{2}$$

$$\rho \frac{\partial e}{\partial t} + \rho u \cdot \nabla e = -p\,\nabla \cdot u + q \tag{3}$$

where ρ, u, and e are density, velocity, and internal energy per unit volume, p, and q are pressure and a volumetric heat release contribution and the spatial Laplacians describe cylindrical coordinates.

Using a series of assumptions relating to the boundary conditions which can be found in [19] results in a pair of partial differential equations on the annular domain,

$$\frac{\partial u_\Theta}{\partial t} = -a^2 \frac{\partial p}{\partial \Theta} \tag{4}$$

$$\frac{\partial p}{\partial t} + \frac{\partial u_\Theta}{\partial \Theta} = -\zeta p + q \tag{5}$$

where Θ is the spatial rotational coordinate, ζ is a damping constant, a is the acoustic wavespeed, and q is a driving heat release mechanism.

2.1 Heat Release. Equations (4) and (5) are self-contained with the exception of the heat release function. The form of the heat release function (q) is the driving component in the feedback loop. Because of the complexity of combustion dynamics, harsh conditions, high noise levels, and lack of adequate sensing apparatus, an analytical form is not yet available. The heat released from combustion is most frequently modeled as a function of acoustic velocity that contains a *saturation-like* quality as in [1,3,16–18]. With this in mind we denote the heat release contribution as

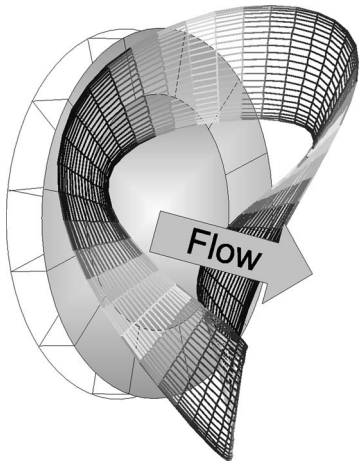

Fig. 2 Schematic representation of the spectral modes of the annular combustor

$$q = \sigma[u] + \alpha[u^3] \tag{6}$$

where σ is a linear destabilizing effect, and α is a parameter that introduces the limiting effect ($\alpha < 0$ is chosen).

2.2 Asymmetry Parameter. Prior to discretizing the equations into a modal representation, the acoustic wavespeed is parameterized to have a spatial preference. A perturbation is added to the wavespeed in the form of the second spatial harmonic. The reason for this choice is that using linear analysis in a previous study [19], it was found that altering the wavespeed in this pattern effected the stability the most. The resulting spatially perturbed acoustic wavespeed is

$$a = a_0 + \sqrt{2}\delta \cos(2\Theta) \tag{7}$$

where a_0 is a nominal wavespeed and δ is the asymmetry parameter with second harmonic preference.

2.3 Discretization. The discretized equations are obtained by projecting the rotational coordinate onto spatial Fourier modes. The first two spatial modes are retained: $\sin(\Theta)$, $\cos(\Theta)$. A spatio-temporal response in these coordinates is

$$p(\Theta,t) = \frac{1}{\sqrt{\pi}}(p_{\sin}(t)\sin(\Theta) + p_{\cos}(t)\cos(\Theta)) \tag{8}$$

$$u(\Theta,t) = \frac{1}{\sqrt{\pi}}(u_{\sin}(t)\sin(\Theta) + u_{\cos}(t)\cos(\Theta)) \tag{9}$$

where $p_{\sin}$, $p_{\cos}$ and $u_{\sin}$, $u_{\cos}$ are the time dependent modal amplitudes which become the states of our dynamical system. A schematic of these modes on the annular domain is presented in Fig. 2.

The relative amplitude and phase of the temporal coefficients impact the presence of either standing or traveling waves. A standing wave is characterized with an amplitude that depends on position (i.e., a response that has clear nodes and antinodes), while a traveling wave retains a constant amplitude with space. These wave motions have reciprocal relations in that traveling waves can be described using combination of standing waves and vice versa [20]. We are particularly interested in traveling wave solutions and keep in mind that using $\sin(\Theta)$ and $\cos(\Theta)$ as a basis for the dynamics, a traveling wave exists when the amplitudes of the temporal coefficients are equal with a phase difference of $\pi/2$ (and solutions that are trigonometrically symmetric to this).

When using the first two Fourier modes as a basis, the cubic nonlinearity acts through the velocity component and is projected onto the modes as follows:

Table 1 Nominal parameters

a_0	ζ	σ	α	δ
1.0	0.2	0.5	−0.0018	0.0

$$q_{\sin} = \frac{\alpha}{\sqrt{\pi}}\int_0^{2\pi} \sin(\Theta)(u_{\sin}(t)\sin(\Theta) + u_{\cos}(t)\cos(\Theta))^3 d\Theta = \alpha\left(\frac{3\sqrt{\pi}}{4}u_{\sin}(u_{\sin}^2 + u_{\cos}^2)\right) \tag{10}$$

$$q_{\cos} = \frac{\alpha}{\sqrt{\pi}}\int_0^{2\pi} \cos(\Theta)(u_{\sin}(t)\sin(\Theta) + u_{\cos}(t)\cos(\Theta))^3 d\Theta = \alpha\left(\frac{3\sqrt{\pi}}{4}u_{\cos}(u_{\sin}^2 + u_{\cos}^2)\right) \tag{11}$$

and projecting the assumed modal solution onto (4) and (5) results in the system of ODEs,

$$\begin{bmatrix} \dot{u}_{\sin} \\ \dot{u}_{\cos} \\ \dot{p}_{\sin} \\ \dot{p}_{\cos} \end{bmatrix} = \begin{bmatrix} 0 & 0 & 0 & a_0^2 - \delta \\ 0 & 0 & -a_0^2 - \delta & \\ \sigma & 1 & -\zeta & 0 \\ -1 & \sigma & 0 & -\zeta \end{bmatrix} \begin{bmatrix} u_{\sin} \\ u_{\cos} \\ p_{\sin} \\ p_{\cos} \end{bmatrix} + \begin{bmatrix} 0 \\ 0 \\ \alpha\left(\frac{3\sqrt{\pi}}{4}u_{\sin}(u_{\sin}^2 + u_{\cos}^2)\right) \\ \alpha\left(\frac{3\sqrt{\pi}}{4}u_{\cos}(u_{\sin}^2 + u_{\cos}^2)\right) \end{bmatrix}$$

To get these equations in the form coupled oscillators, we take $[u_{\sin}, u_{\cos}]$ as $[x_1, x_2]$ which results in the following second order coupled nonlinear differential equations:

$$x_1'' + \zeta x_1' + (a_0^2 - \delta)x_1 = x_2(a_0^2 - \delta)\left(\sigma - \alpha\left(\frac{3\sqrt{\pi}}{4}(x_1^2 + x_2^2)\right)\right) \tag{12}$$

$$x_2'' + \zeta x_2' + (a_0^2 + \delta)x_2 = -x_1(a_0^2 + \delta)\left(\sigma + \alpha\left(\frac{3\sqrt{\pi}}{4}(x_1^2 + x_2^2)\right)\right) \tag{13}$$

From this representation, the architecture of the system becomes clear. Once projected onto the two modes, the dynamics are two stable oscillators with skew symmetric coupling due to the heat release.

For the remainder of this study, we will investigate the behavior of systems (12) and (13) specifically focusing on two parameters; σ which is the skew symmetric coupling parameter from heat release, and δ which is the asymmetry parameter. We begin by studying behavior of the global equilibrium and continue by investigating the periodic equilibria and their stability. For the analysis to follow, we will use the values in Table 1 as a set of *nominal* parameters.

3 Equilibrium Analysis

The systems (12) and (13) contain one equilibrium point at the origin, and in this section we investigate the stability of this equilibrium with respect to both the linear coupling parameter, and the asymmetry parameter. When the asymmetry parameter (δ) and coupling term (σ) are zero, evaluation of the Jacobian at the origin reveals a set of co-located stable eigenvalue pairs at $\frac{1}{2}(-\zeta \pm \sqrt{-4a_0^2 + \xi_0^2})$.

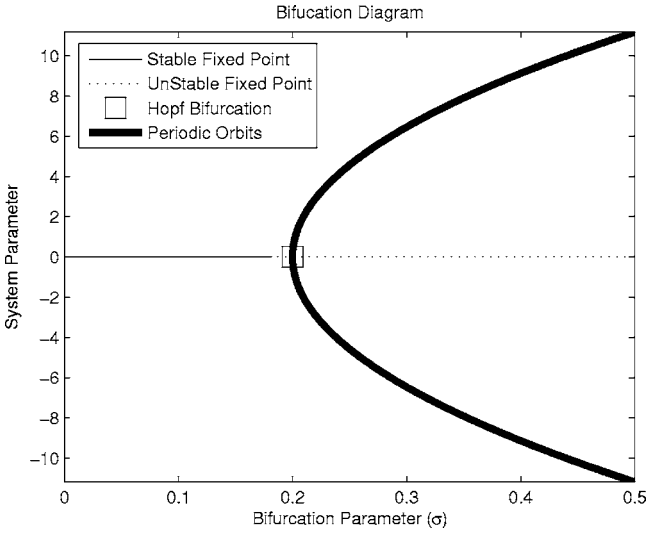

Fig. 3 Bifurcation solutions representing the destabilizing effect of the parameter σ

When the coupling is increased from zero these complex eigenvalues become

$$\lambda_{1,2} = \frac{-\zeta - \sqrt{\zeta^2 - 4a_0^2 \pm 4\sqrt{-\sigma^2 a_0^4}}}{2}$$

$$\lambda_{3,4} = \frac{-\zeta + \sqrt{\zeta^2 - 4a_0^2 \pm 4\sqrt{-\sigma^2 a_0^4}}}{2} \tag{14}$$

It is evident that with sufficiently large values of positive or negative coupling the eigenvalues break apart, moving left and right in the complex plane. Physically, the case with $\sigma=0$ represents zero combustion (the eigenvalues are purely acoustic), and the case with nonzero σ portrays the case with the driving combustion process. With sufficient heat addition, one pair of complex eigenvalues eventually crosses the imaginary axis. The value of the coupling parameter such that the eigenvalues cross the imaginary axis is,

$$\sigma_{\text{crit}} = \frac{\zeta}{a_0} \tag{15}$$

From this we see that instability occurs when the coupling from positive feedback exceeds the acoustic damping normalized by the nominal wavespeed. When the coupling from heat release is further increased the eigenvalues continue to become more unstable, the oscillations grow, and are eventually limited by nonlinearity. Figure 3 shows results from the numerical bifurcation analysis tool AUTO illustrating the Hopf bifurcation leading to instability without any modification of symmetry (the *system parameter* is oscillation amplitude).

The stabilizing effect of adding asymmetry to the combustion dynamics is performed by investigating the behavior of the system under variations of the asymmetry parameter δ. Taking a nonzero positive value for σ which insures oscillations in the dynamics, we perform eigenvalue analysis in a similar way. The results show that increasing asymmetry provides a stabilizing mechanism, and the critical value that returns the eigenvalues to the stable half of the complex plane is

$$\delta_{\text{crit}}^2 = \frac{a_0\sqrt{a_0^2\sigma^2 - \zeta^2}}{\sqrt{1 + \sigma^2}} \tag{16}$$

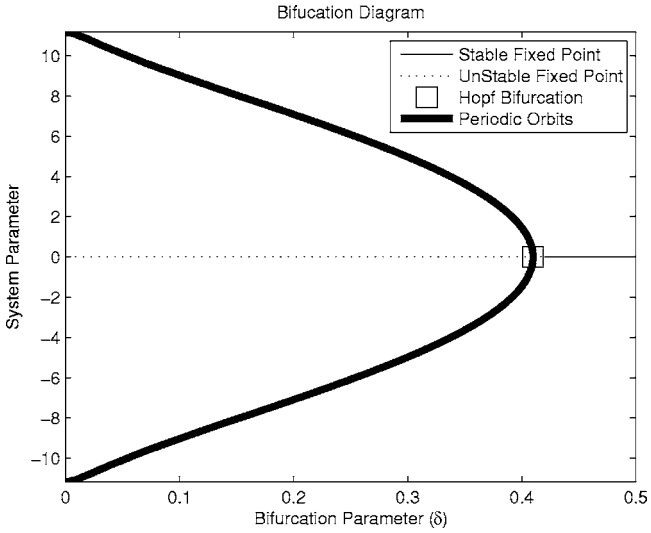

Fig. 4 Bifurcation solutions representing the stabilizing effect of the parameter δ

Similar numerical bifurcation results of the system with its symmetry altered showing its stabilizing effect are found in Fig. 4.

The focus of this study is to generate both analytical and numerical results which are similar to the schematics of Figs. 3 and 4. Specifically, we investigate the amplitude and stability of the limit cycle when $\sigma > \sigma_{\text{crit}}$ and $0 < \delta < \delta_{\text{crit}}$.

4 Periodic Solutions

To analyze the bifurcation branches and periodic behavior of the combustion system, we rely on the characteristic that the dynamics are nearly linear. The linearity of the system is addressed by rearranging the terms of the nonlinear systems (12) and (13) into a standard oscillator form and entering in the nominal parameters. The equations become

$$x_1'' + x_1 = -0.2x_1' + \delta x_1 + 0.5(-\delta + 1)x_2 + 0.0024(\delta - 1)x_1^2 x_2 + 0.0024(\delta - 1)x_2^3$$

$$x_2'' + x_2 = -0.2x_2' - \delta x_2 + 0.5(-\delta - 1)x_1 + 0.0024(\delta + 1)x_1 x_2^2 + 0.0024(\delta + 1)x_1^3 \quad (17)$$

With small variation in the asymmetry parameter δ the system remains *closely linear* in its behavior. This is also confirmed by the mostly sinusoidal response of equations from time integration (i.e., simulation with an ODE solver). Another point of interest which is evident in (17) is that the terms on the right-hand side consist of driving from heat addition and dissipation from damping in the acoustics. It is a balance of these two mechanisms that is the manifestation of the periodic response of the system.

Since the dynamics of the system appear to first order as those of a linear oscillator with small perturbation, we have a few options for the approximate analysis of the dynamics. Below we present two approaches relying on averaging (in two different coordinate systems), and harmonic balance to obtain the *slow flow* dynamics of the trajectories.

4.1 Averaging. The first approach to obtain the slow flow of Eqs. (12) and (13) includes the use of time averaging (see [21]). We perform this approximation using two different bases; polar coordinates, and using action angle variables. We show that the averaged results are identical using either approach.

The averaging approach includes making a harmonic assumption of the limit cycle response exploiting a time scale assumption on the assumed solution (i.e., variation of parameters), and integration in time (averaging). What results is the slow flow (i.e., amplitude and phase ODEs). We will investigate the equilibria of this reduced system both with and without asymmetry.

4.1.1 Averaging in Polar Coordinates. We begin by making the assumption that the response is harmonic with slowly varying amplitude and phase parameters,

$$x_i(t) = R_i(t)\cos(\omega t + \phi_i(t)) \quad (18)$$

where i relates to the two oscillators describing the amplitudes of the sine and cosine acoustic modes. For this study, we are concerned with solutions where the period of each oscillation is equal and stationary. Differentiation in time results in

$$x'(t) = -\omega R_i(t)\sin(\omega t + \phi_i(t)) - \phi_i'(t)R_i(t)\sin(\omega t + \phi_i(t)) + R_i'(t)\cos(\omega t + \phi_i(t)) \quad (19)$$

where $(.)'$ represents differentiation with respect to time. The assumption that the amplitude and phase of the assumed solution vary slowly with time reveals that their time derivative has negligible contribution to the velocity states which is equivalent to solution of the ODE using *variation of parameters* [22]. With this in mind, we assume

$$0 = -\phi_i'(t)R_i(t)\sin(\omega t + \phi_i(t)) + R_i'(t)\cos(\omega t + \phi_i(t)) \quad (20)$$

which results in the velocity state as

$$x'(t) = -\omega R_i(t)\sin(\omega t + \phi_i(t)) \quad (21)$$

The assumed solutions (18) and (21), and the time derivative of (21) are substituted into the equations of motion. Using this equation and (20) results in two equations and two unknowns for each oscillator. Isolating the time derivatives of the unknowns $(R_i'(t), \phi_i'(t))$ results in an ODE describing the slow evolution of the amplitude and phase of the limit cycle. This differential equation system will contain the parameters of the system $(\sigma, \alpha, a_0, \xi_0)$, the states of the slow flow $(R_i(t), \phi_i(t))$, and resonant terms (i.e., $\cos(\omega t)$, $\sin(\omega t)$). The next step is to remove the resonant terms by averaging over one period of oscillation. Before doing this we change the coordinates to consider relative phase variables

$$\psi_+ = \tfrac{1}{2}(\theta_1 + \theta_2)$$

$$\psi_- = \theta_1 - \theta_2$$

or

$$\theta_1 = \frac{\psi_-}{2} + \psi_+$$

$$\theta_2 = \psi_+ - \frac{\psi_-}{2} \quad (22)$$

and perform the averaging

$$\frac{d\bar{R}_i}{dt} = \frac{1}{T}\int_0^T f(R, \psi, t)dt \quad (23)$$

$$\frac{d\bar{\psi}_i}{dt} = \frac{1}{T}\int_0^T f(R, \psi, t)dt \quad (24)$$

where $T = 2\pi/\omega$, and the function $f(R, \psi, t)$ contains information from both oscillators due to the coupling, and the overbar denotes averaged quantities. The resulting system is

$$\bar{\psi}_+' = \frac{\cos(\bar{\psi}_-)(16\sigma + 9\sqrt{\pi}\alpha(\bar{R}_1^2 + \bar{R}_2^2))((\bar{R}_1 - \bar{R}_2)(\bar{R}_1 + \bar{R}_2)a_0^2 + \delta(\bar{R}_1^2 + \bar{R}_2^2))}{64a_0\bar{R}_1\bar{R}_2}$$

$$\bar{\psi}_-' = -\frac{32\delta\bar{R}_1\bar{R}_2 + \cos(\bar{\psi}_-)((a_0^2 + \delta)\bar{R}_1^2 + (a_0^2 - \delta)\bar{R}_2^2)(16\sigma + 9\sqrt{\pi}\alpha(\bar{R}_1^2 + \bar{R}_2^2))}{32a_0\bar{R}_1\bar{R}_2}$$

$$\bar{R}_1' = -\frac{16\zeta a_0\bar{R}_1 + \sin(\bar{\psi}_-)(a_0^2 - \delta)\bar{R}_2(16\sigma + 3\sqrt{\pi}\alpha(\bar{R}_1^2 + 3\bar{R}_2^2))}{32a_0}$$

$$\bar{R}_2' = -\frac{16\zeta a_0\bar{R}_2 + \sin(\bar{\psi}_-)(a_0^2 + \delta)\bar{R}_1(16\sigma + 3\sqrt{\pi}\alpha(3\bar{R}_1^2 + \bar{R}_2^2))}{32a_0} \tag{25}$$

Studying the equilibrium points of (25) reveals the amplitude and phase of the limit cycle when the limit cycle in the system exists due to sufficient heat release (i.e., $\sigma > \sigma_{crit}$). We will study these equilibria and how they are effected by assymmetry in Sec. 5.

4.1.2 Averaging in Action Angle Coordinates. To perform the averaging in action angle coordinates, we first define the canonical transformation,

$$x_1(t) = \sqrt{2J_1(t)}\cos(\theta_1(t))$$

$$x_1(t)' = \sqrt{2J_1(t)}\sin(\theta_1(t)) \tag{26}$$

$$x_2(t) = \sqrt{2J_2(t)}\cos(\theta_2(t))$$

$$x_2(t)' = \sqrt{2J_2(t)}\sin(\theta_2(t)) \tag{27}$$

where again as designated, the action and angle variables are functions of time. The second derivative in time is found from differentiation of the above relations (i.e., $x_1'' = d(x_1')/dt$) and after substituting the coordinate transforms, we have two equations and four differential variables $(J_1, J_2, \theta_1, \theta_2)$. Two additional equations are realized by the constraint equations (again from variation of parameters):

$$\frac{dx_1}{dt} = x_1'$$

$$\frac{dx_2}{dt} = x_2' \tag{28}$$

for the assumed quantities in (26) and (27).

After these substitutions, we can solve for the differential variables of the system $(J_1', J_2', \theta_1', \theta_2')$ resulting in a fourth order ordinary differential equation system. Again, we transform the phase variables to the form in Eq. (22) resulting in a differential equation system $(J_1', J_2', \psi_+', \psi_-')$. In this coordinate system, the phase variable ψ_+ acts like time and hence we average the dynamics over this variable,

$$\bar{f} = \frac{1}{2\pi}\int_0^{2\pi} f d\psi_+ \tag{29}$$

The averaged system in action angle coordinates is then

$$\bar{\psi}_+' = -\frac{16\sqrt{\bar{J}_1}\sqrt{\bar{J}_2}(a_0^2 + 1) + \cos(\bar{\psi}_-)(8\sigma + 9\sqrt{\pi}\alpha(\bar{J}_1 + \bar{J}_2))((\bar{J}_1 - \bar{J}_2)a_0^2 + \delta(\bar{J}_1 + \bar{J}_2))}{32\sqrt{\bar{J}_1}\sqrt{\bar{J}_2}}$$

$$\bar{\psi}_-' = \delta + \frac{\cos(\bar{\psi}_-)(8\sigma + 9\sqrt{\pi}\alpha(\bar{J}_1 + \bar{J}_2))((\bar{J}_1 + \bar{J}_2)a_0^2 + \delta(\bar{J}_1 - \bar{J}_2))}{16\sqrt{\bar{J}_1}\sqrt{\bar{J}_2}}$$

$$\bar{J}_1' = \frac{1}{8}\sqrt{\bar{J}_1}(\sin(\bar{\psi}_-)(a_0^2 - \delta)\sqrt{\bar{J}_2}(8\sigma + 3\sqrt{\pi}\alpha(\bar{J}_1 + 3\bar{J}_2)) - 8\zeta\sqrt{\bar{J}_1})$$

$$\bar{J}_2' = \frac{1}{8}\sqrt{\bar{J}_2}(\sin(\bar{\psi}_-)(a_0^2 + \delta)\sqrt{\bar{J}_1}(8\sigma + 3\sqrt{\pi}\alpha(3\bar{J}_1 + \bar{J}_2)) - 8\zeta\sqrt{\bar{J}_2}) \tag{30}$$

4.2 Harmonic Balance. The variable coefficient harmonic balance method provides another approximation to the limit cycle dynamics and to develop it we begin with the assumed harmonic solution (18), differentiate it as necessary, and insert it into the equations of motion (12) and (13). Similar to the use of *variation of parameters*, the coefficients of the assumed harmonic solution are considered slowly varying. Because of this, as in [23], the second order derivatives of the amplitude and phase coefficients of the assumed solution are considered negligible. By collecting the sine and cosine terms of each equation (the coefficients of the resonant terms) we obtain two differential equations for each oscillator. Similar to the slow flow system derived from averaging this ODE describes the slow evolution of amplitude and phase of the assumed solution. We may again solve for

the time derivatives of the unknown coefficients, and the equilibriums will describe the limit cycle conditions.

If we consider the resonant case, the period of oscillation will be related to the wavespeed and therefore the natural frequency of the assumed solution will equal the wave speed ($\omega = a_0$). After including this into the equations of motion, we have the slow flow system:

$$R_1' = \frac{3\sqrt{\pi}\alpha(3k2\zeta + 2k1a_0)(a_0^2-\delta)R_2R_1^2 + 16\zeta(\delta-2a_0^2)R_1 + (k2\zeta+2k1a_0)(a_0^2-\delta)R_2(9\sqrt{\pi}\alpha R_2^2+16\sigma)}{16(\zeta^2+4a_0^2)}$$

$$R_2' = -\frac{-3\sqrt{\pi}\alpha(2k1a_0-3k2\zeta)(a_0^2+\delta)R_1R_2^2 + 16\zeta(2a_0^2+\delta)R_2 - (2k1a_0-k2\zeta)(a_0^2+\delta)R_1(9\sqrt{\pi}\alpha R_1^2+16\sigma)}{16(\zeta^2+4a_0^2)}$$

$$\psi_-' = \frac{9\sqrt{\pi}\alpha(k1\zeta+2k2a_0)(a_0^2+\delta)R_1^4 + 2(3\sqrt{\pi}\alpha(6k2a_0^3+k1\delta\zeta)R_2^2 + 8\sigma(k1\zeta+2k2a_0)(a_0^2+\delta))R_1^2}{16(\zeta^2+4a_0^2)R_1R_2} + \cdots$$
$$+ \frac{64\delta a_0R_2R_1 + (2k2a_0-k1\zeta)(a_0^2-\delta)R_2^2(9\sqrt{\pi}\alpha R_2^2+16\sigma)}{16(\zeta^2+4a_0^2)R_1R_2}$$

$$\psi_+' = \frac{-9\sqrt{\pi}\alpha(k1\zeta+2k2a_0)(a_0^2+\delta)R_1^4 - 2(3\sqrt{\pi}\alpha a_0(6k2\delta+k1\zeta a_0)R_2^2 + 8\sigma(k1\zeta+2k2a_0)(a_0^2+\delta))R_1^2}{32(\zeta^2+4a_0^2)R_1R_2} + \cdots$$
$$+ \frac{32\zeta^2a_0R_2R_1 + (2k2a_0-k1\zeta)(a_0^2-\delta)R_2^2(9\sqrt{\pi}\alpha R_2^2+16\sigma)}{32(\zeta^2+4a_0^2)R_1R_2} \tag{31}$$

where $k1=\sin\psi_-$ and $k2=\cos\psi_-$.

5 Comparison of Methods and Numerical Results

In this section we compare the results of the different approximation methods. We first present the dynamics when the asymmetry parameter is set to zero (the value of the equilibria, and the associated phase space of the reduced system). A comparison is also presented for the amplitudes of the limit cycle with varying asymmetry. It is shown that the three different approximations to the full nonlinear system are in agreement with each other and that the asymmetry parameter always reduces the amplitude of the limit cycle.

5.1 Reduced Phase Space Comparison. When the asymmetry parameter is set to zero the dynamics are symmetric and therefore the amplitude of the two acoustic modes are identical. This offers a means to investigate the system on a two-dimensional plane.

For the case with averaging in polar coordinates, we let $\bar{R}_1 = \bar{R}_2 = \bar{R}$ and $\delta=0$ in Eq. (25) and obtain the reduced system,

$$\bar{\psi}_+' = 0$$

$$\bar{\psi}_-' = -\tfrac{1}{16}\cos(\bar{\psi}_-)(18\sqrt{\pi}\alpha\bar{R}^2+16\sigma)a_0$$

$$\bar{R} = -\frac{\bar{R}(12\sqrt{\pi}\alpha\bar{R}^2+16\sigma)\sin(\bar{\psi}_-)a_0^2 + 16\zeta\bar{R}a_0}{32a_0} \tag{32}$$

The equilibrium points of (32) are found by setting time derivatives to zero. The nontrivial real solutions are presented in Table 2, with the numerical substitution using the nominal parameters.

In the approximation using averaging in action angle coordinates we investigate the nominal symmetric case by letting $\bar{J}_1 = \bar{J}_2 = \bar{J}$, $\delta=0$ in the differential equation system (30). The resulting equations are

$$\bar{\psi}_+' = \tfrac{1}{2}(-a_0^2-1)$$

$$\bar{\psi}_-' = \tfrac{1}{8}\cos(\bar{\psi}_-)(8\sigma+18\sqrt{\pi}\alpha\bar{J})a_0^2$$

$$\bar{J} = \tfrac{1}{8}\sqrt{\bar{J}}(\sqrt{\bar{J}}(8\sigma+12\sqrt{\pi}\alpha\bar{J})\sin(\bar{\psi}_-)a_0^2 - 8\zeta\sqrt{\bar{J}}) \tag{33}$$

The equilibrium points of (33) are presented in Table 2. Note that the conversion of $R\approx\sqrt{2J}$ provides exact agreement in these results between averaging in polar and action angle coordinates (and the harmonic balance for that matter).

For the case where harmonic balance is utilized as an approximation, we investigate the symmetric case by letting $R_1=R_2=R$ and $\delta=0$ resulting in

$$R'(t) = \frac{Ra_0^2((9\sqrt{\pi}\alpha R^2+8\sigma)\cos(\psi_-)\zeta - 16\zeta + 4(3\sqrt{\pi}\alpha R^2+4\sigma)\sin(\psi_-)a_0)}{8(\zeta^2+4a_0^2)}$$

$$R'(t) = \frac{Ra_0^2(4(3\sqrt{\pi}\alpha R^2+4\sigma)\sin(\psi_-)a_0 - \zeta((9\sqrt{\pi}\alpha R^2+8\sigma)\cos(\psi_-)+16))}{8(\zeta^2+4a_0^2)}$$

$$\psi'_- = \frac{(9\sqrt{\pi}\alpha R^2 + 8\sigma)\cos(\psi_-)a_0^3}{2(\zeta^2 + 4a_0^2)}$$

$$\psi'_+ = \frac{\zeta a_0(4\zeta - (3\sqrt{\pi}\alpha R^2 + 4\sigma)\sin(\psi_-)a_0)}{4(\zeta^2 + 4a_0^2)} \tag{34}$$

In this system, the term ψ_+ is a decoupled nonequilibrium state that acts similar to time. Therefore we omit this differential equation and perform the steady state analysis. The nontrivial real equilibria of the symmetric system are presented in Table 2.

As seen in Table 2 there is agreement between all three approximate methods. Additionally, since the system has been reduced to a second order system, we can investigate its phase space graphically. The phase space of the averaged system (32) is presented in Fig. 5 (the phase space for all three methods is indistinguishable graphically, so for brevity we present the vector field from averaging in polar coordinates). From this, we find that the equilibrium point $\bar{R}=11.19$, $\bar{\psi}_-=-(\pi/2)$ is stable (square), while the other equilibria are unstable (star), which was confirmed by evaluation of the Jacobian at these equilibria.

5.2 Amplitude Comparisons. Now that we are familiar with the approximate systems when the asymmetry parameter is zero, we investigate the response of the limit cycle amplitude when the symmetry of the acoustic wavespeed is modified on the annular domain. In this section we provide a comparison of oscillator amplitudes (12) and (13) using three different methods including averaging in polar and action angle coordinates, as well as the harmonic balance with nonzero asymmetry. In each case, fixed points of the ordinary differential equations were found by time integration of the system of equations, retaining the final point when the dynamics have settled. In all cases, the nominal system parameters are those described in Sec. 2, while the symmetry parameter is varied as the independent variable. Figure 6 illustrates the amplitude of the limit cycle for each acoustic mode (each oscillator in (12) and (13)).

Table 2 Equilibria for the symmetric case comparing different methods (when the conversion $R\approx\sqrt{2J}$ is used, all values agree)

	Averaging (polar)	Averaging (action-angle)	Harmonic balance
Amplitude	$\bar{R}=\frac{2\sqrt{\pm\zeta-\sigma a_0}}{\pi^{1/4}\sqrt{3\alpha a_0}}$	$\bar{J}=\pm\frac{2(\zeta\mp\sigma a_0^2)}{3\sqrt{\pi}\alpha a_0^2}$	$R=\frac{2\sqrt{\pm\zeta-\sigma a_0}}{\pi^{1/4}\sqrt{3\alpha a_0}}$
	$=\{17.10, 11.19\}$	$=\{62.68,146.27\}$	$=\{17.10,11.19\}$
Phase	$\bar{\psi}_-=\pm\frac{\pi}{2},\pm\frac{\pi}{2}$	$\bar{\psi}_-=\pm\frac{\pi}{2},\pm\frac{\pi}{2}$	$\psi_-=\pm\frac{\pi}{2},\pm\frac{\pi}{2}$

In this figure, the influence of the asymmetry parameter (δ) presents an attenuating influence on the amplitudes of the oscillations ultimately quenching the response. In addition, we notice that these amplitudes decrease at different rates which occurs because when altering the symmetry of the system, the dynamics prefer one spatial mode over the other, and the corresponding state variable behaves accordingly. It is also clear that the solutions agree quite well between the original and approximate dynamics.

The above plots trace the stable solutions of the system in both its full and approximate state. We are also interested in the effect of asymmetry on the unstable solutions. In Fig. 7 we trace both the stable and unstable branches as the asymmetry is increased. For this we simply use a gradient search on the right-hand sides of the approximate differential equations (seeking zero).

This figure shows that when $\delta=0$ and $R_1=R_2$ there exists two values (11.19,17.10) corresponding to the stable and unstable equilibria. With an increase in δ the stable solution begins to decrease in amplitude (R_1 and R_2 at different rates) and eventually reaches zero. For the unstable solution which starts at 17.10 increasing δ also effects the amplitudes (at different rates) but it is evident that these solutions do not interact with the stable branch.

5.3 Orbit Stability. As we have shown, symmetry effects amplitudes while to be sufficiently applicable for engineering application, these new orbits must be stable to account for unmodeled characteristics or external influences. Therefore, it is necessary to assess the stability of the periodic solutions of this system under influence of the asymmetry to characterize the robustness of the use symmetry in the system to reduce oscillation amplitudes. To perform this analysis, the slow flow equations developed from the averaging method in action angle coordinates (30) are linearized about the stable equilibria in Fig. 7. The eigenvalues of these fixed points is presented in Fig. 8.

Figure 8 illustrates that the orbits remain stable under all conditions where the slow flow equations are valid. The behavior of these dynamics are such that all solutions are stable and real when the symmetry parameter is set to zero. Upon increasing this parameter, two eigenvalues break apart and become complex pairs. Clearly these eigenvalues are associated with the amplitude evolution dynamics (as verified by investigating the eigenvectors),

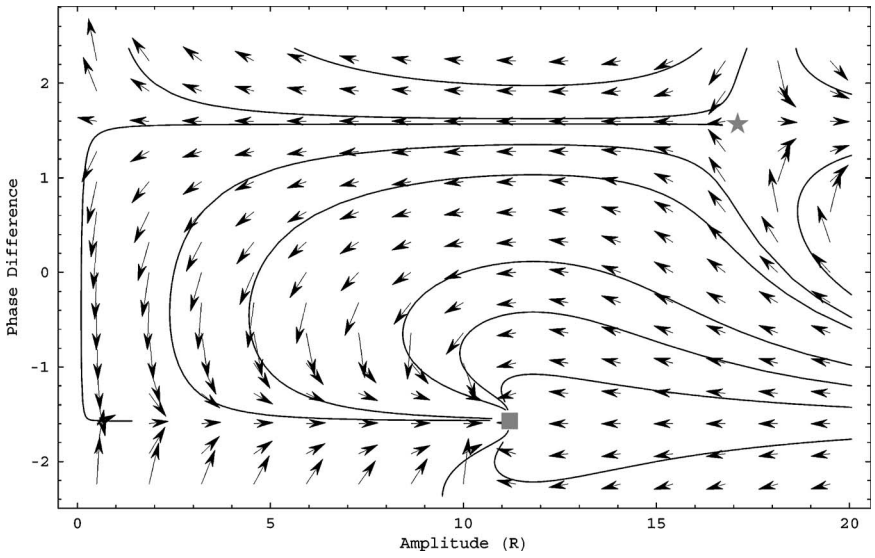

Fig. 5 Phase space of the nominally symmetric system reduced to a 2D field

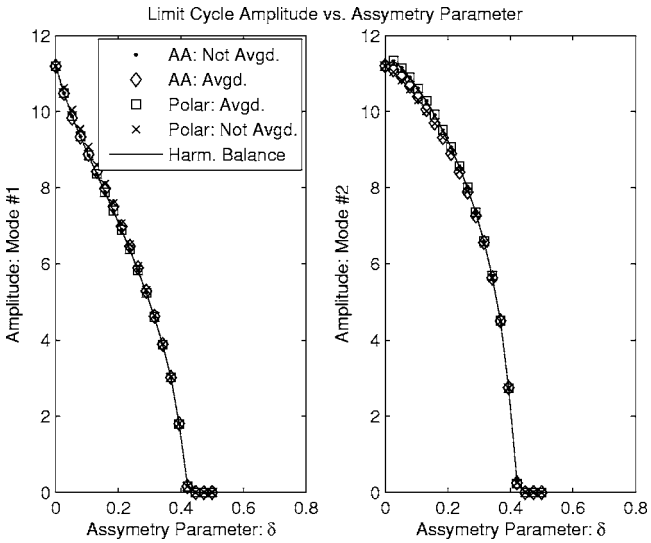

Fig. 6 Mode amplitudes as a function of the asymmetry parameter (the action angle results are scaled)

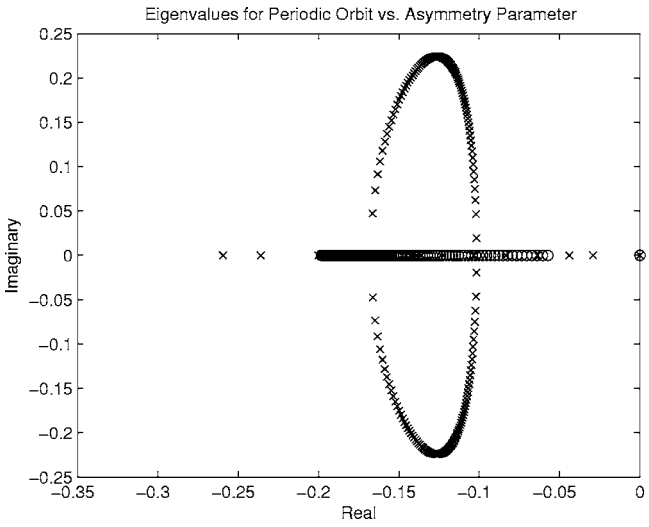

Fig. 8 Eigenvalues of the periodic orbits with the influence of asymmetry

while the third eigenvalue remains real and is associated with the differential phase between the two oscillator dynamics. This particular eigenvalue approaches instability as the amplitude equilibrium approaches zero but remains stable.

6 Summary

In this paper we have modeled thermoacoustic dynamics in an annular combustor and reduced these dynamics to a coupled oscillator system including a parameter for the spatial symmetry of the passive dynamics. We have shown that the nonlinear coupling due to heat release, always imposes an adverse effect on the system, resulting in a limit cycle exhibited by a traveling acoustic wave. We have also shown that spatial perturbation in the symmetry of the acoustic wavespeed reduces the amplitude of the limit cycle (in a stable way) eventually stabilizing the system. These results have been obtained using three different nonlinear analysis tools that in this problem yield identical results.

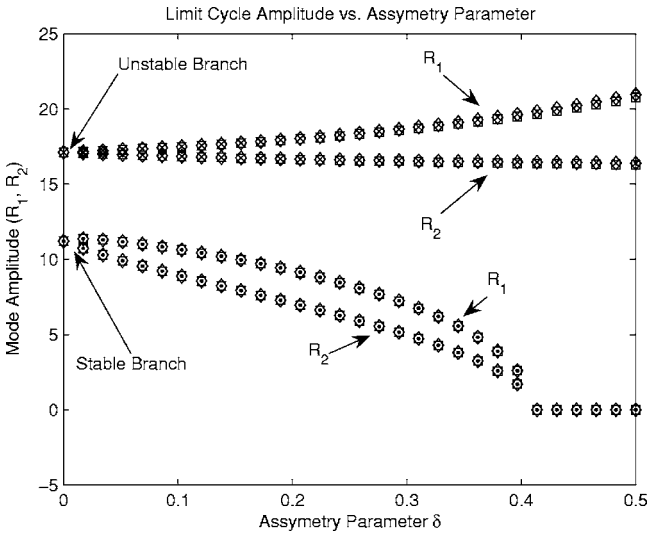

Fig. 7 Mode amplitudes as a function of the asymmetry parameter for three different approximations (note all approximations are nearly equivalent, and the action angle results are scaled)

Acknowledgment

This work was supported by AFOSR Contract No. F49620-01-C-0021, which is gratefully acknowledged. The authors would also like to thank Dr. Prashant Mehta (University of Illinois, Urbana-Champaign), Dr. Umesh Vaidya (Iowa State University), and Dr. Tamás Kalmár-Nagy (Texas A&M) for many fruitful discussions.

References

[1] Dowling, A. P., 1997, "Nonlinear Self-Excited Oscillations of a Ducted Flame," J. Fluid Mech., **346**, pp. 271–290.

[2] Fleifil, M., Annaswamy, A. M., Ghoneim, Z. A., and Ghoniem, A. F., 1996, "Response of a Laminar Premixed Flame to Flow Oscillations: A Kinematic Modal and Thermoacoustic Instability Results," Combust. Flame, **106**, pp. 487–510.

[3] Peracchio, A., and Proscia, W., 1998, "Nonlinear Heat Release/Acoustic Model for Thermoacoustic Instability in Lean Premixed Combustors," ASME Paper No. 98-GT-269.

[4] Jacobson, C. A., Khibnik, A. I., Banaszuk, A., Cohen, J., and Proscia, W., 2000, "Active Control of Combustion Instabilities in Gas Turbine Engines for Low Emissions—Part 1: Physics-Based and Experimentally Identified Models of Combustion Instability," Applied-Vehicle Technology Panel Symposium on Active Control Technology, Brauschweig, Germany, 2000.

[5] Stow, S., and Dowling, A., 2001, "Thermoacoustic Oscillations in an Annular Combustor," ASME Paper No. 2001-GT-0037.

[6] Stow, S., and Dowling, A., 2003, "Modelling of Circumferential Modal Coupling Due to Helmholtz Resonators," ASME Paper No. 2003-GT-38168.

[7] Stow, S., and Dowling, A., 2004, "Low-Order Modelling of Thermoacoustic Limit Cycles," ASME Paper No. GT2004-54245.

[8] Kunze, K., Hirsch, C., and Sattelmayer, T., 2003, "Thermoacoustic Modeling and Control of Multiburner Combustion Systems," ASME Paper No. 2003-GT-38688.

[9] Krebs, W., Walz, G., and Hoffmann, S., 1999, "Thermoacoustic Analysis of Annular Combustor," AIAA Paper No. 99-1971.

[10] Candel, S. M., 1992, "Combustion Instabilities Coupled by Pressure Waves and Their Active Control," Fourth International Symposium on Combustion, The Combustion Institute, pp. 1277–1296.

[11] Paschereit, C. O., and Gutmark, E., 2004, "The Effectiveness of Passive Combustion Control Methods," *Proceedings of the ASME Turbo Expo*, Vienna, Austria.

[12] Banaszuk, A., Hagen, G., Mehta, P., and Oppelstrup, J., 2003, "A Linear Model for Control of Thermoacoustic Instabilities on an Annular Domain," *Proceedings of the IEEE Conference on Decision and Control*.

[13] Krstic, M., and Banaszuk, A., 2006, "Multivariable Adaptive Control of Instabilities Arising in Jet Engines," Control Eng. Pract., **14**, 833–842.

[14] Schuermans, B., Bellucci, V., and Paschereit, C. O., 2003, "Thermoacoustic Modeling and Control of Multiburner Combustion Systems," *Proceedings of the ASME Turbo Expo*, Atlanta, Georgia.

[15] Culick, F. E. C., 1987, "A Note on Rayleigh's Criterion," Combust. Sci. Technol., **56**, pp. 159–166.

[16] Balachandran, R., Ayoola, B. O., Kaminski, C. F., Dowling, A. P., and Mastorakos, E., 2005, "Experimental Investigation of the Nonlinear Response of Turbulent Premixed Flames to Imposed Inlet Velocity Oscillations," Combust.

Flame, **143**, pp. 37–55.
[17] Lieuwen, T., and Neumeier, Y., 2002, "Nonlinear Pressure-Heat Release Transfer Function Measurements in a Premixed Combustor," Proc. Combust. Inst., **29**, pp. 99–105.
[18] Lieuwen, T., and Bellows, B., 2002, "Nonlinear Kinematic Response of Premixed Flames to Harmonic Velocity Disturbances," *Proceedings of the Third Joint Meeting of the U.S. Sections of the Combustion Institute*.
[19] Hagen, G., and Banaszuk, A., 2004, "Uncertainty Propagation in a Reduced Order Thermo-Acoustic Model," 43rd IEEE Conference on Decision and Control.
[20] Kinsler, L. E., Frey, A. R., et al., 1982, *Fundamentals of Acoustics*, 3rd ed., Wiley, New York.
[21] Guckenheimer, J., and Holmes, P. J., 1983, *Nonlinear Oscillations, Dynamical Systems and Bifurcations of Vector Fields*, Springer, New York.
[22] Newman, W. I., and Efroimsky, M., 2003, "The Method of Variation of Constants and Multiple Time Scales in Orbital Mechanics," 34th Meeting of the AAS Division on Dynamical Astronomy.
[23] Van Der Pol, B., 1927, "Forced Oscillations in a Circuit With Non-Linear Resistance," Philos. Mag., **3**, pp. 65–80.

Fast Fourier Transform Based Numerical Methods for Elasto-Plastic Contacts of Nominally Flat Surfaces

W. Wayne Chen
Department of Mechanical Engineering,
Northwestern University,
Evanston, IL 60208

Shuangbiao Liu
Technology and Solutions Division,
E854, Caterpillar Inc.,
Peoria, IL 61656-1875

Q. Jane Wang
Department of Mechanical Engineering,
Northwestern University,
Evanston, IL 60208

This paper presents a three-dimensional numerical elasto-plastic model for the contact of nominally flat surfaces based on the periodic expandability of surface topography. This model is built on two algorithms: the continuous convolution and Fourier transform (CC-FT) and discrete convolution and fast Fourier transform (DC-FFT), modified with duplicated padding. This model considers the effect of asperity interactions and gives a detailed description of subsurface stress and strain fields caused by the contact of elasto-plastic solids with rough surfaces. Formulas of the frequency response functions (FRF) for elastic/plastic stresses and residual displacement are given in this paper. The model is verified by comparing the numerical results to several analytical solutions. The model is utilized to simulate the contacts involving a two-dimensional wavy surface and an engineering rough surface in order to examine its capability of evaluating the elasto-plastic contact behaviors of nominally flat surfaces. [DOI: 10.1115/1.2755158]

1 Introduction

Analyzing contact stress is of a significant importance to the design of mechanical components. When two elements are brought into contact and relative motion, interfacial normal and shear tractions occur either due to either the direct interaction of the asperities of two surfaces in a dry contact or the entrainment of a pressurized fluid in a mixed lubrication process. The knowledge of surface interaction makes the analysis of subsurface stress analysis feasible. Moreover, the subsurface stress field could be perturbed by surface irregularities and internal eigenstrains (such as plastic strain). The contact stress field information provides the foundation for the investigation of many surface-related phenomena, such as roll-contact fatigue [1], crack propagation [2], and wear [3].

Engineering surfaces are inevitably rough, and asperities may deform plastically until the contact area becomes sufficiently large and the elementary pressure can hold the applied load [4]. A pioneered work has been done by Greenwood and Williamson [5], who assumed that asperities have spherical tips with uniform radius but the Gaussian height distribution. This basic model was extended by Chang et al. [6] to take into account the volume conservation of the plastic zone. A thorough review of numerical models and simulations of multiple asperity contacts has been given by Bhushan [7].

On the other hand, contact problems can be formulated by means of the explicit relationship between excitation and material response. Tripp et al. [8] developed analytical solutions for the internal stress field induced by bisinusoidal normal and tangential tractions. A complete solution for the elastic contact of one-dimensional sinusoidal surface with a flat surface was investigated by Westergaard [9] and Dundurs et al. [10]. Experimental results reported in [11] showed the difficulty of predicting the shape of contact areas for two-dimensional sinusoidal surfaces, and thus, a numerical method, rather than an analytical approach, was employed to investigate the contact situation. Gao et al. [12] conducted an extensive study on the plastic contact between a rigid, flat body and an elastic–perfectly plastic solid with a one-dimensional sinusoidal surface by using the finite element method (FEM). They identified two parameters characterizing the type of the asperity contact behavior. Recently, Kim et al. [13] analyzed both frictionless and frictional contacts of a rigid surface with an elastic–perfectly plastic solid with a non-Gaussian rough surface generated by computer based on different statistical parameters.

The accurate description of the real contact area requires fine discretization with a large number of grids, which means a heavy computational burden. In addition, the mesh size along the depth should be small enough in order to obtain an accurate subsurface stress field. Considering the fact that many linear convolutions exist in several mathematical formulations of contact problems, the fast Fourier transform (FFT) [2,14–18] technique is utilized to accelerate the numerical process of contact simulation. Liu et al. [16] proposed a DC-FFT method with twice domain extension in each dimension to circumvent the otherwise encountered border aliasing error. This method is widely used for the analysis of the contact of counterformal rough surfaces, where the contact area is small compared to the sizes of contact bodies. However, the contact of two nominally flat surfaces involves a large nominal contact area, and the grid number needed to discretize surface asperities is beyond the power of a regular personal computer. Because a periodic similarity may exist in surface topography [4], the contact of nominally flat, but actually rough, surfaces may be solved on a characteristic domain that can be periodically extended to the entire contact region. Wang et al. [19] utilized the continuous convolution and Fourier transform (CC-FT) method, based on the frequency response function (FRF), to investigate the asperity contact in mixed lubrication, where the rough surface of a half-space was assumed to be periodic. This method is extended here to solve the elasto-plastic contact involving infinitely large rough surfaces by means of periodic domain extension.

Extensive modeling work has been done to study elasto-plastic counterformal contacts. Jacq et al. [20] developed a fast semi-analytical method to study the elasticplastic response of solid materials. Furthermore, frictional heating was introduced by Boucly et al. [21] into the model mentioned above. Wang and Keer [22] investigated the effect of various strain-hardening laws on the elasto-plastic indentation behaviors of materials.

The current work, based on Jacq's model [20], aims to develop

Contributed by the Applied Mechanics Division of ASME for publication in the JOURNAL OF APPLIED MECHANICS. Manuscript received December 4, 2006; final manuscript received May 14, 2007; published online February 15, 2008. Review conducted by Antoinette Maniatty.

a three-dimensional numerical elasto-plastic contact model for nominally flat surfaces, employing the CC-FT approach or the DC-FFT approach modified with duplicated padding. This model utilizes the explicit formula for material response (the Green's function and the frequency response function) to calculate the results of contact area, contact pressure, subsurface stress, and plastic strain. The frequency response functions for elastic fields caused by surface tractions and plastic strains are discussed in detail in this paper. The present model does not make any assumption on the asperity shape; it fully considers the interactions of neighboring contact asperities and the bulk deformation. The numerical results obtained from this model are compared to analytical solutions for verification. This model is also applied to evaluate the elasto-plastic contacts involving a sinusoidal surface and an engineering rough surface.

2 Theoretical Background

2.1 Contact Models. The general contact model with boundary constraints used by many researchers is repeated here for clarity

$$W = \int_{\Gamma_c} p(x,y)d\Gamma$$

$$h(x,y) = h_i(x,y) + u_3^{B1+B2}(x,y) - \delta \geqslant 0$$

$$p(x,y) \geqslant 0 \tag{1}$$

$$h(x,y)p(x,y) = 0$$

$$p(x,y) = 0 \subset \Gamma_c, \quad h(x,y) = 0 \not\subset \Gamma_c$$

Here, W is the applied load, Γ_c the real contact surface, p the pressure, u_3 the vertical displacement of two surfaces, and $h_i(x,y)$ and δ are the initial gap and rigid-body approach, respectively. The deformation can be related to loading through the Green's function. Therefore, the contact problem can be described by a linear equation system subjected to the constraints of nontensile contact pressure and impenetrable contact bodies, as indicated in Eq. (1). The iterative method based on the conjugate gradient method (CGM) [23] is introduced to solve this linear equation system for rough-surface contact problems efficiently, with which contact pressure and contact area can be determined simultaneously.

The elastic normal displacement caused by contact pressure $p(x,y)$ is given by the Boussinesq formulas [24]

$$u_3^p(x,y) = \int_{-\infty}^{\infty}\int_{-\infty}^{\infty} G^p(x-x',y-y')p(x',y')dx'dy' = G^p * p \tag{2}$$

where $G^p(x,y) = 1/\pi E^* \sqrt{x^2+y^2}$ and $E^* = E/1-\nu^2$. The domain of interest needs to be discretized into mesh elements, as indicated in Fig. 1. The numerical evaluation uses the discrete influence coefficient (IC), D_j, instead of the continuous Green's function. The general form of ICs can be found in [24], which is the integral of the product of the shape function, $Y(x)$, and the Green's function, $G(x)$, over $[-\Delta/2, \Delta/2]$,

$$D_j = \int_{-\Delta/2}^{\Delta/2} G(\Delta j - \xi)Y(\xi)d\xi \tag{3}$$

Then, the displacement u_i can be expressed in the form of the cyclic convolution,

$$u_i = \sum_{r=0}^{N-1} p_r D_{\text{mod}(i-r) \text{ of } N} \quad i = 0, \ldots, N-1 \tag{4}$$

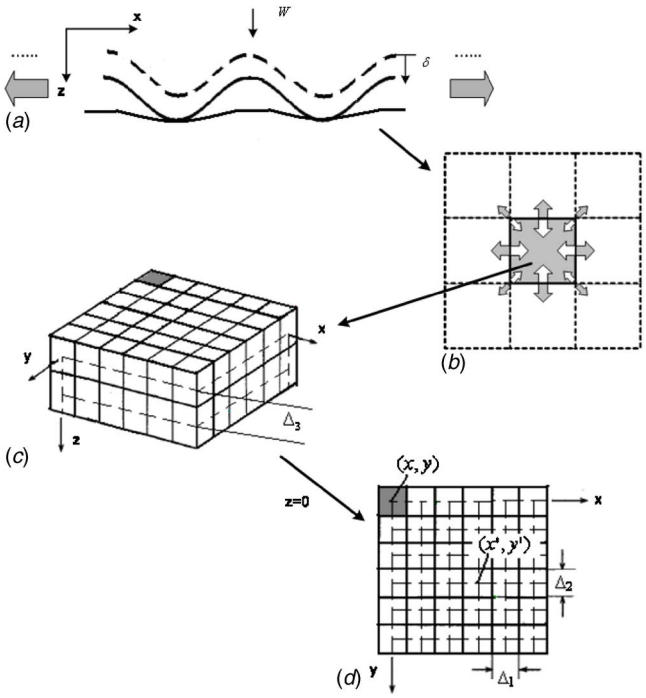

Fig. 1 Contact problem description: (*a*) contact of nominally flat surfaces, (*b*) periodic extension of a representative region, (*c*) characteristic domain with a mesh in a 3D view, and (*d*) characteristic domain of a contact surface with a mesh

With the continuous convolution theorem, the application of the Fourier transform on both sides of Eq. (2) should result in simple multiplication of the Fourier transform of pressure and the frequency response function (FRF). FRFs of surface normal displacements induced by pressure and shear tractions are listed in [25], as shown in

$$\tilde{\tilde{G}}^p(m,n) = \frac{2}{E^*\sqrt{m^2+n^2}}; \quad \tilde{\tilde{G}}^s(m,n) = -\frac{2im}{\mu_e(m^2+n^2)} \tag{5}$$

where the shear traction is applied along the positive x-axis, and m and n are coordinates in the frequency domain. The formula should be applied on both contact bodies to obtain the total surface deformation. Displacements caused by plastic strain can be directly included into the total displacement expression given in Eq. (1) for a solution of elasto-plastic contact. In Secs. 2.2–2.4, the frequency response functions of elastic/residual stresses and displacements are discussed.

2.2 FRF of Stress Field in Half-Space. The FRFs of normal surface displacement and subsurface elastic stress components caused by the surface tractions, shown below in Eqs. (6*a*) and (6*b*) have been derived based on the general expressions given by Liu and Wang [17] for known pressure $p(x,y)$ and tangential traction $s(x,y)$

$$2\mu\tilde{\tilde{u}}_3(m,n,z) = \left(\frac{2(1-\nu)}{\alpha} + z\right)e^{-\alpha z}\cdot\tilde{\tilde{p}} + i\left(\frac{2\nu-1}{\alpha^2} - \frac{z}{\alpha}\right)me^{-\alpha z}\cdot\tilde{\tilde{s}} \tag{6a}$$

$$\tilde{\tilde{\sigma}}_{11}(m,n,z) = [m^2(\alpha z-1) - 2\nu n^2]\alpha^{-2}e^{-\alpha z}\cdot\tilde{\tilde{p}} + i[2(1+\nu)m\alpha^{-1} - 2\nu m^3\alpha^{-3} - m^3\alpha^{-2}z]e^{-\alpha z}\cdot\tilde{\tilde{s}}$$

$$\tilde{\tilde{\sigma}}_{22}(m,n,z) = [n^2(\alpha z-1) - 2\nu m^2]\alpha^{-2}e^{-\alpha z}\cdot\tilde{\tilde{p}} + i[2\nu m\alpha^{-1} - 2\nu mn^2\alpha^{-3} - mn^2\alpha^{-2}z]e^{-\alpha z}\cdot\tilde{\tilde{s}}$$

$$\tilde{\sigma}_{33}(m,n,z) = -(\alpha z+1)e^{-\alpha z}\cdot\tilde{p} + imze^{-\alpha z}\cdot\tilde{s} \tag{6b}$$

$$\tilde{\sigma}_{12}(m,n,z) = mn(\alpha z-1+2\nu)\alpha^{-2}e^{-\alpha z}\cdot\tilde{p} + i[n\alpha^{-1}-2\nu nm^2\alpha^{-3}-nm^2\alpha^{-2}z]e^{-\alpha z}\cdot\tilde{s}$$

$$\tilde{\sigma}_{13}(m,n,z) = imze^{-\alpha z}\cdot\tilde{p} + (m^2z\alpha^{-1}-1)e^{-\alpha z}\cdot\tilde{s}$$

$$\tilde{\sigma}_{23}(m,n,z) = inze^{-\alpha z}\cdot\tilde{p} + mnz\alpha^{-1}e^{-\alpha z}\cdot\tilde{s}$$

Here, $\alpha=\sqrt{m^2+n^2}$, $\tilde{p}$ and $\tilde{s}$ are the double Fourier transforms of surface tractions with respect to coordinates x and y. One quick verification can be conducted through considering the surface displacement caused by a unit concentrated tangential force on the origin, i.e., $\tilde{s}=1$, $\tilde{p}=0$ and $z=0$, the FRF of the normal displacement in Eq. (6*a*) reduces to that for the Cerruti problem in Eq. (5)

$$\tilde{u}_3(m,n,0) = im\frac{2\nu-1}{2\alpha^2\mu} = -\frac{2(1+\nu)(1-2\nu)im}{2\alpha^2E} = -\frac{2im}{\alpha^2\mu_e} = \tilde{G}^s \tag{7}$$

2.3 FRF of Surface Normal Residual Displacement. The reciprocal theorem was employed by Jacq et al. [20] to study the residual displacement due to the plastic strain ε_{ij}^p. The normal residual displacement u_3^r can be expressed as an integration as follows, which can be found from Eq. (1.23) in [20]:

$$u_3^r(x,y) = 2\mu\int_{-\infty}^{\infty}\int_{-\infty}^{\infty}\int_{-\infty}^{\infty}\varepsilon_{ij}^p(x',y',z') \times\overset{*}{\varepsilon}_{ij}(x'-x,y'-y,z')dx'dy'dz' \tag{8}$$

where $\overset{*}{\varepsilon}_{ij}(x'-x,y'-y,z')$ is the elastic strain in the half-space at point (x',y',z'), which is induced by the unit concentrated normal force applied on surface point (x,y). Applying double Fourier transform on the residual displacement formula with respect to coordinates x and y (FT_{xy}) and using the FT property shown in the Appendix, Eq. (8) becomes

$$\tilde{u}_3^r(m,n) = 2\mu\int_{-\infty}^{\infty}\tilde{\varepsilon}_{ij}^p(m,n,z')\tilde{\overset{*}{\varepsilon}}_{ij}(-m,-n,z')dz' \tag{9}$$

Thus far, the horizontal coordinates are in the frequency domain, and the vertical coordinate z is in the space domain. The subsurface domain is divided into N_z equispaced layers along the z-axis, and the observation points locate on the centers of layers. The residual displacement can be rewritten as the superposition of the contributions of all layers, where plastic strains have nonzero value

$$\tilde{u}_3^r(m,n) = 2\mu\sum_{k=1}^{N_z}\left[\int_{\Delta(k-1/2)}^{\Delta(k+1/2)}\tilde{\varepsilon}_{ij}^p(m,n,z')\tilde{\overset{*}{\varepsilon}}_{ij}(-m,-n,z')dz'\right] \tag{10}$$

The plastic strains are assumed to be independent of the z coordinate in each layer, and then they can be factored from the integral,

$$\tilde{u}_3^r(m,n) = 2\mu\sum_{k=1}^{N_z}\left[\tilde{\varepsilon}_{ijk}^p(m,n)\int_{\Delta(k-1/2)}^{\Delta(k+1/2)}\tilde{\overset{*}{\varepsilon}}_{ij}(-m,-n,z')dz'\right] = \sum_{k=1}^{N_z}\tilde{\varepsilon}_{ijk}^p(m,n)\tilde{G}_{ijk}^*(m,n) \tag{11}$$

Here, $\tilde{\varepsilon}_{ijk}^p$ means the double Fourier transform of the plastic strain component ε_{ij} at the kth layer, and $\tilde{\tilde{G}}_{ijk}^*(m,n)=2\mu\int_{\Delta(k-1/2)}^{\Delta(k+1/2)}\tilde{\overset{*}{\varepsilon}}_{ij}(-m,-n,z')dz'$ is called the FRF of the surface residual displacement corresponding to $\tilde{\varepsilon}_{ijk}^p$. Considering the strain and displacement relationship, $\tilde{\overset{*}{\varepsilon}}_{ij}$ can be expressed as

$$\tilde{\overset{*}{\varepsilon}}_{ij} = \frac{FT_{xy}(u_{i,j}^*)+FT_{xy}(u_{j,i}^*)}{2} \tag{12}$$

Following the procedure shown in [17], the FRF of displacements $\tilde{u}_i^*$ due to the concentrated normal force can be derived and listed in the Appendix . Thus, $\tilde{\tilde{\varepsilon}}_{ij}^*$ can be developed, for instance,

$$2\mu\tilde{\overset{*}{\varepsilon}}_{11}(-m,-n,z') = FT_{xy}[2\mu u_{1,1}^*](-m,-n,z') = [im2\mu\tilde{u}_1^*](-m,-n,z') = (2\nu-1+z'\alpha)\frac{m^2}{\alpha^2}e^{-\alpha z'}$$

$$2\mu\tilde{\overset{*}{\varepsilon}}_{13}(-m,-n,z') = [\mu\tilde{u}_{1,3}^* + im\mu\tilde{u}_3^*](-m,-n,z') = -imz'e^{-\alpha z'} \tag{13}$$

Performing definite integral over terms $\tilde{\tilde{\varepsilon}}_{ij}^*$ results in the following FRFs:

$$\tilde{\tilde{G}}_{ijk}^*(m,n) = F_{ij}[m,n,z=\Delta(k+1/2)] - F_{ij}\left[m,n,z=\Delta\left(k-\tfrac{1}{2}\right)\right] \tag{14}$$

The functions F_{ij} are defined by $\partial F_{ij}(m,n,z)/\partial z = 2\mu\tilde{\tilde{\varepsilon}}_{ij}^*(-m,-n,z)$ and listed as follows:

$$F_{11}(m,n,z) = -\frac{m^2(2\nu+\alpha z)e^{-\alpha z}}{\alpha^3};\quad F_{22}(m,n,z) = F_{11}(n,m,z)$$

$$F_{33}(m,n,z) = \left(\frac{2(1-\nu)}{\alpha}+z\right)e^{-\alpha z};$$

$$F_{12}(m,n,z) = -mn\frac{(2\nu+\alpha z)}{\alpha^3}e^{-\alpha z} \tag{15}$$

$$F_{13}(m,n,z) = i\frac{m(1+\alpha z)}{\alpha^2}e^{-\alpha z};\quad F_{23}(m,n,z) = F_{13}(n,m,z)$$

2.4 FRF of Residual Stress in Half-Space by a Numerical Approach. However, for the residual stress field in the half-space caused by the plastic strain, the analytical form of FRF is unavailable, and the derivation needs significant analytical endeavor. On the other hand, the method for calculating influence coefficients D can be found from existing literatures [20,27]. An efficient way needs to be explored to obtain the discrete series of FRF from IC. As shown in Eq. (3), IC is the continuous convolution of the Green's function and the shape function over the discrete element; therefore,

$$\tilde{D} = \tilde{G}\cdot\tilde{Y} \tag{16}$$

The relationship between the FT and DFT series is

$$\hat{D}_i = \frac{\sum_{r=-\infty}^{\infty}\tilde{D}[(2\pi i/n\Delta)-(2\pi r/\Delta)]}{\Delta} \approx \frac{\tilde{D}(2\pi i/n\Delta)}{\Delta} \quad i=0,\ldots,n-1 \tag{17}$$

The approximation relationship holds if the interval Δ is sufficiently small. Only one term at $r=0$ is significant in the summation. Under this simplification, $\tilde{G}$ becomes

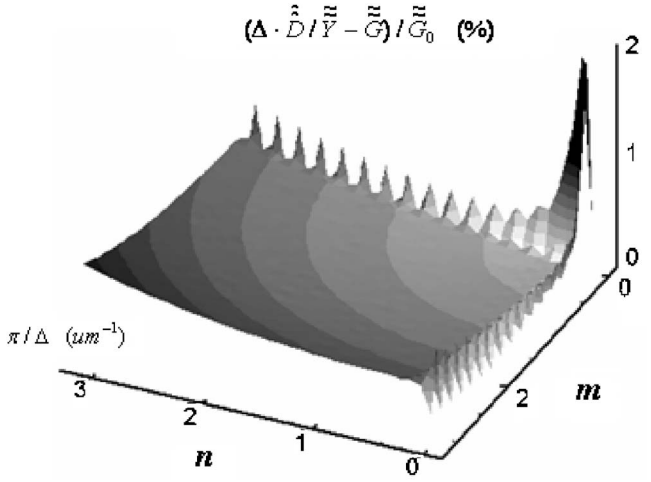

Fig. 2 Relative error of the FRF transformed from the IC for the Boussinesq problem

$$\tilde{G}_i = \tilde{G}\left(\frac{2\pi i}{n\Delta}\right) = \frac{\tilde{D}(2\pi i/n\Delta)}{\tilde{Y}(2\pi i/n\Delta)} \approx \frac{\Delta \cdot \hat{D}_i}{\tilde{Y}(2\pi i/n\Delta)} \quad i = 0, \ldots, n-1 \tag{18}$$

$\hat{D}_i$ can be obtained by applying the FFT on the discrete IC series. A rectangular pulse (zero order of continuity) whose continuous Fourier transform is given in [18] is usually used as the shape function. Based on Eq. (18), the discrete series of FRF $\tilde{G}_i$ can be calculated for further use.

The verification for this procedure is made through the comparison of the approximated FRF converted from IC with the exact FRF for the surface displacement induced by a normal pressure. The approach obtaining IC from the Boussinesq problem in [25] used the rectangular pulse as the shape function, and the FRF is shown in Eq. (5). The element size is $\Delta = 1$ μm, and the mesh dimensions are 64×64. As shown in Fig. 2, the relative error of the numerically approximated procedure is $<2\%$ (one-quarter of the frequency domain is shown, and $\tilde{\tilde{G}}_0$ is the average value of the FRF over the element at the origin). Thus, the FRF obtained from IC in this case is a good substitution for the analytical one. Note that the accuracy of Eq. (18) depends on the contribution from aliasing in Eq. (17), and the approximation is particularly suitable for the fast decaying $\tilde{D}$.

2.5 Numerical Formation of a Nominally Flat Surface. A typical contact involving a nominally flat surface with a large nominal contact area is shown in Fig. 1(*a*). Statistical methods are often used to obtain stochastic parameters that describe a group of rough engineering surfaces [4–6]. However, contact analyses based on surface statistics can hardly predict the interaction among asperities and the subsurface stress-strain behavior. On the other hand, the deterministic expression of a surface can be done with the assistance of modern measurement technologies. However, measurement can only result in a digitized surface sample over a finite area.

It is reasonable to use a sampled rough surface area as the representative domain to form a large rough surface by periodically extending this domain, as shown in Fig. 1(*b*). The characteristic domain can be retrieved as the object under investigation. Figures 1(*c*) and 1(*d*) give the representative space and surface with discrete grids, respectively. Such a periodical domain extension is in favor of the application of the CC-FT algorithm, and the response should have the same period as the excitation load.

2.6 Plasticity Consideration. For the plasticity modeling, the von Mises criterion, as indicated in Eq. (19), is chosen as the rule to identify the transition to plastic deformation

$$f = \sigma_{VM} - \sigma_Y = \sqrt{\frac{3}{2} S_{ij} : S_{ij}} - \sigma_Y \tag{19}$$

where σ_Y and σ_{VM} are the yield limit and the von Mises stress, respectively, and $S_{ij} = \sigma_{ij} - (1/3)\sigma_{kk}\delta_{ij}$. The isotropic Swift hardening law is used in the current study, where the yield limit can be represented in terms of the effective plastic strain as follows:

$$\sigma_Y = B(C + \varepsilon^p)^n \tag{20}$$

Here, B, C, and n are the work hardening parameters for the Swift law, and ε^p is the effective plastic strain, defined as $\varepsilon^p = \int \sqrt{(2/3)\varepsilon^p_{ij} : \varepsilon^p_{ij}}$.

Yield occurs when $f > 0$, i.e., when the von Mises stress is larger than the current yield strength $\sigma_Y(\varepsilon^p)$. The increment in the plastic strain enhances the level of yield strength and reduces the intensity of von Mises stress. The actual increment of the effective plastic strain $\delta\varepsilon^p$ should draw the stress-strain state back onto the yield surface, i.e., $f(\varepsilon^p + \delta\varepsilon^p) = 0$. An increment-based approach [20] can be used to determine the variation of the effective plastic strain, which is a function of stresses σ_{ij}, variations of stresses $\delta\sigma_{ij}$, existing plastic strains ε^p, and strain hardening parameters. The increment of plastic strain components is then calculated based on the plastic flow rule shown

$$\Delta\varepsilon^p_{ij} = \delta\varepsilon^p \frac{3S_{ij}}{2\sigma_{VM}} \tag{21}$$

3 FFT-Based Algorithms

3.1 DC-FFT. The contact response is a continuous convolution between excitation and the Green's function. As discussed by Brigham [26], the discrete convolution (also named cyclic convolution) via using the discrete Fourier transform (DFT) technique requires sampling both the excitation and the Green's function in a finite domain and forming a periodic series. If the excitation is nonperiodic, the alias phenomenon may occur along the domain boundary. In order to avoid this error, Liu et al. [16] proposed a DC-FFT algorithm, which is summarized in Fig. 3(*a*), at the cost of only doubling the problem domain. The FFT technique is applied to execute the DFT efficiently. For contact problems of nominally flat surfaces with periodic roughness, however, the DC-FFT algorithm is not immediately applicable.

3.2 CC-FT. On the other hand, the domain periodic extension strategy in Sec. 2.2 validates the use of the FRF-based CC-FT algorithm following the continuous convolution theorem. If the period of the contact domain is L, all contact variables, such as pressure and deformation, should also be periodic functions with the same period. This periodic characteristic automatically fulfills the periodic extension required by the DFT technique. Therefore, only a single period is needed in the Fourier transform procedure without any domain extension involved in the analysis. For the detailed proof, readers may refer to Sec. 2.2 in [16]. The procedure of CC-FT is illustrated graphically in Fig. 2(*b*).

The discrete series $\tilde{G}$ is obtained by sampling the FRF at the corresponding coordinates in the frequency domain. If the value of a FRF at the frequency domain origin, which equals the area under the corresponding Green's function, is singular, than the average value of the FRF over the element located at the origin can be a substitution value at this point [17].

3.3 DCD-FFT and a Mixed Algorithm. Another approach for problems with periodic roughness can be developed based on the DC-FFT method with certain modifications. As mentioned by Liu et al. [16], zero padding of excitation variables is one of the measures to circumvent the alias error occurring on the boundary

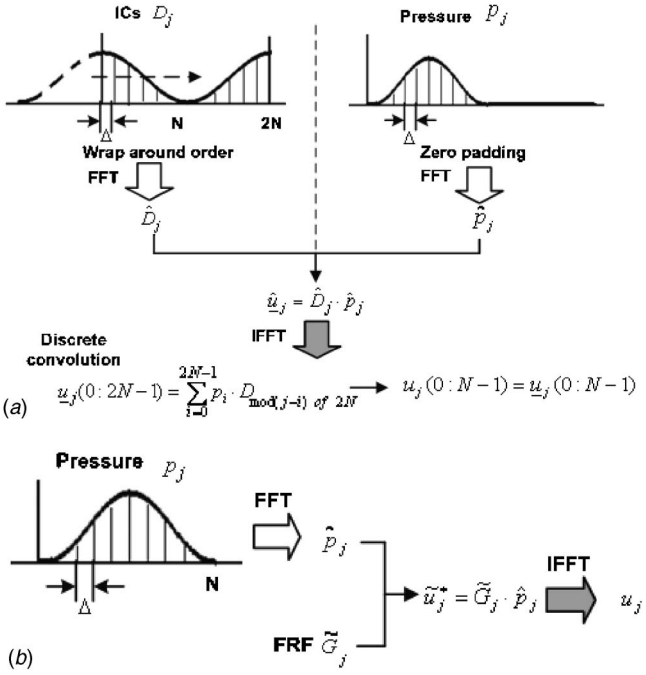

Fig. 3 Schematic illustrations of FFT-based algorithms: (*a*) the DC-FFT algorithm, and (*b*) the CC-FT algorithm

of nonperiodic problems. On the contrary, in order to reproduce periodic loading in neighboring periods, loading on the extended domain can be directly duplicated from the original domain, rather than zero padding. The modified DC-FFT algorithm with duplicated padding is denoted as DCD-FFT in the paper.

Intuitively, the DCD-FFT algorithm is not as accurate and efficient for periodic problems as the CC-FT algorithm, and it is indeed supported by numerical examples discussed in the verification section (Sec. 4) because it involves greater error and costs more in computation power due to the double extension. However, the DCD-FFT algorithm can be used for certain specific problems that the CC-FT algorithm can not readily handle. For example, line-contact problems involve an infinite geometry in one direction but finite geometry in the other. Surface roughness can be formed through periodic extension along the direction with infinite geometry. Neither CC-FT nor DC-FFT alone is valid for this one-dimensional periodic and one-dimensional nonperiodic problem. An approximate method can be developed, i.e., duplicated padding pressure in the periodic direction (the DCD-FFT algorithm) and zero padding pressure in the nonperiodic direction (the DC-FFT algorithm). This mixed method is depicted in Fig. 4.

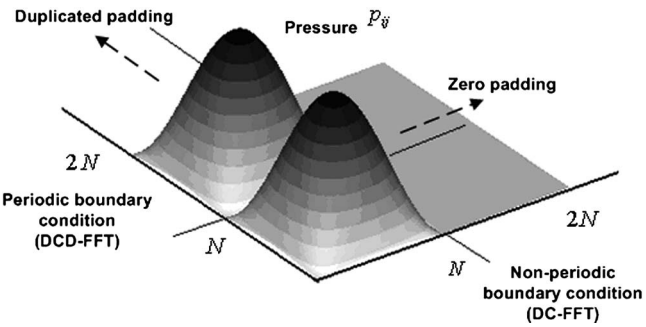

Fig. 4 Mixed method for one-dimensional periodic problems (DCD-FFT and DC-FFT)

4 Verifications and Application Results

Verifications of the FFT-based methods for periodic contact problems were made through the comparision between the numerical results obtained with these methods and the corresponding analytical solutions. Elastioplastic contacts involving a bisinusoidal surface and a engineering surface were then numerically investigated.

4.1 Verification, Stress Field due to a Bisinusoidal Surface Pressure. Assuming a bisinusoidal pressure distribution in the form of

$$p(x,y) = -p_0 \cos\left(\frac{2\pi}{\lambda}x\right)\cos\left(\frac{2\pi}{\lambda}y\right) \tag{22}$$

is applied on a frictionless half-space. Here, λ is the wavelength of the pressure distribution and p_0 the maximum pressure. The analytical solution of the subsurface stress field caused by the bisinusoidal surface tractions were given by Tripp et al. [8]. The stresses in the half-space were calculated numerically with the FFT-based methods in Sec. 3 in a physical domain of $2\lambda \times 2\lambda \times \lambda$. The frequency response functions listed in Sec. 2.2 were applied. When this problem was simplified into a nonperiodic problem subjected to only one period of pressure, the solution can be determined by the DC-FFT algorithm, whose results were also included in the following discussion for comparisons.

Figure 5(*a*) presents the dimensionless von Mises stress profiles along the x-axis below the surface at $z=\lambda/4$, where one-half of the simulated region is shown. The domain was meshed into $128 \times 128 \times 64$ grids. The coordinates were normalized by the pressure wavelength. The results obtained with the CC-FT and DCD-FFT algorithms agree well with the analytical solution in the entire simulation domain. The result with the DC-FFT algorithm is close to the exact solution in the domain center but quickly deviates from the analytical one near the boundary. In order to further compare methods on the domain boundary, the dimensionless von Mises stress profiles along the depth on the boundary of the simulation region is given in Fig. 5(*b*). Good agreements are still found for the results with the CC-FT and DCD-FFT algorithms, but those from the nonperiodic algorithm overestimate the near surface stress and underestimate the values at deeper locations because it neglects the tractions on neighboring regions.

The relative error of the von Mises stress is defined as the absolute difference between the analytical value and the numerical result divided by the maximum pressure p_0. These relative errors calculated for results with different approaches along the x-axis at the depth of $z=\lambda/4$, are shown in Fig. 6, where σ_{VM}^* is the analytical stress value. Different grid numbers, $64 \times 64 \times 32$, $128 \times 128 \times 64$, $256 \times 256 \times 128$ are chosen to study the effect of mesh size. It is found from Fig. 6(*a*) that relative errors for the results from the CC-FT algorithm are hardly visible, $<10^{-6}$. The increase in grid number does not result in less relative error. In Fig. 6(*b*), errors from the results obtained with the DCD-FFT algorithm are $<0.15\%$ for all mesh sizes and has the same period as the von Mises stress. The mesh refinement improves the numerical result obviously (the relative error decreases to 0.01% for the mesh size $256 \times 256 \times 128$). Relative errors for the nonperiodic solution obtained from the DC-FFT algorithm is negligible in the domain center and becomes significant on the domain edge, $>18\%$. It should be mentioned that the grid number has little effect on the results from the DC-FFT algorithm. Therefore, the CC-FT algorithm should be used for periodic problems because of its efficiency and accuracy.

4.2 Verification, Stresses due to a Cylindrical Contact. The Hertz theory indicates that the elastic frictionless line contact between a cylinder and a flat surface produces a contact pressure in the form of

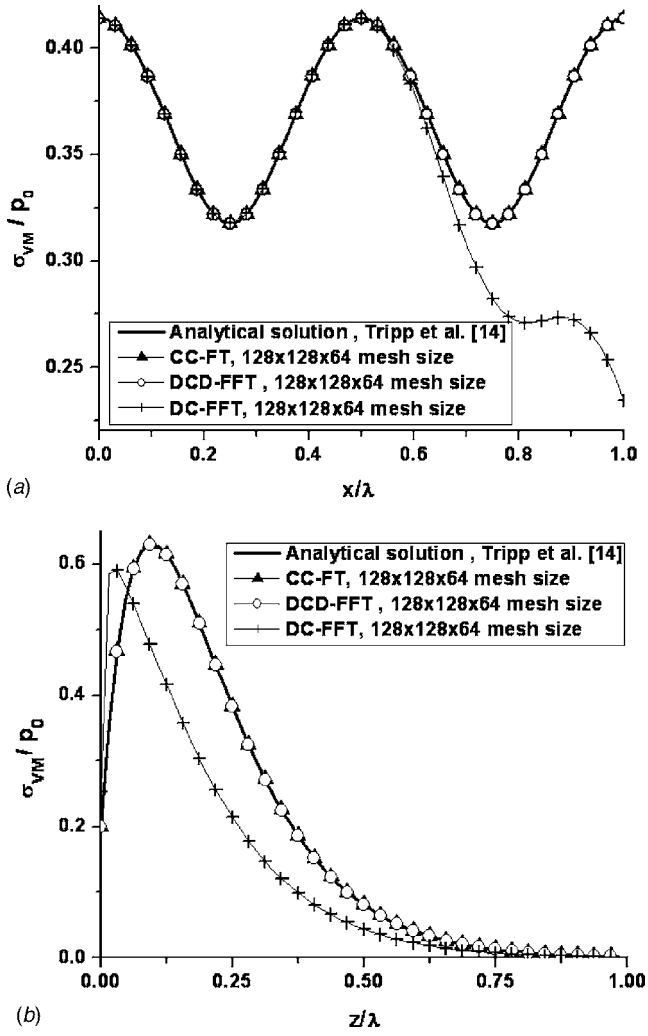

Fig. 5 Comparisons of dimensionless von Mises stress profiles (*a*) along the *x*-axis at $z=\lambda/4$, and (*b*) along depth *z* on the domain boundary ($x=\lambda$, $y=0$)

$$p(x)=\begin{cases} p_0\sqrt{1-x^2/a_H^2}, & |x|\leq a_H \\ 0, & \text{otherwise} \end{cases} \tag{23}$$

where a_H is the Hertizan half contact width and p_0 is the maximum contact pressure. For this line contact problem, the periodic boundary condition can be applied along the cylinder axis, and the nonperiodic contact condition along the perpendicular direction. The DCD-FFT and DC-FFT algorithms should be applied on the periodic direction and nonperiodic direction, respectively (the mixed method in Sec. 3.3). The size of the simulation domain is $4a_H\times 16a_H\times 8a_H$, which was divided into $256\times 256\times 128$ grid points.

The analytical solution of stresses due to the cylindrical contact can be found in [24]. The maximum shear stress τ_1, given in Eq. (24), is used for comparison to the exact solution in [24]

$$\tau_1=\frac{1}{2}\sqrt{(\sigma_{11}-\sigma_{33})^2+4\sigma_{13}^2} \tag{24}$$

On the other hand, a nonperiodic solution, ignoring the pressure on the neighborhood, can be calculated by the DC-FFT algorithm alone in order to examine the advantage of the mixed method. The results of the dimensionless maximum shear stress versus depth at the origin and an edge point are presented in Figs. 7(*a*) and 7(*b*). It can be observed that both the mixed method and DC-FFT algorithms yield reasonably good solutions at the domain center as compared to the exact one. The mixed method keeps the same accuracy on the computational boundary $y=8a_H$, while the results obtained with the DC-FFT algorithm alone notably deviates away

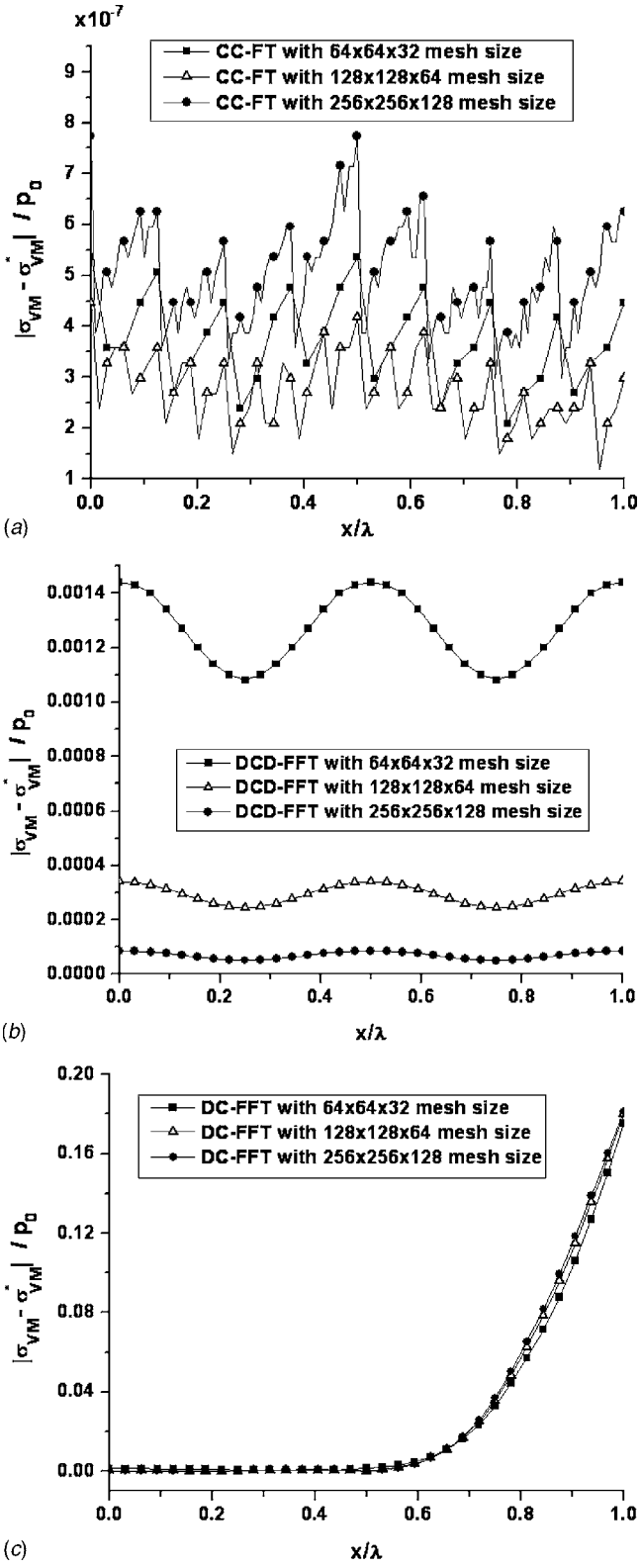

Fig. 6 Relative errors for the von Mises stress along the *x*-axis at the depth of $z=\lambda/4$ for the results obtained with (*a*) the CC-FT algorithm, (*b*) the DCD-FFT algorithm, and (*c*) the nonperiodic approach (DC-FFT)

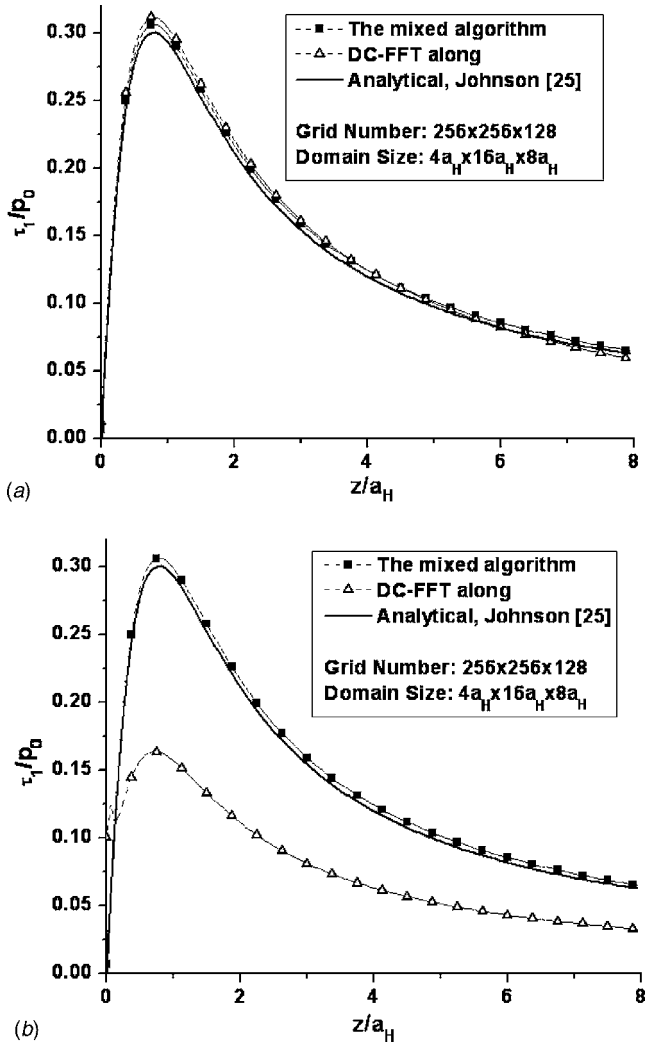

Fig. 7 Comparisons of the dimensionless maximum shear stress along the depth: (*a*) at the origin point and (*b*) on the domain boundary at $y=8a_H$

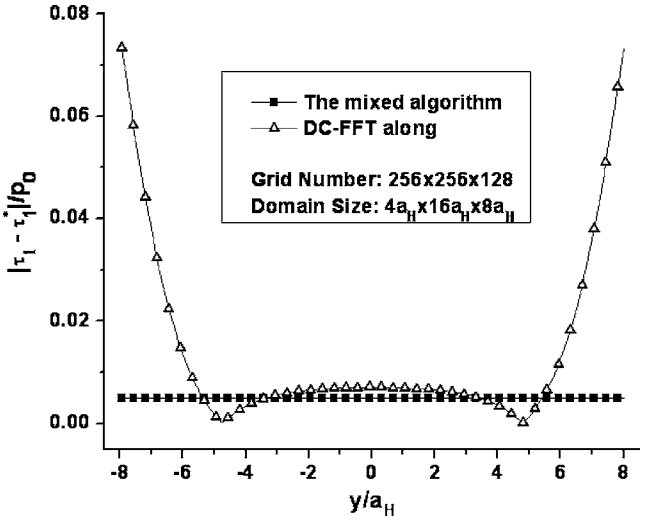

Fig. 8 Relative errors of the maximum shear stress along the cylindrical axis at $z=0.78a_H$ below the surface

from the analytical data. Here, the DC-FFT algorithm underestimates the stress because the pressure influence from neighborhood periods is neglected.

Relative errors of the maximum shear stress along the cylinder axis at $z=0.78a_H$, where the exact maximum value occurs, are plotted in the Fig. 8 for the results obtained with different approaches, and τ_1^* is the analytical maximum shear stress. The mixed method has uniform and small relative errors, $\sim 0.7\%$, over the entire domain. The relative error obtained from the nonperiodic approach is $<2\%$ in the middle of the computational domain, may be comparable to that of the mixed method. However, the error increases rapidly when the observation point is $6a_H$ away from the center point, and even differs by one order of magnitude from that of the mixed method at the boundary. Table 1 lists the maximum relative error from the mixed approach over the entire space for different mesh numbers and computation domain sizes. Under the same domain size, mesh refinement does not improve the result. On the other hand, even using the coarse mesh, $64\times64\times32$, the mixed algorithm still yields good solutions if a large extended computation domain, $4a_H\times16a_H\times8a_H$ is used. In addition, the domain extension along the cylindrical axis (0.67% for $4a_H\times16a_H\times8a_H$) seems more helpful than that along the perpendicular direction (0.99% for $8a_H\times16a_H\times8a_H$). Therefore, the mixed padding approach is capable of solving the one-dimensional periodic line-contact problem, and the domain extension along the periodic dimension may help reduce the numerical error.

4.3 Application, Elasto-Plastic Contact Involving a Bisinusoidal Surface. This section considers the contact of a rigid flat plane with an elasto-plastic body with a bisinusoidal surface, whose initial geometry h_i is given by

$$h_i(x,y)=A_p\left[1-\cos\left(\frac{2\pi x}{\lambda}\right)\cos\left(\frac{2\pi y}{\lambda}\right)\right] \tag{25}$$

where A_p and λ are the amplitude and wavelength of the sinusoidal surface. Figure 9(*a*) gives the cross-sectional view the contact. Suppose the flat surface is brought into contact with the sinusoidal crests under a mean pressure $\bar{p}$. According to Johnson et al. [11], if the mean pressure $\bar{p}$ exceeds a certain value, p^*

Table 1 Maximum relative errors of the Tresca stress obtained from the mixed algorithm for different mesh numbers and domain sizes

	Domain size			
	$4a_H\times4a_H\times2a_H$	$8a_H\times8a_H\times4a_H$	$8a_H\times16a_H\times8a_H$	$4a_H\times16a_H\times8a_H$
Grid number	Relative error (%)			
$64\times64\times32$	2.50	1.87	0.99	0.67
$128\times128\times64$	2.47	1.62	0.83	0.64
$256\times256\times128$	2.46	1.46	0.74	0.62

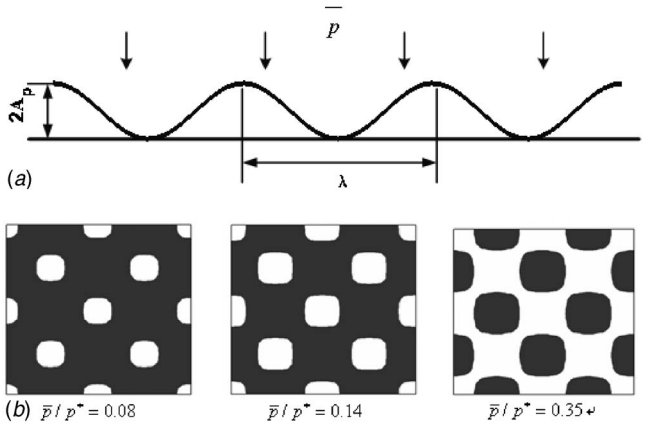

Fig. 9 Contact involving a bisinusoidal elasto-plastic surface: (*a*) cross section of the contact and (*b*) variations of the contact area of the two-dimensional wavy surface as the pressure ratio increases. White zones are the contact areas, and black ones are noncontact areas.

$= \sqrt{2}\pi E^* A_p/\lambda$, then the gap between the flat plane and valleys of the sinusoidal surface should be completely closed. Here, E^* is the equivalent Young's modulus. If $\bar{p} < p^*$, then only partial contact occurs.

The exact solution for the contact pressure of the two-dimensional wavy surface is not available; therefore, the CGM-based iterative procedure [23] was employed here to obtain the contact pressure and actual contact area. The increment of plastic strain and residual displacement were determined by using the semi-analytical approach discussed in [20]. Following the formula in Sec. 2, the FRF discrete series should be obtained for the stress and displacement when the plastic behavior was considered. Because of the periodicity of the sinusoidal surface, the CC-FT algorithm was used as the core numerical technique to accelerate the stress evaluation process. The dimension of the characteristic domain from the infinite body is $2\lambda \times 2\lambda \times \lambda$, which was meshed into $64 \times 64 \times 32$ grid elements. Parameters in the simulation were listed in Table 2.

Table 2 Parameters in the simulation

Parameters	Value	Parameters	Value
B	945 MPa	A_p	0.1 um
C	20	λ	32 um
n	0.085	$\bar{p}/p^*$	0.08, 0.14, and 0.35
E	210 GPa	Δ	1 um
ν	0.3	μ_f	0.3
σ_Y	1219 MPa		

Table 3 Ratios of real to apparent contact area

$\bar{p}/p^*$	0.08	0.14	0.35
Numerical results	0.173	0.275	0.583
Experimental results	0.170	0.280	0.520

Because of the difficulty in predicting the contact area for this problem, Johnson et al. [11] performed an experimental investiga-

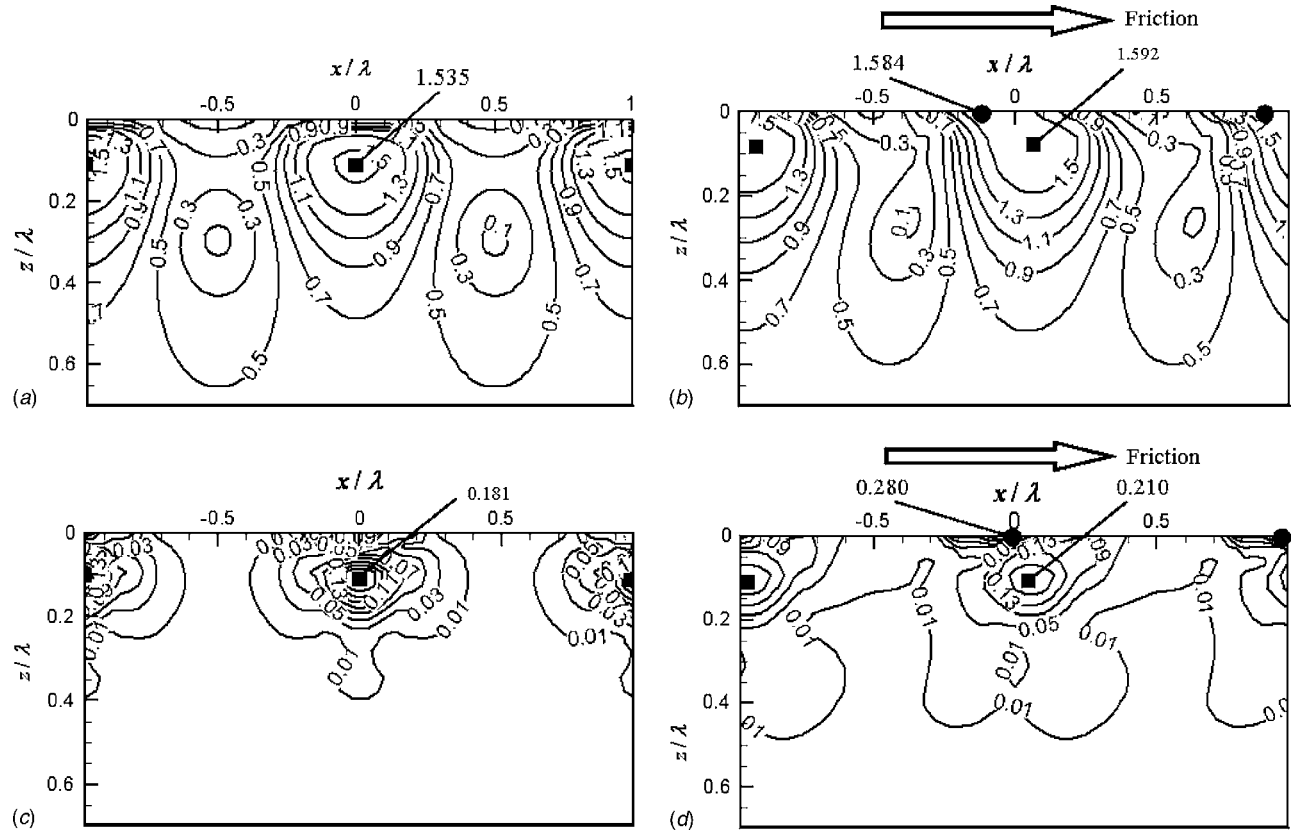

Fig. 10 Dimensionless stress contours in the plane $y=0$ when the external load is applied: (*a*) the total von Mises stress without friction, (*b*) the total von Mises stress with friction, $\mu_f=0.3$, (*c*) the residual von Mises stress without friction, and (*d*) the residual von Mises stress with friction, $\mu_f=0.3$. Rectangles mark the maximum stresses in the body and circles mark the maximum stresses on the surface. The maximum values are labeled above the figures.

tion of the variation of the contact area as a function of the external load for a purely elastic contact. The current work evaluated the contact areas at three pressure ratios, $\bar{p}/p^*=0.08$, 0.14, and 0.35. The shape and size of the contact area for these cases are presented in Fig. 9(*b*). The contact spots are approximately circular at the light load, $\bar{p}/p^*=0.08$ and then become rectangles at $\bar{p}/p^*=0.14$. When the pressure ratio, $\bar{p}/p^*$, further increases up to 0.35, the separate contact spots link to each other and form a continuous region embracing rectangular noncontact areas. The ratios of real to apparent contact area obtained from the numerical simulation and the experiment are listed in Table 3. The numerical results show a satisfactory agreement with the experimental observations in [11]. Note that the axes of Fig. 9 in [11] are at 45 deg to those of Fig. 9(*b*) in this paper.

In order to study the effect of shear traction, a surface shear stress, equal to the production of a friction coefficient and the normal pressure, was applied along the positive *x*-axis. $\mu_f=0.3$ and $\bar{p}=0.35p^*$ were chosen.

Figure 10 plots the contours of dimensionless von Mises stress in the vertical plane of $y=0$ for the total value and the residual part, respectively. The von Mises stress was normalized by the yield strength σ_Y, and the coordinates *x* and *z* were normalized by the sinusoidal wavelength λ. Both the total and residual von Mises stress have the period of λ in the space domain no matter whether the shear is applied or not. For the frictionless case, the maximum values of the total and residual stress are located at about $z=0.1\lambda$ below the sinusoidal crests. When friction is applied, the maximum total stress increases by 4% while the maximum residual stress increases significantly by 55%. In addition, there are two local maximum values for the total and residual stress for the frictional case; one is at the same location as that in frictionless contact case, marked by the rectangle in Fig. 10, whereas the other is on the contact surface, marked by the circle in Fig. 10.

The effect of friction on the residual surface displacement and subsurface effective plastic strain are given in Fig. 11. The residual displacement and plastic strain still have the same periodic properties as the surface geometry. With the presence of the shear traction, the maximum plastic strain increases ~52% and the depths of residual dents caused by the plastic strain also increase ~67%. In addition to that, the peaks of effective plastic strain offset along the direction of shear traction. On the other hand, the valleys of surface residual dents remain in the same position. Humps of the residual displacement can be found on the leading edges of the dents while the shear is applied.

4.4 Application, Elasto-Plastic Contact Involving a Rough Surface. A real ground rough surface patch was digitized with a phase-shift interferometer. The sampling mesh dimension is 128 × 128, and the mesh element is 7 μm × 7 μm in size. A virtual ground rough surface can be formed through periodically extending this representative patch along two dimensions. Figure 12(*a*) presents the representative domain in a perspective view. Along the depth direction, the domain was discretized into 32 layers spaced with 7 μm each. This rough surface is brought into contact with a smooth flat surface under a mean pressure equal to $0.2\sigma_Y$. The material properties are the same as those used in Sec. 4.3.

The dimensionless contact pressure is given in Fig. 12(*b*). Sporadic pressure peaks can be found on the rough surface, and the real contact area is only 7.54% of the apparent contact area at this loading condition. Figures 12(*c*) and 12(*d*) plot the dimensionless total and residual von Mises stresses at the depth of $z=4R_q$, where R_q is the rms roughness. The maximum value of the residual stress differs by one order of magnitude from that of the total stress. Because of the effect of the residual deformation, the rms roughness on the releasing of load reduces to 1.66 μm from its original value of 1.68 μm.

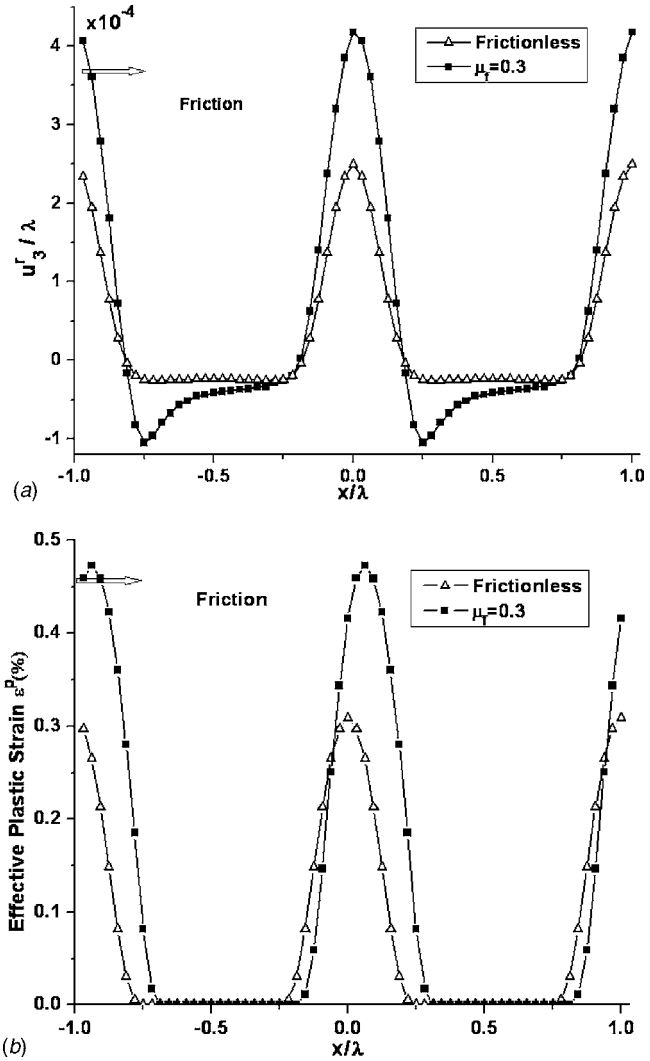

Fig. 11 Comparisons of plastic contact with and without friction: (*a*) the dimensionless residual normal surface displacement along the *x*-axis and (*b*) the effective plastic strain along the *x*-axis at the depth of $z=0.1\lambda$

5 Conclusions

This paper presents a three-dimensional numerical model, based on the continuous convolution and Fourier transform (CC-FT) algorithm and the discrete convolution and fast Fourier transform algorithm modified with duplicated padding (DCD-FFT), for solving the elasto-plastic contact of nominally flat surface. For periodic problems, the CC-FT method yields the most accurate solution and does not require any computation domain extension. A mixed algorithm, DCD-FFT and DC-FFT, is developed for simulating the line contact involving a nominally flat surface.

The FRFs of the elastic subsurface stress and the residual surface displacement have been derived analytically. A numerical approximation approach of transforming IC into the discrete series of FRF was utilized to obtain the FRF of the residual stress.

Model verification was conducted by comparing the numerical results of the half-space stress field induced by a periodic surface pressure to analytical solutions. The results show that the CC-FT algorithm is more accurate and efficient than the DCD-FFT algorithm. The ability of the mixed algorithms was examined with a line contact problem, and the results indicate that this method is sufficiently accurate.

The CC-FT algorithm was applied to evaluate an elasto-plastic contact involving a bisinusoidal surface, including both the nor-

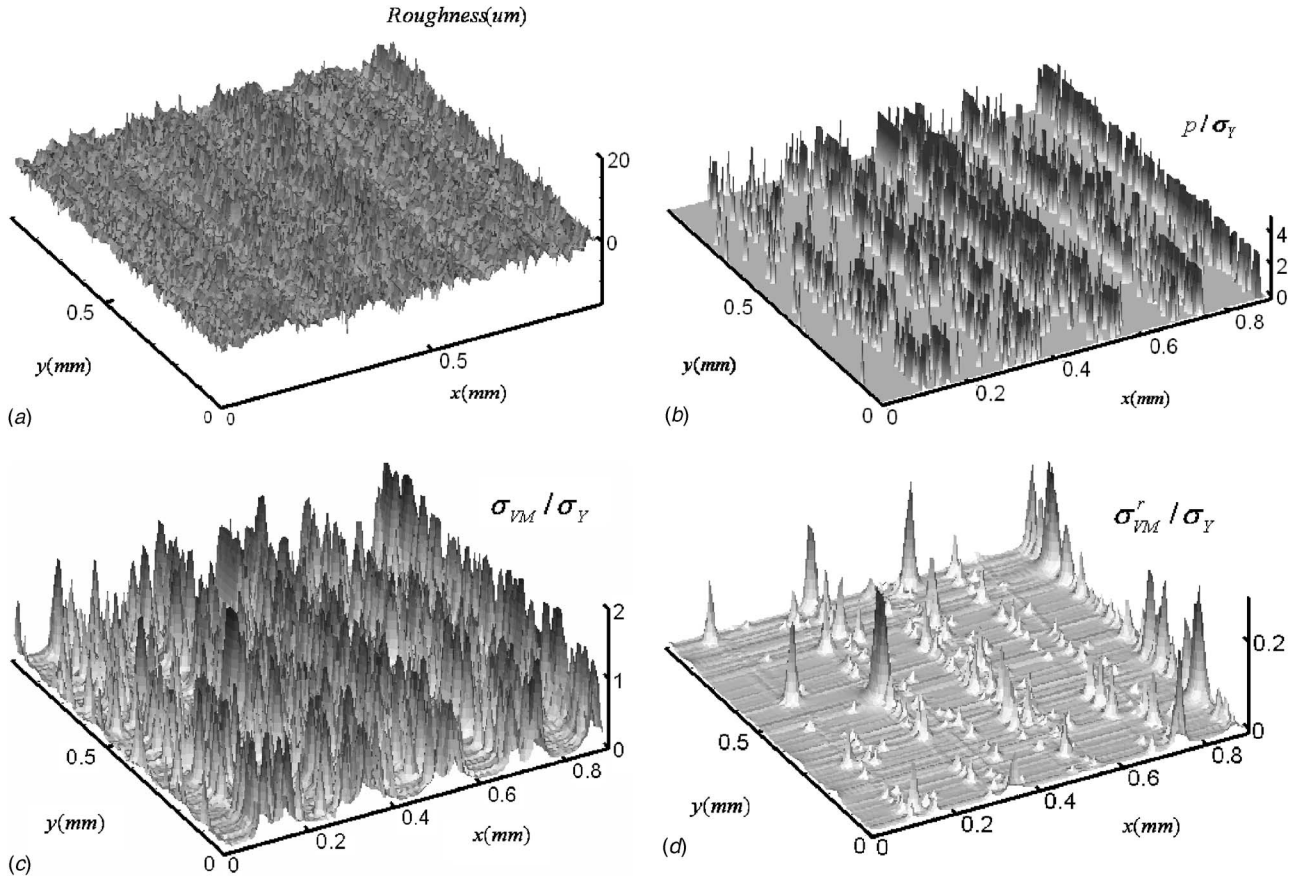

Fig. 12 Simulation results of the elasto-plastic contact involving a ground surface (mean pressure, $\bar{p}=0.2\sigma_Y$): (*a*) The surface geometry of the ground surface (rms roughness, $R_q=1.68$ um), (*b*) dimensionless surface pressure, (*c*) dimensionless total von Mises stress at $z=4R_q$, and (*d*) dimensionless residual von Mises stress at $z=4R_q$

mal and tangential loading. The increase in the mean normal pressure changes the contact spots from circles to rectangles and, finally, to a continuous region. The introduction of the shear traction evidently enhances the intensity of the residual stress and the plastic deformations. The positions of the maximum values of the stress and the plastic strain also shift toward the surface. This model was further used to simulate an elasto-plastic contact involving a flat ground surface. A reduction in roughness due to the residual deformation has been identified.

Acknowledgment

The authors would like to acknowledge financial support from the National Science Foundation, Office of Naval Research, and Ford Motor Company. The authors would also like to express their sincere gratitude to Dr. Fan Wang, Professor Leon Keer and Professor Daniel Nelias, and Vincent Boucly for helpful discussions.

Nomenclature

p, s = pressure and shear tractions, MPa
$\bar{p}$ = average pressure applied on the contact interface
u_i = displacement
u_3^r = normal residual displacement
$\sigma_{ij}, \varepsilon_{ij}$ = stress, strain
σ_{VM}, σ_Y = von Mises equivalent stress, Yield Strength
ε_{ij}^p = plastic strain
$G, \tilde{G}$ = Green's functions, the Frequency response function
D, Y = influence coefficient, Shape function
μ = shear modulus, $\mu=2E/(1+\nu)$, GPa
μ_e = equivalent shear modulus, $1/\mu_e=(1+\nu)(1-2\nu)/2E$, GPa
μ_f = friction coefficient
E, ν = Young's modulus, GPa, Poisson ratio
E^* = equivalent Young's modulus, GPa, $E^*=E/(1-\nu^2)$
x, y, z = space coordinates
m, n = frequency coordinates corresponding to x, y
$(\,)_{,}$ = partial differential operator
$\tilde{}$ $\hat{}$ = continuous FT operator, Discrete FT operator
$*$ = continuous convolution
i = pure imaginary unit, $\sqrt{-1}$
λ = wavelength of sinusoidal geometry or pressure distribution
A_p = amplitude of sinusoidal geometry
Δ = space grid size
a_H = Hertzian half contact width (cylinder contact)
τ_1 = maximum shear stress
ε^p = effective plastic strain
B, C, n = work hardening parameters of the Swift law
R_q = rms, the root mean square of surface roughness

Appendix

1 One of the Properties of Fourier Transform

$$\text{If } f(x)=\int_{-\infty}^{\infty} g(\tau)h(\tau-x)d\tau$$

$$\tilde{f}(m)=\int_{-\infty}^{\infty}\left(\int_{-\infty}^{\infty} g(\tau)h(\tau-x)d\tau\right)e^{-imx}dx$$

$$set\ \sigma = \tau - x$$

$$\tilde{f}(m) = \left(\int_{-\infty}^{\infty} g(\tau) e^{-im\tau} d\tau \right) \cdot \left(\int_{-\infty}^{\infty} h(\sigma) e^{-i\cdot(-m)\cdot\sigma} d\sigma \right)$$

$$= \tilde{g}(m) \cdot \tilde{h}(-m)$$

2 FRF of Displacement Due to a Unit Concentrated Normal Force

$$\tilde{\tilde{p}}(m,n) = 1, \quad \tilde{\tilde{s}}(m,n) = 0$$

$$2\mu \tilde{\tilde{u}}_1^*(m,n,z) = -im \frac{2\nu - 1 + z\alpha}{\alpha^2} e^{-az}$$

$$2\mu \tilde{\tilde{u}}_2^*(m,n,z) = -in \frac{2\nu - 1 + z\alpha}{\alpha^2} e^{-az}$$

$$2\mu \tilde{\tilde{u}}_3^*(m,n,z) = \left(\frac{2(1-\nu)}{\alpha} + z \right) e^{-az}$$

References

[1] Epstein, D., Keer, L. M., Wang, Q., and Cheng, H. S., 2003, "Effect of Surface Topography on Contact Fatigue in Mixed Lubrication," Tribol. Trans., **46**(4), pp. 506–513.

[2] Polonsky, I. A., and Keer, L. M., 2001, "Stress Analysis of Layered Elastic Solids With Cracks Using the Fast Fourier Transform and Conjugate Gradient Techniques," ASME J. Appl. Mech., **68**, pp. 708–714.

[3] Johnson, K. L., 1995, "Contact Mechanics and the Wear of Metals," Wear, **190**, pp. 162–170.

[4] Arnell, R. D., Davies, P. B., Halling, J., and Whomes, T. L., 1991, *Tribology, Principles and Design Applications*, Springer-Verlag, New York.

[5] Greenwood, J. A., and Williamson, J. B. P., 1966, "Contact of Nominally Flat Surfaces," Proc. R. Soc. London, Ser. A, **295**, pp. 300–319.

[6] Chang, W. R., Etsion, I., and Bogy, D. B., 1987, "Elastic Plastic Model for the Contact of Rough Surfaces," ASME J. Tribol., **109**, pp. 257–263.

[7] Bhushan, B., 1998, "Contact Mechanics of Rough Surfaces in Tribology: Multiple Asperity Contact," Tribol. Lett., **4**, pp. 1–35.

[8] Tripp, J. H., Kuilenburg, J. V., Morales-Espejel, G. E., and Lugt, P. M., 2003, "Frequency Response Functions and Rough Surface Stress Analysis," Tribol. Trans., **46**(3), pp. 376–382.

[9] Westergaard, H. M., 1939, "Bearing Pressures and Cracks," ASME J. Appl. Mech., **6**, pp. 49–53.

[10] Dunders, J., Tsai, K. C., and Keer, L. M., 1973, "Contact Between Elastic Bodies With Wavy Surfaces," J. Elast., **3**, pp. 109–115.

[11] Johnson, K. L., Greenwood, J. A., and Higginson, J. G., 1985, "The Contact of Elastic Regular Wavy Surfaces," Int. J. Mech. Sci., **27**, pp. 383–396.

[12] Gao, Y. F., Bower, A. F., Kim, K.-S., Lev, L., and Cheng, Y. T., 2006, "The Behavior of an Elastic-Perfectly Plastic Sinusoidal Surface Under Contact Loading," Wear, **261**(2), pp. 145–154.

[13] Kim, T. W., Bhushan, B., and Cho, Y. J., 2006, "The Contact Behavior of Elastic/Plastic Non-Gaussian Rough Surfaces," Tribol. Lett., **22**(1), pp. 1–13.

[14] Ju, Y., and Farris, T. N., 1996, "Spectral Analysis of Two-Dimensional Contact Problems," ASME J. Tribol., **118**, pp. 320–328.

[15] Lee, S. C., and Ren, N., 1996, "Behavior of Elastic-Plastic Rough Surface Contacts as Affected by the Surface Topography, Load and Material," STLE Tribol. Trans., **39**, pp. 67–74.

[16] Liu, S. B., Wang, Q., and Liu, G., 2000, "A Versatile Method of Discrete Convolution and FFT (DC-FFT) for Contact Analyses," Wear, **243**, pp. 101–111.

[17] Liu, S. B., and Wang, Q., 2002, "Study Contact Stress Fields Caused by Surface Tractions With a Discrete Convolution and Fast Fourier Transform Algorithm," ASME J. Tribol., **124**, pp. 36–45.

[18] Liu, S. B., Hua, D., Chen, W. W., and Wang, Q., 2007, "Tribological Modeling: Application of Fast Fourier Transform," Tribol. Int. **40**, pp. 1284–1293.

[19] Wang, Q., Zhu, D., Yu, T., Cheng, H. S., Jiang, J., and Liu, S. B., 2004, "Mixed Lubrication Analyses by a Micro-Macro Approach and a Full-Scale Micro EHL Model," ASME J. Tribol., **126**, pp. 81–91.

[20] Jacq, C., Nelias, D., Lormand, G., and Girodin, D., 2002, "Development of a Three-Dimensional Semi-Analytical Elastic-Plastic Contact Code," ASME J. Tribol., **124**, pp. 653–667.

[21] Boucly, V., Nelias, D., Liu, S. B., Wang, Q., and Keer, L. M., 2005, "Contact Analyses for Bodies With Frictional Heating and Plastic Behavior," ASME J. Tribol., **127**, pp. 355–364.

[22] Wang, F., and Keer, L. M., 2005, "Numerical Simulation for Three Dimensional Elastic-Plastic Contact With Hardening Behavior," ASME J. Tribol., **127**, pp. 494–502.

[23] Polonsky, I. A., and Keer, L. M., 1999, "A Numerical Method for Solving Rough Contact Problems Based on Multi-Level Multi-Summation and Conjugate Gradient Techniques," Wear, **231**, pp. 206–219.

[24] Johnson, K. L., 1985, *Contact Mechanics*, Cambridge University Press, Cambridge, England.

[25] Liu, S. B., and Wang, Q., 2001, "A Three-Dimensional Thermomechanical Model of Contact Between Non-Conforming Rough Surfaces," ASME J. Tribol., **123**, pp. 17–26.

[26] Brigham, E. O., 1974, *The Fast Fourier Transform*, Prentice-Hall, Englewood Cliffs, NJ.

[27] Liu, S. B., and Wang, Q., 2005, "Elastic Fields Due to Eigenstrains in a Half-Space," ASME J. Appl. Mech., **72**, pp. 871–878.

A Functionally Graded Plane With a Circular Inclusion Under Uniform Antiplane Eigenstrain

X. Wang

E. Pan[1]
ASME Member

Department of Civil Engineering
and Department of Applied Mathematics,
University of Akron,
Akron, OH 44325-3905

A. K. Roy
ASME Fellow
Air Force Research Laboratory,
AFRL/MLBCM, Bldg. 654,
2941 Hobson Way
Wright-Patterson AFB, OH 45433-7750

The problem of a functionally graded plane with a circular inclusion under a uniform antiplane eigenstrain is investigated, where the shear modulus varies exponentially along the x direction. By introducing a new function which satisfies the Helmholtz equation, the general solution to the original problem is derived in terms of series expansion. Numerical results are then presented which demonstrate clearly that for a functionally graded plane, the strain and stress fields inside the circular inclusion under uniform antiplane eigenstrains are intrinsically nonuniform. This phenomenon differs from the corresponding homogeneous material case where both the strain and stress fields are uniform inside the circular inclusion. [DOI: 10.1115/1.2745391]

Keywords: functionally graded material, Eshelby eigenstrain, circular inclusion, antiplane deformation

1 Introduction

The well-known result of Eshelby [1] for an elastic space shows that the strain and stress fields inside an ellipsoidal (and elliptical) inclusion under uniform eigenstrains are uniform. Eshelby's result is based on the assumption that the infinite elastic space is isotropic and homogeneous. Recently, this classic Eshelby problem has been extended to material anisotropy and even piezoelectric coupling [2–4], with applications in novel strained semiconductor quantum structures (see, e.g., [5,6]).

As a new type of composites, functionally graded materials (FGMs) were initially designed as thermal barrier materials for aerospace structures (Koizumi [7]), in which the volume fractions of different constituent materials vary continuously from one side to the other, resulting in smooth variation of material properties. If a FGM space contains an ellipsoidal or elliptical inclusion with uniform eigenstrains, are the strain and stress fields inside the inclusion still uniform? To the best of the authors' knowledge, the Eshelby problem in FGMs has not been addressed, although the fracture problem (see, e.g., [8]) and some Green's function problems (see, e.g., [9–13]) in FGMs were investigated before. Since the general Eshelby problem in FGMs is very difficult, we consider here only the simple situation in which a FGM plane contains a circular cylindrical inclusion under uniform antiplane eigenstrains. Furthermore we assume that the shear modulus of the FGM varies exponentially along a fixed direction, say the x direction, as adopted by Erdogan et al. [8]. In doing so, it is possible for us to derive a general solution to this problem by introducing a new function φ which satisfies the Helmholtz equation. The final series solution is expressed in terms of the modified Bessel functions.

2 General Solution

We consider an infinite FGM in the x-y plane as shown in Fig. 1, and assume that the shear modulus μ of the FGM varies exponentially in the x direction as (e.g., [8])

$$\mu = e^{2\beta x}\mu_0 \tag{1}$$

where μ_0 is the homogeneous shear modulus and β is the gradient factor of the FGM.

We point out that while various processing techniques have been proposed for FGMs (e.g. [14–17]), including the isotropic FGM as a special case [15], the exponential variation described by Eq. (1) could be difficult to achieve experimentally. Therefore, Eq. (1) should be regarded as a simplified FGM model to the more complicated FGMs fabricated from laboratories. We further mention that an isotropic FGM, as the one assumed here, could be realized only for certain spatial variations of composition [14] since random distributed microstructures (i.e., two distinct phases distributed in a disordered fashion) would be locally *anisotropic* [18–20], with the latter requires more involved analysis.

We also assume that, within the FGM, there is a circular inclusion $r=\sqrt{x^2+y^2}\leqslant R$ which undergoes uniform antiplane eigenstrains ε^*_{zx} and ε^*_{zy}. The boundary condition along the inclusion-matrix interface $r=R$ is assumed to be fully bonded, and can be expressed in terms of the out-of-plane elastic displacements $w^{(1)}$ inside the inclusion and $w^{(2)}$ outside, as

$$\begin{aligned} w^{(1)} + w^* &= w^{(2)} \\ \frac{\partial w^{(1)}}{\partial r} &= \frac{\partial w^{(2)}}{\partial r} \qquad (r=R) \end{aligned} \tag{2}$$

where $w^*=r(\varepsilon^*_{zx}-\mathrm{i}\varepsilon^*_{zy})e^{\mathrm{i}\theta}+r(\varepsilon^*_{zx}+\mathrm{i}\varepsilon^*_{zy})e^{\mathrm{i}\theta}$ is the additional displacement corresponding to the uniform eigenstrains $\varepsilon^*_{zx}, \varepsilon^*_{zy}$. The first condition in Eq. (2) states that the displacement is continuous across the interface; while the second one in Eq. (2) implies that the traction σ_{zr} is continuous across the interface. Furthermore, it is easy to show that $w^{(1)}$ and $w^{(2)}$ satisfy the following partial differential equations:

$$\begin{aligned} &\frac{\partial^2 w^{(1)}}{\partial x^2} + \frac{\partial^2 w^{(1)}}{\partial y^2} + 2\beta\frac{\partial w^{(1)}}{\partial x} = 0 \quad \sqrt{x^2+y^2} \leqslant R \\ &\frac{\partial^2 w^{(2)}}{\partial x^2} + \frac{\partial^2 w^{(2)}}{\partial y^2} + 2\beta\frac{\partial w^{(2)}}{\partial x} = 0 \quad \sqrt{x^2+y^2} \geqslant R \end{aligned} \tag{3}$$

We now introduce a new function φ which is related to w through the following relation:

$$w = e^{-\beta x}\varphi \tag{4}$$

It is easy to show that, in terms of the new function φ, the boundary condition (2) can be equivalently expressed as

$$\begin{aligned} \varphi^{(2)} - \varphi^{(1)} &= e^{\beta x} w^* \\ \frac{\partial \varphi^{(2)}}{\partial r} - \frac{\partial \varphi^{(1)}}{\partial r} &= \beta e^{\beta x}\cos\theta w^* \qquad (r=R) \end{aligned} \tag{5}$$

where $\varphi^{(1)}$ and $\varphi^{(2)}$ are within and outside the inclusion, respectively. They satisfy the following Helmholtz equations:

[1]Corresponding author.

Contributed by the Applied Mechanics Division of ASME for publication in the JOURNAL OF APPLIED MECHANICS. Manuscript received October 14, 2006; final manuscript received March 19, 2007; published online January 11, 2008. Review conducted by Martin Ostoja-Starzewski.

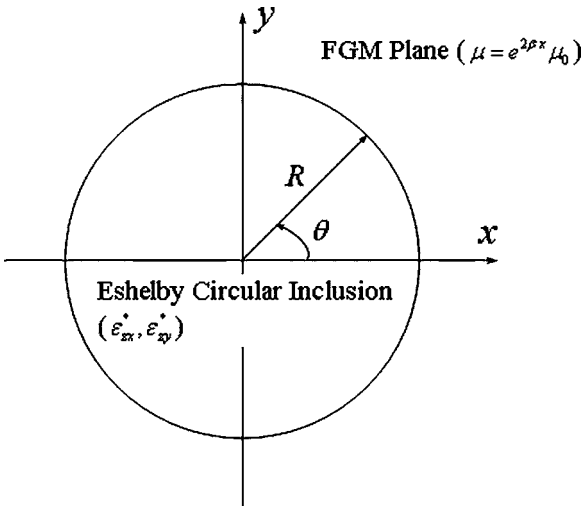

Fig. 1 An infinite FGM plane containing a circular inclusion with uniform antiplane eigenstrains

$$\frac{\partial^2\varphi^{(1)}}{\partial x^2}+\frac{\partial^2\varphi^{(1)}}{\partial y^2}-\beta^2\varphi^{(1)}=0 \quad \sqrt{x^2+y^2}\leqslant R$$

$$\frac{\partial^2\varphi^{(2)}}{\partial x^2}+\frac{\partial^2\varphi^{(2)}}{\partial y^2}-\beta^2\varphi^{(2)}=0 \quad \sqrt{x^2+y^2}\geqslant R \tag{6}$$

In view of Eq. (6), $\varphi^{(1)}$ and $\varphi^{(2)}$ can be expressed in terms of series expansion as

$$\varphi^{(1)}=\sum_{n=-\infty}^{+\infty}A_n^{(1)}I_n(|\beta|r)e^{in\theta} \quad 0\leqslant r\leqslant R \tag{7}$$

$$\varphi^{(2)}=\sum_{n=-\infty}^{+\infty}A_n^{(2)}K_n(|\beta|r)e^{in\theta} \quad r\geqslant R \tag{8}$$

where I_n and K_n are the modified nth-order Bessel functions of the first and second kinds, respectively; $A_n^{(1)}$ and $A_n^{(2)}$ are unknown coefficients to be determined. In addition, the exponential function $e^{\beta x}$ can be expanded as follows:

$$e^{\beta x}=\sum_{n=-\infty}^{+\infty}I_n(\beta r)e^{in\theta} \tag{9}$$

Therefore, the two terms on the right-hand side of Eq. (5) can be expanded as

$$e^{\beta x}w^*=R\sum_{n=-\infty}^{+\infty}[I_{n-1}(\beta R)(\varepsilon^*_{zx}-i\varepsilon^*_{zy})+I_{n+1}(\beta R)(\varepsilon^*_{zx}+i\varepsilon^*_{zy})]e^{in\theta} \tag{10}$$

$$\beta\cos\theta e^{\beta x}w^*=\frac{\beta R}{2}\sum_{n=-\infty}^{+\infty}\{[I_{n-2}(\beta R)+I_n(\beta R)](\varepsilon^*_{zx}-i\varepsilon^*_{zy})+[I_n(\beta R)+I_{n+2}(\beta R)](\varepsilon^*_{zx}+i\varepsilon^*_{zy})\}e^{in\theta} \tag{11}$$

By enforcing the boundary condition (5), we determine the unknown expansion coefficients in Eqs. (7) and (8) as

$$\begin{bmatrix}A_n^{(1)}\\A_n^{(2)}\end{bmatrix}=\frac{R}{K_n(|\beta|R)I_n'(|\beta|R)-I_n(|\beta|R)K_n'(|\beta|R)}\begin{bmatrix}K_n'(|\beta|R) & -K_n(|\beta|R)\\ I_n'(|\beta|R) & -I_n(|\beta|R)\end{bmatrix}\times\begin{bmatrix}I_{n-1}(\beta R)(\varepsilon^*_{zx}-i\varepsilon^*_{zy})+I_{n+1}(\beta R)(\varepsilon^*_{zx}+i\varepsilon^*_{zy})\\ \frac{\beta}{2|\beta|}\{[I_{n-2}(\beta R)+I_n(\beta R)](\varepsilon^*_{zx}-i\varepsilon^*_{zy})+[I_n(\beta R)+I_{n+2}(\beta R)](\varepsilon^*_{zx}+i\varepsilon^*_{zy})\}\end{bmatrix} \tag{12}$$

where the prime ($'$) denotes the derivative with respect to the variable in the parentheses.

We mention that the following identities are useful in the calculation of the coefficients:

$$I_n'(x)=\frac{I_{n-1}(x)+I_{n+1}(x)}{2}$$

$$K_n'(x)=-\frac{K_{n-1}(x)+K_{n+1}(x)}{2} \tag{13}$$

which can be easily derived using the definitions that

$$I_n(x)=i^{-n}J_n(ix)$$

$$K_n(x)=\frac{\pi}{2}i^{n+1}H_n^{(1)}(ix) \tag{14}$$

where J_n and $H_n^{(1)}$ are the nth order Bessel and Hankel functions of the first kind. The other useful identities are

$$J_n'(x)=\frac{J_{n-1}(x)-J_{n+1}(x)}{2}$$

$$H_n^{(1)\prime}(x)=\frac{H_{n-1}^{(1)}(x)-H_{n+1}^{(1)}(x)}{2} \tag{15}$$

We add that Eq. (9) can be easily derived from the following Jacobi-Anger expansion [21]:

$$e^{ikx}=\sum_{n=-\infty}^{+\infty}i^nJ_n(kr)e^{in\theta} \tag{16}$$

by taking $\beta=ik$ and using the definition of I_n in Eq. (14).

3 Numerical Results

As a numerical example, we consider a circular inclusion with uniform eigenstrains $\varepsilon^*_{zx}\neq 0$ and $\varepsilon^*_{zy}=0$. We truncate the series in Eqs. (7) and (8) at $n=\pm 10$ in order to obtain a result with a relative truncation error less than 0.1%.

Figure 2 shows the distribution of the normalized stress component

$$\sigma=-\frac{\sigma_{zx}}{\mu_0\varepsilon^*_{zx}}$$

where

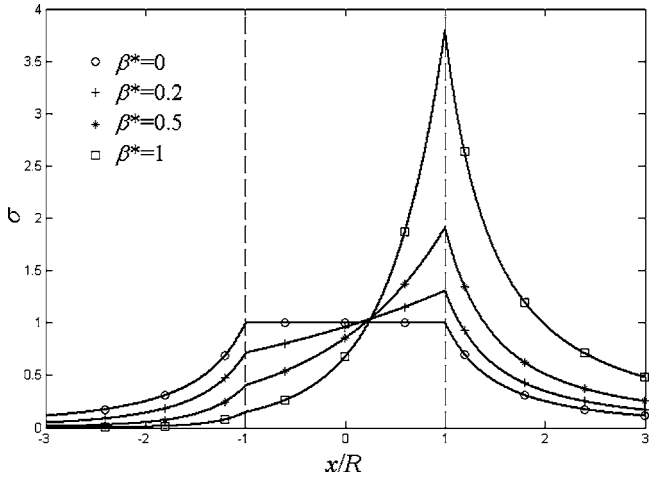

Fig. 2 Distribution of the normalized stress component $\sigma = -(\sigma_{zx}/\mu_0\varepsilon^*_{zx})$ along the x axis for different gradient parameters $\beta^* = \beta R = 0, 0.2, 0.5, 1$

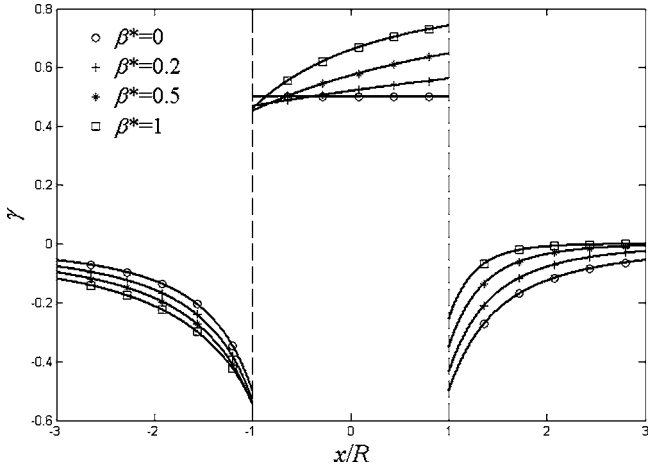

Fig. 4 Distribution of the normalized total strain component γ along the x axis for different gradient parameters $\beta^* = 0, 0.2, 0.5, 1$

$$\sigma_{zx} = \mu \frac{\partial w}{\partial x} = \mu_0 e^{\beta x}\left(-\beta\varphi + \frac{\partial \varphi}{\partial x}\right)$$

along the x axis for four different gradient parameters $\beta^* = \beta R = 0, 0.2, 0.5, 1$. It is noted that, for $\beta^* = 0$, which corresponds to a homogeneous plane, variation of σ obeys the following exact expression, which can also be derived from the result of Ru and Schiavone [22]:

$$\sigma = \begin{cases} 1, & |x| \leqslant R \\ \left(\dfrac{R}{x}\right)^2, & |x| \geqslant R \end{cases} \tag{17}$$

It is well known that the stress field inside the circular inclusion is uniform when the plane is homogeneous, which is the classic Eshelby result. When $\beta^* \neq 0$ for an FGM plane, however, the stress field inside the circular inclusion is no longer uniform with its maximum value being always reached at $x = R$ (Fig. 2).

Figure 3 shows the variation of the maximum stress $\sigma_{\max}$ as a function of β^*. It is observed that $\sigma_{\max}$ is a monotonic increasing function of β^*. The influence of the gradient parameter β^* on $\sigma_{\max}$ is significant. For example, when $\beta^* = 3$, $\sigma_{\max} = 98.3133$, a value nearly 100 times of the one corresponding to the homogeneous material case ($\sigma_{\max} = 1$ for $\beta^* = 0$).

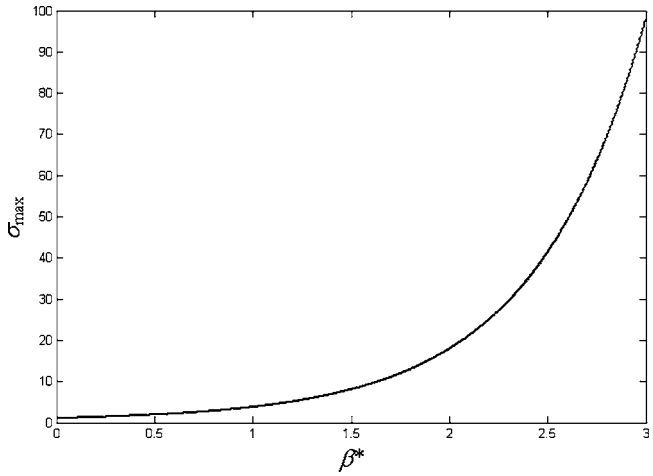

Fig. 3 Variation of the maximum stress $\sigma_{\max}$ as a function of β^*

Besides the stress distribution, we also show in Fig. 4 the distribution of the normalized total strain component (being an element of the Eshelby tensor [1])

$$\gamma = \begin{cases} (\varepsilon^{(1)}_{zx} + \varepsilon^*_{zx})/\varepsilon^*_{zx}, & |x| \leqslant R \\ \varepsilon^{(2)}_{zx}/\varepsilon^*_{zx}, & |x| \geqslant R \end{cases} \tag{18}$$

along the x axis for four different gradient parameters $\beta^* = 0, 0.2, 0.5, 1$. In Eq. (18),

$$\varepsilon^{(1)}_{zx} = \frac{1}{2}\frac{\partial w^{(1)}}{\partial x}$$

and

$$\varepsilon^{(2)}_{zx} = \frac{1}{2}\frac{\partial w^{(2)}}{\partial x}$$

are the elastic strains inside and outside the inclusion, respectively. Similarly, Fig. 4 demonstrates that the Eshelby tensor within the circular inclusion is no longer uniform for an FGM plane ($\beta^* \neq 0$).

Figure 5 shows the distribution of the normalized total displacement

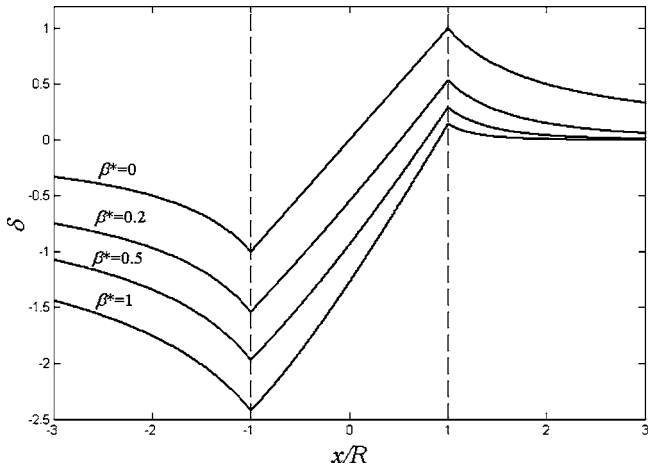

Fig. 5 Distribution of the normalized total displacement δ along the x axis for different gradient parameters $\beta^* = 0, 0.2, 0.5, 1$

$$\delta = \begin{cases} (w^{(1)} + w^*)/R\varepsilon^*_{zx}, & |x| \leq R \\ w^{(2)}/R\varepsilon^*_{zx}, & |x| \geq R \end{cases} \tag{19}$$

along the x axis for four different gradient parameters $\beta^* = 0, 0.2, 0.5, 1$. It is observed that the displacement field inside the circular inclusion in an FGM plane (especially when $\beta^* = 1$) is no longer a linear function of the coordinate x. Furthermore, the magnitude of δ for $x \geq R$ is very small when the gradient parameter β^* is large. For example, for a large β^*, say $\beta^* \geq 1$, the magnitude of δ at $x = R$ is $\delta \approx 0$. It is further interesting that, for a large β^*, the corresponding stress σ at $x = R$ is also large ($\sigma > 3.5$ at $x = R$). On the other hand, for $\beta^* \geq 1$, the magnitude of δ at $x = -R$ is very large ($\delta < -2.5$ at $x = -R$) while that of σ at $x = -R$ is small ($\sigma \approx 0$ at $x = -R$). Finally, when $\beta^* = 0$, i.e., for the corresponding homogeneous material case, the displacement δ along the x axis obeys the following exact expression [22]:

$$\delta = \begin{cases} x/R, & |x| \leq R \\ R/x, & |x| \geq R \end{cases} \tag{20}$$

which implies that δ within the inclusion is proportional to the coordinate x, while outside the inclusion δ is inversely proportional to the coordinate x.

We remark that the dimensionless gradient parameter β^* cannot be arbitrarily large as this would result in a FGM with a very large shear modulus. For example, the modulus corresponding to $\beta^* = 3$ at $x = R$ would be more than 400 times larger than the one corresponding to the homogeneous material case (i.e., μ_0 when $\beta^* = 0$).

4 Conclusions

We have analyzed the displacement, strain, and stress fields for an infinite FGM plane containing a circular inclusion under uniform antiplane eigenstrains. The solution is expressed in terms of series expansion by virtue of a new function. Numerical results show that, inside the circular inclusion, the stress and strain fields are nonuniform and the displacement field is no longer a linear function of the coordinates x and y when the elastic plane is functionally graded (or inhomogeneous in shear modulus). A similar problem that could be addressed in the future is for the corresponding transversely isotropic and piezoelectric FGM plane with a circular inclusion under uniform antiplane eigenstrains and in-plane eigenelectric fields. Finally we indicate again that the FGM plane studied in this research is assumed to be isotropic and exponentially graded to simplify the analysis. Introduction of local anisotropy [18–20] to our model will require more involved investigation and thus form the subject of future research.

Acknowledgment

This project was supported by AFRL 06-S531-060-C1. The authors would also like to thank both reviewers and the associate editor for their constructive comments.

References

[1] Eshelby, J. D., 1957, "The Determination of the Elastic Field of an Ellipsoidal Inclusion and Related Problems," Proc. R. Soc. London, Ser. A, **241**, pp. 376–396.

[2] Ru, C. Q., 2000, "Eshelby's Problem for a Two Dimensional Piezoelectric Inclusion of Arbitrary Shape," Proc. R. Soc. London, Ser. A, **456**, pp. 1051–1068.

[3] Ru, C. Q., 2001, "A Two Dimensional Eshelby Problem for Two Bonded Piezoelectric Half-planes," Proc. R. Soc. London, Ser. A, **457**, pp. 865–883.

[4] Ru, C. Q., 2003, "Eshelby Inclusion of Arbitrary Shape in an Anisotropic Plane or Half-Plane," Acta Mech., **160**, pp. 219–234.

[5] Pan, E., 2004, "Eshelby Problem of Polygonal Inclusions in Anisotropic Piezoelectric Full- and Half-Planes," J. Mech. Phys. Solids, **52**, pp. 567–589.

[6] Pan, E., Han, F., and Albrecht, J. D., 2005, "Strain Fields in InAs/GaAs Quantum Wire Structures: Inclusion versus Inhomogeneity," J. Appl. Phys., **98**, pp. 013534-12.

[7] Koizumi, M., 1993, "The Concept of FGM," Ceram. Trans., **34**, pp. 3–10.

[8] Erdogan, F., Kaya, A. C., and Joseph, P. F., 1991, "The Mode-III Crack Problem in Bonded Materials With a Nonhomogeneous Interfacial Zone," ASME J. Appl. Mech., **58**, pp. 419–427.

[9] Shaw, R. P., and Gipson, G. S., 1995, "Interrelated Fundamental Solutions for Various Heterogeneous Potential, Wave and Advective-Diffusive Problems," Eng. Anal. Boundary Elem., **16**, pp. 29–34.

[10] Gray, L. J., Kaplan, T., Richardson, J. D., and Paulino, G. H., 2003, "Green's Functions and Boundary Integral Analysis for Exponentially Graded Materials: Heat Conduction," ASME J. Appl. Mech., **70**, pp. 543–549.

[11] Chan, Y. S., Gray, L. J., Kaplan, T., and Paulino, G. H., 2004, "Green's Functions for a Two-Dimensional Exponentially Graded Elastic Media," Proc. R. Soc. London, Ser. A, **460**, pp. 1689–1706.

[12] Sutradhar, A., and Paulino, G. H., 2004, "A Simple Boundary Element Method for Problems of Potential Problems in Nonhomogeneous Media," Int. J. Numer. Methods Eng., **60**, pp. 2203–2230.

[13] Pan, E., and Han, F., 2005, "Green's Functions for Transversely Isotropic Piezoelectric Functionally Graded Multilayered Half Spaces," Int. J. Solids Struct., **42**, pp. 3207–3233.

[14] Markworth, A. J., Ramesh, K. S., and Parks, W. P., 1995, "Review: Modelling Studies Applied to Functionally Graded Materials," J. Mater. Sci., **30**, pp. 2183–2193.

[15] Lambros, J., Santare, M. H., Li, H., and Sapna III, G. H., 1999, "A Novel Technique for the Fabrication of Laboratory Scale Model Functionally Graded Materials," Exp. Mech., **39**, pp. 184–190.

[16] Kieback, B., Neubrand, A., and Riedel, H., 2003, "Processing Techniques for Functionally Graded Materials," Mater. Sci. Eng., A, **362**, pp. 81–105.

[17] Lafdi, K., 2005, "TEM Characterization of the Interface Property Between the Fibre and Matrix," private communication.

[18] Ostoja-Starzewski, M., Jasiuk, I., Wang, W., and Alzebdeh, K., 1996, "Composites With Functionally Graded Interfaces: Meso-Continuum Concept and Effective Properties," Acta Mater., **44**, pp. 2057–2066.

[19] Ostoja-Starzewski, M., 1998, "Random Field Models of Heterogeneous Materials," Int. J. Solids Struct., **35**, pp. 2429–2455.

[20] Ostoja-Starzewski, M., 2005, "On the Admissibility of an Isotropic, Smooth Elastic Continuum," Arch. Mech., **57**(4), pp. 345–355.

[21] Chew, W. C., 1995, *Waves and Fields in Inhomogeneous Media*, IEEE, New York.

[22] Ru, C. Q., and Schiavone, P., 1997, "A Circular Inclusion With Circumferentially Inhomogeneous Interface in Antiplane Shear," Proc. R. Soc. London, Ser. A, **453**, pp. 2551–2572.

Dynamic Viscoelastic Rod Stability Modeling by Fractional Differential Operator

D. Ingman
QA&R, Technion-I.I.T.,
Technion City, Haifa 32000, Israel
e-mail: qadov@tx.technion.ac.il

J. Suzdalnitsky[1]
QA&R, Technion-I.I.T.,
Technion City, Haifa 32000, Israel
e-mail: iosef@tx.technion.ac.il

The need to take into account the oscillation of a system is a special feature in the linear problem of the stability of a cantilevered rod under a follower force. Involvement of viscoelastic materials leads to damping of the oscillation hence to overestimation of critical loads. This new problem is solved here by means of an additional term introduced into the constitutive equation and proportional to the fractional time derivative with complex order—besides the inertial one. The effects contributed by the damping ratio, the real part of the order and the corrective role of its imaginary part on the shape of the bifurcation line, on its maximum and on the disposition of the inflection and maximal deflection points on the centerline of the deformed rod during the secondary loss of stability, are discussed. [DOI: 10.1115/1.2745825]

Keywords: damping, fractional calculus, stability, viscoelasticity

Introduction

In many recent studies of the viscoelastic deformation processes, it was shown that the behavior of the material can be described with a high degree of accuracy with the aid of models containing a fractional differential operator. Its order is chosen either the same for the entire data base e.g., [1,2], as constant over a certain intervals of the parameters [3], or as a certain continuous function [4]. In the last case, the time-dependent order function accumulates at each moment the previous history of the deformation process. Theoretical studies of oscillating processes showed that the presence in the constitutive equation of a term proportional to a fractional derivative is equivalent to introduction into the system of an element acting either as an additional damper (viscous element), or as stiffness (spring). The character of this action is determined by the order of the operator. Existence of order values, for which the fractional differential term in the equation leads to intensification of the stiffness, was shown in [5]. A method for calculating the boundary between the respective regions in which the two properties of the introduced element predominate was proposed in [6].

In the studies mentioned above and close to the discussed theme studies, it was assumed that the operator order is real. The first attempt to construct a model involving an operator with a complex fractional order was undertaken in [7]. Modeling of oscillating processes gives rise to an additional parameter, which permits more accurate description of the mechanical properties of viscoelastic deformation. The authors of [7] demonstrated this assertion on two models via comparison of numerical and experimental results.

In the proposed work, the authors' goal is utilization of the properties of the differential operator with complex fractional order in the analysis of dynamic stability of a rod subjected to a follower force and capable of dissipation. The problem consists in the following. Let us consider a rod, rigidly fixed at one end (cantilever) and loaded by a follower force at the other. The force is called "follower," if in the process of loss of stability its direction obeys some particular law other than that of gravity. Such, in particular, is the force whose direction remains tangent to the axis of the rod as it deforms (Fig. 1). In Euler's well-known problem on the stability of a rectilinear rod the force is assumed to be aligned with its initial axis and therefore is not a follower (dead force). In fact in the case of a follower force, Euler's problem is unsolvable in its linear static setting: the rod cannot lose stability whatever the compressive force. For a solution to exist a dynamic stability criterion is needed, with the constitutive equation of the process containing, besides the terms of stiffness and force, also one of inertia. After subordinating the general solution of this differential equation to the boundary conditions at the rod ends, we will obtain the final equation for determining the eigenvalues. The latter makes it possible to establish the dependence between the critical force P and the frequency ω. The plotted function $P=P(\omega)$ is shown in Fig. 2 (solid line). On the left side of the loop, the loss of stability predominates with respect to the first mode; on the right, to the second. At its maximum, P exceeds the critical Euler's force for the same rod approximately eight times. The damping effect in [8] is obtainable by introducing an additional term in the constitutive equation proportional to the first time derivative. An analogous situation exists in the case of dynamic stability of the flexible tubes carrying a flowing liquid [9].

The stability problem of rods loaded by follower forces remains of interest in the field of mechanics because of the need for better evaluation of the strength characteristics of structures, especially those of airborne vehicles. Study of bending of a rod in the second mode frequently proves of particular importance, since in this case, the points appear at which structural failure can occur as a result of rupture of the bearing elements. In a recent article [10], new results about the supercritical behavior of a rod were obtained on the basis of the nonlinear theory of the bending of rods, with special attention to the disposition of critical points (inflection and maximal pressurization) along the rod line. Damping, however, is not discussed.

The present paper deals with the dynamic stability of a cantilever rod in the presence of dissipation, simulated by a fractional differential operator with complex order. The damping effect of the real and imaginary parts of the order on the loss of stability under tangential follower forces is evaluated.

Stability of Viscoelastic Rod

Consider a thin elastic rod of constant section, loaded by a tangential force P and undergoing small oscillations in plane xOz about its undeformed rectilinear equilibrium configuration (Fig. 1). Let $w(x,t)$ be a small deviation at any point x of the rod, EJ the flexural rigidity of its section, and m its mass per unit length. The equation of these small oscillations takes the form [8]

$$EJ\frac{\partial^4 w}{\partial x^4}+P\frac{\partial^2 w}{\partial x^2}+m\frac{\partial^2 w}{\partial t^2}=0 \tag{1}$$

The model of viscoelastic deformation entails introduction in Eq. (1) of additional term dissipation. This correction is usually effected through replacement of the constant quantity E by the differential operator $E^*=E(1+\eta(\partial/\partial t))$. Our study being carried out within the framework of fractional differentiation, we take the relaxation modulus of elasticity as

[1]Corresponding author.

Contributed by the Applied Mechanics Division of ASME for publication in the JOURNAL OF APPLIED MECHANICS. Manuscript received February 1, 2007; final manuscript received March 22, 2007; published online January 14, 2008. Review conducted by K. Ravi-Chandar.

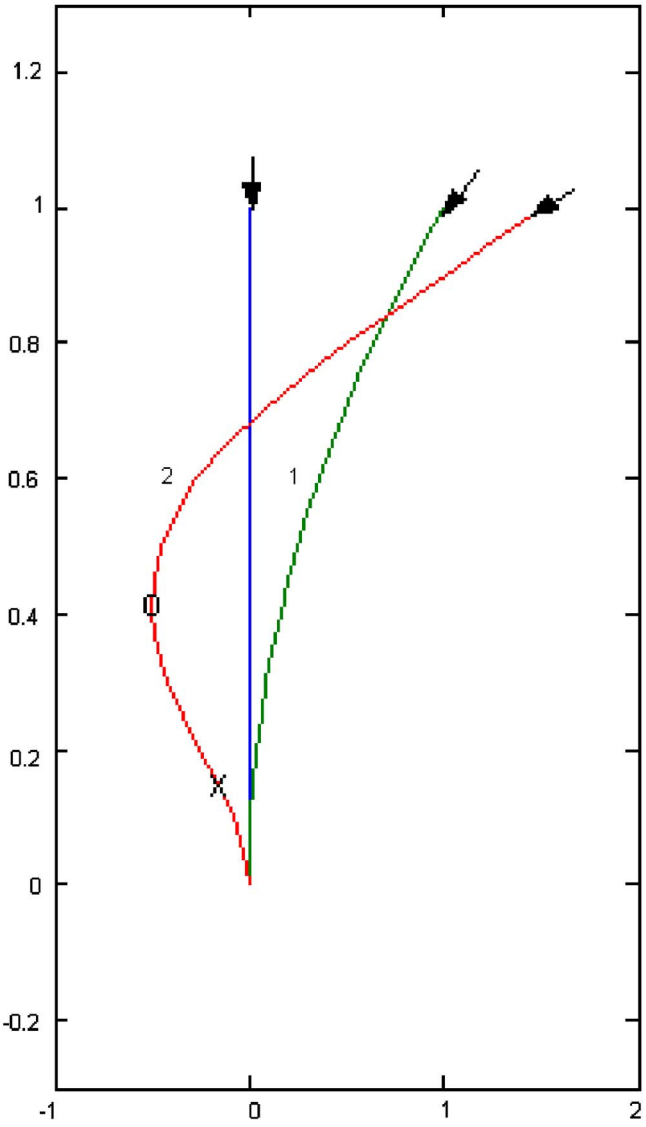

Fig. 1 Modes of equilibrium state of rod: 1–first; 2–second. Critical points: x–inflection, o–maximal deflection

$$E^* = E\left[1 + \left(\eta_0 \frac{\partial}{\partial t}\right)^{\alpha+i\beta}\right] \quad D_t^\gamma f(t) = \frac{1}{\Gamma(m-\alpha)} \int_{-\infty}^{t} (t - \tau)^{m-1-\gamma} f(\tau) d\tau \tag{2}$$

where m is the integer part of $1+\mathrm{Re}\ \gamma$. We use the Weyl definition of a fractional differential operator. The damping ratio η_0 has the dimensionality s.

The boundary conditions at the fixed end, i.e., $x=0$, and at the free end, i.e., $x=L$, read

$$w(0,t) = \frac{\partial}{\partial x} w(0,t) = 0 \quad \frac{\partial^2}{\partial x^2} w(L,t) = \frac{\partial^3}{\partial x^3} w(L,t) = 0 \tag{3}$$

Equation (1) with the relaxation modulus (2) satisfies the function $w(x,t)=V(x)\exp(i\Omega t)$, where $V(x)$ and Ω are an unknown function and an unknown constant. Substituting it in (1), we obtain an equation which, after introduction of dimensionless variables and parameters,

$$\xi = x/L \quad v(\xi) = V(x)/L \quad u = PL^2/EJ \quad \omega = \Omega L^2 \sqrt{m/EL}$$

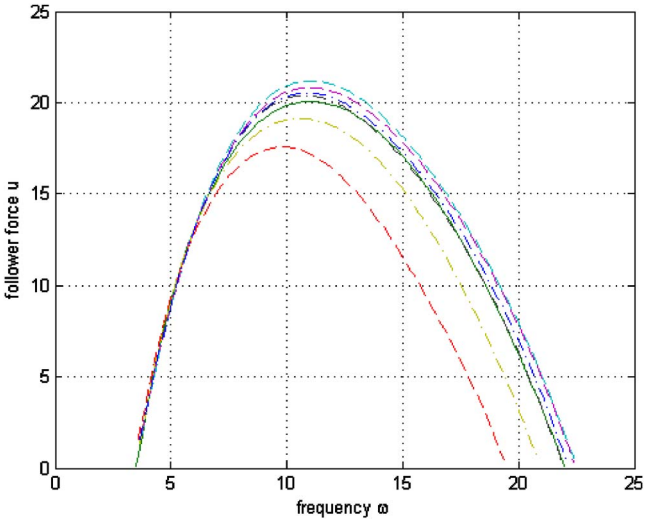

Fig. 2 Bifurcation lines $u=u(\omega)$

$$\eta = \eta_0 \sqrt{EJ/mL^4}$$

takes the form $[1+(i\eta\omega)^{\alpha+i\beta}]v'''' + uv'' - \omega^2 v = 0$.

We seek the solution of this linear equation with constant coefficients in the form $v(\xi)=\exp(r\xi)$. The characteristic biquadratic equation

$$[1 + (i\eta\omega)^{\alpha+i\beta}]r^4 + ur^2 - \omega^2 = 0 \tag{4}$$

has four roots $r_j=\rho_j+i\delta_j$ $r_{j+2}=-r_j$ $j=1,2$.

Applying to the general solution,

$$v(\xi) = \sum_{j=1}^{4} A_j e^{r_j \xi} \tag{5}$$

the boundary conditions (3), we obtain a homogeneous set of linear algebraic equations:

$$\sum_{j=1}^{4} A_j = 0 \quad \sum_{j=1}^{4} A_j(\rho_j + i\delta_j) = 0 \quad \sum_{j=1}^{4} A_j(\rho_j + i\delta_j)^2 \exp(\rho_j + i\delta_j) = 0$$

$$\sum_{j=1}^{4} A_j(\rho_j + i\delta_j)^3 \exp(\rho_j + i\delta_j) = 0 \tag{6}$$

The existence condition for a nonzero solution of this set is a zero value of the determinant $D(u,\omega,\eta,\alpha,\beta)$ of the matrix comprising the coefficients adjoining A_j in set (6). The interdependence of the parameters u and ω for each triad η, α, β is readily found by Newton's iteration technique. In the calculations, the initial value of $\omega^{(0)}$ was chosen as 10 for the first mode and 20 for the second, $\Delta\omega=0.02$. Convergence was sufficiently fast, so that the first four significant digits were established after 5–6 iterations.

The numerical and graphical results demonstrated below present the real part of the output characteristics. Let us note the following. For $\beta=0$, two roots of Eq. (4) are real and two imaginary. In this case all calculation results of interest are real. For $\beta\neq 0$ these results become complex; in evaluating the influence of the imaginary part on the data the real part was replaced by its absolute value (for example, $\mathrm{Re}(u_{\max})$ by $|u_{\max}|$ or $\mathrm{Re}\ \xi$ by $|\xi|$). However, within the accepted limitations on the external parameters ($0\leq\eta\leq 0.005$, $0.7\leq\alpha\leq 1$, $|\beta|\leq 0.5$), no sufficiently noticeable changes were observed either in the qualitative or in the quantitative pattern.

Table 1 Dependence of u_{max} on parameters α and β

α	β=−0.5	−0.25	0	0.25	0.5
0.7	17.56	19.73	21.19	21.22	20.81
0.85	18.44	19.45	20.62	20.77	20.63
1	19.14	19.51	20.37	20.54	20.52

Damping Effect of the Differential Operator Parameters

Study of the dynamic stability of a rod involves the dependence $u=u(\omega)$ between the parameters ω and u, proportional to the oscillation frequency and compressive follower force, respectively. Each point on the graph of this dependence corresponds to bifurcation of the equilibrium state of the rod. The left-hand branch corresponds to loss of stability with respect to the first mode and right-hand to the second (lines 1 and 2 in Fig. 1, respectively). Plotted functions for some values of parameters α, β, and η are shown in Fig. 2. The solid line refers to $\eta=0$ (Bolotin's bifurcation line), the dashed lines refer to $\eta=0.002$, $\alpha=0.7$ and the dot-dashed lines to $\eta=0.002$, $\alpha=1$. The parameter β was assigned the values of −0.5, 0, 0.5. The most noticeable differences occur in the second-mode bifurcation (right-hand branches in the graphs). Therefore, in considering the calculation results further, we confine ourselves to the special features in the behavior of the maximal value of bifurcation line or of its right-hand branch. In other words, we are concerned with the influence of the parameters α, β, and η on the maximal critical force and the secondary loss of stability.

For $\beta<0$, the bifurcation lines lie below Bolotin's line, and move upwards as β increases. The lines for $\alpha=0.7$ initially lie below those for $\alpha=1$, and subsequently rise above it. The same features are demonstrated in Table 1.

Bolotin's line has $u_{max}=20.05$. It can be noted that for each α, the line $\beta=0$ plays the role of a "distorting mirror" for matched lines with opposite sign of β.

In Figs. 3(*a*) and 3(*b*) are given sections of the surface $u_{max}(\alpha,\beta)$ for β=const (β=−0.3, −0.2, 0, 0.2, 0.3: lines 1–5, respectively) and for α=const (α=1, 0.9, 0.8, 0.7: lines 1–4). For $\beta\geq 0$ with increase of α, u_{max} decreases monotonically. An increase in the parameter α corresponds to higher viscosity of the system, which leads to loss of stability on the lower bifurcation line. For $\beta<0$, u_{max} loses its monotonicity, although the downward trend persists. The lines in the α=const sections are nonmonotonic. Each line in Fig. 3(*b*) has a maximum, which is shifted to the left with decrease of α. For $\beta<0$, the surface $u_{max}(\alpha,\beta)$ becomes folded.

Figure 4 shows the upper arcs of the bifurcation lines for η =0.0005, 0.0045, α=0.8, 1.0, and β=0. u_{max} increases with damping ratio η and decreases with α.

It was established in [11], in a study of the oscillations of a system with a single degree of freedom, that inclusion of a term

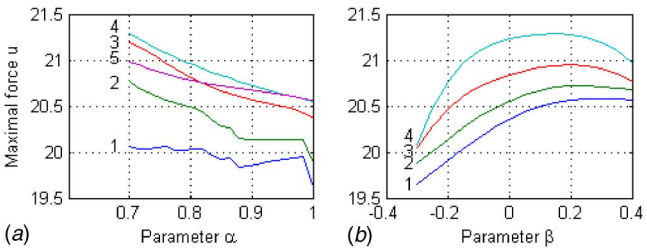

Fig. 3 Sections of surface $u_{max}(\alpha,\beta)$: (*a*) β=const and (*b*) α =const

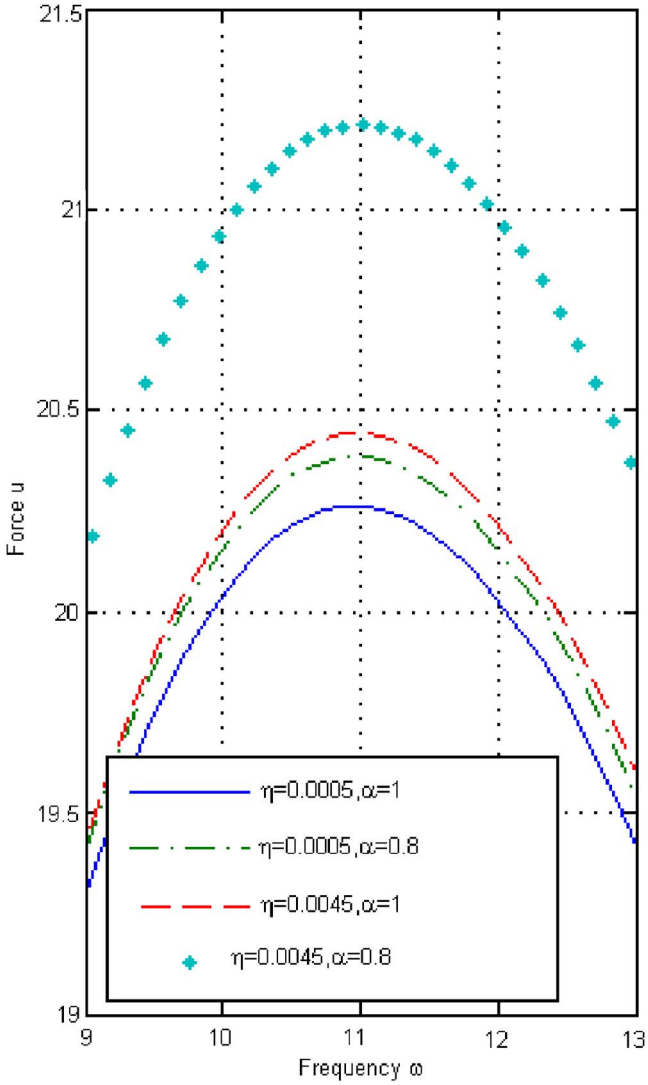

Fig. 4 Upper arcs of bifurcation lines for β=0

proportional to the fractional derivative of real order in the constitutive equation of motion is equivalent to appearance of an additional element in the system with properties determined by the damping ratio η and the order of differentiation α. The oscillations of this system undergo damping, their frequency ω decreasing with increase of η and decrease of α. The layout of the lines in Fig. 4 shows prevalence this effect also in the present system with infinite degrees of freedom. Decrease of the oscillation frequency under a constant compressive force renders the system more stable, and a stronger force is needed to revert to the bifurcation state. As consequence, the bifurcation line moves upwards together with increase of η and decrease of α.

Critical Points

The point at which the second derivative $d^2v/d\xi^2$ vanishes is the inflection point of the rod centerline. The first mode has a single inflection point at the clamped end. In the second mode, a second inflection point appears, whose coordinate we denote by ξ_1. The point at which the tangent and the centerline of the undeformed rod (the x-axis) coincide is the point of maximal deflection, whose coordinate for the second mode we denote by ξ_0.

The displacement of the rod point with loss of stability cannot be determined unambiguously under the linear deformation theory, but the following assumption can be made: the lower the

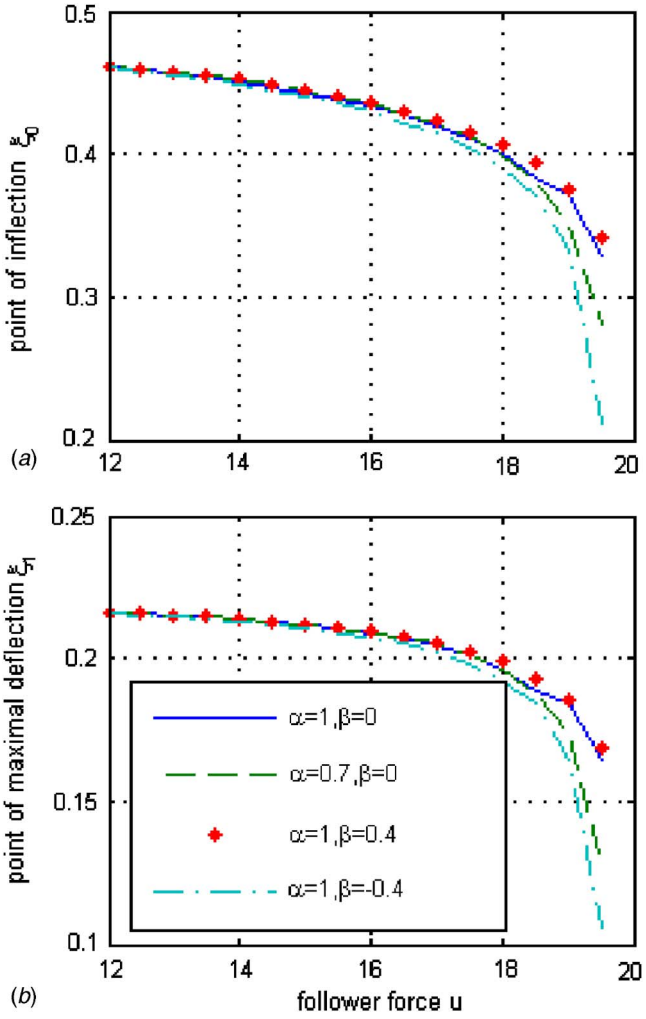

Fig. 5 Pattern of critical points on second mode: (*a*) inflection point ξ_0 and (*b*) maximal deflection ξ_1

point of inflection, the higher the curvature of the deformed rod at the point of maximal deflection, which is the likeliest site this point of rupture in the second mode.

Let us derive the equations for the coordinates of these points. Using the first three equations of set (6), we can write coefficients A_j in the form $A_j = A\mu_j$, where

$$\mu_1 = r_2^2(r_1 - r_2)e^{r_1+2r_2} + 2r_1^2 r_2 e^{r_2} - r_2^2(r_1 + r_2)e^{r_1}$$

$$\mu_2 = [(r_1 + r_2)\mu_1 + 2r_2\mu_3]/(r_1 - r2)$$

$$\mu_3 = r_1^2(r_2 - r_1)e^{2r_1+r_2} + 2r_2^2 r_1 e^{r_1} - r_1^2(r_1 + r_2)e^{r_2}$$

$$\mu_4 = [(r_1 + r_2)\mu_3 + 2r_1\mu_1]/(r_2 - r_1)$$

r_1, r_2 being the roots of the characteristic Eq. (4) that correspond to the second mode. Substituting the above in the general solution (5) and equating the first and second derivatives to zero, we have

$$v'(\xi_0) = A\sum_{j=1}^{4} \mu_j r_j \exp(r_j\xi_0) = 0 \quad v''(\xi_1) = A\sum_{j=1}^{4} \mu_j r_j^2 \exp(r_j\xi_1) = 0$$

The graphs of the coordinate functions $\xi_0(u)$ and $\xi_1(u)$ for certain combinations of the parameters α, β, and η are shown in Figs. 5(*a*) and 5(*b*). The higher the line, the larger α and β and the smaller η. As $u(\omega)$ approaches its maximum, the divergence of the graphs becomes more significant and points $\xi_0(u)$ and $\xi_1(u)$ descend towards the fixed end of the rod. For $u \leq 12$, ξ_0 and ξ_1 depend on the compressive force, but are practically independent of the other parameters.

Conclusion

In this work, the authors posed two problems: first, estimation of the influence of viscoelasticity on the dynamic stability of the rod, by recourse to the tool of fractional differentiation; second, assessment of the approximational possibilities of the imaginary part of the order of the differential operator. In publications on fractional integro-differentiation in analysis of viscoelastic deformation processes, the order of the operator is assumed, as a rule, to be real, especially where experimental determination of the order for real materials is concerned. In [7], a complex order of the differential operator made it possible to enlist the second parameter (imaginary part of the order) in approximating the dependences in the investigated process. Here, however, our results show that smooth behavior can be expected only for $\beta \geq 0$. For $\beta < 0$, it may occur that a small change in the input data would lead to an unjustifiably large one in the output: a phenomenon given the name of "fold catastrophe." The unavoidable conclusion is that the imaginary part of the order of the differential operator as leveling parameter secures a smooth approximation only in the region of its positive values. Accordingly, only results associated with the condition $\beta \geq 0$ are retained in the sequel.

Inclusion of a term proportional to the differential operator, with damping ratio $\eta > 0$, in the constitutive equation of motion, leads to damped oscillations whose frequency increases with η. Secondary bifurcation occurs at higher values u_{max} and with decrease of the coordinates of the inflection point ξ_1 and of the maximal deflection ξ_0. An increase in the maximal compressive force u_{max} "propels" the entire bifurcation line upwards, with simultaneous downward movement of the critical points.

The parameter α for values close to 1 imparts to the additional device the properties of a viscous element, but with a decrease of α, the device is transformed into a stiff spring. The frequency of the damped oscillations increases as α decreases, u_{max} increases, and the critical points descend. In other words, decrease of α has the same consequences as an increase of η. Transfer of the bifurcation line to a higher state makes for a higher stability of the rod, but lowering of the critical points increases the likelihood of rupture at point ξ_0.

The coordinates ξ_0 and ξ_1 depend on β and increase monotonically, whereas u_{max} changes with β non-monotonically.

Loss of stability can occur at any combination of u and ω linked in a bifurcational dependence, but as the right-hand branch ascends, the critical points descend.

The onset of "anomalous" (term in [5]; see also [6]) behavior of the frequencies, in which the eigenfrequency of fractional differential model exceeds the analogous value in the purely elastic oscillator, influences the duration of the initial period, after which second-mode motion develops in the viscoelastic material.

Acknowledgment

The authors wish to express their gratitude to E. Goldberg for his valuable help and advice in preparation of the manuscript.

References

[1] Alcoutlabi, M., and Martinez-Vega, J. J., 1998, "Application of Fractional Calculus to Viscoelastic Behaviour Modelling and to the Physical Ageing Phenomenon in Glassy Amorphous Polymers," Polymer, **39**(25), pp. 6269–6277.
[2] Deng, R., Davies, P., and Bajaj, A. K., 2003, "Flexible Polyurethane Foam Modeling and Identification of Viscoelastic Parameters for Automotive Seating Applications," J. Sound Vib., **262**, pp. 391–417.
[3] Hernandez-Jimenez, A., Hernandez-Santiago, J., Macias-Garcia, A., and Sanchez-Gonzalez, J., 2002, "Relaxation Modulus in PMMA and PTFE Fitting by Fractional Maxwell Model," Polym. Test., **21**, pp. 325–331.
[4] Ingman, D., Suzdalnitsky, J., and Zeifman, M., 2000, "Constitutive Dynamic-Order Model for Nonlinear Contact Phenomena," ASME J. Appl. Mech., **67**, pp. 383–390.

[5] Rossikhin, Yu. A., and Shitikova, M. V., 1997, "Applications of Fractional Calculus to Dynamic Problems of Linear and Nonlinear Hereditary Mechanics of Solids," Appl. Mech. Rev. **50**(1), pp. 15–57.
[6] Ingman, D., and Suzdalnitsky, J., 2004, "Control of Damping Oscillations by Fractional Differential Operator With Time-Dependent Order," Comput. Methods Appl. Mech. Eng., **193**(52), pp. 5585–5595.
[7] Makris, N., and Constantinou, M. C., 1993, "Models of Viscoelasticity With Complex-Order Derivatives," J. Eng. Mech., **119**(7), pp. 1453–1464.
[8] Bolotin, V. V., 1963, *Nonconservative Problems of the Theory of Elastic Stability*, Pergamon Press, Oxford.
[9] Paidoussis, M. P., 1998, *Fluid-Structure Interactions*, Vol. 1, Academic Press, New York.
[10] Zakharov, Yu. V., Okhotkin, K. G., and Skorobogatov, A. D., 2004, "Bending of Bars Under a Follower Load," J. Appl. Mech. Tech. Phys., **45**(5), pp. 756–763.
[11] Ingman, D., and Suzdalnitsky, J., 2001, "Iteration Method for Equation of Viscoelastic Motion With Fractional Differential Operator of Damping," Comput. Methods Appl. Mech. Eng., **190**, pp. 5027–5036.

An Upper Bound on the Error in Linear Quasi-Shallow Shell Theory

J. G. Simmonds
Fellow ASME
Department of Civil Engineering,
University of Virginia,
Charlottesville, VA 22904-4742
e-mail: jgs@virginia.edu

For a completely clamped elastic shell, an explicit upper bound is derived for the error in the energy norm of a solution of the linear, quasi-shallow shell equations as compared to the corresponding solution of the Sanders-Koiter equations.
[DOI: 10.1115/1.2745827]

1 Introduction

Quasi-shallow (Q-S) shell theory, the independent extension by Libai [1] and Koiter [2] of Marguerre's shallow shell theory [3], assumes only that L, a typical wavelength of the deformation pattern (Koiter's phrase), is small compared to R, a typical radius of curvature of the shell's reference surface. (Q-S theory is sometimes called D-M-V theory, after Donnell, Mushtari, and Vlasov.) Compared to the Sanders-Koiter (S-K) linear shell equations [4], the equations of quasi-shallow shell theory are much simpler, involving, for example, only two unknowns, the normal displacement and a stress function, as opposed to, for example, three displacement components and three stress functions.

The present Note derives a rigorous upper bound, in the energy norm, on the difference between solutions of the S-K and Q-S equations. A key is to regard the Q-S equations as the S-K equations with distributed surface loads. This idea was used in a recent estimate [5] of the error in Novozhilov's equations for general (non-circular) elastically isotropic cylindrical shells. There, a second key step was to obtain a particular solution of a cylindrical membrane under arbitrary surface loads. However, for arbitrary shells, such solutions do not seem to be readily available so, instead of obtaining an *exact* error estimate via the Prager-Synge hypercircle theorem [6] as in [5], we are forced to accept an *upper* bound on the error of a fully clamped shell that involves the solution of the (presumed known) static Q-S equations in addition to the *lowest natural extensional frequency* predicted by these same equations. Despite its limitations, such an estimate yields both quantitative and qualitative information. For example, as boundary conditions of complete clamping are relaxed, the estimate suggests that the error in the Q-S equations degrades.

2 Differential Geometry

Let $\mathbf{x}(\vartheta^1,\vartheta^2)$ denote the twice differentiable position of the orientable shell reference surface $\mathcal{S}$, where $(\vartheta^1,\vartheta^2)$ are Gaussian coordinates, and let $\mathbf{n}(\mathbf{x})$ denote a unit normal to $\mathcal{S}$ at $\mathbf{x}$. In standard notation, the covariant base vectors on $\mathcal{S}$ are defined and denoted by $\mathbf{a}_\alpha \equiv \mathbf{x},_\alpha \equiv \partial\mathbf{x}/\partial\vartheta^\alpha$, $\alpha=1,2$, the covariant and contravariant components of the surface metric tensor by $a_{\alpha\beta}\equiv\mathbf{a}_\alpha\bullet\mathbf{a}_\beta$ and $a^{\alpha\gamma}a_{\beta\gamma}=\delta^\alpha_\beta$, the Kronecker delta, the covariant components of the surface curvature by $b_{\alpha\beta}=\mathbf{n}\bullet\mathbf{x},_{\alpha\beta}$, and the contravariant components of the surface permutation tensor by $\varepsilon^{\alpha\beta}$. Covariant differentiation on $\mathcal{S}$ will be denoted by a vertical bar, indices, as usual, are raised or lowered with respect to the components of the metric tensor, and $\mathbf{n},_\alpha=-b^\beta_\alpha\mathbf{a}_\beta$.

3 The Sanders-Koiter (S-K) and Quasi-Shallow (Q-S) Shell Equations

The equilibrium equations of S-K theory may be written

$$\mathbf{N}^\alpha|_\alpha+\mathbf{p}=\mathbf{0} \tag{1}$$

where

$$\mathbf{N}^\alpha=\left(N^{\alpha\beta}+\underline{\frac{1}{2}\varepsilon^{\alpha\beta}S_{\lambda\mu}M^{\lambda\mu}}\right)\mathbf{a}_\beta-M^{\alpha\beta}|_\beta\mathbf{n} \tag{2}$$

is the reduced contravariant stress resultant,

$$\mathbf{p}=p^\alpha\mathbf{a}_\alpha+p\mathbf{n} \tag{3}$$

is the external surface load, and

$$S_{\alpha\beta}=\frac{1}{2}(\varepsilon_{\alpha\gamma}b^\gamma_\beta+\varepsilon_{\beta\gamma}b^\gamma_\alpha) \tag{4}$$

are the covariant components of Sanders' tensor. Note that $a^{\alpha\beta}S_{\alpha\beta}=b^{\alpha\beta}S_{\alpha\beta}=0$. In (2), $N^{\alpha\beta}$ and $M^{\alpha\beta}$ are, respectively, the contravariant components of the (modified, symmetric) stress resultant and stress couple of S-K theory [4]. The underlined term in (2) and in the equations to follow are absent in Q-S theory.

Taking the dot product of (1) with

$$\mathbf{u}=u^\alpha\mathbf{a}_\alpha+w\mathbf{n} \tag{5}$$

the displacement of the reference surface $\mathcal{S}$, integrating over $\mathcal{S}$, and applying the divergence theorem, we obtain the *mechanical work identity*:

$$\int_{\partial\mathcal{S}}\nu_\alpha\mathbf{N}^\alpha\bullet\mathbf{u}ds+\int_{\mathcal{S}}\mathbf{p}\bullet\mathbf{u}dS\equiv\int_{\mathcal{S}}\mathbf{N}^\alpha\bullet\mathbf{u},_\alpha dS \tag{6}$$

where $\partial\mathcal{S}$ is the (assumed) piecewise smooth boundary of $\mathcal{S}$, the ν_α are the covariant components of the outward unit normal to $\partial\mathcal{S}$ tangent to $\mathcal{S}$, and s is arc length along $\partial\mathcal{S}$. Because

$$\mathbf{u},_\alpha=(E_{\alpha\beta}+\varepsilon_{\alpha\beta}\omega)\mathbf{a}^\beta+\varphi_\alpha\mathbf{n} \tag{7}$$

where

$$E_{\alpha\beta}=\frac{1}{2}(u_{\alpha|\beta}+u_{\beta|\alpha})-b_{\alpha\beta}w \tag{8}$$

is the extensional strain,

$$\omega=\frac{1}{2}\varepsilon^{\alpha\beta}u_{\beta|\alpha} \tag{9}$$

is the rotation about the normal, and

$$\varphi_\alpha=w,_\alpha+\underline{b^\beta_\alpha u_\beta} \tag{10}$$

is the rotation about $\varepsilon^{\beta\alpha}\mathbf{a}_\beta$,

$$\mathbf{N}^\alpha\bullet\mathbf{u},_\alpha=N^{\alpha\beta}E_{\alpha\beta}+\underline{S_{\alpha\beta}M^{\alpha\beta}\omega}-M^{\alpha\beta}|_\beta\varphi_\alpha \tag{11}$$

Now,

$$\int_{\mathcal{S}}M^{\alpha\beta}|_\beta\varphi_\alpha dS=\int_{\partial\mathcal{S}}[M\varphi-H(dw/ds+\underline{b^\beta_\alpha\tau^\alpha u_\beta})]ds-\int_{\mathcal{S}}M^{\alpha\beta}\varphi_{\alpha|\beta}dS \tag{12}$$

where $\varphi=\varphi_\alpha\nu^\alpha$ is the edge rotation, $M=M^{\alpha\beta}\nu_\alpha\nu_\beta$ is the edge bending moment, $H=-M^{\alpha\beta}\nu_\alpha\tau_\beta$ is the edge twisting moment, and the τ^α are the contravariant components of a unit tangent vector along $\partial\mathcal{S}$ in the direction of increasing arc length.

Contributed by the Applied Mechanics Division of ASME for publication in the JOURNAL OF APPLIED MECHANICS. Manuscript received February 27, 2007; final manuscript received April 16, 2007; published online January 14, 2008. Review conducted by Robert M. McMeeking.

Inserting (2) and (11) into (6) and then (12) into the resulting equation and integrating $H\,dw/ds$ by parts along $\partial\mathcal{S}$, we obtain the final form of the mechanical work identity in S-K theory:

$$\int_{\partial\mathcal{S}}\left[\left(N^{\alpha\beta}+\underline{\frac{1}{2}\varepsilon^{\alpha\beta}S_{\lambda\mu}M^{\lambda\mu}-\tau^{\beta}b^{\alpha}_{\beta}H}\right)\nu_{\alpha}u_{\beta}+(dH/ds-\ M^{\alpha\beta}|_{\beta}\nu_{\alpha})w+M\varphi\right]ds+\sum_{s_i}[\![H]\!]w+\int_{\mathcal{S}}(p^{\alpha}u_{\alpha}+pw)dS$$
$$\equiv\int_{\mathcal{S}}(N^{\alpha\beta}E_{\alpha\beta}+M^{\alpha\beta}K_{\alpha\beta})dS \tag{13}$$

where

$$K_{\alpha\beta}=\frac{1}{2}(\varphi_{\ \alpha|\beta}+\varphi_{\ \beta|\alpha})+\underline{S_{\alpha\beta}\omega} \tag{14}$$

is the bending strain, the s_i locate the corners of $\partial\mathcal{S}$, and $[\![H]\!]$ is the jump in the edge twisting moment at those corners. Boundary conditions may be read off from the boundary integral and sum on the left side of (13).

The S-K and Q-S theories are completed by the addition of stress-strain relations. For simplicity, we confine ourselves to elastic isotropy so that

$$N^{\alpha\beta}=C[(1-\nu)E^{\alpha\beta}(\mathbf{u})+\nu a^{\alpha\beta}E^{\gamma}_{\gamma}(\mathbf{u})] \tag{15}$$

$$M^{\alpha\beta}=D[(1-\nu)K^{\alpha\beta}(\mathbf{u})+\nu a^{\alpha\beta}K^{\gamma}_{\gamma}(\mathbf{u})] \tag{16}$$

where

$$C=\frac{Eh}{(1-\nu^2)}\quad\text{and}\quad D=\frac{Eh^3}{12(1-\nu^2)} \tag{17}$$

E is Young's modulus, h is the constant shell thickness, and ν is Poisson's ratio.

4 The Error Estimate

Let an unknown with an overbar denote a solution of the Q-S equations and a tilde denote an unknown depending on $\bar{\mathbf{u}}$ but using expressions from S-K theory. Thus, $\bar{N}^{\alpha\beta}=\tilde{N}^{\alpha\beta}$, but $\bar{M}^{\alpha\beta}=D[(1-\nu)\bar{w}|_{\alpha\beta}+\nu a^{\alpha\beta}\bar{w}|^{\gamma}_{\gamma}]$ and

$$\tilde{M}^{\alpha\beta}=D[(1-\nu)\tilde{K}^{\alpha\beta}(\bar{\mathbf{u}})+\nu a^{\alpha\beta}\tilde{K}^{\gamma}_{\gamma}(\bar{\mathbf{u}})]\equiv\bar{M}^{\alpha\beta}(\bar{w})+\hat{M}^{\alpha\beta}(\bar{\mathbf{u}}) \tag{18}$$

where

$$\hat{M}^{\alpha\beta}=D\left\{\frac{1}{2}(1-\nu)[\ (b^{\alpha\gamma}\bar{u}_{\gamma})|^{\beta}+\ (b^{\beta\gamma}\bar{u}_{\gamma})|^{\alpha}+2S_{\alpha\beta}\bar{\omega}]+\nu a^{\alpha\beta}\,(b^{\lambda\mu}\bar{u}_{\mu})|_{\lambda}\right\} \tag{19}$$

Now from (1) and (2) observe that $\bar{\mathbf{u}}$ *satisfied the S-K equations with* $\mathbf{p}$ *replaced by*

$$\mathbf{p}-\left[\ \frac{1}{2}\varepsilon^{\alpha\beta}(S_{\lambda\mu}\tilde{M}^{\lambda\mu})\Big|_{\alpha}+\ b^{\beta}_{\gamma}\tilde{M}^{\alpha\gamma}|_{\alpha}\right]\mathbf{a}_{\beta}-\ \tilde{M}^{\alpha\beta}|_{\alpha\beta}\mathbf{n}\equiv\mathbf{p}-\tilde{\mathbf{p}}(\bar{\mathbf{u}}) \tag{20}$$

so that the difference $\Delta\mathbf{N}^{\alpha}\equiv\mathbf{N}^{\alpha}-\tilde{\mathbf{N}}^{\alpha}$ satisfies the equation

$$\Delta\mathbf{N}^{\alpha}|_{\alpha}+\tilde{\mathbf{p}}=\mathbf{0} \tag{21}$$

We now restrict attention to *clamped boundary conditions*. With $\Delta\mathbf{u}=\mathbf{u}-\bar{\mathbf{u}}$, we have, from (10) and (13), $\Delta\mathbf{u}|_{\partial\mathcal{S}}=\mathbf{0}$ and $(\varphi-\tilde{\varphi})|_{\partial\mathcal{S}}=0$, so that (21) and these boundary conditions imply the mechanical work identity

$$\int_{\mathcal{S}}\tilde{\mathbf{p}}\cdot\Delta\mathbf{u}dS\equiv 2V[\Delta\mathbf{u}] \tag{22}$$

where, by (15) and (16), the strain-energy of any twice-differentiable displacement field is

$$V[\mathbf{u}]r=\frac{1}{2}\int_{\mathcal{S}}\{C[(1-\nu)E^{\alpha\beta}E_{\alpha\beta}+\nu E^{\alpha}_{\alpha}E^{\beta}_{\beta}]+D[(1-\nu)K^{\alpha\beta}K_{\alpha\beta}+\nu K^{\alpha}_{\alpha}K^{\beta}_{\beta}]\}dS\equiv V_e[\mathbf{u}]+V_b[\mathbf{u}]>0$$
$$\text{if }\mathbf{u}\neq\text{ a rigid body displacement} \tag{23}$$

By Schwarz' inequality, $\int_{\mathcal{S}}\tilde{\mathbf{p}}\cdot\Delta\mathbf{u}dS\leq\int|\tilde{\mathbf{p}}||\Delta\mathbf{u}|dS\leq\|\tilde{\mathbf{p}}\|\|\Delta\mathbf{u}\||\mathcal{S}|$, where $|\mathcal{S}|\|\cdot\|^2\equiv\int_{\mathcal{S}}|\cdot|^2dS$ and $|\mathcal{S}|$ denotes the area of the reference surface. Thus,

$$2V[\Delta\mathbf{u}]\leq\|\tilde{\mathbf{p}}(\bar{\mathbf{u}})\|\|\Delta\mathbf{u}\||\mathcal{S}| \tag{24}$$

Let

$$\lambda[\hat{\mathbf{u}}]=\min\frac{\sqrt{V[\mathbf{u}]}}{\|\mathbf{u}\|\sqrt{|\mathcal{S}|}}\quad\forall\ \|\mathbf{u}\|\neq 0,\ \mathbf{u}|_{\partial\mathcal{S}}=0 \tag{25}$$

Physically, $\lambda/\sqrt{m}$ is *the lowest natural frequency of the fully clamped shell* predicted by S-K theory, where m is the mass per unit area of the reference surface $\mathcal{S}$. In writing "min" instead of "inf" and $\lambda[\hat{\mathbf{u}}]$ instead of λ, we are assuming that there is a twice differentiable displacement field $\hat{\mathbf{u}}$ for which the minimum in (25) is actually achieved.

The substitution of (25) with $\mathbf{u}$ replaced by $\Delta\mathbf{u}$ into (24) gives us a bound on $\Delta\mathbf{u}$ in the energy norm:

$$\sqrt{V[\Delta\mathbf{u}]}\leq(2\lambda)^{-1}\|\tilde{\mathbf{p}}(\bar{\mathbf{u}})\|\sqrt{|\mathcal{S}|} \tag{26}$$

5 A Computable Upper Bound

The obvious problem with computing the right side of (26) is that the scalar λ comes from S-K theory—the very theory to be approximated by the simpler Q-S theory. To work with quantities coming exclusively from Q-S theory, note that in *membrane theory* ($M^{\alpha\beta}=0$), the field equations and boundary conditions of both theories are identical and that complete clamping means $u_{\alpha}|_{\partial\mathcal{S}}=0$; nothing can be said about the boundary values of w or its normal derivative. Thus, let

$$\Lambda[\hat{\mathbf{u}}]\equiv\min\frac{\sqrt{V_e[\mathbf{u}]}}{\|\mathbf{u}\|\sqrt{|\mathcal{S}|}}\quad\forall\ \|\mathbf{u}\|\neq 0\quad\mathbf{u}|_{\partial\mathcal{S}}=0 \tag{27}$$

Then,

$$\Lambda[\hat{\mathbf{u}}]\leq\frac{\sqrt{V_e[\hat{\mathbf{u}}]+V_b[\hat{\mathbf{u}}]}}{\|\hat{\mathbf{u}}\|\sqrt{|\mathcal{S}|}}=\lambda[\hat{\mathbf{u}}] \tag{28}$$

so that from (26),

$$\sqrt{V[\Delta\mathbf{u}]}\leq(2\Lambda)^{-1}\|\tilde{\mathbf{p}}(\bar{\mathbf{u}})\|\sqrt{|\mathcal{S}|} \tag{29}$$

6 A Qualitative Error Estimate

If L denotes the "wavelength" associated with the deformation we are trying to approximate by a solution of the Q-S equations where, typically, L measures the width of an edge-zone layer, then, from (16), (19), (20), (23), and (27),

$$\|\tilde{\mathbf{p}}\|=\mathrm{O}(Eh^3\|\bar{\mathbf{u}}\|/L^2R^2),\quad\Lambda[\hat{\mathbf{u}}]=\mathrm{O}(\sqrt{Eh}/L) \tag{30}$$

Thus,

$$\sqrt{V[\Delta\mathbf{u}]}=\mathrm{O}(\sqrt{Eh|\mathcal{S}|}h^2\|\bar{\mathbf{u}}\|/LR^2) \tag{31}$$

7 Conclusions

Our final error estimate (29) involves solutions of the Q-S equations only, although in addition to a given static problem an auxiliary eigenvalue problem must be solved. However, assuming the numerical machinery is in place to handle the Q-S equations, this additional calculation should require little additional effort.

References

[1] Libai, A., 1962, "On the Nonlinear Elastokinetics of Shells and Beams," J. Aerosp. Sci., **29**, pp. 1190–1195, 1209.

[2] Koiter, W. T., 1966, "On the Nonlinear Theory of Thin Elastic Shells," Proc. K. Ned. Akad. Wet., Ser. B: Phys. Sci., **69**, pp. 1–54.

[3] Marguerre, K., 1938, "Zur Theorie der Gekrümmten Platte Grosser Formänderung," *Proc. 5th Int. Cong. Appl. Mechanics*, John Wiley, New York), pp. 93–101.

[4] Budiansky, B., and Sanders, J. L., Jr., 1963, "On the 'Best' First-Order Linear Shell Theory," *Progress in Applied Mechanics* (Prager Anniversary Volume), Macmillan, New York, pp. 129–140.

[5] Simmonds, J. G., 2007, "The Hypercircle Theorem for Elastic Shells and the Accuracy of Novozhilov's Simplified Equations for General Cylindrical Shells," Discrete Contin. Dyn. Syst., **7**, pp. 643–650.

[6] Prager, W., and Synge, J. L., 1947, "Approximations in Elasticity Based on the Concept of Function Space," Q. Appl. Math., **5**, pp. 241–269.

Wave Propagation Analysis in Anisotropic Plate Using Wavelet Spectral Element Approach

Mira Mitra

S. Gopalakrishnan[1]
e-mail: krishnan@aero.iisc.ernet.in

Department of Aerospace Engineering,
Indian Institute of Science,
Bangalore 560 012, India

In this paper, a 2D wavelet-based spectral finite element (WSFE) is developed for a anisotropic laminated composite plate to study wave propagation. Spectral element model captures the exact inertial distribution as the governing partial differential equations (PDEs) are solved exactly in the transformed frequency-wave-number domain. Thus, the method results in large computational savings compared to conventional finite element (FE) modeling, particularly for wave propagation analysis. In this approach, first, Daubechies scaling function approximation is used in both time and one spatial dimensions to reduce the coupled PDEs to a set of ordinary differential equations (ODEs). Similar to the conventional fast Fourier transform (FFT) based spectral finite element (FSFE), the frequency-dependent wave characteristics can also be extracted directly from the present formulation. However, most importantly, the use of localized basis functions in the present 2D WSFE method circumvents several limitations of the corresponding 2D FSFE technique. Here, the formulated element is used to study wave propagation in laminated composite plates with different ply orientations, both in time and frequency domains. [DOI: 10.1115/1.2755125]

1 Introduction

Composites are being used in aircraft structures because of their several favorable properties. Study of wave propagation in such composite structures is of much relevance because it helps one to understand their behavior under high-frequency impact load encountered in gust, bird hit, tool drop, etc. Apart from this, wave propagation analysis finds important applications in structural health monitoring using diagnostic waves, control of noise, and vibration. However, the behavior of composites at high frequencies is more complicated than it is for their metallic counterpart because of the presence of anisotropy, and very little literature is specifically available on transient wave propagation analysis of composite structures.

Wave propagation deals with loading of high-frequency content and FE formulation for such problems is computationally prohibitive because it requires large system size to capture all the higher modes. These problems are usually solved in the transformed frequency domain using Fourier methods and FSFE [1] is one such method, especially tailored for wave propagation analysis.

In FSFE formulation for 2D structures [1], nodal displacements are related to nodal tractions through a frequency-wave-number-dependent stiffness matrix. The mass distribution is captured exactly, and the accurate elemental dynamic stiffness matrix is derived. Consequently, in the absence of any discontinuities, one element is sufficient to model a plate structure of any length, but unbounded along the other lateral direction.

The main drawback of FSFE is that it cannot handle waveguides of short lengths. This is because the required assumption of periodicity in time approximation results in a "wrap-around" problem for a smaller time window, which totally distorts the response. However, in WSFE formulation, use of Daubechies compactly supported wavelets [2] with localized basis for temporal approximation removes the wraparound problem and can efficiently model undamped finite length waveguides. In addition, for 2D problems, FSFEs [1] are essentially semi-infinite, i.e., they are bounded only in one direction. Thus, the effect of one lateral boundary cannot be captured, and this can be attributed to the global basis functions of the Fourier series approximation of the spatial dimension. The formulated 2D WSFE also overcomes the above problem and can accurately model 2D plate structures of finite dimensions. This is again due to the use of localized Daubechies scaling functions as the basis for approximation of the spatial dimension.

The steps followed in 2D WSFE formulation are as follows. Here, first Daubechies scaling functions are used for approximation in time and this reduces the governing partial differential equation (PDE) into a set of coupled PDEs in spatial dimensions. The wavelet extrapolation technique [3] is used for adapting wavelets in finite domain and imposition of initial conditions. The coupled transformed PDEs are decoupled through eigenanalysis. This temporal approximation, imposition of initial conditions, and decoupling of the reduced PDEs are very similar to that done in WSFE formulation for 1D waveguides [4]. Next, each of these decoupled PDEs are further reduced to a set of coupled ODEs by using the same Daubechies scaling functions for approximation of the spatial dimension. Unlike the temporal approximation, here, the scaling function coefficients lying outside the finite domain are not extrapolated but obtained through periodic extension for unrestrained, i.e., free lateral edges. Each set of ODEs are also coupled, and decoupling is again done using eigenvalue analysis.

Presence of elastic coupling in anisotropic laminated composite plate results in coupled governing differential equations. Thus, the final reduced ODEs after spatial and temporal approximations are in the form of a set of coupled ODEs, for each temporal and spatial sampling point. The solution of these ODEs to derive the exact shape function involves determination of wave numbers and the amplitude ratio matrix. Unlike isotropic cases, here the process of solution is more complicated and is done by posing it as polynomial eigenvalue problem (PEP).

It should be mentioned here that similar to 2D FSFE, the frequency-dependent wave characteristics corresponding to each lateral (Y) wave number, can be extracted directly from the present 2D WSFE formulation. However, unlike FSFE, the wave numbers will be accurate only up to a certain fraction of Nyquist frequency [5].

2 Daubechies Compactly Supported Wavelets

In this section, a concise review of orthogonal basis of Daubechies wavelets [2] is provided. Wavelets $\psi_{j,k}(t)$ forms a compactly supported orthonormal basis for $\mathbf{L}^2(\mathbf{R})$. The wavelets and associated scaling functions $\varphi_{j,k}(t)$ are obtained by translation and dilation of single functions $\psi(t)$ and $\varphi(t)$, respectively,

$$\psi_{j,k}(t) = 2^{j/2}\psi(2^j t - k), \quad j,\ k \in \mathbf{Z} \tag{1}$$

$$\varphi_{j,k}(t) = 2^{j/2}\varphi(2^j t - k), \quad j,\ k \in \mathbf{Z} \tag{2}$$

The scaling functions $\varphi(t)$ are derived from the dilation or scaling equation,

[1]Corresponding author.

Contributed by the Applied Mechanics Division of ASME for publication in the JOURNAL OF APPLIED MECHANICS. Manuscript received July 25, 2006; final manuscript received May 3, 2007; published online January 16, 2008. Review conducted by Sridhar Krishnaswamy.

$$\varphi(t) = \sum_k a_k \varphi(2t-k) \tag{3}$$

and the wavelet function $\psi(t)$ is obtained as

$$\psi(t) = \sum_k (-1)^k a_{1-k} \varphi(2t-k) \tag{4}$$

a_k are the filter coefficients, which are fixed for a specific wavelet or scaling function basis. For compactly supported wavelets, only a finite number of a_k are nonzero. The filter coefficients a_k are derived by imposing certain constraints on the scaling functions.

Let $P_j(f)(t)$ be the approximation of a function $f(t)$ in $\mathbf{L}^2(\mathbf{R})$ using $\varphi_{j,k}(t)$ as the basis, at a certain level (resolution) j, then

$$P_j(f)(t) = \sum_k c_{j,k} \varphi_{j,k}(t), \quad k \in \mathbf{Z} \tag{5}$$

where $c_{j,k}$ are the approximation coefficients.

3 Reduction of Wave Equations to ODEs

3.1 Governing Differential Equations. Using classical laminated plate theory (CLPT) [6], the three governing equations with respect to the three degrees of freedom u_0, v_0, and w are given below. Here, $u_0(x,y,t)$, $v_0(x,y,t)$, and $w(x,y,t)$ are the axial and transverse displacements in x, y and z directions, respectively, along the midplane, which is at $z=0$

$$\frac{A_{11}\partial^2 u_0}{\partial x^2} + \frac{(A_{12}+A_{66})\partial^2 v_0}{\partial x\,\partial y} + \frac{A_{66}\partial^2 u_0}{\partial y^2} - \frac{B_{11}\partial^3 w}{\partial y^3} - \frac{(B_{12}+2B_{66})\partial^3 w}{\partial x\,\partial y^2} = I_0 \ddot{u}_0 \tag{6}$$

$$\frac{A_{66}\partial^2 v_0}{\partial x^2} + \frac{(A_{12}+A_{66})\partial^2 u_0}{\partial x\,\partial y} + \frac{A_{22}\partial^2 v_0}{\partial y^2} - \frac{(B_{12}+2B_{66})\,\partial w^3}{\partial x^2\,\partial y} - \frac{B_{22}\,\partial w^3}{\partial y^3} = I_0 \ddot{v}_0 \tag{7}$$

$$\frac{B_{11}\partial^3 u_0}{\partial x^3} + \frac{(B_{12}+2B_{66})\partial^3 u_0}{\partial x^2\,\partial y} + \frac{(B_{12}+2B_{66})\partial^3 v_0}{\partial x\,\partial y^2} + \frac{B_{11}\partial^3 v_0}{\partial x^3} - \frac{D_{11}\partial^4 w}{\partial x^4} - \frac{2(D_{12}+2D_{66})\partial^4 w}{\partial x^2\,\partial y^2} - \frac{D_{22}\partial^4 w}{\partial y^4} = I_0 \ddot{w} - I_2\left(\frac{\partial^2 \ddot{w}}{\partial x^2} + \frac{\partial^2 \ddot{w}}{\partial y^2}\right) \tag{8}$$

The stiffness coefficients A_{ij}, B_{ij}, D_{ij} and the inertial coefficients I_0, I_2 are defined as

$$[A_{ij},B_{ij},D_{ij}] = \int_A Q_{ij}[1,z,z^2]dA \quad [I_0,I_2] = \int_A \rho[1,z^2]dA$$

where Q_{ij} is the stiffness constant of the lamina and ρ is the mass density. The associated boundary conditions for edges parallel to Y-axis are

$$N_x = \frac{A_{11}\,\partial u_0}{\partial x} + \frac{A_{12}\,\partial v_0}{\partial y} - \frac{B_{11}\partial^2 w}{\partial x^2} - \frac{B_{12}\partial^2 w}{\partial y^2} \tag{9}$$

$$N_y = A_{66}\left(\frac{\partial u_0}{\partial y} + \frac{\partial v_0}{\partial x}\right) - \frac{2B_{66}\partial^2 w}{\partial x\,\partial y} \tag{10}$$

$$M_y = -\frac{B_{11}\,\partial u_0}{\partial x} - \frac{B_{12}\,\partial v_0}{\partial y} + \frac{D_{11}\partial^2 w}{\partial x^2} + \frac{D_{12}\partial^2 w}{\partial y^2} \tag{11}$$

$$V = \frac{B_{11}\partial^2 u_0}{\partial x^2} + \frac{B_{12}\partial^2 v_0}{\partial x\,\partial y} - \frac{D_{11}\partial^3 w}{\partial x^3} - \frac{D_{12}\partial^3 w}{\partial x\,\partial y^2} + \frac{I_2\,\partial \ddot{w}}{\partial x} \tag{12}$$

where N_x and N_y are the normal forces in x and y direction, respectively. M_y and M_x are the moments about x- and y-axis. The shear resultant or the Kirchoff shear [1] V is obtained as

$$V = Q - \frac{\partial M_{xy}}{\partial y} \tag{13}$$

where Q is the transverse shear force in the z direction. Next, governing PDEs and the associated boundary conditions derived here are reduced to a set of ODEs using Daubechies scaling function approximation in time and one spatial (Y) dimension.

3.2 Temporal Approximation. The first step in the formulation of the 2D WSFE is the reduction of each of the three governing differential equations given by Eqs. (6)–(8) to a set of PDEs by Daubechies scaling function-based transformation in time. The procedure is exactly similar to that in the formulation of the 1D WSFE [4]. However, the key steps are stated here very briefly for completeness. Let $u_0(x,y,t)$ be discretized at n points in the time window $[0t_f]$. Let $\tau=0,1,\ldots,n-1$ be the sampling points, then

$$t = \triangle t\,\tau \tag{14}$$

where $\triangle t$ is the time interval between two sampling points. The function $u_0(x,y,t)$ can be approximated by scaling function $\varphi(\tau)$ at an arbitrary scale as

$$u_0(x,y,t) = u_0(x,y,\tau) = \sum_k u_{0k}(x,y)\varphi(\tau-k), \quad k \in \mathbf{Z} \tag{15}$$

where $u_{0k}(x,y)$ (referred as u_{0k} hereafter) are the approximation coefficients at a certain spatial dimension x and y. The other displacements $v_0(x,y,t), w(x,y,t)$ can be transformed similarly. Substituting these approximations in Eq. (6), using the orthogonality property of the translates of the scaling functions and the definition of connection coefficients [7], the transformed coupled PDEs obtained are of the form

$$A_{11}\left\{\frac{\partial^2 u_{0j}}{\partial x^2}\right\} + (A_{12}+A_{66})\left\{\frac{\partial^2 v_{0j}}{\partial x\,\partial y}\right\} + A_{66}\left\{\frac{\partial^2 u_{0j}}{\partial y^2}\right\} - B_{11}\left\{\frac{\partial^3 w_j}{\partial x^3}\right\} - (B_{12}+2B_{66})\left\{\frac{\partial^3 w_j}{\partial x\,\partial y^2}\right\} = [\Gamma^1]^2 I_0\{u_{0j}\} \tag{16}$$

where Γ^1 is the first-order connection coefficient matrix obtained after using the wavelet extrapolation technique [3]. These coupled PDEs are decoupled using eigenvalue analysis of Γ^1 as given in Ref. [4]. The final decoupled form of the reduced PDEs given in Eq. (16) is

$$A_{11}\frac{\partial^2 \hat{u}_{0j}}{\partial x^2} + (A_{12}+A_{66})\frac{\partial^2 \hat{v}_{0j}}{\partial x\,\partial y} + A_{66}\frac{\partial^2 \hat{u}_{0j}}{\partial y^2} - B_{11}\frac{\partial^3 \hat{w}_j}{\partial x^3} - (B_{12}+2B_{66})\frac{\partial^3 \hat{w}_j}{\partial x\,\partial y^2} = -I_0\gamma_j^2 \hat{u}_{0j} \quad j=0,1,\ldots,n-1 \tag{17}$$

where $\hat{u}_{0j}$ and similarly other transformed displacements are

$$\hat{u}_{0j} = \Phi^{-1} u_{0j} \tag{18}$$

where Φ is the eigenvector matrix of Γ^1 and $_1\gamma_j$ are the corresponding eigenvalues. Following exactly similar steps, the two other governing differential equations (Eqs. (7) and (8)) and the force boundary conditions (Eqs. (9)–(12)) are transformed to PDEs in x and y.

It should be mentioned here that the sampling rate $\triangle t$ should be less than a certain value to avoid spurious dispersion in the simulation using WSFE. In Ref. [5], a numerical study has been pre-

sented from which the required $\triangle t$ can be determined depending on the order N of the Daubechies scaling function and frequency content of the load.

3.3 Spatial (Y) Approximation. As said in Sec. 1, the next step involved is to further reduce each of the transformed and decoupled PDEs given by Eq. (17) (similarly for the other transformed governing differential equations corresponding to (7) and (8)) for $j=0,1,\ldots,n-1$ to a set of coupled ODEs using Daubechies scaling function approximation in one of the spatial (Y) direction. Similar to time approximation, the transformed variable $\hat{u}_{0j}$ be discretized at m points in the spatial window $[0, L_Y]$, where L_Y is the length in Y direction. Let $\zeta=0,1,\ldots,m-1$ be the sampling points, then

$$y = \triangle Y \zeta \tag{19}$$

where $\triangle Y$ is the spatial interval between two sampling points. The function $\hat{u}_{0j}(x,y)$ can be approximated by scaling function $\varphi(\zeta)$ at an arbitrary scale as

$$\hat{u}_{0j}(x,y) = \hat{u}_{0j}(x,\zeta) = \sum_k \hat{u}_{0lj}(x)\varphi(\zeta - l), \quad l \in \mathbf{Z} \tag{20}$$

where $\hat{u}_{0lj}(x,y)$ (referred as $\hat{u}_{0lj}$ hereafter) are the approximation coefficients at a certain spatial dimension x. The other displacements $\hat{v}_{0j}(x,y), \hat{w}_j(x,y)$ can be similarly transformed. Following similar steps as the time approximation, substituting the above approximations in Eq. (17) and taking inner product on both sides with the translates of scaling functions $\varphi(\zeta - i)$, where $i=0,1,\ldots,m-1$ and using their orthogonal properties, we get m simultaneous ODEs as follows:

$$\begin{aligned} &A_{11}\frac{d^2\hat{u}_{0ij}}{dx^2} + (A_{12}+A_{66})\frac{1}{\triangle Y}\sum_{l=i-N+2}^{i+N-2}\frac{d\hat{v}_{0lj}}{dx}\Omega^1_{i-l} \\ &\quad + A_{66}\frac{1}{\triangle Y^2}\sum_{l=i-N+2}^{i+N-2}\hat{u}_{0lj}\Omega^2_{i-l} - B_{11}\frac{d^3\hat{w}_{ij}}{dx^3} - (B_{12}+2B_{66}) \\ &\quad \times\frac{1}{\triangle Y^2}\sum_{l=i-N+2}^{i+N-2}\frac{d\hat{w}_{lj}}{dx}\Omega^2_{i-l} = -I_0\gamma_j^2\hat{u}_{0ij} \quad i=0,1,\ldots,m-1 \end{aligned} \tag{21}$$

where N is the order of Daubechies wavelet and Ω^1_{i-l} and Ω^2_{i-l} are the connection coefficients for first- and second-order derivative defined in Ref. [7].

It can be seen from the ODEs given by Eq. (21), that, similar to time approximation, here also certain coefficients $\hat{u}_{0ij}$ near the vicinity of the boundaries ($i=0$ and $i=m-1$) lie outside the spatial window $[0L_Y]$ defined by $i=0,1,\ldots,m-1$. These coefficients must be treated properly for finite domain analysis. However, here, unlike time approximation, these coefficients are obtained through periodic extension, but only for free lateral edges, while other boundary conditions may be imposed quite differently using a restraint matrix [8]. The unrestrained, i.e., free-free boundary conditions may also be imposed in a similar way using a restraint matrix, but interestingly, it has been seen from the numerical experiments that the use of periodic extension gives accurate results. In addition, it allows decoupling of the ODEs using eigenvalue analysis and thus reduces the computational cost. Here, after expressing the unknown coefficients lying outside the finite domain in terms of the inner coefficients considering periodic extension, the ODEs given by Eq. (21) can be written as a matrix equation of the form

$$\begin{aligned} &A_{11}\left\{\frac{d^2\hat{u}_{0ij}}{dx^2}\right\} + (A_{12}+A_{66})[\Lambda^1]\left\{\frac{d\hat{v}_{0ij}}{dx}\right\} + A_{66}[\Lambda^1]^2\{\hat{u}_{0lj}\} \\ &\quad = -B_{11}\left\{\frac{d^3\hat{w}_{ij}}{dx^3}\right\} - (B_{12}+2B_{66})[\Lambda^1]^2\left\{\frac{d\hat{w}_{lj}}{dx}\right\} - I_0\gamma_j^2\{\hat{u}_{0ij}\} \end{aligned} \tag{22}$$

where Λ^1 is the first-order connection coefficient matrix obtained after periodic extension. The coupled ODEs given by Eq. (22) are decoupled using eigenvalue analysis similar to that done in time approximation. It should be mentioned here that matrix Λ^1 obtained after periodic extension has a circulant form and its eigenparameters are known analytically [9]. Let the eigenvalues be $\imath\beta_i$, then the decoupled ODEs corresponding to Eqs. (22) are

$$\begin{aligned} &A_{11}\frac{d^2\tilde{u}_{0ij}}{dx^2} - \imath\beta_i(A_{12}+A_{66})\frac{d\tilde{v}_{0ij}}{dx} - \beta_i^2 A_{66}\tilde{u}_{0ij} - B_{11}\frac{d^3\tilde{w}_{ij}}{dx^3} \\ &\quad + \beta_i^2(B_{12}+2B_{66})\frac{d\tilde{w}_{ij}}{dx} = -I_0\gamma_j^2\tilde{u}_{0ij} \quad i=0,1,\ldots,m-1 \end{aligned} \tag{23}$$

where $\tilde{u}_{0j}$ and similarly other transformed displacements are

$$\tilde{u}_{0j} = \Psi^{-1}\hat{u}_{0j} \tag{24}$$

where Ψ is the eigenvector matrix of Λ^1.

Following exactly similar steps, the final transformed and decoupled form of the Eqs. (7) and (8) (following reduction using temporal approximation) are

$$\begin{aligned} &A_{66}\frac{d^2\tilde{v}_{0ij}}{dx^2} - \imath\beta_i(A_{12}+A_{66})\frac{d\tilde{u}_{0ij}}{dx} - \beta_i^2 A_{22}\tilde{v}_{0ij} \\ &\quad + \imath\beta_i(B_{12}+2B_{66})\frac{d^2\tilde{w}_{ij}}{dx^2} - \imath\beta_i^3 B_{22}\tilde{w}_{ij} = -I_0\gamma_j^2\tilde{v}_{0ij} \end{aligned} \tag{25}$$

$$\begin{aligned} &B_{11}\frac{d^3\tilde{u}_{0ij}}{dx^3} - \beta_i^2(B_{12}+2B_{66})\frac{d\tilde{u}_{0ij}}{dx} - \imath\beta_i(B_{12}+2B_{66})\frac{d^2\tilde{v}_{0ij}}{dx^2} \\ &\quad + \imath\beta_i^3 B_{22}\tilde{v}_{0ij} - D_{11}\frac{d^4\tilde{w}_{ij}}{dx^4} + 2\beta_i^2(D_{12}+2D_{66})\frac{d^2\tilde{w}_{ij}}{dx^2} - \beta_i^4 D_{22}\tilde{w}_{ij} \\ &\quad = -I_0\gamma_j^2\tilde{w}_{ij} + I_2\gamma_j^2\left(\frac{d^2\tilde{w}_{ij}}{dx^2} - \beta_i^2\tilde{w}_{ij}\right) \end{aligned} \tag{26}$$

Similarly, the transformed form of the force boundary conditions given by Eqs. (9)–(12) (following reduction using temporal approximation) are

$$A_{11}\frac{d\tilde{u}_{0ij}}{dx} - \imath\beta_i A_{12}\tilde{v}_{0ij} - B_{11}\frac{d^2\tilde{w}_{ij}}{dx^2} + \beta_i^2(B_{12}+2B_{66})\tilde{w}_{ij} = \tilde{N}_{xij} \tag{27}$$

$$A_{66}\left(-\imath\beta_i\tilde{u}_{0ij} + \frac{d\tilde{v}_{0ij}}{dx}\right) + 2\imath\beta_i B_{66}\frac{d\tilde{w}_{ij}}{dx} = \tilde{N}_{yij} \tag{28}$$

$$-B_{11}\frac{d\tilde{u}_{0ij}}{dx} + \imath\beta_i B_{12}\tilde{v}_{0ij} + D_{11}\frac{d^2\tilde{w}_{ij}}{dx^2} - \beta_i^2 D_{12}\tilde{w}_{ij} = \tilde{M}_{yij} \tag{29}$$

$$\begin{aligned} &B_{11}\frac{d^2\tilde{u}_{0ij}}{dx^2} - \imath\beta_i B_{12}\frac{d\tilde{v}_{0ij}}{dx} - D_{11}\frac{d^3\tilde{w}_{ij}}{dx^3} + \beta_i^2 D_{12}\frac{d^2\tilde{w}_{ij}}{dx^2} - I_2\gamma_j^2\frac{d\tilde{w}_{ij}}{dx} \\ &\quad = \tilde{V}_{ij} \quad i=0,1,\ldots,m-1 \end{aligned} \tag{30}$$

The final transformed ODEs given by Eqs. (23), (25), and (26) and the boundary conditions Eqs. (28)–(30) are used for 2D

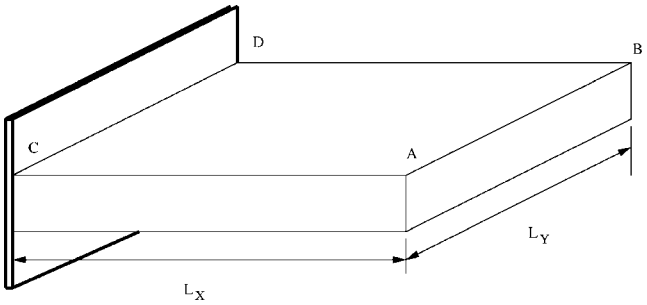

Fig. 1 Uniform cantilever plate

WSFE formulation similar to the 2D FSFE technique [1].

Similar to the temporal approximation, the spatial sampling rate $\triangle Y$ is also determined from the order N of the scaling function used for spatial approximation and the spatial distribution of the load.

The four degrees of freedom per node associated with the element formulation are $\tilde{u}_{0ij}, \tilde{v}_{0ij}, \tilde{w}_{ij}$, and $\partial\tilde{w}_{ij}/\partial x$. The corresponding nodal forces are $\tilde{N}_{xij}$, $\tilde{N}_{yij}$, $\tilde{M}_{yij}$ and $\tilde{V}_{ij}$. From the previous sections, for unrestrained lateral edges we get a set of decoupled ODEs (Eqs. (23), (25), and (26)) for an isotopic plate using CLPT, in a transformed wavelet domain. These equations are required to be solved for $\tilde{u}_{0ij}$, $\tilde{v}_{0ij}\tilde{w}_{0ij}$, and the actual solutions $u_0(x,y,t)$, $v_0(x,y,t)$, $w(x,y,t)$ are obtained using inverse wavelet transform twice for spatial Y dimension and time.

It can be seen that the transformed decoupled ODEs have a form that is similar to that in FSFE [1], and thus, the formulation of WSFE from here is similar to FSFE formulation or 1-D WSFE formulation given in Ref. [4]. Thus, the formulation is not repeated here. Finally, the transformed nodal forces $\{\tilde{\mathbf{F}}^{\mathbf{e}}\}$ and transformed nodal displacements $\{\tilde{\mathbf{u}}^{\mathbf{e}}\}$ are related as

$$\{\tilde{\mathbf{F}}^{\mathbf{e}}\} = [\tilde{\mathbf{K}}^{e}]\{\tilde{\mathbf{u}}^{e}\} \tag{31}$$

where $[\tilde{\mathbf{K}}^{\mathbf{e}}]$ is the exact elemental dynamic stiffness matrix. The solution of the Eq. (31) and the assembly of the elemental stiffness matrices to obtain the global stiffness matrix is exactly similar to conventional FE technique.

4 Numerical Experiments

Here, the formulated 2D WSFE is used to study axial and transverse wave propagation in composite graphite-epoxy AS/3501 plates of different configurations and ply orientations. The analysis results are presented in both time and frequency domains. The responses simulated using the formulated element is first validated with 2D FE analysis. In addition, comparisons to corresponding responses obtained using FSFE are also provided. This highlights the advantages of WSFE over FSFE in modeling 2D structures with finite dimensions. The example used (shown in Fig. 1) consist of uniform cantilever plate. The material properties are as follows, $E_1=144.48$ GPa, $E_2=E_3=9.63$ GPa, $G_{23}=G_{13}=G_{12}=4.128$ GPa, $\nu_{23}=0.3$, $\nu_{13}=\nu_{12}=0.02$, and $\rho=1389$ kg/m^3.

In all the examples provided, the load applied is a unit impulse of time duration 50 μs and occurs between 100 and 150 μs, with frequency content 44 kHz. The load is applied at the edge along the Y-axis and has a spatial distribution of

$$F(Y) = e^{-(Y/\alpha)^2} \tag{32}$$

where α is a constant and can be varied to change the Y-axis variation of the load.

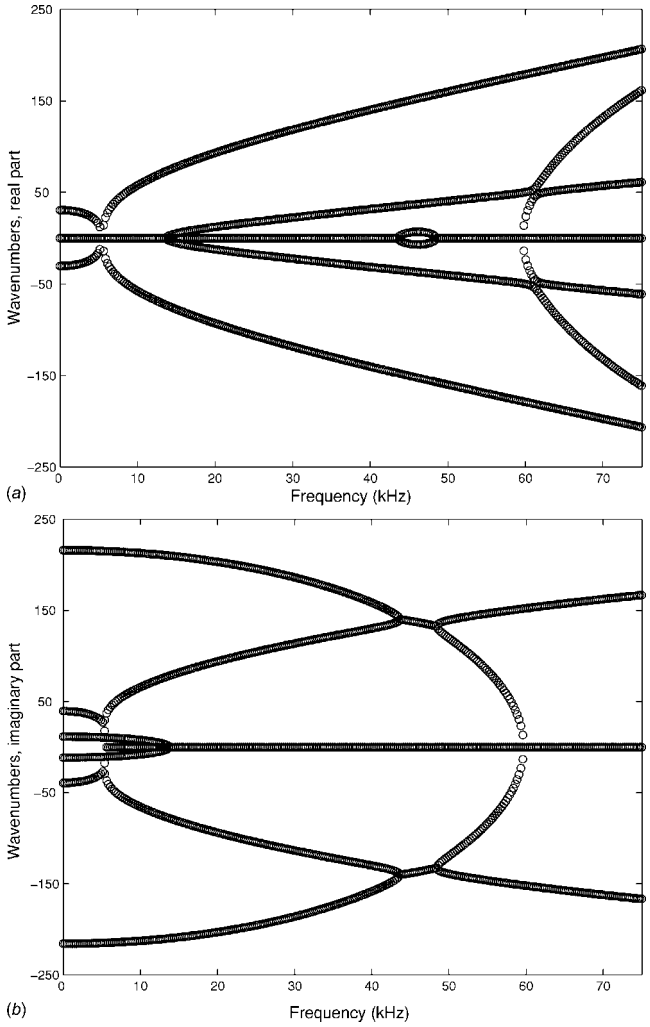

Fig. 2 The (*a*) real and (*b*) imaginary parts of the wave number of a plate with asymmetric ply layup of $[0_4/90_4]$

The 2D WSFE model is formulated with the Daubechies scaling function of order $N=22$ for temporal approximation and $N=4$ for spatial approximation. The time sampling rate is $\triangle t=2$ μs, unless otherwise mentioned, while the spatial sampling rate $\triangle Y$ is varied depending on L_Y and load distribution $F(y)$.

The uniform cantilever plate shown in Fig. 1 is fixed at one edge (CD) and free at the other edge AB along Y-axis. Numerical experiments are performed by considering the other two edges (AC) and (BD) along X-axis to be free-free. The dimensions are L_X and L_Y along X and Y axis, respectively, while the depth ($=2h$) is kept fixed at 0.01 m with eight laminates.

4.1 Spectrum Relations. The spectrum relation for the plate with $L_Y=0.25$ m and asymmetric ply lay up of $[0_4/90_4]$ are plotted in Fig. 2. Figures 2(*a*) and 2(*b*) respectively show the real and imaginary parts of the wave numbers for a Y wave number of 50. It can be seen that the wave number has significant real and imaginary parts. This implies that the waves are inhomogeneous in nature, i.e., it attenuates as it propagates. The wave numbers have been obtained with $\triangle t=4$ μs, i.e, for a Nyquist frequency of $f_{nyq}=125$ kHz. As said earlier [5], WSFE predicts accurate wave numbers only up to a certain fraction p_N of Nyquist frequency f_{nyq}. This fraction p_N for $N=22$ is ~ 0.6. Thus in Figs. 2(*a*) and 2(*b*), the wave numbers are plotted up to a frequency $f_N=p_N f_{nyq}=75$ kHz. There are three cutoff frequencies, which vary with the wave number.

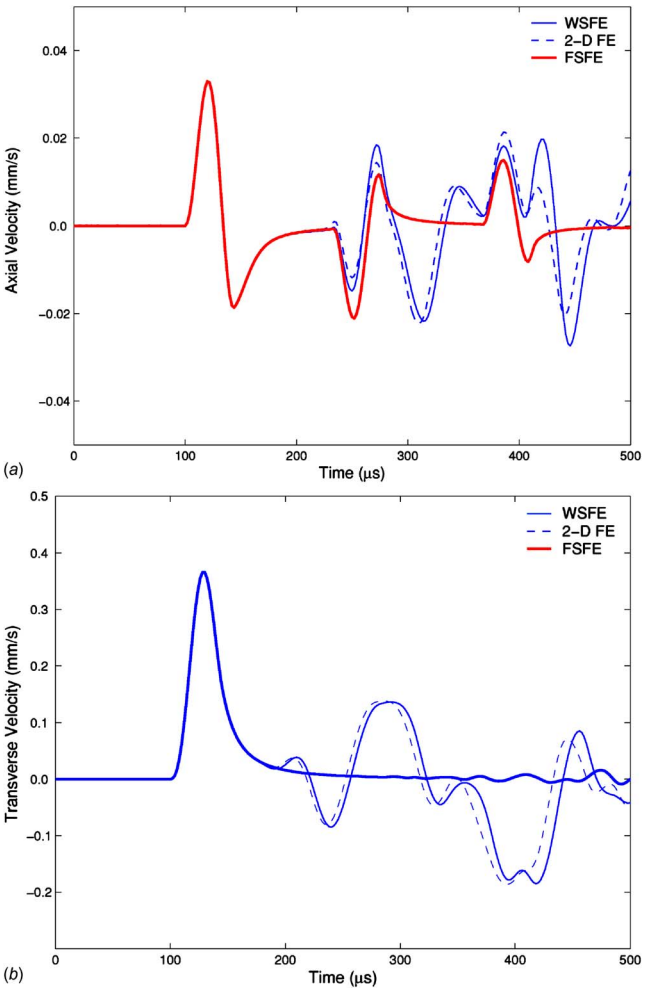

Fig. 3 (*a*) Axial and (*b*) transverse velocities at midpoint of edge AB in a $[0_4/90_4]$ cantilever plate (see Fig. 1) with L_X =0.5 m and L_Y=0.25 m due to tip impulse load applied in axial and transverse directions along AB, respectively

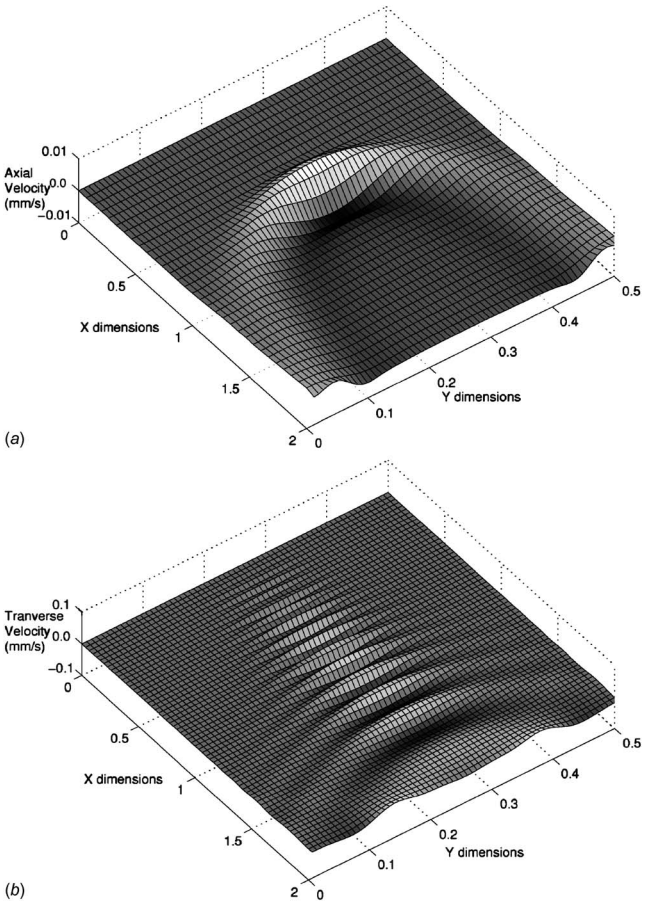

Fig. 4 Snapshots of (*a*) axial velocities at time instance T =250 μs and (*b*) transverse velocities at time instance T =1000 μs in a $[0]_8$ cantilever plate (see Fig. 1) with L_X=2.0 m and L_Y=0.5 m due to tip impulse load applied in axial direction

4.2 Response Analysis. Next, the time domain responses of a plate with L_X=0.5 m, L_Y=0.25 m and asymmetric ply orientation of $[0_4/90_4]$, simulated using the WSFE method are validated with 2D FE results. In Figs. 3(*a*) and 3(*b*), respectively, the axial and transverse velocities measured at the midpoint of edge AB (see Fig. 1) of the cantilever plate are plotted and compared to 2D FE results. The impulse loads are applied along AB correspondingly in axial and transverse directions. The Y variation of the load is obtained using α=0.03 in Eq. (32). As mentioned earlier, only one WSFE is used to model the structure and the time window is kept to T_w=512 μs. The number of discretization points along Y-axis is m=64, and thus, the spatial sampling rate is $\triangle Y = L_Y/(m-1)$ =0.004 m. A very refined mesh with 6432 four-noded plane stress quadrilateral elements were used for the 2D FE analysis, while Newmark's scheme with time step 1 μs was used for time integration. It can be seen that WSFE and FE results match very well. A comparison is also provided to FSFE results. As stated earlier, it can be seen from these results that unlike WSFE, FSFE is unable to accurately capture the reflections from the lateral edges AC and BD in this example. The velocities obtained from FSFE modeling show only the reflection from the fixed edge CD. Thus, for structures with finite or short dimensions, FSFE results will deviate substantially from the actual responses. In addition, simulation with FSFE requires a "throw-off"element to impart artificial damping to the structure and a large time window T_w =16,384 μs to remove the distortions due to the wraparound problem. It should be restated here that the accuracy of the response simulated using WSFE is independent of the time window T_w, which is chosen, as required, for observation.

Figures 4(*a*) and 4(*b*) show the snapshots of the axial and transverse velocities of the cantilever plate shown in Fig. 1 with a symmetric ply orientation of $[0_8]$ at time instances T=250 μs and T=1000 μs, respectively. The plate dimensions are L_X=2.0 m and L_Y=0.5 m, and is modeled using a single WSFE with m=64 sampling points in the Y direction. The impulse load as explained earlier is applied along edge AB in the axial and transverse directions, and the Y variation is obtained with α=0.05. The snapshot at T=250 μs (Fig. 4(*a*)) shows the forward-moving axial wave. Similarly, Fig. 4(*b*) shows the forward-moving transverse waves, which are dissipative in nature. It should be mentioned here that the velocities at all the sampling points along Y direction and at any points along X direction used to obtain the snapshots are obtained from a single simulation.

5 Conclusions

In this paper, a 2D wavelet-based spectral finite element is formulated to study wave propagation in an anisotropic plate. The spectral finite element method is an efficient alternative to FE analysis and decreases the computational cost substantially. The present wavelet-based technique circumvents several major limitations of the conventional FFT based spectral finite element method, while retaining the advantages of low computational cost and simultaneous time and frequency-domain analysis. The local-

ized nature of the Daubechies basis functions for the WSFE method allows modeling of plate structures with finite dimensions, which is otherwise not possible with the corresponding FFT-based method. In addition, 2D WSFE is also free from the wraparound problem associated with FSFE due to the assumption of periodicity in the time approximation. As a result of FSFE, unlike WSFE, we cannot model undamped finite length structures and, even in the presence of damping, a larger time window is needed to remove the distortions arising from wraparound.

First, the responses simulated using the formulated WSFE is validated with 2D FE results. Comparisons to the corresponding FSFE simulations are also provided to emphasize the advantages of WSFE over FSFE, particularly for analyzing structures with finite/short dimensions. Numerical experiments are performed to study wave propagation in plates with different asymmetric ply layup in both the time and frequency domains.

References

[1] Doyle, J. F., 1999, *Wave Propagation in Structures*, Springer, New York.
[2] Daubechies, I., 1992, *Ten Lectures on Wavelets*, CBMS-NSF Series in Applied Mathematics, SIAM, Philadelphia.
[3] Williams, J. R., and Amaratunga, K., 1997, "A Discrete Wavelet Transform Without Edge Effects Using Wavelet Extrapolation," J. Fourier Anal. Appl., **3**(4), pp. 435–449.
[4] Mitra, M., and Gopalakrishnan, S., 2005, "Spectrally Formulated Wavelet Finite Element for Wave Propagation and Impact Force Identification in Connected 1D Waveguides," Int. J. Solids Struct., **42**, 4695–4721.
[5] Mitra, M., and Gopalakrishnan, S., 2006, "Extraction of Wave Characteristics From Wavelet Based Spectral Finite Element Formulation," Mech. Syst. Signal Process., **20**, pp. 2046–2079.
[6] Reddy, J. N., 1997, *Mechanics of Laminated Plates*, CRC Press, Boca Raton.
[7] Beylkin, G., 1992, "On the Representation of Operators in Bases of Compactly Supported Wavelets," SIAM (Soc. Ind. Appl. Math.) J. Numer. Anal., **6**(6), pp. 1716–1740.
[8] Chen, M. Q., Hwang, C., and Shih, P., 2006, "The Computation of Wavelet-Galerkin Approximation on a Bounded Interval," Int. J. Numer. Methods Eng., **39**, pp. 2921–2944.
[9] Davis, P. J., 1963, *Interpolation and Approximation*, Blaisdell, New York.

Simple Formula to Study the Large Amplitude Free Vibrations of Beams and Plates

G. Venkateswara Rao[1]
INAE Distinguished Professor
e-mail: hydrao1944@yahoo.co.in

K. Meera Saheb
Assistant Professor
e-mail: meera_recw@rediffmail.com

Department of Mechanical Engineering,
Sreenidhi Institute of Science & Technology,
Yamnampet, Ghatkesar, Hyderabad - 501 301, India

G. Ranga Janardhan
Associate Professor
Department of Mechanical Engineering,
Jawaharlal Nehru Technological University,
Kukatpally, Hyderabad - 500 072, India
e-mail: rangajanardhan@yahoo.co.in

A simple formula to study the large amplitude free vibration behavior of structural members, such as beams and plates, is developed. The nonlinearity considered is of von Karman type, and after eliminating the space variable(s), the corresponding temporal equation is a homogeneous Duffing equation. The simple formula uses the tension(s) developed in the structural members due to large deflections along with the corresponding buckling load obtained when the structural members are subjected to the end axial or edge compressive load(s) and are equal in magnitude of the tension(s). The ratios of the nonlinear to the linear radian frequencies for beams and the nonlinear to linear time periods for plates are obtained as a function of the maximum amplitude ratio. The numerical results, for the first mode of free vibration obtained from the present simple formula compare very well to those available in the literature obtained by applying the standard analytical or numerical methods with relatively complex formulations.
[DOI: 10.1115/1.2755147]

Keywords: free vibrations, geometric nonlinearity, beams, plates

1 Introduction

Evaluation of the large amplitude free vibrations of basic structural members, such as beams, plates, and shells, is essential for studying the behavior of the present-day highly optimized and cost-effective structural members subjected to a severe dynamic environment. The basic study involved is to find the variation of the frequency or time period of vibration, for a given mode, with respect to a given maximum amplitude ratio. Based on this information, further investigations on the dynamic behavior of these structural elements can follow. This paper covers the study of the large amplitude free vibrations of uniform slender beams and thin plates made of isotropic materials, henceforth referred as beams and plates.

The classic work on the topic of large amplitude free vibrations of hinged-hinged beams (called as bars in the paper) is initially due to Woinowsky-Krieger [1]. This formulation basically takes the nonlinearity involved in the strain-displacement relation (von Karman type) and is taken into account by evaluating the constant axial tension, developed because of the large deflections with the axially immovable end conditions. This tension term, when included in the dynamic equation of equilibrium, becomes a homogenous Duffing equation of the hardening type, and the solution is obtained in terms of the elliptic integrals, with an assumed space mode for the beams. Extensive studies by other researchers on the large amplitude free vibration of beams by using either continuum methods or a numerical method, such as the versatile finite element method, considering the axially immovable end conditions of the beam (henceforth called beams with immovable ends), with some simplifying assumptions on the axial displacements, linearization of the strain-displacement relations, treating that the nonlinear vibrations also exhibit simple harmonic motion (SHM), etc. A detailed study on the effect of these assumptions on the large amplitude vibrations of hinged-hinged beams is presented by Singh et al. [2]. Marur [3] has systematically classified the various formulations on the large amplitude free vibrations of beams. Excellent review articles by Sathyamoorthy [4,5] give the developments that took place on the nonlinear analysis of beams up to the 1980 and an exhaustive presentation of the developments in the area of nonlinear analysis of structural members until recently [6].

For the plates, the large amplitude free vibration problem becomes a cubic nonlinear one of hardening type, with the edges immovable in the normal direction in the plane of the plates (henceforth called plates with immovable edges), either by using the approach of Woinowsky-Krieger [1,7] or the stress function approach [8], and the corresponding results are given in a systematic way by Leissa [9]. These formulations, whether continuum or finite element based, are relatively complex in nature and are not easily amenable for obtaining simple, accurate, and reliable closed-form solutions.

It is the endeavor of the first author to develop simple and, at the same time, accurate and reliable solutions to some complex problems of practical interest in structural mechanics, and he successfully developed simple formulas for predicting the fundamental frequency parameter of the initially loaded (stressed) structural members [10–13] and their thermal post-buckling behavior [14–16].

With the same spirit and following the earlier work [10–13], the authors have successfully developed a simple formulation for studying the large amplitude free vibration behavior of structural members with immovable ends or edges, for beams and plates, respectively, where the nonlinearity exists in the strain-displacement relation(s) of von Karman type, which yields a homogenous cubic nonlinear temporal equation (homogeneous Duffing equation) with an assumed space mode. It is emphasized here that the formula is developed based on the knowledge of the two totally unrelated quantities to the free vibrations, such as the tensile load(s) developed in these structural members due to the large deflections and the corresponding buckling loads that are obtained from the same pattern of compressive load(s) as the tensile load(s), where "s" in the parentheses is applicable for rectangular plates representing the two biaxial tensile loads that exist in the directions of the 2D rectangular Cartesian frame.

Numerical results, obtained using the simple formula, for the large amplitude free vibrations of typical immovable beams and plates are presented for the first mode of free vibration. The present numerical results compare very well to those available in the literature, indicating that the present simple formula developed based on the physical concepts of the problem and the subsequent logical deductions with much less mathematical treatment is

[1]Corresponding author.

Contributed by the Applied Mechanics Division of ASME for publication in the JOURNAL OF APPLIED MECHANICS. Manuscript received November 6, 2006; final manuscript received May 9, 2007; published online January 16, 2008. Review conducted by Oliver M. O'Reilly.

highly promising to obtain accurate, reliable, and a quick solution for the cubic nonlinear homogeneous temporal equations that are often encountered in the nonlinear structural mechanics.

2 Simple Formula

The frequency parameter of the beams and plates with initial axial or inplane loads, based on the earlier work [10–13], is given by

$$\frac{\lambda_f}{\lambda_{f_o}} \pm \frac{\lambda_i}{\lambda_b} = 1 \tag{1}$$

where λ_f and λ_{f_o} are the frequency parameters of the initially loaded and without initial load, λ_i and λ_b are the initial load and the buckling load parameters of the structural members, respectively. It is to be noted here that both λ_f, λ_{fo} or λ_i and λ_b are the nondimensional parameters that are obtained directly from the nondimensional differential or matrix equations. In Eq. (1), the positive and negative signs represent the compressive or tensile initial loads, respectively.

The condition involved in deriving this formula is that the mode shapes of the load free vibration, initial loaded vibration and the buckling are the same for any given mode. In actual practice, it is difficult to satisfy this condition, except for hinged-hinged beams and rectangular plates with simply supported edges, and is approximately satisfied. Thus, a small error exists in predicting the initially loaded frequency parameter and the magnitude of the error depends on how accurately this condition is satisfied. However, in the case of the use of single-term mode shapes in the analysis, this condition is exactly satisfied and the predicted initially loaded frequency parameter using Eq. (1) is exactly the same as the one evaluated using rigorous continuum or numerical analysis performed using the same single-term mode shapes. These can also be called single-term admissible functions.

The main theme of this note is to transform Eq. (1) to represent the problem of large amplitude free vibrations of structural members. It has already been mentioned earlier that the structural members develop tensile load(s) during large deflections and these load(s) are treated as initial loads in developing the present simple formula. However, these are functions of maximum amplitude ratios as the initial load(s) are dependent on the same for a given mode of vibration.

In the context of large amplitude free vibrations, λ_i can be replaced by λ_T, the initial tensile load parameter, λ_f is the nonlinear frequency parameter λ_{NL} because of the initial load developed due to large deflections and λ_{f_o} is the linear frequency parameter λ_L without the initial load. Equation (1) can now be written with the negative sign because of the tensile initial loads, as

$$\frac{\lambda_{NL}}{\lambda_L} = 1 + \frac{\lambda_T}{\lambda_b} \tag{2}$$

As Eq. (1) is derived using the assumption of SHM, λ_{NL} obtained with this assumption is approximate. Hence, following the harmonic balance method (HBM) [17], Eq. (2) is corrected using a correction factor [18], to compensate the assumption of SHM for obtaining λ_{NL}. The correction factor of 3/4 is obtained by solving the homogeneous Duffing equation with and without the assumption of SHM and comparing both the solutions. Equation (2) is now written as

$$\frac{\lambda_{NL}}{\lambda_L} = \frac{\omega_{NL}^2}{\omega_L^2} = 1 + \frac{3}{4}\frac{\lambda_T}{\lambda_b} \tag{3}$$

The effectiveness of this simple formula is demonstrated through typical large amplitude free vibration problems of beams and plates.

3 Expressions for Tensile Load Parameters

The expressions for the tensile loads, from which the tensile load parameters are defined, developed because of large deflections are taken from Woinowsky-Krieger [1], Leissa [9], and Rao and Raju [15]. These are

$$T_X = \frac{EI}{2Lr^2}\int_0^L \left(\frac{dw}{dx}\right)^2 dx \tag{4}$$

$$T_R = \frac{12D}{a^2h^2}\int_0^a \left(\frac{dw}{dr}\right)^2 RdR \tag{5}$$

$$T_X = \frac{Eh}{2A}\int_0^A \left[\frac{dw(x)}{dx}\right]^2 dx \tag{6}$$

in the x direction and

$$T_Y = \frac{Eh}{2B}\int_0^B \left[\frac{d(w(y))}{dy}\right]^2 dy \tag{7}$$

in the y direction, for the beams, circular plates with axisymmetric deformations, and rectangular plates respectively, where r is the radius of gyration for beams, h is the thickness for plates is the length of the beam, a is the radius of the circular plate, R is the radius of the circular plate, A and B are the lengths of the plates in the x and y directions, and w is the assumed transverse displacement distributions for the three structural members considered. These tensile loads are dependent on the maximum amplitude ratios $(b/r)^2$ in the case of the beams and $(b/h)^2$ in the case of the plates, where b is the maxim amplitude of the large amplitude free vibration and are constant for a given b/r or b/h.

The initial tensile load parameter due to the large deflections for beams is defined as $T_X L^2/EI$. For the circular plate, with the axisymmetric large deflections, the tensile load parameter is defined as $T_R a^2/D$. And for the rectangular plate, the tensile load parameters are defined $T_X A^2/\pi^2 D$ or $T_Y B^2/\pi^2 D$, where T_x and T_y are the uniform tensile initial loads per unit length developed in the plate due to large deflections. The corresponding buckling load parameters λ_b are obtained using the same type of compressive load system(s) similar to the tensile loads generated. In the study of the rectangular plates, the magnitudes of the compressive loading system has to be taken such that $N_Y/N_X = T_Y/T_X$, where N_X and N_Y are the biaxial compressive loads per unit length in x and y directions acting on the plate.

4 Numerical Results

The proposed simple formula for predicting the large amplitude free vibrations for the first mode is verified through some typical beam and plate problems using the standard single-term admissible functions for the space mode. As the numerical results ω_{NL}/ω_L for beams and T_{NL}/T_L for plates are given in terms of the maximum amplitude ratios, it is necessary to normalize the admissible functions for the transverse displacements chosen with a factor called the normalizing factor, so that the maximum value of the transverse displacement becomes unity. These admissible functions applicable for the first mode of vibration are given in Table 1 along with the normalizing factors, tension, and buckling load parameters obtained by using these admissible functions. It can be seen that the buckling load parameters match very well with the classical solutions [19].

The variation of ω_{NL}/ω_L obtained from the present simple formula with various values of b/r are presented in Table 2 along with those obtained through the elliptic integral of solution [1,20], solutions obtained through direct numerical integration (DNI) using both finite element (FE) and the continuum analyses [21,22] for the hinged-hinged beam. For the clamped-clamped beams the elliptic integral solution is not readily available and hence the

Table 1 Transverse displacement field, normalizing factor, tension, and buckling load parameters for beams, circular, and rectangular plates

Sl. No.	Boundary conditions	Transverse displacement field w	Normalizing factor	Tension parameter λ_T	Buckling load parameter λ_b
1	Hinged-hinged Beam	$b \sin \pi x/L$	1	$(\pi^2/4)(b/r)^2$	π^2
2	Clamped-clamped Beam	$b[1-\cos 2\pi x/L]$	2	$(\pi^2/4)(b/r)^2$	$4\pi^2$
3	Simply supported circular plate	$b\{[(4+v)/2(1+v)]a^3-[(6+3v)/2(1+v)]aR^2+R^3\}$	$1.6539a^3$	$9.5358\ (b/h)^2$	4.2201
4	Clamped circular plate	$b[R^3-(3/2)aR^2+(1/2)a^3]$	$0.5a^3$	$(36/5)(b/h)^2$	14.998
5	Rectangular plate - all edges simply supported (A/B=2)	$b \sin \pi x/A \sin \pi y/B$	1	$3(1-v^2)(b/h)^2$	1.4706
6	Rectangular plate - all edges clamped (A/B=0.5)	$b(1-\cos(2\pi x/A))(1-\cos(2\pi y/B))$	4	$3(1-v^2)(b/h)^2$	4.6275
7	Rectangular plate - all edges clamped (A/B=2)	$b(1-\cos(2\pi x/A))(1-\cos(2\pi y/B))$	4	$3(1-v^2)(b/h)^2$	4.6275
8	Rectangular plate - all edges clamped (A/B=1)	$b(1-\cos(2\pi x/A))(1-\cos(2\pi y/B))$	4	$3(1-v^2)(b/h)^2$	5.3333

present results are compared with those obtained by using the DNI [21,22]. The results obtained by using the HBM [18] are included in Table 2 for the limiting case of slender beams. In any case, the present results match excellently with those obtained through the other solutions. Because the problem of axisymmetric free vibration behavior of circular plates is also a one-dimensional problem, such as beams, and for the sake of brevity, a detailed discussion of the same is not given in this note. However, for $b/h=1$, the values of T_{NL}/T_L obtained from the simple formula for the simply supported and clamped circular plates are 0.6092 and 0.8595 and match well with the values of 0.6154 and 0.8488 [7,23], respectively.

To conclusively verify the present simple formula, the rectangular simply supported plate of aspect ratio 2 is considered and the numerical results in the form of T_{NL}/T_L are present in Table 3. The present results compare well to those of Rao et al. [24], and the consistency of the present simple formula is verified in the case of clamped rectangular plates with the aspect ratios 0.5 and 2.0. These two plates are similar and the present results in terms of T_{NL}/T_L obtained using the tension parameter and buckling load parameter with proper nondimensionalization should be the same; this is seen in Table 3. For clamped square plates, the present results agree excellently with those given in Ref. [6].

5 Conclusions

The efficacy of the developed simple formula for studying the large amplitude free vibrations of structural members with cubic

Table 2 Variation of ω_{NL}/ω_L with maximum amplitude ratio for beams

	Hinged-hinged					Clamped-clamped			
			DNI				DNI		
b/r	Present study	Refined results of [1] taken from [20]	FEM [21]	Continuum [22]	HBM [17,18]	Present study	FEM [21]	Continuum [18]	HBM [17,18]
0.0	1.0000	1.0000	1.0000	1.0000	1.0000	1.0000	1.0000	1.0000	1.0000
0.2	1.0037	1.0037	1.0037	1.0037	1.0037	1.0009	1.0009	1.0009	-
0.4	1.0149	1.0149	1.0148	1.0149	1.0149	1.0037	1.0036	1.0037	-
0.6	1.0332	1.0331	1.0331	1.0331	1.0332	1.0084	1.0080	1.0084	-
0.8	1.0583	1.0580	1.0581	1.0580	1.0583	1.0149	1.0142	1.0149	-
1.0	1.0897	1.0892	1.0892	1.0892	1.0897	1.0232	1.0221	1.0231	1.0232
2.0	1.3229	1.3178	1.3178	1.3178	1.3229	1.0897	1.0854	1.0892	1.0897
3.0	1.6394	1.6257	1.6257	1.6257	1.6394	1.1924	1.1825	1.1902	1.1924
4.0	2.0000	1.9760	1.9761	1.9760	2.0000	1.3229	1.3055	1.3178	1.3229
5.0	2.3848	2.3501	2.3502	2.3501	2.3848	1.4737	1.4474	1.4647	1.4737

Table 3 Variation of T_{NL}/T_L with maximum amplitude ratio for rectangular plates

	All edges simply supported ($A/B=2.0$)		All edges clamped			
			$A/B=0.5$	$A/B=2.0$	$A/B=1.0$	
$\frac{b}{h}$	Present study	Rao et al. [24]	Present study	Present study	Present study	Sathyamoorthy [6]
0.0	1.0000	1.0000	1.0000	1.0000	1.0000	1.0000
0.2	0.9733	0.9767	-	-	-	-
0.4	0.9043	0.9159	-	-	-	-
0.5	-	-	0.9489	0.9489	0.9552	0.9559
0.6	0.8162	0.8363	-	-	-	-
0.8	0.7272	0.7539	-	-	-	-
1.0	0.6465	0.6776	0.8326	0.8326	0.8501	0.8508
1.5	-	-	0.7079	0.7079	0.7325	0.7315

nonlinear temporal equation, such as beams, circular, and rectangular plates, has been conclusively demonstrated in this paper through some typical problems. The authors are of the opinion that the present simple formula, because of the accuracy and the consistency of the numerical results obtained, attracts both analysts and researchers belonging to the basic engineering analysis and research. However, a similar simple formula should to be developed for structural members that exhibit the quadratic nonlinearity also in the cubic nonlinear temporal equation. Furthermore, the large amplitude free vibration behavior for the higher modes of vibration can be studied by using the single-term admissible functions corresponding to the required mode of free vibration.

Acknowledgment

The authors are thankful to the authorities of Sreenidhi Institute of Science & Technology for their encouragement during the course of this work.

References

[1] Woinowsky-Krieger, S., 1950, "The Effect of an Axial Force on the Vibration of Hinged Bars," ASME J. Appl. Mech., **17**, pp. 35–36.
[2] Singh, G., Sharma, A. K., and Rao, G. V., 1990, "Large-Amplitude Free Vibrations of Beams—A Discussion Various Formulations and Assumptions," J. Sound Vib., **142**, pp. 77–85.
[3] Marur, R. S., 2000, "Advances in Nonlinear Vibration Analysis of Structures—Part I, Beams," Sadhana: Proc., Indian Acad. Sci., **26**(3), pp. 243–249.
[4] Sathyamoorthy, M., 1982, "Nonlinear Analysis of Beams—Part I: A Survey of Recent Advances," Shock Vib. Dig., **14**, pp. 19–35.
[5] Sathyamoorthy, M., 1982, "Nonlinear Analysis of Beams—Part II: Finite Element Methods," Shock Vib. Dig., **14**, pp. 7–18.
[6] Sathyamoorthy, M., 1998, *Nonlinear Analysis of Structures*, CRC Press, Boca Raton, CRC Mechanical Engineering Series.
[7] Wah, T., 1963, "Vibration of Circular Plates at Large Amplitudes," J. Engrg. Mech. Div., **89**, pp. 1–15.
[8] Yamaki, N., 1961, "Influence of Large Amplitudes on Flexural Vibrations of Elastic Plates," Z. Angew. Math. Mech., **41**, pp. 501–510.
[9] Leissa, A. W., 1969, *Vibration of Plates*, Scientific and Technical Information Division, Office of Technology Utilization, National Aeronautics and Space Administration, Washington, DC.
[10] Rao, G. V., and Naidu, N. R., 2001, "Prediction of Fundamental Frequencies of Stressed Spring Hinged Tapered Beams," AIAA J., **39**, pp. 186–188.
[11] Rao, G. V., 2001, "A Simple Formula to Predict the Fundamental Frequency of Initially Stressed Square Plates," J. Sound Vib., **246**, pp. 185–189.
[12] Rao, G. V., and Raju, K. K., 2002, "Simple Formula for Evaluating the Fundamental Frequency Parameter of Initially Stressed Uniform Beams on Elastic Foundation," Fire Technol., **124**, pp. 451–454.
[13] Rao, G. V., and Neetha, R., 2003, "Prediction of Fundamental Frequency of Initially Inplane Loaded Thick Circular Plates," J. Sound Vib., **259**, pp. 1265–1268.
[14] Rao, G. V., and Raju, K. K., 2002, "Thermal Postbuckling of Uniform Columns," AIAA J., **40**, pp. 2138–2140.
[15] Rao, G. V., and Raju, K. K., 2004, "Applicability of a Simple Method for Thermal Postbuckling of Square Plates," AIAA J., **42**, pp. 1724–1726.
[16] Rao, G. V., and Raju, K. K., 2005, "A Simple Solution for the Thermal Postbuckling of Uniform Columns and Circular Plates," J. Struct. Eng. (India), **32**, pp. 217–220.
[17] Azrar, L., and White, R. G., 1999, "A Semi Analytical Approach to the Nonlinear Dynamic Response Problems of S-S and C-C Beams at Large Vibration Amplitudes—Part I: General Theory and Application to the Single Mode Approach to Free and Forced Vibration Analysis," J. Sound Vib., **224**, pp. 183–207.
[18] Rao, G. V., Meera Saheb, K., and Ranga Janardhan, G., 2006, "Concept of Coupled Displacement Field for Large Amplitude Free Vibrations of Shear Flexible Beams," Fire Technol., **128**, pp. 251–255.
[19] Timoshenko, S. P., and Gere, G. M., 1961, *Theory of Elastic Stability*, McGraw-Hill, New York.
[20] Chu, M., 1972, "Non-Linear Vibrations of Beams by Matrix Displacement Method," AIAA J., **10**, pp. 355–357.
[21] Singh, G., Rao, G. V., and Iyengar, N. G. R., 1990, "Re-Investigation of Large-Amplitude Free Vibrations of Beams Using Finite Elements," J. Sound Vib., **143**, pp. 351–355.
[22] Rao, G. V., and Raju, K. K., 2003, "Large Amplitude Free Vibrations of Beams—An Energy Approach," Z. Angew. Math. Mech., **7**, pp. 493–498.
[23] Berger, H. M., 1955, "A New Approach to the Analysis of Large Deflection of Plates," ASME J. Appl. Mech., **22**, pp. 465–472.
[24] Rao, G. V., Raju, J. S., and Raju, K. K., 1976, "A Finite Element Formulation for Large Amplitude Flexural Vibrations of Thin Rectangular Plates," Comput. Struct., **6**, pp. 163–167.

Analysis of Unsteady Flow Through a Microtube With Wall Slip and Given Inlet Volume Flow Rate Variations

Chun-I Chen[1]
Department of Industrial Engineering and Management,
I-Shou University,
No. 1, Sec. 1,
Syuecheng Road,
Dashu Township,
Kaohsiung County,
Taiwan 84041

Cha'o-Kuang Chen
e-mail: ckchen@imail.ncku.edu.tw

Heng-Ju Lin

Department of Mechanical Engineering,
National Cheng Kung University,
Tainan, Taiwan 70101

*This study examines the effects of rarefaction of an unsteady flow through a microtube for a given but arbitrary inlet volume flow rate. Four cases of inlet volume flow rate proposed by Das and Arakeri (2000, ASME J. Appl. Mech., **67**, pp. 274–281) are as follows: (1) trapezoidal piston motion, (2) constant acceleration, (3) impulsively started flow, and (4) impulsively blocked fully developed flow. During the analysis process, the Knudsen number (Kn) is used to represent the degree of rarefaction. The analytical results are presented graphically and compared to the results for a continuum under a no-slip condition. The effect of wall-slip became significant with the increasing degrees of rarefaction. The velocity in the boundary layer increased, whereas the velocity in the potential core of the microtube decreased, under the same condition. The influence of the rarefaction for the pressure gradient varied for the four cases.* [DOI: 10.1115/1.2755085]

Keywords: microfluidics, slip-flow, unsteady flow, Knudsen number

1 Introduction

Microsystems, one of the most significant technologies developed in the 21st century, are widely used in the fields of engineering, the sciences, and medicine for applications such as microwave communication, biological technology, optocommunication, automation, sensors, semiconductors, etc. Microfluidics, the primary technology in microsystems, is the principal focus in this study.

Rarefaction phenomena should be considered when fluid flows in a microtube, as compared to macroscale flow. The degree of the rarefaction can be identified by the Knudsen number (Kn), which is a ratio of magnitude of the average mean free molecular path to the characteristic dimension in a flow field. Classification of flow fields by Knudsen number can be divided into the following four regimes [1]: $\mathrm{Kn} < 10^{-3}$, continuum flow; $10^{-3} \leqslant \mathrm{Kn} < 10^{-1}$, slip-flow; $10^{-1} \leqslant \mathrm{Kn} < 10$, transition flow; and $10 \leqslant \mathrm{Kn}$, free molecular flow. When slip-flow occurs, the fluid adjacent to the wall surface no longer attains the velocity of the wall surface, and it slips along the wall surface [2].

In the literature, considerable work deals with the internal macroscale flow, in which a no-slip condition is incorporated. Some researchers solve for exact solutions for laminar flows in a duct with a given pressure gradient varying over time; for example, Szymanski [3] and Uchida [4] presented solutions for an impulsively imposed and sinusoidally varying pressure gradient. For the more complex case of a Maxwell fluid, Rahaman and Ramkissoon [5] provided solutions for a pressure gradient varying exponentially over time, a sinusoidal pulsating pressure gradient, and a constant pressure gradient. Hayat et al. [6] solved exact solutions to some simple flows of an Oldroyd-B fluid between two parallel plates with and without pressure gradients.

In practice, it is generally the inlet volume flow rate that is given, rather than the pressure gradient. For a power law fluid, Pascal and Pascal [7] solved this problem by employing a similarity method. Das and Arakeri [8] developed analytical solutions for various transient volume flow rates for a Newtonian fluid to complement their earlier experimental work [9]. Chen et al. [10–13] extended Das and Arakeri's work by considering various non-Newtonian fluids.

As the microflow is considered, the no-slip condition is no longer valid. In this study, the range of Knudsen number, $0.01 \leqslant \mathrm{Kn} < 0.1$, is chosen as most of the microelectromechanical system mechanism falls into this region [14], and the flow situations proposed by Das and Arakeri [8] are adopted. The results show that the analytic solutions of velocity profile and pressure gradient are affected by the slip conditions.

2 Mathematical Formulation

When investigating the fluid rarefaction effect in a microtube, the Knudsen number is an important nondimensional parameter:

$$\mathrm{Kn} \equiv \lambda / L \tag{1}$$

where λ is the molecular mean free path, which is defined as the mean secondary collision distance of a gas molecule, and L is the characteristic length.

Figure 1 shows the physical configuration of Newtonian fluid flowing in the horizontal microtube. The continuity and momentum equations of this problem are

$$\nabla \cdot (\rho \mathbf{V}) = 0 \tag{2}$$

$$\rho \left[\frac{\partial \mathbf{V}}{\partial t} + \mathbf{V} \cdot \nabla \mathbf{V} \right] = -\nabla P + \mu \nabla^2 \mathbf{V} \tag{3}$$

where ρ is the fluid density, $\mathbf{V}$ is the velocity vector, P is static pressure, and μ is the dynamic viscosity.

Using the cylindrical coordinate system (r, θ, x), the x-axis is taken as the centerline direction of the circular duct, r is in the radius direction, and θ is in the circumferential direction. The velocity vector is assumed to take the form:

$$\mathbf{V} = u(r,t)\mathbf{i} \tag{4}$$

where u is the velocity in the x-coordinate direction, and $\mathbf{i}$ is the unit vector in the x-coordinate direction. This effectively assumes that the flow is fully developed at all points in time. The governing equations can be derived as

$$\frac{\partial u}{\partial t} = -\frac{1}{\rho}\frac{\partial P}{\partial x} + \nu \left(\frac{\partial^2 u}{\partial r^2} + \frac{1}{r}\frac{\partial u}{\partial r} \right) \tag{5}$$

[1]Corresponding author.

Contributed by the Applied Mechanics Division of ASME for publication in the JOURNAL OF APPLIED MECHANICS. Manuscript received March 8, 2005; final manuscript received April 25, 2007; published online February 6, 2008. Review conducted by Bassam A. Younis. Paper presented at the 2002 ASME Wind Energy Symposium (WIND2002), Reno, NV, January 14–17, 2002.

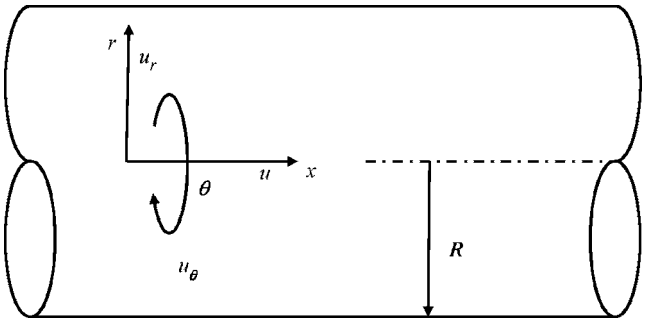

Fig. 1 Schematic representation of the problem considered

$$\frac{\partial P}{\partial r} = \frac{\partial P}{\partial \theta} = 0 \tag{6}$$

where ν is the kinematic viscosity.

With R the radius of duct, the boundary conditions are:

$$u(R,t) = -\beta_\nu \lambda \frac{\partial u(R,t)}{\partial r} \tag{7}$$

$$\frac{\partial u(0,t)}{\partial r} = 0 \tag{8}$$

where $\beta_\nu \lambda$ is the velocity slip coefficient and is defined as

$$\beta_\nu = \frac{2 - F_\nu}{F_\nu} \tag{9}$$

and F_ν is the tangential momentum accommodation coefficient and is defined as

$$F_\nu \equiv \frac{u_i - u_{\mathrm{re}}}{u_i - U_w} \tag{10}$$

where u_i, u_{re}, and U_w are tangential momentum of incoming molecules, reflected molecules, and re-emitted molecules, respectively. F_ν is the material parameter that describes the interaction between fluid and wall, and is related to constituents of fluid, temperature, velocity, wall temperature, roughness, and chemical status.

The problem can be solved if the pressure gradient function is known. In this study, the pressure gradient is determined indirectly by the given inlet volume flow rate. Velocity is related to the inlet volume flow rate by

$$\int_0^R 2\pi r u(r,t) dr = u_p(t)\pi R^2 = Q(t) \tag{11}$$

where u_p is a known inlet velocity function.

Taking the Laplace transformation of Eqs. (5), (7), (8), and (11) yields the following equations

$$\frac{\partial^2 \bar{u}(r,s)}{\partial r^2} + \frac{1}{r}\frac{\partial \bar{u}(r,s)}{\partial r} - \frac{s}{\nu}\bar{u}(r,s) = \frac{1}{u}\frac{\partial \bar{P}(x,s)}{\partial x} - \frac{1}{\nu}u(r,0) \tag{12}$$

$$\bar{u}(R,s) = -\beta_\nu \lambda \frac{\partial \bar{u}(R,s)}{\partial r} \tag{13}$$

$$\frac{\partial \bar{u}(0,s)}{\partial r} = 0 \tag{14}$$

$$\bar{Q}(s) = \int_0^R 2\pi r \bar{u}(r,t) dr = \bar{u}_p(s)\pi R^2 \tag{15}$$

where $\bar{u}(r,s) = \int_0^\infty e^{-st} u(r,t) dt$, $\bar{P}(x,s) = \int_0^\infty e^{-st} P(x,t) dt$, and $\bar{u}_p(s) = \int_0^\infty e^{-st} u_p(t) dt$.

Equation (12) is a second-order nonhomogeneous ordinary differential equation. The homogeneous part is the modified Bessel's equation of zeroth order, and if the particular solution is assumed to be ϕ_p, the complete solution is

$$\bar{u}(r,s) = C_1 I_0(mr) + C_2 K_0(mr) + \phi_p \tag{16}$$

where $m = \sqrt{s/\nu}$.

The boundary conditions (13) and (14) are used to solve for the two arbitrary coefficients C_1 and C_2, respectively. Substituting C_1 and C_2 into Eq. (16), we get

$$\bar{u}(r,s) = \phi_p \left(1 - \frac{I_0(mr)}{[I_0(mR) + \beta_\nu \lambda p I_1(mR)]}\right) \tag{17}$$

where I_1 is the modified Bessel's equation of the first order.

In order to solve for unknown ϕ_p, substitute Eq. (17) into (15) and ϕ_p is obtained as

$$\phi_p = \frac{\bar{u}_p(s)}{\left\{1 - \dfrac{2I_1(mR)}{mR[I_0(mR) + \beta_\nu \lambda p I_1(mR)]}\right\}} \tag{18}$$

Substituting ϕ_p into Eq. (17) gives

$$\bar{u}(r,s) = \bar{u}_p(s)\bar{G}(r,s) \tag{19}$$

where

$$\bar{G}(r,s) = \frac{[I_0(B\sqrt{s}) + \alpha B\sqrt{s} I_1(B\sqrt{s})] - I_0(A\sqrt{s})}{[I_0(B\sqrt{s}) + \alpha B\sqrt{s} I_1(B\sqrt{s})] - \dfrac{2I_1(B\sqrt{s})}{B\sqrt{s}}} \tag{20}$$

$\alpha = \beta_\nu \lambda / R = \beta_\nu \,\mathrm{Kn} \approx \mathrm{Kn}$ and $A = r/\sqrt{\nu}$, $B = R/\sqrt{\nu}$.

Taking the inverse Laplace transform, the velocity profile is

$$u(r,t) = \frac{1}{2\pi i}\int_{r-i\infty}^{r+i\infty} \bar{u}_p(s)\bar{G}(r,s)e^{st} ds \tag{21}$$

Furthermore, the pressure gradient is found by substituting Eq. (17) into Eq. (12) to give

$$\frac{d\bar{P}(x,s)}{dx} = -\bar{u}_p(s)\frac{[I_0(B\sqrt{s}) - \alpha B\sqrt{s} I_1(B\sqrt{s})]}{[I_0(B\sqrt{s}) - \alpha B\sqrt{s} I_1(B\sqrt{s})] - \dfrac{2I_1(B\sqrt{s})}{B\sqrt{s}}} \tag{22}$$

Using the inverse Laplace transform formula, the pressure gradient distribution can also be obtained.

3 Illustration of Examples

Examples will be considered in this study to demonstrate the effect of wall-slip conditions on the unsteady flow patterns in a microtube.

3.1 First Example: Trapezoidal Piston Motion. The trapezoidal piston motion has three stages: constant acceleration of piston starting from rest, a period of constant velocity, and a constant deceleration of the piston to a stop. The prescribed piston velocity is assumed to vary with time as follows:

$$u_p(t)=\begin{cases}\dfrac{U_p}{t_0}t & \text{for } 0\leqslant t\leqslant t_0\\ U_p & \text{for } t_0\leqslant t\leqslant t_1\\ U_p\dfrac{(t_2-t)}{(t_2-t_1)} & \text{for } t_1\leqslant t\leqslant t_2\\ 0 & \text{for } t_2\leqslant t\leqslant\infty\end{cases} \tag{23}$$

where U_p is the constant velocity after acceleration, and t_0, t_1, and t_2 are the time periods for changing piston velocity. The piston motion can be described by the Heaviside unit step function

$$u_p(t)=\frac{U_p}{t_0}tH(t)-\frac{U_p}{t_0}tH(t-t_0)+U_pH(t-t_0)-U_pH(t-t_1)+U_p\frac{t_2-t}{t_2-t_1}H(t-t_1)-U_p\frac{t_2-t}{t_2-t}H(t-t_2) \tag{24}$$

During the constant acceleration period ($0\leqslant t\leqslant t_0$), the velocity distribution can be calculated by Eq. (21) as

$$u(r,s)=\frac{1}{2\pi i}\left(2\pi i\sum_{j=1}R_j\right) \tag{25}$$

where R_j is the residual of $f(s)=U_pe^{st}\bar{G}(r,s)/t_0s^2$ at $s=s_j$ and is defined as

$$R_j=\operatorname*{Res}_{s=s_j}\left[\frac{\phi(s)}{s^2}\right] \tag{26}$$

where

$$\phi(s)=\frac{U_p}{t_0}e^{st}\bar{G}(r,s) \tag{27}$$

It is easily observed that $s=0$ is a pole of order 2. Therefore, the residue at $s=0$ is

$$\mathrm{Res}(0)=\frac{U_p}{t_0}\left\{\frac{(2t)[1-(r/R)^2+2\alpha]+\dfrac{B^2}{8}[1-(r/R)^4+4\alpha]}{1+4\alpha}-\frac{\dfrac{B^2}{6}[1-(r/R)^2+2\alpha](1+6\alpha)}{(1+4\alpha)^2}\right\} \tag{28}$$

The other singular points are the roots of the following transcendental equation

$$[I_0(B\sqrt{s})+\alpha B\sqrt{s}I_1(B\sqrt{s})]-\frac{2I_1(B\sqrt{s})}{B\sqrt{s}}=0 \tag{29}$$

Setting $B\sqrt{s}=mR=i\nu$, we find that

$$\alpha\upsilon J_1(\upsilon)+J_2(\upsilon)=0 \tag{30}$$

If ν_n, $n=1,2,3,\ldots,\infty$ are zeros of Eq. (30), then $s_n=-\nu_n^2/B^2$, $n=1,2,3,\ldots,\infty$ are the simple poles, and residues at all these poles can be obtained as

$$R_n=\operatorname*{Res}_{s=s_n}[f(s)]=\lim_{s\to s_n}[(s-s_n)f(s)]=\lim_{s\to s_n}\left[\frac{U_p(s-s_n)}{t_0s^2}e^{st}\bar{G}(r,s)\right]=\frac{U_pR^2}{t_0\nu}\left\{e^{-(\nu_n/B)^2t}\frac{2\left[J_0(\upsilon_n)-\alpha\upsilon_nJ_1(\upsilon_n)-J_0\left(\dfrac{r}{R}\upsilon_n\right)\right]}{[(1+2\alpha)\upsilon_n^3J_1(\upsilon_n)+\alpha\upsilon_n^4J_0(\upsilon_n)]}\right\} \tag{31}$$

Substituting Eqs. (28) and (31) into (26), the dimensionless velocity distribution is obtained as

$$u^*(c,t^*)=\frac{1}{t_0^*}\left[\frac{(2t^*)(1-c^2+2\alpha)+\dfrac{1}{8}(1-c^4+16\alpha)}{1+4\alpha}-\frac{\dfrac{1}{6}(1-c^2+2\alpha)(1+6\alpha)}{(1+4\alpha)^2}\right]+\frac{2}{t_0^*}\sum_{n=1}^{\infty}\left\{e^{-\upsilon_n^2t^*}\frac{[J_0(\upsilon_n)-\alpha\upsilon_nJ_1(\upsilon_n)-J_0(c\upsilon_n)]}{[(1+2\alpha)\upsilon_n^3J_1(\upsilon_n)+\alpha\upsilon_n^4J_0(\upsilon_n)]}\right\} \tag{32}$$

where $u^*=u_p/U_p$, $c=r/R$, $\alpha=\beta_\nu\mathrm{Kn}$, $t^*=t\nu/R^2=t/B^2$, $t_0^*=t_0\nu/R^2=t_0/B^2$.

By the same method, the dimensionless velocity profile in the time period of $t_0\leqslant t\leqslant t_1$ is obtained as

$$u^*(c,t^*)=2\left[\frac{(1-c^2)+2\alpha}{1+4\alpha}\right]+\frac{1}{t_0^*}\left\{e^{-\upsilon_n^2t^*}(1-e^{-\upsilon_n^2t_0^*})\times\frac{[J_0(\upsilon_n)-\alpha\upsilon_nJ_1(\upsilon_n)-J_0(c\upsilon_n)]}{[(1+2\alpha)\upsilon_n^3J_1(\upsilon_n)+\alpha\upsilon_n^4J_0(\upsilon_n)]}\right\} \tag{33}$$

During the constant deceleration period ($t_1\leqslant t\leqslant t_2$)

$$u^*(c,t^*)=\frac{1}{(t_2^*-t_1^*)}\left[\frac{2(t_2^*-t_1^*)(1-c^2+2\alpha)-\dfrac{1}{8}(1-c^4+4\alpha)}{1+4\alpha}+\frac{\dfrac{1}{6}(1-c^2+2\alpha)(1+6\alpha)}{(1+4\alpha)^2}\right]+2\sum_{n=1}^{\infty}\left[\frac{[e^{-\upsilon_n^2t^*}-e^{-\upsilon_n^2(t^*-t_0^*)}]}{t_0^*}-\frac{e^{-\upsilon_n^2(t^*-t_1^*)}}{(t_2^*-t_1^*)}\right]\frac{[J_0(\upsilon_n)-\alpha\upsilon_nJ_1(\upsilon_n)-J_0(c\upsilon_n)]}{[(1+2\alpha)\upsilon_n^3J_1(\upsilon_n)+\alpha\upsilon_n^4J_0(\upsilon_n)]}, \tag{34}$$

where $t_1^*=t_1\nu/R^2=t_1/B^2$, $t_2^*=t_2\nu/R^2=t_2/B^2$.

After the piston has stopped ($t_2\leqslant t\leqslant\infty$):

$$u^*(c,t^*)=2\sum_{n=1}^{\infty}\left[\frac{e^{-\upsilon_n^2t^*}-e^{-\upsilon_n^2(t^*-t_0^*)}}{t_0^*}-\frac{(e^{-\upsilon_n^2(t^*-t_1^*)}-e^{-\upsilon_n^2(t^*-t_2^*)})}{(t_2^*-t_1^*)}\right]\times\frac{[J_0(\upsilon_n)-\alpha\upsilon_nJ_1(\upsilon_n)-J_0(c\upsilon_n)]}{[(1+2\alpha)\upsilon_n^3J_1(\upsilon_n)+\alpha\upsilon_n^4J_0(\upsilon_n)]} \tag{35}$$

In addition, the dimensionless pressure gradient is also found during these four different stages:

(i) During the constant acceleration period ($0\leqslant t\leqslant t_0$):

$$\frac{dP^*}{dx^*}=-\frac{1}{t_0^*}\left[\frac{t^*+\dfrac{\alpha}{2}+\dfrac{1}{4}}{(1+4\alpha)}-\frac{\dfrac{1}{12}+\dfrac{\alpha}{2}}{(1+4\alpha)^2}\right]+\sum_{n=1}^{\infty}\frac{1}{4t_0^*}\frac{e^{-\nu_n^2t^*}[J_0(\nu)-\alpha\nu J_1(\nu)]}{[(1+2\alpha)\nu_nJ_1(\nu_n)+\alpha\nu_n^2J_0(\nu_n)]} \tag{36}$$

where $P^*=P/(8\mu U_p/R)$, $x^*=x/R$.

(ii) During the constant velocity period ($t_0\leqslant t\leqslant t_1$):

$$\frac{dP^*}{dx^*}=-\frac{1}{1+4\alpha}+\sum_{n=1}^{\infty}\frac{1}{4t_0^*}\frac{e^{-\nu_n^2t^*}(1-e^{-\nu_n^2t_0^*})[J_0(\nu)-\alpha\nu J_1(\nu)]}{[(1+2\alpha)\nu_nJ_1(\nu_n)+\alpha\nu_n^2J_0(\nu_n)]} \tag{37}$$

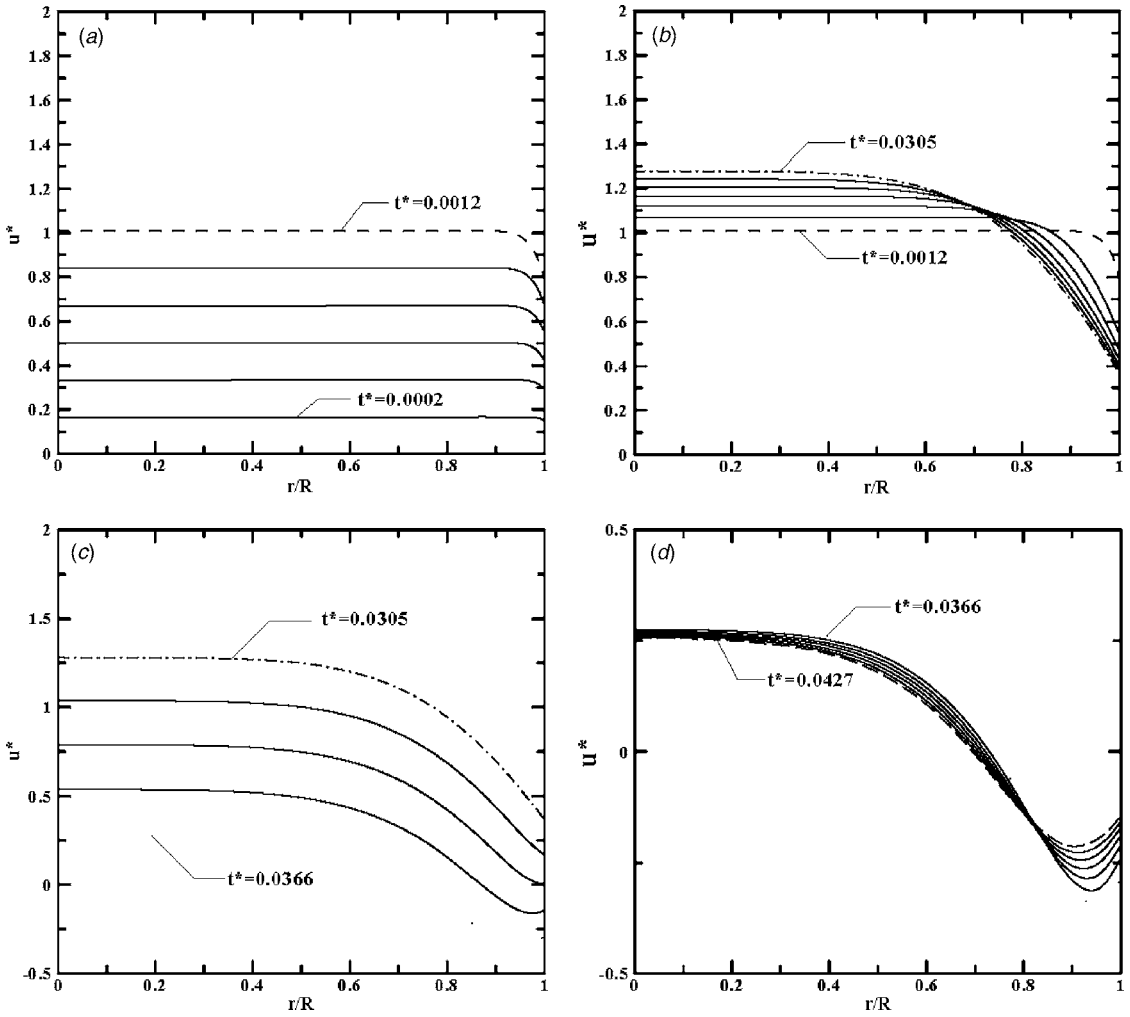

Fig. 2 Velocity profiles at different phases at Kn=0.1 (*a*) during the acceleration of the piston motion (profiles are shown at time intervals of $t_0^*/6$), (*b*) when the piston velocity is constant (time intervals of $(t_1^*-t_0^*)/6$), (*c*) during the deceleration of the piston velocity (time intervals of $(t_2^*-t_1^*)/4$), and (*d*) after the piston motion has stopped (time intervals of $(0.0427-t_2^*)/6$)

(iii) During the constant deceleration period ($t_1 \leqslant t \leqslant t_2$):

$$\frac{dP^*}{dx^*} = \frac{-1}{(t_2^*-t_1^*)}\left[\frac{(t_2^*-t_1^*)-\left(\frac{\alpha}{2}+\frac{1}{4}\right)}{(1+4\alpha)}+\frac{\frac{1}{12}+\frac{\alpha}{2}}{(1+4\alpha)^2}\right] + \sum_{n=1}^{\alpha}\left\{\frac{1}{4t_0^*}\left[e^{-\nu_n^2 t^*}-e^{-\nu_n^2(t^*-t_0^*)}\right] - \frac{1}{4(t_2^*-t_1^*)}\left[e^{-\nu_n^2(t^*-t_1^*)}\right]\right\} \times \frac{[J_0(\nu)-\alpha\nu J_1(\nu)]}{[(1+2\alpha)\nu_n J_1(\nu_n)+\alpha\nu_n^2 J_0(\nu_n)]} \tag{38}$$

(iv) After the piston has stopped ($t_2 \leqslant t \leqslant \infty$):

$$\frac{dP^*}{dx^*} = \sum_{n=1}^{\alpha}\left\{\frac{1}{4t_0^*}\left[e^{-\nu_n^2 t^*}-e^{-\nu_n^2(t^*-t_0^*)}\right] - \frac{1}{4(t_2^*-t_1^*)}\left[e^{-\nu_n^2(t^*-t_1^*)} - e^{-\nu_n^2(t^*-t_2^*)}\right]\right\} \frac{[J_0(\nu)-\alpha\nu J_1(\nu)]}{[(1+2\alpha)\nu_n J_1(\nu_n)+\alpha\nu_n^2 J_0(\nu_n)]} \tag{39}$$

Figure 2 shows the velocity profiles calculated for trapezoidal piston motion at Kn=0.1 for different nondimensional times ($t^*=t\nu/R^2$) with $t^*=0.0012$, $t^*=0.0305$, and $t^*=0.0366$. These values are chosen for the purpose of comparing the results obtained by this study with those obtained by Das and Arakeri [8]. When $\alpha=0$ (no-slip condition), the velocity profiles in Eqs. (33)–(36) are identical to Das and Arakeri's results. Figure 2 shows the phenomenon of slippage on the microtube wall during four different time periods. The development of velocity profiles is similar to that in Das and Arakeri's work; however, the change of velocity from the wall to centerline is smoother than that in Das and Arakeri's work as a result of the existence of slippage. Figure 3 shows the variation of nondimensional pressure gradients over different time pe-

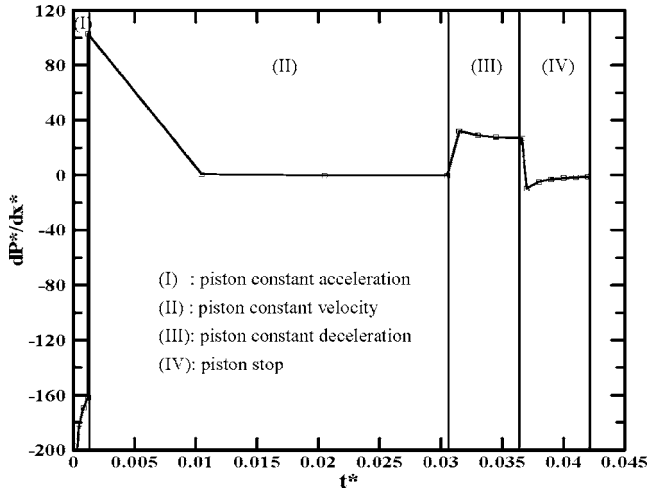

Fig. 3 The variation of pressure gradient with time for trapezoidal piston motion at Kn=0.1

riods at Kn=0.1. During the acceleration phase, the pressure gradient is negative as the pressure is higher at upstream due to the piston acceleration. This negative pressure gradient decreases with time as the induced flow resistance increased at downstream. When the piston comes to constant velocity phase, the pressure gradient changes drastically from negative to positive due to the disappearance of acceleration motion. With the time increased, the flow reaches the equilibrium state, which causes the pressure gradient to approach zero. As the piston starts to decelerate, the pressure gradient is increased as this sudden decrease in velocity, which causes the flow to lose its momentum. Finally, when the piston stops, the pressure gradient decays to zero. Figure 4 shows the effect of Kn various (Kn=0,0.05,0.1) values on the velocity profiles. During the four phases of piston motion, the larger Kn values flatten the velocity profile. The degree of flatness is proportional to the Kn value. Figure 5 shows the effect of different Kn values on the pressure gradient for trapezoidal piston motion. The analytical result demonstrates that a larger Kn value will increase the pressure gradient to move the fluid inside the microtube.

3.2 Second Example: Constant Acceleration Piston Motion. The piston motion of constant acceleration can be described by the following equation:

$$u_p(t) = a_p t = \left(\frac{U_p}{t_0}\right) t \tag{40}$$

where a_p is the constant acceleration, U_p is the final velocity after acceleration, and t_0 is the time period of acceleration.

The velocity profile can be found by setting $t=t_0$ of Eq. (33):

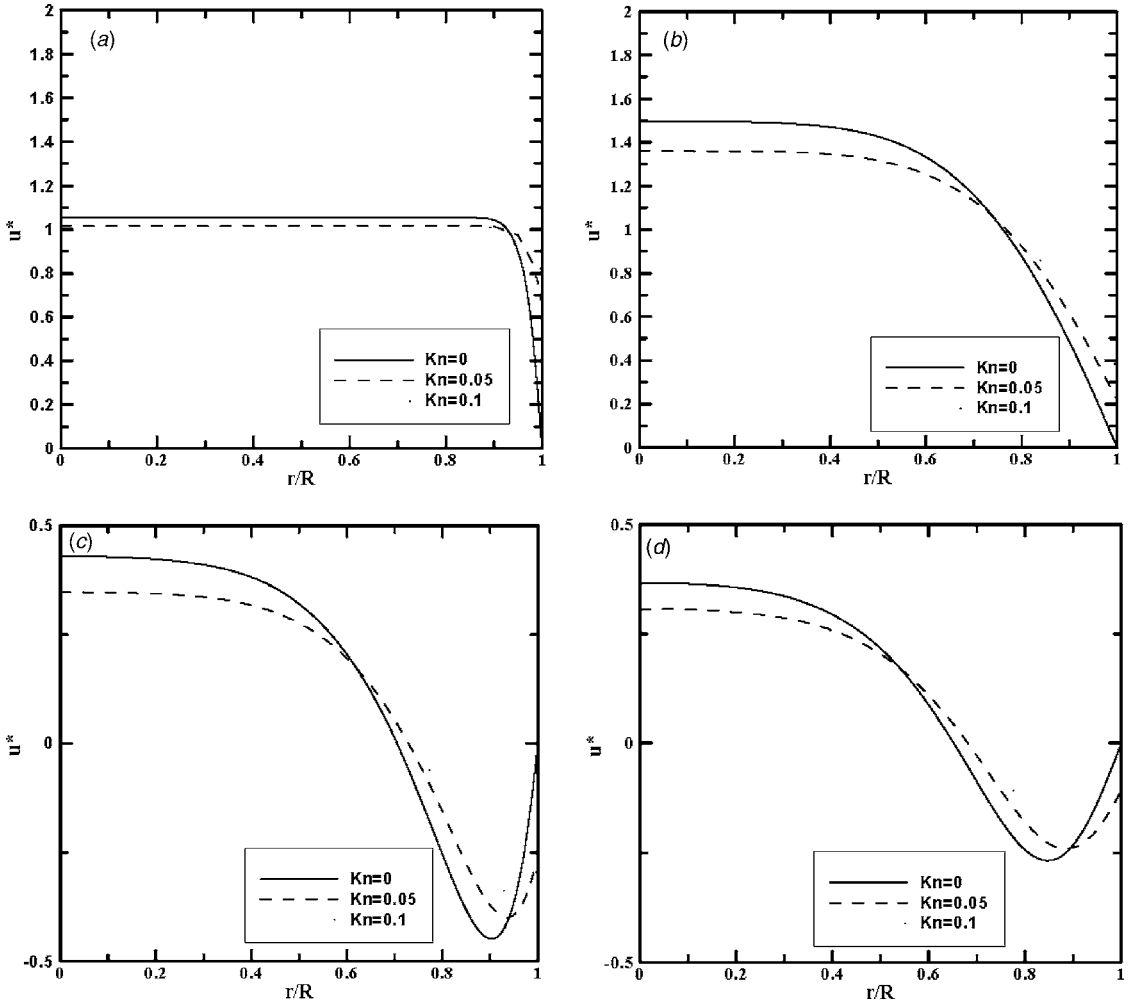

Fig. 4 The effect of different Kn values on the velocity profiles for trapezoidal piston motion: (*a*) $t^*=0.0012$, (*b*) $t^*=0.0305$, (*c*) $t^*=0.0366$, and (*d*) $t^*=0.0427$

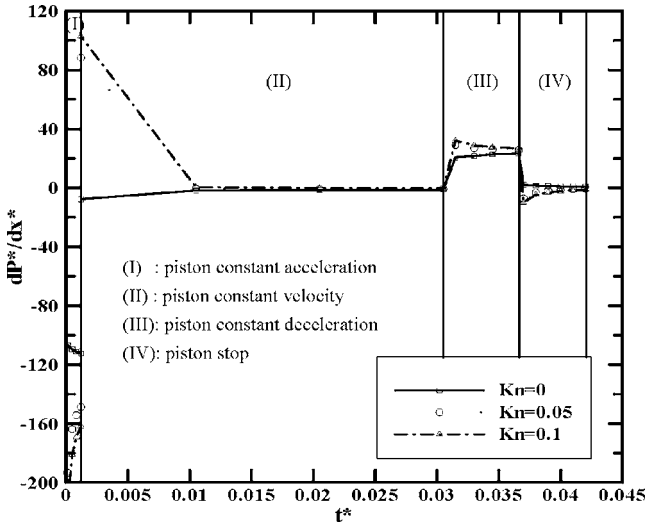

Fig. 5 The effect of different Kn values on the pressure gradient for trapezoidal piston motion

$$u^*(c,t^*) = \frac{1}{t^*}\left[\frac{(2t^*)(1-c^2+2\alpha)+\frac{1}{8}(1-c^4+16\alpha)}{1+4\alpha} - \frac{\frac{1}{6}(1-c^2+2\alpha)(1+6\alpha)}{(1+4\alpha)^2}\right] + \frac{2}{t^*}\sum_{n=1}^{\infty}\left\{e^{-\nu_n^2 t^*}\frac{[J_0(\nu_n)-\alpha\nu_n J_1(\nu_n)-J_0(c\nu_n)]}{[(1+2\alpha)\nu_n^3 J_1(\nu_n)+\alpha\nu_n^4 J_0(\nu_n)]}\right\} \tag{41}$$

and when the time approaches infinity, the pressure gradient is

$$\frac{dP^*}{dx^*} = -\frac{1}{(1+4\alpha)} - \frac{\left(\frac{\alpha}{2}+\frac{1}{4}\right)a_P R^2}{(1+4\alpha)\nu u_P} + \frac{\left(\frac{1}{12}+\frac{\alpha}{2}\right)a_P R^2}{(1+4\alpha)^2\nu u_P} - \frac{1}{t^*}\left[\frac{t^*+\frac{\alpha}{2}+\frac{1}{4}}{(1+4\alpha)} - \frac{\left(\frac{1}{12}+\frac{\alpha}{2}\right)}{(1+4\alpha)^2}\right] \tag{42}$$

3.3 Third Example: Suddenly Started Flow. For a suddenly started flow in a circular duct:

$$u_p = 0 \text{ for } t \leqslant 0$$

$$\text{and } = U_p \quad \text{for } t > 0 \tag{43}$$

where U_p is the constant velocity. In this case, the dimensionless velocity profile is:

$$u^*(c,t^*) = 2\frac{(1-c^2)+2\alpha}{1+4\alpha} - 2\sum_{n=1}^{\infty} e^{-\nu_n^2 t^*}\frac{[J_0(\nu_n)-\alpha\nu_n J_1(\nu_n)-J_0(c\nu_n)]}{[\nu_n J_1(\nu_n)+2\alpha\nu_n J_1(\nu_n)+\alpha\nu_n^2 J_0(\nu_n)]} \tag{44}$$

and the pressure gradient is:

$$\frac{dP^*}{dx^*} = -\frac{1}{(1+4\alpha)} - \frac{1}{4}\sum_{n=1}^{\infty} e^{-\nu_n^2 t^*}\frac{\nu_n[J_0(\nu)-\alpha\nu J_1(\nu)]}{[(1+2\alpha)J_1(\nu_n)+\alpha\nu_n J_0(\nu_n)]} \tag{45}$$

3.4 Fourth Example: Suddenly Blocked Fully Developed Flow. The exact solution of this problem was considered by Weinbaum and Parker [15] with a no-slip wall condition, under the initial condition, i.e., $u(r,0)=1-c^2$, and with the mass flow condition, i.e., $\int_0^R 2\pi r u dr = 0$. The resulting dimensionless velocity profile is:

$$u^*(c,t^*) = -2\sum_{n=1}^{\infty} e^{-\nu_n^2 t^*}\frac{J_0(\nu_n)-J_0(c\nu_n)}{\nu_n J_1(\nu_n)} \tag{46}$$

When wall-slip is considered, the solutions for the velocity profile and pressure gradient are

$$u^*(c,t^*) = -2\sum_{n=1}^{\infty} e^{-\nu_n^2 t^*}\frac{J_0(\nu_n)-\alpha\nu_n J_1(\nu_n)-J_0(c\nu_n)}{\nu_n J_1(\nu_n)+2\alpha\nu_n J_1(\nu_n)+\alpha\nu_n^2 J_0(\nu_n)} \tag{47}$$

$$\frac{dP^*}{dx^*} = \frac{1}{4t_0^*}\sum_{n=1}^{\infty} e^{-\nu_n^2 t^*}\frac{[J_0(\nu_n)-\alpha\nu J_1(\nu_n)]}{[(1+2\alpha)\nu_n J_1(\nu_n)+\alpha\nu_n^2 J_0(\nu_n)]} \tag{48}$$

4 Conclusion

The exact solutions of velocity profiles and pressure gradients with wall slippage phenomenon for unsteady flow through microtube subject to known inlet volume flow rate conditions are given. The analytical results are compared to those obtained by Das and Arakeri's work [8] for no-slip flow, and we found that the Kn value, which represents the degree of rarefaction, plays a significant role in influencing the velocity profile. The larger the Kn value, the less drastic is the change of velocity distribution. Due to wall slippage, the effort to move fluid at one cross section is larger than at a cross section without slippage. Therefore, the pressure gradient is also increased when the fluid has a high Kn value.

Acknowledgment

The authors would like to thank the reviewers, who gave us many valuable suggestions.

Nomenclature

A = $r/\sqrt{\nu}$
B = $R/\sqrt{\nu}$
c = r/R
C_1, C_2 = arbitrary coefficients
$F\nu$ = tangential momentum accommodation coefficient
$H(t)$ = Heaviside unit step function
I_0, I_1 = modified Bessel's function of the first kind of zeroth and first order
Kn = Knudsen number (Kn$\equiv\lambda/L$)
K_0, K_1 = modified Bessel's function of the second kind of zeroth and first order, respectively
L = characteristic length of the microtube
m = $\sqrt{s/\nu}$
P = static pressure
P^* = nondimensional pressure ($p^*=P/(8\eta U_p/R)$)
Q = inlet volume flow rate
R = radius of microtube
r, θ, x = cylindrical coordinates
s = parameter of the Laplace transform
t = time

t_0, t_1, t_2 = time period of acceleration, constant velocity, and deceleration, respectively.
u_r, u_θ, u = velocity components in the r-, θ-, and x-directions, respectively
u_{re} = tangential momentum of reflected molecules
u_i = tangential momentum of incoming molecules
u_p = average velocity over cross section
u^* = nondimensional average velocity over cross section
U_p = constant inlet piston velocity
U_w = tangential momentum of re-emitted molecules
$\mathbf{V}$ = velocity vector

Greek Symbols

α = nondimensional velocity slip coefficient
β_v = velocity slip parameter
λ = molecular mean free path
ϕ_p = assumed particular solution
ρ = fluid density
ν = kinematic viscosity
μ = dynamic viscosity

References

[1] Beskok, A., and Karniadakis, G. E., 1992, "Simulation of Slip-Flows in Complex Micro-Geometries," In ASME Proceedings Vol. DSC-40, pp. 355–470.
[2] Maxwell, J. C., 1890, "On the Condition to be Satisfied by a Gas at the Surface of a Solid Body," *The Scientific Papers of James Clerk Maxwell*, Vol. 2, Cambridge University Press, London, p. 704.
[3] Szymanski, P., 1932, "Some Exact Solution of the Hydrodynamic Equations of a Viscous Fluid in the Case of a Cylindrical Tube," J. Math. Pures Appl., **11**, pp. 67–107.
[4] Uchida, S., 1956, "The Pulsating Viscous Flow Superposed on the Steady Laminar Motion of Incompressible Fluids in a Circular Pipe," Z. Angew. Math. Phys., **7**, pp. 403–422.
[5] Rahaman, K. D., and Ramkissoon, H., 1995, "Unsteady Axial Viscoelastic Pipe Flows," J. Non-Newtonian Fluid Mech., **57**, pp. 27–38.
[6] Hayat, T., Siddiqui, A. M., and Asghar, S., 2001, "Some Simple Flows of an Oldroyd-B Fluid," Int. J. Eng. Sci., **39**, pp. 135–147.
[7] Pascal, J. P., and Pascal, H., 1995, "On Some Non-Linear Shear Flows of Non-Newtonian Fluids," Int. J. Non-Linear Mech., **30**, pp. 487–500.
[8] Das, D., and Arakeri, J. H., 2000, "Unsteady Laminar Duct Flow With a Given Volume Flow Rate," ASME J. Appl. Mech., **67**, pp. 274–281.
[9] Das, D., and Arakeri, J. H., 1998, "Transition of Unsteady Velocity Profiles With Reverse Flow," J. Fluid Mech., **374**, pp. 251–283.
[10] Chen, C. K., Chen, C. I., and Yang, Y. T., 2002, "Unsteady Unidirectional Flow of a Maxwell Fluid in a Circular Duct With Different Given Volume Flow Rate Conditions," Proc. Inst. Mech. Eng., Part C: J. Mech. Eng. Sci., **216**(5), pp. 583–590.
[11] Chen, C. I., Chen, C. K., and Yang, Y. T., 2004, "Unsteady Unidirectional Flow of an Oldroyd-B Fluid in a Circular Duct With Different Given Volume Flow Rate Conditions," Heat Mass Transfer, **40**, pp. 203–209.
[12] Chen, C.-I., 2004, "The Effect of Known Inlet Volume Flow Rate on Transient Flow Pattern of a Second Grade Fluid in a Tube," J. Chin. Soc. Mech. Eng., **25**(2), pp. 125–132.
[13] Chen, C. I., Chen, C. K., and Yang, Y. T., 2004, "Unsteady Unidirectional Flow of Voigt Fluid in the Circular Duct With Different Given Volume Flow Rate Conditions," Heat Mass Transfer, **41**(1), pp. 37–43.
[14] Karnidakis, G. E., and Beskok, A., 2002, *Micro Flow*, Springer, New York.
[15] Weinbaum, S., and Parker, K., 1975, "The Laminar Decay of Suddenly Blocked Channel and Pipe Flows," J. Fluid Mech., **69**, pp. 729–752.

A Device for Mechanically Folding Yarns and Woven Fabrics of Ballistic Fibers

J. H. Kim
Polymers Division,
Characterization and Methods Development Group,
National Institute of Standards and Technology,
100 Bureau Drive Stop 8541,
Gaithersburg, MD 20899-8541

N. Brandenburg
Fabrication Technology Division, Shops,
National Institute of Standards and Technology,
100 Bureau Drive Stop 8250,
Gaithersburg, MD 20899-8250

W. McDonough

W. Blair

G. A. Holmes[1]

Polymers Division,
Characterization and Methods Development Group,
National Institute of Standards and Technology,
100 Bureau Drive Stop 8541,
Gaithersburg, MD 20899-8541

A device was designed and built that attaches to servohydraulic machines that typically perform material fatigue testing. The device was designed to systematically fold woven fabric and yarns of ballistic fibers to assess the impact of mechanical folding, such as may occur during use, on ballistic fiber properties. Initial tests indicate that the device repeatedly folds a piece of woven fabric at the same location. However, when the device is in the open position, a consistent 1 cm *movement of the fabric was observed. A slight modification of the device is required to eliminate this movement. After cycling a piece of woven poly(benzoxazole) (PBO) fabric for 5500 cycles, an 18% reduction in the ultimate tensile strength and strain to failure of the PBO fibers was observed. Research is continuing to determine a relevant and optimized testing protocol.* [DOI: 10.1115/1.2755131]

1 Introduction

It has been suggested that folding of the ballistic fibers that comprise soft body armor may also be a factor in the performance deterioration observed worn in soft body armor. In an attempt to quantify the impact of this mechanism, a device was designed and built to simulate the folding that may occur to the ballistic fibers while the vest is in use. This effort is part of a research program being conducted by the National Institute of Standards and Technology Office of Law Enforcement and Standards (NIST-OLES) under the auspices of the National Institute of Justice (NIJ). A key objective of this research program is to develop relevant and nondestructive test procedures that link personal body-armor performance to fundamental and measurable properties of the materials that are used in its construction. One long-term goal of the folding research on ballistic fibers is the development of a controlled procedure for simulating the folding that occurs in an actual vest during various stages of its proposed lifespan. This type of procedure would then allow ballistic fiber tests to be performed on body armor whose wear and deformation history are known. Such tests on controlled materials should help to establish the link between use and life expectancy of the body armor.

The device described in this report was designed to fold individual yarns and single and multiple layers of woven fabrics of ballistic fibers by using servohydraulic testing equipment that is often available in laboratories that perform fatigue testing of materials. Since the concept is new, a major design goal was to incorporate sufficient flexibility into the design to allow most of the deformation parameter space that occurs during actual use to be systematically probed, with the end result being an optimized and relevant deformation protocol. Furthermore, the use of off-the-shelf testing equipment, such as the servohydraulic testing equipment, should facilitate peer review and use by others.

2 Motivation: The Single-Fold Test

The research of Cunniff and Auerbach [1] has shown that, within the elastic limit, a correlation exists between the ballistic fiber properties and ballistic performance if the energy absorbed by the ballistic fibers is decoupled from the absorbed energy associated with the vest construction, i.e., the areal density. That is, the material properties of the fiber are decoupled from the vest construction parameters known to depend on a manufacturer's vest design. From their research, the correlation between ballistic performance and the mechanical properties of the active fiber is quantified by the $(U^*)^{1/3}$ parameter shown in Eq. (1). Therefore, $(U^*)^{1/3}$ is a theoretical parameter that estimates the maximum velocity of a bullet that the fibers of a vest can stop and is independent of vest construction. This equation has also been derived theoretically by Phoenix and Porwal [2,3].

$$[U^*]^{1/3} = \left[\frac{\sigma_f^u \varepsilon_f^u}{2\rho} \sqrt{\frac{E_{1f}}{\rho}} \right]^{1/3} \tag{1}$$

where σ_f^u is the fiber ultimate axial tensile strength (UTS), ε_f^u is the fiber ultimate tensile strain, ρ is the fiber density, and E_{1f} is the longitudinal linear elastic fiber modulus.

In a previous publication, it was shown that a *modified* single fiber test (m-SFT) [4], based on ASTM C1557-03 [5], could be used to obtain the fiber properties for Eq. (1). In another report [6], it was shown that changes in ballistic performance could be detected in a worn vest that was presumed to arise from ultraviolet (UV) exposure and hydrolytic action. Since it is probable that mechanically induced degradation may also induce subtle changes in ballistic fiber properties, 50 fibers were extracted from a single yarn of virgin poly(benzoxazole) (PBO) fibers and placed uniformly across two pieces of poster board (see Fig. 1). The two adjoined poster boards were then folded together, and 11.8 kg bricks were placed on the folded poster boards and left overnight to simulate a worst-case scenario. The visible damage induced by the single fold is shown in Fig. 2. To ascertain the effect of this damage on the mechanical properties of the fiber, 50 folded and 50 nonfolded virgin PBO fibers were tested randomly using the m-SFT.

Fiber diameters were measured on each specimen by using an optical micrometer (Excel Technologies Inc., Model VIA-100[2])

[1]Corresponding author. This paper is declared a work of the U.S. Government and is not subject to copyright protection in the United States.

Contributed by the Applied Mechanics Division of ASME for publication in the JOURNAL OF APPLIED MECHANICS. Manuscript received September 29, 2006; final manuscript received May 14, 2007; published online January 16, 2008. Review conducted by Thomas W. Shield.

[2]Certain commercial materials and equipment are identified in this paper to specify adequately the experimental procedure. In no case does such identification imply recommendation or endorsement by the National Institute of Standards and Technology, nor does it imply necessarily that the product is the best available for the purpose.

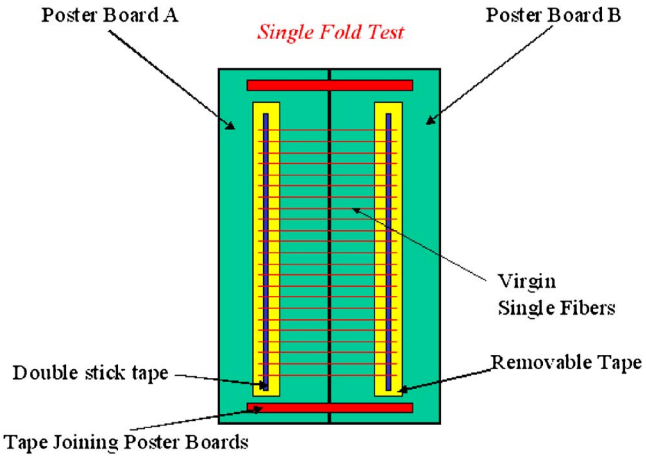

Fig. 1 Pictorial representation of single fibers stretched across two adjoining pieces of poster board

attached to a Nikon Optiphot-POL microscope equipped with a video camera (Optronix LX-450 RGB Remote Head microscope camera). The fiber image was viewed on a Sony PVM-1344Q color video monitor. All fiber samples had diameter measurements made at five equally spaced locations along the 6 cm gage length.

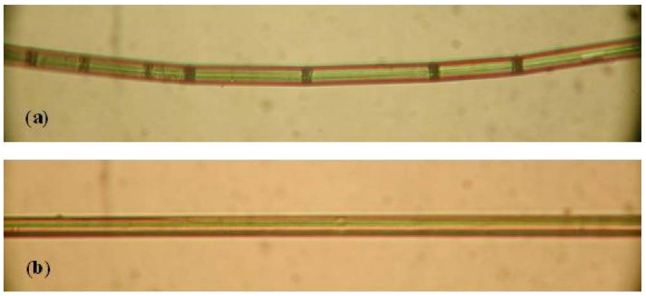

Fig. 2 (*a*) Damage induced by single fold of PBO fiber, (*b*) nonfolded virgin PBO fiber

The five individual diameter measurements were averaged to give an average diameter value for each fiber sample. The average fiber diameters from the folded specimens were found to be (12.6 ± 0.5) μm, and those of the nonfolded specimens were found to be (12.5 ± 0.5) μm. The folded and nonfolded populations of average fiber diameter values were indistinguishable at the 95% confidence level ($p=0.125$).

From the m-SFT, the strain-to-failure and ultimate tensile strength of the folded virgin PBO fiber was reduced by $\sim$10% relative to the nonfolded fibers ($p=0.011$ and 0.004, respectively). Histograms depicting the shift in the distributions are shown in Fig. 3. In contrast to previous results on worn vests, the modulus of the virgin fiber was also found to decrease about 15% from (164 ± 9) GPa to (156 ± 12) GPa. These results indicate that the property changes in folding should be quantifiable and that the m-SFT is sensitive enough to observe these changes.

2.1 Device Design and Operation. The design of the experimental device was motivated by the desire to use the controlled fatigue testing features inherent in most servohydraulic test machines. To minimize damage to the servohydraulic machine by the device, it was designed to fit on a 250 kN (55 kip) Model 810.25 MTS machine equipped with a 158.5 mm dia piston rod. To convert the precise linear motion of the servohydraulic machine to precise rotational motion, a bracket was fitted to the piston rod that containing a spur gear and rack as shown in Fig. 4. The 28 teeth spur gear was a 16 pitch −12.70 mm face width with the following specifications: (i) pitch diameter: 44.45 mm, (ii) hub diameter: 38.10 mm, (iii) outer diameter: 47.75 mm, and (iv) overall width (including face width): 25.40 mm. This spur gear required a bore size between 12.70 mm and 22.23 mm.

To effect the folding of the ballistic fiber material, a two-piece clamshell design is employed (see Fig. 5). To minimize mass, most of the device is constructed using aluminum, except where otherwise specified. The lower plate is connected to a platform that is attached to the servohydraulic machine through the column mounting brackets. Interchangeable folding rods were constructed out of 0.635 cm dia and 1.27 cm dia stainless steel and attached to this plate. The upper plate is attached to a 1.27 cm^2 stainless steel rod that is turned at each end to 1.27 cm dia to conform to the required bore size of the spur gear. The top plate is attached to the platform using two base-mount ball bearings that accommodate a

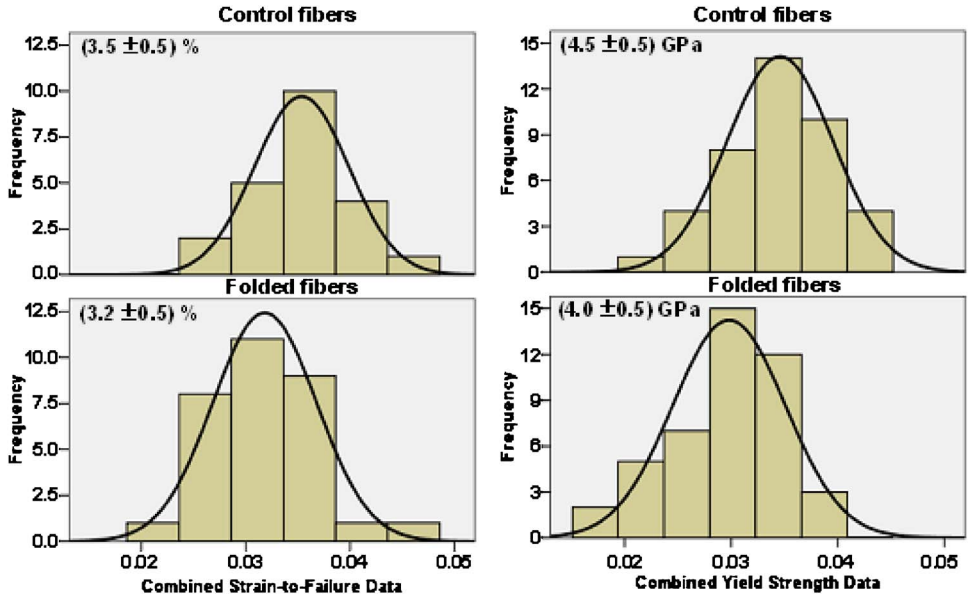

Fig. 3 Histograms showing the change in strain-to-failure and ultimate tensile strength of virgin PBO fibers caused by the single-fold test

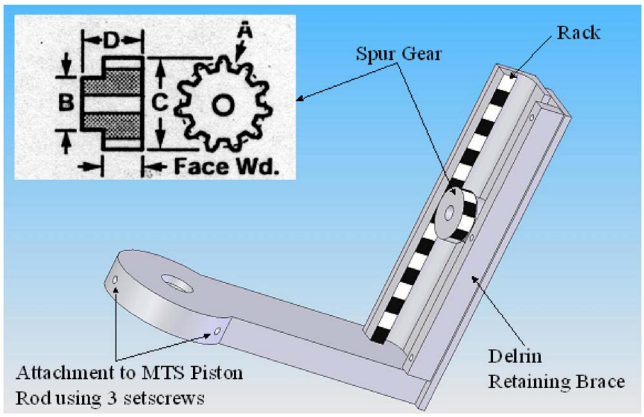

Fig. 4 Piston rod bracket for converting linear motion of MTS 810.25 servohydraulic machine into rotational motion. Inset shows schematics of spur gear with detail specifications given in the text. Delrin is polyoxymethylene.

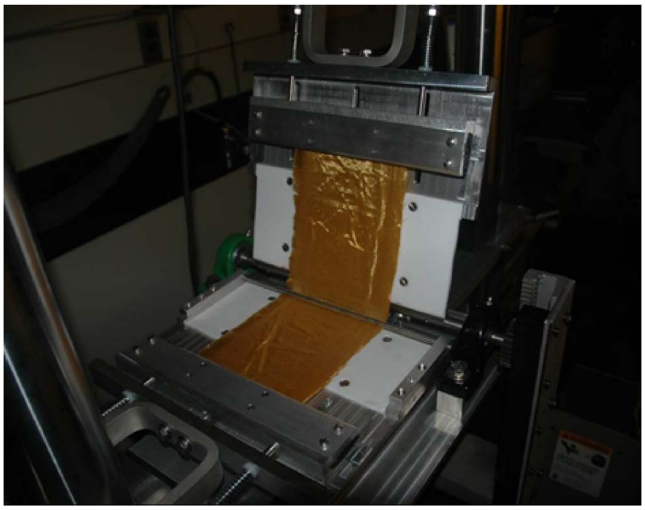

Fig. 6 Folding device with fabric clamped in the sliding brackets and around the folding rod

shaft diameter of 1.27 cm.

Each plate is equipped with teflon sheets to minimize friction between the ballistic material and the plate surface, and in order to hold the fabric or yarn in place, each plate is equipped with a sliding bracket. Each sliding bracket is held in place by two 0.635 cm dia stainless steel rods that attaches to constant force springs (rods not shown in Fig. 5). The constant force springs were rated for 40,000 cycles and are used to maintain constant tension on the woven fabric or yarn.

2.2 m-SFT. This test procedure was described in a previous publication [4] and is repeated here for the reader's convenience. Fifty individual fibers, each ~30–40 cm long, were obtained from a harvested yarn and mounted onto a paper tensile testing template. The template, printed on typical 21.6 cm by 27.9 cm printer paper that contains 1 cm major graduations and 1 mm minor graduations, held two or three rows of five fibers. Therefore, one fiber strand generated two or three test samples, each with a 6 cm gage length. Individual fibers were initially attached temporarily to the paper template outside the region of the fiber that would undergo diameter measurement and tensile testing with double-sided tape (3M Stationary Products Division, St. Paul, MN). Prior to epoxy gluing, small strips (approximately 1.2 cm $\times$ 0.2 cm) of silver reflective tape (United Calibration Corp.) were applied to the template at the top and bottom of the gage section of each fiber sample. The reflective tape allows elongation measurements to be made by the laser extensometer (United Calibration Corp. Model EXT 62 LOE) while the sample is undergoing tensile testing. The fibers were then permanently bonded to the template by epoxy adhesive (Hardman Water-Clear Epoxy, Double/Bubble Green Package No. 04004). The epoxy adhesive was allowed to cover up to 0.1 cm thickness of the reflective tape to avoid the slip between fiber, paper template, and reflective tape.

The five individual diameter measurements were averaged for each fiber sample. Between steps in the mounting, diameter measuring, and tensile testing processes, fiber samples were stored in the dark, in wooden map cabinets.

Although the compliance method in ASTM C1557-03 has been found to be satisfactory for quantifying the properties of new fibers, the use of noncontact extensometers to detect gage section elongation directly is often suggested if a more accurate measure of strain is required, since specimen fragility prevents the use of normal strain-sensing devices, such as strain gages or mechanical extensometers. Consistent with this recommendation, a United Calibration Corporation Model EXT-62-LOE laser extensometer was used.

An initial gage length of 5.1 cm or greater is required for optimum performance of the laser extensometer. Furthermore, because fiber strength is typically gage-length dependent, a specimen length reflective of the amount of material that may be deformed during ballistic action is probably necessary. Therefore, a gage length of 6.0 cm was chosen. The laser extensometer was calibrated using an Epsilon extensometer calibrator Model 3590C that has 10 cm of travel. The standard uncertainty in the strain at 6.1 cm associated with this measurement is 0.0001. The standard uncertainty in the load cell at 100 g is 0.001 g.

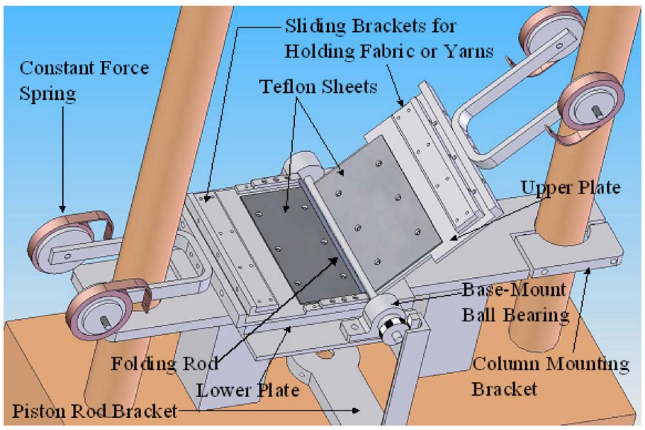

Fig. 5 Basic design of folding device attached to servohydraulic machine. Constant force springs attach to sliding brackets using 0.635 cm dia stainless steel rods (not shown). Note: Delrin brace on piston rod bracket removed to better show clamshell design.

3 Results and Discussions

To test the effectiveness of the device, a piece of woven fabric (12.7 cm $\times$ 38.1 cm) was attached to each sliding bracket and under the 0.635 cm folding rod (see Figs. 5 and 6). The device was rotated through 90 deg ($\pi/2$ rad) as shown in Fig. 7 and held at each end point for ~15 s. The movement of the linear actuator was controlled at 25.4 mm/s. Manual markings were made in permanent ink on the edge of the sample to monitor movement of the folded region as the specimen was repeatedly folded for approximately 5500 cycles. The folded region location remained constant throughout the test. However, in the open position

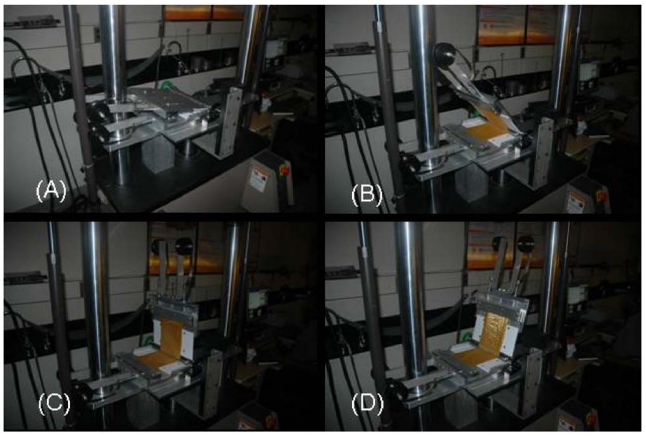

Fig. 7 Collage showing the fabric as it goes from a closed position (A) to the fully open position (D)

(90 deg), the fabric moved a consistent 1 cm distance away from the folded region. Analysis of the motion of the device indicates that immobilizing the sliding bracket on the lower plate and adjusting the travel distance on the sliding bracket of the upper plate can eliminate this movement.

Under the folding conditions with both brackets sliding, the strain-to-failure and ultimate tensile strength as measured by the m-SFT decreased by ~18% when subject to 5500 cycles (see Table 1). The modulus and fiber diameter were unchanged.

4 Conclusions

The device as designed can consistently fold woven fabrics and yarns in a manner useful for test measurements. After the cyclic folding of the woven fabric using this device, the tensile strain and strength of the fibers collected from the folded woven fabric showed an 18% reduction compared to the nonfolded fibers. Although slight modifications are needed to control the damage that may occur to the fibers due to frictional sliding on the folding rod, the folding device introduces a controlled damage region in the fiber that can be quantitatively assessed by the modified single fiber tensile test. More testing is planned to determine the optimum and relevant testing conditions required to simulate the impact of mechanical folding over a period of 5–10 years of use. Further tests are underway to quantify the mechanism of mechanical degradation.

Table 1 Effect of repeated folding (5500 cycles) on woven fabrics composted of poly(benzoxazole) fibers

Fiber properties	Control (NF_14)	Folded (FF_15)	ANOVA statistics for 95% confidence level	
			F	F_{crit}
Fiber diameter (μm)	13.14±0.67	13.24±0.27	0.276	4.210
Modulus (GPa)	145±11	144±10	0.122	4.210
Strain-to-failure	3.14±0.26	2.59±0.54	12.364	4.210
UTS (GPa)	3.54±0.23	290±0.49	19.884	4.210

References

[1] Cunniff, P. M., and Auerbach, M. A., 2002, "High Performance "M5" Fiber for Ballistics/Structural Composites," 23rd Army Science Conference, Orlando, AO-04

[2] Phoenix, S. L., and Porwal, P. K., 2003, A New Membrane Model for the Ballistic Impact Response and V-50 Performance of Multi-Ply Fibrous Systems," Int. J. Solids Struct., **40**, pp. 6723–6765.

[3] Phoenix, S. L., and Porwal, P. K., 2005, "Modeling System Effects in Ballistic Impact Into Multi-Layered Fibrous Materials for Soft Body Armor," Int. J. Fract., **135**, (1-4), pp. 217–249.

[4] Kim, J. H., McDonough, W. G., Blair, W., and Holmes, G. A., 2007, "The Single Fiber Test: A Methodology for Monitoring Ballistic Performance," Journal of Applied Polymer Science (accepted).

[5] ASTM D 3379-75, 1982, "Standard test method for tensile strength and young's modulus for high-modulus single-filament materials," ASTM, Philadelphia.

[6] Holmes, G. A., Rice, K., and Snyder, C. R., 2006, "Ballistic Fibers: A Review of the Thermal, Ultraviolet and Hydrolytic Stability of the Benzoxazole Ring Structure," J. Mater. Sci., **41**, pp. 4105–4116.